Doctoral Thesis

Quantum-to-continuum mechanics in 2D: from graphene to concrete slabs

submitted in satisfaction of the requirements for the degree of
Doctor of Science in Civil Engineering
of the TU Wien, Faculty of Civil Engineering

Dissertation

Mehrskalen-2D-Mechanik: von Quanten zu Festkörpern, von Graphen zu Betonplatten

ausgeführt zum Zwecke der Erlangung des akademischen Grades eines
Doktors der technischen Wissenschaften
eingereicht an der Technischen Universität Wien, Fakultät für Bauingenieurwesen

von

Dipl.-Ing. **Raphael Höller**, BSc
Matr.Nr.: 1028779

Betreuer: Univ.Prof. Dipl.-Ing. Dr.techn. **Christian Hellmich**
Institut für Mechanik der Werkstoffe und Strukturen
Technische Universität Wien
Karlsplatz 13/202, 1040 Wien, Österreich

Betreuer: Assoc.Prof. Dipl.-Ing. Dr.techn. **Florian Libisch**
Institut für Theoretische Physik
Technische Universität Wien
Wiedner Haupstrasse 8-10/136, 1040 Wien, Österreich

Gutachter: Univ.Prof. Dipl.-Ing. Dr.techn. **Andreas Kolbitsch**
Institut für Hochbau, Baudynamik und Gebäudetechnik
Technische Universität Wien
Karlsplatz 13/208-02, 1040 Wien, Österreich

Gutachter: Ao.Univ.Prof. Dr. **Christian Teichert**
Institut für Physik
Montanuniversität Leoben
Franz-Josef-Straße 18, 8700 Leoben, Österreich

Wien, im Juni 2020

Danksagung

Die vorliegende Arbeit ist am Institut für Mechanik der Werkstoffe und Strukturen (IMWS) sowie im Rahmen des TU-D Doktoratskollegs an der Technischen Universität Wien entstanden. In diesem Zusammenhang danke ich der TU Wien für die Ermöglichung der Arbeit und für die finanzielle Unterstützung.

An dieser Stelle möchte ich mich bei meinem Hauptbetreuer, Herrn *Univ.Prof. Dipl.-Ing. Dr.techn. Christian Hellmich*, Vorstand des IMWS, herzlich bedanken. Durch seine langjährige Erfahrung in der Wissenschaft und sein großes Fachwissen im Bereich der Kontinuumsmechanik, konnte er mich stets in die richtige Bahn lenken und verhalf mir das Anfertigen von wissenschaftlichen Berichten zu erlernen. Die nötige Freiheit, die er mir bei den behandelten Themenstellungen entgegengebracht hat, habe ich sehr geschätzt. Seine motivierenden Worte haben stets dazu geführt, Lösungsansätze recheneffizient und am neuesten Stand der Technik zu gestalten.

Ein großer Dank gilt auch meinem Co-Betreuer, Herrn *Assoc.Prof. Dipl.-Ing. Dr.techn. Florian Libisch*, Leiter des TU-D Doktoratskollegs, ein Zusammenschluss von Doktoratsstudierenden aus den Fachbereichen Physik, Chemie, Elektrotechnik, Mathematik, und Bauingenieurwesen. Seine Expertise im Bereich der theoretischen Physik konnte mir vor allem bei der quantenmechanischen Berechnung von Graphenmembranen sehr weiterhelfen. Somit konnte ich notwendige Details der breitgefächerten Physik auf meine Forschungsaufgaben anwenden. Für die wertvollen und äußerst effizienten Besprechungen bin ich sehr dankbar.

Ein besonderer Dank gilt Herrn *Univ.Prof. Dipl.-Ing. Dr.techn. Bernhard Pichler*, Betreuer meiner Bachelorarbeit. Er hat mir in weiterer Folge die Erstellung meiner Diplomarbeit bei Prof. Hellmich ermöglicht, welche schließlich zur Anstellung als Dissertant geführt hat. Ohne ihn wäre die vorliegende Arbeit am IMWS also nicht möglich gewesen. Auch im Rahmen der Dissertation danke ich für wertvolle Besprechungen und für seine Kooperation bei Strukturanalysen von Betonplatten.

Herrn *Ass.Prof. Dipl.-Ing. Dr.techn. Mehdi Aminbaghai* sei an dieser Stelle für die exzellente Zusammenarbeit und für die gemeinsam erarbeiteten Lösungsansätze im Forschungsbereich der elastisch gebetteten Platten gedankt. Von seiner unermüdlichen Hilfsbereitschaft und seinen versierten Programmierkenntnissen konnte ich sehr profitieren.

Meinem Festigkeitslehre-Team, *Dipl.-Ing. Dr.techn. Johannes Kalliauer, Dipl.-Ing. Valentina Kumbolder*, und *Dipl.-Ing. Robert Plachy*, danke ich für die hervorragende Zusammenarbeit im Zuge der Organisation und Abwicklung unserer betreuten Lehrveranstaltungen am IMWS.

Natürlich danke ich auch meiner Familie und Lebensgefährtin für die Ermöglichung meines Studiums und für die Unterstützung während der dreijährigen Dissertation. In schwierigen Phasen habe ich stets Rückhalt und Motivation erhalten, um die vielseitigen Forschungsaufgaben zu bewältigen.

Kurzfassung

2D Mechanik von dünnen Strukturelementen in Kombination mit Fourierreihen-basierten Verschiebungsansätzen dient als eine effiziente Art und Weise zur Bestimmung von Deformations- und Spannungsgrößen. Neben der Recheneffizienz infolge der gewählten kinematischen Annahmen bezüglich des Strukturelements, werden energetisch konsistente Kontinuummodelle für thermoelastische dünne Platten und Membrane für beliebige Randbedingungen hergeleitet. In diesem Zusammenhang wird das Prinzip der virtuellen Leistungen angewendet, um die strikte Unterscheidung zwischen internen und externen Kräften sicherzustellen. Dieses vielseitige Prinzip liefert weiters ein Lösungsverfahren in Form von algebraischen Gleichungssystemen zur Bestimmung der Fourierkoeffizienten der obengenannten Reihendarstellung der gesuchten Verschiebungen.

In der vorliegenden Arbeit wird die semianalytische Methode auf Strukturprobleme von dünnen elastisch gebetteten Betonplatten sowie von freistehenden Graphenmembranen unter großen Deformationen angewendet. Die Modellierung der Betonplatten erfolgt durch Kirchhoffsche Platten auf elastischer Winkler Bettung mit spannungsfreien Randbedingungen. Dabei wird von klassischen linear-thermoelastischen Spannungs-Dehungsbeziehungen zur Beschreibung des isotropen Materialverhalten ausgegangen. Das konstitutive Materialverhalten von Graphen hingegen ist noch in der Anfangsphase der Entwicklung. Hierbei handelt es sich um das erste tatsächliche 2D Material mit unübertroffenen mechanischen Eigenschaften, bestehend aus Kohlenstoffatomen, die in einem einschichtigen hexagonalen Gitter angeordnet sind. Als Lösungsansatz für diese Situation wird eine invariante hyperelastische Formulierung des vollständig nichtlinearen anisotropen Materialverhalten entwickelt. Dieses verfeinerte Model basiert auf quantenmechanischen Energiesimulationen von Zehntausenden beliebigen biaxialen Verzerrungszuständen, bis zu den elastischen Stabilitätsgrenzen von Graphen.

Solch dünne Strukturelemente werden mehreren Typen von vertikalen mechanischen Kräften sowie Temperaturgradienten über die Elementdicke unterworfen. Die temperaturinduzierten Belastungen werden durch Simulationen von extremen Wetterverhältnissen motiviert, nämlich Hagelschauer nach starker Sonneneinstrahlung auf Straßen oder Flugplätzen. Die numerischen Ergebnisse der bereitgestellten Anwendungen werden durch Vergleich mit Daten von experimentellen Messungen und Finite Elemente Analysen validiert. In Bezug auf letztere kann das reihenbasierte Lösungsverfahren die Rechenzeit um einen Faktor von bis zu vierzig verkürzen.

Abstract

2D mechanics of thin structural elements in combination with Fourier series-based approximative displacement fields serves as an efficient way to determine deformation and stress measures. Along with computational efficiency due to the kinematic assumptions regarding the structural element, energetically consistent continuum models for thermoelastic thin plates and membranes with arbitrary boundary conditions are derived. In this context, the Principle of Virtual Power is applied in order to ensure a rigorous discrimination of internal and external forces. This versatile principle further yields a solution procedure in form of an algebraic system of equations for the Fourier coefficients of the aforementioned series representation of the sought displacements.

In the present thesis, the semi-analytical method is applied to structural problems of thin elastically supported concrete slabs and to suspended graphene membranes undergoing large deformations. The concrete slabs are modeled as Kirchhoff plates resting on elastic Winkler foundations with stress-free boundary conditions, where classical linear thermoelastic stress-strain relations are used for describing the constitutive isotropic material behavior. For graphene, the first true 2D material with unsurpassed mechanical properties, consisting of carbon atoms arranged in a monolayer hexagonal lattice, the constitutive material behavior is still in its infancy. As a remedy to this situation, an invariant hyperelastic formulation of the fully nonlinear anisotropic material behavior is developed. This refined model is based on quantum mechanics-rooted energy simulations associated with tens of thousands of arbitrary biaxial strain states up to graphene's elastic stability limits.

Such thin structural elements are subjected to several types of vertical mechanical forces and to temperature gradients along the element's thickness. The temperature-induced loads are motivated to simulate extreme weather events, namely hail showers following significant solar heating, appearing on roads and airfields for example. The numerical results of the provided applications are validated through comparison with predictions obtained from experimental measurements and Finite Element analysis. With respect to the latter, the series-based solution procedure may reduce computer time by a factor of almost forty.

Contents

4   Concrete pavements subjected to hail showers: A semi-analytical thermoelastic multiscale analysis   **100**

5   Energy landscapes of graphene under general deformations: DFT-to-hyperelasticity upscaling   **133**

List of Figures

List of Tables

Chapter 1

Introduction

Two-dimensional (2D) structural mechanics is an eminent modeling-tool for many engineering applications, including the design of thin plates, shells, walls, and membranes in building and bridge construction [Deplazes, 2008; Chen and Duan, 2014; Pech et al., 2018], or of thin concrete slabs resting on elastic foundations for roads, airfields, and floor screeds [Teller and Sutherland, 1943; Bowles, 1997; Delatte, 2008]. The shape of such *thin structural elements* (surface structures) is characterized by one dimension (thickness t), measured normal to the *midplane*, which is significantly smaller than all other in-plane dimensions of the element (height h, side lengths $a \times b$, radius R, etc.). The latter is typically at least ten times larger than the dimension of the thickness, see Fig. 1.1. The midplane represents the symmetry plane of the top- and bottom
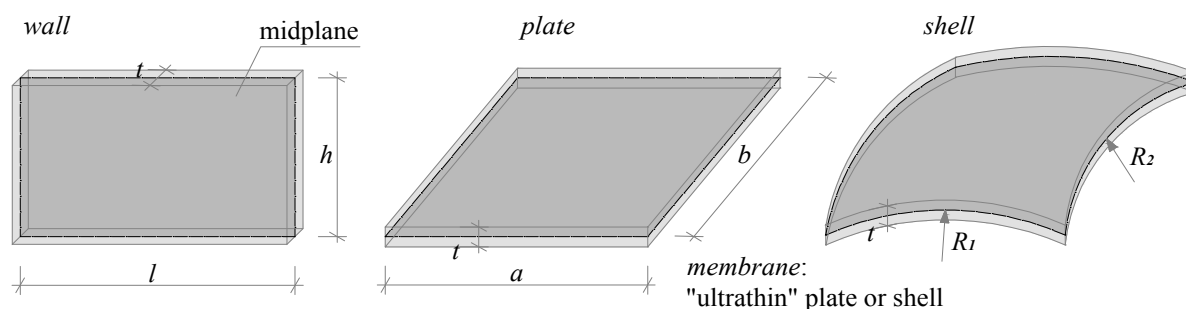
Fig. 1.1: Thin structural elements characterized by a 2D midplane and by a corresponding thickness t of the surface structure: walls, plates, shells, and membranes.

surface of a thin structural element, also called "neutral plane" in the case of pure bending. While plates and walls have a flat midplane in the undeformed reference configuration, a thin structural element with a curved midplane before deformation processes is called shell. Membranes, namely structural elements even thinner than plates and shells, can have both a flat or a curved midplane. When taking advantage of the *smallness of the thickness*, it is not mandatory to use computation-intensive three-dimensional (3D) elasticity models for calculating the six independent strain and stress components acting throughout all points of the continuum [Salençon, 2001], as provided by the 3D Finite Element method [Bathe and Wilson, 1976; Zienkiewicz and Taylor, 2000] or by the theory of layered elastic halfspaces [Pan, 1989; Höller, 2017]. Thus, a much more *efficient* way to determine stress- and strain distributions in such plane continua is that of *2D structural mechanics*: In this concept, the possibilities of deformations of the body are constraint to its essential forms of deformation, but remain geometric compatible and being sufficient to satisfy the equilibrium of internal and external powers. Depending on the applied kinematic constraint, so-called *2D theories for plates, shells, and membranes* [Timoshenko and Woinowsky-Krieger, 1959; Gould, 1988; Ventsel and Krauthammer, 2001; Reddy, 2007] are obtained.

1.1 Kinematics and stress resultants of thin plates – Winkler foundation model

Focusing on thin plates, the deformations standardly arise from mechanical and thermal loads causing bending and stretching of the plate. The magnitude of the deformations depends on the stiffnesses of the plate, namely the stretching rigidity and the flexural rigidity, as well as on the dimensions and boundary conditions of the plate. The corresponding displacement field vector **u** for a thin plate is based on the *Kirchhoff-Love hypothesis*[1], built on the assumption that straight lines (generators) orthogonal to the undeformed midplane of the plate remain, throughout the deformation process, *straight*, constant in length (*rigid body motion*), and *orthogonal* to the (then deformed) midplane of the plate [Love, 1888], see Fig. 1.2. This hypothesis for thin plates forms
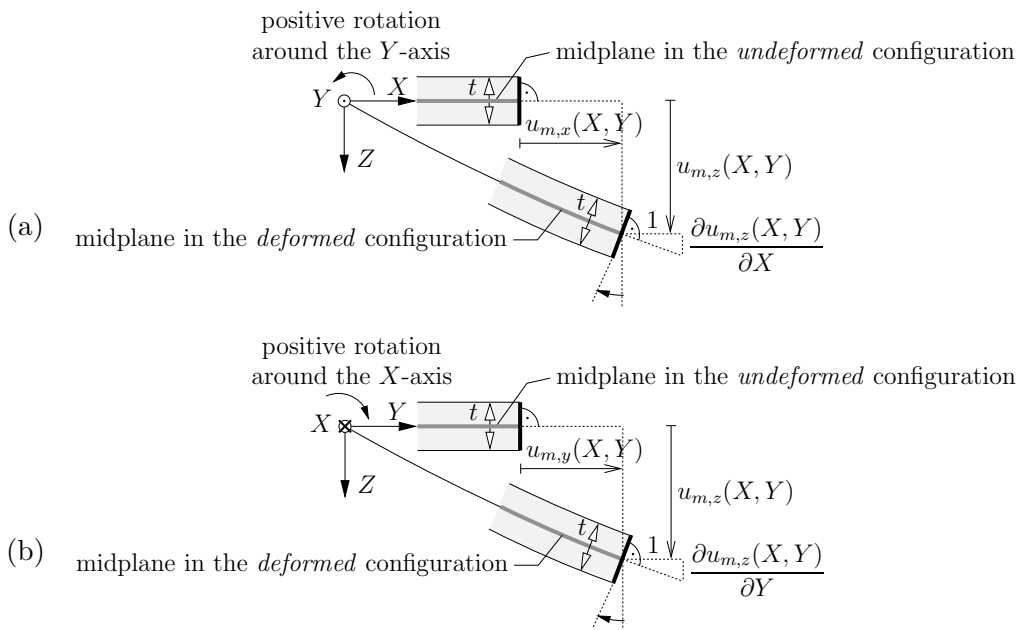
Fig. 1.2: Sideviews of the midplane and a corresponding plate generator in the undeformed and deformed configuration, according to the Kirchhoff-Love hypothesis [Love, 1888] for the kimematics of thin plates (1.1): (a) X, Z-plane and (b) Y, Z-plane.

the basis for classical plate theories, described by a displacement field of the format[2]

$$\mathbf{u}(\mathbf{X}) = \left[u_{m,x}(X,Y) - \frac{\partial u_{m,z}(X,Y)}{\partial X} Z \right] \mathbf{e}_x + \left[u_{m,y}(X,Y) - \frac{\partial u_{m,z}(X,Y)}{\partial Y} Z \right] \mathbf{e}_y + u_{m,z}(X,Y) \mathbf{e}_z .$$
(1.1)

In Eq. (1.1), $u_{m,x}$, $u_{m,y}$, and $u_{m,z}$ are the displacement components of $\mathbf{u}_m$ along the directions of the coordinates X, Y, and Z, respectively, with $\mathbf{u}_m$ being the displacement field of the midplane of the plate. The corresponding deflection gradients of the midplane, $\partial u_{m,z}/\partial X$ and $\partial u_{m,z}/\partial Y$, represent the rotations of the generators around the Y-axis and X-axis, respectively. The hypothesis concerning rigid body motions of the generators (i.e. the thickness of the plate

---

[1] The theory was developed by the physicist Gustav Robert Kirchhoff (1824-1887) and the mathematician Augustus Edward Hough Love (1863-1940).

[2] Any location vector $\mathbf{X}$ of material points throughout the *undeformed* solid plate and its boundaries is described by a Cartesian coordinate system, with an origin located in the midplane of the plate, and with base vectors $\mathbf{e}_x$, $\mathbf{e}_y$, and $\mathbf{e}_z$, whereby $\mathbf{e}_z$ is orthogonal to the midplane of the plate. Accordingly, we measure the location coordinates, $\mathbf{X} = X \mathbf{e}_x + Y \mathbf{e}_y + Z \mathbf{e}_z$.

remains constant) implies a zero normal strain in direction of the thickness, and consequently a vertical displacement u_z independent of coordinate Z, i.e. equivalent to the vertical displacement of the midplane of the plate: $u_z(X, Y, Z) = u_{m,z}(X, Y)$. Furthermore, the hypothesis concerning generators being both straight and perpendicular to the midplane implies zero transverse shear strains, indicating a so-called *shear-rigidity* of the plate. Summarizing, the kinematic assumptions (1.1) for thin plates clarifies, that knowledge regarding the displacement field of the midplane is sufficient to reconstruct the displacement field for all points of the plate, giving access to the determination of strains and stresses acting throughout the plane continuum. In other words, a 3D continuum description of thin structural elements can be replaced by a *2D structural theory*.

Application of the continuum mechanical description of the characteristic kinematics regarding a thin plate (1.1) to 2D structural theories requires further information concerning the magnitude of the displacement field and its corresponding gradients, i.e. we have to distinguish between "small" and "large" deformations: In general, solid continua undergoing small deformations are characterized by displacements which are small when compared to the dimensions of the continuum, resulting in a deformed configuration (described by location vectors $\mathbf{x}$) which differ insignificantly from the undeformed configuration (described by location vectors $\mathbf{X}$), with $\mathbf{X} \approx \mathbf{x}$. Thus, equilibrium equations of forces, moments, and powers acting in the deformed continuum can also be formulated in the *known* undeformed reference configuration. Furthermore, small deformations imply that the norm of the displacement gradient tensor is much smaller than 1, namely $\|\partial\mathbf{u}/\partial\mathbf{X}\| \ll 1$, yielding the concept of *linear elasticity* (linearized theory) using the linearized strain tensor [Mang and Hofstetter, 2000]. Thin plates undergoing small deformations can then be described by the so-called *Kirchhoff plate theory*. In this linear 2D theory, thermal loads and external mechanical loads, $p_x(x, y)$, $p_y(x, y)$, and $p_z(x, y)$, are carried by internal in-plane (membrane) forces per unit length, namely $n_{xx}(x, y)$, $n_{xy}(x, y)$, and $n_{yy}(x, y)$; as well as by internal bending moments per unit length, $m_{xx}(x, y)$, $m_{yy}(x, y)$, and internal twisting moments per unit length $m_{xy}(x, y)$, acting on the midplane of the plate [Ventsel and Krauthammer, 2001]. It is noted, that the stretching problem and the bending problem of a Kirchhoff plate are not coupled and can be treated separately, see Fig. 1.3. On the other hand, when considering
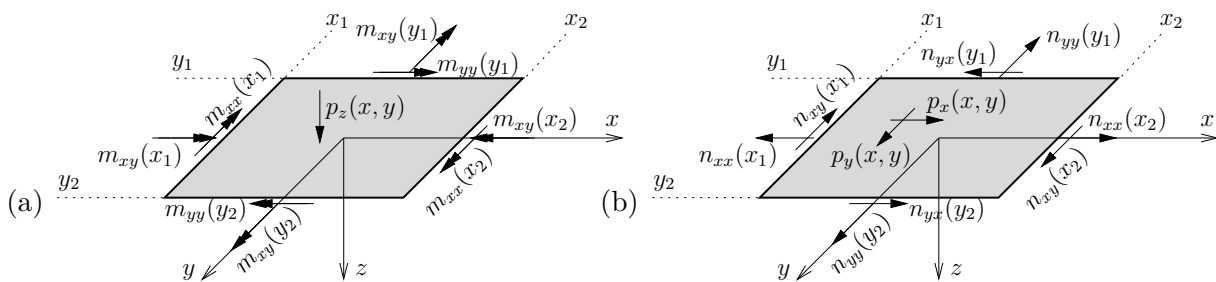
Fig. 1.3: Schematical illustration of internal and external stress resultants acting on a section of a thin Kirchhoff plate, spanning from x_1 to x_2, and from y_1 to y_2: decoupled (a) bending problem and (b) stretching problem.

large deformations, the displacements are not small when compared to the dimensions of the continuum, resulting in a significant change in position of a material point moving from the geometric point $\mathbf{X}$ in the undeformed configuration to the geometric point $\mathbf{x}$ in the deformed configuration, with $\mathbf{X} \neq \mathbf{x}$. Thus, for large deformations, the concept of linear elasticity does not hold anymore, which in turn requires *nonlinear* elastic theories. One theory concerning thin plates was proposed by Theodore von Kármán (1881-1963), allowing the generator of the plate undergoing moderate rotations (in the range of 10-15 degrees of angle) yielding the so-called *von*

Kármán plate theory. In this nonlinear 2D theory the stretching and bending problem become *coupled* [von Kármán, 1910; Reddy, 2007], in contrast to the Kirchhoff plate theory. The basic concepts for the continuum mechanical description of such theories, including the definitions of strain and stress measures (for small and large deformations) as well as of the corresponding thermodynamical description together with power principles[3], can be found in Chapter 2 of the present thesis.

As regards thin plates resting on elastic foundations (*"swimming" plates*), the mechanical interaction between the plate and the underlying continuous elastic subgrade (underground) is taken into account: For roads, airfields, and plate foundations, the modeled underground represents the soil, while the modeled underground of floor screeds typically represents the impact sound insulation. The by far most popular mechanical model for this interaction problem is that of the *elastic Winkler foundation* [Winkler, 1867], in reference to the civil engineer Emil Winkler (1835-1888). This model represents the subgrade medium as a system of an infinite set of closely spaced, *uncoupled* vertical linear elastic springs on which the plate is lying on. In analogy to Hooke's law[4] of linear elastic single springs [Hooke, 1678], the Winkler springs are characterized by a spring constant c (force per unit area per unit length) also denoted as Winkler elastic modulus of subgrade reaction. Corresponding *subgrade reaction forces* in vertical direction are defined as external traction forces T_z^c (force per unit area) acting on the bottom surface of the plate, being in direct *interaction* with usually applied vertical surface loads per unit area p_z acting on the top surface of the plate, see Fig. 1.4. In this context, the same assumption of the
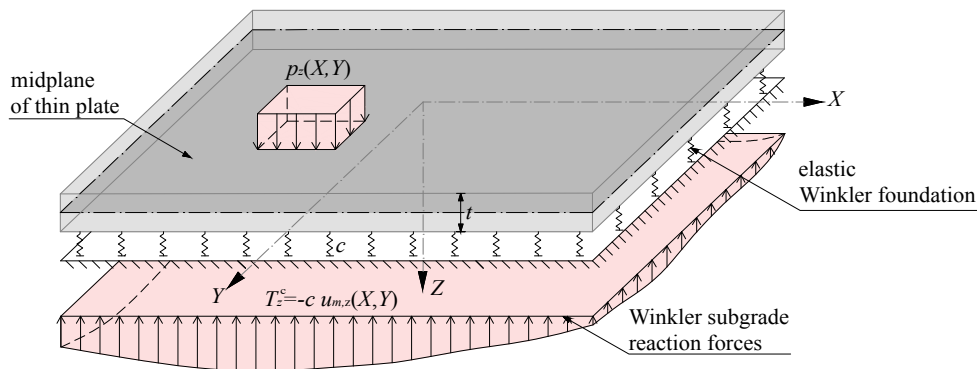
Fig. 1.4: Thin plate on elastic Winkler foundation ("swimming" plate) with thickness t and Winkler elastic modulus c, subjected to vertical surface loads p_z and Winkler subgrade reaction forces T_z^c.

displacement field (1.1) holds for thin plates on elastic foundations, but also serves as a part of the external subgrade reaction forces T_z^c, namely the product of the Winkler elastic modulus c and the negative deflection function in vertical direction $u_{m,z}$, reading as

$$T_z^c(X,Y) = -c\,u_{m,z}(X,Y)\,. \tag{1.2}$$

It is noted, that the kinematic assumptions of the Kirchhoff-Love hypothesis result in a vertical displacement of the bottom surface of the plate equivalent to the vertical displacement of the midplane of the plate. For such plates in bending mode, the external forces, namely the subrade

---

[3]A common formulation for the equilibrium of internal and external powers is the so-called *Principle of Virtual Power* (PVP) [Germain, 1973a,b; Maugin, 2013] giving access to theories of structural elements, as documented by Paul Germain (1920-2009) and Gérard A. Maugin (1944-2016).

[4]The Hooke's law is named after the physicist Robert Hooke (1635-1703) and states that the extension or compression of an elastic spring is directly proportional to the applied force [Hooke, 1678].

reaction forces T_z^c (1.2), the surface loads p_z, and thermal loads, as well as the dimensions and stiffnesses referring to the plate form an elastic system for the determination of the unknown displacement field of the midplane of the plate $\mathbf{u}_m$.

Analytical expressions for the sought deflection function are mostly complex or strictly not solvable. Only for simple loading cases, namely vertical forces acting on the edge, corner, and center of a thin Kirchhoff plate, the civil engineer Harold M. Westergaard (1888-1950) derived analytical formulae for the maximum deflections and maximum tensile stresses in such plates when resting on elastic Winkler foundations [Westergaard, 1926, 1939, 1948]. As a remedy, one can resort to the numerical 2D Finite Element method for more complex systems, subdividing the midplane of the plate into a sufficient finite number of elements (discretisation), whereas the displacement field between the corner points of the elements is typically approximated by means of linear or quadratic interpolation functions [Ko et al., 2016; Neto et al., 2015]. A further popular semi-analytical method for this problem is that put forward by the mathematician and engineer Claude L. M. H. Navier (1785-1836), representing the displacement field of the midplane of the plate as a series of double trigonometric *ansatz functions* [Navier, 1823], reading as (with respect to the deflection $u_{m,z}$)

$$u_{m,z}(X,Y) = \sum_{m=1}^{N_m} \sum_{n=1}^{N_n} c_{m,n}\, w_{m,n}(X,Y)\,, \tag{1.3}$$

with $c_{m,n}$ and $w_{m,n}$ as the amplitudes (Fourier coefficients) and the trigonometric deflection modes, respectively. The approximative solution for the deflection is the more precise the more series deflection members (being $N_m \times N_n$ in number) are employed. While *Navier's solution* holds for a rectangular plate with simply supported boundaries, his followers Vasily Z. Vlasov (1906-1958) and Nikolai N. Leont'ev (1926-2009) provided extended (symmetrical and antimetrical) trigonometric ansatz functions according to plates on elastic foundations with free boundaries [Vlasov and Leont'ev, 1966]. Another noteworthy pioneer in developing semi-analytical solutions for the deflections was Stepan P. Timoshenko (1878-1972), who published a series of ansatz functions for the displacement fields of plates with various shapes and boundary conditions (combined simply supported, clamped, and free boundaries) [Timoshenko and Woinowsky-Krieger, 1959]. In the present thesis, a theoretical approach of a structural plate-subgrade-interaction problem is developed in form of a concrete slab with free boundaries resting on elastic Winkler foundations [Höller et al., 2019; Wang et al., 2019a]. The freely "swimming" plate is subjected to vertical surface loads and temperature gradients along the thickness of the plate, where the latter results in a temperature-induced eigencurvature of the plate. The sought vertical deflections of the midplane of the slab are approximated by Vlasov-type ansatz functions in form of 2D Fourier series, see Chapter 3 and Chapter 4 of the present thesis.

1.2 Kinematics and stress resultants of 2D membranes – Graphene

At this point, we introduced theories for thin plates, mechanically described by means of the displacement field of the midplane together with an assigned constant thickness t of the plate. However, for an "ultrathin" structural element, characterized by a thickness at least 80 to 100 times smaller than the other in-plane dimensions, the thickness can be regarded as negligible small, with $t \to 0$. Then such structural elements are called *membranes* [Gould, 1988], finding applications for wide-span roof structures and pneumatic (air-supported) structures in building construction, or for silos, pressure vessels, tanks, etc. in industrial construction. In the case of an infinitesimal small thickness of the membrane, also the coordinate of the location vector in

direction of the thickness is negligible small, with $Z \to 0$. Hence, starting from (1.1) and taking into account the boundary value $Z \to 0$, yields the kinematics of a 2D membrane fully described in form of the displacement field of the aforementioned midplane, being in good approximation the displacement field of the membrane itself (see Fig. 1.5), reading as
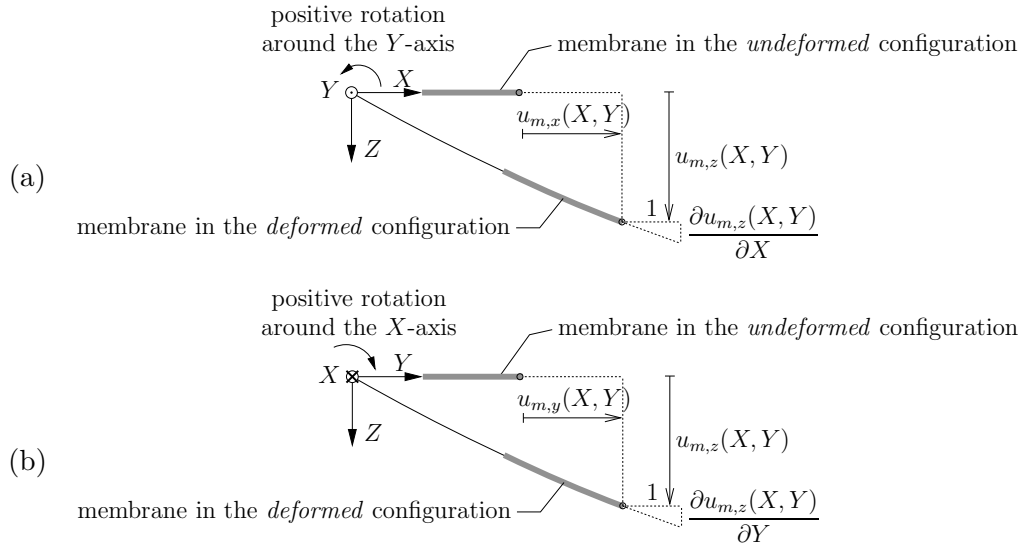
Fig. 1.5: Sideviews of a membrane in the undeformed and deformed configuration, according to the kimematic assumption (1.4): (a) X, Z-plane and (b) Y, Z-plane.

$$\mathbf{u}_m(\mathbf{X}) = u_{m,x}(X,Y)\,\mathbf{e}_x + u_{m,y}(X,Y)\,\mathbf{e}_y + u_{m,z}(X,Y)\,\mathbf{e}_z\,. \tag{1.4}$$

It is easily seen, that the assumption of the displacement field (1.4) only depends on the in-plane coordinates X and Y (there are no terms related to the deflection gradients). For membranes in bending mode, the out of plane deflections $u_{m,z}$ are in general *large* when compared to the (infinitesimal small) thickness of the membrane. Obviously, this results in a significant change in position of a material point moving from the geometric point $\mathbf{X}$ in the undeformed configuration to the geometric point $\mathbf{x}$ in the deformed configuration, indicating the necessity of a large deformation theory. In this context, it is useful to formulate strain and stress resultants as functions of the *known* location vector $\mathbf{X}$ in the undeformed configuration – in other words, strains and stresses are formulated in *Lagrangian representation*, in reference to the mathematician and astronomer Joseph-Louis Lagrange (1736-1813). The large deformations (1.4) arise from external loads causing bending and stretching of the membrane. However, the latter is devoid of flexural rigidity and shear rigidity due to the vanishing thickness of the membrane, which results in either zero or negligible small bending and twisting moments. Thus, the dominating stretching rigidity referring to the membrane indicates that external Lagrangian loads, $p_{L,x}(X,Y)$, $p_{L,y}(X,Y)$, and $p_{L,z}(X,Y)$, are carried by internal Lagrangian *membrane forces* per unit length, namely normal forces $n_{L,xx}(X,Y)$, $n_{L,yy}(X,Y)$, and in-plane shear forces $n_{L,xy}(X,Y)$, see Fig.1.6. This load transfer can be imagined as a natural extension of one-dimensional theories for rope (wire) structures, where external loads are carried by an internal normal force [Salençon, 2001]. Moreover, membranes undergoing large deformations imply no limitations of displacement gradients in contrast to the moderate gradients within the von Kármán plate theory. Thus, more general theories for large deformations are required, including informations of nonlinear constitutive relations. A valuable classical tool is the concept of *hyperelasticity* (also called Green elasticity), developed by the mathematical physicist George Green (1793-1841) and followers [Green, 1837;
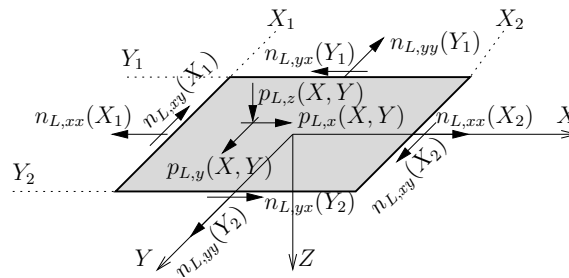
Fig. 1.6: Schematical illustration of internal and external Lagrangian stress resultants acting on a section of a membrane, spanning from X_1 to X_2, and from Y_1 to Y_2.

Truesdell and Noll, 1965; Rajagopal, 2011]: Lagrangian stresses acting in a hyperelastic material are associated to a stored energy in the system, namely the Helmholtz free energy[5], which in turn is a function of applied Lagrangian strains, yielding nonlinear stress-strain relations, see also Chapter 2 of the present thesis.

When dealing with membrane theories, the question arises if there do exist real 2D membranes? Initially 2D materials were thought to be thermodynamically unstable [Mermin, 1968]. However, the physicists Andre Geim and Konstantin Novoselov (and co-workers) indeed discovered the first stable 2D material in 2004, namely *graphene* an isolated single-layer from graphite [Novoselov et al., 2004]. Their outstanding research was acknowledged by the Nobel Prize in Physics in 2010 "for groundbreaking experiments regarding the two-dimensional material graphene." Graphene is a perfect *one-atom-thick* membrane (without defined thickness), consisting of strongly bonded carbon atoms, arranged in a hexagonal *honeycomb lattice*, see Fig. 1.7(a). The equilibrium bond length of two neighboring carbon atoms in the undeformed configuration is called lattice constant of graphene, with a dimension of about 0.14 nm [Castro Neto et al., 2009]. The strongly bonded atoms in graphene can be imagined as follows: Within the graphene layer, plane sp^2 hybridized carbon atoms result in covalent bonds formed by overlaps of the electronic orbitals (wavefunctions), see Fig. 1.7(b). The electronic wavefunctions describe the motion of electrons around their carbon atom on which they belong. As regards geometric properties, graphene is an *anisotropic* material due to its two characterizing "zigzag" and "armchair" directions, which are repeated over periods of $\pi/3$. This 2D material is the basic structural element for other allotropes of carbon, including graphite, carbon nanotubes, and fullerenes. For graphite, the graphene layers are stacked on top of each other and are bonded by Van der Waals forces[6] resulting in an established interlayer distance of 0.335 nm [Franklin, 1951]. On the other hand, carbon nanotubes are obtained by rolling up a graphene membrane into a cylinder; while fullerenes are formed by unfolding graphene into a spherical shape. Graphene, neither a metal nor a semiconductor but a *semimetal*, is characterized by a number of intriguing properties [Lau et al., 2012], attracting considerable attention in the fields of physics, chemistry, and material science: The most famous ones are high thermal conductivity, weak optical absorptivity, and extremely high electron mobility [Balandin et al., 2008; Nair et al., 2008; Bolotin et al., 2008]. Furthermore, graphene has motivated studies in the fields of experimental mechanics and of continuum mechanical modeling, reporting a modulus of elasticity of about 1000 GPa (for small deformations) and a tensile strength of over 100 GPa [Liu et al., 2007; Lee et al., 2008]. These examples of mechanical characteristics of graphene exceed those of any other material and are obtained when assigning

---

[5]The physician and physicist Hermann von Helmholtz (1821-1894) introduced the term "free energy" in 1883. It is the part of the internal energy which can be converted back into effective mechanical work.

[6]The distance-dependent weak interaction between atoms is named after the theoretical physicist Johannes Diderik van der Waals (1837-1923).
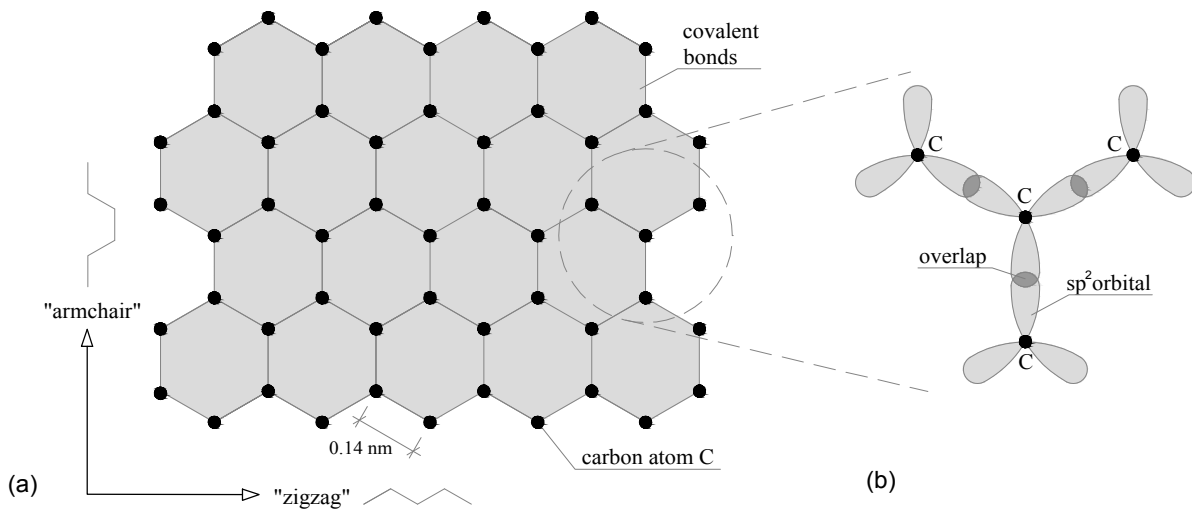
Fig. 1.7: 2D graphene membrane consisting of strongly bonded carbon atoms: (a) hexagonal one-atom-thick honeycomb lattice of graphene with "zigzag" and "armchair" directions, (b) illustration of sp^2 hybridized carbon atoms with covalenty bonded electronic orbitals.

an effective thickness to graphene, namely the interlayer distance of graphite – a common practice for comparison to 3D materials. In the context of mechanical properties, we have to overcome the transition from quantum mechanics, dealing with the motion of atoms and electrons (*electronic densities*) on nanoscopic levels, to classical theories of continuum mechanics, dealing with macroscopic strains, stresses, and stiffnesses of a solid material. This "upscaling" process can be realized by means of the aforementioned concept of hyperelasticity, which resorts to the Helmholtz free energy in the system, a physical quantity known in both scales. Thus, this essential energy can be determined by various quantum mechanics-rooted methods, the most popular ones are: The *Density Functional Theory* (DFT) approximately solves the electronic *Schrödinger equation*[7] by expressing the internal energy as a functional of the electronic density [Hohenberg and Kohn, 1964; Kohn and Sham, 1965]. A fictitious system of noninteracting electrons is then used for determining the electronic wavefunctions, electronic densities, and the sought internal energy in an iterative self-consistent manner [Parr and Yang, 1989]. A computationally more efficient method, compared to DFT, represents the semi-empirical tight-binding (TB) method [Slater and Koster, 1954], in which electrons are assumed to be tightly bound to the atom on which they belong, resulting in an electronic wave function rather similar to the atomic orbital. Molecular dynamics (MD) simulations can be applied for describing the interactions of neighboring atoms (chemical binding energy). Frequently used interatomic potentials are the Lennard-Jones potential [Lennard-Jones, 1924] and the reactive empirical bond-order (REBO) potentials (also called Brenner potentials) based on the Abell-Tersoff covalent-bonding formalism [Abell, 1985; Tersoff, 1988]. For graphene, we here use the most accurate one of the aforementioned quantum mechanical methods for describing the electronic structure, namely the Density Functional Theory. Knowing the strain-induced free energy for any material direction of graphene, the anisotropic hyperelastic material modeling gives us access to macroscopic *nonlinear* stress-strain relations and stiffnesses, as well as to corresponding mechanical properties of graphene [Höller et al., 2020a], see Chapter 5 of the present thesis. Based on the mechanical material behavior (stress-strain

---

[7]The Schrödinger equation was developed by the physicist Erwin Schrödinger (1887-1961) in 1926. The equation, initially known as "wave equation", governs the form of the wavefunction of electrons in a quantum mechanical system [Schrödinger, 1926] and was awarded by the Nobel Prize in Physics in 1933.

relations) of graphene, of course structural theories of membranes can be investigated using the kinematic characteristics according to Eq. (1.4). The corresponding solution for the deflection function of a membrane with various shapes and boundary conditions can again be approximated by the numerical 2D Finite Element method and by the semi-analytical series-based solution procedure. For suspended (freestanding) graphene sheets with simply supported boundaries, it is advisable to use the efficient series-based Navier's solution (1.3), which automatically assumes deflections to be zero at the boundaries. Hence, the latter approach as well as the Principle of Virtual Power are applied to circular graphene sheets with simply supported boundaries. The derived membrane theory finally yields a nonlinear system of equations for the sought deflection function [Höller et al., 2020b], see Chapter 6 of the present thesis.

1.3 Outline of the thesis

The individual chapters of the present thesis contain basic concepts of continuum mechanics and either already published and submitted papers in peer-reviewed scientific journals. Thus, the doctoral thesis is structured as follows:

- A collection and derivation of the definitions of continuum mechanical measures as strains (deformations) and stresses, as well as of the Principle of Virtual Power and thermodynamics of deformable continua is provided in *Chapter* 2. All these basic quantities are further used in the following chapters concerning 2D mechanics.

- *Chapter* 3 is devoted to structural mechanics of thin elastic Kirchhoff plates with free boundaries resting on elastic Winkler foundations (swimming plates). In this context, the deflection function is approximated by Vlasov-type 2D Fourier series, where the Principle of Virtual Power yields an complete and energetically consistent mechanical description of the structural problem. The resulting linear algebraic system of equations for the unknown Fourier coefficients is applied to relevant problems in pavement engineering, appearing as an efficient alternative to the standardly applied Finite Element method.

  Rigorous amendment of Vlasov's theory for thin elastic plates on elastic Winkler foundations, based on the Principle of Virtual Power

  Authored by: R. Höller, M. Aminbaghai, L. Eberhardsteiner, J. Eberhardsteiner,
  R. Blab, B.L.A. Pichler, and C. Hellmich

  Published in: *European Journal of Mechanics / A Solids* 73 (2019) 449-482

- *Chapter* 4 presents concrete pavements subjected to extreme weather events, namely hail showers, following solar heating. In this thermoelastic analysis, the thermal expansion coefficient and the modulus of elasticity of microscopic concrete constituents are homogenized using multiscale material modeling. The series-based structural problem of concrete slabs resting on elastic Winkler foundations is then used for calculating macroscopic stresses. Finally, top-down scaling to the microscopic stresses of the concrete constituents show that these stresses are likely to reach the tensile strength of concrete.

  Concrete pavements subjected to hail showers: A semi-analytical thermoelastic multiscale analysis

  Authored by: H. Wang, R. Höller, M. Aminbaghai, C. Hellmich, Y. Yuan, H.A. Mang,
  and B.L.A. Pichler

  Published in: *Engineering Structures* 200 (2019) 109677

- *Chapter* 5 describes the mechanical material modeling of graphene using the concept of hyperelasticity. The related free energy density is calculated by DFT for tens of thousands of biaxial strain states, providing a full set of strain-induced energy landscapes of graphene. The latter are formulated in an invariant manner including the anisotropic behavior in form of a structural tensor. Thereafter, the material law of hyperelasticity yields power-conjugate nonlinear stress-strain relations for general deformations, giving access to the stiffness tensor and to the elastic stability limits of graphene.

  Energy landscapes of graphene under general deformations: DFT-to-hyperelasticity upscaling

  Authored by: R. Höller, V. Smejkal, F. Libisch, and C. Hellmich

  Under review: *International Journal of Engineering Science*

- *Chapter* 6 provides the structural modeling of circular graphene sheets with simply supported boundaries. A membrane theory for large deformations is derived including hyperelastic stress-strain relations as well as Navier-type ansatz functions for the sought deflections. In this context, the Principle of Virtual Power yields a nonlinear system of equations for the unknown Fourier coefficients, which is solved iteratively. This efficient solution procedure is applied to relevant mechanical problems of graphene and is validated by experimental nanoindentation measurements.

  A membrane theory for circular graphene sheets, based on a hyperelastic material model for large deformations

  Authored by: R. Höller, F. Libisch, and C. Hellmich.

  Submitted to: *Mechanics of Advanced Materials and Structures*

The doctoral thesis concludes with a discussion of the results, followed by perspectives on future research, see *Chapter* 7. Based on the developments of the present thesis, a potential further study for graphene is the application of advanced continuum mechanics theories, as the exploration of corresponding electro-magneto-mechanical couplings. In this context, classical continuum mechanical definitions (according to Chapter 2) are in strong interaction with applied electric and magnetic fields. The provided theory for this interaction problem is based on Gérard A. Maugin (1944-2016) [Maugin, 1988] and can serve as a starting point for research in the growing field of the mechanics of graphene and other comparable nanomaterials.

Chapter 2

Basics of continuum mechanics – Definitions of strain and stress measures

The following provided overview of the continuum mechanical concepts is based on the academic lectures of Prof. Christian Hellmich [Hellmich, 2012, 2018], where he was inspired by former works concerning classical continuum mechanics [Salençon, 2001; Fung and Tong, 2001; Mang and Hofstetter, 2000].

2.1 Deformation – strains

Forces acting on a body typically cause changes in shape (*deformations*). We consider bodies composed of mathematical points – where the points physically correspond to *material volumes*, which are significantly smaller than the dimensions of the body or the dimensions of the acting loads. For the description of the deformation of the continuum, we use the concept of *neighboring points*: By changes in position of neighboring points, the changes in shape of our deformed body can be mathematically captured. Since we deal with points and their neighbors, the mathematical terms of *vector fields* and their derivatives play a central role. Ultimately, this concept leads to the introduction of additional tensor quantities, namely *strains*. This will be explained in detail in the following sections.

2.1.1 Deformation gradient and strain tensor

Imagine a deformable body as a set of material points. In the *undeformed* reference configuration, the location of the material points (particles) is described by the location vector $\mathbf{X}$. In the *deformed* momentan configuration, these material particles are located at the positions $\mathbf{x}$ (see Fig. 2.1). The corresponding mapping reads as

$$\mathbf{x} = \boldsymbol{\varphi}(\mathbf{X}) \,. \tag{2.1}$$

In order to formulate a mathematical description of the deformation of a body, we also consider neighbor points of $\mathbf{X}$. The neighbor $\mathbf{X} + d\mathbf{X}$ moves according to (2.1)

$$\mathbf{x} + d\mathbf{x} = \boldsymbol{\varphi}(\mathbf{X} + d\mathbf{X}) \,. \tag{2.2}$$

The neighborhood is expressed by the fact that function values at neighboring points $\boldsymbol{\varphi}(d\mathbf{X})$ are defined by spatial derivatives of $\boldsymbol{\varphi}(\mathbf{X})$ times distance vectors $d\mathbf{X}$

$$\boldsymbol{\varphi}(\mathbf{X} + d\mathbf{X}) = \boldsymbol{\varphi}(\mathbf{X}) + \mathbf{F} \cdot d\mathbf{X} \,, \qquad \text{with} \qquad \mathbf{F} = \frac{\partial \boldsymbol{\varphi}}{\partial \mathbf{X}}(\mathbf{X}) \,. \tag{2.3}$$
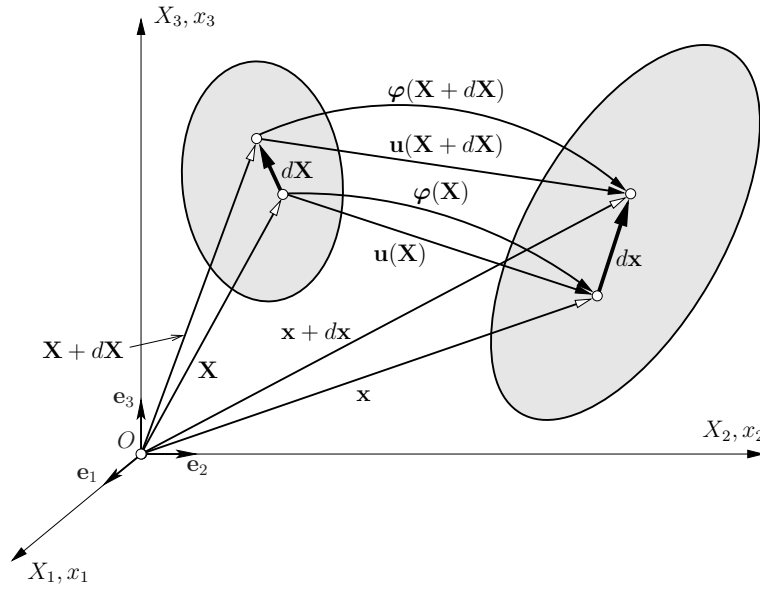
Fig. 2.1: Reference configuration and momentan configuration of a deformable continuum.

In Eq. (2.3), $\mathbf{F}$ is the so-called *deformation gradient* (in general a nonsymmetrical tensor of second order), which represents the spatial derivative $\partial\boldsymbol{\varphi}/\partial\mathbf{X}$. Substitution of (2.1) and (2.2) into (2.3) results in a relation between deformed and undeformed neighbor vectors:

$$d\mathbf{x} = \mathbf{F} \cdot d\mathbf{X}\,. \tag{2.4}$$

The deformation of the body is characterized by changes in lengths and angles between two distance vectors, namely $d\mathbf{X}$ and $\overline{d\mathbf{X}}$. Such changes in length and angle can be represented simply by the difference between inner products, $d\mathbf{x} \cdot \overline{d\mathbf{x}} - d\mathbf{X} \cdot \overline{d\mathbf{X}}$: Substitution of (2.4) into the inner products yields

$$d\mathbf{x} \cdot \overline{d\mathbf{x}} - d\mathbf{X} \cdot \overline{d\mathbf{X}} = d\mathbf{X} \cdot (\mathbf{F}^T \cdot \mathbf{F} - \mathbf{1}) \cdot \overline{d\mathbf{X}} = d\mathbf{X} \cdot 2\mathbf{E} \cdot \overline{d\mathbf{X}}\,, \tag{2.5}$$

where $\mathbf{E}$ is the so-called *Green-Lagrange strain tensor* defined as:

$$\mathbf{E} = \frac{1}{2}(\mathbf{F}^T \cdot \mathbf{F} - \mathbf{1})\,, \tag{2.6}$$

named after George Green (1793-1841) and Joseph-Louis Lagrange (1736-1813). Its is noted, that the strain tensor $\mathbf{E}$ is *symmetric*, due to the inner product of the unsymmetrical tensor $\mathbf{F}$ with its transpose, see (2.6). It is also useful to introduce the field of displacement vectors $\mathbf{u}(\mathbf{X})$,

$$\mathbf{u}(\mathbf{X}) = \mathbf{x} - \mathbf{X} = \boldsymbol{\varphi}(\mathbf{X}) - \mathbf{X}\,, \tag{2.7}$$

which points from its material point $\mathbf{X}$ in the reference configuration to its point $\mathbf{x}$ in the momentan configuration (see Fig. 2.1). Derivation of (2.7) with respect to $\mathbf{X}$ and considering the definition of the deformation gradient (2.3) yields the relation between the deformation gradient $\mathbf{F}$ and displacement field $\mathbf{u}$,

$$\mathbf{F} = \frac{\partial\mathbf{u}}{\partial\mathbf{X}} + \mathbf{1}\,, \tag{2.8}$$

with $\mathbf{1}$ being the second-order identity tensor. Use of (2.8) in expression (2.6) provides an alternative representation of the Green-Lagrange strain tensor,

$$\mathbf{E} = \frac{1}{2}\left[\frac{\partial \mathbf{u}}{\partial \mathbf{X}} + \left(\frac{\partial \mathbf{u}}{\partial \mathbf{X}}\right)^T + \left(\frac{\partial \mathbf{u}}{\partial \mathbf{X}}\right)^T \cdot \frac{\partial \mathbf{u}}{\partial \mathbf{X}}\right] = \sum_{i=1}^{3}\sum_{j=1}^{3} E_{ij}\mathbf{e}_i \otimes \mathbf{e}_j\,, \tag{2.9}$$

as function of the displacement field $\mathbf{u}$. The components of the strain tensor $\mathbf{E}$ read as

$$E_{ij} = \frac{1}{2}\left(\frac{\partial u_i}{\partial X_j} + \frac{\partial u_j}{\partial X_i} + \sum_{k=1}^{3}\frac{\partial u_k}{\partial X_i}\frac{\partial u_k}{\partial X_j}\right)\,, \qquad i,j = 1,2,3\,, \tag{2.10}$$

or individually,

$$E_{11} = \frac{\partial u_1}{\partial X_1} + \frac{1}{2}\left[\left(\frac{\partial u_1}{\partial X_1}\right)^2 + \left(\frac{\partial u_2}{\partial X_1}\right)^2 + \left(\frac{\partial u_3}{\partial X_1}\right)^2\right]\,, \tag{2.11}$$

$$E_{12} = E_{21} = \frac{1}{2}\left[\frac{\partial u_1}{\partial X_2} + \frac{\partial u_2}{\partial X_1} + \frac{\partial u_1}{\partial X_1}\frac{\partial u_1}{\partial X_2} + \frac{\partial u_2}{\partial X_1}\frac{\partial u_2}{\partial X_2} + \frac{\partial u_3}{\partial X_1}\frac{\partial u_3}{\partial X_2}\right]\,, \tag{2.12}$$

$$E_{13} = E_{31} = \frac{1}{2}\left[\frac{\partial u_1}{\partial X_3} + \frac{\partial u_3}{\partial X_1} + \frac{\partial u_1}{\partial X_1}\frac{\partial u_1}{\partial X_3} + \frac{\partial u_2}{\partial X_1}\frac{\partial u_2}{\partial X_3} + \frac{\partial u_3}{\partial X_1}\frac{\partial u_3}{\partial X_3}\right]\,, \tag{2.13}$$

$$E_{22} = \frac{\partial u_2}{\partial X_2} + \frac{1}{2}\left[\left(\frac{\partial u_1}{\partial X_2}\right)^2 + \left(\frac{\partial u_2}{\partial X_2}\right)^2 + \left(\frac{\partial u_3}{\partial X_2}\right)^2\right]\,, \tag{2.14}$$

$$E_{23} = E_{32} = \frac{1}{2}\left[\frac{\partial u_2}{\partial X_3} + \frac{\partial u_3}{\partial X_2} + \frac{\partial u_1}{\partial X_2}\frac{\partial u_1}{\partial X_3} + \frac{\partial u_2}{\partial X_2}\frac{\partial u_2}{\partial X_3} + \frac{\partial u_3}{\partial X_2}\frac{\partial u_3}{\partial X_3}\right]\,, \tag{2.15}$$

$$E_{33} = \frac{\partial u_3}{\partial X_3} + \frac{1}{2}\left[\left(\frac{\partial u_1}{\partial X_3}\right)^2 + \left(\frac{\partial u_2}{\partial X_3}\right)^2 + \left(\frac{\partial u_3}{\partial X_3}\right)^2\right]\,. \tag{2.16}$$

2.1.2 Interpretation of strain tensor components – volume change – principal strains

For interpretation of the normal strain components E_{11}, E_{22}, and E_{33}, we make use of Eq. (2.5), specified for one neighbor vector (infinitesimal line element $\overline{d\mathbf{X}} = d\mathbf{X}$) which is parallel to one of the basis vectors, with lengths $|d\mathbf{X}| = \sqrt{d\mathbf{X} \cdot d\mathbf{X}} = dL_i$, and $|d\mathbf{x}| = \sqrt{d\mathbf{x} \cdot d\mathbf{x}} = dl_i$, $i = 1,2,3$, see Fig. 2.2:

$$dl_i^2 - dL_i^2 = 2E_{ii}dL_i^2 \quad \Leftrightarrow \quad dl_i = \sqrt{2E_{ii}+1}\,dL_i, \quad i = 1,2,3\,. \tag{2.17}$$

Obviously, E_{ii} is a function of the change in length of a line element oriented in $\mathbf{e}_i$-direction in

$$E_{11} = \frac{1}{2}[(\frac{dl_1}{dL_1})^2 - 1]$$

$$E_{12} = \frac{1}{2}\sin(\gamma_{12})\sqrt{(2E_{11}+1)(2E_{22}+1)}$$
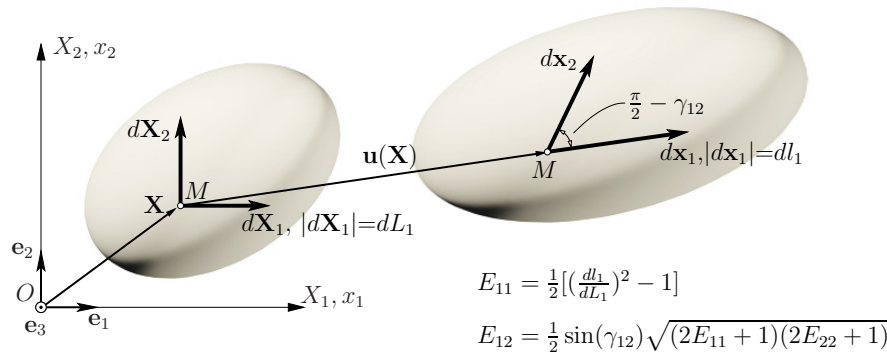
Fig. 2.2: Interpretation of normal- and shear strain components in the $\mathbf{e}_1$-$\mathbf{e}_2$-plane.

reference configuration. This can be expressed by the *engineering strain* ϵ_i and by the *stretch* λ_i, respectively

$$\epsilon_i = \frac{dl_i - dL_i}{dL_i} \quad \Leftrightarrow \quad \lambda_i = \frac{dl_i}{dL_i} = \epsilon_i + 1\,. \tag{2.18}$$

Hence, substitution of (2.17) into (2.18) delivers

$$E_{ii} = \frac{1}{2}[(\epsilon_i + 1)^2 - 1] = \frac{1}{2}\left[\lambda_i^2 - 1\right], \quad i = 1, 2, 3\,. \tag{2.19}$$

Furthermore, for the interpretation of the shear strain components E_{12}, E_{13}, and E_{23}, again we make use of Eq. (2.5) specified for two neighbor vectors (infinitesimal line elements) in $\mathbf{e}_i$- and $\mathbf{e}_j$-direction, respectively, with $d\mathbf{X} = dL_1\mathbf{e}_1$ and $\overline{d\mathbf{X}} = dL_2\mathbf{e}_2$. In the deformed configuration, these line elements are described by the vectors $d\mathbf{x} = d\mathbf{x}_1$ (with length dl_1) and $\overline{d\mathbf{x}} = d\mathbf{x}_2$ (with length dl_2), which include an angle ($\pi/2 - \gamma_{ij}$), i.e. shear deformation provokes a *change in the initial right angle* between two initial orthonormal line elements. For this spacial case, Eq. (2.5) reads as

$$d\mathbf{x} \cdot \overline{d\mathbf{x}} = dl_i dl_j \sin(\gamma_{ij}) = 2E_{ij}dL_i dL_j, \quad i, j = 1, 2, 3, \ i \neq j\,. \tag{2.20}$$

Thus, use of Eqs. (2.20) and (2.17) yields

$$E_{ij} = \frac{1}{2}\sin(\gamma_{ij})\sqrt{(2E_{ii} + 1)(2E_{jj} + 1)} \quad i, j = 1, 2, 3, \ i \neq j\,. \tag{2.21}$$

Volume changes, regarding to deformations in a continuous body, can be quantified by considering three line elements $d\mathbf{X} = dL_1\mathbf{e}_1$, $\overline{d\mathbf{X}} = dL_2\mathbf{e}_2$, and $\overline{\overline{d\mathbf{X}}} = dL_3\mathbf{e}_3$, parallel to the mutually orthogonal unit vectors $\mathbf{e}_1$, $\mathbf{e}_2$, and $\mathbf{e}_3$ (see Fig. 2.3), yielding the initial volume of a cuboid

$$dV_0 = dL_1\, dL_2\, dL_3\,. \tag{2.22}$$

The volume of the deformed cuboid is spanned by the vectors $d\mathbf{x}$, $\overline{d\mathbf{x}}$, $\overline{\overline{d\mathbf{x}}}$, which can be obtained
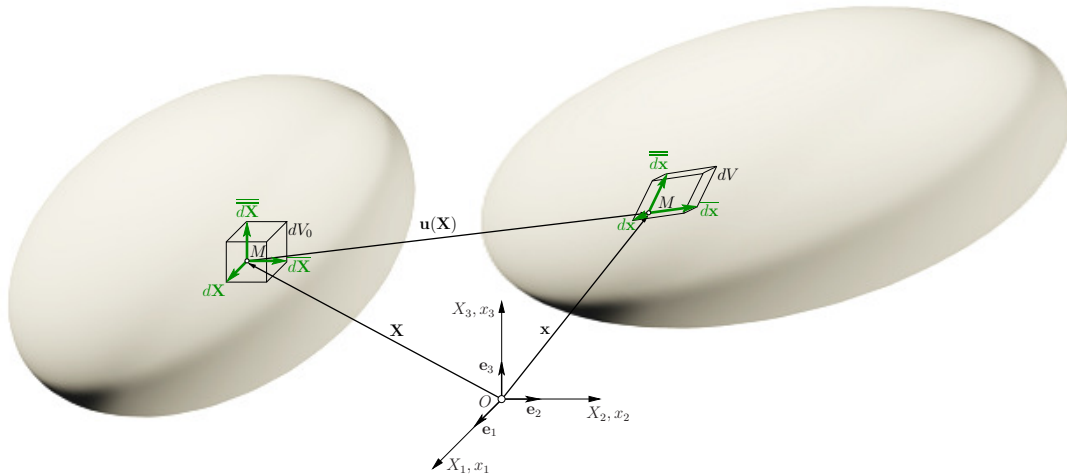
Fig. 2.3: Volume changes around material points M, arising from deformation of continuous bodies.

by means of the triple product,

$$dV = (d\mathbf{x} \times \overline{d\mathbf{x}}) \cdot \overline{\overline{d\mathbf{x}}} = \det \begin{pmatrix} dx_1 & \overline{dx}_1 & \overline{\overline{dx}}_1 \\ dx_2 & \overline{dx}_2 & \overline{\overline{dx}}_2 \\ dx_3 & \overline{dx}_3 & \overline{\overline{dx}}_3 \end{pmatrix} . \tag{2.23}$$

The line elements, bounding the deformed volume element, are expressed by specification of (2.4) for the edges of the initial cuboid,

$$d\mathbf{x} = F_{11}dL_1\mathbf{e}_1 + F_{21}dL_1\mathbf{e}_2 + F_{31}dL_1\mathbf{e}_3 , \tag{2.24}$$

$$\overline{d\mathbf{x}} = F_{12}dL_2\mathbf{e}_1 + F_{22}dL_2\mathbf{e}_2 + F_{32}dL_2\mathbf{e}_3 , \tag{2.25}$$

$$\overline{\overline{d\mathbf{x}}} = F_{13}dL_3\mathbf{e}_1 + F_{23}dL_3\mathbf{e}_2 + F_{33}dL_3\mathbf{e}_3 . \tag{2.26}$$

Substitution of (2.24)-(2.26) into (2.23) finally delivers relation between the undeformed and the deformed volume element, reading as

$$dV = \det\mathbf{F}dV_0 = JdV_0 , \tag{2.27}$$

with $J = \det\mathbf{F}$ as the so-called *Jacobi-determinant*, in reference to Carl Gustav Jacob Jacobi (1804-1851).

Let us us now investigate special directions induced by the strain tensor $\mathbf{E}$. These direction are defined by the orientation vectors $\mathbf{n}$, used in the context of the *eigenvalue-problem*

$$\mathbf{E} \cdot \mathbf{n}_i = E_i\mathbf{n}_i, \quad i = \mathrm{I}, \mathrm{II}, \mathrm{III} , \tag{2.28}$$

with eigenvalues E_I, E_II, E_III, and eigenvectors $\mathbf{n}_\mathrm{I}$, $\mathbf{n}_\mathrm{II}$, $\mathbf{n}_\mathrm{III}$. The eigenvalues can be obtained by solving the following characteristic polynomial

$$\det(\mathbf{E} - E\mathbf{1}) = 0 = -E^3 + I_1^E E^2 - I_2^E E + I_3^E , \tag{2.29}$$

where the coefficients of the characteristic polynomial

$$I_1^E = \mathrm{tr}\mathbf{E} = E_{11} + E_{22} + E_{33} , \tag{2.30}$$

$$I_2^E = \frac{1}{2}\left[(\mathrm{tr}\mathbf{E})^2 - \mathrm{tr}\left(\mathbf{E}^2\right)\right] = \begin{vmatrix} E_{22} & E_{23} \\ E_{32} & E_{33} \end{vmatrix} + \begin{vmatrix} E_{11} & E_{13} \\ E_{31} & E_{33} \end{vmatrix} + \begin{vmatrix} E_{11} & E_{12} \\ E_{21} & E_{22} \end{vmatrix} , \tag{2.31}$$

$$I_3^E = \det\mathbf{E} = \begin{vmatrix} E_{11} & E_{12} & E_{13} \\ E_{21} & E_{22} & E_{23} \\ E_{31} & E_{32} & E_{33} \end{vmatrix} \tag{2.32}$$

are the principal invariants of the Green-Lagrange strain tensor. The three real solutions of Eq. (2.29) are called *principal strains E_i*, $i = \mathrm{I}, \mathrm{II}, \mathrm{III}$. Substitution of these eigenvalues into Eq. (2.28) yields three orthonormal eigenvectors $\mathbf{n}_i$, $i = \mathrm{I}, \mathrm{II}, \mathrm{III}$, which are called *principal strain directions*. Use of these eigenvectors as basis vectors of length one $\mathbf{e}_\mathrm{I}$, $\mathbf{e}_\mathrm{II}$, $\mathbf{e}_\mathrm{III}$, results in the following notation for the strain tensor $\mathbf{E}$

$$\mathbf{E} = E_\mathrm{I}\mathbf{e}_\mathrm{I} \otimes \mathbf{e}_\mathrm{I} + E_\mathrm{II}\mathbf{e}_\mathrm{II} \otimes \mathbf{e}_\mathrm{II} + E_\mathrm{III}\mathbf{e}_\mathrm{III} \otimes \mathbf{e}_\mathrm{III} . \tag{2.33}$$

Eq. (2.33) shows that deformations in principal strain directions provoke vanishing shear strain components.

2.1.3 Small displacement derivatives – linearized strain tensor

In the next step, we want to achieve simplifications of the strain expression (2.9): Therefore, we investigate cases, where the norm of the displacement gradient tensor $\partial\mathbf{u}/\partial\mathbf{X}$ is much smaller than 1:

$$\|\partial\mathbf{u}/\partial\mathbf{X}\| \ll 1 \Leftrightarrow |\frac{\partial u_i}{\partial X_j}| \ll 1 \; \forall i,j \in \{1,2,3\}\,. \tag{2.34}$$

Let us consider the strain tensor components Eqs. (2.11)-(2.16) as functions of nine variables, namely, the displacement derivative components $\partial u_i/\partial X_j$, $i,j = 1,2,3$. Since these quantities are all very small, we are interested in the functional values of E_{ij} in the neighborhood of $(0,0,0,0,0,0,0,0,0)$. These values can be approximated by component-specific Taylor series, which are canceled after the linear terms. As a result of this procedure, the linear approximations of the strain components E_{ij} are

$$
\begin{aligned}
E_{11}\left(\frac{\partial u_1}{\partial X_1}, \frac{\partial u_2}{\partial X_1}, \frac{\partial u_3}{\partial X_1}\right) &\approx \frac{\partial u_1}{\partial X_1} = \varepsilon_{11}\,,\\
E_{12}\left(\frac{\partial u_1}{\partial X_1}, \frac{\partial u_1}{\partial X_2}, \frac{\partial u_2}{\partial X_1}, \frac{\partial u_2}{\partial X_2}, \frac{\partial u_3}{\partial X_1}, \frac{\partial u_3}{\partial X_2}\right) &\approx \frac{1}{2}\left(\frac{\partial u_1}{\partial X_2} + \frac{\partial u_2}{\partial X_1}\right) = \varepsilon_{12}\,,\\
E_{13}\left(\frac{\partial u_1}{\partial X_1}, \frac{\partial u_1}{\partial X_3}, \frac{\partial u_2}{\partial X_1}, \frac{\partial u_2}{\partial X_3}, \frac{\partial u_3}{\partial X_1}, \frac{\partial u_3}{\partial X_3}\right) &\approx \frac{1}{2}\left(\frac{\partial u_1}{\partial X_3} + \frac{\partial u_3}{\partial X_1}\right) = \varepsilon_{13}\,,\\
E_{22}\left(\frac{\partial u_1}{\partial X_2}, \frac{\partial u_2}{\partial X_2}, \frac{\partial u_3}{\partial X_2}\right) &\approx \frac{\partial u_2}{\partial X_2} = \varepsilon_{22}\,,\\
E_{23}\left(\frac{\partial u_1}{\partial X_2}, \frac{\partial u_1}{\partial X_3}, \frac{\partial u_2}{\partial X_2}, \frac{\partial u_2}{\partial X_3}, \frac{\partial u_3}{\partial X_2}, \frac{\partial u_3}{\partial X_3}\right) &\approx \frac{1}{2}\left(\frac{\partial u_2}{\partial X_3} + \frac{\partial u_3}{\partial X_2}\right) = \varepsilon_{23}\,,\\
E_{33}\left(\frac{\partial u_1}{\partial X_3}, \frac{\partial u_2}{\partial X_3}, \frac{\partial u_3}{\partial X_3}\right) &\approx \frac{\partial u_3}{\partial X_3} = \varepsilon_{33}\,.
\end{aligned}
\tag{2.35}
$$

These linear approximations are components of the so-called *linearized strain tensor*, $\boldsymbol{\varepsilon}$. Thus, in a compact notation, the linearized strain tensor $\boldsymbol{\varepsilon}$ reads as

$$\boldsymbol{\varepsilon} = \frac{1}{2}\left[\frac{\partial\mathbf{u}}{\partial\mathbf{X}} + \left(\frac{\partial\mathbf{u}}{\partial\mathbf{X}}\right)^T\right] = \sum_{i=1}^{3}\sum_{j=1}^{3}\varepsilon_{ij}\mathbf{e}_i \otimes \mathbf{e}_j\,, \tag{2.36}$$

with the components

$$\varepsilon_{ij} = \frac{1}{2}\left(\frac{\partial u_i}{\partial X_j} + \frac{\partial u_j}{\partial X_i}\right)\,, \qquad i,j = 1,2,3\,. \tag{2.37}$$

In the case of small (infinitesimal) displacement derivatives, the normal components of the linearized strain tensor correspond to the physical elongation in the directions of the selected base vectors

$$\epsilon_1 \approx \varepsilon_{11}\,, \quad \epsilon_2 \approx \varepsilon_{22}\,, \quad \epsilon_3 \approx \varepsilon_{33}\,. \tag{2.38}$$

Furthermore, in this specific case, the shear components of the linearized strain tensor can be interpreted as angle changes from the original right angle γ (by making use of $\sin\gamma \approx \gamma$)

$$\gamma_{12} \approx 2\varepsilon_{12}\,, \quad \gamma_{23} \approx 2\varepsilon_{23}\,, \quad \gamma_{13} \approx 2\varepsilon_{13}\,. \tag{2.39}$$

2.2 Stresses

Deformation and failure of a material is determined by physical quantities of dimension *force per area*, also called *stress* (pressure, for example, represents a special case of stress). It is noted, that both the force and the area are generally vectorial quantities. In other words, they are defined by a *scalar* (magnitude) and a *direction*. In this context, Augustin Louis Cauchy (1789-1857) presented a concept in 1829, from which the *stress tensor* was developed. The physical and mathematical basis for this stress tensor will be discussed in the following sections.

2.2.1 Equilibrium conditions – Cauchy stress tensor

Our starting point is the description of surface- and volume forces, acting on a continuum in the *deformed configuration*. First, we consider elementary surface elements dS on the surface of the body with orientation $\mathbf{n}(\mathbf{x})$. The unit vector $\mathbf{n}$ is orthogonal to the surface element dS and points outwards. On these surface elements, *traction vectors* $\mathbf{T}$ (dimension force per unit area) are acting. The traction vectors depend only on the orientation of the surface elements $\mathbf{n}$ and on the location $\mathbf{x}$: $\mathbf{T} = \mathbf{T}(\mathbf{x}, \mathbf{n})$. Secondly, we define elementary volume elements dV of the body. On these volume elements, *force density vectors* $\mathbf{f}$ (dimension force per unit volume) are acting. The force density vectors depend only on the location $\mathbf{x}$: $\mathbf{f} = \mathbf{f}(\mathbf{x})$, see Fig. 2.4a. For this continuous force system, the mechanical equilibrium conditions, namely the force- and moment equilibrium in the static case read as[1]

$$\int_V \mathbf{f}(\mathbf{x})\, dV + \int_S \mathbf{T}(\mathbf{x}, \mathbf{n})\, dS = 0\,, \tag{2.40}$$

$$\int_V \mathbf{x} \times \mathbf{f}(\mathbf{x})\, dV + \int_S \mathbf{x} \times \mathbf{T}(\mathbf{x}, \mathbf{n})\, dS = 0\,. \tag{2.41}$$
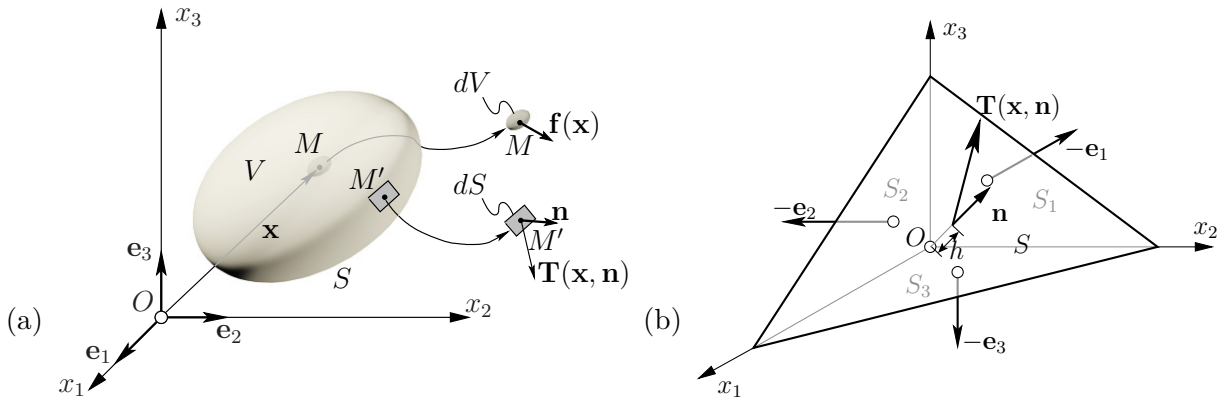
Fig. 2.4: (a) Volume forces $\mathbf{f}\,dV$ and surface forces $\mathbf{T}\,dS$, acting on a 3D continuum in the *deformed* configuration, and (b) Cauchy tetrahedron.

Based on the described continuous forces system, we want to obtain definitions of stresses and stress tensors, respectively. Consequently, we consider a tetrahedron with the following geometry:

---

[1]In the dynamic case (where the velocity of motions can not be neglected), Eqs. (2.40) and (2.41) must be extended to $\int_V \mathbf{f}(\mathbf{x})\, dV + \int_S \mathbf{T}(\mathbf{x}, \mathbf{n})\, dS = \int_V \rho \frac{\partial^2 \mathbf{x}}{\partial t^2}\, dV$ and $\int_V \mathbf{x} \times \mathbf{f}(\mathbf{x})\, dV + \int_S \mathbf{x} \times \mathbf{T}(\mathbf{x}, \mathbf{n})\, dS = \int_V \mathbf{x} \times \rho \frac{\partial^2 \mathbf{x}}{\partial t^2}\, dV$, respectively, with ρ as the mass density in point $\mathbf{x}$. These equilibrium conditions are only applicable, if the position vectors are measured in a spatially fixed or Galilean coordinate system.

Its three side faces S_i are orthogonal to the unit vectors $\mathbf{e}_i$, and the base area S is orthogonal to the unit normal vector $\mathbf{n} = n_1\mathbf{e}_1 + n_2\mathbf{e}_2 + n_3\mathbf{e}_3$. In this case, the side surfaces are functions of the base area, $S_i = Sn_i$, and the volume of the tetrahedron with height h is $V = \frac{1}{3}Sh$, see Fig. 2.4b. Specification of the force equilibrium (2.40) for the tetrahedron yields

$$\int_V \mathbf{f}(\mathbf{x})\,dV + \int_S \mathbf{T}(\mathbf{x},\mathbf{n})\,dS + \sum_{i=1}^{3} \int_{S_i} \mathbf{T}(\mathbf{x},-\mathbf{e}_i)\,dS_i = 0\,. \tag{2.42}$$

Subsequently, we use average surface- and volume forces, resulting in

$$\frac{1}{3}Sh\langle\mathbf{f}(\mathbf{x})\rangle_V + S\langle\mathbf{T}(\mathbf{x},\mathbf{n})\rangle_S + \sum_{i=1}^{3} S_i\langle\mathbf{T}(\mathbf{x},-\mathbf{e}_i)\rangle_S = 0\,. \tag{2.43}$$

Since the relation (2.43) has to be valid for any size of the tetrahedron, it is permissible to consider the boundary transition $h \to 0$. Then, all means remain finite, $\mathbf{x} \to 0$, and one obtains, using the *action-reaction-law* $\mathbf{T}(\mathbf{x},\mathbf{n}) = -\mathbf{T}(\mathbf{x},-\mathbf{n})$ and division by S

$$\mathbf{T}(0,\mathbf{n}) = \sum_{i=1}^{3} n_i\mathbf{T}(0,\mathbf{e}_i)\,. \tag{2.44}$$

In French and American literature, Eq. (2.44) is often called the *tetrahedron-lemma*. Eq. (2.44) defines an operation which *linearly* relates the traction forces acting on three mutually orthogonal surfaces with the components of the normal vector onto an arbitrarily oriented surface, in order to quantify the traction vector acting on this surface. This multilinear function induces the existence of the so-called (symmetric) *Cauchy stress tensor* $\boldsymbol{\sigma}$ in the context of the operation

$$\mathbf{T}(\mathbf{n}) = \boldsymbol{\sigma}\cdot\mathbf{n}\,, \tag{2.45}$$

where the second-order tensor $\boldsymbol{\sigma}$ links the normal vector $\mathbf{n}$ to the traction vector $\mathbf{T}$ in a multilinear manner by means of an inner product. In German literature, Eq. (2.45) is often called *Cauchy's formula.*

As an alternative to the formulation of the equilibrium on the entire body (2.40), we derive a so-called equilibrium condition at the level of a single material point $\mathbf{x}$. In this context, use of Cauchy's formula (2.45) in equilibrium condition (2.40), as well as use of Gauss's divergence theorem[2] yields

$$\int_V [\mathbf{f}(\mathbf{x}) + \mathrm{div}\boldsymbol{\sigma}(\mathbf{x})]\,dV = 0\,, \tag{2.46}$$

where the divergence theorem for the second-order tensor $\boldsymbol{\sigma}$ for an orthonormal basic system $\mathbf{e}_1$, $\mathbf{e}_2$, $\mathbf{e}_3$, is defined as follows

$$\int_V \mathrm{div}\boldsymbol{\sigma}\,dV = \int_V \sum_{i=1}^{3}\sum_{j=1}^{3} \frac{\partial\sigma_{ij}}{\partial x_j}\,\mathbf{e}_i\,dV = \int_S \sum_{i=1}^{3}\sum_{j=1}^{3} \sigma_{ij}\cdot n_j\,\mathbf{e}_i\,dS = \int_S \boldsymbol{\sigma}\cdot\mathbf{n}\,dS\,. \tag{2.47}$$

---

[2]The theorem was first documented by Joseph-Louis Lagrange in 1762 and then later independently rediscovered by the mathematician Carl Friedrich Gauss (1777-1855) in 1813.

Since Eq. (2.46) is valid for any size of a continuum, the integrand in (2.46) must vanish, and we obtain the so-called *local equilibrium condition*[3]

$$\mathbf{f}(\mathbf{x}) + \text{div}\boldsymbol{\sigma}(\mathbf{x}) = 0\,. \tag{2.48}$$

In transition to components of an orthonormal basis $\mathbf{e}_1$, $\mathbf{e}_2$, $\mathbf{e}_3$, the equilibrium condition in notation of components reads as

$$f_1 + \frac{\partial \sigma_{11}}{\partial x_1} + \frac{\partial \sigma_{12}}{\partial x_2} + \frac{\partial \sigma_{13}}{\partial x_3} = 0\,, \tag{2.49}$$

$$f_2 + \frac{\partial \sigma_{21}}{\partial x_1} + \frac{\partial \sigma_{22}}{\partial x_2} + \frac{\partial \sigma_{23}}{\partial x_3} = 0\,, \tag{2.50}$$

$$f_3 + \frac{\partial \sigma_{31}}{\partial x_1} + \frac{\partial \sigma_{32}}{\partial x_2} + \frac{\partial \sigma_{33}}{\partial x_3} = 0\,. \tag{2.51}$$

2.2.2 Symmetry of the stress tensor – interpretation of stress tensor components

Finally, we want to prove the symmetry of the Cauchy stress tensor. In this context, we refer to the moment equilibrium condition (2.41) in notation of components of an orthogonal basis $\mathbf{e}_1$, $\mathbf{e}_2$, $\mathbf{e}_3$

$$
\begin{aligned}
\left[\int_V (x_2 f_3 - x_3 f_2) dV + \int_S (x_2 T_3 - x_3 T_2) dS\right] \mathbf{e}_1 \quad & + \\
\left[\int_V (x_3 f_1 - x_1 f_3) dV + \int_S (x_3 T_1 - x_1 T_3) dS\right] \mathbf{e}_2 \quad & + \\
\left[\int_V (x_1 f_2 - x_2 f_1) dV + \int_S (x_1 T_2 - x_2 T_1) dS\right] \mathbf{e}_3 \quad & = \quad 0\,,
\end{aligned}
\tag{2.52}
$$

which requires, that the three expressions in the brackets are equal to zero. In the following, we regard to the multiplier of $\mathbf{e}_1$: Use of Cauchy's formula (2.45), and the local force equilibrium conditions (2.50) and (2.51), as well as use of Gauss's divergence theorem yields

$$
\begin{aligned}
0 = \int_V \Big(-x_2 \frac{\partial \sigma_{31}}{\partial x_1} - x_2 \frac{\partial \sigma_{32}}{\partial x_2} - x_2 \frac{\partial \sigma_{33}}{\partial x_3} + x_3 \frac{\partial \sigma_{21}}{\partial x_1} + x_3 \frac{\partial \sigma_{22}}{\partial x_2} + x_3 \frac{\partial \sigma_{23}}{\partial x_3} \\
+ x_2 \frac{\partial \sigma_{31}}{\partial x_1} + \sigma_{32} + x_2 \frac{\partial \sigma_{32}}{\partial x_2} + x_2 \frac{\partial \sigma_{33}}{\partial x_3} - x_3 \frac{\partial \sigma_{21}}{\partial x_1} - x_3 \frac{\partial \sigma_{22}}{\partial x_2} - \sigma_{23} - x_3 \frac{\partial \sigma_{23}}{\partial x_3} \Big) dV\,.
\end{aligned}
\tag{2.53}
$$

Since Eq. (2.53) is valid for any size of a continuum, the integrand must vanish, and we obtain

$$\sigma_{23} = \sigma_{32}\,. \tag{2.54}$$

Analogous transformations of the multipliers of $\mathbf{e}_2$ and $\mathbf{e}_3$ in (2.52) delivers

$$\sigma_{13} = \sigma_{31} \quad \text{and} \quad \sigma_{12} = \sigma_{21}\,, \tag{2.55}$$

which allows us to write in general

$$\boldsymbol{\sigma} = \boldsymbol{\sigma}^T \quad \text{or} \quad \sigma_{ij} = \sigma_{ji} \quad \forall i \neq j\,. \tag{2.56}$$

Hence, in the pure mechanical case, we can state that the Cauchy stress tensor is *symmetric*.

---

[3]In the dynamic case (where the velocity of motions can not be neglected), Eq. (2.48) must be extended to $\mathbf{f}(\mathbf{x}) + \text{div}\boldsymbol{\sigma}(\mathbf{x}) = \rho \frac{\partial^2 \mathbf{x}}{\partial t^2}$.

After the derivation of the continuous force system, including volume forces, traction forces, as well as the characteristics of the Cauchy stress tensor, we want to provide the interpretation of the six independent components of the Cauchy stress tensor (symmetric second-order tensor), namely σ_{11}, $\sigma_{12} = \sigma_{21}$, $\sigma_{13} = \sigma_{31}$, σ_{22}, $\sigma_{23} = \sigma_{32}$ and σ_{33}. This interpretation follows from the specification of the Cauchy's formula for the directions of the basis vectors $\mathbf{e}_1$, $\mathbf{e}_2$ and $\mathbf{e}_3$. Thus, evaluation of (2.45) for $\mathbf{n} = \mathbf{e}_1$ yields

$$\mathbf{T}(\mathbf{e}_1) = \boldsymbol{\sigma} \cdot \mathbf{e}_1 \quad = \quad \sigma_{11}\mathbf{e}_1 + \sigma_{21}\mathbf{e}_2 + \sigma_{31}\mathbf{e}_3 \,. \tag{2.57}$$

In other words, Eq. (2.57) states, that the components of the Cauchy stress tensor with suffix "1": σ_{i1} denote the components of the traction vector $\mathbf{T}$ acting on the surface element with the normal direction $\mathbf{e}_1$, see Fig. 2.5. In analogy, the components of the Cauchy stress tensor with suffix "2": σ_{i2} and suffix "3": σ_{i3}, can be interpreted as the components of the traction vector acting on the surface element with the normal direction $\mathbf{e}_2$, and $\mathbf{e}_3$, respectively, see Fig. 2.5

$$\mathbf{T}(\mathbf{e}_2) = \boldsymbol{\sigma} \cdot \mathbf{e}_2 \quad = \quad \sigma_{12}\mathbf{e}_1 + \sigma_{22}\mathbf{e}_2 + \sigma_{32}\mathbf{e}_3 \,, \tag{2.58}$$

$$\mathbf{T}(\mathbf{e}_3) = \boldsymbol{\sigma} \cdot \mathbf{e}_3 \quad = \quad \sigma_{13}\mathbf{e}_1 + \sigma_{23}\mathbf{e}_2 + \sigma_{33}\mathbf{e}_3 \,. \tag{2.59}$$
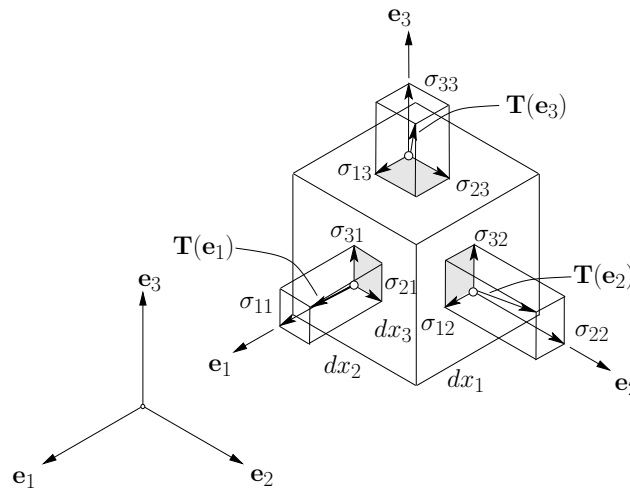
Fig. 2.5: Interpretation of the components of the Cauchy stress tensor.

2.3 The Principle of Virtual Power

The *Principle of Virtual Power* (PVP) is a versatile and safe method for the formulation of complex structural theories of continua. For the pure mechanical case, we can provide a short derivation in the following way: Our starting point is the investigation of power characteristics of forces in equilibrium, acting on a continuous body. Thus, an continuous system of volume forces $\mathbf{f}$ and surface forces $\mathbf{T}$ perform virtual power $\mathcal{P}$ along *geometrically compatible*[4] virtual velocities $\hat{\mathbf{v}}$, reading as

$$\mathcal{P} = \int_V \mathbf{f}(\mathbf{x}) \cdot \hat{\mathbf{v}}(\mathbf{x}) \, dV + \int_S \mathbf{T}(\mathbf{x}, \mathbf{n}) \cdot \hat{\mathbf{v}}(\mathbf{x}) \, dS \,, \tag{2.60}$$

---

[4]Geometrically compatible means that all points of a body can only move in such a way that neighbor points remain neighbors after deformation of the body.

representing the power of forces acting in a *deformed* continuum, see Fig. 2.6. In order to obtain
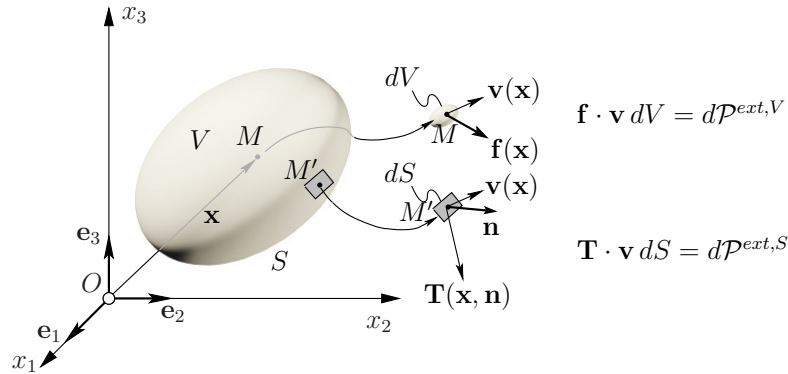
Fig. 2.6: Power of volume- and surface forces, acting on a 3D continuum in the *deformed* configuration.

the so-called Principle of Virtual Power, we reformulate the power expression (2.60): Use of Cauchy's formula (2.45) and Gauss's divergence theorem yields

$$\mathcal{P} = \int_V \left(\mathbf{f} \cdot \hat{\mathbf{v}} + \mathrm{div}(\hat{\mathbf{v}} \cdot \boldsymbol{\sigma}) \right) dV = \int_V \left(\mathbf{f} \cdot \hat{\mathbf{v}} + \mathrm{grad}\hat{\mathbf{v}} : \boldsymbol{\sigma} + \hat{\mathbf{v}} \cdot \mathrm{div}\boldsymbol{\sigma} \right) dV \,. \qquad (2.61)$$

Taking into account the local equilibrium condition (2.48), as well as the relation deriving from the symmetry of the Cauchy stress tensor ($\mathrm{grad}\hat{\mathbf{v}} : \boldsymbol{\sigma} = \boldsymbol{\sigma} : \hat{\mathbf{d}}$), delivers the remarkable expression

$$\mathcal{P} = \int_V \boldsymbol{\sigma} : \hat{\mathbf{d}} \, dV \,, \qquad (2.62)$$

with $\hat{\mathbf{d}}$ as the (virtual) *Eulerian strain rate tensor*

$$\hat{\mathbf{d}} = \nabla^S \hat{\mathbf{v}} = \frac{1}{2} \left[\frac{\partial \hat{\mathbf{v}}}{\partial \mathbf{x}} + \left(\frac{\partial \hat{\mathbf{v}}}{\partial \mathbf{x}} \right)^T \right] \,, \qquad (2.63)$$

named after the mathematician Leonhard Euler (1707-1783). Equating the power expressions (2.60) and (2.62), which are called virtual power of external forces and virtual power of internal forces, respectively, results in the sought Principle of Virtual Power in the (deformed) Eulerian representation. The provided format of this principle was also provided by the modern French engineering mechanics schools, as documented by Paul Germain (1920–2009) and Gérard A. Maugin (1944-2016). Summarizing, for a standard 3D solid continuum in the mechanical and static case, the Principle of Virtual Power [Germain, 1972, 1973a,b; Maugin, 2013; Salençon, 2001] reads as

$$\mathcal{P}^{ext} + \mathcal{P}^{int} = 0 \,, \qquad (2.64)$$

with

$$\mathcal{P}^{ext} = +\int_V \mathbf{f}(\mathbf{x}) \cdot \hat{\mathbf{v}}(\mathbf{x}) \, dV + \int_S \mathbf{T}(\mathbf{x}, \mathbf{n}) \cdot \hat{\mathbf{v}}(\mathbf{x}) \, dS \,, \qquad (2.65)$$

$$\mathcal{P}^{int} = -\int_V \boldsymbol{\sigma} : \hat{\mathbf{d}} \, dV \,, \qquad (2.66)$$

where $\mathcal{P}^{ext}$ and $\mathcal{P}^{int}$ denote the virtual power of the external forces and the virtual power of the internal forces, respectively; $\mathbf{x}$ denotes the location vectors throughout the deformed continuum and at its boundaries with outward normals $\mathbf{n}$; $\mathbf{f}$ denotes volume forces; $\mathbf{T}$ denotes traction (surface) forces; $\hat{\mathbf{v}}$ denotes the virtual velocity; $\boldsymbol{\sigma}$ denotes the Cauchy stress tensor; $\hat{\mathbf{d}}$ denotes the virtual Eulerian strain rate; and the operator ":" denotes the second-order tensor contraction[5].

In the case, that displacements are not small in comparison to the measurements of the continuum, we have to formulate strains, surface forces, volume forces and stresses as a function of the particle position vector $\mathbf{X}$ in the *undeformed configuration* (Lagrangian representation). In order to formulate the Principle of Virtual Power in the *undeformed* configuration, we relate the Eulerian strain rate with the rate of the Green-Lagrange strain tensor,[6]

$$\hat{\mathbf{d}}(\mathbf{x}, t) = \mathbf{F}^{-T} \cdot \dot{\hat{\mathbf{E}}}(\mathbf{X}, t) \cdot \mathbf{F}^{-1}, \tag{2.67}$$

where $\mathbf{F}$ is the deformation gradient, see (2.4). Use of (2.67) in the expression of the virtual power of internal forces (2.66), and considering the volume change (2.27), yields

$$-\int_V \boldsymbol{\sigma} : \hat{\mathbf{d}}(\mathbf{x}, t) \, dV = -\int_{V_0} \boldsymbol{\sigma} : \mathbf{F}^{-T} \cdot \dot{\hat{\mathbf{E}}}(\mathbf{X}, t) \cdot \mathbf{F}^{-1} J \, dV_0 = -\int_{V_0} J \mathbf{F}^{-1} \cdot \boldsymbol{\sigma} \cdot \mathbf{F}^{-T} : \dot{\hat{\mathbf{E}}} \, dV_0 , \tag{2.68}$$

where $J = \det\mathbf{F}$ is the Jacobi-determinant. The multiplier of $\dot{\mathbf{E}}$ in (2.68) is called *second Piola-Kirchhoff stress tensor*

$$\boldsymbol{\pi} = J \mathbf{F}^{-1} \cdot \boldsymbol{\sigma} \cdot \mathbf{F}^{-T}, \tag{2.69}$$

named after the mathematician Gabrio Piola (1794-1850) and physicist Gustav Robert Kirchhoff (1824–1887). It is noted, that the stress tensor $\boldsymbol{\pi}$ is *symmetric*, due to the inner products of the two unsymmetrical deformation gradients and the symmetric Cauchy stress tensor. Hence, the virtual power of the internal forces with respect to the undeformed position reads as

$$\mathcal{P}^{int} = -\int_{V_0} \boldsymbol{\pi} : \dot{\hat{\mathbf{E}}} \, dV_0 . \tag{2.70}$$

Next, we want to express the virtual power of external forces in the Lagrangian representation: The virtual power of external volume forces related to the undeformed configuration, using (2.1) and (2.27), reads as

$$\int_V \mathbf{f}(\mathbf{x}) \cdot \hat{\mathbf{v}} \, dV = \int_{V_0} \mathbf{f}[\boldsymbol{\varphi}(\mathbf{X})] \cdot \hat{\mathbf{v}} \, J \, dV_0 \quad \text{with} \quad dV = J dV_0 , \tag{2.71}$$

where $\mathbf{f}[\boldsymbol{\varphi}(\mathbf{X})]$ denotes the field of the volume forces, which is transformed from the the deformed to the undeformed continuum. Based on Cauchy's formula (2.45) as well as on the geometric relation $\mathbf{n} \, dS = J \mathbf{F}^{-T} \cdot \mathbf{N} \, dS_0$, with $\mathbf{N}$ as the unit vector pointing outwards and orthogonal to

---

[5]The second-order tensor contraction is indicated by the symbol ":" and assigns two second-order tensors, $\mathbf{A}$ and $\mathbf{B}$ to a scalar λ, in the format $\mathbf{A} : \mathbf{B} = \sum_{i=1}^3 \sum_{j=1}^3 A_{ij} B_{ij} = \lambda$ for an orthogonal basis $\mathbf{e}_1$, $\mathbf{e}_2$, $\mathbf{e}_3$. The second-order tensor contraction is also called inner product of two second-order tensors.

[6]The existence of Eq. (2.67) can be proved by inverse calculation of the rate of the Green-Lagrange strain tensor, $\dot{\mathbf{E}} = \frac{1}{2} \left[\frac{\partial \mathbf{v}}{\partial \mathbf{X}} + \left(\frac{\partial \mathbf{v}}{\partial \mathbf{X}} \right)^T + \left(\frac{\partial \mathbf{v}}{\partial \mathbf{X}} \right)^T \cdot \frac{\partial \mathbf{u}}{\partial \mathbf{X}} + \left(\frac{\partial \mathbf{u}}{\partial \mathbf{X}} \right)^T \frac{\partial \mathbf{v}}{\partial \mathbf{X}} \right]$. This is done by substitution of the deformation gradient, $\mathbf{F} = \frac{\partial \mathbf{x}}{\partial \mathbf{X}}$ and of the Eulerian strain rate $\mathbf{d} = \frac{1}{2} \left[\frac{\partial \mathbf{v}}{\partial \mathbf{x}} + \left(\frac{\partial \mathbf{v}}{\partial \mathbf{x}} \right)^T \right]$ into $\dot{\mathbf{E}} = \mathbf{F}^T \cdot \mathbf{d} \cdot \mathbf{F}$ resulting in $\dot{\mathbf{E}} = \frac{1}{2} \left[\frac{\partial \mathbf{v}}{\partial \mathbf{X}} \cdot \left(\frac{\partial \mathbf{x}}{\partial \mathbf{X}} \right)^T + \left(\frac{\partial \mathbf{v}}{\partial \mathbf{X}} \right)^T \cdot \frac{\partial \mathbf{x}}{\partial \mathbf{X}} \right]$, with $\mathbf{x} = \mathbf{u} + \mathbf{X}$.

the undeformed surface element dS_0, the virtual power of external surface forces related to the undeformed configuration reads as

$$\int_S \mathbf{T}\cdot\hat{\mathbf{v}}\,dS = \int_S \boldsymbol{\sigma}\cdot\mathbf{n}\cdot\hat{\mathbf{v}}\,dS = \int_{S_0} J\,\boldsymbol{\sigma}\cdot\mathbf{F}^{-T}\cdot\mathbf{N}\cdot\hat{\mathbf{v}}\,dS_0 = \int_{S_0}\mathbf{F}\cdot\boldsymbol{\pi}\cdot\mathbf{N}\cdot\hat{\mathbf{v}}\,dS_0 = \int_{S_0}\mathbf{F}\cdot\boldsymbol{\mathcal{T}}\cdot\hat{\mathbf{v}}\,dS_0\,, \quad (2.72)$$

taking into account the definition (2.69) of the second Piola-Kirchhoff tensor $\boldsymbol{\pi}$, as well as the definition of the so-called *Piola-Lagrange traction* $\boldsymbol{\mathcal{T}} = \boldsymbol{\pi}\cdot\mathbf{N}$, in analogy to Cauchy's formula (2.45). Thus, in Lagrangian representation, the Principle of Virtual Power of external forces reads as:

$$\mathcal{P}^{ext} = \int_{V_0}\mathbf{f}[\boldsymbol{\varphi}(\mathbf{X})]\cdot\hat{\mathbf{v}}\,J\,dV_0 + \int_{S_0}\mathbf{F}\cdot\boldsymbol{\mathcal{T}}\cdot\hat{\mathbf{v}}\,dS_0\,. \quad (2.73)$$

Finally, we obtain the formulation of the Principle of Virtual Power in Lagrangian representation:

$$\mathcal{P}^{ext} + \mathcal{P}^{int} = 0\,, \quad (2.74)$$

with

$$\mathcal{P}^{ext} = +\int_{V_0}\mathbf{f}[\boldsymbol{\varphi}(\mathbf{X})]\cdot\hat{\mathbf{v}}\,J\,dV_0 + \int_{S_0}\mathbf{F}\cdot\boldsymbol{\mathcal{T}}\cdot\hat{\mathbf{v}}\,dS_0\,, \quad (2.75)$$

$$\mathcal{P}^{int} = -\int_{V_0}\boldsymbol{\pi}:\dot{\hat{\mathbf{E}}}\,dV_0\,. \quad (2.76)$$

2.4 Thermodynamics

Very often, the work which is put into a solid body is not entirely stored as elastic energy, i.e. it can not be recovered completely in the form of mechanical work. The work is only partly stored as elastic energy, the rest of the work is transformed into another type of energy, namely heat energy (such heat can also be applied directly to the body).

2.4.1 Law of energy conservation, entropy and dissipation − small deformations

For small deformations (and small rigid body movements), the position, shape and volume of a body change only insignificantly during the transition from the reference- in the current configuration. The same applies to all infinitesimal volume elements $dV(\mathbf{x})$ that enclose a material point located at position $\mathbf{x}$, with $dV(\mathbf{x}) \approx dV_0(\mathbf{X})$. Thus, the context $\psi = \psi(\mathbf{x})$ clarifies that the energy density characterizes a material point in the geometric point $\mathbf{x}$. First, we start with the thermodynamical description in the deformed configuration (Eulerian representation). The conservation of all forms of energy in the case of electromagnetic deformable continua is formulated as follows (*first law of thermodynamics*): mechanical work, electromagnetic energy, and heat given to a body per unit time is equal to the increase of its *internal energy* E[7]

$$\dot{E} = \int_V \dot{e}\,dV = \int_V \mathbf{f}\cdot\mathbf{v}\,dV + \int_S \mathbf{T}\cdot\mathbf{v}\,dS - \int_S \mathbf{q}\cdot\mathbf{n}\,dS + \int_V r\,dV\,, \quad (2.77)$$

where e is the internal energy density; r is the per unit volume and per time Eulerian heat supply; and $\mathbf{q}$ is the heat flux vector (heat per unit area) in the Eulerian representation. Use of the Principle of Virtual Power (2.64)-(2.66) assuming small displacement derivatives so that $\mathbf{d} \approx \dot{\boldsymbol{\varepsilon}}$,

---

[7]For small deformations, we can state that $\dot{E} = \frac{D}{Dt}\int_V e\,dV = \int_V \dot{e}\,dV$ because of the insignificant volume change $\dot{dV} = 0$. On the other hand, if the deformations are not small, the rate of the internal energy can be determined by means of internal energies per unit mass.

as well as the divergence theorem, allows the reformulation of (2.77) for any body (integrands must vanish)

$$\dot{e} = \boldsymbol{\sigma} : \dot{\boldsymbol{\varepsilon}} - \text{div}\mathbf{q} + r\,, \tag{2.78}$$

which is called the local form of the *law of energy conservation* in Eulerian representation.

Thereby, the conversion of heat energy into effective mechanical energy is limited, which is expressed by the *second law of thermodynamics*: The rate of the internal entropy S is greater or equal to the externally supplied entropy (heat per absolute temperature)

$$\frac{\partial S}{\partial t} = \int_V \dot{s}\, dV \geq \int_V \frac{r}{T}\, dV - \int_S \frac{\mathbf{q} \cdot \mathbf{n}}{T}\, dS\,, \tag{2.79}$$

where s is the internal entropy density, and T is the absolute Temperature. Use of the divergence theorem, allows the reformulation of (2.79) for any body (integrands must vanish) yielding the *local form of the second law of thermodynamics*

$$\dot{s} + \text{div}\left(\frac{\mathbf{q}}{T}\right) - \frac{r}{T} \geq 0\,. \tag{2.80}$$

Evaluation of the divergence term according to the differentiation rule for quotients and multiplication by the absolute temperature T yields

$$T\dot{s} + \text{div}\mathbf{q} - \frac{\mathbf{q}}{T} \cdot \text{grad}T - r \geq 0\,. \tag{2.81}$$

Now, we link the local forms of the second law of thermodynamics (2.81) and first law of thermodynamics (2.78), by expressing the heat supply terms $(r - \text{div}\mathbf{q})$ by internal energy changes and external work

$$\boldsymbol{\sigma} : \dot{\boldsymbol{\varepsilon}} + T\dot{s} - \dot{e} - \frac{\mathbf{q}}{T} \cdot \text{grad}T \geq 0\,. \tag{2.82}$$

The internal energy density can be split into a part which can be changed back into effective mechanical energy, the *Helmholtz[8] free energy density* ψ, and an energy component sT, which is only in heat form

$$e = \psi + Ts\,. \tag{2.83}$$

Energy differentiation (2.83) allows us to attribute the energy inequality (2.82) as a function of the free energy density ψ

$$\phi = \boldsymbol{\sigma} : \dot{\boldsymbol{\varepsilon}} - \dot{\psi} - s\dot{T} - \frac{\mathbf{q}}{T} \cdot \text{grad}T \geq 0\,. \tag{2.84}$$

This inequality is called *Clausius-Duhem inequality* (dissipation inequality) in reference to Rudolf Clausius (1822-1888) and Pierre Duhem (1861-1916). In (2.84), the positive semidefinite quantity ϕ is the *dissipation*, which is the energy per unit of time, which is irreversibly converted from effective mechanical energy into heat.

2.4.2 Thermoelasticity for small deformations

The material behavior is now described by the form of the free energy density ψ, which is a function of so-called *state variables*. In the case of thermoelasticity, there are two such

---

[8]The physician and physicist Hermann von Helmholtz (1821-1894) introduced the term "free energy" in 1883.

state variables, namely the linearized strain tensor $\boldsymbol{\varepsilon}$ (as before we assume small displacement derivatives) and the absolute temperature T.

$$\psi = \psi(\boldsymbol{\varepsilon}, T). \tag{2.85}$$

Use of the dependence (2.85), the dissipation inequality (2.84) can be reformulated as follows

$$\phi = \boldsymbol{\sigma} : \dot{\boldsymbol{\varepsilon}} - \frac{\partial \psi}{\partial \boldsymbol{\varepsilon}} \dot{\boldsymbol{\varepsilon}} - \frac{\partial \psi}{\partial T} \dot{T} - s\dot{T} - \frac{\mathbf{q}}{T} \cdot \mathrm{grad}T \geq 0. \tag{2.86}$$

This inequality must be valid for any evolutions of the linearized strain tensor $\boldsymbol{\varepsilon}$ and of the absolute temperature T (and temperature gradients). Therefore, the fulfillment of the dissipation inequality (2.86) implies that,

$$\boldsymbol{\sigma} = \frac{\partial \psi}{\partial \boldsymbol{\varepsilon}}(\boldsymbol{\varepsilon}, T), \qquad s = -\frac{\partial \psi}{\partial T}(\boldsymbol{\varepsilon}, T). \tag{2.87}$$

In light of small strains, $\|\boldsymbol{\varepsilon}\| \ll 1$, and small temperature changes around T_0, $|(T - T_0)/T_0| \ll 1$, we perform a Taylor series expansion of $\boldsymbol{\sigma}$ $(2.87)_1$ about $\boldsymbol{\varepsilon} = 0$ and $T = T_0$, where at most linear terms are considered

$$\boldsymbol{\sigma} \approx \frac{\partial^2 \psi}{\partial \boldsymbol{\varepsilon} \partial \boldsymbol{\varepsilon}} : \boldsymbol{\varepsilon} + \frac{\partial^2 \psi}{\partial \boldsymbol{\varepsilon} \partial T}(T - T_0). \tag{2.88}$$

For isothermal states, $T = T_0$, we see that the the tensor of fourth order, $\partial^2\psi/\partial\boldsymbol{\varepsilon}\partial\boldsymbol{\varepsilon}$, is the so-called linear elasticity tensor $\mathbb{C}$, i.e. the any stress tensor can be expressed by the corresponding strain tensor and vice versa. For constrained strains, $\boldsymbol{\varepsilon} = 0$, temperature changes induce so-called thermal stresses, which are the result of temperature-induced strains

$$\boldsymbol{\varepsilon}_T = \boldsymbol{\alpha}_T(T - T_0), \tag{2.89}$$

with $\boldsymbol{\alpha}_T$ being the a second order tensor with components $\alpha_{T,ij}$, which are called thermal expansion coefficients. Hence, the total strain tensor consists of stress-induced and temperature-induced strains, reading as

$$\boldsymbol{\varepsilon} = \mathbb{C}^{-1} : \boldsymbol{\sigma} + \boldsymbol{\alpha}_T(T - T_0), \tag{2.90}$$

where the second energy derivative in (2.88) is identified as, $\partial^2\psi/\partial\boldsymbol{\varepsilon}\partial T = -\mathbb{C} : \boldsymbol{\alpha}_T$. On the other hand, the stress tensor is a function of the total strains and of the temperature-induced strains

$$\boldsymbol{\sigma} = \mathbb{C} : [\boldsymbol{\varepsilon} - \boldsymbol{\alpha}_T(T - T_0)], \tag{2.91}$$

which is called linear thermoelastic *generalized Hooke's law*. In the case of an isotropic material behavior, (2.91) reads as (in Kelvin-Mandel matrix-vector notation)

$$\begin{pmatrix} \sigma_{11} \\ \sigma_{22} \\ \sigma_{33} \\ \sqrt{2}\sigma_{23} \\ \sqrt{2}\sigma_{13} \\ \sqrt{2}\sigma_{12} \end{pmatrix} = \frac{E}{(1+\nu)} \begin{pmatrix} \frac{1-\nu}{1-2\nu} & \frac{\nu}{1-2\nu} & \frac{\nu}{1-2\nu} & 0 & 0 & 0 \\ \frac{\nu}{1-2\nu} & \frac{1-\nu}{1-2\nu} & \frac{\nu}{1-2\nu} & 0 & 0 & 0 \\ \frac{\nu}{1-2\nu} & \frac{\nu}{1-2\nu} & \frac{1-\nu}{1-2\nu} & 0 & 0 & 0 \\ 0 & 0 & 0 & 1 & 0 & 0 \\ 0 & 0 & 0 & 0 & 1 & 0 \\ 0 & 0 & 0 & 0 & 0 & 1 \end{pmatrix} \begin{pmatrix} \varepsilon_{11} - \alpha_T(T - T_0) \\ \varepsilon_{22} - \alpha_T(T - T_0) \\ \varepsilon_{33} - \alpha_T(T - T_0) \\ \sqrt{2}\varepsilon_{23} \\ \sqrt{2}\varepsilon_{13} \\ \sqrt{2}\varepsilon_{12} \end{pmatrix}. \tag{2.92}$$

with E and ν being the elastic Young's modulus and Poisson's ratio, respectively.

2.4.3 Material behavior in the case of large deformations − hyperelasticity

In the case of large deformations, the statement of insignificant changes in position, shape and volume of a body (as mentioned in Section 2.4.1) is no longer valid: A material point (described by an energy state ψ) moves from the geometric point $\mathbf{X}$ in the reference configuration to the geometric point $\mathbf{x}$ in the current configuration; and the enclosing infinitesimal volume element is also subjected to change, from $dV_0(\mathbf{X})$ to $dV(\mathbf{x})$. However, one quantity which remains *constant* during large deformations is the *mass* („conservation of mass"). Hence, for the mass element dm (corresponding to the material volume element), we can state

$$dm = \rho_0(\mathbf{X})\, dV_0 = \rho(\mathbf{x}, t)\, dV = \rho(\mathbf{x}, t)\, J\, dV_0\,, \tag{2.93}$$

with ρ as the actual volumetric mass density; ρ_0 as the initial volumetric mass density; and J as the Jacobi-determinant regarding to the identity for volume changes (2.27). Eq. (2.93) indicates the following relations

$$J = \frac{dV}{dV_0} = \frac{\rho_0}{\rho}\,. \tag{2.94}$$

Obviously, it makes sense not to assign the elastic energy density to a (variable) volume element but rather to a constant mass element – in other words, we make a transition from a volumetric density („energy per volume") to a gravimetric density („energy per mass"). The (gravimetric) specific Helmholtz free energy density will be denoted by ψ_m, being defined as

$$\frac{\psi(\mathbf{x})}{\rho(\mathbf{x})} = \psi_m(\mathbf{x})\,. \tag{2.95}$$

In analogy, we also introduce a specific internal energy density $e_m(\mathbf{x})$, a specific internal entropy density $s_m(\mathbf{x})$, and a specific dissipation $\phi_m(\mathbf{x})$, in the form:

$$\frac{e(\mathbf{x})}{\rho(\mathbf{x})} = e_m(\mathbf{x}), \qquad \frac{s(\mathbf{x})}{\rho(\mathbf{x})} = s_m(\mathbf{x}), \qquad \frac{\phi(\mathbf{x})}{\rho(\mathbf{x})} = \phi_m(\mathbf{x})\,. \tag{2.96}$$

Use of these new quantities and restriction to isothermal, dissipation-free states, the first law of thermodynamics (2.77) can be reformulated as follows[9]

$$\dot{E} = \int_{V_0} \rho_0\, \dot{e}_m\, dV_0 = \int_{V_0} \mathbf{f}[\boldsymbol{\varphi}(\mathbf{X})] \cdot \mathbf{v}\, J\, dV_0 + \int_{S_0} \mathbf{F} \cdot \boldsymbol{\mathcal{T}} \cdot \mathbf{v}\, dS_0\,. \tag{2.97}$$

Substitution of the Principle of Virtual Power (2.74)-(2.76) into (2.97) yields the local form of the first law of thermodynamics in Lagrangian representation (integrands must vanish)

$$\rho_0\, \dot{e}_m = \boldsymbol{\pi} : \dot{\mathbf{E}}\,. \tag{2.98}$$

Since for isothermal states the entropy density is not taken into account, the free energy density is equal to the internal energy density $\psi_m = e_m$, resulting in the following Clausius-Duhem inequality

$$\phi = \rho\, \phi_m = \boldsymbol{\pi} : \dot{\mathbf{E}} - \rho_0\, \dot{\psi}_m = 0\,. \tag{2.99}$$

---

[9]For deformations with significant volume changes ($\dot{dV} \neq 0$), the identitiy $\dot{E} = \int_{V_0} \rho_0\, \dot{e}_m\, dV_0$ can be proved as follows: Use of the identity of the volume change (2.94) in the definition of the rate of the internal energy, $\dot{E} = \frac{D}{Dt} \int_V e\, dV = \frac{D}{Dt} \int_V \rho\, e_m\, dV$, results in $\dot{E} = \frac{D}{Dt} \int_{V_0} \rho_0\, e_m\, dV_0$. Since the rate of the initial volume dV_0 and initial mass density ρ_0 is zero, we easily obtain $\dot{E} = \int_{V_0} \rho_0\, \dot{e}_m\, dV_0$.

The free energy density ψ_m is a thermodynamic state variable and therefore must not depend on time or on time rates of other quantities. Thus, the condition (2.99) can be satisfied by the form $\psi = \psi(\mathbf{E})$,

$$\boldsymbol{\pi} : \dot{\mathbf{E}} - \rho_0 \frac{\partial \psi_m(\mathbf{E})}{\partial \mathbf{E}} : \dot{\mathbf{E}} = 0 \,. \tag{2.100}$$

Validity of (2.100) for all time rates $\dot{\mathbf{E}}$ delivers the *material law of hyperelasticity* reading as:

$$\boldsymbol{\pi} = \rho_0 \frac{\partial \psi_m(\mathbf{E})}{\partial \mathbf{E}} \,. \tag{2.101}$$

2.5 Remarks to objectivity of some quantities in continuum mechanics

Objective vectors, tensors as well as objective time rates are important for the formulation of constitutive equations. In other words, these fundamental equations have to be independent of the movement of an *observer*. A physical quantity is called objective or frame-indifferent, if two observers, $\mathcal{O}$ and $\mathcal{O}'$ (performing measurements relative to the basis systems $\mathbf{e}_1$, $\mathbf{e}_2$, $\mathbf{e}_3$ and $\mathbf{e}'_1$, $\mathbf{e}'_2$, $\mathbf{e}'_3$), obtain numerical results, which can be transformed in the same manner as the components of the corresponding quantities from basis $\mathbf{e}_1$, $\mathbf{e}_2$, $\mathbf{e}_3$ to basis $\mathbf{e}'_1$, $\mathbf{e}'_2$, $\mathbf{e}'_3$. In the case of a scalar quantity, we trivially obtain the same results measured by both observers, with $a' = a$. For vectors, the components $\mathcal{V}_1$, $\mathcal{V}_2$, $\mathcal{V}_3$, measured by observer $\mathcal{O}$ in basis system $\mathbf{e}_1$, $\mathbf{e}_2$, $\mathbf{e}_3$ have to be related to the components $\mathcal{V}'_1$, $\mathcal{V}'_2$, $\mathcal{V}'_3$, measured by observer $\mathcal{O}'$ in basis system $\mathbf{e}'_1$, $\mathbf{e}'_2$, $\mathbf{e}'_3$, according to the component transformation rule for vectors:

$$\begin{pmatrix} \mathcal{V}'_1 \\ \mathcal{V}'_2 \\ \mathcal{V}'_3 \end{pmatrix}_{\mathbf{e}'_1, \mathbf{e}'_2, \mathbf{e}'_3} = \mathbf{Q} \cdot \begin{pmatrix} \mathcal{V}_1 \\ \mathcal{V}_2 \\ \mathcal{V}_3 \end{pmatrix}_{\mathbf{e}_1, \mathbf{e}_2, \mathbf{e}_3} \qquad \Leftrightarrow \qquad \boldsymbol{\mathcal{V}}' = \mathbf{Q} \cdot \boldsymbol{\mathcal{V}} \tag{2.102}$$

with $\mathbf{Q}$ being the 3×3 transformation (orthogonal) matrix. The corresponding components Q_{ij} are defined as follows

$$Q_{ij} = \cos \alpha_{ij} = \cos(\angle \mathbf{e}'_i, \mathbf{e}_j) = \frac{\mathbf{e}'_i \cdot \mathbf{e}_j}{|\mathbf{e}'_i||\mathbf{e}_j|} = \mathbf{e}'_i \cdot \mathbf{e}_j \,. \tag{2.103}$$

In the case of general second order tensors $\boldsymbol{\mathcal{M}}$, the components $\mathcal{M}_{11}$, $\mathcal{M}_{12}$, $\mathcal{M}_{13}$, $\mathcal{M}_{21}$, $\mathcal{M}_{22}$, $\mathcal{M}_{23}$, $\mathcal{M}_{31}$, $\mathcal{M}_{32}$, $\mathcal{M}_{33}$, measured by observer $\mathcal{O}$ in basis system $\mathbf{e}_1$, $\mathbf{e}_2$, $\mathbf{e}_3$ have to be related to the components $\mathcal{M}'_{11}$, $\mathcal{M}'_{12}$, $\mathcal{M}'_{13}$, $\mathcal{M}'_{21}$, $\mathcal{M}'_{22}$, $\mathcal{M}'_{23}$, $\mathcal{M}'_{31}$, $\mathcal{M}'_{32}$, $\mathcal{M}'_{33}$, measured by observer $\mathcal{O}'$ in basis system $\mathbf{e}'_1$, $\mathbf{e}'_2$, $\mathbf{e}'_3$, according to the component transformation rule for second order tensors:

$$\begin{bmatrix} \mathcal{M}'_{11} & \mathcal{M}'_{12} & \mathcal{M}'_{13} \\ \mathcal{M}'_{21} & \mathcal{M}'_{22} & \mathcal{M}'_{23} \\ \mathcal{M}'_{31} & \mathcal{M}'_{32} & \mathcal{M}'_{33} \end{bmatrix}_{\mathbf{e}'_1, \mathbf{e}'_2, \mathbf{e}'_3} = \mathbf{Q} \cdot \begin{bmatrix} \mathcal{M}_{11} & \mathcal{M}_{12} & \mathcal{M}_{13} \\ \mathcal{M}_{21} & \mathcal{M}_{22} & \mathcal{M}_{23} \\ \mathcal{M}_{31} & \mathcal{M}_{32} & \mathcal{M}_{33} \end{bmatrix}_{\mathbf{e}_1, \mathbf{e}_2, \mathbf{e}_3} \cdot \mathbf{Q}^T \tag{2.104}$$

or in compact notation

$$\boldsymbol{\mathcal{M}}' = \mathbf{Q} \cdot \boldsymbol{\mathcal{M}} \cdot \mathbf{Q}^T \,. \tag{2.105}$$

Let us now investigate the objectivity of some physical quantities used in continuum mechanics. First, we start with strains and strain rates:

- The deformation gradient $\mathbf{F}$, which transforms between the undeformed distance vector $d\mathbf{X}$ (reference configuration) and the deformed distance vector $d\mathbf{x}$ (current configuration), reading as

$$\mathbf{F} = \frac{d\mathbf{x}}{d\mathbf{X}} = \frac{dx_i}{dX_L}\, \mathbf{e}_i \otimes \mathbf{e}_L \quad \Leftrightarrow \quad \mathbf{F}' = \frac{d\mathbf{x}'}{d\mathbf{X}} = \frac{dx_i'}{dX_L}\, \mathbf{e}_i' \otimes \mathbf{e}_L \,, \tag{2.106}$$

  where the index L describes the reference (undeformed) coordinates X_L, which are independent of the observers's basis system, i.e frame-indifferent with $X_L = X_L'$. Substitution of the transformation rule for vectors (2.102) into (2.106) while taking into account the frame-indifference of vectors in Lagrangian representation, yields

$$\mathbf{F}' = \frac{d\mathbf{x}'}{d\mathbf{X}} = \mathbf{Q}\frac{d\mathbf{x}}{d\mathbf{X}} = \mathbf{Q}\,\mathbf{F}\,. \tag{2.107}$$

  Even though (2.107) does not satisfy the general tranformation rule for second order tensors (2.105), the deformation gradient is objective. This is because the deformation gradient is a so-called two-point second order tensor, which transforms between the reference- and current configuration. In other words, one index describes the current configuration and the other index describes the reference configuration. Thus, frame-transformation behavior of the deformation gradient corresponds to the transformation rule of vectors (2.102).

- In addition, objectivity of the determinant of the deformation gradient (Jacobi determinant) J is described as follows:

$$J = \det\mathbf{F} \quad \Leftrightarrow \quad J' = \det\mathbf{F}' = \det(\mathbf{Q}\mathbf{F}) = J\,. \tag{2.108}$$

  where we considered the property of orthogonal tensor, $\det\mathbf{Q} = 1$. Thus, the Jacobi determinant J is independent of the observer and an objective scalar.

- Next, we discuss the effect of an observer transformation on the Green-Lagrange strain tensor $\mathbf{E}$.

$$\mathbf{E}' = \frac{1}{2}\left[\mathbf{F}'^T \cdot \mathbf{F}' - \mathbf{1}\right] = \frac{1}{2}\left[\left((\mathbf{F})^T\,\mathbf{Q}\right)^T\right)\cdot(\mathbf{Q}\,\mathbf{F}) - \mathbf{1}\right] = \frac{1}{2}\left[\mathbf{F}^T\cdot\mathbf{F} - \mathbf{1}\right] = \mathbf{E}\,. \tag{2.109}$$

  Hence, the Green-Lagrange strain tensor is objective, since this kinematic quantity is defined in the reference configuration. Based on the transformation behavior of $\mathbf{E}$ (2.109), it is easily seen that the rate of the Green-Lagrange strain tensor is also objective,

$$\dot{\mathbf{E}}' = \dot{\mathbf{E}}\,. \tag{2.110}$$

- The objectivity of the Eulerian strain rate $\mathbf{d}$ (representing the symmetric gradient of the velocity $\nabla^S\mathbf{v}$) can be proved using the following relation

$$\mathbf{d} = \mathbf{F}^{-T}\cdot\dot{\mathbf{E}}\cdot\mathbf{F}^{-1}\,, \quad \Leftrightarrow \quad \mathbf{d}' = \mathbf{F}'^{-T}\cdot\dot{\mathbf{E}}'\cdot\mathbf{F}'^{-1}\,. \tag{2.111}$$

  Substitution of (2.107) and (2.110) into (2.111) yields

$$\mathbf{d}' = (\mathbf{Q}\,\mathbf{F})^{-T}\cdot\dot{\mathbf{E}}\cdot(\mathbf{Q}\,\mathbf{F})^{-1} = \mathbf{Q}(\mathbf{F}^{-T}\cdot\dot{\mathbf{E}}\cdot\mathbf{F}^{-1})\mathbf{Q}^T = \mathbf{Q}\,\mathbf{d}\,\mathbf{Q}^T\,, \tag{2.112}$$

  resulting in an frame-indifferent Eulerian strain rate satisfying the tansformation rule for second order tensors (2.105).

- Since the Eulerian strain rate represents the symmetric gradient of the velocity, this motivates us to investigate the velocity gradient $\nabla \mathbf{v}$. This strain rate can be expressed as a function of the deformation gradient, reading as[10]

$$\nabla \mathbf{v} = \dot{\mathbf{F}} \, \mathbf{F}^{-1} \quad \Leftrightarrow \quad \nabla \mathbf{v}' = \dot{\mathbf{F}}' \, \mathbf{F}'^{-1} \tag{2.113}$$

Again, we make use of the transformation for the deformation gradient (2.107), which results in the equivalent expression

$$\nabla \mathbf{v}' = (\mathbf{Q} \, \dot{\mathbf{F}} + \dot{\mathbf{Q}} \, \mathbf{F}) \, (\mathbf{Q} \, \mathbf{F})^{-1} = \mathbf{Q} \, \dot{\mathbf{F}} \, \mathbf{F}^{-1} \mathbf{Q}^T + \dot{\mathbf{Q}} \, \mathbf{Q}^T = \mathbf{Q} \, \nabla \mathbf{v} \mathbf{Q}^T + \boldsymbol{\Omega} \, . \tag{2.114}$$

One can see, that (2.114) does not coincide with the transformation rule for second order tensors (2.105) due to the existence of the last term on the right-hand side $\boldsymbol{\Omega} = \dot{\mathbf{Q}} \, \mathbf{Q}^T$, which is also called angular velocity tensor. Hence, in contrast to the Eulerian strain rate, we can state that the velocity gradient is not objective. This fact is the motivation to make use of the Eulerian strain rate in the Principle of virtual power or in thermodynamic laws.

Finally, we also want to provide objectivity-studies for common stress measures used in continuum mechanics:

- The Cauchy stress tensor $\boldsymbol{\sigma}$ relates the normal vector $\mathbf{n}$ (orthogonal to a surface element) to the corresponding traction vector $\mathbf{T}$. For both observers Cauchy's formula reads as

$$\mathbf{T} = \boldsymbol{\sigma} \cdot \mathbf{n} \quad \Leftrightarrow \quad \mathbf{T}' = \boldsymbol{\sigma}' \cdot \mathbf{n}' \, . \tag{2.115}$$

Substitution of the transformation rule for vectors (2.102) into (2.115)$_2$ delivers

$$\mathbf{Q} \, \mathbf{T} = \boldsymbol{\sigma}' \, \mathbf{Q} \, \mathbf{n} \, . \tag{2.116}$$

Comparison of (2.116) with (2.102)$_1$ results in the general transformation rule for second order tensors

$$\mathbf{Q} \, \boldsymbol{\sigma} \, \mathbf{n} = \boldsymbol{\sigma}' \, \mathbf{Q} \, \mathbf{n} \quad \Rightarrow \quad \boldsymbol{\sigma}' = \mathbf{Q} \, \boldsymbol{\sigma} \, \mathbf{Q}^T \, . \tag{2.117}$$

Thus, the Cauchy stress tensor is independent of the observer's motion and is objective.

- The last quantity we want to describe, is the second Piola-Kirchhoff stress tensor, which is used for large deformations. Since this quantity is defined in the reference configuration (in analogy to the Green-Lagrange strain tensor), it should be independent of observer transformations. This is proved by the following relation:

$$\boldsymbol{\pi} = J \, \mathbf{F}^{-1} \cdot \boldsymbol{\sigma} \cdot \mathbf{F}^{-T} \quad \Leftrightarrow \quad \boldsymbol{\pi}' = J' \, \mathbf{F}'^{-1} \cdot \boldsymbol{\sigma}' \cdot \mathbf{F}'^{-T} \, . \tag{2.118}$$

Substitution of the transformations for the deformation gradient (2.107) and Jacobi determinant (2.108) as well as for the Cauchy stress tensor (2.117) yields

$$\boldsymbol{\pi}' = J \, (\mathbf{Q} \mathbf{F})^{-1} \cdot (\mathbf{Q} \, \boldsymbol{\sigma} \, \mathbf{Q}^T) \cdot (\mathbf{Q} \mathbf{F})^{-T} = J \, \mathbf{F}^{-1} \cdot \boldsymbol{\sigma} \cdot \mathbf{F}^{-T} = \boldsymbol{\pi} \, . \tag{2.119}$$

Indeed, the second Piola-Kirchhoff stress tensor is frame-indifferent and objective.

Summarizing, all used physical strain and stress quantities in constitutive equations are independent of the observer, i.e. we obtained invariant formulations for the thermodynamical description of a continuum.

---

[10]The relation (2.113) can be easily proved, by substitution of the rate of the deformation gradient, $\dot{\mathbf{F}} = \partial \mathbf{v}/\partial \mathbf{X}$ as well as of the inverse deformation gradient, $\mathbf{F}^{-1} = \partial \mathbf{X}/\partial \mathbf{x}$, resulting in $\nabla \mathbf{v} = \partial \mathbf{v}/\partial \mathbf{X} \cdot \partial \mathbf{X}/\partial \mathbf{x} = \partial \mathbf{v}/\partial \mathbf{x} = \nabla \mathbf{v}$.

Chapter 3

Rigorous amendment of Vlasov's theory for thin elastic plates on elastic Winkler foundations, based on the Principle of Virtual Power

Authored by: Raphael Höller, Mehdi Aminbaghai, Lukas Eberhardsteiner, Josef Eberhardsteiner, Ronald Blab, Bernhard L.A. Pichler, and Christian Hellmich

Abstract

Deflection modes relevant for plates with rigidly supported edges are commonly used as kind of "approximation" for the deformation behavior of plates which are freely swimming on an elastic foundation. However, this approach entails systematic errors at the boundaries. As a remedy to this problem, we here rigorously derive a theory for elastically supported thin plates for arbitrary boundary conditions, based on the Principle of Virtual Power. Somewhat surprisingly, it appears that the well-known Laplace-type differential equation for the deflections needs to be extended by additional boundary integrals entailing moments and shear forces, so as to actually "release" the boundaries from "spuriously" acting external moments and shear forces. When approximating the deflections through 2D Fourier series, the Principle of Virtual Power yields an algebraic system of equations, the solution of which provides the Fourier coefficients of the aforementioned series representation. The latter converges, with increasing number of series members, to the true solution for the plate deflections. The new method is applied to relevant problems in pavement engineering, and it is validated through comparison of the numerical results it provides, with predictions obtained from Finite Element analysis. With respect to the latter, the new series-based method reduces the required computer time by a factor between one and a half and almost forty.

Contribution of the author: The author of the present thesis developed the new method for energetically consistent structural problems of thin plates on elastic Winkler foundations, based on the Principle of Virtual Power. Furthermore, he performed extensive literature research, prepared the Matlab code for the series-based solution procedure, and documented most of the manuscript.

List of symbols

a	side length of the plate in x-direction
b	side length of the plate in y-direction
c	Winkler elastic modulus of subgrade reaction
C	spring stiffness
$c_{m,n}$	Fourier coefficient of deflection approximation
$\mathring{c}_{k,l}$	Fourier coefficient in approximation of virtual deflection rate
$\check{\mathbf{d}}$	virtual Eulerian strain rate
$\check{d}_{xx}$	normal component of $\check{\mathbf{d}}$, in x-direction
$\check{d}_{xy}$	shear component of $\check{\mathbf{d}}$, in x-y plane
$\check{d}_{yy}$	normal component of $\check{\mathbf{d}}$, in y-direction
$\mathbf{e}_x, \mathbf{e}_y, \mathbf{e}_z$	base vectors of Cartesian coordinate system
E	elastic Young's modulus
$\mathbf{f}$	volume force vector
f_x, f_y, f_z	components of $\mathbf{f}$, in x, y, and z-direction
h	thickness of plate
k	index of summation / of vector component
K	flexural rigidity of the plate
k_x, k_y	external moments per unit area
L	index of summation / of vector component
l	index of summation / of vector component
M	index of summation / of vector component
m	index of summation / of vector component
M_{klmn}^c	"stiffness matrix element" associated to Winkler foundation
M_{klmn}^C	"stiffness matrix element" associated to single springs
M_{klmn}^m	"stiffness matrix element" associated to bending and twisting moments
m_{xx}	bending moments per unit length, around the y-axis
m_{xy}	twisting moments per unit length
m_{yy}	bending moments per unit length, around the x-axis
n	index of summation / of vector component
$\mathbf{n}$	outward normal vector onto the boundaries of a plates
N_C	number of single springs
N_m	number of Fourier series members approximating a function along x-direction, for constant y-direction
N_n	number of Fourier series members approximating a function along y-direction, for constant x-direction
N_P	number of single forces
$N_{\overline{p}}$	number of "patched loads"
P	single force acting in vertical direction (z)
$\overline{p}$	vertical plate load per unit area, acting over specific rectangular area ("patched load")
p	vertical plate load per unit area, acting over entire plate
PVP	Principle of Virtual Power
$\mathcal{P}^{ext}$	virtual power of external forces
$\mathcal{P}^{int}$	virtual power of internal forces
q_x	shear force per unit length, acting on cross section orthogonal to x
q_y	shear force per unit length, acting on cross section orthogonal to y
s	index of summation / of vector component

t	time
T	temperature field
T_{ref}	uniform (initial) reference temperature field
$\mathbf{T}$	traction vector
T_x, T_y, T_z	components of $\mathbf{T}$, in x, y, z-directions
$\mathbf{u}$	displacement vector
$\check{\mathbf{v}} = \dot{\check{\mathbf{u}}}$	virtual velocity vector
$V_{kl}^{\kappa_T^e}$	"load vector element" associated to temperature gradient
V_{kl}^{p}	"load vector element" associated to surface load acting on entire plate
$V_{kl}^{\bar{p}}$	"load vector element" associated to patched surface load
V_{kl}^{P}	"load vector element" associated to single force
w	deflection of the plate's midplane
$w_{m,n}$	(m,n)-th deflection mode associated to 2D Fourier series
$\check{w}$	virtual deflection of the plate's midplane
$\dot{\check{w}}$	virtual deflection rate of the plate's midplane
$\mathbf{x}$	location vector throughout the plate and its boundaries
x, y	horizontal coordinates of the Cartesian coordinate system
x_a, y_a	horizontal coordinates of the beginning of the plate
x_e, y_e	horizontal coordinates of the end of the plate
x_s, y_s	horizontal coordinates of the vertical single force P, and/or single spring force $C\,w$
$x_{\bar{s}}, y_{\bar{s}}$	horizontal central point coordinates of the surface load $\bar{p}$
z	vertical coordinate of the Cartesian coordinate system
α_T	thermal expansion coefficient
δ	two-dimensional Dirac delta function
Δ	Laplace operator
ΔT_κ	temperature difference between the bottom and the top of the plate
$\boldsymbol{\varepsilon}$	linearized strain tensor
ε_{xx}	normal strain in the x-direction
ε_{xy}	shear strain in the x-y plane
ε_{yy}	normal strain in the y-direction
$\dot{\check{\boldsymbol{\varepsilon}}}$	rate of the virtual linearized strain tensor
$\dot{\check{\varepsilon}}_{xx}$	virtual normal strain rate in the x-direction
$\dot{\check{\varepsilon}}_{xy}$	virtual shear strain rate in the x-y plane
$\dot{\check{\varepsilon}}_{yy}$	virtual normal strain rate in the y-direction
$\eta_{\bar{s}}, \xi_{\bar{s}}$	side lengths of the surface load $\bar{p}$
κ_T^e	temperature-induced eigencurvature of the plate
λ	scaling factor
∇^S	symmetric gradient
ν	Poisson's ratio
Π	dimensionless stress and deformation quantities
$\boldsymbol{\sigma}$	Cauchy stress tensor
σ_{xx}	normal stress in the x-direction
σ_{xy}	shear stress in the x-y plane
σ_{xz}	shear stress in the x-z plane
σ_{yz}	shear stress in the y-z plane
σ_{yy}	normal stress in the y-direction
$\sum$	summation operator

3.1 Introduction

Plates on elastic foundations play an eminent role in many engineering applications, including the design of pavements for roads and airfields [Delatte, 2008; Stenzel, 2005; Eisenmann, 1979; Blab and Harvey, 2002; Westergaard, 1926, 1939, 1948; Teller and Sutherland, 1943; Caliendo and Parisi, 2010; Hajek, 2011] and of foundations and floating floor screeds in building construction [Pech et al., 2016; Bowles, 1997; Das, 2010; Kameswara Rao, 2011; Terzaghi, 1943, 1948; Deplazes, 2008] The by far most popular method for the solution of related mathematical problems is that put forward in the landmark book of Vlasov and Leont'ev [Vlasov and Leont'ev, 1966], which has been the basis for many scientific contributions up to the present day [Fo-van and Siao-mei, 1984; Yao and Yih, 1987; Xiang-sheng, 1988; Straughan, 1990; Ke-rang, 1990; Jun-Yu, 1991; Xiang-sheng, 1992; Turhan, 1992; Shi et al., 1994; Kang et al., 1995] For a "swimming" rectangular plate with side lengths a and b, and boundaries free from being subjected to any type of mechanical forces, the corresponding governing equation given by Vlasov and Leont'ev [Vlasov and Leont'ev, 1966], when specified for a Winkler foundation [Winkler, 1867], reads as

$$\sum_{m=0}^{N_m} \sum_{n=0}^{N_n} c_{m,n} \int_{-a/2}^{a/2} \int_{-b/2}^{b/2} \left[K \left(\frac{\partial^4 w_{m,n}}{\partial x^4} + 2 \frac{\partial^4 w_{m,n}}{\partial x^2 \partial y^2} + \frac{\partial^4 w_{m,n}}{\partial y^4} \right) + c\, w_{m,n} - p \right] w_{k,l} \; dx \; dy = 0 \,,$$

$$\text{for} \quad k = 0, ..., N_m; \quad l = 0, ..., N_n \,, \tag{3.1}$$

with $c_{m,n}$ and $w_{m,n}$ as the amplitudes (Fourier coefficients) and the deflection modes, respectively, which jointly quantify the deflections according to Navier's proposal [Navier, 1823] as

$$w(x, y) = \sum_{m=0}^{N_m} \sum_{n=0}^{N_n} c_{m,n} w_{m,n}(x, y) \,, \tag{3.2}$$

with $(N_m \times N_n)$ as the number of employed deflection modes, see Section 3.4 for mathematical details on Fourier series. Furthermore, c is the elastic Winkler modulus of subgrade reaction, p denotes plate loads per unit area, and K is the flexural rigidity of the plate, being defined as

$$K = \frac{E\, h^3}{12(1 - \nu^2)} \,, \tag{3.3}$$

where E is the elastic Young's modulus, ν is the Poisson's ratio, and h is the thickness of the plate.

Let us now evaluate Eq. (3.1) for $N_m = N_n = 4$ and for a vertical single force P acting in the center of the horizontal quadratic plate, i.e. for "surface" loads of the format

$$p = P\, \delta(0, 0) \,, \tag{3.4}$$

with δ being the two-dimensional Dirac distribution. This evaluation, when employing a plate property set characteristic for concrete pavements, namely for $E/(c\, h) = 1.2 \times 10^3$, yields the deflection mode depicted in Fig. 3.1. Obviously, the actually "free" boundary conditions at the edges are violated, as the plate undergoes deflection gradients *along* the edges, implying non-zero moments and shear forces at the edges of the plate, see Fig. 3.2. The latter quantities were computed according to Vlasov and Leont'ev's formulae, reading as

$$m_{xx} = -K \left[\frac{\partial^2 w}{\partial x^2} + \nu \frac{\partial^2 w}{\partial y^2} \right] \,,$$
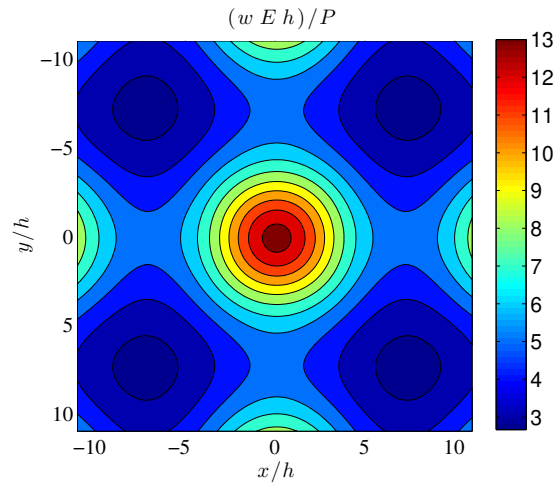
Fig. 3.1: Dimensionless deflections $[w\,E\,h\,/P]$ according to Vlasov and Leont'ev [Vlasov and Leont'ev, 1966], arising from a vertical single force P acting in the center of a quadratic plate with side length a, thickness h, elastic Young's modulus E, and Winkler modulus c, whereby $E/(c\,h) = 1.2 \times 10^3$ and $a/h = 22$.

$$
\begin{aligned}
m_{yy} &= -K\left[\frac{\partial^2 w}{\partial y^2} + \nu\,\frac{\partial^2 w}{\partial x^2}\right], \\[2mm]
m_{xy} = m_{yx} &= -K\,(1-\nu)\frac{\partial^2 w}{\partial x\,\partial y}, \\[2mm]
q_x &= -K\,\frac{\partial}{\partial x}\left[\frac{\partial^2 w}{\partial x^2} + \frac{\partial^2 w}{\partial y^2}\right], \\[2mm]
q_y &= -K\,\frac{\partial}{\partial y}\left[\frac{\partial^2 w}{\partial x^2} + \frac{\partial^2 w}{\partial y^2}\right].
\end{aligned}
\tag{3.5}
$$

Vlasov and Leont'ev therefore state that their function (3.2) were merely an "approximation". This explanation is somewhat unsatisfactory, as the use of a higher number $(N_m \times N_n)$ of series deflection members does not lead to a solution which converges towards the actual "free" boundary condition.

As a remedy, we here present a more rigorous reason for that expression (3.1) violates the plate's boundary conditions. Therefore, we resort to the Principle of Virtual Power (PVP) [Maugin, 2013; Germain, 1972, 1973a,b; Maugin and Goudjo, 1982; Germain et al., 1983; Salençon, 2001; Zhang et al., 2017] which we specify for the kinematic characteristics of a thin elastic plate embedded on an elastic Winkler foundation, in Section 3.2. In Section 3.3, the aforementioned developments are extended towards thermoelasticity, and towards generalized boundary conditions. The latter allow for mechanical modeling of plates which are anchored, at their boundaries, to the compliant ground which they are lying on. In this context, we consider rectangular plates subjected to several types of vertical forces, namely to single forces or to surface loads acting on rectangular areas, whereby the action points and the areas form symmetric or antimetric patterns with respect to the plate directions x and y. Such kinds of patched loads allow for consideration of heavy vehicle pressures acting on the surfaces of concrete pavements [Blab and Harvey, 2002]. In Section 3.4, the system of algebraic equations for determining the unknown Fourier coefficients $c_{m,n}$, is derived from the PVP as well. Section 3.5 is devoted to numerical investigations in the form of three representative examples, and of comparison of respective results with Finite Element
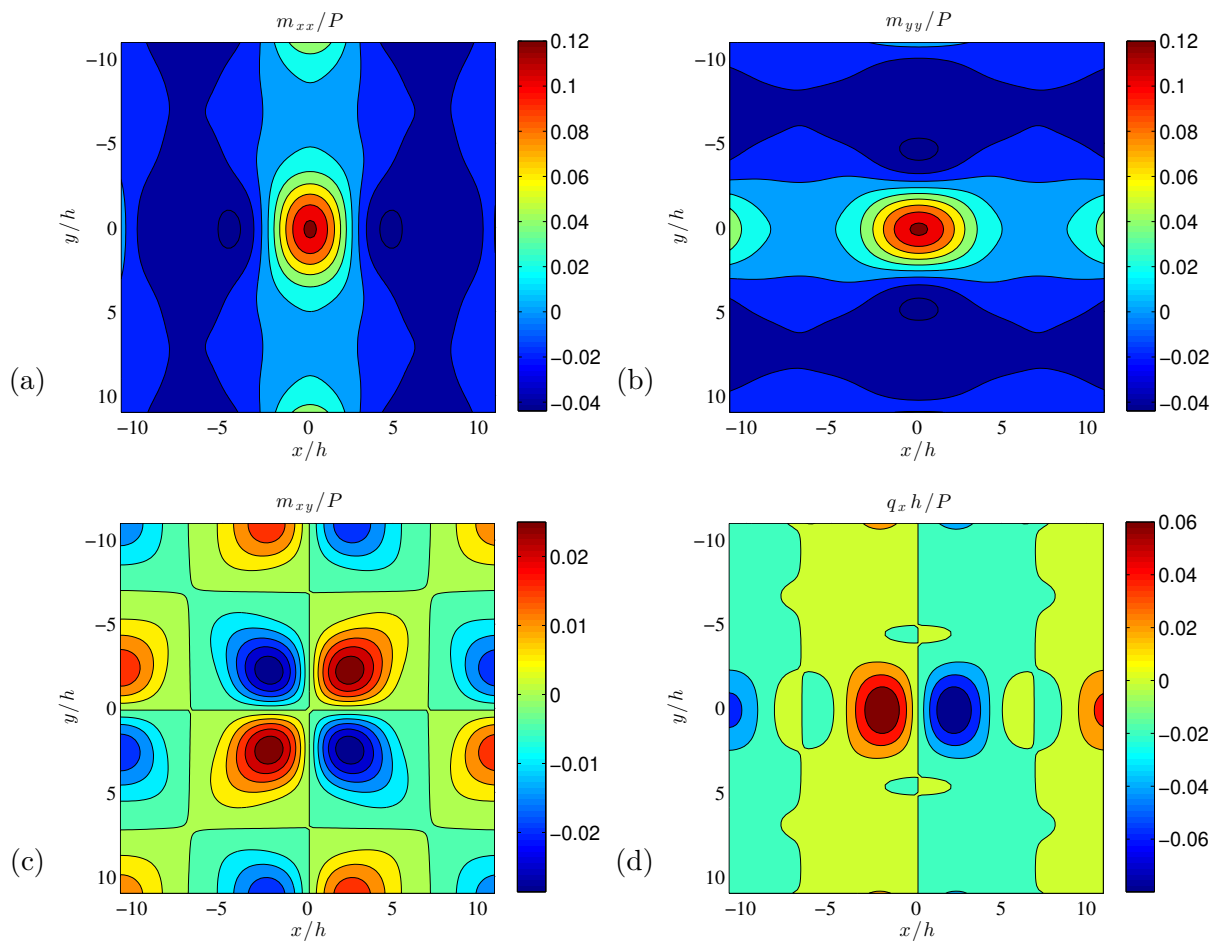
Fig. 3.2: Dimensionless stress resultants according to Vlasov and Leont'ev [Vlasov and Leont'ev, 1966], arising from a vertical single force P acting in the center of a quadratic plate with side length a, thickness h, elastic Young's modulus E, and Winkler modulus c, whereby $E/(c\,h) = 1.2 \times 10^3$ and $a/h = 22$: (a) bending moment around y-axis $[m_{xx}/P]$, (b) bending moment around x-axis $[m_{yy}/P]$, (c) twisting moment $[m_{xy}/P]$, and (d) shear force $[q_x h/P]$.

solutions. Finally, concluding remarks are provided in Section 3.6. Appendix A contains the elements of the system of algebraic equations for the three aforementioned numerical examples, in order to solve the unknown Fourier coefficients.

3.2 Kinematics and stress resultants of a thin elastic plate on an elastic foundation – reviewed in the context of the Principle of Virtual Power

3.2.1 Basics

We share the assessment of Maugin [Maugin, 2013] that the Principle of Virtual Power (PVP) "is an efficient and safe way to construct theories of structural members", setting our focus point on thin "Kirchhoff" plates embedded on an elastic foundation. Our starting point is the formulation of the PVP for the standard 3D continuum, in the format put forward by Germain and followers

[Germain, 1972, 1973a,b; Germain et al., 1983; Maugin and Goudjo, 1982; Salençon, 2001; Zhang et al., 2017],

$$\mathcal{P}^{ext} + \mathcal{P}^{int} = 0 \, , \tag{3.6}$$

with

$$\mathcal{P}^{ext} \;=\; + \int\limits_V \mathbf{f}(\mathbf{x}) \cdot \check{\mathbf{v}}(\mathbf{x}) \, dV + \int\limits_{\partial V} \mathbf{T}(\mathbf{n}, \mathbf{x}) \cdot \check{\mathbf{v}}(\mathbf{x}) \, dA \, , \tag{3.7}$$

$$\mathcal{P}^{int} \;=\; - \int\limits_V \boldsymbol{\sigma} : \check{\mathbf{d}} \, dV \, , \tag{3.8}$$

where $\mathcal{P}^{ext}$ and $\mathcal{P}^{int}$ denote the virtual power of the external forces and of the internal forces, respectively; $\mathbf{x}$ denotes the location vectors throughout the continuum and at its boundaries with outward normals $\mathbf{n}$; $\mathbf{f}$ denotes volume forces; $\mathbf{T}$ denotes traction (surface) forces; $\check{\mathbf{v}}$ denotes the virtual velocity; $\boldsymbol{\sigma}$ denotes the Cauchy stress; and $\check{\mathbf{d}}$ denotes the virtual Eulerian strain rate. The Principle of Virtual Power implies both kinematic compatibility and equilibrium of the 3D solid continuum. In our case, we consider thin (thermo-)elastic rectangular plates with constant thickness h, resting on Winkler foundations, and undergoing small deformations. Any position within the volume and the surface of such a plate is described by a Cartesian coordinate system, with an origin located in the midplane of the plate, and with base vectors $\mathbf{e}_x, \mathbf{e}_y$, and $\mathbf{e}_z$, whereby $\mathbf{e}_x$ and $\mathbf{e}_y$ are parallel to the edges of the plate, and $\mathbf{e}_z$ is orthogonal to the midplane of the plate.

3.2.2 Kinematics

A thin plate in so-called bending mode is characterized by the following kinematic features:

1. Each plate generator[1] performs a *rigid body motion*.

2. Generator rotations are *small*, and the plate thickness is constant, such that all points of a generator have, in good approximation, the same displacement in z-direction, namely the deflection of the midplane $w(x, y)$.

3. All plate generators remain, at any time, both *straight* and *orthogonal* to the midplane of the plate (see also Fig. 3.3).

4. The displacements are small when compared with the thickness of the plate.

Under the aforementioned kinematic conditions, the displacement field of the plate reads as

$$\mathbf{u}(\mathbf{x}) = \left[-\frac{\partial w(x, y)}{\partial x} \, z \right] \mathbf{e}_x + \left[-\frac{\partial w(x, y)}{\partial y} \, z \right] \mathbf{e}_y + w(x, y) \, \mathbf{e}_z \, , \tag{3.9}$$

and the corresponding virtual velocity field follows from a virtual displacement field of the form

$$\check{\mathbf{u}}(\mathbf{x}; t) = \left[-\frac{\partial \check{w}(x, y; t)}{\partial x} \, z \right] \mathbf{e}_x + \left[-\frac{\partial \check{w}(x, y; t)}{\partial y} \, z \right] \mathbf{e}_y + \check{w}(x, y; t) \, \mathbf{e}_z \, . \tag{3.10}$$

---

[1] The plate generator is the set of all points which are on a normal to the midplane of the plate in the undeformed configuration.

positive rotation
around the x-axis

x

y

generator in the undeformed configuration

z

generator in the deformed configuration

1

$\dfrac{\partial w(x,y)}{\partial y}$ ... positive,

$w(x,y)$ increases with increasing y

(a)

generator rotates
positively around the x-axis

positive rotation
around the y-axis

y

x

generator in the undeformed configuration

z

generator in the deformed configuration

1

$\dfrac{\partial w(x,y)}{\partial x}$ ... positive

$w(x,y)$ increases with increasing x

(b)

generator rotates
negatively around the y-axis

Fig. 3.3: Sideviews of a plate generator in the undeformed and in the deformed configuration:
(a) in the y,z-plane, a positive rotation of the generator corresponds to a positive
deflection gradient $\partial w(x,y)/\partial y$; and (b) in the x,z-plane, a negative rotation of the
generator corresponds to a positive deflection gradient $\partial w(x,y)/\partial x$.

Namely, temporal derivation of (6.7) yields the virtual velocity field as

$$\check{\mathbf{v}}(\mathbf{x}) = \dot{\check{\mathbf{u}}}(\mathbf{x}) = \left[-\frac{\partial \dot{\check{w}}(x,y)}{\partial x}\, z \right] \mathbf{e}_x + \left[-\frac{\partial \dot{\check{w}}(x,y)}{\partial y}\, z \right] \mathbf{e}_y + \dot{\check{w}}(x,y)\, \mathbf{e}_z\,, \tag{3.11}$$

with $\dot{\check{w}}$ as the temporal derivative of the time-dependent virtual displacement $\check{w}(x,y;t)$.

Displacement field (3.9) implies a strain field $\boldsymbol{\varepsilon} = \nabla^S \mathbf{u}$, the non-zero components of which
read as

$$\varepsilon_{xx}(x,y,z) = -\frac{\partial^2 w(x,y)}{\partial x^2}\, z\,,$$

$$\varepsilon_{yy}(x,y,z) = -\frac{\partial^2 w(x,y)}{\partial y^2}\, z\,,$$

$$\varepsilon_{xy}(x,y,z) = -\frac{\partial^2 w(x,y)}{\partial y\, \partial x}\, z\,. \tag{3.12}$$

Vanishing of the shear strains, ε_{xz} and ε_{yz}, indicates the so-called shear rigidity of the Kirchhoff
plate. In linearized geometrical settings, the virtual Eulerian strain rate tensor $\check{\mathbf{d}}$ is equal to the

temporal derivative of the virtual linearized strain tensor $\dot{\check{\boldsymbol{\varepsilon}}}$, so that the non-zero components of the former reads for the considered plate as

$$
\begin{aligned}
\check{d}_{xx}(x,y,z) = \dot{\check{\varepsilon}}_{xx}(x,y,z) &= -\frac{\partial^2 \dot{\check{w}}(x,y)}{\partial x^2}\, z\,, \\
\check{d}_{yy}(x,y,z) = \dot{\check{\varepsilon}}_{yy}(x,y,z) &= -\frac{\partial^2 \dot{\check{w}}(x,y)}{\partial y^2}\, z\,, \\
\check{d}_{xy}(x,y,z) = \dot{\check{\varepsilon}}_{xy}(x,y,z) &= -\frac{\partial^2 \dot{\check{w}}(x,y)}{\partial y\, \partial x}\, z\,.
\end{aligned}
\tag{3.13}
$$

3.2.3 Virtual power of the external forces on elastically embedded plates – stress resultants

Evaluation of Eq. (6.2) for kinematics (3.11) and for forces with components

$$
\mathbf{f}(x,y,z) = f_x(x,y,z)\mathbf{e}_x + f_y(x,y,z)\mathbf{e}_y + f_z(x,y,z)\mathbf{e}_z\,,
\tag{3.14}
$$

$$
\mathbf{T}(\mathbf{n};x,y,z) = T_x(x,y,z)\mathbf{e}_x + T_y(x,y,z)\mathbf{e}_y + T_z(x,y,z)\mathbf{e}_z\,,
\tag{3.15}
$$

whereby the Winkler foundation implies that

$$
T_z(\mathbf{e}_z; x,y,z=\tfrac{h}{2}) = -c\, w(x,y)\,,
\tag{3.16}
$$

yields, when considering a plate according to Fig. 3.4,
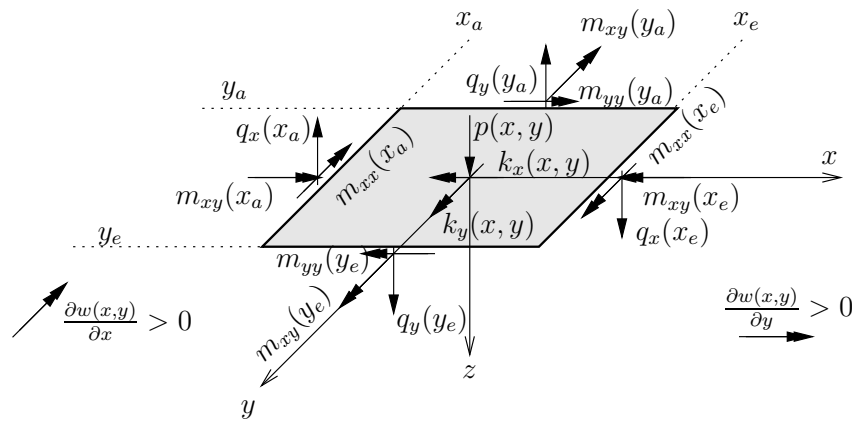
Fig. 3.4: Schematical illustration of stress resultants acting on a thin plate, spanning from $x_a = -a/2$ to $x_e = a/2$, and from $y_a = -b/2$ to $y_e = b/2$.

$$
\begin{aligned}
\mathcal{P}^{ext} &= + \int\limits_{-b/2}^{b/2} \int\limits_{-a/2}^{a/2} \left[\int\limits_{-\frac{h}{2}}^{+\frac{h}{2}} f_z(x,y,z)\, dz + T_z(-\mathbf{e}_z; x,y,-\tfrac{h}{2}) \right] \dot{\check{w}}(x,y)\, dx\, dy \\
&\quad + \int\limits_{-b/2}^{b/2} \int\limits_{-a/2}^{a/2} -c\, w(x,y)\, \dot{\check{w}}(x,y)\, dx\, dy
\end{aligned}
$$

$$
- \int\limits_{-b/2}^{b/2} \int\limits_{-a/2}^{a/2} \left[\int\limits_{-\frac{h}{2}}^{+\frac{h}{2}} f_y(x,y,z)\, z\, dz - \frac{h}{2}\, T_y(\mathbf{e}_z; x,y,\tfrac{h}{2}) + \frac{h}{2}\, T_y(-\mathbf{e}_z; x,y,-\tfrac{h}{2}) \right] \frac{\partial \overset{\scriptscriptstyle\vee}{\dot{w}}(x,y)}{\partial x}\, dx\, dy
$$

$$
- \int\limits_{-b/2}^{b/2} \int\limits_{-a/2}^{a/2} \left[\int\limits_{-\frac{h}{2}}^{+\frac{h}{2}} f_x(x,y,z)\, z\, dz + \frac{h}{2}\, T_x(\mathbf{e}_z; x,y,\tfrac{h}{2}) - \frac{h}{2}\, T_x(-\mathbf{e}_z; x,y,-\tfrac{h}{2}) \right] \frac{\partial \overset{\scriptscriptstyle\vee}{\dot{w}}(x,y)}{\partial y}\, dx\, dy
$$

$$
+ \int\limits_{-b/2}^{b/2} \left[\int\limits_{-\frac{h}{2}}^{+\frac{h}{2}} T_z(\mathbf{e}_x; x,y,z)\, dz \right] \overset{\scriptscriptstyle\vee}{\dot{w}}(x,y) \Big|_{-a/2}^{a/2} dy + \int\limits_{-a/2}^{a/2} \left[\int\limits_{-\frac{h}{2}}^{+\frac{h}{2}} T_z(\mathbf{e}_y; x,y,z)\, dz \right] \overset{\scriptscriptstyle\vee}{\dot{w}}(x,y) \Big|_{-b/2}^{b/2} dx
$$

$$
- \int\limits_{-b/2}^{b/2} \left[\int\limits_{-\frac{h}{2}}^{+\frac{h}{2}} T_x(\mathbf{e}_x; x,y,z)\, z\, dz \right] \frac{\partial \overset{\scriptscriptstyle\vee}{\dot{w}}(x,y)}{\partial x} + \left[\int\limits_{-\frac{h}{2}}^{+\frac{h}{2}} T_y(\mathbf{e}_x; x,y,z)\, z\, dz \right] \frac{\partial \overset{\scriptscriptstyle\vee}{\dot{w}}(x,y)}{\partial y} \Big|_{-a/2}^{a/2} dy
$$

$$
- \int\limits_{-a/2}^{a/2} \left[\int\limits_{-\frac{h}{2}}^{+\frac{h}{2}} T_x(\mathbf{e}_y; x,y,z)\, z\, dz \right] \frac{\partial \overset{\scriptscriptstyle\vee}{\dot{w}}(x,y)}{\partial x} + \left[\int\limits_{-\frac{h}{2}}^{+\frac{h}{2}} T_y(\mathbf{e}_y; x,y,z)\, z\, dz \right] \frac{\partial \overset{\scriptscriptstyle\vee}{\dot{w}}(x,y)}{\partial y} \Big|_{-b/2}^{b/2} dx \,.
$$

$$(3.17)$$

Eq. (3.17) indicates that the plate-specific "degrees of freedom" $\overset{\scriptscriptstyle\vee}{\dot{w}}$, $\partial \overset{\scriptscriptstyle\vee}{\dot{w}}/\partial y$, and $\partial \overset{\scriptscriptstyle\vee}{\dot{w}}/\partial x$ induce force quantities called stress resultants, namely those on which they produce power. These stress resultants are called plate loads $p(x,y)$, external moments per unit area, $k_x(x,y)$ and $k_y(x,y)$, shear forces per unit length, $q_x(x,y)$ and $q_y(x,y)$, bending moments per unit length, $m_{xx}(x,y)$ and $m_{yy}(x,y)$, and twisting moments per unit length, $m_{xy}(x,y)$; and they refer to the following mathematical expressions

$$
p(x,y) \;=\; \int\limits_{-\frac{h}{2}}^{+\frac{h}{2}} f_z(x,y,z)\, dz + T_z(-\mathbf{e}_z; x,y,-\tfrac{h}{2})\,, \tag{3.18}
$$

$$
k_x(x,y) \;=\; \int\limits_{-\frac{h}{2}}^{+\frac{h}{2}} f_y(x,y,z)\, z\, dz - \frac{h}{2}\, T_y(\mathbf{e}_z; x,y,\tfrac{h}{2}) + \frac{h}{2}\, T_y(-\mathbf{e}_z; x,y,-\tfrac{h}{2})\,, \tag{3.19}
$$

$$
k_y(x,y) \;=\; \int\limits_{-\frac{h}{2}}^{+\frac{h}{2}} f_x(x,y,z)\, z\, dz + \frac{h}{2}\, T_x(\mathbf{e}_z; x,y,\tfrac{h}{2}) - \frac{h}{2}\, T_x(-\mathbf{e}_z; x,y,-\tfrac{h}{2})\,, \tag{3.20}
$$

$$
q_x(x,y) \;=\; \int\limits_{-\frac{h}{2}}^{+\frac{h}{2}} T_z(\mathbf{n}\!=\!\mathbf{e}_x; x,y,z)\, dz = \int\limits_{-\frac{h}{2}}^{+\frac{h}{2}} \sigma_{xz}(x,y,z)\, dz\,, \tag{3.21}
$$

$$q_y(x,y) \;=\; \int\limits_{-\frac{h}{2}}^{+\frac{h}{2}} T_z(\mathbf{n}{=}\mathbf{e}_y; x,y,z)\; dz = \int\limits_{-\frac{h}{2}}^{+\frac{h}{2}} \sigma_{yz}(x,y,z)\; dz\,, \tag{3.22}$$

$$m_{xx}(x,y) \;=\; \int\limits_{-\frac{h}{2}}^{+\frac{h}{2}} T_x(\mathbf{n}{=}\mathbf{e}_x; x,y,z)\; z\; dz = \int\limits_{-\frac{h}{2}}^{+\frac{h}{2}} \sigma_{xx}(x,y,z)\; z\; dz\,, \tag{3.23}$$

$$m_{yy}(x,y) \;=\; \int\limits_{-\frac{h}{2}}^{+\frac{h}{2}} T_y(\mathbf{n}{=}\mathbf{e}_y; x,y,z)\; z\; dz = \int\limits_{-\frac{h}{2}}^{+\frac{h}{2}} \sigma_{yy}(x,y,z)\; z\; dz\,, \tag{3.24}$$

$$m_{xy}(x,y) \;=\; \int\limits_{-\frac{h}{2}}^{+\frac{h}{2}} T_y(\mathbf{n}{=}\mathbf{e}_x; x,y,z)\; z\; dz = \int\limits_{-\frac{h}{2}}^{+\frac{h}{2}} T_x(\mathbf{n}{=}\mathbf{e}_y; x,y,z)\; z\; dz =$$

$$= \int\limits_{-\frac{h}{2}}^{+\frac{h}{2}} \sigma_{xy}(x,y,z)\; z\; dz\,. \tag{3.25}$$

Back-insertion of the definitions (3.18)-(3.25) into the power expression (3.17), yields the power of external forces in the following form

$$
\begin{aligned}
\mathcal{P}^{ext} \;=\; & + \int\limits_{-b/2}^{b/2}\int\limits_{-a/2}^{a/2} [p(x,y) - c\,w(x,y)]\; \dot{\breve{w}}(x,y)\; dx\; dy \\
& - \int\limits_{-b/2}^{b/2}\int\limits_{-a/2}^{a/2} k_x(x,y)\; \frac{\partial \dot{\breve{w}}(x,y)}{\partial x}\; dx\; dy - \int\limits_{-b/2}^{b/2}\int\limits_{-a/2}^{a/2} k_y(x,y)\; \frac{\partial \dot{\breve{w}}(x,y)}{\partial y}\; dx\; dy \\
& + \int\limits_{-b/2}^{b/2} q_x(x,y)\; \dot{\breve{w}}(x,y) \Big|_{-a/2}^{a/2}\; dy + \int\limits_{-a/2}^{a/2} q_y(x,y)\; \dot{\breve{w}}(x,y) \Big|_{-b/2}^{b/2}\; dx \\
& - \int\limits_{-b/2}^{b/2} m_{xx}(x,y)\; \frac{\partial \dot{\breve{w}}(x,y)}{\partial x} + m_{xy}(x,y)\; \frac{\partial \dot{\breve{w}}(x,y)}{\partial y} \Big|_{-a/2}^{a/2}\; dy \\
& - \int\limits_{-a/2}^{a/2} m_{xy}(x,y)\; \frac{\partial \dot{\breve{w}}(x,y)}{\partial x} + m_{yy}(x,y)\; \frac{\partial \dot{\breve{w}}(x,y)}{\partial y} \Big|_{-b/2}^{b/2}\; dx\,.
\end{aligned} \tag{3.26}
$$

For an only vertically loaded, "freely swimming" plate with traction-free boundaries, i.e. with vanishing moments per unit length, $m_{xy}(x = -a/2) = m_{xy}(x = a/2) = m_{xy}(y = -b/2) = m_{xy}(y = b/2) = m_{yy}(y = -b/2) = m_{yy}(y = b/2) = m_{xx}(x = -a/2) = m_{xx}(x = a/2) = 0$, and

vanishing shear forces per unit length, $q_x(x = -a/2) = q_x(x = a/2) = q_y(y = -b/2) = q_y(y = b/2) = 0$, Eq. (3.26) reduces to

$$\mathcal{P}^{ext} = + \int\limits_{-b/2}^{b/2} \int\limits_{-a/2}^{a/2} [p(x,y) - c\, w(x,y)] \, \mathring{\dot{w}}(x,y) \, dx \, dy \,. \tag{3.27}$$

3.2.4 Virtual power of the internal forces, plate elasticity, and PVP-based governing equation

As regards specification of the virtual power of internal forces (6.3) for thin plates, the virtual strain rates (3.13) imply that only stresses σ_{xx}, σ_{yy} and $\sigma_{xy} = \sigma_{yx}$ perform power along the virtual strain rates $\mathring{\dot{\varepsilon}}_{xx}$, $\mathring{\dot{\varepsilon}}_{yy}$ and $\mathring{\dot{\varepsilon}}_{xy} = \mathring{\dot{\varepsilon}}_{yx}$. Hence, the virtual power of the internal forces reads as

$$
\begin{aligned}
\mathcal{P}^{int} = {} & -\int\limits_{V} \sigma_{xx}\, \mathring{\dot{\varepsilon}}_{xx} + \sigma_{yy}\, \mathring{\dot{\varepsilon}}_{yy} + 2\, \sigma_{xy}\, \mathring{\dot{\varepsilon}}_{xy} \, dV \\
= {} & -\int\limits_{-a/2}^{a/2} \int\limits_{-b/2}^{b/2} \int\limits_{-\frac{h}{2}}^{+\frac{h}{2}} \sigma_{xx}(x,y,z) \left[-\frac{\partial^2 \mathring{\dot{w}}(x,y)}{\partial x^2}\, z \right] dx \, dy \, dz \\
& -\int\limits_{-a/2}^{a/2} \int\limits_{-b/2}^{b/2} \int\limits_{-\frac{h}{2}}^{+\frac{h}{2}} \sigma_{yy}(x,y,z) \left[-\frac{\partial^2 \mathring{\dot{w}}(x,y)}{\partial y^2}\, z \right] dx \, dy \, dz \\
& -\int\limits_{-a/2}^{a/2} \int\limits_{-b/2}^{b/2} \int\limits_{-\frac{h}{2}}^{+\frac{h}{2}} 2\, \sigma_{xy}(x,y,z) \left[-\frac{\partial^2 \mathring{\dot{w}}(x,y)}{\partial y\, \partial x}\, z \right] dx \, dy \, dz \,.
\end{aligned}
\tag{3.28}
$$

Substitution of Eqs. (3.23)-(3.25) into Eq. (3.28) yields the following expression for the virtual power of internal forces in terms of bending moments and twisting moments

$$
\begin{aligned}
\mathcal{P}^{int} = {} & + \int\limits_{-a/2}^{a/2} \int\limits_{-b/2}^{b/2} m_{xx}(x,y)\, \frac{\partial^2 \mathring{\dot{w}}(x,y)}{\partial x^2} \, dy \, dx + \int\limits_{-a/2}^{a/2} \int\limits_{-b/2}^{b/2} m_{yy}(x,y)\, \frac{\partial^2 \mathring{\dot{w}}(x,y)}{\partial y^2} \, dy \, dx \\
& + \int\limits_{-a/2}^{a/2} \int\limits_{-b/2}^{b/2} 2\, m_{xy}(x,y) \frac{\partial^2 \mathring{\dot{w}}(x,y)}{\partial y\, \partial x} \, dy \, dx \,.
\end{aligned}
\tag{3.29}
$$

For a linear elastic isotropic, homogeneous plate with elastic Young's modulus E and Poisson's ratio ν, insertion of Hooke's law into the definitions of the moments (3.23) to (3.25) yields the moment-curvature relations

$$
\begin{aligned}
m_{xx}(x,y) &= -K\left[\frac{\partial^2 w(x,y)}{\partial x^2} + \nu\,\frac{\partial^2 w(x,y)}{\partial y^2}\right], \\
m_{yy}(x,y) &= -K\left[\frac{\partial^2 w(x,y)}{\partial y^2} + \nu\,\frac{\partial^2 w(x,y)}{\partial x^2}\right], \\
m_{xy}(x,y) &= -K\,(1-\nu)\frac{\partial^2 w(x,y)}{\partial x\,\partial y}\,.
\end{aligned}
\tag{3.30}
$$

Use of (3.30) in (3.29), and subsequent insertion of the resulting expression for the virtual power of the internal forces, as well as of the expression (3.27) for the virtual power of the external forces, into the PVP (6.1), yields, after twofold partial integration

$$
\begin{aligned}
\mathcal{P}^{ext} + \mathcal{P}^{int} = & +\int_{-a/2}^{a/2}\int_{-b/2}^{b/2}\left[K\left(\frac{\partial^4 w}{\partial x^4} + 2\,\frac{\partial^4 w}{\partial x^2\,\partial y^2} + \frac{\partial^4 w}{\partial y^4}\right) + c\,w - p\right]\mathring{\dot{w}}\,dx\,dy \\
& -\int_{-b/2}^{b/2}\left[m_{xx}\frac{\partial\mathring{\dot{w}}}{\partial x} + m_{xy}\frac{\partial\mathring{\dot{w}}}{\partial y}\right]\bigg|_{-a/2}^{a/2}\,dy - \int_{-a/2}^{a/2}\left[m_{xy}\frac{\partial\mathring{\dot{w}}}{\partial x} + m_{yy}\frac{\partial\mathring{\dot{w}}}{\partial y}\right]\bigg|_{-b/2}^{b/2}\,dx \\
& +\int_{-b/2}^{b/2}\left[\frac{\partial m_{xx}}{\partial x} + \frac{\partial m_{xy}}{\partial y}\right]\mathring{\dot{w}}\bigg|_{-a/2}^{a/2}\,dy + \int_{-a/2}^{a/2}\left[\frac{\partial m_{yy}}{\partial y} + \frac{\partial m_{xy}}{\partial x}\right]\mathring{\dot{w}}\bigg|_{-b/2}^{b/2}\,dx = 0\,.
\end{aligned}
\tag{3.31}
$$

Comparing (3.31) with (3.1) shows that Vlasov and Leont'ev were missing *internal* force-related terms associated to the plate's boundary. It is the consideration of these internal force-related power terms, which ensures the "force free nature" of the boundary of the "swimming" plate. After approximation of the deflection mode into a Fourier series with (4×4) members, see Section 3.4 for details, we obtain the deflection mode depicted in Fig. 3.5: the plate boundaries are obviously free of forces.

On the other hand, Vlasov and Leont'ev actually did not make any considerations concerning boundary conditions. This is readily seen when specifying Eq. (3.26) just for vanishing surface moments per unit area, $k_x = k_y = 0$, while leaving all the moment and shear force terms unspecified. Namely, letting the Principle of Virtual Power, $\mathcal{P}^{ext} + \mathcal{P}^{int}$ be fulfilled by the aforementioned specification of Eq. (3.26), as well as by Eq. (3.29); and partially integrating twice, indeed yields Vlasov and Leont'ev's original proposition, namely Eq. (3.1).

3.3 Extension to thermoelasticity, and to generalized boundary conditions

The aforementioned developments can be straightforwardly extended to more complex material behavior and to load types going beyond continuous functions $p(x,y)$ as occurring in Eq. (3.27).
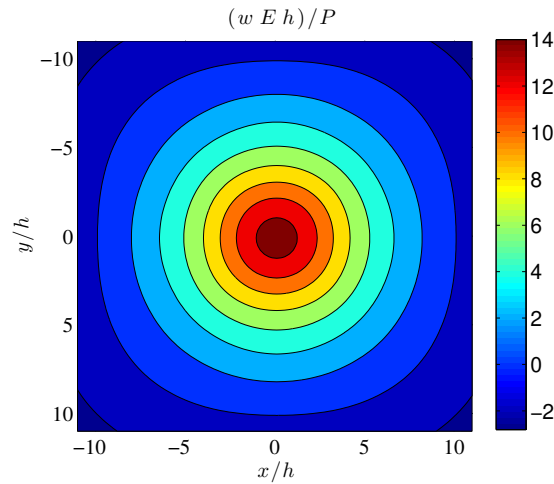
Fig. 3.5: Dimensionless deflections $[wEh/P]$ according to the Principle of Virtual Power (3.31), arising from a vertical single force P acting in the center of a quadratic plate with side length a, thickness h, elastic Young's modulus E, and Winkler modulus c, whereby $E/(c\,h) = 1.2 \times 10^3$ and $a/h = 22$.

As regards material behavior, we here consider thermoelastic behavior, which for the plane stress state found in thin plates reads as

$$
\begin{bmatrix} \sigma_{xx} \\ \sigma_{yy} \\ \sqrt{2}\,\sigma_{xy} \end{bmatrix} = \frac{E}{1-\nu^2} \begin{bmatrix} 1 & \nu & 0 \\ \nu & 1 & 0 \\ 0 & 0 & 1-\nu \end{bmatrix} \begin{bmatrix} \varepsilon_{xx} - \alpha_T\,(T - T_{ref}) \\ \varepsilon_{yy} - \alpha_T\,(T - T_{ref}) \\ \sqrt{2}\,\varepsilon_{xy} \end{bmatrix} , \tag{3.32}
$$

with E and ν as the elastic Young's modulus and Poisson's ratio, respectively; ε_{xx}, ε_{yy}, and ε_{yy} as the plate's dominant strain components according to Eq. (3.12); α_T as the thermal expansion coefficient; T_{ref} as the uniform (initial) reference temperature; and T as the temperature field in the deformed configuration. The latter is introduced as

$$
T = T_{ref} + \Delta T_\kappa\,\frac{z}{h} , \tag{3.33}
$$

where $\Delta T_\kappa = T_{lower} - T_{upper}$ denotes the temperature difference between the lower and the upper surface of the plate. Specifying the thermoelastic law (3.32) for plate-specific strains (3.12) and for the temperature field (3.33), and insertion of the corresponding result into Eq. (3.23)-(3.25), delivers

$$
\begin{aligned}
m_{xx}(x,y) &= -K\left[\frac{\partial^2 w(x,y)}{\partial x^2} + \nu\,\frac{\partial^2 w(x,y)}{\partial y^2} + \kappa_T^e\right], \\
m_{yy}(x,y) &= -K\left[\frac{\partial^2 w(x,y)}{\partial y^2} + \nu\,\frac{\partial^2 w(x,y)}{\partial x^2} + \kappa_T^e\right], \\
m_{xy}(x,y) &= -K\,(1-\nu)\frac{\partial^2 w(x,y)}{\partial x\,\partial y} ,
\end{aligned} \tag{3.34}
$$

where K is the flexural rigidity, see (3.3), and

$$\kappa_T^e = \frac{(1+\nu)\alpha_T}{h}\Delta T_\kappa \tag{3.35}$$

is the temperature-induced eigencurvature of the plate. The relation between stresses and stress resultants follows from inserting Eq. (3.12) into Eq. (3.32), and comparing the result with the Eqs. (3.34) while considering rigidity definition (3.3). This yields

$$\sigma_{xx}(x,y,z) = \frac{m_{xx}(x,y)}{h^3/12}\,z\,, \quad \sigma_{yy}(x,y,z) = \frac{m_{yy}(x,y)}{h^3/12}\,z\,, \quad \sigma_{xy}(x,y,z) = \frac{m_{xy}(x,y)}{h^3/12}\,z\,. \tag{3.36}$$

As regards more complex loading states, Eq. (3.27) can be straightforwardly extended to plates loaded by surfaces loads per unit area $p(x,y)$ over the entire plate, distributed forces $\overline{p}_s$ over the rectangular area of side lengths $\xi_{\overline{s}} \times \eta_{\overline{s}}$ with coordinates $x_{\overline{s}}$ and $y_{\overline{s}}$, and vertical single forces P_s with coordinates x_s and y_s (see Fig. 3.6); or to plates with elastically supported edges, e.g. in the form of single springs exerting, on the plate, vertical forces of magnitude $C_s\,w(x_s,y_s)$ (see Fig. 3.7). In this context, the virtual power of external forces for a plate on elastic foundation
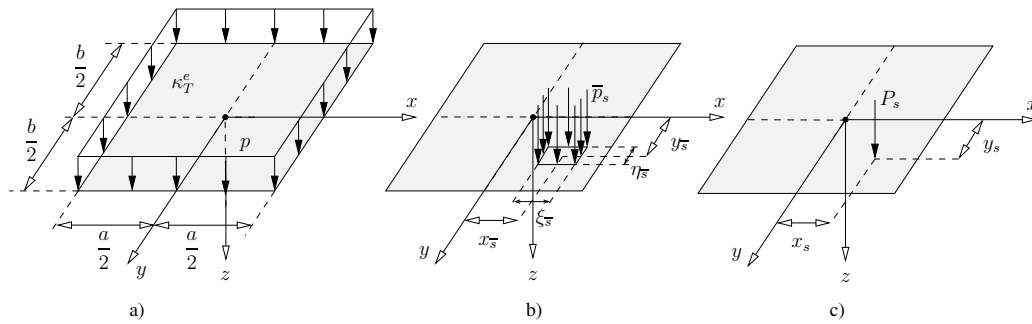
Fig. 3.6: a) Vertical distributed forces p and the temperature-induced eigencurvature κ_T^e over the plate, b) Distributed forces $\overline{p}_s$ over the rectangular area of side lengths $\xi_{\overline{s}} \times \eta_{\overline{s}}$ and the central point coordinates $x_{\overline{s}}$ and $y_{\overline{s}}$, c) Vertical single forces P_s with coordinates x_s and y_s.
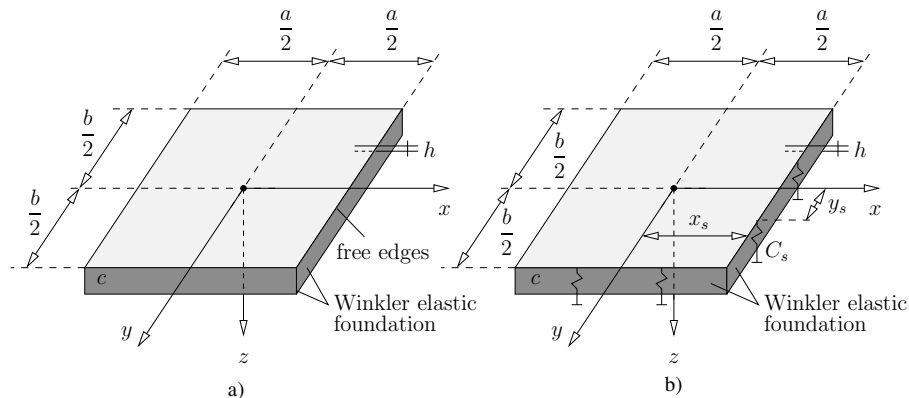
Fig. 3.7: A rectangular plate on Winkler elastic foundation of side lengths $a \times b$ and thickness h, with a) free edges b) elastic boundary conditions in the form of single springs exerting forces.

with arbitrary boundary conditions reads as

$$
\begin{aligned}
\mathcal{P}^{ext} \;=\; & +\int_{-b/2}^{b/2}\int_{-a/2}^{a/2}\Big[p(x,y)-c\,w(x,y)\Big]\,\mathring{w}(x,y)\;dx\;dy \\
& +\sum_{s=1}^{N\overline{p}}\overline{p}_s\int_{x_{\overline{s}}-\frac{\xi_{\overline{s}}}{2}}^{x_{\overline{s}}+\frac{\xi_{\overline{s}}}{2}}\int_{y_{\overline{s}}-\frac{\eta_{\overline{s}}}{2}}^{y_{\overline{s}}+\frac{\eta_{\overline{s}}}{2}}\mathring{w}(x,y)\;dx\;dy+\sum_{s=1}^{N_P}P_s\mathring{w}(x,y)\Big|_{\substack{x=x_s\\y=y_s}} \\
& -\sum_{s=1}^{N_C}C_s w\,(x,y)\,\mathring{w}(x,y)\Big|_{\substack{x=x_s\\y=y_s}}.
\end{aligned}
\tag{3.37}
$$

Use of thermoelastic law (3.34) in (3.29), and insertion of the resulting expression for the virtual power of the internal forces, as well as of the expression (3.37) for the virtual power of the external forces for arbitrary loads, into the Principle of Virtual Power (6.1), yields

$$
\begin{aligned}
\mathcal{P}^{ext}+\mathcal{P}^{int} \;=\; & +\int_{-b/2}^{b/2}\int_{-a/2}^{a/2}\Big[p-c\,w\Big]\,\mathring{w}\;dx\;dy-K\kappa_T^e\int_{-b/2}^{b/2}\int_{-a/2}^{a/2}\left(\frac{\partial^2\mathring{w}}{\partial x^2}+\frac{\partial^2\mathring{w}}{\partial y^2}\right)\;dx\;dy \\
& +\sum_{s=1}^{N\overline{p}}\overline{p}_s\int_{x_{\overline{s}}-\frac{\xi_{\overline{s}}}{2}}^{x_{\overline{s}}+\frac{\xi_{\overline{s}}}{2}}\int_{y_{\overline{s}}-\frac{\eta_{\overline{s}}}{2}}^{y_{\overline{s}}+\frac{\eta_{\overline{s}}}{2}}\mathring{w}\;dx\;dy+\sum_{s=1}^{N_P}P_s\mathring{w}\Big|_{\substack{x=x_s\\y=y_s}}-\sum_{s=1}^{N_C}C_s w\,\mathring{w}\Big|_{\substack{x=x_s\\y=y_s}} \\
& -K\int_{-b/2}^{b/2}\int_{-a/2}^{a/2}\left[\left(\frac{\partial^2 w}{\partial x^2}+\nu\frac{\partial^2 w}{\partial y^2}\right)\frac{\partial^2\mathring{w}}{\partial x^2}+\left(\frac{\partial^2 w}{\partial y^2}+\nu\frac{\partial^2 w}{\partial x^2}\right)\frac{\partial^2\mathring{w}}{\partial y^2}\right. \\
& \left.+\left(2\,(1-\nu)\frac{\partial^2 w}{\partial y\,\partial x}\right)\frac{\partial^2\mathring{w}}{\partial y\,\partial x}\right]\;dx\;dy=0\,.
\end{aligned}
\tag{3.38}
$$

The PVP in the format (3.38) is the basis for the determination of the sought deflection function $w(x,y)$. Therefore, the latter is expanded into a Fourier series, which leads to the so-called Galerkin method, as described in Section 3.4.

3.4 Mathematical solution procedure

The Principle of Virtual Power in the format (3.38) can also be used for constructing an algebraic system of equations giving access to the deflection field $w(x,y)$, and then, via (3.34) and (3.36), to the stresses acting throughout the plate. For this purpose, we resort to Eq. (3.2), representing the deflection function $w(x,y)$ as a series of double trigonometric functions, i.e. a two dimensional Fourier series

$$
w\,(x,y)=\sum_{m=0}^{N_m}\sum_{n=0}^{N_n}\sum_{M=I}^{IV}c_{m,n}^M\,w_{m,n}^M\,(x,y)\,,
\tag{3.39}
$$

where $w_{m,n}^M$ are trigonometric functions, and $c_{m,n}^M$ denote the corresponding unknown Fourier coefficients. Subscripts m and n refer to the number of waves related to the trigonometric functions, whereas superscript M indicates four different types of functions, being symmetrical

or antimetrical with respect to the x- or y-axis, respectively. Accordingly, the aforementioned trigonometric functions read as

$$w_{m,n}^I(x,y) \;=\; \cos\frac{m\pi x}{a}\,\cos\frac{n\pi y}{b} \qquad \text{for} \quad m=0,1,3..., \quad n=0,1,3... \tag{3.40}$$

$$w_{m,n}^{II}(x,y) \;=\; \begin{cases} \dfrac{2x}{a}\,\cos\dfrac{n\pi y}{b} & m=0, \qquad\quad n=0,1,3... \\[2ex] \sin\dfrac{m\pi x}{a}\,\cos\dfrac{n\pi y}{b} & m=2,4,6..., \quad n=0,1,3... \end{cases} \qquad\text{for} \tag{3.41}$$

$$w_{m,n}^{III}(x,y) \;=\; \begin{cases} \dfrac{2y}{b}\,\cos\dfrac{m\pi x}{a} & m=0,1,3..., \quad n=0 \\[2ex] \sin\dfrac{n\pi y}{b}\,\cos\dfrac{m\pi x}{a} & m=0,1,3..., \quad n=2,4,6... \end{cases} \qquad\text{for} \tag{3.42}$$

$$w_{m,n}^{IV}(x,y) \;=\; \begin{cases} \dfrac{4xy}{ab} & m=0, \qquad\quad n=0 \\[2ex] \dfrac{2y}{b}\,\sin\dfrac{m\pi x}{a} & m=2,4,6..., \quad n=0 \\[2ex] \dfrac{2x}{a}\,\sin\dfrac{n\pi y}{b} & m=0, \qquad\quad n=2,4,6... \\[2ex] \sin\dfrac{n\pi y}{b}\,\sin\dfrac{m\pi x}{a} & m=2,4,6..., \quad n=2,4,6... \end{cases} \qquad\text{for} \tag{3.43}$$

It is easily seen that $w_{m,n}^I$ is symmetric with respect to both the x- and the y-axis; that $w_{m,n}^{II}$ is symmetric with respect to the x-axis and antimetric with respect to the y-axis; that $w_{m,n}^{III}$ is antimetric with respect to the x-axis and symmetric with respect to the y-axis, and that $w_{m,n}^{IV}$ is antimetric with respect to both axes.

Similar choices are made for the virtual velocities $\mathring{w}(x,y)$, through introduction of Ansatz functions identical to those in Eq. (3.39),

$$\mathring{w}(x,y) = \sum_{k=0}^{N_k}\sum_{l=0}^{N_l}\sum_{L=I}^{IV} \mathring{c}_{k,l}^L\, w_{k,l}^L(x,y)\;, \tag{3.44}$$

with the virtual velocity coefficient $\mathring{c}_{k,l}$. Insertion of (3.44) and of (3.39), together with (3.40) to (3.43), into Eq. (3.38), yields the following Galerkin-type solution scheme

$$
\begin{aligned}
\mathcal{P}^{ext}+\mathcal{P}^{int} \;=\; &\sum_{k=0}^{N_k}\sum_{l=0}^{N_l}\sum_{L=I}^{IV}\mathring{c}_{k,l}^L\Bigg\{ \int_{-b/2}^{b/2}\int_{-a/2}^{a/2} p\,w_{k,l}^L\;dx\;dy \\[1ex]
&+\sum_{s=1}^{N_{\overline{p}}}\overline{p}_s\int_{x_{\overline{s}}-\frac{\xi_{\overline{s}}}{2}}^{x_{\overline{s}}+\frac{\xi_{\overline{s}}}{2}}\int_{y_{\overline{s}}-\frac{\eta_{\overline{s}}}{2}}^{y_{\overline{s}}+\frac{\eta_{\overline{s}}}{2}} w_{k,l}^L\;dx\;dy + \sum_{s=1}^{N_P}P_s w_{k,l}^L\Big|_{\substack{x=x_s\\y=y_s}} \\[1ex]
&-K\,\kappa_T^e\int_{-b/2}^{b/2}\int_{-a/2}^{a/2}\left(\frac{\partial^2 w_{k,l}^L}{\partial x^2}+\frac{\partial^2 w_{k,l}^L}{\partial y^2}\right)dx\;dy \\[1ex]
&+\sum_{m=0}^{N_m}\sum_{n=0}^{N_n}\sum_{M=I}^{IV}c_{m,n}^M\left(-K\int_{-b/2}^{b/2}\int_{-a/2}^{a/2}\left[\left(\frac{\partial^2 w_{m,n}^M}{\partial x^2}+\nu\frac{\partial^2 w_{m,n}^M}{\partial y^2}\right)\frac{\partial^2 w_{k,l}^L}{\partial x^2}\right.\right.
\end{aligned}
$$

$$+ \left(\frac{\partial^2 w_{m,n}^M}{\partial y^2} + \nu \frac{\partial^2 w_{m,n}^M}{\partial x^2} \right) \frac{\partial^2 w_{k,l}^L}{\partial y^2} + \left(2\,(1-\nu)\, \frac{\partial^2 w_{m,n}^M}{\partial y\,\partial x} \right) \frac{\partial^2 w_{k,l}^L}{\partial y\,\partial x} \bigg] \; dx \; dy$$

$$- \int\limits_{-b/2}^{b/2} \int\limits_{-a/2}^{a/2} c\, w_{m,n}^M\, w_{k,l}^L \; dx \; dy - \sum_{s=1}^{N_C} C_s\, w_{m,n}^M\, w_{k,l}^L \bigg|_{\substack{x=x_s \\ y=y_s}} \Bigg) \Bigg\} = 0 \,.$$

$$(3.45)$$

Requiring validity of (3.45) for *any* combination of virtual coefficients $\dot{\check{c}}_{k,l}$, and taking into account the orthogonality of the double trigonometric functions, i.e. of

$$\int\limits_{-b/2}^{b/2} \int\limits_{-a/2}^{a/2} \frac{\partial^2 w_{m,n}^M}{\partial x^2} \frac{\partial^2 w_{k,l}^L}{\partial x^2} \; dx \; dy = \int\limits_{-b/2}^{b/2} \int\limits_{-a/2}^{a/2} \frac{\partial^2 w_{m,n}^M}{\partial y^2} \frac{\partial^2 w_{k,l}^L}{\partial x^2} \; dx \; dy$$

$$= \int\limits_{-b/2}^{b/2} \int\limits_{-a/2}^{a/2} \frac{\partial^2 w_{m,n}^M}{\partial y^2} \frac{\partial^2 w_{k,l}^L}{\partial y^2} \; dx \; dy = \int\limits_{-b/2}^{b/2} \int\limits_{-a/2}^{a/2} \frac{\partial^2 w_{m,n}^M}{\partial y\,\partial x} \frac{\partial^2 w_{k,l}^L}{\partial y\,\partial x} \; dx \; dy$$

$$= \int\limits_{-b/2}^{b/2} \int\limits_{-a/2}^{a/2} w_{m,n}^M\, w_{k,l}^L \; dx \; dy = 0 \qquad \text{for} \quad M \neq L \,, \tag{3.46}$$

yields a system of $(N_m \times N_n)$ algebraic equations for the unknowns $c_{m,n}^L$; reading as

$$\int\limits_{-b/2}^{b/2} \int\limits_{-a/2}^{a/2} p\, w_{k,l}^L \; dx \; dy + \sum_{s=1}^{N_{\overline{p}}} \overline{p}_s \int_{x_{\overline{s}}-\frac{\xi_{\overline{s}}}{2}}^{x_{\overline{s}}+\frac{\xi_{\overline{s}}}{2}} \int_{y_{\overline{s}}-\frac{\eta_{\overline{s}}}{2}}^{y_{\overline{s}}+\frac{\eta_{\overline{s}}}{2}} w_{k,l}^L \; dx \; dy + \sum_{s=1}^{N_P} P_s w_{k,l}^L \bigg|_{\substack{x=x_s \\ y=y_s}}$$

$$- K\, \kappa_T^e \int\limits_{-b/2}^{b/2} \int\limits_{-a/2}^{a/2} \left(\frac{\partial^2 w_{k,l}^L}{\partial x^2} + \frac{\partial^2 w_{k,l}^L}{\partial y^2} \right) \; dx \; dy$$

$$+ \sum_{m=0}^{N_m} \sum_{n=0}^{N_n} c_{m,n}^L \Bigg\{ -K \int\limits_{-b/2}^{b/2} \int\limits_{-a/2}^{a/2} \Bigg[\left(\frac{\partial^2 w_{m,n}^L}{\partial x^2} + \nu \frac{\partial^2 w_{m,n}^L}{\partial y^2} \right) \frac{\partial^2 w_{k,l}^L}{\partial x^2}$$

$$+ \left(\frac{\partial^2 w_{m,n}^L}{\partial y^2} + \nu \frac{\partial^2 w_{m,n}^L}{\partial x^2} \right) \frac{\partial^2 w_{k,l}^L}{\partial y^2} + \left(2\,(1-\nu)\, \frac{\partial^2 w_{m,n}^L}{\partial y\,\partial x} \right) \frac{\partial^2 w_{k,l}^L}{\partial y\,\partial x} \bigg] \; dx \; dy$$

$$- \int\limits_{-b/2}^{b/2} \int\limits_{-a/2}^{a/2} c\, w_{m,n}^L\, w_{k,l}^L \; dx \; dy - \sum_{s=1}^{N_C} C_s\, w_{m,n}^L\, w_{k,l}^L \bigg|_{\substack{x=x_s \\ y=y_s}} \Bigg\} = 0 \,,$$

$$\text{for} \quad k = 0, ..., N_m; \qquad l = 0, ..., N_n; \qquad L = I, ..., IV \,. \tag{3.47}$$

It is suitable to reformulate Eq. (3.47) in matrix form, yielding

$$
\begin{bmatrix}
M_{0000}^{m,L} + M_{0000}^{c,L} + M_{0000}^{C,L} & \cdot & & \cdot \\
\cdot & \cdot & & \cdot \\
\cdot & M_{klmn}^{m,L} + M_{klmn}^{c,L} + M_{klmn}^{C,L} & & \cdot \\
\cdot & \cdot & & \cdot \\
\cdot & \cdot & & M_{N_m}^{m,L} + M_{N_m}^{c,L} + M_{N_m}^{C,L}
\end{bmatrix}
\cdot
\begin{bmatrix}
c_{00}^L \\
\cdot \\
c_{mn}^L \\
\cdot \\
c_{N_m}^L
\end{bmatrix}
=
$$

$$
=
\begin{bmatrix}
-V_{00}^{\kappa_T^e,L} - V_{00}^{p,L} - V_{00}^{\overline{p},L} - V_{00}^{P,L} \\
\cdot \\
-V_{kl}^{\kappa_T^e,L} - V_{kl}^{p,L} - V_{kl}^{\overline{p},L} - V_{kl}^{P,L} \\
\cdot \\
-V_{N_m}^{\kappa_T^e,L} - V_{N_m}^{p,L} - V_{N_m}^{\overline{p},L} - V_{N_m}^{P,L}
\end{bmatrix},
\tag{3.48}
$$

with

$$
\begin{aligned}
M_{klmn}^{m,L} \;=\; & -K \int\limits_{-b/2}^{b/2} \int\limits_{-a/2}^{a/2} \left[\left(\frac{\partial^2 w_{m,n}^L}{\partial x^2} + \nu \frac{\partial^2 w_{m,n}^L}{\partial y^2} \right) \frac{\partial^2 w_{k,l}^L}{\partial x^2} \right. \\
& \left. + \left(\frac{\partial^2 w_{m,n}^L}{\partial y^2} + \nu \frac{\partial^2 w_{m,n}^L}{\partial x^2} \right) \frac{\partial^2 w_{k,l}^L}{\partial y^2} + \left(2\,(1-\nu)\,\frac{\partial^2 w_{m,n}^L}{\partial y\,\partial x} \right) \frac{\partial^2 w_{k,l}^L}{\partial y\,\partial x} \right] \, dx\; dy\,,
\end{aligned}
\tag{3.49}
$$

as the stiffness matrix elements associated to bending and twisting moments (see the Appendix A, Eq. (3.A.5)-(3.A.29), and (3.A.39)-(3.A.113) for analytical expressions concerning (3.49));

$$
M_{klmn}^{c,L} \;=\; -\int\limits_{-b/2}^{b/2} \int\limits_{-a/2}^{a/2} c\, w_{m,n}^L\, w_{k,l}^L \; dx\; dy\,,
\tag{3.50}
$$

as the stiffness matrix elements associated to the Winkler foundation (see the Appendix A, Eq. (3.A.5)-(3.A.29), and (3.A.39)-(3.A.113) for analytical expressions concerning (3.50));

$$
M_{klmn}^{C,L} \;=\; -\sum_{s=1}^{N_C} C_s w_{m,n}^L\, w_{k,l}^L \Big|_{\substack{x=x_s \\ y=y_s}} ,
\tag{3.51}
$$

as the stiffness matrix elements associated to single springs (see the Appendix A, Eq. (3.A.30), and (3.A.39)-(3.A.113) for analytical expressions concerning (3.51));

$$
V_{kl}^{\kappa_T^e,L} \;=\; -K\, \kappa_T^e \int\limits_{-b/2}^{b/2} \int\limits_{-a/2}^{a/2} \left(\frac{\partial^2 w_{k,l}^L}{\partial x^2} + \frac{\partial^2 w_{k,l}^L}{\partial y^2} \right) \, dx\; dy\,,
\tag{3.52}
$$

as the load vector elements associated to temperature gradients (see the Appendix A, Eq. (3.A.31)-(3.A.34) for analytical expressions concerning (3.52));

$$V_{kl}^{p,L} = \int_{-b/2}^{b/2} \int_{-a/2}^{a/2} p\, w_{k,l}^L \; dx\; dy\,, \tag{3.53}$$

as the load vector elements associated to the surface load acting on the entire plate (see the Appendix A, Eq. (3.A.1)-(3.A.4) for analytical expressions concerning (3.53));

$$V_{kl}^{\overline{p},L} = \sum_{s=1}^{N\overline{p}} \overline{p}_s \int_{x_{\overline{s}}-\frac{\xi_{\overline{s}}}{2}}^{x_{\overline{s}}+\frac{\xi_{\overline{s}}}{2}} \int_{y_{\overline{s}}-\frac{\eta_{\overline{s}}}{2}}^{y_{\overline{s}}+\frac{\eta_{\overline{s}}}{2}} w_{k,l}^L \; dx\; dy\,, \tag{3.54}$$

as the load vector elements associated to patched surface loads (see the Appendix A, Eq. (3.A.35)-(3.A.38) for analytical expressions concerning (3.54)); and

$$V_{kl}^{P,L} = \sum_{s=1}^{N_P} P_s w_{k,l}^L \Big|_{\substack{x=x_s \\ y=y_s}}\,, \tag{3.55}$$

as the load vector elements associated to single forces. The corresponding approximative solution for $w(x,y)$ is the more precise the more series deflection members (being $N_m \times N_n$ in number) are employed.

3.5 Application to pavement engineering problems, and validation by means of the Finite Element Method

The structural problem (3.48)-(3.55) is now applied to the analysis of a quadratic plate of $a = b = 5.5\,\text{m}$ side length and of $h = 0.25\,\text{m}$ height. Considering situations encountered in pavement engineering, an elastic Young's modulus of $E = 30 \times 10^6\,\text{kN/m}^2$, a Poisson's ratio of $\nu = 0.167$, and a coefficient of linear thermal expansion of $\alpha_T = 1 \times 10^{-5}\,\text{K}^{-1}$ refer to concrete [Eisenmann, 1979]. An embedment for concrete pavements is characterized by a modulus of $c = 0.1\,\text{GPa/m}$ [Lang, 2010; Ullrich, 2016]. In the following, this plate is subjected to different mechanical loads and temperature variations; and corresponding results will be presented in a dimensionless way, which does not only comprise the actual deformations and stress resultants arising from the aforementioned material, structural, and loading characteristics, but which reflects infinitely many additional problems which are associated with different plate thicknesses, different elastic Young's moduli, different temperature gradients, and different mechanical loads. In more detail, we consider a dimensional analysis [Barenblatt, 1996] of the deflection function (3.39) arising from the solution of (3.48), together of (3.49) to (3.55). This yields the following dimensionless relations (provided all patched loads exhibit the same magnitude $\overline{p}$ and all bolts exhibit the same stiffness C)

$$\begin{aligned} \Pi &= \left(\frac{p}{E} + \frac{\overline{p}}{E} + \alpha_T \Delta T_\kappa \right) \\ &\quad \times [\Pi]_0 \left(\frac{x}{h}, \frac{y}{h}, \frac{a}{h}, \frac{x_1}{h}, ..., \frac{x_s}{h}, ..., \frac{x_{N_C}}{h}, \frac{y_1}{h}, ..., \frac{y_s}{h}, ..., \frac{y_{N_C}}{h}, \right. \\ &\qquad\quad \left. \frac{x_{\overline{1}}}{h}, \frac{x_{\overline{2}}}{h}, \frac{y_{\overline{1}}}{h}, \frac{y_{\overline{2}}}{h}, \frac{\xi_{\overline{1}}}{h}, \frac{\xi_{\overline{2}}}{h}, \frac{\eta_{\overline{1}}}{h}, \frac{\eta_{\overline{2}}}{h}, \nu, \frac{c\,h}{E}, \frac{C}{h\,E} \right)\,, \end{aligned}$$

$$\text{for} \qquad \Pi = \frac{w}{h}, \varepsilon_{xx}, \varepsilon_{xy}, \varepsilon_{yy}, \frac{m_{xx}}{E\,h^2}, \frac{m_{xy}}{E\,h^2}, \frac{m_{yy}}{E\,h^2}, \frac{q_x}{E\,h}, \frac{q_y}{E\,h}. \qquad (3.56)$$

(6.43) elucidates that basic dimensionless functions Π_0, which depend on geometrical and embedment/bolt stiffnesses, can be multiplied with a sum of dimensionless quantities related to mechanical and thermal loadings, so as to deliver dimensionless quantities related to deflections, strains, and stress resultants.

These relations, depicted in the format of $\Pi = \Pi_0(x/h, y/h, a/h = x_1/h = ... = x_s/h = ... = x_{N_C}/h = y_1/h = ... = y_s/h = ... = y_{N_C}/h = x_{\overline{1}}/h = x_{\overline{2}}/h = y_{\overline{1}}/h = y_{\overline{2}}/h = \xi_{\overline{1}}/h = \xi_{\overline{2}}/h = \eta_{\overline{1}}/h = \eta_{\overline{2}}/h = \nu = c\,h/E = C/(hE) = \text{constant})$ in Figures 3.9, 3.10, 3.12, 3.13, 3.15, and 3.16, are valid for any loading types p, $\overline{p}$, and $\alpha_T \Delta T_\kappa$. Furthermore, they hold for any change $h \to \lambda\,h$, once $x \to \lambda\,x$, $y \to \lambda\,y$, $a \to \lambda\,a$, $x_1 \to \lambda\,x_1$, ..., $x_s \to \lambda\,x_s$, ..., $x_{N_C} \to \lambda\,x_{N_C}$, $y_1 \to \lambda\,y_1$, ..., $y_s \to \lambda\,y_s$, ..., $y_{N_C} \to \lambda\,y_{N_C}$, $x_{\overline{1}} \to \lambda\,x_{\overline{1}}$, $x_{\overline{2}} \to \lambda\,x_{\overline{2}}$, $y_{\overline{1}} \to \lambda\,y_{\overline{1}}$, $y_{\overline{2}} \to \lambda\,y_{\overline{2}}$, $\xi_{\overline{1}} \to \lambda\,\xi_{\overline{1}}$, $\xi_{\overline{2}} \to \lambda\,\xi_{\overline{2}}$, $\eta_{\overline{1}} \to \lambda\,\eta_{\overline{1}}$, $\eta_{\overline{2}} \to \lambda\,\eta_{\overline{2}}$, $c \to c/\lambda$, and $C \to \lambda\,C$; and they hold for any change $E \to \lambda\,E$, once $c \to \lambda\,c$ and $C \to \lambda\,C$.

3.5.1 Example 1: Elastically supported plate, with loose anchor bolt connections at its edges, subjected to uniform surface load

Anchor bolts represented by single springs with stiffness $C = 410000\,\text{kN/m}$ are distributed along the plate's edges, at distances of $a/3 = b/3 = 1.833\,\text{m}$. The plate is subjected to a uniform surface load $p(x,y) = \text{constant} = p$, representing the deadload of a concrete plate for example, see Fig. 3.8. As this load is obviously symmetric with respect to both the x-axis and the y-axis, the
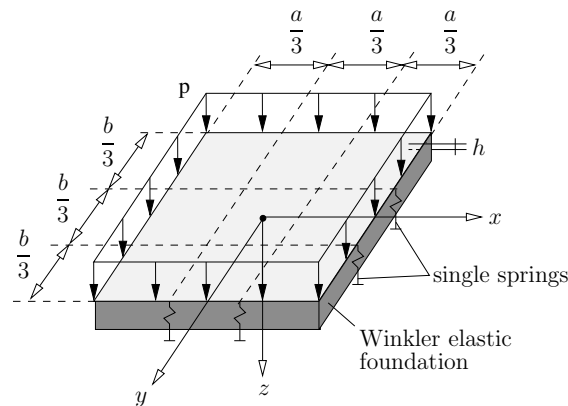
Fig. 3.8: Example 1: quadratic plate on elastic foundation with loose anchor bolt connections at its edges, side length a, thickness h, elastic Young's modulus E, and Winkler modulus c, subjected to uniform surface load p.

evaluation of the elements occurring in (3.48) can be restricted to double-symmetric trigonometric functions, i.e. to $w_{m,n}^I$, see Appendix 3.A.1 for the load vector elements, and for the stiffness matrix elements, respectively. The approximative solution for the dimensionless deflection $[w/h]_0$ at the plate's center as well as that for the dimensionless bending moment $[m_{xx}/(E\,h^2)]_0$ at the same location, can be regarded as converged once $N_m \times N_n = 8 \times 8 = 64$ series members are employed, see Figures 3.9(e) and 3.10(f). With Matlab version R2012b [Mathworks, 2012] running on a computer AMD Phenom(tm) II X6 1090T with 8GB RAM, this related to 0.8 seconds computing time, see Fig. 3.9(f). Considering corresponding fields, the deflections close to the corners of the plate are larger than those in the midpoints of the plate's sides, see Fig. 3.9(a). This is an effect of the single springs (bolts) located at the plate's sides. These bolts also provoke significant strain and stress resultant concentrations, see Figures 3.9(b-d) and 3.10(a-e).
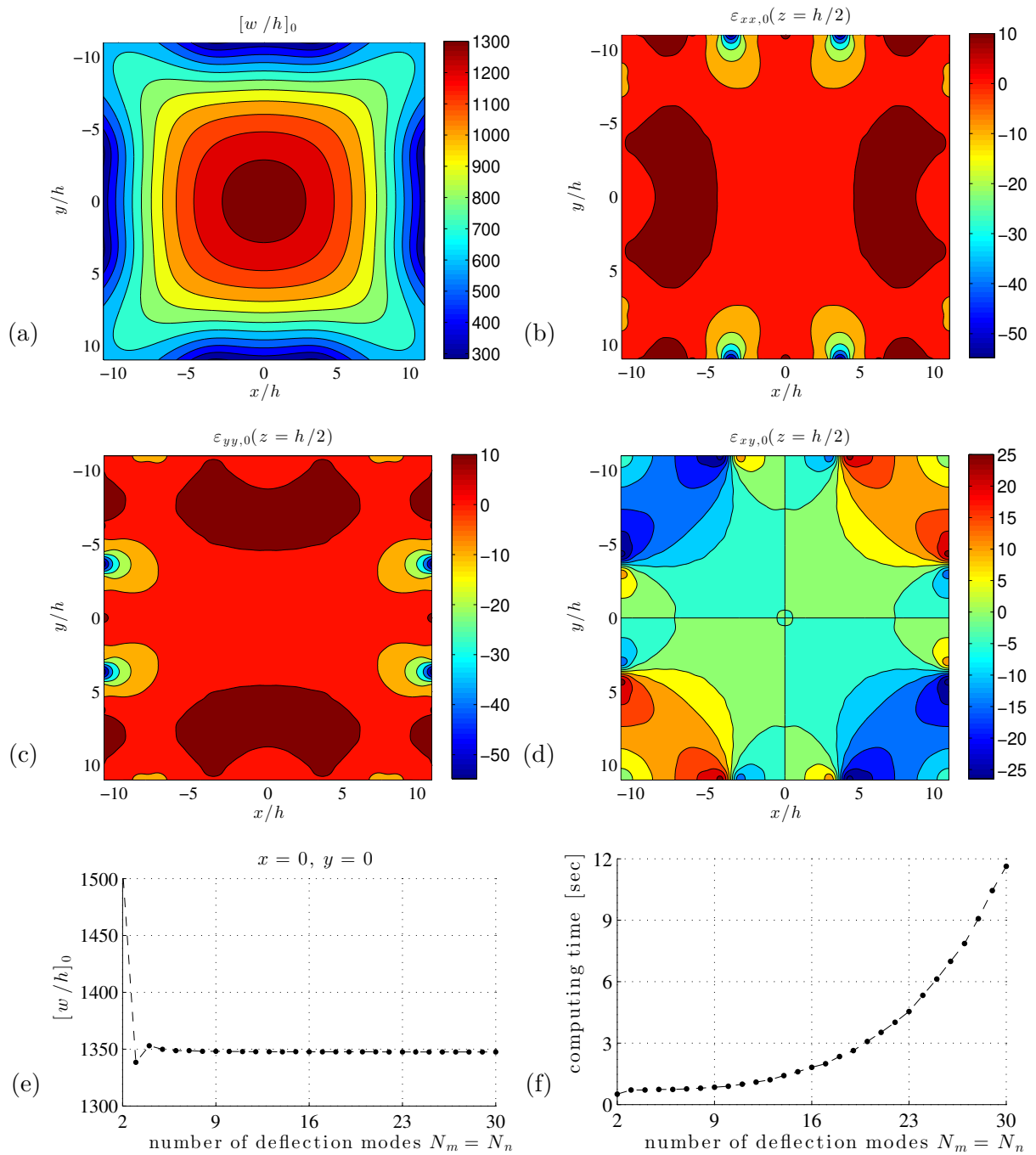
Fig. 3.9: Dimensionless deformation quantities in elastically supported plate, with loose anchor bolt connections at its edges, subjected to uniform surface load p: (a) dimensionless deflections $[w/h]_0$, (b) normal strain $\varepsilon_{xx,0}$, (c) normal strain $\varepsilon_{yy,0}$, (d) shear strain $\varepsilon_{xy,0}$, (e) convergence study of the dimensionless deflection $[w/h]_0$ located at $x = y = 0$ as a function of the number of deflection modes $N_m = N_n$, and (f) corresponding computing time for results associated to one point of the plate.
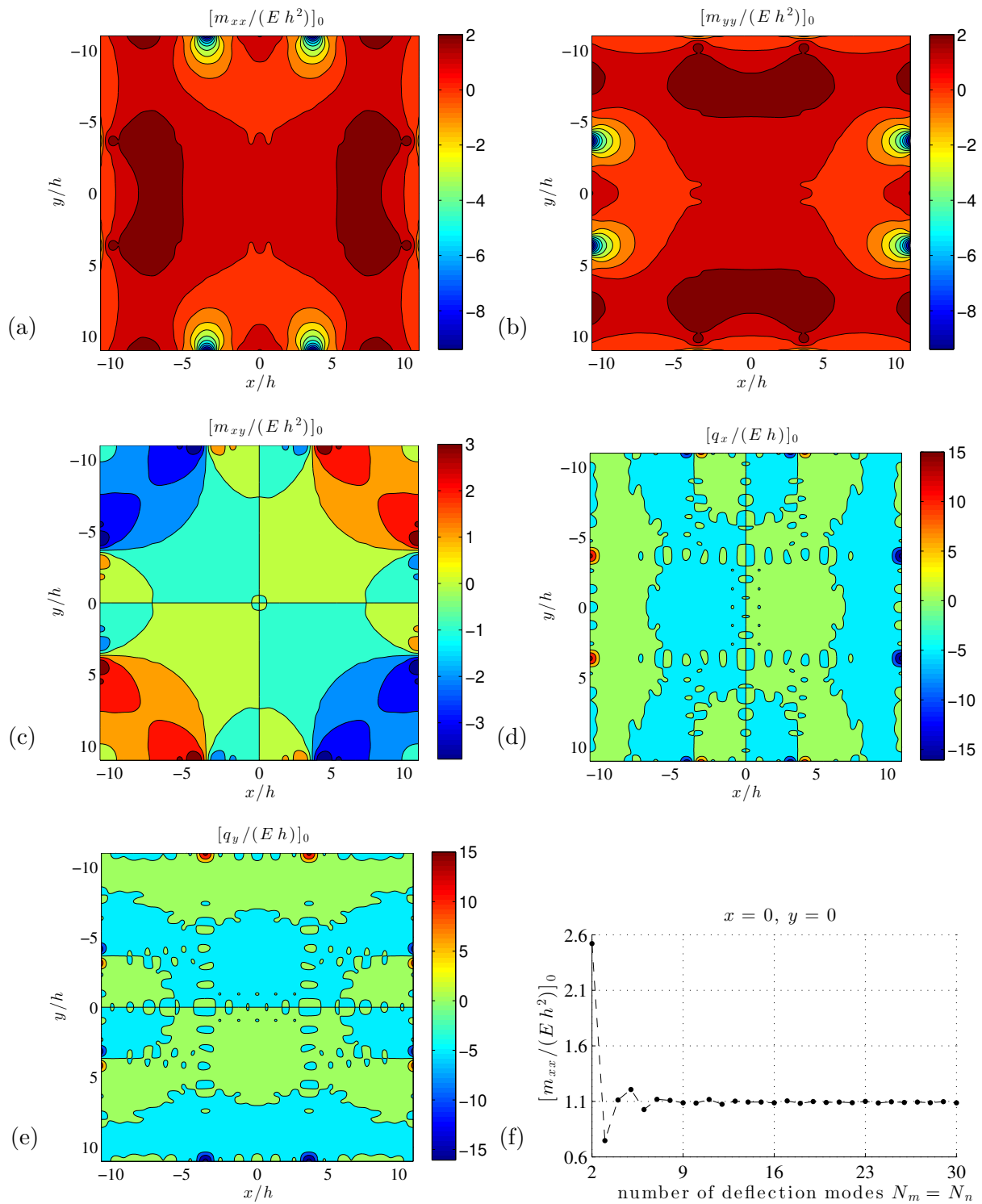
Fig. 3.10: Dimensionless stress resultants in elastically supported plate, with loose anchor bolt connections at its edges, subjected to uniform surface load p: (a) bending moment around y-axis $[m_{xx}/(E\,h^2)]_0$, (b) bending moment around x-axis $[m_{yy}/(E\,p\,h^2)]_0$, (c) twisting moment $[m_{xy}/(E\,h^2)]_0$, (d) shear force $[q_x/(E\,h)]_0$, (e) shear force $[q_y/(E\,h)]_0$, and (f) convergence study of the dimensionless moment $[m_{xx}/(E\,h^2)]_0$ located at $x = y = 0$ as a function of the number of deflection modes $N_m = N_n$.

These results are compared to those stemming from a Finite Element analysis performed with the commercial software RFEM [Dlubal, 2016], based on 47 961 rectangular Kirchhoff plate elements (MITC4 elements [Ko et al., 2016] with a dimension of $0.1\,h$). Maximum differences between FE results and series-based results according to (3.47) are as low as $0.05\,\%$ for the displacements, and $1.56\,\%$ for the moments. The ratio of CPU times needed for the FE-based and the series-based analysis (pointwise calculation performed for $N_m = N_n = 8$), respectively, amounted to 39.

3.5.2 Example 2: Elastically supported plate, with dense anchor bolt connections at its edges, subjected to temperature gradient

Anchor bolts represented by single springs with stiffness $C = 410000\,\mathrm{kN/m}$ are distributed along the plate's edges, at distances of $a/20 = b/20 = 0.275\,\mathrm{m}$. The plate is subjected to a temperature difference ΔT_κ between the lower and the upper surfaces, see Fig. 3.11. As this load is
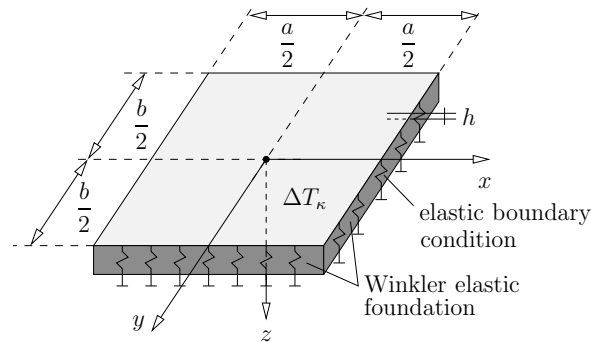
Fig. 3.11: Example 2: quadratic plate on elastic foundation with dense anchor bolt connections at its edges, side length a, thickness h, elastic Young's modulus E, and Winkler modulus c, subjected to the temperature difference ΔT_κ.

obviously symmetric with respect to both the x-axis and the y-axis, the evaluation of the elements occurring in (3.48) can be restricted to double-symmetric trigonometric functions, i.e. to $w_{m,n}^I$, see Appendix 3.A.2, (3.A.31)-(3.A.34), for the load vector elements, and Appendix 3.A.1, (3.A.5)-(3.A.30), for the stiffness matrix elements. The approximative solution for the dimensionless deflection $[w/h]_0$ located at $x = y = 6.2\,h$ as well as that for the dimensionless bending moment $[m_{xx}/(E\,h^2)]_0$ at the plate's center, can be regarded as converged once $N_m \times N_n = 9 \times 9 = 81$ series members are employed, see Figures 3.12(e) and 3.13(f). With Matlab version R2012b running on a computer AMD Phenom(tm) II X6 1090T with 8GB RAM, this related to 0.95 seconds computing time, see Fig. 3.12(f). Considering corresponding fields, the maximum deflections do not occur at the plate's center, but half way between the center and the corners of the plate, see Fig. 3.12(a). Obviously, the temperature-driven curvatures provoke larger reaction forces from the Winkler embedment at the plate's center than in regions closer to the plate's boundaries. As compared to Example 1, no significant strain and stress concentrations are observed around the bolts, since the distances between the bolts have been significantly reduced, compare Figure 3.12(b-d) to Figure 3.9(b-d); and compare Figure 3.13(a-e) to Figure3.10(a-e).

These results are compared to those stemming from a Finite Element analysis performed with the commercial software RFEM, based on 48 400 rectangular Kirchhoff plate elements (MITC4 elements with a dimension of $0.1\,h$). Maximum differences between FE results and series-based results according to (3.47) are as low as $0.32\,\%$ for the displacements, and $0.74\,\%$ for
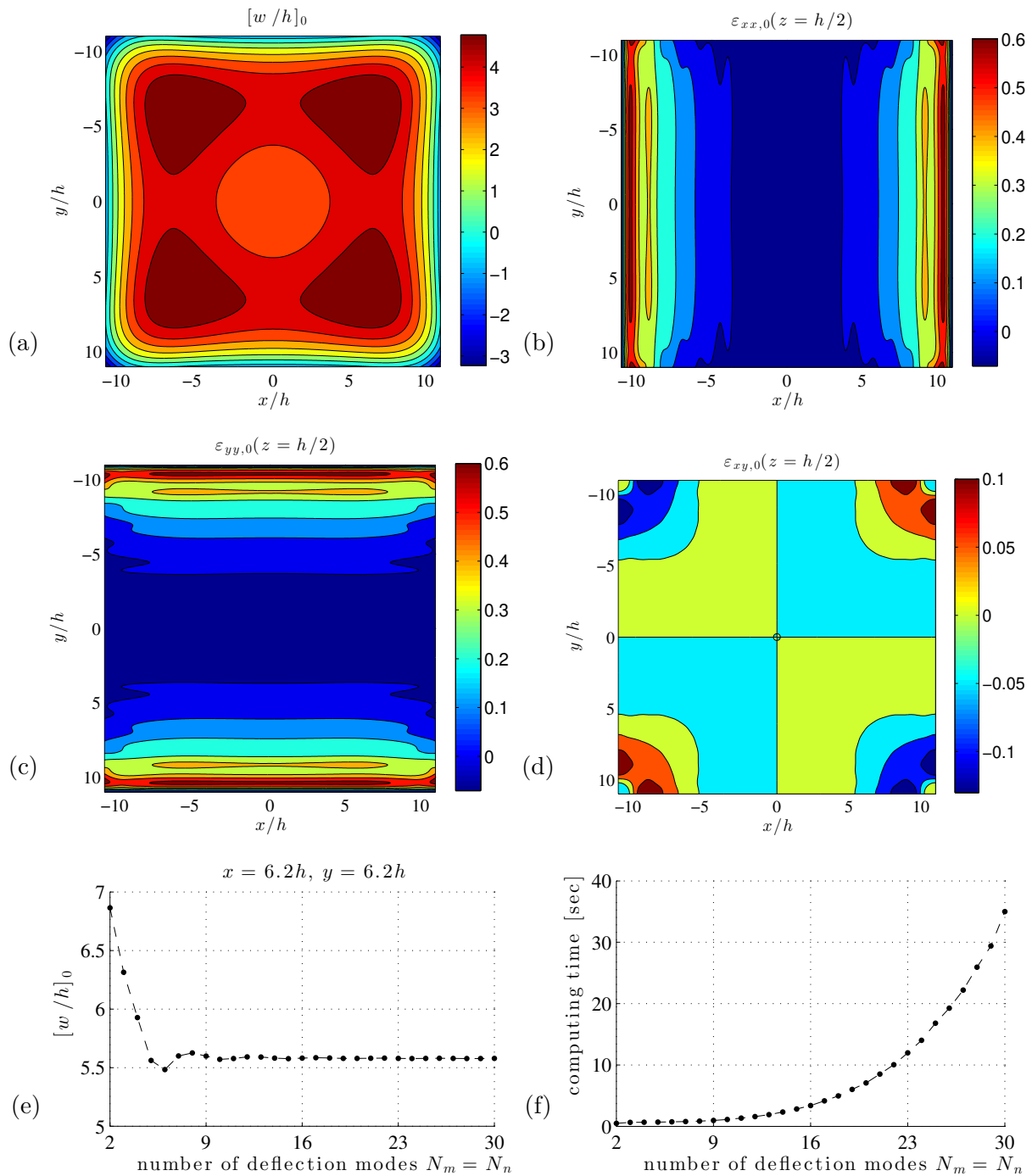
Fig. 3.12: Dimensionless deformation quantities in elastically supported plate, with dense anchor bolt connections at its edges, subjected to temperature gradient $\Delta T_\kappa/h$: (a) dimensionless deflections $[w/h]_0$, (b) normal strain $\varepsilon_{xx,0}$, (c) normal strain $\varepsilon_{yy,0}$, (d) shear strain $\varepsilon_{xy,0}$, (e) convergence study of the dimensionless deflection $[w/h]_0$ located at $x = y = 6.2\,h$ as a function of the number of deflection modes $N_m = N_n$, and (f) corresponding computing time for results associated to one point of the plate.
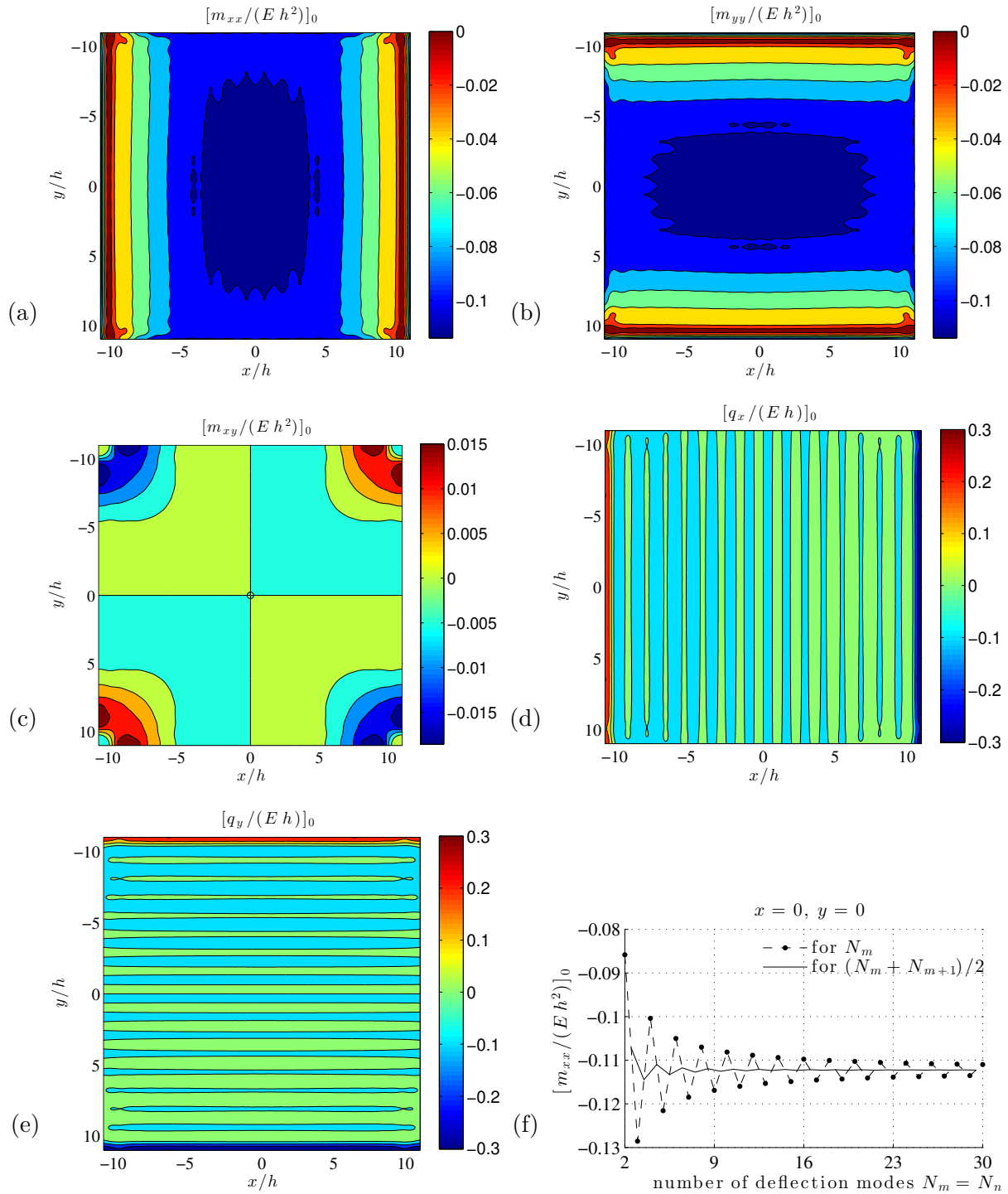
Fig. 3.13: Dimensionless stress resultants in elastically supported plate, with dense anchor bolt connections at its edges, subjected to temperature gradient $\Delta T_\kappa/h$: (a) bending moment around y-axis $[m_{xx}/(E\,h^2)]_0$, (b) bending moment around x-axis $[m_{yy}/(E\,h^2)]_0$, (c) twisting moment $[m_{xy}/(E\,h^2)]_0$, (d) shear force $[q_x/(E\,h)]_0$, (e) shear force $[q_y/(E\,h)]_0$, and (f) convergence study of the dimensionless moment $[m_{xx}/(E\,h^2)]_0$ located at $x = y = 0$ as a function of the number of deflection modes $N_m = N_n$.

the moments. The ratio of CPU times needed for the FE-based and the series-based analysis (pointwise calculation performed for $N_m = N_n = 9$), respectively, amounted to 22.

3.5.3 Example 3: Elastically supported plate, with dense anchor bolt connections at its edges, subjected to patched loads

Anchor bolts represented by single springs with stiffness $C = 410000\,\text{kN/m}$ are distributed along the plate's edges, at distances of $a/20 = b/20 = 0.275\,\text{m}$. The plate is subjected to patched loads $\bar{p}_1 = \bar{p}_2 = \bar{p}$, which are distributed over rectangular areas of side lengths $\xi_{\bar{1}} = \xi_{\bar{2}} = 0.25\,\text{m}$, $\eta_{\bar{1}} = \eta_{\bar{2}} = 0.25\,\text{m}$, with coordinates of the central points of these rectangular areas $x_{\bar{1}} = -0.5\,\text{m}$, $y_{\bar{1}} = 1\,\text{m}$, and $x_{\bar{2}} = 1.5\,\text{m}$, $y_{\bar{2}} = 1\,\text{m}$, see Fig. 3.14. These patched loads represent the pressures
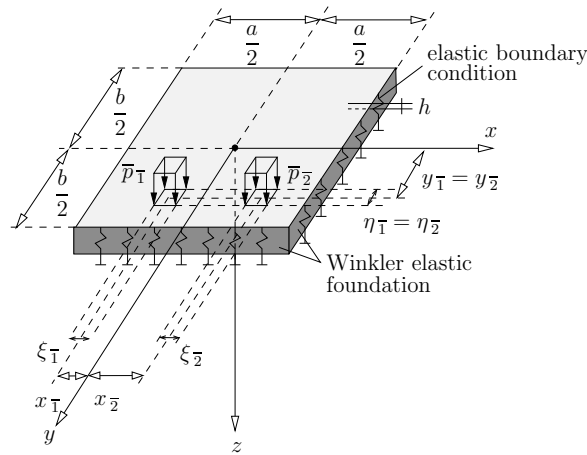
Fig. 3.14: Example 3: quadratic plate on elastic foundation with dense anchor bolt connections at its edges, side length a, thickness h, elastic Young's modulus E, and Winkler modulus c, subjected to patched loads $\bar{p}_1 = \bar{p}_2$.

of two tires of a car on the road surface made of concrete slabs. As these loads are obviously antimetric with respect to both the x-axis and the y-axis, the evaluation of the elements occurring in (3.48) is realized for all four types of trigonometric functions, $w_{m,n}^I$, $w_{m,n}^{II}$, $w_{m,n}^{III}$, $w_{m,n}^{IV}$, see Appendix 3.A.3 for the load vector and stiffness matrix elements, respectively. The approximative solution for the dimensionless deflection $[w/h]_0$ located at $x = -2\,h$, $y = 4\,h$ as well as that for the dimensionless bending moment $[m_{yy}/(E\,h^2)]_0$ at at the same location, can be regarded as converged once $N_m \times N_n \times 4 = 18 \times 18 \times 4 = 1296$ series members are employed, see Figures 3.15(e) and 3.16(f). With Matlab version R2012b running on a computer AMD Phenom(tm) II X6 1090T with 8GB RAM, this related to 18.86 seconds computing time, see Fig. 3.15(f). Considering corresponding fields, the maximum deflections occur at the acting areas of the patched loads, see Fig. 3.15(a). These patched loads also provoke significant strain and stress resultant concentrations, see Figures 3.15(b-d) and 3.16(a-e).

These results are compared to those stemming from a Finite Element analysis performed with the commercial software RFEM, based on 87 400 rectangular Kirchhoff plate elements (MITC4 elements with a dimension of $0.08\,h$). Maximum differences between FE results and series-based results according to (3.47) are as low as 1.44 % for the displacements, and 0.35 % for the moments. The ratio of CPU times needed for the FE-based and the series-based analysis (pointwise calculation performed for $N_m = N_n = 18$), respectively, amounted to 1.5.
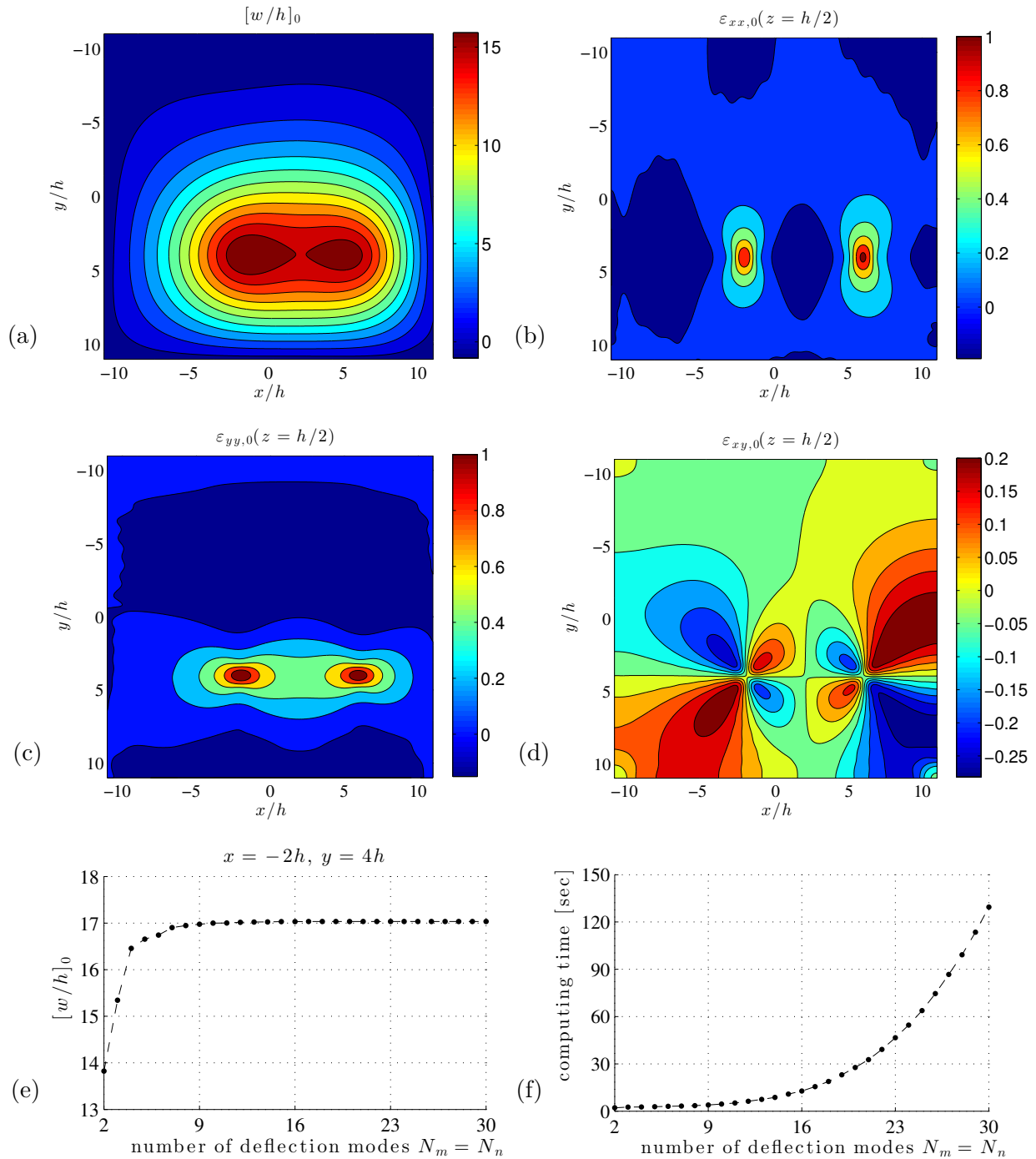
Fig. 3.15: Dimensionless deformation quantities in elastically supported plate, with dense anchor bolt connections at its edges, subjected to patched loads $\overline{p}$: (a) dimensionless deflections $[w/h]_0$, (b) normal strain $\varepsilon_{xx,0}$, (c) normal strain $\varepsilon_{yy,0}$, (d) shear strain $\varepsilon_{xy,0}$, (e) convergence study of the dimensionless deflection $[w/h]_0$ located at $x = -2\,h$, $y = 4\,h$ as a function of the number of deflection modes $N_m = N_n$, and (f) corresponding computing time for results associated to one point of the plate.
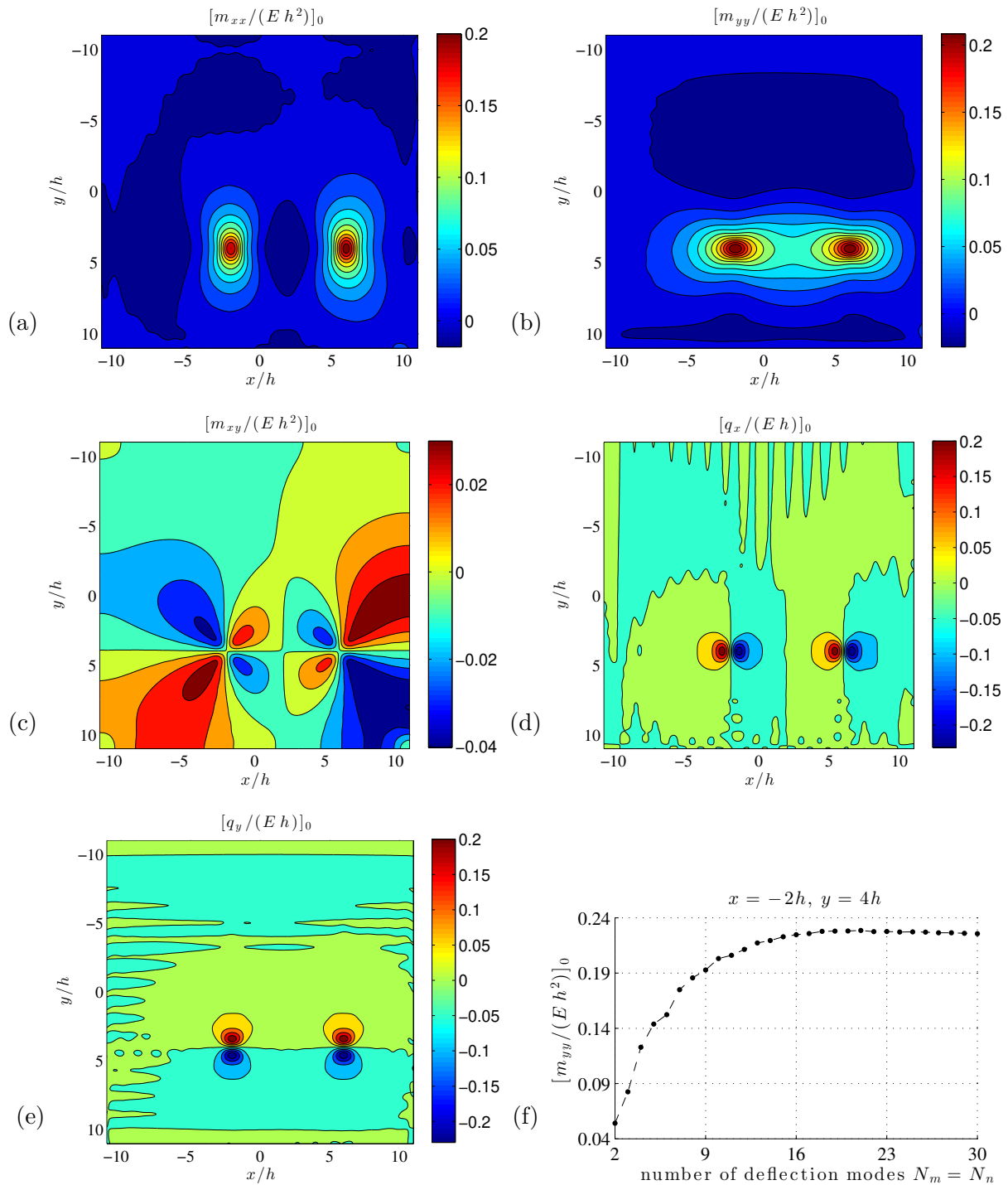
Fig. 3.16: Dimensionless stress resultants in elastically supported plate, with dense anchor bolt connections at its edges, subjected to patched loads $\bar{p}$: (a) bending moment around y-axis $[m_{xx}/(E\,h^2)]_0$, (b) bending moment around x-axis $[m_{yy}/(E\,h^2)]_0$, (c) twisting moment $[m_{xy}/(E\,h^2)]_0$, (d) shear force $[q_x/(E\,h)]_0$, (e) shear force $[q_y/(E\,h)]_0$, and (f) convergence study of the dimensionless moment $[m_{yy}/(E\,h^2)]_0$ located at $x = -2\,h$, $y = 4\,h$ as a function of the number of deflection modes $N_m = N_n$.

3.6 Conclusion

The Principle of Virtual Power, with rigorous discrimination of internal versus external forces, was applied to the problem of a Kirchhoff plate on a flexible foundation. The resulting, Fourier series-based Galerkin-type solution procedure allowed for overcoming "spurious" external moments and shear forces, as they are encountered with the widely used plate theories of the Vlasov-type. For specific problems in pavement engineering, the aforementioned solution procedure also appears as an efficient alternative to the standardly applied Finite Element method. Namely, it may reduce computing times by a factor of almost forty. We regard this as an interesting example for energetically consistent formulations appearing as the basis for particularly relevant and reliable solutions to everyday engineering problems; comparable to similar cases known from the field of stability analysis [Ji et al., 2010; Bažant et al., 2012; Bažant and Vorel, 2014], of ferromagnetic plates [Maugin and Goudjo, 1982], of large strain beam theory [Jelenić and Saje, 1995], of shear deformable beams [Polizzotto, 2015], of gradient elastic beams and plates [Polizzotto, 2016], and of virtual fields used for elastic parameter identification [Grédiac et al., 2006].

Acknowlegements

3.A Stiffness matrix and load vector elements for provided examples

In order to determine the unknown coefficients c_{mn}^L, we have to solve the system of algebraic equations (3.48) with the corresponding stiffness matrix- and load vector elements (3.49)-(3.55), for the chosen number of deflection modes N_m and N_n, respectively. These matrix- and vector elements are specified for the three provided examples, as discussed in the following Sections.

3.A.1 Stiffness matrix and load vector elements for Example 1

As the loading in Example 1 is symmetric with respect to both the x-axis and the y-axis, only the trigonometric functions of type $w_{m,n}^I$ are employed to solve the system of equations (3.48). Hence, substituting the deflection modes $w_{m,n}^I$ and $w_{k,l}^I$ according to (3.40) into (3.49)-(3.55) yields, after integration, the elements for Example 1. First, we provide the load vector elements associated to surface load over the entire plate p (3.53), for any combinations of k, and l:

(i) Load vector element associated to surface load p, for $k = l = 0$:

$$V_{00}^{p,I} = p\,a\,b\,, \tag{3.A.1}$$

(ii) Load vector element associated to surface load p, for $k = 0$ and $l \neq 0$:

$$V_{0l}^{p,I} = 2\,p\,a\,b\sin\left(1/2\,l\pi\right)/\left(l\pi\right). \tag{3.A.2}$$

(iii) Load vector element associated to surface load p, for $k \neq 0$ and $l = 0$:

$$V_{k0}^{p,I} = 2\,p\,a\,b\sin\left(1/2\,k\pi\right)/\left(k\pi\right). \tag{3.A.3}$$

(iv) Load vector element associated to surface load p, for $k \neq 0$ and $l \neq 0$:

$$V_{kl}^{p,I} = 4\, p\, a\, b\, \sin\left(1/2\, k\pi\right) \sin\left(1/2\, l\pi\right) / \left(\pi^2 k\, l\right). \tag{3.A.4}$$

Next, we provide the stiffness matrix elements for the employed trigonometric functions of type $w_{m,n}^I$, see (3.49)-(3.51), for 25 combinations of k, l, m, and n:

1. Stiffness matrix elements for $k = l = m = n = 0$:

$$M_{0000}^{m,I} = 0\,, \qquad M_{0000}^{c,I} = -c\, a\, b\,. \tag{3.A.5}$$

2. Stiffness matrix elements for $k = l = m = 0$, and $n \neq 0$:

$$M_{000n}^{m,I} = 0\,, \qquad M_{000n}^{c,I} = -\frac{2\, cab \sin\left(1/2\, n\pi\right)}{n\pi}\,. \tag{3.A.6}$$

3. Stiffness matrix elements for $k = l = n = 0$, and $m \neq 0$:

$$M_{00m0}^{m,I} = 0\,, \qquad M_{00m0}^{c,I} = -\frac{2\, cab \sin\left(1/2\, m\pi\right)}{m\pi}\,. \tag{3.A.7}$$

4. Stiffness matrix elements for $k = l = 0$, and $m \neq 0$, $n \neq 0$:

$$M_{00mn}^{m,I} = 0\,, \qquad M_{00mn}^{c,I} = -\frac{4\, cab \sin\left(1/2\, m\pi\right) \sin\left(1/2\, n\pi\right)}{m\pi^2 n}\,. \tag{3.A.8}$$

5. Stiffness matrix elements for $m = k = 0$, and $n \neq 0$, $l \neq 0$ with $l \neq n$:

$$
\begin{aligned}
M_{0l0n}^{m,I} &= \frac{2\, Kl^2\pi^3 n^2 a \left(-l \sin\left(1/2\, l\pi\right) \cos\left(1/2\, n\pi\right) + n \cos\left(1/2\, l\pi\right) \sin\left(1/2\, n\pi\right)\right)}{b^3 l^2 - b^3 n^2}\,, \\
M_{0l0n}^{c,I} &= \frac{2\, cab \left(-l \sin\left(1/2\, l\pi\right) \cos\left(1/2\, n\pi\right) + n \cos\left(1/2\, l\pi\right) \sin\left(1/2\, n\pi\right)\right)}{\pi\, l^2 - \pi\, n^2}\,. \tag{3.A.9}
\end{aligned}
$$

6. Stiffness matrix elements for $m = k = 0$, and $n \neq 0$, $l \neq 0$ with $l = n$:

$$
\begin{aligned}
M_{0n0n}^{m,I} &= -\frac{Kn^3\pi^3 a \left(2\, \cos\left(1/2\, n\pi\right) \sin\left(1/2\, n\pi\right) + n\pi\right)}{2\, b^3}\,, \\
M_{0n0n}^{c,I} &= -\frac{cab \left(2\, \cos\left(1/2\, n\pi\right) \sin\left(1/2\, n\pi\right) + n\pi\right)}{2\, n\pi}\,. \tag{3.A.10}
\end{aligned}
$$

7. Stiffness matrix elements for $n = k = 0$, and $m \neq 0$, $l \neq 0$:

$$
\begin{aligned}
M_{0lm0}^{m,I} &= -\frac{4\, Kvl\pi^2 m \sin\left(1/2\, m\pi\right) \sin\left(1/2\, l\pi\right)}{ba}\,, \\
M_{0lm0}^{c,I} &= -\frac{4\, cab \sin\left(1/2\, m\pi\right) \sin\left(1/2\, l\pi\right)}{m\pi^2 l}\,. \tag{3.A.11}
\end{aligned}
$$

8. Stiffness matrix elements for $k = 0$, and $m \neq 0$, $n \neq 0$, $l \neq 0$ with $l \neq n$:

$$
\begin{aligned}
M_{0lmn}^{m,I} &= -\frac{4\, K\, \pi^2 l^2 \sin\left(1/2\, m\pi\right) \left(b^2 m^2 v + a^2 n^2\right)}{b^3 a \left(l^2 - n^2\right) m} \cdot \\
&\quad \cdot \left(l \sin\left(1/2\, l\pi\right) \cos\left(1/2\, n\pi\right) - n \cos\left(1/2\, l\pi\right) \sin\left(1/2\, n\pi\right)\right)\,, \\
M_{0lmn}^{c,I} &= -\frac{4\, cab \sin\left(1/2\, m\pi\right) \left(l \sin\left(1/2\, l\pi\right) \cos\left(1/2\, n\pi\right) - n \cos\left(1/2\, l\pi\right) \sin\left(1/2\, n\pi\right)\right)}{\pi^2 m \left(l^2 - n^2\right)}\,.
\end{aligned}
$$
$$\tag{3.A.12}$$

9. Stiffness matrix elements for $k = 0$, and $m \neq 0$, $n \neq 0$, $l \neq 0$ with $l = n$:

$$
\begin{aligned}
M_{mn0n}^{m,I} &= -\frac{K n \pi^2 \sin\left(1/2\, m\pi\right) \left(b^2 m^2 v + a^2 n^2\right) \left(2 \cos\left(1/2\, n\pi\right) \sin\left(1/2\, n\pi\right) + n\pi\right)}{b^3 a m}, \\
M_{mn0n}^{c,I} &= -\frac{cab \sin\left(1/2\, m\pi\right) \left(2 \cos\left(1/2\, n\pi\right) \sin\left(1/2\, n\pi\right) + n\pi\right)}{m\pi^2 n}.
\end{aligned}
\tag{3.A.13}
$$

10. Stiffness matrix elements for $m = l = 0$, and $n \neq 0$, $k \neq 0$:

$$
\begin{aligned}
M_{k00n}^{m,I} &= -\frac{4 K v n \pi^2 k \sin\left(1/2\, k\pi\right) \sin\left(1/2\, n\pi\right)}{ba}, \\
M_{k00n}^{c,I} &= -\frac{4 cab \sin\left(1/2\, k\pi\right) \sin\left(1/2\, n\pi\right)}{\pi^2 k n}.
\end{aligned}
\tag{3.A.14}
$$

11. Stiffness matrix elements for $n = l = 0$, and $m \neq 0$, $k \neq 0$ with $k \neq m$:

$$
\begin{aligned}
M_{k0m0}^{m,I} &= \frac{2 K k^2 \pi^3 m^2 \left(-k \sin\left(1/2\, k\pi\right) \cos\left(1/2\, m\pi\right) + m \cos\left(1/2\, k\pi\right) \sin\left(1/2\, m\pi\right)\right) b}{a^3 k^2 - a^3 m^2}, \\
M_{k0m0}^{c,I} &= \frac{2 cab \left(-k \sin\left(1/2\, k\pi\right) \cos\left(1/2\, m\pi\right) + m \cos\left(1/2\, k\pi\right) \sin\left(1/2\, m\pi\right)\right)}{\pi k^2 - \pi m^2}.
\end{aligned}
\tag{3.A.15}
$$

12. Stiffness matrix elements for $n = l = 0$, and $m \neq 0$, $k \neq 0$ with $k = m$:

$$
\begin{aligned}
M_{m0m0}^{m,I} &= -\frac{K m^3 \pi^3 b \left(2 \cos\left(1/2\, m\pi\right) \sin\left(1/2\, m\pi\right) + m\pi\right)}{2 a^3}, \\
M_{m0m0}^{c,I} &= -\frac{cab \left(2 \cos\left(1/2\, m\pi\right) \sin\left(1/2\, m\pi\right) + m\pi\right)}{2 m\pi}.
\end{aligned}
\tag{3.A.16}
$$

13. Stiffness matrix elements for $l = 0$, and $m \neq 0$, $n \neq 0$, $k \neq 0$ with $k \neq m$:

$$
\begin{aligned}
M_{k0mn}^{m,I} &= -\frac{4 K \sin\left(1/2\, n\pi\right) \pi^2 k^2 \left(a^2 n^2 v + b^2 m^2\right)}{a^3 b \left(k^2 - m^2\right) n} \times \\
&\quad \times \left(k \sin\left(1/2\, k\pi\right) \cos\left(1/2\, m\pi\right) - m \cos\left(1/2\, k\pi\right) \sin\left(1/2\, m\pi\right)\right), \\
M_{k0mn}^{c,I} &= -\frac{4 cab \left(k \sin\left(1/2\, k\pi\right) \cos\left(1/2\, m\pi\right) - m \cos\left(1/2\, k\pi\right) \sin\left(1/2\, m\pi\right)\right) \sin\left(1/2\, n\pi\right)}{\pi^2 \left(k^2 - m^2\right) n}.
\end{aligned}
\tag{3.A.17}
$$

14. Stiffness matrix elements for $l = 0$, and $m \neq 0$, $n \neq 0$, $k \neq 0$ with $k = m$:

$$
\begin{aligned}
M_{mnm0}^{m,I} &= -\frac{K \sin\left(1/2\, n\pi\right) m\pi^2 \left(2 \cos\left(1/2\, m\pi\right) \sin\left(1/2\, m\pi\right) + m\pi\right) \left(a^2 n^2 v + b^2 m^2\right)}{ba^3 n}, \\
M_{mnm0}^{c,I} &= -\frac{cab \left(2 \cos\left(1/2\, m\pi\right) \sin\left(1/2\, m\pi\right) + m\pi\right) \sin\left(1/2\, n\pi\right)}{m\pi^2 n}.
\end{aligned}
\tag{3.A.18}
$$

15. Stiffness matrix elements for $m = 0$, and $n \neq 0$, $k \neq 0$, $l \neq 0$ with $l \neq n$:

$$
\begin{aligned}
M_{kl0n}^{m,I} &= -\frac{4 K \pi^2 \sin\left(1/2\, k\pi\right) n^2 \left(b^2 k^2 v + a^2 l^2\right)}{b^3 a \left(l^2 - n^2\right) k} \times \\
&\quad \times \left(l \sin\left(1/2\, l\pi\right) \cos\left(1/2\, n\pi\right) - n \cos\left(1/2\, l\pi\right) \sin\left(1/2\, n\pi\right)\right), \\
M_{kl0n}^{c,I} &= -\frac{4 cab \sin\left(1/2\, k\pi\right) \left(l \sin\left(1/2\, l\pi\right) \cos\left(1/2\, n\pi\right) - n \cos\left(1/2\, l\pi\right) \sin\left(1/2\, n\pi\right)\right)}{\pi^2 k \left(l^2 - n^2\right)}.
\end{aligned}
$$

$$(3.A.19)$$

16. Stiffness matrix elements for $m = 0$, and $n \neq 0$, $k \neq 0$, $l \neq 0$ with $l = n$:

$$
\begin{aligned}
M_{kn0n}^{m,I} &= -\frac{K n \pi^2 \left(b^2 k^2 v + a^2 n^2\right) \sin\left(1/2\,k\pi\right) \left(2 \cos\left(1/2\,n\pi\right) \sin\left(1/2\,n\pi\right) + n\pi\right)}{b^3 a k}, \\
M_{kn0n}^{c,I} &= -\frac{c a b \sin\left(1/2\,k\pi\right) \left(2 \cos\left(1/2\,n\pi\right) \sin\left(1/2\,n\pi\right) + n\pi\right)}{\pi^2 k n}.
\end{aligned}
\tag{3.A.20}
$$

17. Stiffness matrix elements for $n = 0$, and $m \neq 0$, $k \neq 0$, $l \neq 0$ with $k \neq m$:

$$
\begin{aligned}
M_{klm0}^{m,I} &= -\frac{4\,K\,m^2\pi^2 \sin\left(1/2\,l\pi\right) \left(a^2 l^2 v + b^2 k^2\right)}{a^3 b \left(k^2 - m^2\right) l} \times \\
&\quad \times \left(k \sin\left(1/2\,k\pi\right) \cos\left(1/2\,m\pi\right) - m \cos\left(1/2\,k\pi\right) \sin\left(1/2\,m\pi\right)\right), \\
M_{klm0}^{c,I} &= -\frac{4\,c a b \left(k \sin\left(1/2\,k\pi\right) \cos\left(1/2\,m\pi\right) - m \cos\left(1/2\,k\pi\right) \sin\left(1/2\,m\pi\right)\right) \sin\left(1/2\,l\pi\right)}{\pi^2 \left(k^2 - m^2\right) l}.
\end{aligned}
\tag{3.A.21}
$$

18. Stiffness matrix elements for $n = 0$, and $m \neq 0$, $k \neq 0$, $l \neq 0$ with $k = m$:

$$
\begin{aligned}
M_{mlm0}^{m,I} &= -\frac{K\,\pi^2 m \sin\left(1/2\,l\pi\right) \left(a^2 l^2 v + b^2 m^2\right) \left(m\pi + 2 \cos\left(1/2\,m\pi\right) \sin\left(1/2\,m\pi\right)\right)}{a^3 b l}, \\
M_{mlm0}^{c,I} &= -\frac{c a b \left(m\pi + 2 \cos\left(1/2\,m\pi\right) \sin\left(1/2\,m\pi\right)\right) \sin\left(1/2\,l\pi\right)}{m\pi^2 l}.
\end{aligned}
\tag{3.A.22}
$$

19. Stiffness matrix elements for $m = n = k = 0$, and $l \neq 0$:

$$
M_{0l00}^{m,I} = 0, \qquad M_{0l00}^{c,I} = -\frac{2\,c a b \sin\left(1/2\,l\pi\right)}{l\pi}.
\tag{3.A.23}
$$

20. Stiffness matrix elements for $m = n = l = 0$, and $k \neq 0$:

$$
M_{k000}^{m,I} = 0, \qquad M_{k000}^{c,I} = -\frac{2\,c a b \sin\left(1/2\,k\pi\right)}{k\pi}.
\tag{3.A.24}
$$

21. Stiffness matrix elements for $m = n = 0$, and $k \neq 0$, $l \neq 0$:

$$
M_{kl00}^{m,I} = 0, \qquad M_{kl00}^{c,I} = -\frac{4\,c a b \sin\left(1/2\,k\pi\right) \sin\left(1/2\,l\pi\right)}{\pi^2 k l}.
\tag{3.A.25}
$$

22. Stiffness matrix elements for $k \neq 0$, $l \neq 0$, $m \neq 0$ and $n \neq 0$, with $k \neq m$ and $l \neq n$:

$$
\begin{aligned}
M_{klmn}^{m,I} &= -\frac{4\,K\pi^2}{b^3 a^3 \left(l - n\right) \left(l + n\right) \left(k - m\right) \left(k + m\right)} \Big(m \Big(\sin\left(1/2\,n\pi\right) n \Big(-2 \left(a^2 \left(v - 1\right) l^2 \right. \\
&\quad \left. -1/2\,a^2 n^2 v - 1/2\,b^2 m^2\right) b^2 k^2 + a^2 l^2 \left(b^2 m^2 v + a^2 n^2\right)\Big) \cos\left(1/2\,l\pi\right) \\
&\quad - \left(\left(b^2 m^2 - a^2 n^2 \left(v - 2\right)\right) b^2 k^2 + a^2 l^2 \left(b^2 m^2 v + a^2 n^2\right)\right) \cos\left(1/2\,n\pi\right) \times \\
&\quad \times \sin\left(1/2\,l\pi\right) l\Big) \sin\left(1/2\,m\pi\right) \cos\left(1/2\,k\pi\right) - k \sin\left(1/2\,k\pi\right) \cos\left(1/2\,m\pi\right) \times \\
&\quad \times \Big(\sin\left(1/2\,n\pi\right) n \left(b^2 \left(a^2 n^2 v + b^2 m^2\right) k^2 + a^2 \left(-b^2 \left(v - 2\right) m^2 + a^2 n^2\right) l^2\right) \times \\
&\quad \times \cos\left(1/2\,l\pi\right) - \cos\left(1/2\,n\pi\right) \sin\left(1/2\,l\pi\right) \left(b^2 \left(a^2 n^2 v + b^2 m^2\right) k^2 \right. \\
&\quad \left. + a^2 \left(\left(b^2 m^2 v + a^2 n^2\right) l^2 - 2 b^2 m^2 n^2 \left(v - 1\right)\right)\right) l\Big)\Big),
\end{aligned}
$$

$$M_{klmn}^{c,I} = -\frac{4\,cab\left[-k\sin\left(1/2\,k\pi\right)\cos\left(1/2\,m\pi\right)+m\cos\left(1/2\,k\pi\right)\sin\left(1/2\,m\pi\right)\right]}{\pi^2\left(k^2-m^2\right)\left(l^2-n^2\right)} \times$$
$$\times\left[-l\sin\left(1/2\,l\pi\right)\cos\left(1/2\,n\pi\right)+n\cos\left(1/2\,l\pi\right)\sin\left(1/2\,n\pi\right)\right]. \tag{3.A.26}$$

23. Stiffness matrix elements for $k\neq0$, $l\neq0$, $m\neq0$ and $n\neq0$, with $k=m$ and $l\neq n$:

$$M_{mlmn}^{m,I} = -\frac{2\,K\,\pi^2}{a^3b^3m\left(l^2-n^2\right)}\left(-n\sin\left(1/2\,n\pi\right)\left(\left(m^4b^4+3\,a^2\left((v-2/3)\,l^2\right.\right.\right.\right.$$
$$\left.+1/3\,n^2v\right)b^2m^2+a^4l^2n^2\Big)\sin\left(1/2\,m\pi\right)\cos\left(1/2\,m\pi\right)+1/2\left(m^4b^4\right.$$
$$\left.-a^2\left((v-2)\,l^2-n^2v\right)b^2m^2+a^4l^2n^2\right)\pi\,m\Big)\cos\left(1/2\,l\pi\right)+l\cos\left(1/2\,n\pi\right)\times$$
$$\times\left(\left(\left(m^4b^4+\left(l^2v+3\,n^2\,(v-2/3)\right)a^2b^2m^2+a^4l^2n^2\right)\sin\left(1/2\,m\pi\right)\cos\left(1/2\,m\pi\right)\right.\right.$$
$$\left.\left.+1/2\left(m^4b^4+\left(l^2v-n^2\,(v-2)\right)a^2b^2m^2+a^4l^2n^2\right)\pi\,m\right)\sin\left(1/2\,l\pi\right)\right),$$

$$M_{mlmn}^{c,I} = \frac{cab\left[m\pi+2\,\cos\left(1/2\,m\pi\right)\sin\left(1/2\,m\pi\right)\right]}{m\pi^2\left(l^2-n^2\right)}\times$$
$$\times\left[-l\sin\left(1/2\,l\pi\right)\cos\left(1/2\,n\pi\right)+n\cos\left(1/2\,l\pi\right)\sin\left(1/2\,n\pi\right)\right]. \tag{3.A.27}$$

24. Stiffness matrix elements for $k\neq0$, $l\neq0$, $m\neq0$ and $n\neq0$, with $k\neq m$ and $l=n$:

$$M_{knmn}^{m,I} = \frac{2\,K\,\pi^2}{b^3\left(k^2-m^2\right)a^3n}\left[\left(\left(a^4n^4+3\,a^2\left((v-2/3)\,k^2+1/3\,m^2v\right)b^2n^2+b^4k^2m^2\right)\times\right.\right.$$
$$\times\sin\left(1/2\,n\pi\right)\cos\left(1/2\,n\pi\right)+1/2\,n\pi\left(a^4n^4-a^2b^2\left((v-2)\,k^2-m^2v\right)n^2\right.$$
$$\left.+b^4k^2m^2\right)\Big)\sin\left(1/2\,m\pi\right)m\cos\left(1/2\,k\pi\right)-k\left(\left(a^4n^4+a^2b^2\left(k^2v\right.\right.\right.$$
$$\left.+3\,(v-2/3)\,m^2\right)n^2+b^4k^2m^2\Big)\sin\left(1/2\,n\pi\right)\cos\left(1/2\,n\pi\right)+1/2\left(a^4n^4\right.$$
$$\left.\left.+\left(k^2v-m^2\,(v-2)\right)a^2b^2n^2+b^4k^2m^2\right)n\pi\right)\cos\left(1/2\,m\pi\right)\sin\left(1/2\,k\pi\right)\right],$$

$$M_{knmn}^{c,I} = -\frac{cab\left[k\sin\left(1/2\,k\pi\right)\cos\left(1/2\,m\pi\right)-m\cos\left(1/2\,k\pi\right)\sin\left(1/2\,m\pi\right)\right]}{\pi^2\left(k^2-m^2\right)n}\times$$
$$\times\left[2\,\cos\left(1/2\,n\pi\right)\sin\left(1/2\,n\pi\right)+n\pi\right]. \tag{3.A.28}$$

25. Stiffness matrix elements for $k\neq0$, $l\neq0$, $m\neq0$ and $n\neq0$, with $k=m$ and $l=n$:

$$M_{mnmn}^{m,I} = -\frac{K\,\pi^2}{a^3b^3nm}\left[\left(\sin\left(1/2\,n\pi\right)\left(a^2n^2+b^2m^2\right)^2\cos\left(1/2\,n\pi\right)+1/2\left(m^4b^4\right.\right.\right.$$
$$\left.+4\,a^2\,(v-1/2)\,b^2n^2m^2+a^4n^4\right)\pi\,n\Big)\sin\left(1/2\,m\pi\right)\cos\left(1/2\,m\pi\right)$$
$$+1/2\,m\pi\left(\sin\left(1/2\,n\pi\right)\left(m^4b^4+4\,a^2\,(v-1/2)\,b^2n^2m^2+a^4n^4\right)\times\right.$$
$$\left.\left.\times\cos\left(1/2\,n\pi\right)+1/2\,n\pi\left(a^2n^2+b^2m^2\right)^2\right)\right],$$

$$M_{mnmn}^{c,I} = -\frac{cab\left(m\pi+2\,\cos\left(1/2\,m\pi\right)\sin\left(1/2\,m\pi\right)\right)\left(2\,\cos\left(1/2\,n\pi\right)\sin\left(1/2\,n\pi\right)+n\pi\right)}{4\,m\pi^2n}.$$
$$\tag{3.A.29}$$

where the stiffness matrix element associated to single springs is defined as

$$M_{klmn}^{C,I} = -\sum_{s=1}^{N_C} C_s \cos\left(\frac{m\pi\,x_s}{a}\right) \cos\left(\frac{n\pi\,y_s}{b}\right) \cos\left(\frac{k\pi\,x_s}{a}\right) \cos\left(\frac{l\pi\,y_s}{b}\right). \qquad (3.A.30)$$

3.A.2 Stiffness matrix and load vector elements for Example 2

As the temperature loading in Example 2 is symmetric with respect to both the x-axis and the y-axis, only the trigonometric functions of type $w_{m,n}^I$ are employed to solve the system of equations(3.48). Hence, substituting the deflection modes $w_{m,n}^I$ and $w_{k,l}^I$ according to (3.40) into (3.49)-(3.55) yields, after integration, the elements for Example 2. First, we provide the load vector elements associated to temperature gradients (3.52), for any combinations of k, and l:

(i) Load vector elements for $k = l = 0$:

$$V_{00}^{\kappa_T^e,I} = 0. \qquad (3.A.31)$$

(ii) Load vector elements for $k = 0$ and $l \neq 0$:

$$V_{0l}^{\kappa_T^e,I} = 2\,K\kappa_T^e\,l\pi\,a\sin\left(1/2\,l\pi\right)/b. \qquad (3.A.32)$$

(iii) Load vector elements for $k \neq 0$ and $l = 0$:

$$V_{k0}^{\kappa_T^e,I} = 2\,K\kappa_T^e\,k\pi\,b\sin\left(1/2\,k\pi\right)/a. \qquad (3.A.33)$$

(iv) Load vector elements for $k \neq 0$ and $l \neq 0$:

$$V_{kl}^{\kappa_T^e,I} = \frac{4\,K\kappa_T^e\,\sin\left(1/2\,l\pi\right)\left(a^2l^2 + b^2k^2\right)\sin\left(1/2\,k\pi\right)}{abkl}. \qquad (3.A.34)$$

The stiffness matrix elements $M_{klmn}^{m,I}$, $M_{klmn}^{c,I}$, and $M_{klmn}^{C,I}$ for the employed trigonometric functions of type $w_{m,n}^I$ can be found by analogy to Example 1, see (3.A.5)-(3.A.30).

3.A.3 Stiffness matrix and load vector elements for Example 3

As the patched loads in Example 3 are antimetric with respect to both the x-axis and the y-axis, the trigonometric functions of type $w_{m,n}^I$-$w_{m,n}^{IV}$ according to Eq. (3.40)-(3.43) are employed to solve the system of equations (3.48). Hence, substituting the deflection modes $w_{m,n}^I$-$w_{m,n}^{IV}$ and $w_{k,l}^I$-$w_{k,l}^{IV}$, respectively, according to (3.40)-(3.43) into (3.49)-(3.55) yields, after integration, the elements for Example 3.

3.A.3.1 Load vector elements for the employed trigonometric functions of type $w_{m,n}^I$-$w_{m,n}^{IV}$

First, we provide the load vector elements, see (3.52)-(3.55), for any combinations of k, and l:

(i) Load vector elements for $k = l = 0$:

$$V_{00}^{\overline{p},I} = \sum_{s=1}^{N\overline{p}} \overline{p}_s\,\xi_{\overline{s}}\,\eta_{\overline{s}},$$

$$
\begin{aligned}
V_{00}^{\overline{p},II} &= \sum_{s=1}^{N\overline{p}} 2\,\overline{p}_s\,x_{\overline{s}}\,\xi_{\overline{s}}\,\eta_{\overline{s}}\,/a\,, \\
V_{00}^{\overline{p},III} &= \sum_{s=1}^{N\overline{p}} 2\,\overline{p}_s\,y_{\overline{s}}\,\xi_{\overline{s}}\,\eta_{\overline{s}}\,/b\,, \\
V_{00}^{\overline{p},IV} &= \sum_{s=1}^{N\overline{p}} 4\,\frac{\overline{p}_s\,x_{\overline{s}}\xi_{\overline{s}}\,y_{\overline{s}}\,\eta}{ab}\,.
\end{aligned}
\tag{3.A.35}
$$

(ii) Load vector elements for $k = 0$ and $l \neq 0$:

$$
\begin{aligned}
V_{0l}^{\overline{p},I} &= \sum_{s=1}^{N\overline{p}} \frac{\overline{p}_s\,\xi_{\overline{s}}\,b}{l\pi}\left[\sin\left(\frac{l\pi\,(-2\,y_{\overline{s}}+\eta_{\overline{s}})}{2\,b}\right) + \sin\left(\frac{l\pi\,(2\,y_{\overline{s}}+\eta_{\overline{s}})}{2\,b}\right)\right], \\
V_{0l}^{\overline{p},II} &= \sum_{s=1}^{N\overline{p}} 2\,\frac{\overline{p}_s x_{\overline{s}}\,\xi_{\overline{s}}\,b}{a\,l\pi}\left[\sin\left(\frac{l\pi\,(-2\,y_{\overline{s}}+\eta_{\overline{s}})}{2\,b}\right) + \sin\left(\frac{l\pi\,(2\,y_{\overline{s}}+\eta_{\overline{s}})}{2\,b}\right)\right], \\
V_{0l}^{\overline{p},III} &= \sum_{s=1}^{N\overline{p}} \frac{\overline{p}_s\,\xi_{\overline{s}}\,b}{l\pi}\left[\cos\left(\frac{l\pi\,(-2\,y_{\overline{s}}+\eta_{\overline{s}})}{2\,b}\right) - \cos\left(\frac{l\pi\,(2\,y_{\overline{s}}+\eta_{\overline{s}})}{2\,b}\right)\right], \\
V_{0l}^{\overline{p},IV} &= \sum_{s=1}^{N\overline{p}} 2\,\frac{\overline{p}_s\,x_{\overline{s}}\xi_{\overline{s}}\,b}{al\pi}\left[\cos\left(\frac{l\pi\,(-2\,y_{\overline{s}}+\eta_{\overline{s}})}{2\,b}\right) - \cos\left(\frac{l\pi\,(2\,y_{\overline{s}}+\eta_{\overline{s}})}{2\,b}\right)\right].
\end{aligned}
\tag{3.A.36}
$$

(iii) Load vector elements for $k \neq 0$ and $l = 0$:

$$
\begin{aligned}
V_{k0}^{\overline{p},I} &= \sum_{s=1}^{N\overline{p}} \frac{\overline{p}_s\,a\eta_{\overline{s}}}{k\pi}\left[\sin\left(\frac{k\pi\,(-2\,x_{\overline{s}}+\xi_{\overline{s}})}{2\,a}\right) + \sin\left(\frac{k\pi\,(2\,x_{\overline{s}}+\xi_{\overline{s}})}{2\,a}\right)\right], \\
V_{k0}^{\overline{p},II} &= \sum_{s=1}^{N\overline{p}} \frac{\overline{p}_s\,a\eta_{\overline{s}}}{k\pi}\left[\cos\left(\frac{k\pi\,(-2\,x_{\overline{s}}+\xi_{\overline{s}})}{2\,a}\right) - \cos\left(\frac{k\pi\,(2\,x_{\overline{s}}+\xi_{\overline{s}})}{2\,a}\right)\right], \\
V_{k0}^{\overline{p},III} &= \sum_{s=1}^{N\overline{p}} 2\,\frac{\overline{p}_s\,a\,y_s\,\eta_{\overline{s}}}{k\pi\,b}\left[\sin\left(\frac{k\pi\,(-2\,x_{\overline{s}}+\xi_{\overline{s}})}{2\,a}\right) + \sin\left(\frac{k\pi\,(2\,x_{\overline{s}}+\xi_{\overline{s}})}{2\,a}\right)\right], \\
V_{k0}^{\overline{p},IV} &= \sum_{s=1}^{N\overline{p}} 2\,\frac{\overline{p}_s\,a\,y_{\overline{s}}\,\eta_{\overline{s}}}{k\pi\,b}\left[\cos\left(\frac{k\pi\,(-2\,x_{\overline{s}}+\xi_{\overline{s}})}{2\,a}\right) - \cos\left(\frac{k\pi\,(2\,x_{\overline{s}}+\xi_{\overline{s}})}{2\,a}\right)\right].
\end{aligned}
\tag{3.A.37}
$$

(iv) Load vector elements for $k \neq 0$ and $l \neq 0$:

$$
\begin{aligned}
V_{kl}^{\overline{p},I} &= \sum_{s=1}^{N\overline{p}} \frac{\overline{p}_s ab}{k\pi^2 l}\left[\sin\left(\frac{k\pi\,(-2\,x_{\overline{s}}+\xi_{\overline{s}})}{2\,a}\right) + \sin\left(\frac{k\pi\,(2\,x_{\overline{s}}+\xi_{\overline{s}})}{2\,a}\right)\right] \times \\
&\quad \times \left[\sin\left(\frac{l\pi\,(-2\,y_{\overline{s}}+\eta_{\overline{s}})}{2\,b}\right) + \sin\left(\frac{l\pi\,(2\,y_{\overline{s}}+\eta_{\overline{s}})}{2\,b}\right)\right], \\
V_{kl}^{\overline{p},II} &= \sum_{s=1}^{N\overline{p}} \frac{\overline{p}_s ab}{k\pi^2 l}\left[\cos\left(\frac{k\pi\,(-2\,x_{\overline{s}}+\xi_{\overline{s}})}{2\,a}\right) - \cos\left(\frac{k\pi\,(2\,x_{\overline{s}}+\xi_{\overline{s}})}{2\,a}\right)\right] \times \\
&\quad \times \left[\sin\left(\frac{l\pi\,(-2\,y_{\overline{s}}+\eta_{\overline{s}})}{2\,b}\right) + \sin\left(\frac{l\pi\,(2\,y_{\overline{s}}+\eta_{\overline{s}})}{2\,b}\right)\right],
\end{aligned}
$$

$$
\begin{aligned}
V_{kl}^{\overline{p},III} &= \sum_{s=1}^{N\overline{p}} \frac{\overline{p}_s\, a\, b}{k\pi^2 l} \left[\sin\left(\frac{k\pi\,(-2\,x_{\overline{s}} + \xi_{\overline{s}})}{2\,a}\right) + \sin\left(\frac{k\pi\,(2\,x_{\overline{s}} + \xi_{\overline{s}})}{2\,a}\right) \right] \times \\
&\quad \times \left[\cos\left(\frac{l\pi\,(-2\,y_{\overline{s}} + \eta_{\overline{s}})}{2\,b}\right) - \cos\left(\frac{l\pi\,(2\,y_{\overline{s}} + \eta_{\overline{s}})}{2\,b}\right) \right], \\
V_{kl}^{\overline{p},IV} &= \sum_{s=1}^{N\overline{p}} \frac{\overline{p}_s\, a b}{k\pi^2 l} \left[\cos\left(\frac{k\pi\,(-2\,x_{\overline{s}} + \xi_{\overline{s}})}{2\,a}\right) - \cos\left(\frac{k\pi\,(2\,x_{\overline{s}} + \xi_{\overline{s}})}{2\,a}\right) \right] \times \\
&\quad \times \left[\cos\left(\frac{l\pi\,(-2\,y_{\overline{s}} + \eta_{\overline{s}})}{2\,b}\right) - \cos\left(\frac{l\pi\,(2\,y_{\overline{s}} + \eta_{\overline{s}})}{2\,b}\right) \right].
\end{aligned}
\tag{3.A.38}
$$

3.A.3.2 Stiffness matrix elements for the employed trigonometric functions of type $w_{m,n}^{I}$

The stiffness matrix elements $M_{klmn}^{m,I}$, $M_{klmn}^{c,I}$, and $M_{klmn}^{C,I}$ for the employed trigonometric functions of type $w_{m,n}^{I}$ can be found by analogy to Example 1, see (3.A.5)-(3.A.30).

3.A.3.3 Stiffness matrix elements for the employed trigonometric functions of type $w_{m,n}^{II}$

The stiffness matrix elements $M_{klmn}^{m,II}$, $M_{klmn}^{c,II}$, and $M_{klmn}^{C,II}$ for the employed trigonometric functions of type $w_{m,n}^{II}$, for 25 combinations of k, l, m, and n, read as:

1. Stiffness matrix elements for $k = l = m = n = 0$:

$$
M_{0000}^{m,II} = 0\,, \qquad M_{0000}^{c,II} = -\frac{1}{3}\, c\, a\, b\,, \qquad M_{0000}^{C,II} = -\sum_{s=1}^{N_C} 4\, C_s\, x_s^2 / a^2\,.
\tag{3.A.39}
$$

2. Stiffness matrix elements for $k = l = m = 0$, and $n \neq 0$:

$$
M_{000n}^{m,II} = 0\,, \qquad M_{000n}^{c,II} = -\frac{2\,c\,a\,b\sin\left(1/2\,n\,\pi\right)}{3\,n\pi}\,, \qquad M_{000n}^{C,II} = -\sum_{s=1}^{N_C} 4\, \frac{C_s x_s^2}{a^2} \cos\left(\frac{n\,\pi\,y_s}{b}\right).
\tag{3.A.40}
$$

3. Stiffness matrix elements for $k = l = n = 0$, and $m \neq 0$:

$$
\begin{aligned}
M_{00m0}^{m,II} &= 0\,, \\
M_{00m0}^{c,II} &= \frac{2\,c\,a\,b\,(m\pi\,\cos\left(1/2\,m\pi\right) - 2\,\sin\left(1/2\,m\pi\right))}{m^2\pi^2}\,, \\
M_{00m0}^{C,II} &= -\sum_{s=1}^{N_C} 2\,\frac{C_s x_s}{a} \sin\left(\frac{m\pi\,x_s}{a}\right).
\end{aligned}
\tag{3.A.41}
$$

4. Stiffness matrix elements for $k = l = 0$, and $m \neq 0$, $n \neq 0$:

$$
\begin{aligned}
M_{00mn}^{m,II} &= 0\,, \\
M_{00mn}^{c,II} &= \frac{4\,c\,a\,b\,(m\pi\,\cos\left(1/2\,m\pi\right) - 2\,\sin\left(1/2\,m\pi\right))\sin\left(1/2\,n\pi\right)}{m^2\pi^3 n}\,, \\
M_{00mn}^{C,II} &= -\sum_{s=1}^{N_C} 2\,\frac{C_s x_s}{a} \sin\left(\frac{m\pi\,x_s}{a}\right) \cos\left(\frac{n\pi\,y_s}{b}\right).
\end{aligned}
\tag{3.A.42}
$$

5. Stiffness matrix elements for $m = k = 0$, and $n \neq 0$, $l \neq 0$ with $l \neq n$:

$$
\begin{aligned}
M_{0l0n}^{m,II} &= \frac{2\,K\,n\,l\,\pi}{3\,ab^3l^2 - 3\,ab^3n^2}\Big[\sin\left(1/2\,n\pi\right)\left(a^2n^2\pi^2 - 24\,b^2\left(-1+v\right)\right)l\cos\left(1/2\,l\pi\right) \\
&\quad - \cos\left(1/2\,n\pi\right)\left(a^2l^2\pi^2 - 24\,b^2\left(-1+v\right)\right)n\sin\left(1/2\,l\pi\right)\Big]\,, \\
M_{0l0n}^{c,II} &= -\frac{2\,c\,a\,b\,(l\sin\left(1/2\,l\pi\right)\cos\left(1/2\,n\pi\right) - n\cos\left(1/2\,l\pi\right)\sin\left(1/2\,n\pi\right))}{3\,\pi\,(l^2 - n^2)}\,, \\
M_{0l0n}^{C,II} &= -\sum_{s=1}^{N_C} 4\,\frac{C_s{x_s}^2}{a^2}\cos\left(\frac{n\pi\,y_s}{b}\right)\cos\left(\frac{l\pi\,y_s}{b}\right).
\end{aligned}
\tag{3.A.43}
$$

6. Stiffness matrix elements for $m = k = 0$, and $n \neq 0$, $l \neq 0$ with $l = n$:

$$
\begin{aligned}
M_{0n0n}^{m,II} &= -\frac{K\,n\,\pi}{6\,a\,b^3}\Big[2\left(a^2n^2\pi^2 + 24\,b^2\left(-1+v\right)\right)\sin\left(1/2\,n\pi\right)\cos\left(1/2\,n\pi\right) \\
&\quad + \left(a^2n^2\pi^2 - 24\,b^2\left(-1+v\right)\right)n\pi\Big]\,, \\
M_{0n0n}^{c,II} &= -\frac{c\,a\,b\,(2\cos\left(1/2\,n\pi\right)\sin\left(1/2\,n\pi\right) + n\pi)}{6\,n\pi}\,, \\
M_{0n0n}^{C,II} &= -\sum_{s=1}^{N_C} 4\,\frac{C_s{x_s}^2}{a^2}\left(\cos\left(\frac{n\pi\,y_s}{b}\right)\right)^2.
\end{aligned}
\tag{3.A.44}
$$

7. Stiffness matrix elements for $n = k = 0$, and $m \neq 0$, $l \neq 0$:

$$
\begin{aligned}
M_{0lm0}^{m,II} &= -\frac{4\,Kvl\pi\,(-m\pi\cos\left(1/2\,m\pi\right) + 2\sin\left(1/2\,m\pi\right))\sin\left(1/2\,l\pi\right)}{ab}\,, \\
M_{0lm0}^{c,II} &= \frac{4\,cab\,(m\pi\cos\left(1/2\,m\pi\right) - 2\sin\left(1/2\,m\pi\right))\sin\left(1/2\,l\pi\right)}{m^2\pi^3l}\,, \\
M_{0lm0}^{C,II} &= -\sum_{s=1}^{N_C} 2\,\frac{C_s x_s}{a}\sin\left(\frac{m\pi\,x_s}{a}\right)\cos\left(\frac{l\pi\,y_s}{b}\right).
\end{aligned}
\tag{3.A.45}
$$

8. Stiffness matrix elements for $k = 0$, and $m \neq 0$, $n \neq 0$, $l \neq 0$ with $l \neq n$:

$$
\begin{aligned}
M_{0lmn}^{m,II} &= \frac{4\,\pi\,K\,l}{b^3m^2a\,(l^2 - n^2)}\Big[\Big(-2\sin\left(1/2\,l\pi\right)\left(\left(b^2m^2v + a^2n^2\right)l^2\right. \\
&\quad \left. -2\,b^2m^2n^2\left(-1+v\right)\right)\cos\left(1/2\,n\pi\right) + 2\cos\left(1/2\,l\pi\right)\sin\left(1/2\,n\pi\right)\times \\
&\quad \times\left(-b^2\left(v-2\right)m^2 + a^2n^2\right)ln\Big)\sin\left(1/2\,m\pi\right) + \cos\left(1/2\,m\pi\right)lm\pi\times \\
&\quad \times\left(b^2m^2v + a^2n^2\right)(l\sin\left(1/2\,l\pi\right)\cos\left(1/2\,n\pi\right) - n\cos\left(1/2\,l\pi\right)\sin\left(1/2\,n\pi\right))\Big]\,, \\
M_{0lmn}^{c,II} &= -\frac{8cab}{m^2\pi^3\,(l^2 - n^2)}\left[l\sin\left(1/2\,l\pi\right)\cos\left(1/2\,n\pi\right) - n\cos\left(1/2\,l\pi\right)\sin\left(1/2\,n\pi\right)\right]\times \\
&\quad \times\left[-1/2\,m\pi\cos\left(1/2\,m\pi\right) + \sin\left(1/2\,m\pi\right)\right]\,, \\
M_{0lmn}^{C,II} &= -\sum_{s=1}^{N_C} 2\,\frac{C_s x_s}{a}\sin\left(\frac{m\pi\,x_s}{a}\right)\cos\left(\frac{n\pi\,y_s}{b}\right)\cos\left(\frac{l\pi\,y_s}{b}\right).
\end{aligned}
\tag{3.A.46}
$$

9. Stiffness matrix elements for $k = 0$, and $m \neq 0$, $n \neq 0$, $l \neq 0$ with $l = n$:

$$
\begin{aligned}
M_{mn0n}^{m,II} &= -\frac{4\,K\pi\,n}{b^3 m^2 a}\Big[\Big(\sin\left(1/2\,n\pi\right)\left(3\left(v - 2/3\right)b^2 m^2 + a^2 n^2\right)\cos\left(1/2\,n\pi\right) \\
&\quad + 1/2\,n\pi\left(-b^2\left(v - 2\right)m^2 + a^2 n^2\right)\Big)\sin\left(1/2\,m\pi\right) \\
&\quad - 1/2\left(b^2 m^2 v + a^2 n^2\right)\left(\cos\left(1/2\,n\pi\right)\sin\left(1/2\,n\pi\right) + 1/2\,n\pi\right)\cos\left(1/2\,m\pi\right)\pi\,m\Big]\,, \\
M_{mn0n}^{c,II} &= \frac{c\,a\,b\left[m\pi\,\cos\left(1/2\,m\pi\right) - 2\,\sin\left(1/2\,m\pi\right)\right)\left(2\,\cos\left(1/2\,n\pi\right)\sin\left(1/2\,n\pi\right) + n\pi\right]}{m^2\pi^3 n}\,, \\
M_{mn0n}^{C,II} &= -\sum_{s=1}^{N_C} 2\,\frac{C_s x_s}{a}\sin\left(\frac{m\pi\,x_s}{a}\right)\left(\cos\left(\frac{n\pi\,y_s}{b}\right)\right)^2.
\end{aligned}
\tag{3.A.47}
$$

10. Stiffness matrix elements for $m = l = 0$, and $n \neq 0$, $k \neq 0$:

$$
\begin{aligned}
M_{k00n}^{m,II} &= \frac{4\,Kvn\pi\left(k\pi\,\cos\left(1/2\,k\pi\right) - 2\,\sin\left(1/2\,k\pi\right)\right)\sin\left(1/2\,n\pi\right)}{ab}\,, \\
M_{k00n}^{c,II} &= \frac{4\,cab\left(k\pi\,\cos\left(1/2\,k\pi\right) - 2\,\sin\left(1/2\,k\pi\right)\right)\sin\left(1/2\,n\pi\right)}{k^2\pi^3 n}\,, \\
M_{k00n}^{C,II} &= -\sum_{s=1}^{N_C} 2\,\frac{C_s x_s}{a}\cos\left(\frac{n\pi\,y_s}{b}\right)\sin\left(\frac{k\pi\,x_s}{a}\right).
\end{aligned}
\tag{3.A.48}
$$

11. Stiffness matrix elements for $n = l = 0$, and $m \neq 0$, $k \neq 0$ with $k \neq m$:

$$
\begin{aligned}
M_{k0m0}^{m,II} &= \frac{2\,Kk^2\pi^3 m^2\left(k\cos\left(1/2\,k\pi\right)\sin\left(1/2\,m\pi\right) - m\sin\left(1/2\,k\pi\right)\cos\left(1/2\,m\pi\right)\right)b}{a^3\left(k^2 - m^2\right)}\,, \\
M_{k0m0}^{c,II} &= \frac{2\,cab\left(k\cos\left(1/2\,k\pi\right)\sin\left(1/2\,m\pi\right) - m\sin\left(1/2\,k\pi\right)\cos\left(1/2\,m\pi\right)\right)}{\pi\left(k^2 - m^2\right)}\,, \\
M_{k0m0}^{C,II} &= -\sum_{s=1}^{N_C} C_s\sin\left(\frac{m\pi\,x_s}{a}\right)\sin\left(\frac{k\pi\,x_s}{a}\right).
\end{aligned}
\tag{3.A.49}
$$

12. Stiffness matrix elements for $n = l = 0$, and $m \neq 0$, $k \neq 0$ with $k = m$:

$$
\begin{aligned}
M_{m0m0}^{m,II} &= -\frac{Km^3\pi^3\left(m\pi - 2\,\cos\left(1/2\,m\pi\right)\sin\left(1/2\,m\pi\right)\right)b}{2\,a^3}\,, \\
M_{m0m0}^{c,II} &= -\frac{cab\left(m\pi - 2\,\cos\left(1/2\,m\pi\right)\sin\left(1/2\,m\pi\right)\right)}{2\,m\pi}\,, \\
M_{m0m0}^{C,II} &= -\sum_{s=1}^{N_C} C_s\left(\sin\left(\frac{m\pi\,x_s}{a}\right)\right)^2.
\end{aligned}
\tag{3.A.50}
$$

13. Stiffness matrix elements for $l = 0$, and $m \neq 0$, $n \neq 0$, $k \neq 0$ with $k \neq m$:

$$
\begin{aligned}
M_{k0mn}^{m,II} &= -\frac{4\,K\sin\left(1/2\,n\pi\right)\pi^2 k^2\left(a^2 n^2 v + b^2 m^2\right)}{a^3 b\left(k^2 - m^2\right)n} \times \\
&\quad \times\left[-k\cos\left(1/2\,k\pi\right)\sin\left(1/2\,m\pi\right) + m\sin\left(1/2\,k\pi\right)\cos\left(1/2\,m\pi\right)\right]\,, \\
M_{k0mn}^{c,II} &= \frac{4\,c\,a\,b\left(k\cos\left(1/2\,k\pi\right)\sin\left(1/2\,m\pi\right) - m\sin\left(1/2\,k\pi\right)\cos\left(1/2\,m\pi\right)\right)\sin\left(1/2\,n\pi\right)}{\pi^2\left(k^2 - m^2\right)n}\,,
\end{aligned}
$$

$$M_{k0mn}^{C,II} = -\sum_{s=1}^{N_C} C_s \sin\left(\frac{m\pi x_s}{a}\right) \cos\left(\frac{n\pi y_s}{b}\right) \sin\left(\frac{k\pi x_s}{a}\right). \tag{3.A.51}$$

14. Stiffness matrix elements for $l = 0$, and $m \neq 0$, $n \neq 0$, $k \neq 0$ with $k = m$:

$$M_{mnm0}^{m,II} = -\frac{K \sin(1/2\, n\pi)\, m\pi^2 \left(-2\, \cos(1/2\, m\pi) \sin(1/2\, m\pi) + m\pi\right) \left(a^2 n^2 v + b^2 m^2\right)}{a^3 bn},$$

$$M_{mnm0}^{c,II} = -\frac{cab\,(m\pi - 2\, \cos(1/2\, m\pi) \sin(1/2\, m\pi)) \sin(1/2\, n\pi)}{m\pi^2 n},$$

$$M_{mnm0}^{C,II} = -\sum_{s=1}^{N_C} C_s \left(\sin\left(\frac{m\pi x_s}{a}\right)\right)^2 \cos\left(\frac{n\pi y_s}{b}\right). \tag{3.A.52}$$

15. Stiffness matrix elements for $m = 0$, and $n \neq 0$, $k \neq 0$, $l \neq 0$ with $l \neq n$:

$$\begin{aligned}
M_{kl0n}^{m,II} &= \frac{8\pi Kn}{b^3 ak^2\, (l^2 - n^2)} \left[\left(\left(\left(b^2 k^2 v + a^2 l^2\right) n^2 - 2\, b^2 k^2 l^2 (-1 + v)\right) \sin(1/2\, n\pi) \cos(1/2\, l\pi)\right.\right. \\
&\quad \left. - \sin(1/2\, l\pi)\, l \cos(1/2\, n\pi) \left(-b^2 (v - 2) k^2 + a^2 l^2\right) n\right) \sin(1/2\, k\pi) \\
&\quad - 1/2\, \cos(1/2\, k\pi)\, \pi\, kn \left(b^2 k^2 v + a^2 l^2\right) (-l \sin(1/2\, l\pi) \cos(1/2\, n\pi) \\
&\quad \left. + n \cos(1/2\, l\pi) \sin(1/2\, n\pi))\right], \\
M_{kl0n}^{c,II} &= -\frac{8\, c\, a\, b}{k^2 \pi^3\, (l^2 - n^2)} \left[l \sin(1/2\, l\pi) \cos(1/2\, n\pi) - n \cos(1/2\, l\pi) \sin(1/2\, n\pi)\right] \times \\
&\quad \times \left[-1/2\, k\pi\, \cos(1/2\, k\pi) + \sin(1/2\, k\pi)\right], \\
M_{kl0n}^{C,II} &= -\sum_{s=1}^{N_C} 2\, \frac{C_s x_s}{a} \cos\left(\frac{n\pi y_s}{b}\right) \sin\left(\frac{k\pi x_s}{a}\right) \cos\left(\frac{l\pi y_s}{b}\right). \tag{3.A.53}
\end{aligned}$$

16. Stiffness matrix elements for $m = 0$, and $n \neq 0$, $k \neq 0$, $l \neq 0$ with $l = n$:

$$\begin{aligned}
M_{kn0n}^{m,II} &= -\frac{4nK\pi}{b^3 ak^2} \left[\left(\sin(1/2\, n\pi) \left(3\, (v - 2/3)\, b^2 k^2 + a^2 n^2\right) \cos(1/2\, n\pi)\right.\right. \\
&\quad + 1/2\, n\pi \left(-b^2 (v - 2) k^2 + a^2 n^2\right)\right) \sin(1/2\, k\pi) \\
&\quad \left. - 1/2 \left(b^2 k^2 v + a^2 n^2\right) \cos(1/2\, k\pi) (\cos(1/2\, n\pi) \sin(1/2\, n\pi) + 1/2\, n\pi)\, \pi\, k\right], \\
M_{kn0n}^{c,II} &= \frac{c\, a\, b\, [k\pi\, \cos(1/2\, k\pi) - 2\, \sin(1/2\, k\pi)]\, [2\, \cos(1/2\, n\pi) \sin(1/2\, n\pi) + n\pi]}{k^2 \pi^3 n}, \\
M_{kn0n}^{C,II} &= -\sum_{s=1}^{N_C} 2\, \frac{C_s x_s}{a} \left(\cos\left(\frac{n\pi y_s}{b}\right)\right)^2 \sin\left(\frac{k\pi x_s}{a}\right). \tag{3.A.54}
\end{aligned}$$

17. Stiffness matrix elements for $n = 0$, and $m \neq 0$, $k \neq 0$, $l \neq 0$ with $k \neq m$:

$$\begin{aligned}
M_{klm0}^{m,II} &= -\frac{4\, \sin(1/2\, l\pi)\, m^2\pi^2 K \left(a^2 l^2 v + b^2 k^2\right)}{a^3 b\, (k^2 - m^2)\, l} \times \\
&\quad \times \left[-k \cos(1/2\, k\pi) \sin(1/2\, m\pi) + m \sin(1/2\, k\pi) \cos(1/2\, m\pi)\right], \\
M_{klm0}^{c,II} &= \frac{4\, c\, a\, b\, (k \cos(1/2\, k\pi) \sin(1/2\, m\pi) - m \sin(1/2\, k\pi) \cos(1/2\, m\pi)) \sin(1/2\, l\pi)}{\pi^2\, (k^2 - m^2)\, l},
\end{aligned}$$

$$M_{klm0}^{C,II} = -\sum_{s=1}^{N_C} C_s \sin\left(\frac{m\pi\,x_s}{a}\right) \sin\left(\frac{k\pi\,x_s}{a}\right) \cos\left(\frac{l\pi\,y_s}{b}\right). \tag{3.A.55}$$

18. Stiffness matrix elements for $n = 0$, and $m \neq 0$, $k \neq 0$, $l \neq 0$ with $k = m$:

$$M_{mlm0}^{m,II} = \frac{2\,K\,m\,\pi^2 \sin\left(1/2\,l\pi\right)\left(\cos\left(1/2\,m\pi\right)\sin\left(1/2\,m\pi\right) - 1/2\,m\pi\right)\left(a^2 l^2 v + b^2 m^2\right)}{a^3 b\,l},$$

$$M_{mlm0}^{c,II} = -\frac{c\,a\,b\left(m\pi - 2\cos\left(1/2\,m\pi\right)\sin\left(1/2\,m\pi\right)\right)\sin\left(1/2\,l\pi\right)}{m\pi^2 l},$$

$$M_{mlm0}^{C,II} = -\sum_{s=1}^{N_C} C_s \left(\sin\left(\frac{m\pi\,x_s}{a}\right)\right)^2 \cos\left(\frac{l\pi\,y_s}{b}\right). \tag{3.A.56}$$

19. Stiffness matrix elements for $m = n = k = 0$, and $l \neq 0$:

$$M_{0l00}^{m,II} = 0\,, \qquad M_{0l00}^{c,II} = -\frac{2\,cab\sin\left(1/2\,l\pi\right)}{3\,l\pi}\,, \qquad M_{0l00}^{C,II} = -\sum_{s=1}^{N_C} 4\,\frac{C_s x_s{}^2}{a^2}\cos\left(\frac{l\pi\,y_s}{b}\right). \tag{3.A.57}$$

20. Stiffness matrix elements for $m = n = l = 0$, and $k \neq 0$:

$$M_{k000}^{m,II} = 0\,,$$

$$M_{k000}^{c,II} = \frac{2\,cab\left(k\pi\,\cos\left(1/2\,k\pi\right) - 2\sin\left(1/2\,k\pi\right)\right)}{k^2\pi^2}\,,$$

$$M_{k000}^{C,II} = -\sum_{s=1}^{N_C} 2\,\frac{C_s x_s}{a}\sin\left(\frac{k\pi\,x_s}{a}\right). \tag{3.A.58}$$

21. Stiffness matrix elements for $m = n = 0$, and $k \neq 0$, $l \neq 0$:

$$M_{kl00}^{m,II} = 0\,,$$

$$M_{kl00}^{c,II} = \frac{4\,cab\left(k\pi\,\cos\left(1/2\,k\pi\right) - 2\sin\left(1/2\,k\pi\right)\right)\sin\left(1/2\,l\pi\right)}{k^2\pi^3 l}\,,$$

$$M_{kl00}^{C,II} = -\sum_{s=1}^{N_C} 2\,\frac{C_s x_s}{a}\sin\left(\frac{k\pi\,x_s}{a}\right)\cos\left(\frac{l\pi\,y_s}{b}\right). \tag{3.A.59}$$

22. Stiffness matrix elements for $k \neq 0$, $l \neq 0$, $m \neq 0$ and $n \neq 0$, with $k \neq m$ and $l \neq n$:

$$
\begin{aligned}
M_{klmn}^{m,II} = {}& -\frac{4\,K\,\pi^2}{b^3 a^3\,(l-n)\,(l+n)\,(k-m)\,(k+m)}\Bigg[\left(\left(b^2\left(a^2 n^2 v + b^2 m^2\right)k^2\right.\right.\\
& +l^2 a^2\left(-b^2\,(v-2)\,m^2 + a^2 n^2\right)\Big)\sin\left(1/2\,n\pi\right)n\cos\left(1/2\,l\pi\right)\\
& -\cos\left(1/2\,n\pi\right)\sin\left(1/2\,l\pi\right)\left(b^2\left(a^2 n^2 v + b^2 m^2\right)k^2 + \left(\left(b^2 m^2 v + a^2 n^2\right)l^2\right.\right.\\
& \left.-2\,b^2 m^2 n^2\,(-1+v)\right)a^2\Big)\,l\Big)\,k\sin\left(1/2\,m\pi\right)\cos\left(1/2\,k\pi\right)\\
& -\left(\left(2\left(a^2\,(1-v)\,l^2 + 1/2\,a^2 n^2 v + 1/2\,b^2 m^2\right)b^2 k^2\right.\right.\\
& +a^2 l^2\left(b^2 m^2 v + a^2 n^2\right)\Big)\sin\left(1/2\,n\pi\right)n\cos\left(1/2\,l\pi\right)\\
& -\cos\left(1/2\,n\pi\right)\sin\left(1/2\,l\pi\right)\left(\left(b^2 m^2 - a^2 n^2\,(v-2)\right)b^2 k^2\right.\\
& +a^2 l^2\left(b^2 m^2 v + a^2 n^2\right)\Big)\,l\Big)\cos\left(1/2\,m\pi\right)\sin\left(1/2\,k\pi\right)m\Bigg],
\end{aligned}
$$

$$
M_{klmn}^{c,II} = -\frac{4\,c\,a\,b\left[k\cos\left(1/2\,k\pi\right)\sin\left(1/2\,m\pi\right)-m\sin\left(1/2\,k\pi\right)\cos\left(1/2\,m\pi\right)\right]}{\pi^2\left(k^2-m^2\right)\left(l^2-n^2\right)}\times
$$

$$
\times\left[-l\sin\left(1/2\,l\pi\right)\cos\left(1/2\,n\pi\right)+n\cos\left(1/2\,l\pi\right)\sin\left(1/2\,n\pi\right)\right],
$$

$$
M_{klmn}^{C,II} = -\sum_{s=1}^{N_C}C_s\sin\left(\frac{m\pi\,x_s}{a}\right)\cos\left(\frac{n\pi\,y_s}{b}\right)\sin\left(\frac{k\pi\,x_s}{a}\right)\cos\left(\frac{l\pi\,y_s}{b}\right).\tag{3.A.60}
$$

23. Stiffness matrix elements for $k\neq 0$, $l\neq 0$, $m\neq 0$ and $n\neq 0$, with $k=m$ and $l\neq n$:

$$
\begin{aligned}
M_{mlmn}^{m,II} = {}& \frac{2\,K\,\pi^2}{a^3b^3m\left(l^2-n^2\right)}\Big[-\Big(\sin\left(1/2\,m\pi\right)\Big(b^4m^4+3\left(\left(v-2/3\right)l^2+1/3\,n^2v\right)\times\\
& \times a^2b^2m^2+a^4l^2n^2\Big)\cos\left(1/2\,m\pi\right)-1/2\,m\pi\left(b^4m^4-\left(\left(v-2\right)l^2-n^2v\right)\times\right.\\
& \times a^2b^2m^2+a^4l^2n^2\Big)\Big)\sin\left(1/2\,n\pi\right)n\cos\left(1/2\,l\pi\right)+\sin\left(1/2\,l\pi\right)\big(\sin\left(1/2\,m\pi\right)\\
& \left(b^4m^4+\left(l^2v+3\left(v-2/3\right)n^2\right)a^2b^2m^2+a^4l^2n^2\right)\cos\left(1/2\,m\pi\right)\\
& -1/2\,m\left(b^4m^4+a^2b^2\left(l^2v-n^2\left(v-2\right)\right)m^2+a^4l^2n^2\right)\pi\big)\cos\left(1/2\,n\pi\right)l\Big],
\end{aligned}
$$

$$
M_{mlmn}^{c,II} = \frac{c\,a\,b\left(-2\,\cos\left(1/2\,m\pi\right)\sin\left(1/2\,m\pi\right)+m\pi\right)}{m\pi^2\left(l^2-n^2\right)}\times
$$

$$
\times\left(-l\sin\left(1/2\,l\pi\right)\cos\left(1/2\,n\pi\right)+n\cos\left(1/2\,l\pi\right)\sin\left(1/2\,n\pi\right)\right),
$$

$$
M_{mlmn}^{C,II} = -\sum_{s=1}^{N_C}C_s\left(\sin\left(\frac{m\pi\,x_s}{a}\right)\right)^2\cos\left(\frac{n\pi\,y_s}{b}\right)\cos\left(\frac{l\pi\,y_s}{b}\right).\tag{3.A.61}
$$

24. Stiffness matrix elements for $k\neq 0$, $l\neq 0$, $m\neq 0$ and $n\neq 0$, with $k\neq m$ and $l=n$:

$$
\begin{aligned}
M_{knmn}^{m,II} = {}& -\frac{2\,K\,\pi^2}{a^3b^3\left(k^2-m^2\right)n}\Big[-\sin\left(1/2\,m\pi\right)k\left(\left(a^4n^4+a^2b^2\left(k^2v+3\,m^2\left(v-2/3\right)\right)n^2\right.\right.\\
& \left.+b^4k^2m^2\right)\sin\left(1/2\,n\pi\right)\cos\left(1/2\,n\pi\right)+1/2\,\pi\left(a^4n^4+a^2\left(k^2v-m^2\left(v-2\right)\right)b^2n^2\right.\\
& \left.+b^4k^2m^2\right)n\big)\cos\left(1/2\,k\pi\right)+\left(\left(a^4n^4+3\left(\left(v-2/3\right)k^2+1/3\,m^2v\right)a^2b^2n^2\right.\right.\\
& \left.+b^4k^2m^2\right)\sin\left(1/2\,n\pi\right)\cos\left(1/2\,n\pi\right)+1/2\,\pi\,n\left(a^4n^4-a^2\left(\left(v-2\right)k^2-m^2v\right)b^2n^2\right.\\
& \left.+b^4k^2m^2\right)\big)m\sin\left(1/2\,k\pi\right)\cos\left(1/2\,m\pi\right)\Big],
\end{aligned}
$$

$$
M_{knmn}^{c,II} = \frac{cab\left[k\cos\left(1/2\,k\pi\right)\sin\left(1/2\,m\pi\right)-m\sin\left(1/2\,k\pi\right)\cos\left(1/2\,m\pi\right)\right]}{\pi^2\left(k^2-m^2\right)n}\times
$$

$$
\times\left[2\cos\left(1/2\,n\pi\right)\sin\left(1/2\,n\pi\right)+n\pi\right],
$$

$$
M_{knmn}^{C,II} = -\sum_{s=1}^{N_C}C_s\sin\left(\frac{m\pi\,x_s}{a}\right)\left(\cos\left(\frac{n\pi\,y_s}{b}\right)\right)^2\sin\left(\frac{k\pi\,x_s}{a}\right).\tag{3.A.62}
$$

25. Stiffness matrix elements for $k\neq 0$, $l\neq 0$, $m\neq 0$ and $n\neq 0$, with $k=m$ and $l=n$:

$$
\begin{aligned}
M_{mnmn}^{m,II} = {}& \frac{K\pi^2}{a^3b^3mn}\Big[\sin\left(1/2\,m\pi\right)\Big(\sin\left(1/2\,n\pi\right)\left(a^2n^2+b^2m^2\right)^2\cos\left(1/2\,n\pi\right)\\
& +1/2\,n\left(b^4m^4+4\,n^2a^2\left(v-1/2\right)b^2m^2+a^4n^4\right)\pi\Big)\cos\left(1/2\,m\pi\right)\\
& -1/2\left(\left(b^4m^4+4\,n^2a^2\left(v-1/2\right)b^2m^2+a^4n^4\right)\sin\left(1/2\,n\pi\right)\cos\left(1/2\,n\pi\right)\right.
\end{aligned}
$$

$$+1/2\,n\pi\,\left(a^2n^2+b^2m^2\right)^2\right)\pi\,m\bigg]\,,$$

$$M_{mnmn}^{c,II} \;=\; -\frac{cab\left[-2\,\cos\left(1/2\,m\pi\right)\sin\left(1/2\,m\pi\right)+m\pi\right]\left[2\,\cos\left(1/2\,n\pi\right)\sin\left(1/2\,n\pi\right)+n\pi\right]}{4\,m\pi^2 n}\,,$$

$$M_{mnmn}^{C,II} \;=\; -\sum_{s=1}^{N_C} C_s\left(\sin\left(\frac{m\pi\,x_s}{a}\right)\right)^2\left(\cos\left(\frac{n\pi\,y_s}{b}\right)\right)^2. \tag{3.A.63}$$

3.A.3.4 Stiffness matrix elements for the employed trigonometric functions of type $w_{m,n}^{III}$

The stiffness matrix elements $M_{klmn}^{m,III}$, $M_{klmn}^{c,III}$, and $M_{klmn}^{C,III}$ for the employed trigonometric functions of type $w_{m,n}^{III}$, for 25 combinations of k, l, m, and n, read as:

1. Stiffness matrix elements for $k=l=m=n=0$:

$$M_{0000}^{m,III}=0\,,\qquad M_{0000}^{c,III}=-\frac{1}{3}\,c\,a\,b\,,\qquad M_{0000}^{C,III}=-\sum_{s=1}^{N_C} 4\,C_s\,y_s^2\,/b^2. \tag{3.A.64}$$

2. Stiffness matrix elements for $k=l=m=0$, and $n\neq 0$:

$$
\begin{aligned}
M_{000n}^{m,III} &= 0\,,\\
M_{000n}^{c,III} &= \frac{2\,c\,a\,b\left(n\pi\,\cos\left(1/2\,n\pi\right)-2\,\sin\left(1/2\,n\pi\right)\right)}{n^2\pi^2}\,,\\
M_{000n}^{C,III} &= -\sum_{s=1}^{N_C} 2\,\frac{C_s y_s}{b}\,\sin\left(\frac{n\pi\,y_s}{b}\right).
\end{aligned}
\tag{3.A.65}
$$

3. Stiffness matrix elements for $k=l=n=0$, and $m\neq 0$:

$$M_{00m0}^{m,III}=0\,,\qquad M_{00m0}^{c,III}=-\frac{2\,c\,a\,b\sin\left(1/2\,m\,\pi\right)}{3\,m\pi}\,,\qquad M_{00m0}^{C,III}=-\sum_{s=1}^{N_C} 4\,\frac{C_s y_s{}^2}{b^2}\cos\left(\frac{m\,\pi\,x_s}{a}\right). \tag{3.A.66}$$

4. Stiffness matrix elements for $k=l=0$, and $m\neq 0$, $n\neq 0$:

$$
\begin{aligned}
M_{00mn}^{m,III} &= 0\,,\\
M_{00mn}^{c,III} &= \frac{4\,c\,a\,b\left(n\pi\,\cos\left(1/2\,n\pi\right)-2\,\sin\left(1/2\,n\pi\right)\right)\sin\left(1/2\,m\pi\right)}{n^2\pi^3 m}\,,\\
M_{00mn}^{C,III} &= -\sum_{s=1}^{N_C} 2\,\frac{C_s y_s}{b}\,\sin\left(\frac{n\pi\,y_s}{b}\right)\cos\left(\frac{m\pi\,x_s}{a}\right).
\end{aligned}
\tag{3.A.67}
$$

5. Stiffness matrix elements for $m=k=0$, and $n\neq 0$, $l\neq 0$ with $l\neq n$:

$$
\begin{aligned}
M_{0l0n}^{m,III} &= \frac{2\,Kl^2\pi^3 n^2 a\left(l\cos\left(1/2\,l\pi\right)\sin\left(1/2\,n\pi\right)-n\sin\left(1/2\,l\pi\right)\cos\left(1/2\,n\pi\right)\right)}{b^3 l^2-b^3 n^2}\,,\\
M_{0l0n}^{c,III} &= \frac{2\,cab\left(l\cos\left(1/2\,l\pi\right)\sin\left(1/2\,n\pi\right)-n\sin\left(1/2\,l\pi\right)\cos\left(1/2\,n\pi\right)\right)}{\pi\,l^2-\pi\,n^2}\,,\\
M_{0l0n}^{C,III} &= -\sum_{s=1}^{N_C} C_s\sin\left(\frac{n\pi\,y_s}{b}\right)\sin\left(\frac{l\pi\,y_s}{b}\right).
\end{aligned}
\tag{3.A.68}
$$

6. Stiffness matrix elements for $m = k = 0$, and $n \neq 0$, $l \neq 0$ with $l = n$:

$$
\begin{aligned}
M_{0n0n}^{m,III} &= -\frac{K n^3 \pi^3 a \left(-2 \cos\left(1/2\,n\pi\right) \sin\left(1/2\,n\pi\right) + n\pi\right)}{2\,b^3}, \\
M_{0n0n}^{c,III} &= -\frac{cab \left(-2 \cos\left(1/2\,n\pi\right) \sin\left(1/2\,n\pi\right) + n\pi\right)}{2\,n\pi}, \\
M_{0n0n}^{C,III} &= -\sum_{s=1}^{N_C} C_s \left(\sin\left(\frac{n\pi\,y_s}{b}\right)\right)^2.
\end{aligned}
\tag{3.A.69}
$$

7. Stiffness matrix elements for $n = k = 0$, and $m \neq 0$, $l \neq 0$:

$$
\begin{aligned}
M_{0lm0}^{m,III} &= \frac{4\,Kv\pi\,m \sin\left(1/2\,m\pi\right) \left(l\pi \cos\left(1/2\,l\pi\right) - 2 \sin\left(1/2\,l\pi\right)\right)}{ba}, \\
M_{0lm0}^{c,III} &= \frac{4\,cab \sin\left(1/2\,m\pi\right) \left(l\pi \cos\left(1/2\,l\pi\right) - 2 \sin\left(1/2\,l\pi\right)\right)}{\pi^3 m l^2}, \\
M_{0lm0}^{C,III} &= -\sum_{s=1}^{N_C} 2\,\frac{C_s y_s}{b} \cos\left(\frac{m\pi\,x_s}{a}\right) \sin\left(\frac{l\pi\,y_s}{b}\right).
\end{aligned}
\tag{3.A.70}
$$

8. Stiffness matrix elements for $k = 0$, and $m \neq 0$, $n \neq 0$, $l \neq 0$ with $l \neq n$:

$$
\begin{aligned}
M_{0lmn}^{m,III} &= -\frac{4\,K\pi^2 \sin\left(1/2\,m\pi\right) l^2 \left(b^2 m^2 v + a^2 n^2\right)}{b^3 a \left(l^2 - n^2\right) m} \times \\
&\quad \times \left(n \sin\left(1/2\,l\pi\right) \cos\left(1/2\,n\pi\right) - l \cos\left(1/2\,l\pi\right) \sin\left(1/2\,n\pi\right)\right), \\
M_{0lmn}^{c,III} &= \frac{4\,cab \sin\left(1/2\,m\pi\right) \left(l \cos\left(1/2\,l\pi\right) \sin\left(1/2\,n\pi\right) - n \sin\left(1/2\,l\pi\right) \cos\left(1/2\,n\pi\right)\right)}{\pi^2 m \left(l^2 - n^2\right)}, \\
M_{0lmn}^{C,III} &= -\sum_{s=1}^{N_C} C_s \sin\left(\frac{n\pi\,y_s}{b}\right) \cos\left(\frac{m\pi\,x_s}{a}\right) \sin\left(\frac{l\pi\,y_s}{b}\right).
\end{aligned}
\tag{3.A.71}
$$

9. Stiffness matrix elements for $k = 0$, and $m \neq 0$, $n \neq 0$, $l \neq 0$ with $l = n$:

$$
\begin{aligned}
M_{mn0n}^{m,III} &= \frac{2\,K\,\pi^2 n \left(\cos\left(1/2\,n\pi\right) \sin\left(1/2\,n\pi\right) - 1/2\,n\pi\right) \sin\left(1/2\,m\pi\right) \left(b^2 m^2 v + a^2 n^2\right)}{b^3 a m}, \\
M_{mn0n}^{c,III} &= -\frac{cab \left(-2 \cos\left(1/2\,n\pi\right) \sin\left(1/2\,n\pi\right) + n\pi\right)}{2\,n\pi}, \\
M_{mn0n}^{C,III} &= -\sum_{s=1}^{N_C} C_s \left(\sin\left(\frac{n\pi\,y_s}{b}\right)\right)^2 \cos\left(\frac{m\pi\,x_s}{a}\right).
\end{aligned}
\tag{3.A.72}
$$

10. Stiffness matrix elements for $m = l = 0$, and $n \neq 0$, $k \neq 0$:

$$
\begin{aligned}
M_{k00n}^{m,III} &= -\frac{8\,K\pi\,k\,v \sin\left(1/2\,k\pi\right) \left(-1/2\,n\pi \cos\left(1/2\,n\pi\right) + \sin\left(1/2\,n\pi\right)\right)}{ba}, \\
M_{k00n}^{c,III} &= \frac{4\,cab \sin\left(1/2\,k\pi\right) \left(n\pi \cos\left(1/2\,n\pi\right) - 2 \sin\left(1/2\,n\pi\right)\right)}{\pi^3 k n^2}, \\
M_{k00n}^{C,III} &= -\sum_{s=1}^{N_C} 2\,\frac{C_s y_s}{b} \sin\left(\frac{n\pi\,y_s}{b}\right) \cos\left(\frac{k\pi\,x_s}{a}\right).
\end{aligned}
\tag{3.A.73}
$$

11. Stiffness matrix elements for $n = l = 0$, and $m \neq 0$, $k \neq 0$ with $k \neq m$:

$$M_{k0m0}^{m,III} = \frac{48\,m\pi\,kK}{3\,a^3bk^2 - 3\,a^3bm^2}\left[\left(1/24\,b^2m^2\pi^2 - a^2\left(-1+v\right)\right)k\sin\left(1/2\,m\pi\right)\cos\left(1/2\,k\pi\right)\right.$$
$$\left.+m\cos\left(1/2\,m\pi\right)\sin\left(1/2\,k\pi\right)\left(-1/24\,b^2k^2\pi^2 + a^2\left(-1+v\right)\right)\right],$$

$$M_{k0m0}^{c,III} = \frac{2\,cab\left(-k\sin\left(1/2\,k\pi\right)\cos\left(1/2\,m\pi\right) + m\cos\left(1/2\,k\pi\right)\sin\left(1/2\,m\pi\right)\right)}{\left(3\,k^2 - 3\,m^2\right)\pi},$$

$$M_{k0m0}^{C,III} = -\sum_{s=1}^{N_C} 4\,\frac{C_s{y_s}^2}{b^2}\cos\left(\frac{m\pi\,x_s}{a}\right)\cos\left(\frac{k\pi\,x_s}{a}\right). \tag{3.A.74}$$

12. Stiffness matrix elements for $n = l = 0$, and $m \neq 0$, $k \neq 0$ with $k = m$:

$$M_{m0m0}^{m,III} = \frac{4\,m\,K\pi}{a^3b}\left[-2\left(1/24\,b^2m^2\pi^2 + a^2\left(-1+v\right)\right)\sin\left(1/2\,m\pi\right)\cos\left(1/2\,m\pi\right)\right.$$
$$\left.+m\pi\left(-1/24\,b^2m^2\pi^2 + a^2\left(-1+v\right)\right)\right],$$

$$M_{m0m0}^{c,III} = -\frac{cab\left(2\,\cos\left(1/2\,m\pi\right)\sin\left(1/2\,m\pi\right) + m\pi\right)}{6\,m\pi},$$

$$M_{m0m0}^{C,III} = -\sum_{s=1}^{N_C} 4\,\frac{C_s{y_s}^2}{b^2}\left(\cos\left(\frac{m\pi\,x_s}{a}\right)\right)^2. \tag{3.A.75}$$

13. Stiffness matrix elements for $l = 0$, and $m \neq 0$, $n \neq 0$, $k \neq 0$ with $k \neq m$:

$$M_{k0mn}^{m,III} = \frac{4\,k\pi\,K}{ba^3\left(k^2 - m^2\right)n^2}\left[\left(-2\left(\left(a^2n^2v + b^2m^2\right)k^2 - 2\,a^2m^2n^2\left(-1+v\right)\right)\times\right.\right.$$
$$\times\sin\left(1/2\,k\pi\right)\cos\left(1/2\,m\pi\right) - 2\,m\cos\left(1/2\,k\pi\right)k\sin\left(1/2\,m\pi\right)\times$$
$$\times\left(-b^2m^2 + a^2n^2\left(v-2\right)\right)\Big)\sin\left(1/2\,n\pi\right) + \cos\left(1/2\,n\pi\right)kn\pi\left(a^2n^2v + b^2m^2\right)\times$$
$$\left.\times\left(k\sin\left(1/2\,k\pi\right)\cos\left(1/2\,m\pi\right) - m\cos\left(1/2\,k\pi\right)\sin\left(1/2\,m\pi\right)\right)\right],$$

$$M_{k0mn}^{c,III} = \frac{4\,cab\left[k\sin\left(1/2\,k\pi\right)\cos\left(1/2\,m\pi\right) - m\cos\left(1/2\,k\pi\right)\sin\left(1/2\,m\pi\right)\right]}{\pi^3\left(k^2 - m^2\right)n^2}\times$$
$$\times\left[n\pi\,\cos\left(1/2\,n\pi\right) - 2\,\sin\left(1/2\,n\pi\right)\right],$$

$$M_{k0mn}^{C,III} = -\sum_{s=1}^{N_C} 2\,\frac{C_sy_s}{b}\sin\left(\frac{n\pi\,y_s}{b}\right)\cos\left(\frac{m\pi\,x_s}{a}\right)\cos\left(\frac{k\pi\,x_s}{a}\right). \tag{3.A.76}$$

14. Stiffness matrix elements for $l = 0$, and $m \neq 0$, $n \neq 0$, $k \neq 0$ with $k = m$:

$$M_{mnm0}^{m,III} = -\frac{12\,K\,\pi\,m}{ba^3n^2}\left[\left(\sin\left(1/2\,m\pi\right)\left(a^2\left(v-2/3\right)n^2 + 1/3\,b^2m^2\right)\cos\left(1/2\,m\pi\right)\right.\right.$$
$$\left.-1/6\,\pi\,m\left(-b^2m^2 + a^2n^2\left(v-2\right)\right)\right)\sin\left(1/2\,n\pi\right)$$
$$\left.-1/6\,n\cos\left(1/2\,n\pi\right)\pi\,\left(\cos\left(1/2\,m\pi\right)\sin\left(1/2\,m\pi\right) + 1/2\,m\pi\right)\left(a^2n^2v + b^2m^2\right)\right],$$

$$M_{mnm0}^{c,III} = -\frac{2\,cab\left(-1/2\,n\pi\,\cos\left(1/2\,n\pi\right) + \sin\left(1/2\,n\pi\right)\right)\left(2\,\cos\left(1/2\,m\pi\right)\sin\left(1/2\,m\pi\right) + m\pi\right)}{\pi^3mn^2},$$

$$M_{mnm0}^{C,III} = -\sum_{s=1}^{N_C} 2\,\frac{C_sy_s}{b}\sin\left(\frac{n\pi\,y_s}{b}\right)\left(\cos\left(\frac{m\pi\,x_s}{a}\right)\right)^2. \tag{3.A.77}$$

15. Stiffness matrix elements for $m = 0$, and $n \neq 0$, $k \neq 0$, $l \neq 0$ with $l \neq n$:

$$
\begin{aligned}
M_{kl0n}^{m,III} &= -\frac{4\,K\pi^2 \sin(1/2\,k\pi)\,n^2\,(b^2k^2v + a^2l^2)}{b^3 a\,(l^2 - n^2)\,k} \times \\
&\quad \times (n\sin(1/2\,l\pi)\cos(1/2\,n\pi) - l\cos(1/2\,l\pi)\sin(1/2\,n\pi))\,, \\
M_{kl0n}^{c,III} &= \frac{4\,cab\,\sin(1/2\,k\pi)\,(l\cos(1/2\,l\pi)\sin(1/2\,n\pi) - n\sin(1/2\,l\pi)\cos(1/2\,n\pi))}{\pi^2 k\,(l^2 - n^2)}\,, \\
M_{kl0n}^{C,III} &= -\sum_{s=1}^{N_C} C_s \left(\sin\left(\frac{n\pi\,y_s}{b}\right)\right)^2 \cos\left(\frac{k\pi\,x_s}{a}\right).
\end{aligned} \tag{3.A.78}
$$

16. Stiffness matrix elements for $m = 0$, and $n \neq 0$, $k \neq 0$, $l \neq 0$ with $l = n$:

$$
\begin{aligned}
M_{kn0n}^{m,III} &= -\frac{K\pi^2 n\,\sin(1/2\,k\pi)\,(b^2k^2v + a^2n^2)\,(-2\cos(1/2\,n\pi)\sin(1/2\,n\pi) + n\pi)}{b^3 ak}\,, \\
M_{kn0n}^{c,III} &= \frac{cab\,\sin(1/2\,k\pi)\,(2\cos(1/2\,n\pi)\sin(1/2\,n\pi) - n\pi)}{\pi^2 kn}\,, \\
M_{kn0n}^{C,III} &= -\sum_{s=1}^{N_C} C_s \left(\sin\left(\frac{n\pi\,y_s}{b}\right)\right)^2 \cos\left(\frac{k\pi\,x_s}{a}\right).
\end{aligned} \tag{3.A.79}
$$

17. Stiffness matrix elements for $n = 0$, and $m \neq 0$, $k \neq 0$, $l \neq 0$ with $k \neq m$:

$$
\begin{aligned}
M_{klm0}^{m,III} &= \frac{4\,\pi\,K\,m}{ba^3\,(k^2 - m^2)\,l^2} \left[\left(4\left(\left(1/2\,a^2l^2v + 1/2\,b^2k^2\right)m^2 - a^2k^2l^2\,(-1+v)\right) \times \right.\right. \\
&\quad \times \sin(1/2\,m\pi)\cos(1/2\,k\pi) + 2\left(-b^2k^2 + a^2l^2\,(v-2)\right)k\cos(1/2\,m\pi) \times \\
&\quad \times \sin(1/2\,k\pi)\,m)\sin(1/2\,l\pi) + \cos(1/2\,l\pi)\,lm\pi\left(a^2l^2v + b^2k^2\right) \times \\
&\quad \left.\times (k\sin(1/2\,k\pi)\cos(1/2\,m\pi) - m\cos(1/2\,k\pi)\sin(1/2\,m\pi))\right], \\
M_{klm0}^{c,III} &= -\frac{8\,cab\,[-1/2\,l\pi\,\cos(1/2\,l\pi) + \sin(1/2\,l\pi)]}{\pi^3\,(k^2 - m^2)\,l^2} \times \\
&\quad \times [k\sin(1/2\,k\pi)\cos(1/2\,m\pi) - m\cos(1/2\,k\pi)\sin(1/2\,m\pi)]\,, \\
M_{klm0}^{C,III} &= -\sum_{s=1}^{N_C} 2\,\frac{C_s y_s}{b}\cos\left(\frac{m\pi\,x_s}{a}\right)\sin\left(\frac{l\pi\,y_s}{b}\right)\cos\left(\frac{k\pi\,x_s}{a}\right).
\end{aligned} \tag{3.A.80}
$$

18. Stiffness matrix elements for $n = 0$, and $m \neq 0$, $k \neq 0$, $l \neq 0$ with $k = m$:

$$
\begin{aligned}
M_{mlm0}^{m,III} &= -\frac{12\,m\pi\,K}{ba^3 l^2}\left[\left(\left(a^2\,(v - 2/3)\,l^2 + 1/3\,b^2m^2\right)\sin(1/2\,m\pi)\cos(1/2\,m\pi)\right.\right. \\
&\quad -1/6\,m\left(a^2l^2\,(v-2) - b^2m^2\right)\pi\right)\sin(1/2\,l\pi) \\
&\quad \left.-1/6\,\pi\,l\cos(1/2\,l\pi)\,(\cos(1/2\,m\pi)\sin(1/2\,m\pi) + 1/2\,m\pi)\left(a^2l^2v + b^2m^2\right)\right], \\
M_{mlm0}^{c,III} &= \frac{cab\,(2\cos(1/2\,m\pi)\sin(1/2\,m\pi) + m\pi)\,(l\pi\,\cos(1/2\,l\pi) - 2\sin(1/2\,l\pi))}{\pi^3 ml^2}\,, \\
M_{mlm0}^{C,III} &= -\sum_{s=1}^{N_C} 2\,\frac{C_s y_s}{b}\left(\cos\left(\frac{m\pi\,x_s}{a}\right)\right)^2 \sin\left(\frac{l\pi\,y_s}{b}\right).
\end{aligned} \tag{3.A.81}
$$

19. Stiffness matrix elements for $m = n = k = 0$, and $l \neq 0$:

$$
\begin{aligned}
M_{0l00}^{m,III} &= 0\,, \\
M_{0l00}^{c,III} &= \frac{2\,cab\,(l\pi\,\cos\,(1/2\,l\pi) - 2\,\sin\,(1/2\,l\pi))}{l^2\pi^2}\,, \\
M_{0l00}^{C,III} &= -\sum_{s=1}^{N_C} 2\,\frac{C_s y_s}{b}\,\sin\left(\frac{l\pi\,y_s}{b}\right).
\end{aligned}
\tag{3.A.82}
$$

20. Stiffness matrix elements for $m = n = l = 0$, and $k \neq 0$:

$$
M_{k000}^{m,III} = 0\,, \qquad M_{k000}^{c,III} = -\frac{2\,cab\,\sin\,(1/2\,k\pi)}{3\,k\pi}\,, \qquad M_{k000}^{C,III} = -\sum_{s=1}^{N_C} 4\,\frac{C_s y_s{}^2}{b^2}\,\cos\left(\frac{k\pi\,x_s}{a}\right).
\tag{3.A.83}
$$

21. Stiffness matrix elements for $m = n = 0$, and $k \neq 0$, $l \neq 0$:

$$
\begin{aligned}
M_{kl00}^{m,III} &= 0\,, \\
M_{kl00}^{c,III} &= \frac{4\,cab\,\sin\,(1/2\,k\pi)\,(l\pi\,\cos\,(1/2\,l\pi) - 2\,\sin\,(1/2\,l\pi))}{\pi^3 kl^2}\,, \\
M_{kl00}^{C,III} &= -\sum_{s=1}^{N_C} 2\,\frac{C_s y_s}{b}\,\sin\left(\frac{l\pi\,y_s}{b}\right)\cos\left(\frac{k\pi\,x_s}{a}\right).
\end{aligned}
\tag{3.A.84}
$$

22. Stiffness matrix elements for $k \neq 0$, $l \neq 0$, $m \neq 0$ and $n \neq 0$, with $k \neq m$ and $l \neq n$:

$$
\begin{aligned}
M_{klmn}^{m,III} &= -\frac{4\,\pi^2 K}{b^3 a^3\,(l-n)\,(l+n)\,(k-m)\,(k+m)}\Big[\Big(l\Big(-b^2\Big(-b^2 m^2 + a^2 n^2\,(v-2)\Big)k^2 \\
&\quad +a^2 k^2\Big(b^2 m^2 v + a^2 n^2\Big)\Big)\sin\,(1/2\,n\pi)\cos\,(1/2\,l\pi) - n\sin\,(1/2\,l\pi)\cos\,(1/2\,n\pi)\times \\
&\quad \times\Big(-2\,b^2\Big(a^2\,(-1+v)\,l^2 - 1/2\,a^2 n^2 v - 1/2\,b^2 m^2\Big)k^2 + a^2 l^2\Big(b^2 m^2 v + a^2 n^2\Big)\Big)\Big)\times \\
&\quad \times m\sin\,(1/2\,m\pi)\cos\,(1/2\,k\pi) - k\cos\,(1/2\,m\pi)\sin\,(1/2\,k\pi)\,(l\sin\,(1/2\,n\pi)\times \\
&\quad \times\Big(b^2\Big(a^2 n^2 v + b^2 m^2\Big)k^2 + \Big(\Big(b^2 m^2 v + a^2 n^2\Big)l^2 - 2\,b^2 m^2 n^2\,(-1+v)\Big)a^2\Big)\times \\
&\quad \times\cos\,(1/2\,l\pi) - n\sin\,(1/2\,l\pi)\cos\,(1/2\,n\pi)\Big(b^2\Big(a^2 n^2 v + b^2 m^2\Big)k^2 \\
&\quad +l^2 a^2\Big(-b^2\,(v-2)\,m^2 + a^2 n^2\Big)\Big)\Big)\Big]\,, \\
M_{klmn}^{c,III} &= -\frac{4\,cab\,[-k\sin\,(1/2\,k\pi)\cos\,(1/2\,m\pi) + m\cos\,(1/2\,k\pi)\sin\,(1/2\,m\pi)]}{\pi^2\,(k^2 - m^2)\,(l^2 - n^2)}\times \\
&\quad \times [l\cos\,(1/2\,l\pi)\sin\,(1/2\,n\pi) - n\sin\,(1/2\,l\pi)\cos\,(1/2\,n\pi)]\,, \\
M_{klmn}^{C,III} &= -\sum_{s=1}^{N_C} C_s \sin\left(\frac{n\pi\,y_s}{b}\right)\cos\left(\frac{m\pi\,x_s}{a}\right)\sin\left(\frac{l\pi\,y_s}{b}\right)\cos\left(\frac{k\pi\,x_s}{a}\right).
\end{aligned}
\tag{3.A.85}
$$

23. Stiffness matrix elements for $k \neq 0$, $l \neq 0$, $m \neq 0$ and $n \neq 0$, with $k = m$ and $l \neq n$:

$$
\begin{aligned}
M_{mlmn}^{m,III} &= -\frac{2\,\pi^2 K}{a^3 b^3 m\,(l^2 - n^2)}\Big[-l\Big(\Big(b^4 m^4 + b^2\Big(l^2 v + 3\,(v-2/3)\,n^2\Big)a^2 m^2 + a^4 l^2 n^2\Big)\times \\
&\quad \times\sin\,(1/2\,m\pi)\cos\,(1/2\,m\pi) + 1/2\,m\pi\Big(b^4 m^4 + b^2\Big(l^2 v - n^2\,(v-2)\Big)a^2 m^2 \\
&\quad +a^4 l^2 n^2\Big)\Big)\sin\,(1/2\,n\pi)\cos\,(1/2\,l\pi) + \Big(\Big(b^4 m^4 + 3\,b^2\Big((v-2/3)\,l^2 + 1/3\,n^2 v\Big)\times
\end{aligned}
$$

$$\times a^2 m^2 + a^4 l^2 n^2 \Big) \sin\left(1/2\,m\pi\right)\cos\left(1/2\,m\pi\right) + 1/2\,m \left(b^4 m^4 - b^2 \left((v-2)\,l^2 - n^2 v\right) \times\right.$$

$$\left.\times a^2 m^2 + a^4 l^2 n^2 \right) \pi \Big) \cos\left(1/2\,n\pi\right)\sin\left(1/2\,l\pi\right) n \bigg]\ ,$$

$$M_{mlmn}^{c,III} = \frac{cab\left[2\,\cos\left(1/2\,m\pi\right)\sin\left(1/2\,m\pi\right) + m\pi\right]}{\pi^2 m\left(l^2 - n^2\right)} \times$$

$$\times \left[l\,\cos\left(1/2\,l\pi\right)\sin\left(1/2\,n\pi\right) - n\,\sin\left(1/2\,l\pi\right)\cos\left(1/2\,n\pi\right)\right]\ ,$$

$$M_{mlmn}^{C,III} = -\sum_{s=1}^{N_C} C_s \sin\left(\frac{n\pi\,y_s}{b}\right)\left(\cos\left(\frac{m\pi\,x_s}{a}\right)\right)^2 \sin\left(\frac{l\pi\,y_s}{b}\right)\ . \tag{3.A.86}$$

24. Stiffness matrix elements for $k \neq 0$, $l \neq 0$, $m \neq 0$ and $n \neq 0$, with $k \neq m$ and $l = n$:

$$M_{knmn}^{m,III} = \frac{2\,\pi^2 K}{a^3\left(k^2 - m^2\right)nb^3} \Big[-m\,\sin\left(1/2\,m\pi\right)\left(\left(a^4 n^4 + 3\,b^2\left((v-2/3)\,k^2 + 1/3\,m^2 v\right)a^2 n^2\right.\right.$$

$$\left.+ b^4 k^2 m^2\right)\sin\left(1/2\,n\pi\right)\cos\left(1/2\,n\pi\right) - 1/2\,\pi\left(a^4 n^4 - b^2\left((v-2)\,k^2 - m^2 v\right)a^2 n^2\right.$$

$$\left.+ b^4 k^2 m^2\right)n\Big)\cos\left(1/2\,k\pi\right) + k\left(\left(a^4 n^4 + b^2\left(k^2 v + 3\,m^2\left(v-2/3\right)\right)a^2 n^2\right.\right.$$

$$\left.+ b^4 k^2 m^2\right)\sin\left(1/2\,n\pi\right)\cos\left(1/2\,n\pi\right) - 1/2\left(a^4 n^4 + b^2 a^2\left(k^2 v - m^2\left(v-2\right)\right)n^2\right.$$

$$\left.\left.+ b^4 k^2 m^2\right)\pi\,n\right)\sin\left(1/2\,k\pi\right)\cos\left(1/2\,m\pi\right)\Big]\ ,$$

$$M_{knmn}^{c,III} = \frac{2\,cab\left[k\,\sin\left(1/2\,k\pi\right)\cos\left(1/2\,m\pi\right) - m\,\cos\left(1/2\,k\pi\right)\sin\left(1/2\,m\pi\right)\right]}{\pi^2\left(k^2 - m^2\right)n} \times$$

$$\times \left[\cos\left(1/2\,n\pi\right)\sin\left(1/2\,n\pi\right) - 1/2\,n\pi\right]\ ,$$

$$M_{knmn}^{C,III} = -\sum_{s=1}^{N_C} C_s \left(\sin\left(\frac{n\pi\,y_s}{b}\right)\right)^2 \cos\left(\frac{m\pi\,x_s}{a}\right)\cos\left(\frac{k\pi\,x_s}{a}\right)\ . \tag{3.A.87}$$

25. Stiffness matrix elements for $k \neq 0$, $l \neq 0$, $m \neq 0$ and $n \neq 0$, with $k = m$ and $l = n$:

$$M_{mnmn}^{m,III} = \frac{\pi^2 K}{a^3 b^3 nm} \Big[\left(\sin\left(1/2\,n\pi\right)\left(a^2 n^2 + b^2 m^2\right)^2 \cos\left(1/2\,n\pi\right) - 1/2\,n\pi\left(b^4 m^4\right.\right.$$

$$\left.+ 4\,n^2 b^2\left(v-1/2\right)a^2 m^2 + a^4 n^4\right)\Big)\sin\left(1/2\,m\pi\right)\cos\left(1/2\,m\pi\right)$$

$$+ 1/2\,\pi\,m\left(\sin\left(1/2\,n\pi\right)\left(b^4 m^4 + 4\,n^2 b^2\left(v-1/2\right)a^2 m^2 + a^4 n^4\right)\cos\left(1/2\,n\pi\right)\right.$$

$$\left.- 1/2\,n\pi\left(a^2 n^2 + b^2 m^2\right)^2\right)\Big]\ ,$$

$$M_{mnmn}^{c,III} = \frac{cab\left[\cos\left(1/2\,n\pi\right)\sin\left(1/2\,n\pi\right) - 1/2\,n\pi\right]\left[2\,\cos\left(1/2\,m\pi\right)\sin\left(1/2\,m\pi\right) + m\pi\right]}{2\,\pi^2 mn}\ ,$$

$$M_{mnmn}^{C,III} = -\sum_{s=1}^{N_C} C_s \left(\sin\left(\frac{n\pi\,y_s}{b}\right)\right)^2 \left(\cos\left(\frac{m\pi\,x_s}{a}\right)\right)^2 \ . \tag{3.A.88}$$

3.A.3.5   Stiffness matrix elements for the employed trigonometric functions of type $w_{m,n}^{IV}$

The stiffness matrix elements $M_{klmn}^{m,IV}$, $M_{klmn}^{c,IV}$, and $M_{klmn}^{C,IV}$ for the employed trigonometric functions of type $w_{m,n}^{IV}$, for 25 combinations of k, l, m, and n, read as:

1. Stiffness matrix elements for $k = l = m = n = 0$:

$$M_{0000}^{m,IV} = \frac{32\,K\left(-1+v\right)}{ab}\ , \qquad M_{0000}^{c,IV} = -\frac{1}{9}\,c\,a\,b\ , \qquad M_{0000}^{C,IV} = -\sum_{s=1}^{N_C} 16\,\frac{C_s x_s^2 y_s^2}{a^2 b^2}\ . \tag{3.A.89}$$

2. Stiffness matrix elements for $k = l = m = 0$, and $n \neq 0$:

$$
\begin{aligned}
M_{000n}^{m,IV} &= \frac{32\,K\,(-1+v)\,\sin\,(1/2\,n\pi)}{ab}\,, \\
M_{000n}^{c,IV} &= \frac{2\,cab\,(n\pi\,\cos\,(1/2\,n\pi) - 2\,\sin\,(1/2\,n\pi))}{3\,\pi^2 n^2}\,, \\
M_{000n}^{C,IV} &= -\sum_{s=1}^{N_C} 8\,\frac{C_s\,x_s{}^2 y_s}{a^2 b}\,\sin\left(\frac{n\pi\,y_s}{b}\right).
\end{aligned}
\tag{3.A.90}
$$

3. Stiffness matrix elements for $k = l = n = 0$, and $m \neq 0$:

$$
\begin{aligned}
M_{00m0}^{m,IV} &= \frac{32\,K\,(-1+v)\,\sin\,(1/2\,m\pi)}{ab}\,, \\
M_{00m0}^{c,IV} &= \frac{2\,cab\,(m\pi\,\cos\,(1/2\,m\pi) - 2\,\sin\,(1/2\,m\pi))}{3\,\pi^2 m^2}\,, \\
M_{00m0}^{C,IV} &= -\sum_{s=1}^{N_C} 8\,\frac{C_s\,y_s{}^2 x_s}{b^2 a}\,\sin\left(\frac{m\pi\,x_s}{a}\right).
\end{aligned}
\tag{3.A.91}
$$

4. Stiffness matrix elements for $k = l = 0$, and $m \neq 0$, $n \neq 0$:

$$
\begin{aligned}
M_{00mn}^{m,IV} &= \frac{32\,K\,(-1+v)\,\sin\,(1/2\,m\pi)\,\sin\,(1/2\,n\pi)}{ab}\,, \\
M_{00mn}^{c,IV} &= \frac{8\,cab\,(-1/2\,n\pi\,\cos\,(1/2\,n\pi) + \sin\,(1/2\,n\pi))\,(m\pi\,\cos\,(1/2\,m\pi) - 2\,\sin\,(1/2\,m\pi))}{\pi^4 m^2 n^2}\,, \\
M_{00mn}^{C,IV} &= -\sum_{s=1}^{N_C} 4\,\frac{C_s\,x_s\,y_s}{ab}\,\sin\left(\frac{n\pi\,y_s}{b}\right)\sin\left(\frac{m\pi\,x_s}{a}\right).
\end{aligned}
\tag{3.A.92}
$$

5. Stiffness matrix elements for $m = k = 0$, and $n \neq 0$, $l \neq 0$ with $l \neq n$:

$$
\begin{aligned}
M_{0l0n}^{m,IV} &= -\frac{2\,K\pi\,n\,l}{3\,ab^3 l^2 - 3\,ab^3 n^2}\left(-\sin\,(1/2\,n\pi)\left(a^2 l^2 \pi^2 - 24\,b^2\,(-1+v)\right)\times\right. \\
&\qquad \left.\times n\cos\,(1/2\,l\pi) + \sin\,(1/2\,l\pi)\cos\,(1/2\,n\pi)\left(a^2 n^2 \pi^2 - 24\,b^2\,(-1+v)\right)l\right), \\
M_{0l0n}^{c,IV} &= \frac{2\,cab\,(l\cos\,(1/2\,l\pi)\sin\,(1/2\,n\pi) - n\sin\,(1/2\,l\pi)\cos\,(1/2\,n\pi))}{(3\,l^2 - 3\,n^2)\,\pi}\,, \\
M_{0l0n}^{C,IV} &= -\sum_{s=1}^{N_C} 4\,\frac{C_s\,x_s{}^2}{a^2}\,\sin\left(\frac{n\pi\,y_s}{b}\right)\sin\left(\frac{l\pi\,y_s}{b}\right).
\end{aligned}
\tag{3.A.93}
$$

6. Stiffness matrix elements for $m = k = 0$, and $n \neq 0$, $l \neq 0$ with $l = n$:

$$
\begin{aligned}
M_{0n0n}^{m,IV} &= -\frac{K\pi n}{6\,ab^3}\left[-2\left(a^2 n^2 \pi^2 + 24\,b^2\,(-1+v)\right)\sin\,(1/2\,n\pi)\cos\,(1/2\,n\pi)\right. \\
&\qquad \left.+\pi\left(a^2 n^2 \pi^2 - 24\,b^2\,(-1+v)\right)n\right], \\
M_{0n0n}^{c,IV} &= -\frac{cab\,(-2\,\cos\,(1/2\,n\pi)\sin\,(1/2\,n\pi) + n\pi)}{6\,n\pi}\,, \\
M_{0n0n}^{C,IV} &= -\sum_{s=1}^{N_C} 4\,\frac{C_s\,x_s{}^2}{a^2}\left(\sin\left(\frac{n\pi\,y_s}{b}\right)\right)^2.
\end{aligned}
\tag{3.A.94}
$$

7. Stiffness matrix elements for $n = k = 0$, and $m \neq 0$, $l \neq 0$:

$$
\begin{aligned}
M_{0lm0}^{m,IV} &= \frac{16\,K}{ab} \left[\left((v-2)\sin\left(1/2\,m\pi\right) + 1/2\,mv\pi\,\cos\left(1/2\,m\pi\right) \right) \sin\left(1/2\,l\pi\right) \right. \\
&\quad \left. + 1/2\left(-1/2\,m\pi\,\cos\left(1/2\,m\pi\right) + \sin\left(1/2\,m\pi\right)\right) v\pi\,\cos\left(1/2\,l\pi\right) l \right], \\
M_{0lm0}^{c,IV} &= \frac{8\,cab\left(-1/2\,m\pi\,\cos\left(1/2\,m\pi\right) + \sin\left(1/2\,m\pi\right)\right)\left(l\pi\,\cos\left(1/2\,l\pi\right) - 2\sin\left(1/2\,l\pi\right)\right)}{\pi^4 m^2 l^2}, \\
M_{0lm0}^{C,IV} &= -\sum_{s=1}^{N_C} 4\,\frac{C_s\,y_s\,x_s}{ba}\sin\left(\frac{m\pi\,x_s}{a}\right)\sin\left(\frac{l\pi\,y_s}{b}\right).
\end{aligned}
\tag{3.A.95}
$$

8. Stiffness matrix elements for $k = 0$, and $m \neq 0$, $n \neq 0$, $l \neq 0$ with $l \neq n$:

$$
\begin{aligned}
M_{0lmn}^{m,IV} &= \frac{4\,K\pi\,l}{b^3 a m^2\left(l^2-n^2\right)}\left[\left(2\left(\left(b^2 m^2 v + a^2 n^2\right) l^2 - 2 b^2 m^2 n^2\left(-1+v\right)\right)\sin\left(1/2\,n\pi\right) \times \right. \right. \\
&\quad \times \cos\left(1/2\,l\pi\right) - 2 n\cos\left(1/2\,n\pi\right)\sin\left(1/2\,l\pi\right)\left(-b^2\left(v-2\right)m^2 + a^2 n^2\right) l \right) \times \\
&\quad \times \sin\left(1/2\,m\pi\right) + \cos\left(1/2\,m\pi\right) l m\pi\left(b^2 m^2 v + a^2 n^2\right)\left(n\sin\left(1/2\,l\pi\right)\cos\left(1/2\,n\pi\right)\right. \\
&\quad \left.\left. - l\cos\left(1/2\,l\pi\right)\sin\left(1/2\,n\pi\right)\right) \right], \\
M_{0lmn}^{c,IV} &= -8\,\frac{cba\left[n\sin\left(1/2\,l\pi\right)\cos\left(1/2\,n\pi\right) - l\cos\left(1/2\,l\pi\right)\sin\left(1/2\,n\pi\right)\right]}{\pi^3 m^2\left(l^2-n^2\right)} \times \\
&\quad \times \left[-1/2\,m\pi\,\cos\left(1/2\,m\pi\right) + \sin\left(1/2\,m\pi\right)\right], \\
M_{0lmn}^{C,IV} &= -\sum_{s=1}^{N_C} 2\,\frac{C_s x_s}{a}\sin\left(\frac{n\pi\,y_s}{b}\right)\sin\left(\frac{m\pi\,x_s}{a}\right)\sin\left(\frac{l\pi\,y_s}{b}\right).
\end{aligned}
\tag{3.A.96}
$$

9. Stiffness matrix elements for $k = 0$, and $m \neq 0$, $n \neq 0$, $l \neq 0$ with $l = n$:

$$
\begin{aligned}
M_{mn0n}^{m,IV} &= \frac{4\,K\,n\,\pi}{b^3 a m^2}\left[\left(\left(3\left(v-2/3\right)b^2 m^2 + a^2 n^2\right)\sin\left(1/2\,n\pi\right)\cos\left(1/2\,n\pi\right)\right. \right. \\
&\quad \left. - 1/2\,\pi\left(-b^2\left(v-2\right)m^2 + a^2 n^2\right) n\right)\sin\left(1/2\,m\pi\right) - 1/2\,\pi\times \\
&\quad \left. \times\left(b^2 m^2 v + a^2 n^2\right)\cos\left(1/2\,m\pi\right)\left(\cos\left(1/2\,n\pi\right)\sin\left(1/2\,n\pi\right) - 1/2\,n\pi\right)m \right], \\
M_{mn0n}^{c,IV} &= -\frac{2\,cab\left(m\pi\,\cos\left(1/2\,m\pi\right) - 2\sin\left(1/2\,m\pi\right)\right)\left(\cos\left(1/2\,n\pi\right)\sin\left(1/2\,n\pi\right) - 1/2\,n\pi\right)}{\pi^3 m^2 n}, \\
M_{mn0n}^{C,IV} &= -\sum_{s=1}^{N_C} 2\,\frac{C_s x_s}{a}\left(\sin\left(\frac{n\pi\,y_s}{b}\right)\right)^2\sin\left(\frac{m\pi\,x_s}{a}\right).
\end{aligned}
\tag{3.A.97}
$$

10. Stiffness matrix elements for $m = l = 0$, and $n \neq 0$, $k \neq 0$:

$$
\begin{aligned}
M_{k00n}^{m,IV} &= -\frac{16\,K}{ba}\left[\left((v-2)\sin\left(1/2\,n\pi\right) + 1/2\,nv\pi\,\cos\left(1/2\,n\pi\right)\right)\sin\left(1/2\,k\pi\right) \right. \\
&\quad \left. + 1/2\,v\pi\,\cos\left(1/2\,k\pi\right)\left(-1/2\,n\pi\,\cos\left(1/2\,n\pi\right) + \sin\left(1/2\,n\pi\right)\right) k \right], \\
M_{k00n}^{c,IV} &= \frac{8\,cab\left(-1/2\,n\pi\,\cos\left(1/2\,n\pi\right) + \sin\left(1/2\,n\pi\right)\right)\left(k\pi\,\cos\left(1/2\,k\pi\right) - 2\sin\left(1/2\,k\pi\right)\right)}{k^2 \pi^4 n^2}, \\
M_{k00n}^{C,IV} &= -\sum_{s=1}^{N_C} 4\,\frac{C_s x_s\,y_s}{ba}\sin\left(\frac{n\pi\,y_s}{b}\right)\sin\left(\frac{k\pi\,x_s}{a}\right).
\end{aligned}
\tag{3.A.98}
$$

11. Stiffness matrix elements for $n = l = 0$, and $m \neq 0$, $k \neq 0$ with $k \neq m$:

$$
\begin{aligned}
M_{k0m0}^{m,IV} &= \frac{48\,K\,\pi\,m\,k}{3\,a^3bk^2 - 3\,a^3bm^2}\Big[\left(1/24\,b^2k^2\pi^2 - a^2\,(-1+v)\right)\sin\left(1/2\,m\pi\right)m\cos\left(1/2\,k\pi\right) \\
&\quad + \sin\left(1/2\,k\pi\right)\cos\left(1/2\,m\pi\right)\left(-1/24\,b^2m^2\pi^2 + a^2\,(-1+v)\right)k\Big]\,, \\
M_{k0m0}^{c,IV} &= \frac{2\,cab\left(-m\sin\left(1/2\,k\pi\right)\cos\left(1/2\,m\pi\right) + k\cos\left(1/2\,k\pi\right)\sin\left(1/2\,m\pi\right)\right)}{(3\,k^2 - 3\,m^2)\,\pi}\,, \\
M_{k0m0}^{C,IV} &= -\sum_{s=1}^{N_C} 4\,\frac{C_s {y_s}^2}{b^2}\sin\left(\frac{m\pi\,x_s}{a}\right)\sin\left(\frac{k\pi\,x_s}{a}\right)\,. \quad\quad (3.A.99)
\end{aligned}
$$

12. Stiffness matrix elements for $n = l = 0$, and $m \neq 0$, $k \neq 0$ with $k = m$:

$$
\begin{aligned}
M_{m0m0}^{m,IV} &= \frac{4\,\pi\,K\,m}{a^3b}\Big[2\left(1/24\,b^2m^2\pi^2 + a^2\,(-1+v)\right)\sin\left(1/2\,m\pi\right)\cos\left(1/2\,m\pi\right) \\
&\quad + \pi\left(-1/24\,b^2m^2\pi^2 + a^2\,(-1+v)\right)m\Big]\,, \\
M_{m0m0}^{c,IV} &= -\frac{cab\left(-2\cos\left(1/2\,m\pi\right)\sin\left(1/2\,m\pi\right) + m\pi\right)}{6\,m\pi}\,, \\
M_{m0m0}^{C,IV} &= -\sum_{s=1}^{N_C} 4\,\frac{C_s {y_s}^2}{b^2}\left(\sin\left(\frac{m\pi\,x_s}{a}\right)\right)^2\,. \quad\quad (3.A.100)
\end{aligned}
$$

13. Stiffness matrix elements for $l = 0$, and $m \neq 0$, $n \neq 0$, $k \neq 0$ with $k \neq m$:

$$
\begin{aligned}
M_{k0mn}^{m,IV} &= \frac{4\,K\pi\,k}{a^3b\,(k^2 - m^2)\,n^2}\Big[\left(2\sin\left(1/2\,m\pi\right)\left(\left(a^2n^2v + b^2m^2\right)k^2 - 2\,a^2m^2n^2\,(-1+v)\right)\times\right. \\
&\quad \times \cos\left(1/2\,k\pi\right) + 2\cos\left(1/2\,m\pi\right)\left(-b^2m^2 + a^2n^2\,(v-2)\right)\sin\left(1/2\,k\pi\right)m\,k\Big)\times \\
&\quad \times \sin\left(1/2\,n\pi\right) + \cos\left(1/2\,n\pi\right)kn\pi\left(a^2n^2v + b^2m^2\right)\left(m\sin\left(1/2\,k\pi\right)\cos\left(1/2\,m\pi\right)\right. \\
&\quad \left. - k\cos\left(1/2\,k\pi\right)\sin\left(1/2\,m\pi\right)\right)\Big]\,, \\
M_{k0mn}^{c,IV} &= \frac{4\,cab\left[m\sin\left(1/2\,k\pi\right)\cos\left(1/2\,m\pi\right) - k\cos\left(1/2\,k\pi\right)\sin\left(1/2\,m\pi\right)\right]}{\pi^3\,(k^2 - m^2)\,n^2}\times \\
&\quad \times \left[n\pi\cos\left(1/2\,n\pi\right) - 2\sin\left(1/2\,n\pi\right)\right]\,, \\
M_{k0mn}^{C,IV} &= -\sum_{s=1}^{N_C} 2\,\frac{C_s y_s}{b}\sin\left(\frac{n\pi\,y_s}{b}\right)\sin\left(\frac{m\pi\,x_s}{a}\right)\sin\left(\frac{k\pi\,x_s}{a}\right)\,. \quad\quad (3.A.101)
\end{aligned}
$$

14. Stiffness matrix elements for $l = 0$, and $m \neq 0$, $n \neq 0$, $k \neq 0$ with $k = m$:

$$
\begin{aligned}
M_{mnm0}^{m,IV} &= \frac{12\,K\pi\,m}{a^3bn^2}\Big[\left(\sin\left(1/2\,m\pi\right)\left(a^2\,(v - 2/3)\,n^2 + 1/3\,b^2m^2\right)\cos\left(1/2\,m\pi\right)\right. \\
&\quad + 1/6\left(-b^2m^2 + a^2n^2\,(v-2)\right)\pi\,m\Big)\sin\left(1/2\,n\pi\right) - 1/6\left(a^2n^2v + b^2m^2\right)\times \\
&\quad \times \left(\cos\left(1/2\,m\pi\right)\sin\left(1/2\,m\pi\right) - 1/2\,m\pi\cos\left(1/2\,n\pi\right]n\right)\,, \\
M_{mnm0}^{c,IV} &= -\frac{2\,cab\left[-1/2\,n\pi\cos\left(1/2\,n\pi\right) + \sin\left(1/2\,n\pi\right)\right]}{m\pi^3n^2}\times \\
&\quad \times \left[-2\cos\left(1/2\,m\pi\right)\sin\left(1/2\,m\pi\right) + m\pi\right]\,, \\
M_{mnm0}^{C,IV} &= -\sum_{s=1}^{N_C} 2\,\frac{C_s y_s}{b}\sin\left(\frac{n\pi\,y_s}{b}\right)\left(\sin\left(\frac{m\pi\,x_s}{a}\right)\right)^2\,. \quad\quad (3.A.102)
\end{aligned}
$$

15. Stiffness matrix elements for $m = 0$, and $n \neq 0$, $k \neq 0$, $l \neq 0$ with $l \neq n$:

$$
\begin{aligned}
M_{kl0n}^{m,IV} &= \frac{8\,nK\pi}{b^3 k^2 a\,(l^2 - n^2)}\Big[\Big(-\Big(\big(b^2 k^2 v + a^2 l^2\big) n^2 - 2\,b^2 k^2 l^2\,(-1+v)\Big)\sin\left(1/2\,l\pi\right) \\
&\quad \cos\left(1/2\,n\pi\right) + n\cos\left(1/2\,l\pi\right)\Big(-b^2\,(v-2)\,k^2 + a^2 l^2\Big)\sin\left(1/2\,n\pi\right) l\Big) \\
&\quad \sin\left(1/2\,k\pi\right) - 1/2\,\cos\left(1/2\,k\pi\right)\pi\,kn\,\Big(b^2 k^2 v + a^2 l^2\Big)\,\big(l\cos\left(1/2\,l\pi\right)\sin\left(1/2\,n\pi\right) \\
&\quad -n\sin\left(1/2\,l\pi\right)\cos\left(1/2\,n\pi\right)\big)\Big]\,, \\[6pt]
M_{kl0n}^{c,IV} &= -\frac{8\,cab\left[-1/2\,k\pi\,\cos\left(1/2\,k\pi\right) + \sin\left(1/2\,k\pi\right)\right]}{k^2 \pi^3\,(l^2 - n^2)}\times \\
&\quad \times\left[n\sin\left(1/2\,l\pi\right)\cos\left(1/2\,n\pi\right) - l\cos\left(1/2\,l\pi\right)\sin\left(1/2\,n\pi\right)\right]\,, \\[6pt]
M_{kl0n}^{C,IV} &= -\sum_{s=1}^{N_C} 2\,\frac{C_s x_s}{a}\sin\left(\frac{n\pi\,y_s}{b}\right)\sin\left(\frac{l\pi\,y_s}{b}\right)\sin\left(\frac{k\pi\,x_s}{a}\right)\,.
\end{aligned}
\tag{3.A.103}
$$

16. Stiffness matrix elements for $l = 0$, and $m = 0$, and $n \neq 0$, $k \neq 0$, $l \neq 0$ with $l = n$:

$$
\begin{aligned}
M_{kn0n}^{m,IV} &= \frac{4\,K\pi\,n}{ab^3 k^2}\Big[\Big(\big(3\,b^2\,(v - 2/3)\,k^2 + a^2 n^2\big)\sin\left(1/2\,n\pi\right)\cos\left(1/2\,n\pi\right) \\
&\quad -1/2\,\pi\,\big(-b^2\,(v-2)\,k^2 + a^2 n^2\big) n\Big)\sin\left(1/2\,k\pi\right) \\
&\quad -1/2\,\big(\cos\left(1/2\,n\pi\right)\sin\left(1/2\,n\pi\right) - 1/2\,n\pi\big)\pi\,\Big(b^2 k^2 v + a^2 n^2\Big)\cos\left(1/2\,k\pi\right) k\Big]\,, \\[6pt]
M_{kn0n}^{c,IV} &= -\frac{2\,cab\,(k\pi\,\cos\left(1/2\,k\pi\right) - 2\sin\left(1/2\,k\pi\right))\,(\cos\left(1/2\,n\pi\right)\sin\left(1/2\,n\pi\right) - 1/2\,n\pi)}{k^2 \pi^3 n}\,, \\[6pt]
M_{kn0n}^{C,IV} &= -\sum_{s=1}^{N_C} 2\,\frac{C_s x_s}{a}\left(\sin\left(\frac{n\pi\,y_s}{b}\right)\right)^2 \sin\left(\frac{k\pi\,x_s}{a}\right)\,.
\end{aligned}
\tag{3.A.104}
$$

17. Stiffness matrix elements for $n = 0$, and $m \neq 0$, $k \neq 0$, $l \neq 0$ with $k \neq m$:

$$
\begin{aligned}
M_{klm0}^{m,IV} &= \frac{4\,m\,K\pi}{ba^3\,(k^2 - m^2)\,l^2}\Big[\Big(4\,\Big(\big(-1/2\,a^2 l^2 v - 1/2\,b^2 k^2\big) m^2 + a^2 k^2 l^2\,(-1+v)\Big)\times \\
&\quad \times\sin\left(1/2\,k\pi\right)\cos\left(1/2\,m\pi\right) - 2\,m\,\big(-b^2 k^2 + a^2 l^2\,(v-2)\big)\cos\left(1/2\,k\pi\right)\times \\
&\quad \times\sin\left(1/2\,m\pi\right) k\big)\sin\left(1/2\,l\pi\right) + \cos\left(1/2\,l\pi\right) lm\pi\,\Big(a^2 l^2 v + b^2 k^2\Big)\times \\
&\quad \times\big(m\sin\left(1/2\,k\pi\right)\cos\left(1/2\,m\pi\right) - k\cos\left(1/2\,k\pi\right)\sin\left(1/2\,m\pi\right)\big)\Big]\,, \\[6pt]
M_{klm0}^{c,IV} &= -\frac{8\,cab\left[m\sin\left(1/2\,k\pi\right)\cos\left(1/2\,m\pi\right) - k\cos\left(1/2\,k\pi\right)\sin\left(1/2\,m\pi\right)\right]}{\pi^3 l^2\,(k^2 - m^2)}\times \\
&\quad \times\left[-1/2\,l\pi\,\cos\left(1/2\,l\pi\right) + \sin\left(1/2\,l\pi\right)\right]\,, \\[6pt]
M_{klm0}^{C,IV} &= -\sum_{s=1}^{N_C} 2\,\frac{C_s y_s}{b}\sin\left(\frac{m\pi\,x_s}{a}\right)\sin\left(\frac{l\pi\,y_s}{b}\right)\sin\left(\frac{k\pi\,x_s}{a}\right)\,.
\end{aligned}
\tag{3.A.105}
$$

18. Stiffness matrix elements for $n = 0$, and $m \neq 0$, $k \neq 0$, $l \neq 0$ with $k = m$:

$$
\begin{aligned}
M_{mlm0}^{m,IV} &= \frac{12\,K\pi\,m}{ba^3 l^2}\Big[\Big(\sin\left(1/2\,m\pi\right)\Big(a^2\,(v - 2/3)\,l^2 + 1/3\,b^2 m^2\Big)\cos\left(1/2\,m\pi\right) \\
&\quad +1/6\,\Big(a^2 l^2\,(v-2) - b^2 m^2\Big)\pi\,m\Big)\sin\left(1/2\,l\pi\right) - 1/6\,\big(\cos\left(1/2\,m\pi\right)\times \\
&\quad \times\sin\left(1/2\,m\pi\right) - 1/2\,m\pi\big)\Big(a^2 l^2 v + b^2 m^2\Big)\pi\,\cos\left(1/2\,l\pi\right) l\Big]\,,
\end{aligned}
$$

$$M_{mlm0}^{c,IV} = -\frac{2\,cab\,(l\pi\,\cos\,(1/2\,l\pi) - 2\,\sin\,(1/2\,l\pi))\,(\cos\,(1/2\,m\pi)\,\sin\,(1/2\,m\pi) - 1/2\,m\pi)}{m\pi^3 l^2},$$

$$M_{mlm0}^{C,IV} = -\sum_{s=1}^{N_C} 2\,\frac{C_s y_s}{b}\left(\sin\left(\frac{m\pi\,x_s}{a}\right)\right)^2 \sin\left(\frac{l\pi\,y_s}{b}\right). \tag{3.A.106}$$

19. Stiffness matrix elements for $m = n = k = 0$, and $l \neq 0$:

$$M_{0l00}^{m,IV} = \frac{32\,K\,(-1+v)\,\sin\,(1/2\,l\pi)}{ba},$$

$$M_{0l00}^{c,IV} = \frac{2\,cab\,(l\pi\,\cos\,(1/2\,l\pi) - 2\,\sin\,(1/2\,l\pi))}{3\,l^2\pi^2},$$

$$M_{0l00}^{C,IV} = -\sum_{s=1}^{N_C} 8\,\frac{C_s x_s{}^2 y_s}{a^2 b}\,\sin\left(\frac{k\pi\,y_s}{b}\right). \tag{3.A.107}$$

20. Stiffness matrix elements for $m = n = l = 0$, and $k \neq 0$:

$$M_{k000}^{m,IV} = \frac{32\,K\,(-1+v)\,\sin\,(1/2\,k\pi)}{ba},$$

$$M_{k000}^{c,IV} = \frac{2\,cab\,(k\pi\,\cos\,(1/2\,k\pi) - 2\,\sin\,(1/2\,k\pi))}{3\,k^2\pi^2},$$

$$M_{k000}^{C,IV} = -\sum_{s=1}^{N_C} 8\,\frac{C_s x_s y_s{}^2}{ab^2}\,\sin\left(\frac{k\pi\,x_s}{a}\right). \tag{3.A.108}$$

21. Stiffness matrix elements for $m = n = 0$, and $k \neq 0$, $l \neq 0$:

$$M_{kl00}^{m,IV} = \frac{32\,K\,(-1+v)\,\sin\,(1/2\,k\pi)\,\sin\,(1/2\,l\pi)}{ba},$$

$$M_{kl00}^{c,IV} = \frac{8\,cab\,(-1/2\,l\pi\,\cos\,(1/2\,l\pi) + \sin\,(1/2\,l\pi))\,(k\pi\,\cos\,(1/2\,k\pi) - 2\,\sin\,(1/2\,k\pi))}{k^2\pi^4 l^2},$$

$$M_{kl00}^{C,IV} = -\sum_{s=1}^{N_C} 4\,\frac{C_s x_s y_s}{ba}\,\sin\left(\frac{l\pi\,y_s}{b}\right)\sin\left(\frac{k\pi\,x_s}{a}\right). \tag{3.A.109}$$

22. Stiffness matrix elements for $k \neq 0$, $l \neq 0$, $m \neq 0$ and $n \neq 0$, with $k \neq m$ and $l \neq n$:

$$\begin{aligned}
M_{klmn}^{m,IV} &= -\frac{4\,K\pi^2}{b^3 a^3\,(l-n)\,(l+n)\,(k-m)\,(k+m)}\,[\sin\,(1/2\,m\pi)\,(\sin\,(1/2\,n\pi)\,l\times \\
&\quad \times \left(b^2\left(a^2 n^2 v + b^2 m^2\right)k^2 + a^2\left(\left(b^2 m^2 v + a^2 n^2\right)l^2 - 2\,b^2 m^2 n^2\,(-1+v)\right)\right)\times \\
&\quad \times \cos\,(1/2\,l\pi) - \left(b^2\left(a^2 n^2 v + b^2 m^2\right)k^2 + \left(-b^2\,(v-2)\,m^2 + a^2 n^2\right)a^2 l^2\right)\times \\
&\quad \times \cos\,(1/2\,n\pi)\,n\,\sin\,(1/2\,l\pi))\,k\,\cos\,(1/2\,k\pi) - \left(\sin\,(1/2\,n\pi)\left(-b^2\left(-b^2 m^2\right.\right.\right. \\
&\quad \left.\left.+a^2 n^2\,(v-2)\right)k^2 + a^2 l^2\left(b^2 m^2 v + a^2 n^2\right)\right)l\,\cos\,(1/2\,l\pi) - \cos\,(1/2\,n\pi)\,n\times \\
&\quad \times \left(-2\left(a^2\,(-1+v)\,l^2 - 1/2\,a^2 n^2 v - 1/2\,b^2 m^2\right)b^2 k^2 + a^2 l^2\left(b^2 m^2 v + a^2 n^2\right)\right)\times \\
&\quad \times \sin\,(1/2\,l\pi))\,m\,\cos\,(1/2\,m\pi)\,\sin\,(1/2\,k\pi)]\,, \\
M_{klmn}^{c,IV} &= -\frac{4\,cab\,[m\,\sin\,(1/2\,k\pi)\,\cos\,(1/2\,m\pi) - k\,\cos\,(1/2\,k\pi)\,\sin\,(1/2\,m\pi)]}{\pi^2\,(k^2 - m^2)\,(l^2 - n^2)}\,\times \\
&\quad \times [n\,\sin\,(1/2\,l\pi)\,\cos\,(1/2\,n\pi) - l\,\cos\,(1/2\,l\pi)\,\sin\,(1/2\,n\pi)]\,,
\end{aligned}$$

$$M_{klmn}^{C,IV} \;=\; -\sum_{s=1}^{N_C} C_s \sin\left(\frac{n\pi\,y_s}{b}\right) \sin\left(\frac{m\pi\,x_s}{a}\right) \sin\left(\frac{l\pi\,y_s}{b}\right) \sin\left(\frac{k\pi\,x_s}{a}\right). \tag{3.A.110}$$

23. Stiffness matrix elements for $k \neq 0$, $l \neq 0$, $m \neq 0$ and $n \neq 0$, with $k = m$ and $l \neq n$:

$$
\begin{aligned}
M_{mlmn}^{m,IV} \;=\;& \frac{2\,K\pi^2}{a^3 b^3 m\,(l^2 - n^2)}\Big[-\sin\left(1/2\,n\pi\right)\Big(\sin\left(1/2\,m\pi\right)\big(b^4 m^4 + a^2 b^2\,\big(l^2 v \\
& +3\,(v - 2/3)\,n^2\big) m^2 + a^4 l^2 n^2\big)\cos\left(1/2\,m\pi\right) - 1/2\,\pi\,\big(b^4 m^4 + a^2\,\big(l^2 v \\
& -n^2\,(v - 2)\big) b^2 m^2 + a^4 l^2 n^2\big) m\Big) l \cos\left(1/2\,l\pi\right) + \Big(\big(b^4 m^4 + 3\,a^2\,\big((v - 2/3)\,l^2 \\
& +1/3\,n^2 v\big) b^2 m^2 + a^4 l^2 n^2\big)\sin\left(1/2\,m\pi\right)\cos\left(1/2\,m\pi\right) - 1/2\,\big(b^4 m^4 \\
& -\big((v - 2)\,l^2 - n^2 v\big) a^2 b^2 m^2 + a^4 l^2 n^2\big)\pi\,m\big) n\cos\left(1/2\,n\pi\right)\sin\left(1/2\,l\pi\right)\Big], \\
M_{mlmn}^{c,IV} \;=\;& -\frac{cab\left[-2\,\cos\left(1/2\,m\pi\right)\sin\left(1/2\,m\pi\right) + m\pi\right]}{m\pi^2\,(l^2 - n^2)}\times \\
& \times\left[n\sin\left(1/2\,l\pi\right)\cos\left(1/2\,n\pi\right) - l\cos\left(1/2\,l\pi\right)\sin\left(1/2\,n\pi\right)\right], \\
M_{mlmn}^{C,IV} \;=\;& -\sum_{s=1}^{N_C} C_s l \sin\left(\frac{n\pi\,y_s}{b}\right)\left(\sin\left(\frac{m\pi\,x_s}{a}\right)\right)^2 \sin\left(\frac{l\pi\,y_s}{b}\right). \tag{3.A.111}
\end{aligned}
$$

24. Stiffness matrix elements for $k \neq 0$, $l \neq 0$, $m \neq 0$ and $n \neq 0$, with $k \neq m$ and $l = n$:

$$
\begin{aligned}
M_{knmn}^{m,IV} \;=\;& \frac{2\,K\pi^2}{a^3\,(k^2 - m^2)\,b^3 n}\Big[-\sin\left(1/2\,m\pi\right)\Big(\big(a^4 n^4 + a^2\,\big(k^2 v + 3\,m^2\,(v - 2/3)\big) b^2 n^2 \\
& +b^4 k^2 m^2\big)\sin\left(1/2\,n\pi\right)\cos\left(1/2\,n\pi\right) - 1/2\,n\pi\,\big(a^4 n^4 + a^2\,\big(k^2 v - m^2\,(v - 2)\big) b^2 n^2 \\
& +b^4 k^2 m^2\big)\Big) k\cos\left(1/2\,k\pi\right) + \cos\left(1/2\,m\pi\right)\Big(\big(a^4 n^4 + 3\,\big((v - 2/3)\,k^2 + 1/3\,m^2 v\big)\times \\
& \times a^2 b^2 n^2 + b^4 k^2 m^2\big)\sin\left(1/2\,n\pi\right)\cos\left(1/2\,n\pi\right) - 1/2\,\big(a^4 n^4 - a^2\,\big((v - 2)\,k^2 - m^2 v\big)\times \\
& \times b^2 n^2 + b^4 k^2 m^2\big) n\pi\Big)\sin\left(1/2\,k\pi\right) m\Big], \\
M_{knmn}^{c,IV} \;=\;& \frac{2\,cab\left[\cos\left(1/2\,n\pi\right)\sin\left(1/2\,n\pi\right) - 1/2\,n\pi\right]}{\pi^2\,(k^2 - m^2)\,n}\times \\
& \times\left[m\sin\left(1/2\,k\pi\right)\cos\left(1/2\,m\pi\right) - k\cos\left(1/2\,k\pi\right)\sin\left(1/2\,m\pi\right)\right], \\
M_{knmn}^{C,IV} \;=\;& -\sum_{s=1}^{N_C} C_s \left(\sin\left(\frac{n\pi\,y_s}{b}\right)\right)^2 \sin\left(\frac{m\pi\,x_s}{a}\right)\sin\left(\frac{k\pi\,x_s}{a}\right). \tag{3.A.112}
\end{aligned}
$$

25. Stiffness matrix elements for $k \neq 0$, $l \neq 0$, $m \neq 0$ and $n \neq 0$, with $k = m$ and $l = n$:

$$
\begin{aligned}
M_{mnmn}^{m,IV} \;=\;& -\frac{K\pi^2}{a^3 b^3 nm}\Big[\sin\left(1/2\,m\pi\right)\Big(\sin\left(1/2\,n\pi\right)\big(a^2 n^2 + b^2 m^2\big)^2 \cos\left(1/2\,n\pi\right) \\
& -1/2\,\pi\,\big(b^4 m^4 + 4\,a^2\,(v - 1/2)\,b^2 n^2 m^2 + a^4 n^4\big) n\big)\cos\left(1/2\,m\pi\right) \\
& -1/2\,\Big(\sin\left(1/2\,n\pi\right)\big(b^4 m^4 + 4\,a^2\,(v - 1/2)\,b^2 n^2 m^2 + a^4 n^4\big)\cos\left(1/2\,n\pi\right) \\
& -1/2\,n\pi\,\big(a^2 n^2 + b^2 m^2\big)^2\Big)\pi\,m\Big], \\
M_{mnmn}^{c,IV} \;=\;& \frac{cab\left(-2\,\cos\left(1/2\,m\pi\right)\sin\left(1/2\,m\pi\right) + m\pi\right)\left(\cos\left(1/2\,n\pi\right)\sin\left(1/2\,n\pi\right) - 1/2\,n\pi\right)}{2\,m\pi^2 n},
\end{aligned}
$$

$$M_{mnmn}^{C,IV} = -\sum_{s=1}^{N_C} C_s \left(\sin\left(\frac{n\pi\, y_s}{b} \right) \right)^2 \left(\sin\left(\frac{m\pi\, x_s}{a} \right) \right)^2 . \tag{3.A.113}$$

Chapter 4

Concrete pavements subjected to hail showers: A semi-analytical thermoelastic multiscale analysis

Authored by: Hui Wang, Raphael Höller, Mehdi Aminbaghai, Christian Hellmich, Yong Yuan, Herbert A. Mang, and Bernhard L.A. Pichler

Abstract

Climate changes result in an increase of extreme weather events. Concrete pavements e.g. may be subjected more frequently to hail showers, following significant solar heating of their top surface. This scenario is studied by means of multiscale thermoelastic analysis. The semi-analytical solution of the heat conduction problem provides access to the temperature fields inside the pavement plates. The thermal expansion coefficient, the modulus of elasticity, and Poisson's ratio of concrete are homogenized based on the Mori-Tanaka scheme. The thermoelastic analysis of pavement plates, resting on an elastic Winkler foundation, is based on the Kirchhoff hypothesis and a Vlasov-type of structural analysis. This delivers macroscopic stress states of the concrete. Finally, top-down scale transition is used to compute the average stresses, experienced by the three concrete constituents: cement paste, fine aggregates, and coarse aggregates, and by the interfacial transition zones (ITZs), covering the aggregates. This mode of analysis is applied to a realistic pavement plate. It is found that the stresses in concrete pavements subjected to temperature changes are governed by self-equilibrated thermal stresses resulting from non-stationary heat conduction. In case of a sudden hail shower, these stresses are likely to reach the tensile strength of concrete. Cracking starts at the ITZs, representing the weakest link of the microstructure. From quantitative thermoelastic analysis it is concluded that hail showers represent a serious threat for the integrity of the top layer of concrete pavements and, thus, for the long-term durability of such pavements.

Contribution by the author: The author of the present thesis contributed the series-based solution procedure for the structural analysis of the concrete pavement. Corresponding deformation and stress measures were solved iteratively, ensuring an elastic Winkler foundation which is active in compression only. Furthermore, normal stresses induced by the eigendistortions of the generators of the plate were validated by FE simulations.

4.1 Introduction

Concrete pavements are exposed to variable ambient conditions, both in terms of temperature and relative humidity. The stresses/strains in concrete pavements resulting from temperature variations were studied both experimentally Wei et al. [2017] and analytically [Nishizawa et al., 2009; Choubane and Tia, 1992; Zhang et al., 2003]. The stresses were found to be of the same magnitude or even larger than those resulting from the traffic running over the pavements [Mahboub et al., 2004]. Furthermore, the damage resulting from hail showers was reported to increase significantly over the last few decades, possibly related to climate changes [Changnon, 2009; Kunz et al., 2009]. This provides the motivation for the present paper. In this work, semi-analytical formulae for multiscale analysis of concrete pavements, subjected to nonstationary heat conduction in the thickness direction, are used and exemplarily applied to a concrete pavement subjected to a hail shower.

As regards engineering design of concrete pavements subjected to thermal loading, Westergaard [Westergaard, 1927] developed an analytical solution for thin infinite plates, resting on an elastic Winkler foundation. Correction factors for rectangular thin plates with finite dimensions were developed by Bradbury [Bradbury, 1938]. Thick plates, resting on a Pasternak foundation, were analyzed by Shi et al. [Shi et al., 1993, 1994, 2000]. In the USA, design of pavements nowadays follows the Mechanistic Empirical Pavement Design Guide (ME-PDG) [National Cooperative Highway Research Program, 2004]. The described guidelines refer to "temperature gradients", meaning that they are based on the assumption of a *linear* distribution of temperature along the thickness of the plate.

In reality, however, the temperature is typically distributed in a *nonlinear* fashion over the thickness of the pavement plates, see, e.g., [Wei et al., 2017; Teller and Sutherland, 1935]. In order to account for this nonlinearity, Thomlinson [Thomlinson, 1940] subdivided the temperature distributions into a constant, a linear, and a nonlinear part. This has led to several follow-up research activities, e.g. description of temperature distributions using quadratic [Choubane and Tia, 1992; Zhang et al., 2003; Choubane and Tia, 1995] or cubic polynomials [Zhang et al., 2003; Mohamed and Hansen, 1996, 1997] and presentation of a Finite-Element solution to the general problem of multi-layered concrete pavements subjected to arbitrary temperature fields by Ioannides and Khazanovich [Ioannides and Khazanovich, 1998]. These contributions highlighted the importance of the nonlinear part of the temperature profiles for the stress states inside the pavement plates. The nonlinearity of the temperature field will also be explicitly considered in the present paper.

As for scientific research on concrete pavements subjected to thermal loading, structural analysis is nowadays frequently carried out by three-dimensional Finite Element simulations for pavements with free edges [Nishizawa et al., 2009; Pane et al., 1998] or restrained edges because of dowels connecting neighboring plates across joints [Mahboub et al., 2004; Masad et al., 1996; William and Shoukry, 2001], also including implications for design [Ioannides and Peng, 2004]. The semi-analytical solution for thin rectangular plates with free boundaries, resting on an elastic Winkler foundation, developed by Vlasov and Leont'ev [Vlasov and Leont'ev, 1966], is also frequently used. However, this solution was found to entail systematic errors, because it assumes that the ansatz functions satisfy the stress-free boundary conditions prevailing along the edges of pavement plates. Since such ansatz functions do not exist, the free boundary conditions are violated. This results in bending moments and shear forces at the edges of the plate [Höller et al., 2019]. A rigorous amendment of the theory by Vlasov and Leont'ev was recently derived, based on the principle of virtual power [Höller et al., 2019]. This principle will be used in the present paper.

The thermal expansion coefficient of concrete is of prime importance for cracking, faulting, and the reachable service life of pavements subjected to thermal loading [Mallela et al., 2005; McCarthy et al., 2015]. As for cracking, in situ monitoring and laboratory testing of jointed concrete pavements [Kohler and Kannekanti, 2008] and continuously reinforced concrete pavements [McCullough et al., 2000] have clarified that the crack spacing decreases with increasing thermal expansion coefficient of concrete. This provides the motivation for the present paper, wherein special attention is paid to the thermal expansion of concrete.

The thermal expansion coefficient of concrete depends on the initial composition, the age, and the internal relative humidity (RH) of the material [Emanuel and Hulsey, 1977; Sakyi-Bekoe, 2008; Alungbe et al., 1992]. Several experimental studies have elucidated the importance of the type and the volume fraction of the aggregates [Bonnell and Harper, 1950; Mukhopadhyay et al., 2007; Tasneem et al., 2014; Naik et al., 2011; Chung and Shin, 2010; Won, 2005]. In more detail, siliceous aggregates result in a larger thermal expansion coefficient of concrete, compared to carbonate aggregates [Bonnell and Harper, 1950; Mukhopadhyay et al., 2007; Tasneem et al., 2014; Naik et al., 2011]. A linear relation between the thermal expansion coefficient of concrete and the volume fraction of coarse aggregates was reported in [Chung and Shin, 2010; Won, 2005]. In addition, the thermal expansion coefficient of concrete depends on the internal relative humidity [Chung and Shin, 2010; Bonnell and Harper, 1950], because the thermal expansion coefficient of the cement paste is a nonlinear function of this quantity, see Fig. 4.1. Its maximum value occurs around $RH = 65\%$. It is almost twice as large as the minimum value, observed at $RH = 100\%$ [Emanuel and Hulsey, 1977; Wang et al., 2018b]. The rather complex thermal expansion behavior of cement pastes was recently found to be a consequence of spontaneous and reversible uptake/release of water by nanoscopic hydrates, resulting from a decrease/increase of the temperature [Wyrzykowski et al., 2017; Wang et al., 2018b]. As for modeling of thermal
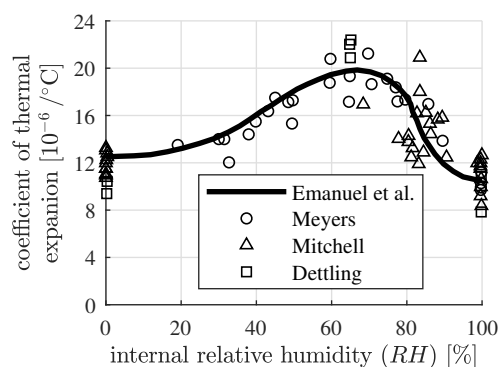
Fig. 4.1: Relation between the thermal expansion coefficient of cement paste and the internal relative humidity: experimental data from Meyers [Meyers, 1951], Mitchell [Mitchell, 1953], and Dettling [Dettling, 1962], measurements on mature cement pastes with initial water-to-cement mass ratios $w/c \in [\,0.12\,,\,0.40\,]$, and regression curve by Emanuel and Hulsey [Emanuel and Hulsey, 1977].

expansion coefficients, there are empirical approaches [Emanuel and Hulsey, 1977; Mukhopadhyay et al., 2007], stochastic multiscale approaches [Liu et al., 2013], and micromechanics models, see, e.g. [Wang et al., 2018b] for the cement paste and [Zhou et al., 2013, 2014; Wang et al., 2018a] for concrete. These models were also utilized for quantification of the thermal expansion coefficients of heterogeneous porous materials [Ghabezloo, 2012] and fiber-reinforced composites [Kundalwal and Ray, 2013, 2014; Kundalwal, 2018]. They link the microscopic properties of the

constituents to the macroscopic behavior of the composite [Wang et al., 2018a; Kundalwal and Ray, 2016]. In the present paper, multiscale methods of continuum micromechanics will be used, see [Wang et al., 2018b,a].

The mismatch of the thermal expansion coefficients of the constituents of concrete [Bažant and Kaplan, 1996], i.e. of the "cement paste" and of the "aggregates", is another source of *micro*scopic stress fluctuations in concrete samples [Sumarac and Krasulja, 1998; Fu et al., 2004a,b,c]. In more detail, Sumarac and Krasulja concluded that already a moderate temperature change can lead to substantial microcracking in the interfacial region between the aggregates and the surrounding cement paste [Sumarac and Krasulja, 1998]. Similar conclusions were drawn by Fu et al., based on Scanning Electron Microscopy [Fu et al., 2004a] and 2D mesoscopic thermoelastic damage modeling [Fu et al., 2004b,c]. Employing a three-phase shear lag model, Ray and Kundalwal [Ray and Kundalwal, 2014] studied the interfacial stresses of heterogeneous composites subjected to thermomechanical loading. This provides the motivation to derive analytical formulae for the stresses of the constituents of concrete and in the interfacial transition zones (ITZs) between the concrete aggregates and the cement paste matrix.

In the present paper, a thermoelastic multiscale model for concrete pavements, subjected to nonstationary heat conduction, is established. Formulae for semi-analytic quantification of macroscopic and microscopic stress states in concrete pavements are derived. At first, a semi-analytical solution of the heat conduction along the thickness of the pavement is presented. This is followed by analytical formulae for bottom-up homogenization of the thermal expansion coefficient, the modulus of elasticity, and Poisson's ratio of concrete. The analysis proceeds with quantifying macroscopic stresses of concrete, based on explicit consideration of the Kirchhoff hypothesis of thin plates. In this framework, macroscopic thermal stresses are quantified as a result of three parts of the thermal eigenstrains: the eigenstretches of the plate, the eigencurvatures of the plate, and the eigendistortions of the generators of the plate. The latter cannot develop, because the generators of the plate must remain straight according to the Kirchhoff hypothesis, and, thus, result in self-equilibrated thermal stresses. The bending-induced stresses, resulting from the eigencurvatures, are quantified by means of structural analysis, referring to a thin rectangular plate that rests on an elastic Winkler foundation. In this context, the approach by Höller et al. [Höller et al., 2019] is extended towards iterative determination of the partial loss of contact between the plate and its subgrade, resulting from the eigencurvature. Based on the computed temperature changes and the macroscopic stresses of the concrete, top-down scale transitions are carried out in order to quantify the average microscopic stresses of the constituents of concrete: cement paste, fine aggregates, and coarse aggregates. New analytical formulae are derived within the conceptual framework of strain concentration and eigenstrain influence tensors [Pichler and Hellmich, 2010]. Finally, stress states in interfacial transition zones are computed, extending the approach of Königsberger et al. [Königsberger et al., 2014a,b] to consideration of temperature changes.

The paper is structured as follows: The elements of multiscale thermoelastic analysis of concrete pavements are described in Section 4.2. Such analysis is then applied exemplarily to a concrete pavement, subjected to a sudden hail shower after solar heating of the top surface, see Section 4.3. Concluding remarks are given in Section 4.4.

4.2 Elements of multiscale thermoelastic analysis of concrete pavements

4.2.1 Semi-analytical analysis of heat conduction in the thickness direction

The temperature distribution inside concrete pavements governs their thermoelastic behavior. In situ measurements indicate large daily temperature changes at the top surface of concrete pavements subjected to solar radiation, and little changes at the bottom surface [Belshe et al., 2010]. As for the further analysis, this situation is idealized as follows: An isothermal initial configuration, characterized by a reference temperature T_{ref}, is assumed to remain constant at the bottom surface of the plate. The temperature at the top surface, however, is assumed to evolve according to a *known* function of time t. The lateral surfaces are treated as thermally insulated. This results in one-dimensional heat conduction in the thickness direction of the plate, i.e. in the z-direction, see Fig. 4.2. The resulting history of the temperature field, $T(z,t)$, is
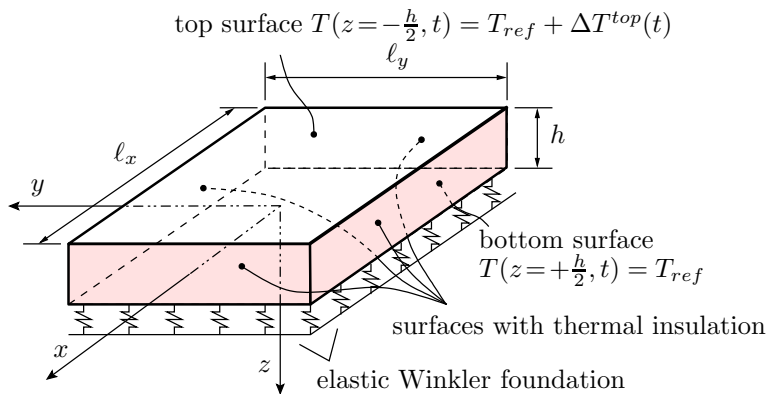
Fig. 4.2: One-dimensional heat conduction over the thickness of the plate.

obtained from the partial differential equation of heat conductivity. For one-dimensional heat conduction, it is given as

$$\frac{\partial T}{\partial t} - a\,\frac{\partial^2 T}{\partial z^2} = 0\,, \tag{4.1}$$

where $a = k/(c_p \cdot \rho)$ stands for the thermal diffusivity of concrete, depending on its thermal conductivity k, its specific heat capacity c_p, and its mass density ρ. Because of the linearity of this partial differential equation, the superposition principle applies. Thus, every given history of the temperature of the top surface can be discretized in a step-wise fashion (Fig. 4.3). This refers to temperature increments ΔT_i^{top} at time instants t_i, with $i = 1, 2, \ldots, N_i$, where N_i stands for the total number of temperature steps considered. The overall solution of the heat conduction problem is obtained by superposition of the solutions for the individual temperature steps [Wang

et al., 2018a; Louhghalam and Ulm, 2016]. Denoting the thickness of the plate as h, the effective temperature change is given as

$$
\begin{aligned}
\Delta T(z,t) = &\sum_{i=1}^{N_i} \Delta T_i^{top} \left(\frac{1}{2} - \frac{z}{h} \right) \\
&- \sum_{n=1}^{\infty} \frac{\Delta T_i^{top} (-1)^n}{n\,\pi} \sin\left(2\,n\,\pi\,\frac{z}{h} \right) \exp\left[-(2\,n\,\pi)^2 \frac{a\,\langle t - t_i \rangle}{h^2} \right] \\
&+ \sum_{n=1}^{\infty} \frac{2\,\Delta T_i^{top} (-1)^n}{(2\,n-1)\,\pi} \cos\left[(2\,n-1)\,\pi\,\frac{z}{h} \right] \exp\left[-(2\,n-1)^2\,\pi^2\,\frac{a\,\langle t - t_i \rangle}{h^2} \right],
\end{aligned}
\tag{4.2}
$$

where $\langle\ \rangle$ stands for the Macaulay operator, defined as

$$
\langle t - t_i \rangle := \frac{1}{2}\Big(t - t_i + |t - t_i| \Big).
\tag{4.3}
$$

The temperature changes over the thickness of the plate, see Eq. (4.2), enter the structural analysis of concrete pavements as input. In addition, also the thermal expansion coefficient of concrete and the elastic stiffness of the material must be quantified. This can be done by means of homogenization, as described in the following.
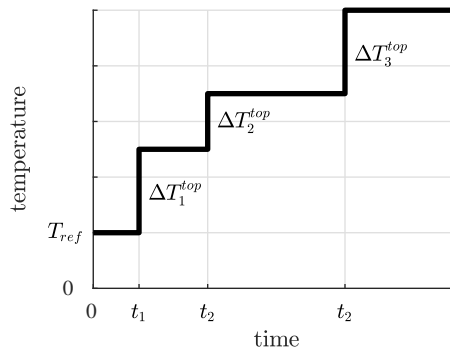
Fig. 4.3: Boundary conditions used for the solution of the heat conduction problem: constant reference temperature, T_{ref}, at the bottom surface of the plate and step-wise evolution of the temperature at the top surface.

4.2.2 Bottom-up homogenization of thermoelastic properties of concrete

Concrete is a matrix-inclusion composite, with coarse aggregates embedded as inclusions in a continuous matrix made of mortar, see Fig. 4.4 (a). At the next smaller scale of observation, also mortar is a matrix-inclusion composite, with fine aggregates embedded as inclusions in a continuous matrix made of cement paste, see Fig. 4.4 (b).

As for homogenization of matrix-inclusion composites, the Mori-Tanaka scheme [Mori and Tanaka, 1973; Benveniste, 1987] is well-suited [Zaoui, 2002]. The required input values are the thermoelastic properties and the volumetric dosages of the two constituents: the matrix phase and the inclusion phase. This work is restricted to *isotropic* material phases and *spherical* inclusions. Denoting the bulk modulus of the matrix as k_m, the shear modulus as μ_m, and the volume fraction as f_m, as well as the corresponding values of the inclusions as k_i, μ_i, and f_i, the
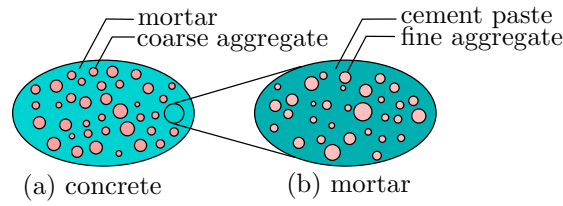
Fig. 4.4: Material organogram of concrete: (a) concrete = spherical coarse aggregates embedded in a mortar matrix, (b) mortar = spherical fine aggregates embedded in a cement paste matrix; two-dimensional sketches of three-dimensional representative volume elements.

homogenized bulk modulus k_{hom} of the composite, and its shear modulus μ_{hom} are obtained as [Wang et al., 2018b]

$$k_{\text{hom}} = \frac{f_i\, k_i \left[1 + \frac{3(k_i - k_m)}{3\,k_m + 4\,\mu_m}\right]^{-1} + f_m\, k_m}{f_i \left[1 + \frac{3(k_i - k_m)}{3\,k_m + 4\,\mu_m}\right]^{-1} + f_m}\,, \tag{4.4}$$

$$\mu_{\text{hom}} = \frac{f_i\, \mu_i \left[1 + \frac{6\,(k_m + 2\,\mu_m)\,(\mu_i - \mu_m)}{5\,\mu_m(3\,k_m + 4\,\mu_m)}\right]^{-1} + f_m\, \mu_m}{f_i \left[1 + \frac{6\,(k_m + 2\,\mu_m)\,(\mu_i - \mu_m)}{5\,\mu_m(3\,k_m + 4\,\mu_m)}\right]^{-1} + f_m}\,. \tag{4.5}$$

The volume fractions satisfy the condition $f_m + f_i = 1$. Denoting the thermal expansion coefficient of the matrix as α_m and the one of the inclusions as α_i, the thermal expansion coefficient of the composite, α_{hom}, reads as [Ghabezloo, 2012; Wang et al., 2018a]

$$\alpha_{\text{hom}} = \frac{3\,k_i\,k_m\,(\alpha_m\, f_m + \alpha_i\, f_i) + 4\,\mu_m\,(\alpha_m\, f_m\, k_m + \alpha_i\, f_i\, k_i)}{3\,k_i\,k_m + 4\,\mu_m\,(f_m\, k_m + f_i\, k_i)}\,. \tag{4.6}$$

As for homogenization of concrete, a two-step homogenization scheme is used. In the first step, mortar is homogenized, based on knowledge regarding the cement paste and the fine aggregates. In the second step, concrete is homogenized, based on knowledge regarding the mortar and the coarse aggregates. Once the homogenized bulk and shear moduli are known, the corresponding values of Young's modulus and Poisson's ratio can be determined based on the standard relations for isotropic materials

$$E = \frac{9\,k\,\mu}{3\,k + \mu}\,, \tag{4.7}$$

$$\nu = \frac{3\,k - 2\,\mu}{6\,k + 2\,\mu}\,. \tag{4.8}$$

4.2.3 Thermoelastic analysis of plates based on the Kirchhoff hypothesis

Temperature changes, see Eq. (4.2), result in thermal eigenstrains. In case of isotropy, the eigenstrains read as:

$$\varepsilon_{xx}^e = \varepsilon_{yy}^e = \varepsilon_{zz}^e = \alpha\,\Delta T\,. \tag{4.9}$$

The question whether they are free to develop, constrained, or prevented from occurring must be answered at two different scales of observation: the larger scale of the entire pavement plate and the smaller scale of the generators of the plate. Notably, a generator is a line normal to the undeformed midplane of the plate.

Theories of thin plates are based on the Kirchhoff hypothesis. It states that the generators remain straight in the deformed configuration of a plate and normal to the tangent plane of the deformed midplane. The corresponding normal strains read as

$$\varepsilon_{xx} = \varepsilon_{x,0} + \kappa_{x,0}\, z\,, \tag{4.10}$$

$$\varepsilon_{yy} = \varepsilon_{y,0} + \kappa_{y,0}\, z\,, \tag{4.11}$$

where $\varepsilon_{x,0} = \frac{\partial u_0}{\partial x}$ and $\varepsilon_{y,0} = \frac{\partial v_0}{\partial y}$ stand for the stretches of the midplane, $\kappa_{x,0} = -\frac{\partial^2 w_0}{\partial x^2}$ and $\kappa_{y,0} = -\frac{\partial^2 w_0}{\partial y^2}$ for the curvatures of the midplane, and $u_0 = u(x,y,z{=}0)$, $v_0 = v(x,y,z{=}0)$, and $w_0 = w(x,y,z{=}0)$ for the three displacement components of an arbitrary point at the midplane of the plate.

Eqs. (4.10) – (4.11) state that assuming the generators of the plate to remain straight is related to normal strains which are *linear* functions of z. It is interesting to discuss this property from the viewpoint of stationary and nonstationary heat conduction:

- Stationary heat conduction in the z-direction refers to the mathematical limit $t \to \infty$ in Eq. (4.2). In this limit, the second line and the third line of Eq. (4.2) are equal to zero. The remaining first line of Eq. (4.2) describes a temperature change which is a *linear* function of z. Thus, the thermal eigenstrains resulting from a steady-state heat conduction problem are compatible with the assumption that the generators of the plate remain straight.

- Nonstationary heat conduction in z-direction refers to temperature changes that are *nonlinear* functions of z. Thus, the thermal eigenstrains resulting from a time-dependent heat conduction problem are incompatible with the assumption that the generators of the plate remain straight, because the nonlinear part of the thermal eigenstrains refers to a distortion of the generators.

The Kirchhoff hypothesis also applies to plates subjected to nonstationary heat conduction. Because the *total* strains must remain *linear* functions of z, the existence of nonlinear *thermal eigen*strains implies the existence of nonlinear *mechanical* ("stress-related") strain such that their superposition results in *total* strains which are linear functions of z. This provides the motivation to split up the thermal eigenstrains into eigenstretches of the plate, eigencurvatures of the plate, and eigendistortions of the generators of the plate. In this context, it is interesting to consider the resultants of the normal stresses, i.e. the normal force per unit length, n_x, and the bending moments per unit length, m_{xx}:

$$n_x = \int\limits_{-h/2}^{+h/2} \sigma_{xx}\, \mathrm{d}z\,, \tag{4.12}$$

$$m_{xx} = \int\limits_{-h/2}^{+h/2} \sigma_{xx}\, z\, \mathrm{d}z\,. \tag{4.13}$$

Notably, n_x and m_{xx} are energetically conjugate to the degrees of freedom u_0 and $\partial w_0/\partial x$ of the generators, for *any* type of material behavior [Höller et al., 2019].

In *thermoelasticity* of thin plates, the stress component σ_{xx} reads as

$$\sigma_{xx} = \frac{E}{1-\nu^2}\left(\varepsilon_{xx}^\sigma + \nu\, \varepsilon_{yy}^\sigma\right)\,, \tag{4.14}$$

where $\varepsilon_{xx}^{\sigma}$ and $\varepsilon_{yy}^{\sigma}$ represent the mechanical normal strains. They are equal to the difference between the total normal strains and the thermal eigenstrains

$$\varepsilon_{xx}^{\sigma} = \varepsilon_{xx} - \varepsilon_{xx}^{e}\,, \tag{4.15}$$

$$\varepsilon_{yy}^{\sigma} = \varepsilon_{yy} - \varepsilon_{yy}^{e}\,. \tag{4.16}$$

Inserting Eqs. (4.9), (4.10), and (4.11) into Eqs. (4.15) and (4.16) and substituting the obtained expressions into Eq. (4.14) allows for reformulating the normal stress component σ_{xx} as

$$\sigma_{xx} = \frac{E}{1-\nu^2}\left[\varepsilon_{x,0} + \kappa_{x,0}\,z - \alpha\,\Delta T + \nu\left(\varepsilon_{y,0} + \kappa_{y,0}\,z - \alpha\,\Delta T\right)\right]. \tag{4.17}$$

Inserting Eq. (4.17) into Eq. (4.12) results in

$$n_x = \frac{E\,h}{1-\nu^2}\left[\varepsilon_{x,0} - \varepsilon_0^e + \nu\left(\varepsilon_{y,0} - \varepsilon_0^e\right)\right], \tag{4.18}$$

with

$$\varepsilon_0^e = \frac{\alpha}{h}\int\limits_{-h/2}^{+h/2}\Delta T\,\mathrm{d}z\,, \tag{4.19}$$

representing the thermal eigenstretches of the plate. Notably, these eigenstretches can be interpreted as the mean value of the eigenstrain distribution. Inserting ΔT according to Eq. (4.2) into Eq. (4.19), and solving the integral, delivers the following expression for the time-dependent evolution of the thermal eigenstretches:

$$\varepsilon_0^e = \sum_{i=1}^{N_i}\alpha\,\Delta T_i^{top}\left\{\frac{1}{2} - \sum_{n=1}^{\infty}\frac{4}{(2\,n-1)^2\,\pi^2}\exp\left[-(2\,n-1)^2\,\pi^2\,\frac{a\,\langle t - t_i\rangle}{h^2}\right]\right\}. \tag{4.20}$$

The question whether the thermal eigenstretches are free to develop, constrained, or prevented must be answered at the scale of the *plate*.

Inserting Eq. (4.17) into Eq. (4.13) results in

$$m_{xx} = \frac{E\,h^3}{12\,(1-\nu^2)}\left[\kappa_{x,0} - \kappa_0^e + \nu\left(\kappa_{y,0} - \kappa_0^e\right)\right], \tag{4.21}$$

with

$$\kappa_0^e = \frac{12\,\alpha}{h^3}\int\limits_{-h/2}^{+h/2}\Delta T\,z\,\mathrm{d}z\,, \tag{4.22}$$

representing the thermal eigencurvatures of plates. Notably, these eigencurvatures can be interpreted as the first-order moment of the eigenstrain distribution. Inserting the temperature changes described by Eq. (4.2) into Eq. (4.22) and solving the integral, delivers the following expression for the time-dependent evolution of the thermal eigencurvatures

$$\kappa_0^e = -\sum_{i=1}^{N_i}\alpha\,\Delta T_i^{top}\frac{1}{h}\left\{1 - \sum_{i=1}^{\infty}\frac{6}{n^2\,\pi^2}\exp\left[-(2\,n\,\pi)^2\,\frac{a\,\langle t - t_i\rangle}{h^2}\right]\right\}. \tag{4.23}$$

The question whether the thermal eigencurvatures are free to develop, constrained, or prevented must also be answered at the scale of the *plate*.

In order to determine the thermal stresses σ_T, Eqs. (4.18) and (4.21) are solved for $\varepsilon_{x,0} + \nu\,\varepsilon_{y,0}$ and $\kappa_{x,0} + \nu\,\kappa_{y,0}$, respectively, and the obtained expressions are back substituted into Eq. (4.17). This yields

$$\sigma_{xx} = \frac{n_x}{h} + \frac{m_{xx}}{h^3/12}\, z + \sigma_T\,, \tag{4.24}$$

with

$$\sigma_T = -\frac{E}{1-\nu}\Big(\alpha\,\Delta T - \varepsilon_0^e - \kappa_0^e\, z\Big)\,. \tag{4.25}$$

In case of stationary heat conduction, the thermal eigenstrain field, $\alpha\,\Delta T$, is a *linear* function of the z-coordinate and, therefore, σ_T vanishes. In case of nonstationary heat conduction, however, the thermal eigenstrain field is a *nonlinear* function of the z-coordinate. The resulting eigendistortions of the generators of the plate, see the expression in brackets of Eq. (4.25), are *prevented* at the scale of the *generators*, because they must remain straight according to the Kirchhoff hypothesis. In other words, the nonlinear eigendistortions activate nonlinear mechanical strains, such that the total strain field is linear in the z-direction and, thus, compatible with the Kirchhoff hypothesis. In addition, the thermal stresses σ_T do not contribute to the stress resultants, because their average value and their first-order moment vanish:

$$\int\limits_{-h/2}^{+h/2} \sigma_T\, \mathrm{d}z = 0\,, \tag{4.26}$$

$$\int\limits_{-h/2}^{+h/2} \sigma_T\, z\, \mathrm{d}z = 0\,. \tag{4.27}$$

By analogy to Eq. (4.24),

$$\sigma_{yy} = \frac{n_y}{h} + \frac{m_{yy}}{h^3/12}\, z + \sigma_T\,. \tag{4.28}$$

The normal forces per unit length, n_x and n_y, and the bending moments per unit length, m_{xx} and m_{yy}, which depend on the mechanical boundary conditions of the pavement plate, are quantified in the following subsection by a semi-analytical method.

4.2.4 Semi-analytical thermoelastic analysis of plates resting on elastic Winkler foundations

A thin rectangular pavement plate with thickness h is considered. It rests on an elastic Winkler foundation, and it undergoes small deflections. The in-plane dimensions in the x and the y-direction are denoted as ℓ_x and ℓ_y. The plate is subjected to dead load p, representing its weight, and to nonstationary heat conduction in the thickness direction. The top surface and the lateral surfaces are stress-free boundaries. Thus, the eigenstretches according to Eq. (4.19) are free to develop, such that the normal forces per unit length vanish:

$$n_x = n_y = 0\,. \tag{4.29}$$

The eigencurvatures according to Eq. (4.22), however, are restrained by the elastic Winkler foundation.

- The absolute values of the reaction forces are equal to the vertical displacement component multiplied by the modulus of subgrade reaction, k, provided that the deflection of the

plate is positive ($w_0 > 0$). In this case, compressive contact stresses prevail in the interface between the plate and the subgrade.

- The reaction forces are equal to zero, provided that the deflection of the plate is negative ($w_0 < 0$). In this case, the plate separates from the subgrade.

In addition, the bottom surface of the plate is free of shear stresses. The bending moments per unit length in Eqs. (4.24) and (4.28) are given as

$$m_{xx} = -K\left[\frac{\partial^2 w_0}{\partial x^2} + \kappa_0^e + \nu\left(\frac{\partial^2 w_0}{\partial y^2} + \kappa_0^e\right)\right], \tag{4.30}$$

$$m_{yy} = -K\left[\frac{\partial^2 w_0}{\partial y^2} + \kappa_0^e + \nu\left(\frac{\partial^2 w_0}{\partial x^2} + \kappa_0^e\right)\right], \tag{4.31}$$

where K is the bending stiffness of the plate, defined as

$$K = \frac{E\,h^3}{12\,(1-\nu^2)}\,. \tag{4.32}$$

The described problem can be solved semi-analytically, based on the principle of virtual power [Höller et al., 2019], which is a rigorous amendment of the theory by Vlasov and Leont'ev [Vlasov and Leont'ev, 1966], entailing systematic errors by violating the free boundary conditions at the edges of the plate. The sought bending surface, w_0, satisfies the following equation:

$$\int\limits_{-\ell_y/2}^{+\ell_y/2}\int\limits_{-\ell_x/2}^{+\ell_x/2}\left[p - k\,w_0\right]\mathring{w}_0\,\mathrm{d}x\,\mathrm{d}y - K\,(1+\nu)\,\kappa_0^e\int\limits_{-\ell_y/2}^{+\ell_y/2}\int\limits_{-\ell_x/2}^{+\ell_x/2}\left(\frac{\partial^2\mathring{w}_0}{\partial x^2} + \frac{\partial^2\mathring{w}_0}{\partial y^2}\right)\mathrm{d}x\,\mathrm{d}y$$

$$- K\int\limits_{-\ell_y/2}^{+\ell_y/2}\int\limits_{-\ell_x/2}^{+\ell_x/2}\left\{\left(\frac{\partial^2 w_0}{\partial x^2} + \nu\frac{\partial^2 w_0}{\partial y^2}\right)\frac{\partial^2\mathring{w}_0}{\partial x^2} + \left(\frac{\partial^2 w_0}{\partial y^2} + \nu\frac{\partial^2 w_0}{\partial x^2}\right)\frac{\partial^2\mathring{w}_0}{\partial y^2}\right. \tag{4.33}$$

$$\left. + \left[2\,(1-\nu)\frac{\partial^2 w_0}{\partial y\,\partial x}\right]\frac{\partial^2\mathring{w}_0}{\partial y\,\partial x}\,\mathrm{d}x\,\mathrm{d}y\right\} = 0\,.$$

Considering the symmetry of the problem with respect to the z-axis, the deflection function $w_0(x,y)$ is represented, in the framework of a Galerkin-type solution scheme [Höller et al., 2019], as a double series of trigonometric functions

$$w_0 = \sum_{s=0}^{N_s}\sum_{t=0}^{N_t} c_{s,t}\,w_{s,t}(x,y)\,, \tag{4.34}$$

where $c_{s,t}$ stands for unknown Fourier coefficients and $w_{s,t}(x,y)$ denotes known ansatz functions

$$w_{s,t} = \cos\frac{s\,\pi\,x}{\ell_x}\,\cos\frac{t\,\pi\,y}{\ell_y}\,, \qquad \begin{array}{l} s = 0,1,3,\ldots,N_s\,, \\ t = 0,1,3,\ldots,N_t\,. \end{array} \tag{4.35}$$

The virtual velocities $\mathring{w}_0(x,y)$ are temporal derivatives of time-dependent virtual displacements. They are introduced by analogy to Eq. (4.34) as

$$\mathring{w}_0 = \sum_{k=0}^{N_k}\sum_{l=0}^{N_l}\mathring{c}_{k,l}\,w_{k,l}(x,y)\,, \tag{4.36}$$

with $\check{\dot{c}}_{k,l}$ denoting the coefficients of the virtual velocity field. Establishing a Galerkin-type solution scheme, Eqs. (4.34) and (4.36) are inserted into Eq. (4.33). Because the obtained expression is valid for arbitrary virtual coefficients $\check{\dot{c}}_{k,l}$, the following system of algebraic equations for determination of the unknown coefficients $c_{s,t}$ is obtained [Höller et al., 2019]:

$$
\begin{aligned}
&\int\limits_{-\ell_y/2}^{+\ell_y/2}\int\limits_{-\ell_x/2}^{+\ell_x/2} p\, w_{k,l}\, \mathrm{d}x\, \mathrm{d}y - K\,(1+\nu)\,\kappa_0^e \int\limits_{-\ell_y/2}^{+\ell_y/2}\int\limits_{-\ell_x/2}^{+\ell_x/2}\left(\frac{\partial^2 w_{k,l}}{\partial x^2} + \frac{\partial^2 w_{k,l}}{\partial y^2}\right)\mathrm{d}x\,\mathrm{d}y \\[2mm]
&+\sum_{s=0}^{N_s}\sum_{t=0}^{N_t} c_{s,t}\left\{-K\int\limits_{-\ell_y/2}^{+\ell_y/2}\int\limits_{-\ell_x/2}^{+\ell_x/2}\left[\left(\frac{\partial^2 w_{s,t}}{\partial x^2}+\nu\frac{\partial^2 w_{s,t}}{\partial y^2}\right)\frac{\partial^2 w_{k,l}}{\partial x^2}\right]\right. \\[2mm]
&+\left(\frac{\partial^2 w_{s,t}}{\partial y^2}+\nu\frac{\partial^2 w_{s,t}}{\partial x^2}\right)\frac{\partial^2 w_{k,l}}{\partial y^2} + \left(2(1-\nu)\frac{\partial^2 w_{s,t}}{\partial y\,\partial x}\right)\frac{\partial^2 w_{k,l}}{\partial y\,\partial x}\ \mathrm{d}x\,\mathrm{d}y \\[2mm]
&\left.-\int\limits_{-\ell_y/2}^{+\ell_y/2}\int\limits_{-\ell_x/2}^{+\ell_x/2} k\, w_{s,t}\, w_{k,l}\, \mathrm{d}x\, \mathrm{d}y\right\}=0 \qquad \text{for}\quad \begin{aligned}k&=0,1,3,\ldots,N_s\,,\\ l&=0,1,3,\ldots,N_t\,.\end{aligned}
\end{aligned}
\tag{4.37}
$$

For details regarding the solution of Eqs. (4.37) see [Höller et al., 2019].

The solution of the problem at hand must be determined iteratively, because the elastic Winkler foundation is active in compression only. In the first iteration step, the modulus of the subgrade reaction, k in Eq. (4.37), is assumed as constant along the entire bottom surface of the plate. Thus, in regions where the deflection is negative, spurious tensile stresses are transmitted between the subgrade and the plate. In order to improve the situation in the second iteration step, the modulus of subgrade reaction is introduced, again in Eq. (4.37), as a two-dimensional step function, which is equal to k in regions where the deflection is positive and equal to zero in regions where it is negative. This strategy is also used in the subsequent iteration steps. Denoting the function of the modulus of subgrade reaction in the iteration step $i+1$ as $k^{(i+1)}$ and the solution for the deflection in the iteration step i as $w_0^{(i)}$, the described step-function can be expressed by means of the Heaviside function H as

$$
k^{(i+1)} = k\, H(w_0^{(i)})\,,
\tag{4.38}
$$

with $H(x)=1$ if $x>0$ and $H(x)=0$ otherwise. The iteration is terminated if the deflection function w_0 remains practically constant for two successive iteration steps. Specifically, the iteration is terminated if

$$
\left|w_{0,\max}^{(i+1)} - w_{0,\max}^{(i)}\right| < 10^{-8}\,\mathrm{m}\,,
\tag{4.39}
$$

where $w_{0,\max}$ is the maximum value of the deflection function and m stands for the SI unit meter.

4.2.5 Top-down quantification of average stresses of the constituents of concrete

This subsection deals with quantification of average stresses and strains of the matrix phase and the inclusion phase, based on knowledge regarding the macroscopic stresses and the temperature change imposed on a representative volume element of a matrix-inclusion composite. Starting at the level of homogenized concrete, the macroscopic stress state reads as

$$
\boldsymbol{\Sigma}_{\mathrm{hom}} = \sigma_{xx}\,\vec{e}_x \otimes \vec{e}_x + \sigma_{yy}\,\vec{e}_y \otimes \vec{e}_y\,,
\tag{4.40}
$$

with σ_{xx} and σ_{yy} taken from Eqs. (4.24) and (4.28). $\vec{e}_x$ and $\vec{e}_y$ are the unit vectors in the direction of the x-axis and y-axis, respectively. The transition from small-case sigmas to a capital sigma follows the tradition of multiscale continuum mechanics, where capital letters are symbolizing *macro*scopic stresses and strains, while lower-case letters are used for *micro*scopic stresses and strains. The macroscopic eigenstrain of homogenized concrete reads as

$$\mathbf{E}^e_{\text{hom}} = \alpha\,\Delta T\Big[\vec{e}_x \otimes \vec{e}_x + \vec{e}_y \otimes \vec{e}_y + \vec{e}_z \otimes \vec{e}_z\Big]\,, \tag{4.41}$$

where $\vec{e}_z$ is the unit vector in the direction of the z-axis, and the homogenized stiffness tensor as

$$\mathbb{C}_{\text{hom}} = 3\,k\,\mathbb{I}_{vol} + 2\,\mu\,\mathbb{I}_{dev}\,, \tag{4.42}$$

where $\mathbb{I}_{vol}$ and $\mathbb{I}_{dev}$ stand for the volumetric and the deviatoric part of the symmetric fourth-order unit tensor $\mathbb{I}$. The $ijkl$-th component of $\mathbb{I}$ reads as $\frac{1}{2}(\delta_{ik}\,\delta_{jl} + \delta_{il}\,\delta_{jk})$ with δ_{ij} denoting the Kronecker delta defined as $\delta_{ij} = 1$ for $i = j$, and $\delta_{ij} = 0$ otherwise. The $ijkl$-th component of $\mathbb{I}_{vol}$ reads as $\frac{1}{3}(\delta_{ij}\,\delta_{kl})$. Finally, $\mathbb{I}_{dev}$ follows as $\mathbb{I}_{dev} = \mathbb{I} - \mathbb{I}_{vol}\,.$

Top-down analysis starts with calculation of the total macroscopic strain:

$$\mathbf{E}_{\text{hom}} = \mathbb{C}^{-1}_{\text{hom}} : \boldsymbol{\Sigma}_{\text{hom}} + \mathbf{E}^e_{\text{hom}}\,, \tag{4.43}$$

with $\mathbb{C}^{-1}_{\text{hom}}$ denoting the inverse of the homogenized elasticity tensor. The scale transition down to the average total microstrains of the matrix and the inclusions is described by the following "concentration-influence relation" [Pichler and Hellmich, 2010]

$$\boldsymbol{\varepsilon}_p = \mathbb{A}_p : \mathbf{E}_{\text{hom}} + \sum_{q=m,i} \mathbb{D}_{pq} : \boldsymbol{\varepsilon}^e_q\,, \qquad p \in [\,m\,;\,i\,]\,, \tag{4.44}$$

where $\mathbb{A}_p$ stands for the strain concentration tensor of the material phase p, $\mathbb{D}_{pq}$ denotes the eigenstrain influence tensor, expressing the effect of the eigenstrain of phase q on the total strain of phase p. For analytical solutions of these tensors, see Appendix A. $\boldsymbol{\varepsilon}^e_q$ stands for the eigenstrains of material phase q, reading as

$$\boldsymbol{\varepsilon}^e_q = \alpha_q\,\Delta T\left[\vec{e}_x \otimes \vec{e}_x + \vec{e}_y \otimes \vec{e}_y + \vec{e}_z \otimes \vec{e}_z\right]\,, \qquad q \in [\,m\,;\,i\,]\,. \tag{4.45}$$

The average microstresses $\boldsymbol{\sigma}_m$ and $\boldsymbol{\sigma}_i$ finally follow from the elasticity law as

$$\boldsymbol{\sigma}_p = \mathbb{C}_p : \left(\boldsymbol{\varepsilon}_p - \boldsymbol{\varepsilon}^e_p\right)\,, \qquad p \in [\,m\,;\,i\,]\,. \tag{4.46}$$

The top-down analysis described by the Eqs. (4.43) – (4.46) is firstly applied to concrete. This leads to the average stresses of the mortar matrix, $\boldsymbol{\sigma}_{mor}$, and of the coarse aggregates, $\boldsymbol{\sigma}_{cagg}$. Thereafter, the described top-down analysis is applied to mortar, in order to compute the average stresses of the cement paste matrix and the fine aggregates. To this end, the Eqs. (4.40), (4.41) and (4.42) are replaced by

$$\boldsymbol{\Sigma}_{\text{hom}} = \boldsymbol{\sigma}_{mor}\,, \tag{4.47}$$

$$\mathbf{E}^e_{\text{hom}} = \alpha_{mor}\,\Delta T\Big[\vec{e}_x \otimes \vec{e}_x + \vec{e}_y \otimes \vec{e}_y + \vec{e}_z \otimes \vec{e}_z\Big]\,, \tag{4.48}$$

$$\mathbb{C}_{\text{hom}} = 3\,k_{mor}\,\mathbb{I}_{vol} + 2\,\mu_{mor}\,\mathbb{I}_{dev}\,. \tag{4.49}$$

4.2.6 Quantification of stress states inside interfacial transition zones

Interfacial transition zones are 15 to $30\,\mu$m thin layers of cement paste covering the aggregates [Ollivier et al., 1995; Scrivener et al., 2004]. The so-called "wall-effect", occurring during mixing of the raw materials, renders ITZs more porous than the rest of the cement paste [Scrivener et al., 2004]. Because ITZs only occupy a small volume of concrete [Simeonov and Ahmad, 1995; Ulrik Nilsen and Monteiro, 1993; Ramesh et al., 1996], they may be idealized as *two-dimensional* interfaces when estimating the homogenized stiffness, see Subsection 4.2.2, and performing the top-down scale transitions described in Subsection 4.2.5. However, microscopic stress states within ITZs are important for estimating the initiation of microcracking of concrete subjected to tensile loading [Königsberger et al., 2014a,b] and for quantifying the strength of the material in case of compressive loading [Königsberger et al., 2018]. In this context, the ITZs are resolved as *three-dimensional* shells covering the aggregates [Königsberger et al., 2014a]. In the following, the scheme for quantification of ITZ stresses by Königsberger et al. [Königsberger et al., 2014a] is extended to consideration of thermal eigenstrains.

Mori-Tanaka estimates of the stresses inside aggregate inclusions, see Eq. (4.46), are based on an Eshelby problem, consisting of a spherical inclusion in an infinite matrix subjected to homogeneous strains at infinity [Zaoui, 2002]. This leads to homogeneous strains inside this inclusion [Eshelby, 1957], suggesting that homogeneous microstrains and microstresses are good approximations of the actual microstress and microstrain states inside the aggregates. Hence, these stress states are also representative for the surfaces of the aggregates.

Assuming that the aggregates are bonded to the surrounding ITZ shell, traction and displacement continuity prevails along their contact surface. In this context, it is beneficial to use a local spherical coordinate system with the zenith angle θ and the azimuth angle ϕ, see Fig. 4.5. The continuity of the traction vectors across the interface implies continuity of the three stress
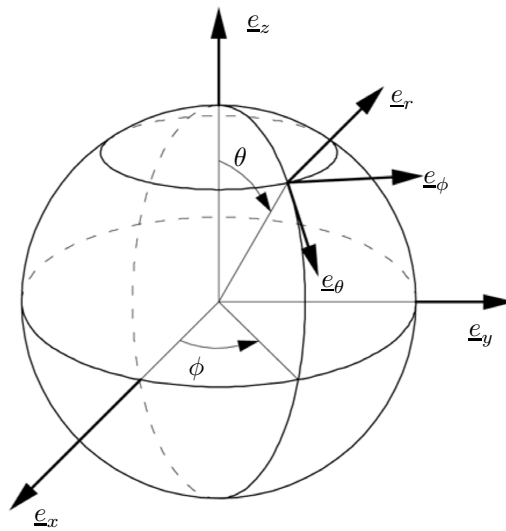
Fig. 4.5: Local spherical coordinate system covering the inclusions.

components with the index r [Königsberger et al., 2014a], resulting in

$$\begin{aligned}
\sigma_{agg,rr}(\theta,\phi) &= \sigma_{ITZ,rr}(\theta,\phi)\,, \\
\sigma_{agg,r\theta}(\theta,\phi) &= \sigma_{ITZ,r\theta}(\theta,\phi)\,, \\
\sigma_{agg,r\phi}(\theta,\phi) &= \sigma_{ITZ,r\phi}(\theta,\phi)\,.
\end{aligned} \tag{4.50}$$

Continuity of the displacements across the interface requires continuity conditions for the three strain components without the index r [Königsberger et al., 2014a]:

$$
\begin{aligned}
\varepsilon_{agg,\theta\theta}(\theta,\phi) &= \varepsilon_{ITZ,\theta\theta}(\theta,\phi)\,, \\
\varepsilon_{agg,\phi\phi}(\theta,\phi) &= \varepsilon_{ITZ,\phi\phi}(\theta,\phi)\,, \\
\varepsilon_{agg,\theta\phi}(\theta,\phi) &= \varepsilon_{ITZ,\theta\phi}(\theta,\phi)\,.
\end{aligned}
\tag{4.51}
$$

The Eqs. (4.50) and (4.51) require the transformation of the Cartesian components of the stress and strain tensors into components related to the local spherical coordinate system. This transformation is performed by means of the following transformation matrix:

$$
\mathbf{Q} = \begin{pmatrix}
\cos\phi\sin\theta & \sin\phi\sin\theta & \cos\theta \\
\cos\phi\cos\theta & \sin\phi\cos\theta & -\sin\theta \\
-\sin\phi & \cos\phi & 0
\end{pmatrix}.
\tag{4.52}
$$

The transformation rule for the stress components reads as

$$
\begin{pmatrix}
\sigma_{agg,rr} & \sigma_{agg,r\theta} & \sigma_{agg,r\phi} \\
\sigma_{agg,r\theta} & \sigma_{agg,\theta\theta} & \sigma_{agg,\theta\phi} \\
\sigma_{agg,r\phi} & \sigma_{agg,\theta\phi} & \sigma_{agg,\phi\phi}
\end{pmatrix}
= \mathbf{Q}\cdot
\begin{pmatrix}
\sigma_{agg,xx} & \sigma_{agg,xy} & \sigma_{agg,xz} \\
\sigma_{agg,xy} & \sigma_{agg,yy} & \sigma_{agg,yz} \\
\sigma_{agg,xz} & \sigma_{agg,yz} & \sigma_{agg,zz}
\end{pmatrix}
\cdot \mathbf{Q}^T,
\tag{4.53}
$$

where $\mathbf{Q}^T$ stands for the transpose of $\mathbf{Q}$. Replacing σ by ε in Eq. (4.53) delivers the corresponding transformation rule for the strain components.

Eqs. (4.50) and (4.51) underline that knowledge of the stresses and the strains of the aggregates allows for determination of three stress and three strain components in the adjacent ITZ. The remaining unknown stress and strain components can be computed based on the generalized Hooke's law for the ITZ, resulting in six equations for the six remaining unknowns. They are give as

$$
\begin{pmatrix}
\sigma_{ITZ,rr} \\
\sigma_{ITZ,\theta\theta} \\
\sigma_{ITZ,\phi\phi} \\
\sqrt{2}\,\sigma_{ITZ,\theta\phi} \\
\sqrt{2}\,\sigma_{ITZ,r\phi} \\
\sqrt{2}\,\sigma_{ITZ,r\theta}
\end{pmatrix}
=
\begin{pmatrix}
k_{ITZ}+\frac{4}{3}\mu_{ITZ} & k_{ITZ}-\frac{2}{3}\mu_{ITZ} & k_{ITZ}-\frac{2}{3}\mu_{ITZ} & 0 & 0 & 0 \\
k_{ITZ}-\frac{2}{3}\mu_{ITZ} & k_{ITZ}+\frac{4}{3}\mu_{ITZ} & k_{ITZ}-\frac{2}{3}\mu_{ITZ} & 0 & 0 & 0 \\
k_{ITZ}-\frac{2}{3}\mu_{ITZ} & k_{ITZ}-\frac{2}{3}\mu_{ITZ} & k_{ITZ}+\frac{4}{3}\mu_{ITZ} & 0 & 0 & 0 \\
0 & 0 & 0 & 2\,\mu_{ITZ} & 0 & 0 \\
0 & 0 & 0 & 0 & 2\,\mu_{ITZ} & 0 \\
0 & 0 & 0 & 0 & 0 & 2\,\mu_{ITZ}
\end{pmatrix}
$$
$$
\cdot
\begin{pmatrix}
\varepsilon_{ITZ,rr} \\
\varepsilon_{ITZ,\theta\theta} \\
\varepsilon_{ITZ,\phi\phi} \\
\sqrt{2}\,\varepsilon_{ITZ,\theta\phi} \\
\sqrt{2}\,\varepsilon_{ITZ,r\phi} \\
\sqrt{2}\,\varepsilon_{ITZ,r\theta}
\end{pmatrix}
-
3\,k_{ITZ}
\begin{pmatrix}
\alpha_{ITZ}\,\Delta T \\
\alpha_{ITZ}\,\Delta T \\
\alpha_{ITZ}\,\Delta T \\
0 \\
0 \\
0
\end{pmatrix},
\tag{4.54}
$$

where k_{ITZ} and μ_{ITZ} denote the bulk and the shear modulus of the ITZ, respectively, and α_{ITZ} stands for the thermal expansion coefficient of the ITZ. The sought three stress components read as

$$
\begin{aligned}
\sigma_{ITZ,\theta\theta}(\theta,\phi) = &\Big[4\,\mu_{ITZ}\,(3\,k_{ITZ} + \mu_{ITZ})\,\varepsilon_{ITZ,\theta\theta} + (3\,k_{ITZ} - 2\,\mu_{ITZ})\,(2\,\mu_{ITZ}\,\varepsilon_{ITZ,\phi\phi} + \sigma_{ITZ,rr}) \\
&- 18\,k_{ITZ}\mu_{ITZ}\,\alpha_{ITZ}\,\Delta T \Big]/(3\,k_{ITZ} + 4\,\mu_{ITZ})
\end{aligned}
\, ,
$$

$$
\begin{aligned}
\sigma_{ITZ,\phi\phi}(\theta,\phi) = &\Big[4\,\mu_{ITZ}\,(3\,k_{ITZ} + \mu_{ITZ})\,\varepsilon_{ITZ,\phi\phi} + (3\,k_{ITZ} - 2\,\mu_{ITZ})\,(2\,\mu_{ITZ}\,\varepsilon_{ITZ,\theta\theta} + \sigma_{ITZ,rr}) \\
&- 18\,k_{ITZ}\mu_{ITZ}\,\alpha_{ITZ}\,\Delta T \Big]/(3\,k_{ITZ} + 4\,\mu_{ITZ})
\end{aligned}
\, ,
$$

$$
\sigma_{ITZ,\theta\phi}(\theta,\phi) = 2\,\mu_{ITZ}\,\varepsilon_{ITZ,\theta\phi}\, ,
$$

$$(4.55)$$

and the sought three strain components as

$$
\varepsilon_{ITZ,rr}(\theta,\phi) = \frac{3\,\sigma_{ITZ,rr} - (3\,k_{ITZ} - 2\,\mu_{ITZ})\,(\varepsilon_{ITZ,\theta\theta} + \varepsilon_{ITZ,\phi\phi}) + 9\,k_{ITZ}\,\mu_{ITZ}\alpha_{ITZ}\,\Delta T}{3\,k_{ITZ} + 4\,\mu_{ITZ}}\, ,
$$

$$
\varepsilon_{ITZ,r\theta}(\theta,\phi) = \frac{\sigma_{ITZ,r\theta}}{2\,\mu_{ITZ}}\, ,
$$

$$
\varepsilon_{ITZ,r\phi}(\theta,\phi) = \frac{\sigma_{ITZ,r\phi}}{2\,\mu_{ITZ}}\, .
$$

$$(4.56)$$

4.3 Exemplary analysis of a concrete pavement subjected to a hail shower

The geometric dimensions of the exemplarily analyzed pavement are given as

$$
\ell_x = 5.00\,\mathrm{m}\, , \quad \ell_y = 3.75\,\mathrm{m}\, , \quad h = 0.25\,\mathrm{m}\, .
\tag{4.57}
$$

The modulus of subgrade reaction, k, is chosen as [Höller et al., 2019]

$$
k = 100\,\mathrm{MPa/m}\, .
\tag{4.58}
$$

The plate is made of concrete, see Table 4.1 for the composition and thermoelastic properties of the constituents. In addition, the thermal diffusivity, a, and the mass density, ρ, of concrete are

Tab. 4.1: Properties of the constituents of concrete: volume fraction, bulk modulus, shear modulus, and thermal expansion coefficient of cement paste, fine aggregates, and coarse aggregates.

material	volume fraction [-]	bulk modulus [GPa]	shear modulus [GPa]	thermal expansion coefficient [$10^{-6}\,/^\circ$C]
cement paste	0.30	10.2	7.7	18.0
fine aggregates (quartz)	0.28	33.8	30.8	11.5
coarse aggregates (granite)	0.42	18.5	12.2	8.0

given as [Wang et al., 2018a]

$$a = 4.73 \times 10^{-7}\,\mathrm{m^2/s}\,, \tag{4.59}$$

$$\rho = 2400\,\mathrm{kg/m^3}\,. \tag{4.60}$$

In the initial configuration, right before sunrise, the pavement plate is considered to be in an isothermal state, at the reference temperature

$$T_{ref} = 17^{\circ}\mathrm{C}\,. \tag{4.61}$$

The temperature at the bottom surface is assumed to be equal to the reference temperature. The evolution of the temperature at the top surface, $T^{top}(t)$, is introduced as an S-shaped function, such that the maximum increase of the temperature at the top surface of the plate, amounting to $45^{\circ}\mathrm{C}$, is reached twelve hours after sunrise, see Fig. 4.6. At that time, a hail shower is assumed to start. It results in a sudden drop of the temperature at the surface of the pavement to $0^{\circ}\mathrm{C}$. This temperature remains constant for 30 minutes, considering that a mix of hailstones and water is covering the plate, see Fig. 4.6. Thus, the mathematical formulation of the evolution of the temperature at the top surface of the pavement plate reads as

$$T^{top}(t) = \begin{cases} 17^{\circ}\mathrm{C} + 45^{\circ}\mathrm{C} \cdot \dfrac{1}{2}\left[1 - \cos\left(\dfrac{t\,\pi}{720\,\mathrm{min}}\right)\right] \dots & 0\,\mathrm{min} \le t < 720\,\mathrm{min}\,, \\ 0^{\circ}\mathrm{C} \;\dots\dots\dots\dots\dots & \dots\; 720\,\mathrm{min} < t \le 750\,\mathrm{min}\,. \end{cases} \tag{4.62}$$
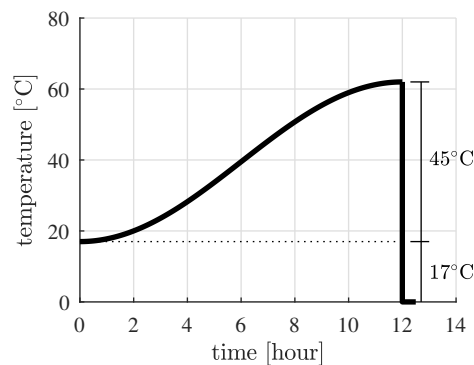
Fig. 4.6: Temperature evolution at the top surface of the pavement plate.

4.3.1 Temperature field of the pavement plate subjected to solar heating and a sudden hail shower

As for the solution of the heat conduction problem, the described evolution of the surface temperature is discretized by time intervals of one minute each:

$$t_i = i \cdot 1\,\mathrm{min}\,, \qquad i = 0, 1, 2, \dots, 750\,. \tag{4.63}$$

The corresponding temperature changes follow from Eq. (4.62) as

$$\Delta T_i^{top} = T^{top}(t_i) - T^{top}(t_{i-1}) \qquad i = 1, 2, \dots, 750\,. \tag{4.64}$$

The temperature distributions inside the pavement plate are computed by inserting Eqs. (4.63) and (4.64) into Eq. (4.2). Thereby, the infinite sums in Eq. (4.2) are approximated very accurately by means of the first 1000 summands each.

Three characteristic time instants are discussed in more detail: the situation right before the hail shower, 3 minutes after its start, and 30 minutes after its start, see Fig. 4.7. Already right
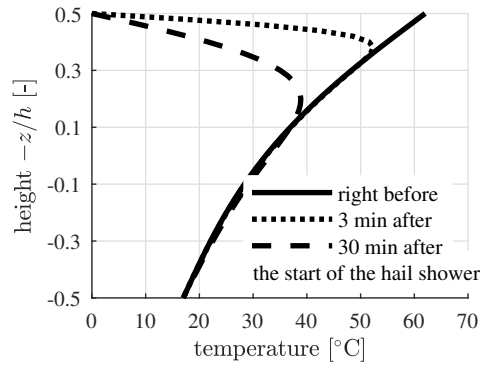
Fig. 4.7: Evolution of the temperature field along the thickness of the pavement plate right before the start of the hail shower, 3 minutes after its start, and 30 minutes after its start, computed based on Eqs. (4.2), (4.63) and (4.64).

before the hail shower, the temperature is nonlinearly distributed across the thickness of the plate. Whereas the black curve is characterized by a monotonic increase of T with increasing $-z/h$, the dotted and the dashed curve have a maximum value of T before decreasing to zero. These temperature distributions are input for the structural analysis of concrete pavements. In addition, also the thermal expansion coefficient of concrete and the elastic stiffness of the material must be quantified. This is done by means of homogenization, as described next.

4.3.2 Bottom-up homogenization of thermoelastic properties of concrete

Homogenization of concrete is carried out in two steps. At first, the matrix-inclusion composite *mortar* is homogenized. The matrix is the cement paste. The inclusions are fine aggregates. The *concrete*-related volumetric dosages of these two constituents, see Table 4.1, are translated into *mortar*-related volume fractions:

$$f_m = \frac{0.30}{0.30 + 0.28} = 0.517\,, \tag{4.65}$$

$$f_i = \frac{0.28}{0.30 + 0.28} = 0.483\,, \tag{4.66}$$

see also Table 4.2. The homogenized elastic stiffness constants and the thermal expansion coefficient of mortar follow from inserting the properties of the matrix and the inclusions, see the second and the third line of Table 4.2, into the Eqs. (4.4), (4.5), and (4.6). The results from homogenization are listed in the last line of Table 4.2.

In the second step, the matrix-inclusion composite *concrete* is homogenized. The matrix is the mortar. The inclusions are the coarse aggregates. Their volume fractions follow from Table 4.1 as

$$f_m = 0.30 + 0.28 = 0.58\,, \tag{4.67}$$

$$f_i = 0.42\,, \tag{4.68}$$

see also Table 4.3. The homogenized elastic constants and the thermal expansion coefficient of concrete follow from inserting the properties of the matrix and the inclusions, see the second and the third line of Table 4.3, into the Eqs. (4.4), (4.5), and (4.6). The results from homogenization are listed in the last line of Table 4.3. Young's modulus and Poisson's ratio of concrete follow from inserting the homogenized bulk and shear modulus, see the last line of Table 4.3, into Eqs. (4.7) and (4.8). They are given as

$$E = 31.8\,\text{GPa}\,, \tag{4.69}$$

$$\nu = 0.20\,. \tag{4.70}$$

4.3.3 Decomposition of thermal eigenstrains into eigenstretches, eigencurvatures, and eigendistortions

The thermal eigenstrains of concrete follow from multiplying the temperature changes, quantified as the differences between the temperature illustrate in Fig. 4.7 and the reference temperature in Eq. (4.61), by the homogenized thermal expansion coefficient of concrete, see the last line of Table 4.3. The three analyzed distributions, see Fig. 4.8 (a), are subdivided into eigenstrains related to eigenstretches of the plate, eigencurvatures of the plate, and eigendistortions of the generators of the plate,

$$\alpha\Delta T = \varepsilon_0^e + \kappa_0^e\,z + \varepsilon_{dist}^e\,, \tag{4.71}$$

see Figs. 4.8 (b), (c), and (d). The eigenstretches and eigencurvatures of the plate, see Fig. 4.8 (b) and Fig. 4.8 (c), follow from inserting Eqs. (4.63) and (4.64) into Eq. (4.20) and Eq. (4.23), respectively; see Table 4.4. Thereby, the infinite sums in Eqs. (4.20) and (4.23) are approximated very accurately by means of the first 1000 summands each. Figs. 4.8 demonstrate that the eigendistortions of the generators of the plate are the *governing* contribution once the hail shower starts.

4.3.4 Thermoelastic structural analysis of the pavement plate

The structural analysis of the pavement plate is carried out as described in Subsection 4.2.4. The values of the dead load $p = \rho\,g\,h$, with the gravitational acceleration g amounting to $9.81\,\text{m/s}^2$, and of the bending stiffness K of the plate, according to Eq. (4.32), follow as

$$p = 5.89\,\text{kN/m}^2\,, \tag{4.72}$$

$$K = 43.1\,\text{MNm}\,. \tag{4.73}$$

The eigencurvatures associated with the investigated scenarios at three different instants of time are input for the analysis, see Table 4.4. The solution for the deflection of the plate is computed

Tab. 4.2: Scale transition 1: homogenization of thermoelastic properties of mortar based on Eqs. (4.4) – (4.6).

material	volume fraction [-]	bulk modulus [GPa]	shear modulus [GPa]	thermal expansion coefficient [$10^{-6}\,/°$C]
cement paste matrix	0.517	10.2	7.7	18.0
fine aggregate inclusions	0.483	33.8	30.8	11.5
homogenized mortar		17.4	14.0	14.2

Tab. 4.3: Scale transition 2: homogenization of thermoelastic properties of concrete based on Eqs. (4.4) – (4.6).

material	volume fraction [-]	bulk modulus [GPa]	shear modulus [GPa]	thermal expansion coefficient [10^{-6} /°C]
mortar matrix	0.58	17.4	14.0	14.2
coarse aggregate inclusions	0.42	18.5	12.2	8.0
homogenized concrete		17.8	13.2	11.5
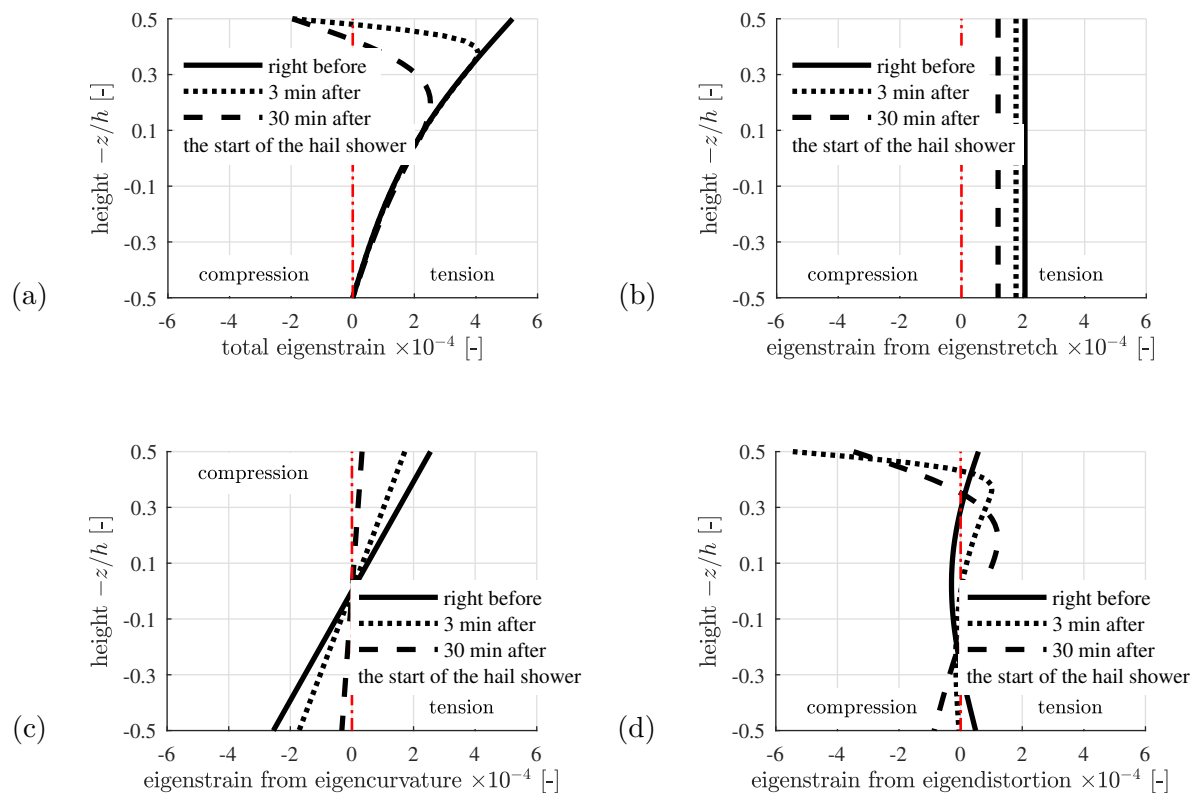
Fig. 4.8: Thermal eigenstrains of the pavement plate right before the start of the hail shower, 3 minutes after its start, and 30 minutes after its start: (a) total eigenstrains, (b) eigenstrains from eigenstretches of the plate, (c) eigenstrains from eigencurvatures of the plate, and (d) eigenstrains from eigendistortions of the generators of the plate.

based on the ansatz function according to Eq. (4.34), using $17 \times 17 = 289$ double trigonometric ansatz functions. The corresponding numerical values of the Fourier coefficients are listed in 4.B. The deflection is positive, i.e. downward, close to the edges of the plate and negative, i.e. upward, in the vicinity of its center, see Fig. 4.9. This underlines that the temperature increase due to solar radiation results in partial separation of the plate from the subgrade. Notably, the numerical values of the deflections were checked against results from Finite Element simulations. Good agreement was obtained.

The bending moments per unit length of the pavement are computed based on Eqs. (4.30) and (4.31), while the twisting moments per unit length, $m_{xy} = m_{yx}$, are equal to zero, considering the

Tab. 4.4: Eigenstretches and eigencurvatures of the pavement right before the start of the hail shower, 3 minutes after its start, and 30 minutes after its start, computed on the basis of Eqs. (4.19) and (4.22) as well as on the temperature distributions illustrated in Fig. 4.7.

time instant	eigenstretches	eigencurvatures
right before the start of the hail shower	2.06×10^{-4}	$-2.04 \times 10^{-3}\,\mathrm{m}^{-1}$
3 min after the start of the hail shower	1.77×10^{-4}	$-1.37 \times 10^{-3}\,\mathrm{m}^{-1}$
30 min after the start of the hail shower	1.19×10^{-4}	$-0.26 \times 10^{-3}\,\mathrm{m}^{-1}$
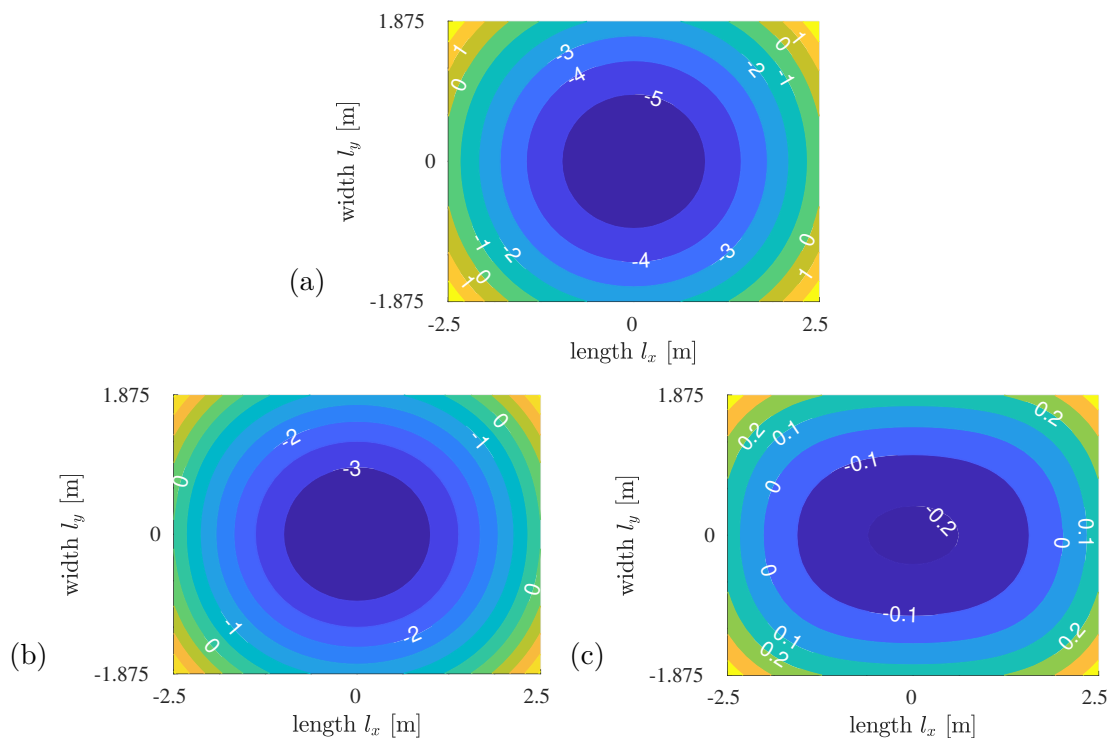
Fig. 4.9: Isolines of the deflection (unit: mm) of the plate (a) right before the start of the hail shower, (b) 3 minutes after its start, and (b) 30 minutes after its start.

symmetry of the problem with respect to z-axis. The maximum bending moments are located at the center of the midplane, see Table 4.5 for the corresponding numerical values. They were checked against results from Finite Element simulations. Good agreement was obtained.

Tab. 4.5: Maximum bending moments per unit length, referring to the center of the pavement, right before the start of the hail shower, 3 minutes after its start, and 30 minutes after its start.

time instant	m_{xx} [kNm/m]	m_{yy} [kNm/m]
right before the start of the hail shower	15.1	6.23
3 min after the start of the hail shower	14.2	5.97
30 min after the start of the hail shower	8.93	5.08

The stresses, induced by the eigendistortions of the generators of the plate, are quantified by Eq. (4.25). They were checked against results from Finite Element simulations. Good agreement was obtained, see 4.C.

The thermoelastic analysis proceeds with calculating the maximum normal stresses in the plate based on Eqs. (4.24), (4.25), (4.28), and (4.29). Thereby, the bending moments per unit length and the thermal eigenstrains are taken from Table 4.5 and from Fig. 4.8, respectively; see also Table 4.4. Because the plate is not quadratic, the values of m_{xx} and m_{yy} are quite different. Still, the macroscopic normal stress components acting in the x- and y-direction are similar, compare Figs. 4.10 (a) and (b). In addition, the stress distributions are qualitatively similar to eigendistortions of the generators of the plate, compare Figs. 4.10 (a) and (b) with Fig. 4.8 (d). This underlines that the macroscopic stresses are governed by the eigendistortions of the generators of the plate, which are prevented to occur, because the generators of the plate must remain straight according to the Kirchhoff hypothesis.
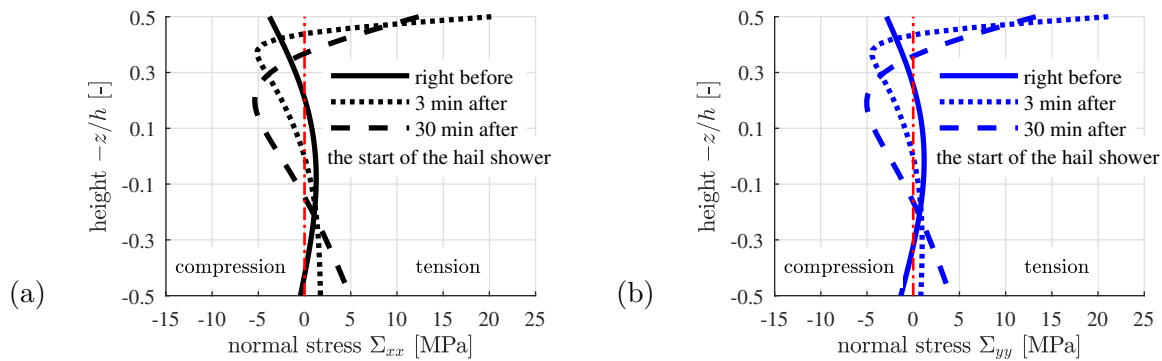
Fig. 4.10: Distribution of macroscopic normal stress components over the thickness of the plate, at the center of the concrete pavement, right before the start of the hail shower, 3 minutes after its start, and 30 minutes after its start: (a) Σ_{xx}, and (b) Σ_{yy}.

Already before the start of the hail shower, the normal stress distributions are nonlinear and, thus, governed by thermal stresses resulting from nonstationary heat conduction. The upper part of the pavement is subjected to macroscopic compressive stresses. They change quickly into tensile stresses, once the hail shower starts. As for the time instant three minutes later, the thermoelastic analysis delivers 21 MPa as the maximum tensile stress. This is by far larger than the tensile strength of concrete. Thus, tensile cracking of concrete will occur close to the exposed top surface of the pavement. Furthermore, the thermoelastic simulation suggests that the uppermost 1.3 cm of concrete experience tensile stresses larger than 3 MPa already three minutes after the start of the hail shower. This tensile zone increases to 2.5 cm another 27 minutes later. At that time, tensile stresses exceeding 3 MPa are also obtained close to the bottom surface of the plate, rendering tensile cracking likely also at the inaccessible bottom of the pavement.

4.3.5 Top-down quantification of average stresses of the constituents of concrete

Average microstresses of the constituents of concrete are quantified following top-down stress concentration, described in Subsection 4.2.5. The computed values of the temperature changes (Fig. 4.7) and the stresses of concrete (Fig. 4.10) are used as macroscopic input quantities. The computed microstresses satisfy the stress average rule

$$\mathbf{\Sigma}_{\text{hom}} = f_i\,\boldsymbol{\sigma}_i + f_m\,\boldsymbol{\sigma}_m\,, \tag{4.74}$$

see Figs. 4.11.

The differences of the microstresses of the matrix and the inclusions originate from two contributions. On the one hand, the stiffer constituent of the statically indeterminate microstructure of the matrix-inclusion composites attracts a larger share of the macroscopic loading, compared to the more compliant other constituent. This is the "mechanical" contribution of the microscopic stress fluctuations. It is governed by the stiffness difference between the matrix and the inclusions, see Tables 4.2 and 4.3. On the other hand, there is also a "thermal" contribution in thermoelasticity, which is governed by the mismatch of thermal expansion coefficients of the matrix and the inclusions [Wang et al., 2018a], see Tables 4.2 and 4.3. In case of a temperature increase, the constituent with the larger/smaller thermal expansion coefficient will be subjected to compression/tension, and to tension/compression in case of a temperature decrease. Anyway, the differences between the average stresses of the matrix and the inclusion phases raises the question concerning the stresses transmitted across the interfaces between them. This provides the motivation to calculate stress states in the ITZs around coarse and fine aggregates.

4.3.6 Quantification of stress states inside the ITZs

ITZs, representing thin layers of cement paste covering the aggregates, are regarded as the "weakest links" within the microstructure of concrete, because they are more porous than the bulk cement paste [Scrivener et al., 2004]. As for the present thermoelastic analysis, the bulk modulus and the shear modulus of the ITZs are set equal to 85% of the corresponding values of the bulk cement paste, see Table 4.2:

$$k_{ITZ} = 8.67\,\text{GPa}\,, \tag{4.75}$$

$$\mu_{ITZ} = 6.55\,\text{GPa}\,. \tag{4.76}$$

This is motivated by nanoindentation results, the Young's modulus of the ITZs is considered to amount to 85% of that of the bulk cement paste, while Poisson's ratio of the ITZs is set equal to that of the bulk cement paste [Königsberger et al., 2014a; Mondal et al., 2009]. The thermal expansion coefficient of the ITZs is set equal to that of the bulk cement paste, see Table 4.2:

$$\alpha_{ITZ} = 18 \times 10^{-6}/^{\circ}\text{C}\,. \tag{4.77}$$

This is motivated by the fact that the thermal expansion coefficient of mature cement pastes is practically independent of the initial water-to-cement mass ratio and, thus, independent of the differences in porosity between the ITZs and the bulk cement paste [Emanuel and Hulsey, 1977; Wang et al., 2018b].

Calculation of stress states in ITZs, covering coarse and fine aggregates, is focusing on the center point of the top surface of the pavement plate and follows the developments in Subsection 4.2.6. Temperature changes, relative to the reference temperature, and the average stress states in the coarse and fine aggregates are used as input, see Table 4.6.

Cracking of the ITZs is caused by the maximum principal normal stress [Königsberger et al., 2014a,b]. Thus, a principal stress analysis is carried out for all positions within the investigated ITZs. Based on the results, the location of the maximum value of the largest principal normal stress is identified. This location is described by the angles ϕ and θ, see Fig. 4.5. Because of

$$\sigma_{cagg,xx} \approx \sigma_{cagg,yy}\,, \tag{4.78}$$

$$\sigma_{fagg,xx} \approx \sigma_{fagg,yy}\,, \tag{4.79}$$
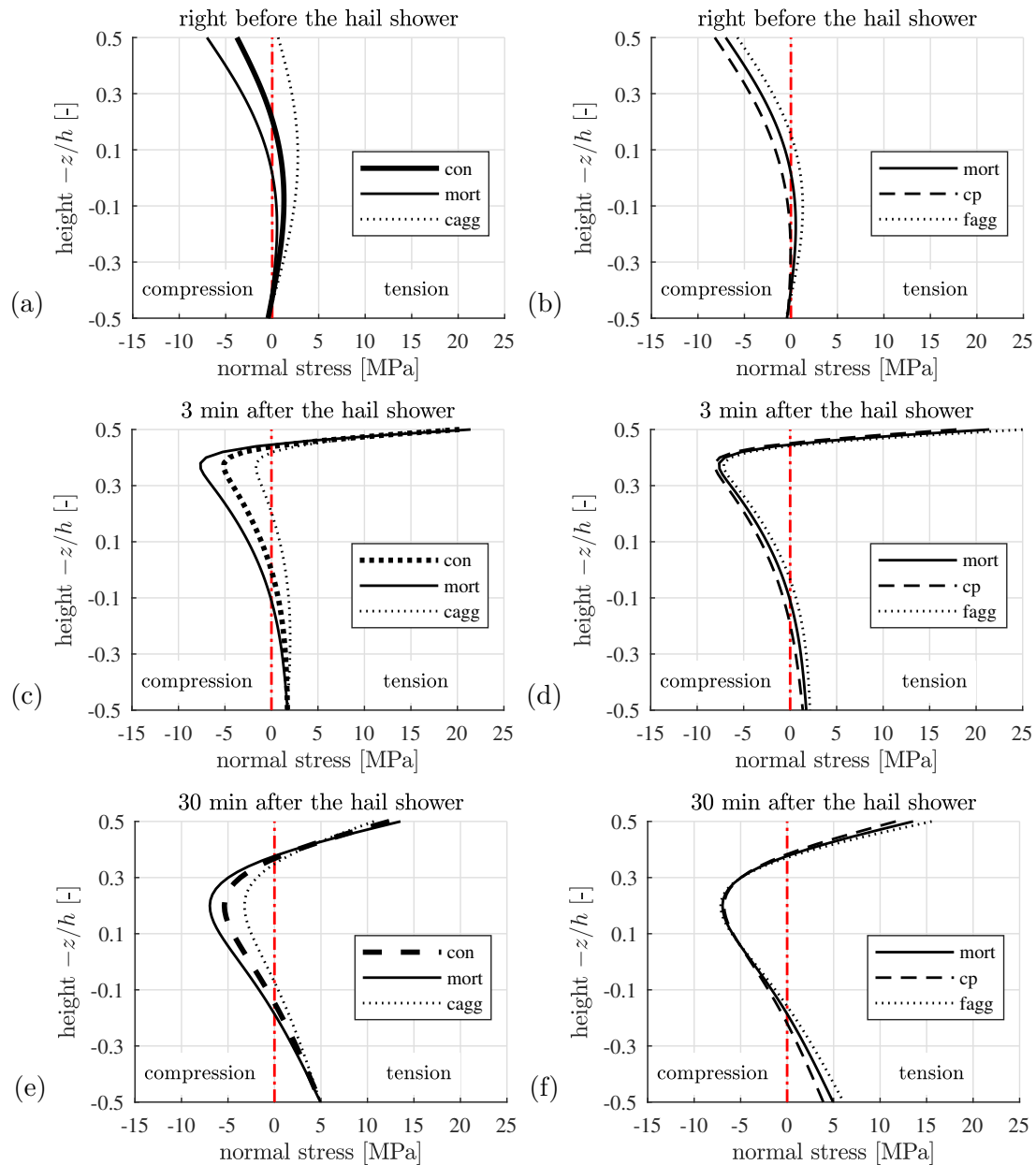
Fig. 4.11: Macroscopic and microscopic normal stresses in the x-direction: (a) and (b) refer to the situation right before the start of the hail shower, (c) and (d) to the one 3 minutes after its start, (e) and (f) to the one 30 minutes after its start; (a), (c), and (e) illustrate macrostresses of the concrete and microstresses of the mortar matrix and the coarse aggregate inclusions; (b), (d), and (f) illustrate macrostresses of the mortar and microstresses of the cement paste matrix and the fine aggregate inclusions.

Tab. 4.6: Temperature changes and nonzero components of the microstress tensors of the coarse and the fine aggregates at the center of the top surface of the pavement right before the start of the hail shower, 3 minutes after its start, and 30 minutes after its start.

time instant	ΔT [°C]	$\sigma_{cagg,xx}$ [MPa]	$\sigma_{cagg,yy}$ [MPa]	$\sigma_{cagg,zz}$ [MPa]
right before the start of the hail shower	+45	+0.65	+1.51	+4.29
3 min after the start of the hail shower	−17	+18.5	+19.4	−0.86
30 min after the start of the hail shower	−17	+10.7	+11.6	−1.17

time instant	ΔT [°C]	$\sigma_{fagg,xx}$ [MPa]	$\sigma_{fagg,yy}$ [MPa]	$\sigma_{fagg,zz}$ [MPa]
right before the start of the hail shower	+45	−5.75	−4.61	−0.91
3 min after the start of the hail shower	−17	+25.2	+26.3	−0.61
30 min after the start of the hail shower	−17	+15.5	+16.7	−0.23

the microstresses of the ITZs only depend weakly on the azimuth angle ϕ. Thus, it is sufficient to show the distribution of the largest principal normal stress along the meridian which contains the maximum principal normal stress, see Fig. 4.12. Because the stress distribution is symmetric with respect to the equator, it is sufficient to illustrate the stresses within the interval $\theta \in [0, \pi/2]$.
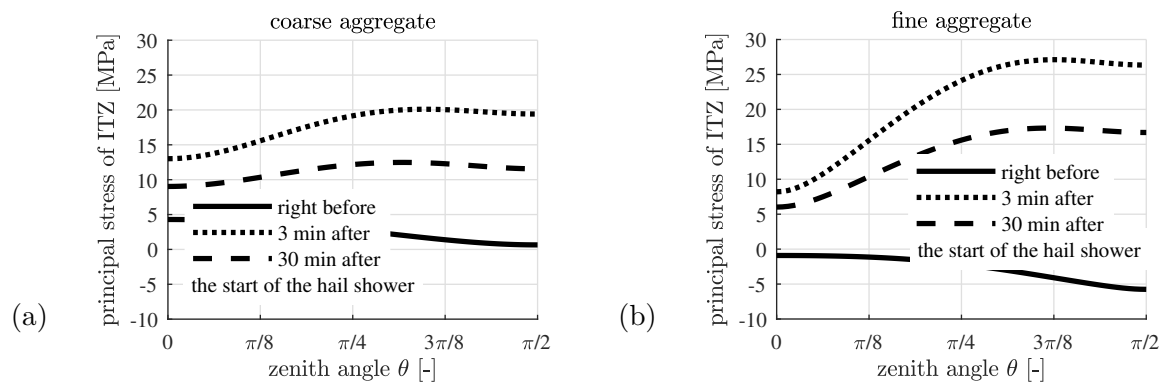
Fig. 4.12: Distribution of the largest principal normal stresses inside ITZs at the center of the top surface of the pavement right before the start of the hail shower, 3 minutes after its start, and 30 minutes after its start: (a) ITZs around coarse aggregates, and (b) ITZs around fine aggregates.

The largest principal normal stresses of the ITZs, right before the start of the hail shower, are much smaller than those after sudden cooling of the top surface. Notably, the maximum value of the largest principal normal stress for both types of analyzed ITZs is even larger than the maximum tensile normal stress of the bulk cement paste, see Fig. 4.12. This underlines that hail showers likely induce tensile cracking along ITZs, at least in regions close to the exposed top surface of pavement plates. Thereby, cracks are likely to develop vertically, in the equatorial regions of the aggregates.

4.3.7 Discussion

Cracking of ITZs is a serious threat for the long-term durability of concrete pavements. Cracks in ITZs close to the top surface of a pavement plate during a hail shower in summer will be filled by water in wet winter periods. If the water is freezing, its volume will increase by some 10%. Once the crystallization pressure reaches the tensile strength of concrete, crack propagation will be encountered [Pichler and Dormieux, 2010a,b]. In order to mitigate the threat to the durability of the pavement, it would be beneficial to (i) cool the top surface of hot pavement plates prior to the start of a hail shower, e.g. by moistening the top surface with water and exploiting the effect of evaporative cooling, and (ii) to avoid freezing of wet pavement plates in winter time, by using anti-freezing agents and/or internal heating of pavement plates. However, these mitigation actions appear to be impractical. Thus, the only practical action is to remove the hailstones as fast as possible, in order to avoid growing of the zones of significant tensile stresses, as was the case in the presented analysis.

The thermal stresses, resulting from the thermal eigenstrains, decrease with decreasing thermal expansion coefficient of concrete. This coefficient can be quantified by the multiscale model in an analytical fashion, based on the composition of the material. This provides the ingredients of a target-oriented mix-design of concrete used for pavements.

- It is recommended to use a rather compliant concrete for pavements. This can be achieved by means of rather compliant coarse and fine aggregates and of a larger volumetric dosage of the more compliant (but expensive) component – the cement paste, see also Eqs. (4.4) and (4.5).

- The thermal expansion coefficient of the cement paste is almost independent of its initial water-to-cement mass ratio, see Fig. 4.1 and [Wang et al., 2018b]. Thus, the remaining design variables are different types and different volumetric dosages of the aggregates, see Eq. (4.6).

- Considering values of relative humidity that are typically encountered in practical applications, the thermal expansion coefficient of the cement paste is, in most cases, larger than that of the aggregates. Thus, moistening of the top surface of the pavement during summer time reduces both the temperature of concrete and the mismatch of the thermal expansion coefficients of the cement paste and of the aggregates. This results in a reduction of the microscopic stress fluctuations.

4.4 Conclusions

Both heating and cooling of the top surface of pavement plates, resulting in nonstationary heat conduction, represent important load cases which deserve careful analysis. From the presented study, the following conclusions are drawn:

- Nonstationary heat conduction is characterized by nonlinear temperature distributions and, thus, by nonlinear distributions of the thermal eigenstrains. They can be subdivided in eigenstretches of the plate, eigencurvatures of the plate, and eigendistortions of the generators of the plate.

- The eigenstretches are free to develop, because of the joints between neighboring plates. The eigencurvatures, in turn, are constrained by the support of the plate resting on the subgrade. Thus, the thermal eigencurvatures of a plate result in bending stresses.

- If the eigendistortions were free to develop, the generators of the plate would be distorted. However, the generators remain straight, because pavements are "thin" plates, the thickness of which is significantly smaller than their in-plane dimensions. Thus, the eigendistortions are prevented at the level of the generators. This results in mechanical strains and, thus, in thermal stresses. The latter are self-equilibrated in the sense of producing no stress resultants in the form of normal forces and bending moments per unit length.

- Stress analysis based on "equivalent" linear temperature distributions appears to be impossible. This is underlined by the fact that the temperature difference between the top and the bottom surface of the pavement plate does not change during the hail shower. Nevertheless, the nonlinear temperature distribution *inside* the plate changes significantly, and this results in a considerable evolution of the thermal stresses.

- In case of a hail shower, following an increase of the temperature of the top surface of the pavement plate, the bending stresses resulting from the restrained thermal eigencurvatures are negligible compared to the thermal stresses induced by the sudden temperature drop to 0°C. Thus, structural analysis of the plate is not necessary. This is beneficial, because partial separation of the plate from the supporting subgrade renders structural analysis of pavements subjected to thermal eigencurvatures a nonlinear task, requiring an iterative solution strategy.

- In order to estimate the maximum macroscopic stresses of the concrete, it is sufficient to know the temperature at the top surface of the pavement plate, $\max T_{surf}$, right before the hail shower, as well as the thermal expansion coefficient α and Young's modulus E of the concrete. Right at the start of the hail shower, the temperature at the top surface of the plate suddenly drops to 0°C. Thus, the sudden temperature change is equal to the initial temperature of the top surface. It would contract, if it was not fixed to the rest of the pavement plate, which is still in a much warmer state. Thus, thermal eigenstrains at the top surface of the plate, resulting from the sudden drop of temperature at the beginning of the hail shower, are practically prevented. This results in a stress-related "mechanical" strain increment, which is equally large as the thermal eigenstrains, but tensile, see Eqs. (4.15) and (4.16). Its multiplication by Young's modulus of concrete delivers the estimate of the thermal stress as

$$\max \sigma_{con} \approx E \, \alpha \, (\max T_{surf}) . \qquad (4.80)$$

In the analyzed scenario, $E = 31.8 \, \text{GPa}$, $\alpha = 11.5 \times 10^{-6}/°\text{C}$ and $\max T_{surf} = 62°\text{C}$, such that $\max \sigma_{con} \approx 22.7 \, \text{MPa}$. This value is only a little larger than $21 \, \text{MPa}$, which is the maximum stress of concrete, computed for the time instant 3 minutes after the start of the hail shower. In this computation, the heat conduction problem and the complex interaction of the pavement plate with the subgrade were considered in detail.

Eq. (4.80) underlines that sudden cooling of a pavement plate resulting from a hail shower represents a serious threat to the integrity of the top layer of concrete, even if the initial temperature at the top surface of the pavement plate is significantly smaller than that considered in the presented analysis. Tensile cracking of concrete is likely going to happen in the ITZs covering the aggregates, because ITZs must transmit tensile stresses which are of similar magnitude as those experienced by the concrete.

Acknowledgments

4.A Analytical solutions for the strain concentration tensors and the eigenstrain influence tensors

The Mori-Tanaka estimates of the strain concentration tensors are given as [Benveniste, 1987; Zaoui, 2002]

$$\mathbb{A}_p = \left[\mathbb{I} + \mathbb{S} : \mathbb{C}_m^{-1} : (\mathbb{C}_p - \mathbb{C}_m) \right]^{-1} : \left\{ \sum_{j=m,i} f_j \left[\mathbb{I} + \mathbb{S} : \mathbb{C}_m^{-1} : (\mathbb{C}_j - \mathbb{C}_m) \right]^{-1} \right\}^{-1}, \qquad p \in [\, m \, ; \, i \,], \tag{4.A.1}$$

where $\mathbb{C}_m$ and $\mathbb{C}_i$ denote the stiffness tensors of the matrix and of the inclusions, respectively. These tensors are isotropic. Analogous to Eq. (4.42), they can be expressed as

$$\mathbb{C}_p = 3 \, k_p \, \mathbb{I}_{vol} + 2 \, \mu_p \, \mathbb{I}_{dev} \,, \qquad p \in [\, m \, ; \, i \,]. \tag{4.A.2}$$

In Eq. (4.A.1), $\mathbb{S}$ denotes the isotropic Eshelby tensor of a spherical inclusion, embedded in an infinite matrix with stiffness $\mathbb{C}_m$. It reads as [Eshelby, 1957]

$$\mathbb{S} = S_{vol} \, \mathbb{I}_{vol} + S_{dev} \, \mathbb{I}_{dev} \,, \tag{4.A.3}$$

with the components

$$S_{vol} = \frac{3 \, k_m}{3 \, k_m + 4 \, \mu_m} \,, \tag{4.A.4}$$

$$S_{dev} = \frac{6 \, (k_m + 2 \, \mu_m)}{5 \, (3 \, k_m + 4 \, \mu_m)} \,. \tag{4.A.5}$$

As for mortars and concretes, consisting of an isotropic matrix and of isotropic inclusions with spherical phase shapes, the strain concentration tensors are also isotropic, reading as

$$\mathbb{A}_p = A_{p,vol} \, \mathbb{I}_{vol} + A_{p,dev} \, \mathbb{I}_{dev} \,, \qquad p \in [\, m \, ; \, i \,], \tag{4.A.6}$$

with the components

$$A_{p,vol} = \left(1 + S_{vol} \frac{k_p - k_m}{k_m} \right)^{-1} \left[\sum_{j=m,i} f_j \left(1 + S_{vol} \frac{k_j - k_m}{k_m} \right)^{-1} \right]^{-1} \,, \tag{4.A.7}$$

$$A_{p,dev} = \left(1 + S_{dev} \frac{\mu_p - \mu_m}{\mu_m} \right)^{-1} \left[\sum_{j=m,i} f_j \left(1 + S_{dev} \frac{\mu_j - \mu_m}{\mu_m} \right)^{-1} \right]^{-1} \,. \tag{4.A.8}$$

The Mori-Tanaka estimates of the eigenstrain influence tensors are given as [Pichler and Hellmich, 2010]

$$
\mathbb{D}_{pp} = [\mathbb{I} - f_p \mathbb{A}_p] : \left[\mathbb{I} + \mathbb{S} : \mathbb{C}_m^{-1} : (\mathbb{C}_p - \mathbb{C}_m)\right]^{-1} : \left(\mathbb{S} : \mathbb{C}_m^{-1}\right) : \mathbb{C}_p \,,
$$
$$
\mathbb{D}_{pq} = -\mathbb{A}_p : f_q \left[\mathbb{I} + \mathbb{S} : \mathbb{C}_m^{-1} : (\mathbb{C}_q - \mathbb{C}_m)\right]^{-1} : \left(\mathbb{S} : \mathbb{C}_m^{-1}\right) : \mathbb{C}_q \,.
$$

(4.A.9)

As for mortars and concretes, consisting of an isotropic matrix and isotropic inclusions with spherical phase shapes, the eigenstrain influence tensors are also isotropic. They read as [Wang et al., 2019b]

$$
\mathbb{D}_{pp} = D_{pp,vol} \, \mathbb{I}_{vol} + D_{pp,dev} \, \mathbb{I}_{dev} \,,
$$
$$
\mathbb{D}_{pq} = D_{pq,vol} \, \mathbb{I}_{vol} + D_{pq,dev} \, \mathbb{I}_{dev} \,,
$$

(4.A.10)

with the components

$$
D_{mm,vol} = (1 - f_m \, A_{m,vol}) \, S_{vol} \,,
$$

(4.A.11)

$$
D_{mm,dev} = (1 - f_m \, A_{m,dev}) \, S_{dev} \,,
$$

(4.A.12)

$$
D_{mi,vol} = -f_i \, A_{m,vol} \left(1 + S_{vol} \frac{k_i - k_m}{k_m}\right)^{-1} S_{vol} \frac{k_i}{k_m} \,,
$$

(4.A.13)

$$
D_{mi,dev} = -f_i \, A_{m,dev} \left(1 + S_{dev} \frac{\mu_i - \mu_m}{\mu_m}\right)^{-1} S_{dev} \frac{\mu_i}{\mu_m} \,,
$$

(4.A.14)

$$
D_{im,vol} = -f_m \, A_{i,vol} \, S_{vol} \,,
$$

(4.A.15)

$$
D_{im,dev} = -f_m \, A_{i,dev} \, S_{dev} \,,
$$

(4.A.16)

$$
D_{ii,vol} = (1 - f_i \, A_{i,vol}) \left(1 + S_{vol} \frac{k_i - k_m}{k_m}\right)^{-1} S_{vol} \frac{k_i}{k_m} \,.
$$

(4.A.17)

$$
D_{ii,dev} = (1 - f_i \, A_{i,dev}) \left(1 + S_{dev} \frac{\mu_i - \mu_m}{\mu_m}\right)^{-1} S_{dev} \frac{\mu_i}{\mu_m} \,.
$$

(4.A.18)

4.B   Numerical values of the Fourier coefficients of the ansatz functions for the deflection of the plate

Höller et al. [Höller et al., 2019] performed convergence analyses regarding the number of ansatz functions considered in Eq. (4.34). They found that the converged solution is approached in a zig-zag fashion. In more detail, if the resolution of the deflection based on 16×16 ansatz functions slightly *under*estimates the converged solution, then 17×17 ansatz functions will slightly *over*estimate the converged solution. The average of the two solutions is a reliable approximation of the converged solution. This is exploited in the present context. Each one of the three plate problems at hand is solved twice, using $16 \times 16 = 256$ ansatz functions ($N_s = N_t = 29$) as well as $17 \times 17 = 289$ ($N_s = N_t = 31$) ansatz functions. Averaging of the two solutions is based on averaging of the computed Fourier coefficients. The obtained averaged coefficients are listed in Table 4.7 for the time instant right before the start of the hail shower, in Table 4.8 for the one 3 minutes after its start, and in Table 4.9 for the one 30 minutes after its start. These averaged solutions were compared with independent Finite Element simulations. Good agreement was obtained. Notably, the coefficients do not only provide access to the deflection at any point of

the plate, see Fig. 4.9 and Eqs. (4.34) and (4.35), but also to the bending moments per unit length at any point of the plate, see Eqs. (4.30) and (4.31). Thus, the stress analysis, which was described in the present paper for the center of the plate, can be repeated for any other point.

4.C Model validation: stresses resulting from the eigendistortions of the generators of the plate

The eigendistortions, see ε_{dist}^e in Eq. (4.71), is prevented to occur at the scale of the plate generators. The resulting thermal stresses can be computed analytically, based on Eq. (4.25). This is checked against the results of a Finite Element (FE) simulation with RFEM [Dlubal, 2016], referring to the time instant 3 minutes after the start of the hail shower. The pavement plate is subdivided into 50 layers in the thickness direction. The thickness of each layer is 0.5 cm. The FE mesh consisted of 375,000 hexahedral finite elements, containing eight nodes with three translational and rotational degrees of freedom each per node [Sevčík]. The eigendistortions are applied by introducing a nonlinear temperature change $\Delta T_{n\ell}$, which generates the same magnitude of eigenstrains, i.e.

$$\alpha \, \Delta T_{n\ell} = \varepsilon_{dist}^e \,. \tag{4.C.1}$$

This temperature field is prescribed by setting the temperature of each layer equal to a constant value, i.e. to the one at its medium z-coordinate. Thus, a piecewise uniform temperature change is prescribed along the thickness of the plate. The numerically quantified normal stresses agree very well with the analytical solution of Eq. (4.25), see Fig. 4.13. This underlines the validity of Eq. (4.25).
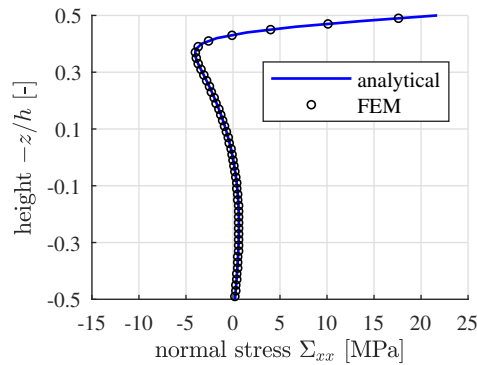
Fig. 4.13: Normal stresses induced by the eigendistortions at the time instant 3 minutes after the start of the hail shower, comparison between the results of the analytical solution following Eq. (4.25) and of the Finite Element simulation.

Tab. 4.7: Fourier coefficients $c_{s,t}$ of the ansatz functions for the deflection of the plate, defined in Eq. (4.34), referring to the configuration right before the start of the hail shower; physical unit of the coefficients [m].

t \ s	0	1	3	5	7	9
0	+2.905655E-03	−5.432520E-03	+2.543635E-04	−5.749035E-05	+2.127335E-05	−9.980030E-06
1	−3.352730E-03	−2.439085E-04	−6.234750E-06	+4.394670E-06	−2.090215E-06	+9.800060E-07
3	+1.506720E-04	−1.076830E-05	+3.077915E-06	−1.214170E-06	+5.935225E-07	−3.061815E-07
5	−3.301395E-05	+3.075700E-06	−1.069220E-06	+4.416545E-07	−2.212110E-07	+1.209825E-07
7	+1.173790E-05	−7.788545E-07	+3.486310E-07	−1.641980E-07	+8.924255E-08	−5.285120E-08
9	−5.510320E-06	+3.570245E-07	−1.755010E-07	+9.201650E-08	−5.425885E-08	+3.454720E-08
11	+3.025140E-06	−2.068605E-07	+1.054680E-07	−5.899950E-08	+3.704500E-08	−2.489490E-08
13	−1.826585E-06	+1.185800E-07	−6.432385E-08	+3.760705E-08	−2.460980E-08	+1.716585E-08
15	+1.155300E-06	−3.472075E-08	+2.950335E-08	−1.781165E-08	+1.264805E-08	−8.934205E-09
17	−7.946970E-07	+2.534775E-08	−2.113820E-08	+1.306290E-08	−9.423325E-09	+6.767370E-09
19	+5.901350E-07	−4.474915E-08	+2.389780E-08	−1.482230E-08	+1.033010E-08	−7.544230E-09
21	−4.401225E-07	+3.705130E-08	−1.914055E-08	+1.186555E-08	−8.306605E-09	+6.154215E-09
23	+3.371790E-07	−3.099255E-08	+1.555230E-08	−9.661450E-09	+6.812635E-09	−5.068650E-09
25	−2.634990E-07	+2.534765E-08	−1.256095E-08	+7.831235E-09	−5.553075E-09	+4.154615E-09
27	+2.098680E-07	−2.101600E-08	+1.027605E-08	−6.446380E-09	+4.587490E-09	−3.466510E-09
29	−1.679675E-07	+1.518695E-08	−7.732965E-09	+4.896785E-09	−3.519100E-09	+2.663985E-09
31	+6.521200E-08	−1.709860E-09	+1.695175E-09	−1.126680E-09	+8.379500E-10	−6.399400E-10

t \ s	11	13	15	17	19	21
0	+5.420420E-06	−3.245890E-06	+2.100905E-06	−1.434415E-06	+1.031640E-06	−7.625290E-07
1	−4.932630E-07	+2.555765E-07	−1.532150E-07	+9.577625E-08	−7.460065E-08	+5.344105E-08
3	+1.695300E-07	−9.798005E-08	+6.401520E-08	−4.348545E-08	+3.412690E-08	−2.555445E-08
5	−7.218545E-08	+4.511990E-08	−3.175750E-08	+2.278270E-08	−1.871665E-08	+1.446360E-08
7	+3.450905E-08	−2.360200E-08	+1.797970E-08	−1.361825E-08	+1.148660E-08	−9.104910E-09
9	−2.395645E-08	+1.728085E-08	−1.341925E-08	+1.033290E-08	−8.670890E-09	+6.828045E-09
11	+1.793100E-08	−1.331525E-08	+1.042820E-08	−8.077660E-09	+6.696970E-09	−5.268375E-09
13	−1.261160E-08	+9.549860E-09	−7.548895E-09	+5.888955E-09	−4.876545E-09	+3.858010E-09
15	+6.851480E-09	−5.306095E-09	+4.313470E-09	−3.431335E-09	+2.913140E-09	−2.463030E-09
17	−5.260045E-09	+4.069885E-09	−7.006610E-09	−6.164790E-10	−2.248425E-09	+1.892755E-09
19	+5.755700E-09	−4.453825E-09	+3.608820E-09	−2.883720E-09	+2.390840E-09	−1.967440E-09
21	−4.734295E-09	+3.719340E-09	−4.610285E-09	+9.291575E-10	−2.046535E-09	+1.691970E-09
23	+3.922235E-09	−3.098540E-09	+3.633485E-09	−1.017307E-09	+1.739545E-09	−1.454555E-09
25	−3.228405E-09	+2.563355E-09	−2.884435E-09	+9.901610E-10	−1.464205E-09	+1.235345E-09
27	+2.703100E-09	−2.147840E-09	+2.330660E-09	−9.311615E-10	+1.247845E-09	−1.062140E-09
29	−2.087505E-09	+1.666935E-09	−1.376720E-09	+1.141925E-09	−9.874760E-10	+8.462270E-10
31	+5.020200E-10	−4.016655E-10	+4.848650E-10	−1.332930E-10	+2.451245E-10	−2.142840E-10

t \ s	23	25	27	29	31
0	+5.857570E-07	−4.557830E-07	+3.631770E-07	−3.336035E-07	+1.016900E-07
1	−4.791865E-08	+3.695565E-08	−3.122975E-08	+8.048400E-08	−4.107625E-08
3	+2.224430E-08	−1.752355E-08	+1.467980E-08	−2.861475E-08	+4.610095E-09
5	−1.273440E-08	+1.010222E-08	−8.552095E-09	+1.293945E-08	−2.295525E-09
7	+8.055500E-09	−6.499140E-09	+5.562915E-09	−8.606315E-09	+1.398455E-09
9	−5.979735E-09	+4.814035E-09	−4.114335E-09	+6.291380E-09	−1.009330E-09
11	+4.564060E-09	−3.684680E-09	+3.130645E-09	−4.765250E-09	+7.774300E-10
13	−3.355905E-09	+2.784255E-09	−2.103515E-09	+3.626840E-09	−5.958350E-10
15	+2.107905E-09	−1.806125E-09	+1.564680E-09	−2.590570E-09	+3.902275E-10
17	−1.653945E-09	+1.425805E-09	−1.251870E-09	+2.042820E-09	−3.126745E-10
19	+1.740375E-09	−1.477815E-09	+1.197525E-09	−1.865690E-09	+3.433640E-10
21	−1.530465E-09	+1.275530E-09	−1.060385E-09	+1.553465E-09	−3.038980E-10
23	+1.323120E-09	−1.111155E-09	+9.398070E-10	−1.316300E-09	+2.705270E-10
25	−1.126625E-09	+9.551050E-10	−8.178290E-10	+1.112085E-09	−2.374615E-10
27	+9.492505E-10	−8.312420E-10	+7.112205E-10	−9.557495E-10	+2.093845E-10
29	−7.582665E-10	+6.622680E-10	−5.753780E-10	+7.796160E-10	−1.677020E-10
31	+2.004405E-10	−1.778535E-10	+1.634635E-10	−2.479635E-10	+8.243800E-11

4 Concrete pavements subjected to hail showers **Tab. 4.8:** Fourier coefficients $c_{s,t}$ of the ansatz functions for the deflection of the plate, defined in Eq. (4.34), referring to the configuration 3 minutes after the start of the hail shower; physical unit of the coefficients [m].

t \ s	0	1	3	5	7	9
0	+2.069520E-03	−3.410800E-03	+1.754000E-04	−4.005905E-05	+1.475810E-05	−6.847220E-06
1	−2.181055E-03	−2.395970E-04	−4.463470E-06	+3.565315E-06	−1.581500E-06	+6.534630E-07
3	+1.057280E-04	−9.616850E-06	+2.656475E-06	−1.017525E-06	+4.725040E-07	−2.228885E-07
5	−2.268610E-05	+2.077755E-06	−7.603765E-07	+3.188195E-07	−1.582900E-07	+8.319645E-08
7	+7.999035E-06	−4.451200E-07	+2.529140E-07	−1.100520E-07	+5.954740E-08	−3.439545E-08
9	−3.734975E-06	+1.770380E-07	−1.181015E-07	+5.987925E-08	−3.547910E-08	+2.219580E-08
11	+2.043000E-06	−9.467785E-08	+6.677920E-08	−3.824915E-08	+2.447185E-08	−1.633980E-08
13	−1.245175E-06	+6.728435E-08	−4.478185E-08	+2.721595E-08	−1.872470E-08	+1.290215E-08
15	+7.433045E-07	+4.120715E-08	+2.399945E-09	−3.127115E-09	+3.095375E-09	−2.385435E-09
17	−5.059550E-07	−3.413630E-08	+6.309650E-11	+1.060350E-09	−1.419030E-09	+1.144546E-09
19	+4.013295E-07	−2.502265E-08	+1.619165E-08	−1.003766E-08	+7.274425E-09	−5.326095E-09
21	−2.992900E-07	+2.119800E-08	−1.298360E-08	+8.302565E-09	−5.840165E-09	+4.280400E-09
23	+2.288980E-07	−1.756170E-08	+1.042750E-08	−6.699670E-09	+4.742280E-09	−3.496160E-09
25	−1.790970E-07	+1.479255E-08	−8.536985E-09	+5.497825E-09	−3.908650E-09	+2.893960E-09
27	+1.425790E-07	−1.227895E-08	+7.000665E-09	−4.506615E-09	+3.214280E-09	−2.386865E-09
29	−1.098775E-07	+3.326995E-09	−3.490600E-09	+1.589630E-09	−1.320275E-09	+1.083185E-09
31	−2.428970E-07	+3.647830E-07	−1.195965E-07	+7.054550E-08	−4.914170E-08	+3.700430E-08

t \ s	11	13	15	17	19	21
0	+3.652220E-06	−2.161345E-06	+1.575220E-06	−8.658395E-07	+7.193815E-07	−5.004635E-07
1	−2.460280E-07	+9.153740E-08	−2.728465E-07	−8.338000E-08	−6.590435E-08	+6.989895E-09
3	+1.030875E-07	−5.192600E-08	+1.006661E-07	+1.095523E-08	+3.171420E-08	−1.026286E-08
5	−4.067930E-08	+2.243975E-08	−9.941120E-08	−3.542490E-08	−1.686200E-08	+6.276545E-09
7	+1.995760E-08	+4.836460E-09	+5.273010E-08	+1.894460E-08	+1.695650E-08	−4.908930E-09
9	−1.389865E-08	+8.348445E-10	−3.081540E-08	−1.017380E-08	−1.063330E-08	+3.429005E-09
11	+1.082610E-08	−2.937435E-09	+1.907415E-08	+5.365195E-09	+7.011870E-09	−2.403210E-09
13	−8.651265E-09	+3.674475E-09	−1.256790E-08	−2.548475E-09	−4.933660E-09	+1.889910E-09
15	+1.518565E-09	+2.005319E-10	+5.844660E-09	+3.082615E-09	+2.037130E-09	−3.776000E-10
17	−6.905035E-10	−1.784417E-10	−3.595775E-09	−2.110655E-09	−1.233485E-09	+1.988681E-10
19	+3.848575E-09	−2.501215E-09	+4.321895E-09	−1.301585E-10	+2.021490E-09	−1.071240E-09
21	−3.173165E-09	+2.187305E-09	−3.292535E-09	+4.073390E-10	−1.638095E-09	+9.435080E-10
23	+2.612060E-09	−1.867665E-09	+2.549860E-09	−5.250655E-10	+1.340165E-09	−8.181620E-10
25	−2.175435E-09	+1.599755E-09	−2.020600E-09	+5.712295E-10	−1.116470E-09	+7.167595E-10
27	+1.795695E-09	−1.387465E-09	+1.615740E-09	−5.627105E-10	+9.113975E-10	−6.265750E-10
29	−8.653075E-10	+7.245650E-10	−9.057490E-10	+2.783985E-10	−5.252820E-10	+3.984335E-10
31	−2.911480E-08	+2.351840E-08	−1.922070E-08	+1.619840E-08	−1.349730E-08	+1.144510E-08

t \ s	23	25	27	29	31
0	+3.913470E-07	−3.050740E-07	+2.473245E-07	−2.061845E-07	+6.961650E-08
1	−1.831995E-08	+1.445385E-08	−1.795070E-08	+2.478095E-08	−2.321370E-08
3	+1.151945E-08	−8.262565E-09	+7.437905E-09	−7.096555E-09	+2.273760E-09
5	−7.854210E-09	+5.733915E-09	−4.863740E-09	+4.250040E-09	−9.649400E-10
7	+5.324295E-09	−3.998890E-09	+3.373090E-09	−2.644625E-09	+5.022550E-10
9	−3.764060E-09	+2.930830E-09	−2.521550E-09	+2.025065E-09	−3.420975E-10
11	+2.665665E-09	−2.150715E-09	+1.911540E-09	−1.646105E-09	+2.603425E-10
13	−1.979650E-09	+1.612650E-09	−1.539830E-09	+1.402070E-09	−2.207025E-10
15	+6.796150E-10	−6.125060E-10	+7.308700E-10	−7.347350E-10	+5.028050E-13
17	−4.454130E-10	+4.307715E-10	−5.636415E-10	+5.550105E-10	+3.052485E-11
19	+1.072072E-09	−9.370525E-10	+9.606580E-10	−8.512680E-10	+1.284725E-10
21	−9.472185E-10	+8.252460E-10	−7.733370E-10	+7.427825E-10	−1.160725E-10
23	+8.065055E-10	−7.045135E-10	+6.625330E-10	−6.445355E-10	+1.026995E-10
25	−6.957770E-10	+6.086235E-10	−5.734035E-10	+5.624155E-10	−9.159350E-11
27	+6.000120E-10	−5.256370E-10	+4.960440E-10	−4.831100E-10	+7.998200E-11
29	−4.641800E-10	+5.236535E-10	−6.730805E-10	+3.139510E-10	−2.187940E-11
31	−9.703100E-09	+8.272700E-09	−7.071450E-09	+6.115900E-09	−5.377450E-09

Die approbierte gedruckte Originalversion dieser Dissertation ist an der TU Wien Bibliothek verfügbar.
The approved original version of this doctoral thesis is available in print at TU Wien Bibliothek.

TU Bibliothek
Your knowledge hub
WIEN

Tab. 4.9: Fourier coefficients $c_{s,t}$ of the ansatz functions for the deflection of the plate, defined in Eq. (4.34), referring to the configuration 30 minutes after the start of the hail shower; physical unit of the coefficients [m].

t \ s	0	1	3	5	7	9
0	+4.709470E-04	−3.487525E-04	+4.162340E-05	−8.498935E-06	+2.908555E-06	−1.328430E-06
1	−3.321465E-04	−5.338485E-05	−4.984020E-06	+7.199045E-07	−1.047665E-07	+2.369860E-08
3	+2.270860E-05	−1.960515E-06	+6.408965E-07	−1.702305E-07	+7.845155E-08	−4.583555E-08
5	−4.552560E-06	+2.884600E-08	−1.456070E-07	+6.704260E-08	−3.849745E-08	+2.254600E-08
7	+1.579220E-06	+6.714440E-08	+6.024990E-08	−3.301175E-08	+1.808585E-08	−1.005131E-08
9	−7.312340E-07	−3.854260E-08	−3.330530E-08	+1.759315E-08	−9.219360E-09	+5.437410E-09
11	+3.987305E-07	+2.020365E-08	+1.975965E-08	−1.015120E-08	+5.414895E-09	−3.555440E-09
13	−2.414040E-07	−1.087590E-08	−1.291950E-08	+6.473065E-09	−3.633915E-09	+2.527115E-09
15	+1.575730E-07	+5.913155E-09	+8.826020E-09	−4.568440E-09	+2.672905E-09	−1.848440E-09
17	−1.085370E-07	−3.361150E-09	−6.216580E-09	+3.285890E-09	−2.006220E-09	+1.359670E-09
19	+7.818225E-08	+1.738595E-09	+4.739310E-09	−2.520200E-09	+1.581300E-09	−1.074080E-09
21	−5.805300E-08	−1.035915E-09	−3.608155E-09	+1.943220E-09	−1.204250E-09	+8.355160E-10
23	+4.440380E-08	+4.836285E-10	+2.859660E-09	−1.549475E-09	+9.675615E-10	−6.841590E-10
25	−3.474335E-08	−1.458479E-10	−2.318765E-09	+1.258270E-09	−7.912640E-10	+5.671580E-10
27	+2.766675E-08	−8.519650E-12	+1.888475E-09	−1.027925E-09	+6.488025E-10	−4.704490E-10
29	−2.255610E-08	+3.053910E-10	−1.626465E-09	+8.899065E-10	−5.976245E-10	+4.261675E-10
31	+9.083200E-09	−3.863795E-10	+5.287650E-10	−2.847835E-10	+1.945815E-10	−1.503135E-10

t \ s	11	13	15	17	19	21
0	+7.128455E-07	−4.280000E-07	+2.398570E-07	−2.161430E-07	+1.362510E-07	−1.011830E-07
1	−4.258255E-09	+1.939290E-09	+4.548555E-08	+3.431695E-08	−1.694335E-09	+1.843975E-09
3	+2.775195E-08	−1.807650E-08	−1.280365E-08	−2.518485E-08	−1.694335E-09	−4.940910E-09
5	−1.299385E-08	+8.081090E-09	+4.616900E-09	+1.126335E-08	−3.000605E-09	+2.396145E-09
7	+5.740665E-09	−3.987615E-09	−8.772385E-10	−5.226730E-09	+1.775395E-09	−1.460445E-09
9	−3.553055E-09	+2.748180E-09	+1.193251E-10	+3.140465E-09	−1.107575E-09	+9.774835E-10
11	+2.537290E-09	−1.820040E-09	+2.340945E-10	−2.005525E-09	+8.270925E-10	−6.760035E-10
13	−1.764175E-09	+1.297380E-09	−2.281840E-10	+1.451210E-09	−6.322000E-10	+5.224315E-10
15	+1.321355E-09	−9.734420E-10	+1.875280E-10	−1.100615E-09	+5.036625E-10	−4.270335E-10
17	−9.814750E-10	+7.662835E-10	−2.286090E-10	+8.315220E-10	−3.943345E-10	+3.293420E-10
19	+7.962030E-10	−6.176645E-10	+2.095225E-10	−6.518825E-10	+3.278870E-10	−2.788065E-10
21	−6.248655E-10	+4.993555E-10	−1.939945E-10	+5.087665E-10	−2.658195E-10	+2.335510E-10
23	+5.160670E-10	−4.139840E-10	+1.850625E-10	−4.058895E-10	+2.240905E-10	−1.965440E-10
25	−4.297180E-10	+3.406135E-10	−1.690315E-10	+3.318995E-10	−1.964855E-10	+1.682800E-10
27	+3.566980E-10	−2.836155E-10	+1.511690E-10	−2.728020E-10	+1.669275E-10	−1.441020E-10
29	−3.164130E-10	+2.531285E-10	−1.445395E-10	+2.363505E-10	−1.497780E-10	+1.300430E-10
31	+1.193865E-10	−9.714700E-11	+5.374150E-11	−9.136800E-11	+5.627650E-11	−4.867995E-11

t \ s	23	25	27	29	31
0	+7.736825E-08	−6.024185E-08	+4.756220E-08	−3.858055E-08	+1.573575E-08
1	−1.978730E-09	+1.376900E-09	−4.947110E-10	+4.551260E-10	−1.792920E-09
3	+4.098555E-09	−3.315950E-09	+2.574780E-09	−1.959660E-09	+5.012300E-10
5	−1.885040E-09	+1.584150E-09	−1.218555E-09	+1.167005E-09	−3.005985E-10
7	+1.171660E-09	−8.779525E-10	+7.074520E-10	−6.303935E-10	+2.329990E-10
9	−8.218500E-10	+6.385995E-10	−4.739020E-10	+4.611680E-10	−1.913580E-10
11	+6.030870E-10	−5.064185E-10	+3.739175E-10	−3.420885E-10	+1.546670E-10
13	−4.471625E-10	+3.953140E-10	−3.044360E-10	+2.488290E-10	−1.171680E-10
15	+3.624750E-10	−3.059760E-10	+2.415680E-10	−2.069955E-10	+9.249150E-11
17	−2.873680E-10	+2.416155E-10	−2.039210E-10	+1.866680E-10	−7.170600E-11
19	+2.445260E-10	−1.958755E-10	+1.718945E-10	−1.535585E-10	+6.181550E-11
21	−2.056110E-10	+1.706045E-10	−1.425710E-10	+1.312735E-10	−5.275000E-11
23	+1.730490E-10	−1.472595E-10	+1.235090E-10	−1.140230E-10	+4.679590E-11
25	−1.468690E-10	+1.279970E-10	−1.079050E-10	+9.742695E-11	−4.160105E-11
27	+1.257015E-10	−1.100700E-10	+9.428170E-11	−8.370115E-11	+3.638145E-11
29	−1.065450E-10	+8.503670E-11	−8.604705E-11	+7.624250E-11	−3.349335E-11
31	+4.305055E-11	−4.631140E-11	+5.534700E-11	−6.402250E-11	−1.574720E-10

Chapter 5

Energy landscapes of graphene under general deformations: DFT-to-hyperelasticity upscaling

Authored by: Raphael Höller, Valerie Smejkal, Florian Libisch, and Christian Hellmich

Under review (minor revisions requested): *International Journal of Engineering Science*

Abstract

Profound investigation of the unsurpassed mechanical properties of suspended graphene motivates the link between classical continuum mechanics (where the notions of "mechanical strength", "mechanical stiffness", and "elastic energy" have actually been coined) and density functional theory (DFT) rooted in quantum mechanics. Namely, the latter quantifies the energetic ground states of systems consisting of atomic nuclei and electrons; and these ground states, in turn, are directly linked to the elastic energy. While the corresponding state-of-the-art typically concerns graphene mechanics under uniaxial or equally biaxial strain states, we here present a fully anisotropic free (strain) energy function reflecting DFT-simulations associated with tens of thousands of arbitrary biaxial strain states. The latter are realized as sets of primitive unit cell vectors spanning a rhomboid unit cell hosting two carbon atoms. The position of the latter follows from internal energy minimization through the Vienna *ab initio* simulation package (VASP). As corresponding continuum mechanical representation we employ hyperelastic, structure tensor-based polynomial models up to the fifth order. The corresponding stress-strain relations are of concave nature, and hence, they provide access to the failure limits of the 2D material undergoing arbitrary loading situations. This is expected to introduce a new level of precision in the growing field of the structural mechanics of graphene.

Contribution of the author: The author of the present thesis developed the refined DFT-based hyperelastic material model for graphene under general deformations. In this context, he performed extensive literature research, performed all quantum mechanical DFT-simulations, prepared the Matlab codes for the fitting process as well as for the provided results, and documented most of the manuscript.

List of symbols

a^0	half width of constant strain triangle ("CST" Finite Element)
$\mathbf{a}_1^0, \mathbf{a}_2^0, \mathbf{a}_3^0$	primitive lattice vectors of graphene in initial configuration
$\mathbf{a}_1, \mathbf{a}_2, \mathbf{a}_3$	primitive lattice vectors of graphene in current configuration
$a_{1,Z}, a_{1,A}$	components of $\mathbf{a}_1$ with respect to base vectors $\mathbf{e}_Z$ and $\mathbf{e}_A$
$a_{2,Z}, a_{2,A}$	components of $\mathbf{a}_2$ with respect to base vectors $\mathbf{e}_Z$ and $\mathbf{e}_A$
A_0	area of parallelogram defined by vectors $\mathbf{a}_1$ and $\mathbf{a}_2$ (initial area of graphene "unit cell")
b^0	height of constant strain triangle (or CST finite element)
$\mathbf{b}_1, \mathbf{b}_2, \mathbf{b}_3$	primitive reciprocal lattice vectors of graphene in initial configuration
$\mathcal{B}$	tensor-valued response functional of Noll's simple materials
c	lattice constant of graphene
c_1-c_{14}	polynomial fitting coefficients
c_{jkm}	Fourier coefficient of Bloch wave
C_1, C_2	carbon atoms
$\mathbb{C}$	2D tangent elasticity tensor, associated with the graphene plane
$\mathbb{C}^{*,1}, \mathbb{C}^{*,2}$	submatrices of $\mathbb{C}$
C_{klmn}^E	components of $\mathbb{C}$ with respect to base vectors $\mathbf{e}_1^E$ and $\mathbf{e}_2^E$
$\hat{\mathcal{C}}$	operator for electron-electron (Coulomb) interaction
$\mathbf{e}_Z, \mathbf{e}_A, \mathbf{e}_T$	orthonormal base frame of Cartesian coordinate system, with $\mathbf{e}_Z$ and $\mathbf{e}_A$ spanning the graphene plane
$\mathbf{e}_1^E, \mathbf{e}_2^E$	principal directions of $\mathbf{E}$ in the graphene plane
$\mathbf{e}_1^\pi, \mathbf{e}_2^\pi$	principal directions of $\boldsymbol{\pi}$ in the graphene plane
$\mathbf{e}_1^\sigma, \mathbf{e}_2^\sigma$	principal directions of $\boldsymbol{\sigma}$ in the graphene plane
e	elementary electron charge
$\bar{E}$	internal energy
E_{cut}	cut-off energy
E_{ee}	electron-electron interaction energy
E_{ext}	nucleus-electron interaction energy
E_H	electrostatic electron-electron interaction energy
E_{xc}	exchange-correlation energy
E_{xc}^{PBE}	generalized gradient approximation of E_{xc} by Perdew, Burke, and Ernzerhof (PBE)
$\mathbf{E}$	Green-Lagrange strain tensor
E_{ZZ}, E_{ZA}, E_{AA}	components of $\mathbf{E}$ with respect to base vectors $\mathbf{e}_Z$ and $\mathbf{e}_A$; lying in the graphene plane
$E_{\mathrm{I}}, E_{\mathrm{II}}$	principal strains of $\mathbf{E}$, in directions $\mathbf{e}_1^E$ and $\mathbf{e}_2^E$
f	periodic function within graphene lattice
f_m	Fourier expansion coefficient of f
$\mathbf{F}$	deformation gradient
F_{ZZ}, F_{ZA}, F_{AA}	components of $\mathbf{F}$ with respect to base vectors $\mathbf{e}_Z$ and $\mathbf{e}_A$
$\mathbf{G}_m$	reciprocal lattice translation vector
G^{2D}	shear modulus associated with 2D elasticity in the graphene plane
G^{3D}	shear modulus associated with pseudo-3D graphene material
h	height of the graphene unit cell
$\hbar$	reduced Planck constant

H	Heaviside step function
$\hat{H}$	Hamiltonian operator
i	imaginary unit
I_1, I_2	principal invariants, associated with isotropic material behavior
I_3	principal invariant, associated with anisotropic material behavior
j, k, l, m, n	index of summation / of vector component
J	Jacobi-determinant
J_1-J_9	main invariants, associated with isotropic material behavior
J_{10}, J_{11}	main invariants, associated with anisotropic material behavior
$\mathbf{k}$	crystal wave vector
$\mathbf{k}_k$	chosen crystal wave vectors in first Brillouin zone
K	corner point of the first Brillouin zone
$\mathcal{L}$	Lagrange function
$\mathbf{M}$	second-order tensor involved in the defintion of structural tensor $\mathbb{P}$
M	center of the confined edge of the first Brillouin zone
m_C	mass of one carbon atom
m_e	mass of one electron
m_{uc}	mass of the graphene unit cell
m_1, m_2, m_3	integers for constructing $\mathbf{G}_m$
$\mathbf{N}$	second-order tensor involved in the defintion of structural tensor $\mathbb{P}$
n_1, n_2, n_3	integers for constructing $\mathbf{R}_n$
N_e	total number of electrons
N_n	total number of nuclei
N_k	total number of wave vector sampling points
$\boldsymbol{\mathcal{N}}$	matrix of linear shape functions
$\mathcal{N}_1, \mathcal{N}_2, \mathcal{N}_3$	values of non-zero elements appearing in $\boldsymbol{\mathcal{N}}$
o, p, q, r, s, t	index of summation / of vector component
$\mathbb{P}$	sixth-order structural tensor of hexagonal lattice (or graphene)
P_{opqrst}	components of $\mathbb{P}$ with respect to base vectors $\mathbf{e}_Z$ and $\mathbf{e}_A$
$\mathbf{q}$	vector collecting nodal displacements
	of the constant strain triangles (or CST finite elements)
$\mathbf{Q}$	orthogonal transformation tensor
Q_{kl}	components of $\mathbf{Q}$ with respect to base vectors $\mathbf{e}_Z$ and $\mathbf{e}_A$
$\mathbf{Q}_{rot}$	rotation tensor of graphene's material symmetry group SO
$\mathbf{Q}_{ref}$	reflection tensor of graphene's material symmetry group SO
$\mathbf{r}$	position vector of electrons
$\mathbf{R}_k$	position vector of k-th nucleus
$\mathbf{R}_n$	lattice translation vector
$\mathbf{S}$	derivative of the principal invariant I_3 with respect to $\mathbf{E}$
S_{ZZ}, S_{ZA}, S_{AA}	components of $\mathbf{S}$ with respect to base vectors $\mathbf{e}_Z$ and $\mathbf{e}_A$
$S_{11}^E, S_{12}^E, S_{22}^E$	components of $\mathbf{S}$ with respect to base vectors $\mathbf{e}_1^E$ and $\mathbf{e}_2^E$
$\mathbb{S}$	derivative of $\mathbf{S}$ with respect to $\mathbf{E}$
SO	material symmetry group of graphene
$\hat{T}_e$	operator for the kinetic energy of electrons
T_e	kinetic energy of electrons
$T_{e,0}$	kinetic energy of non-interacting electrons
t_0	effective thickness of graphene
$\mathbf{u}$	2D displacement vector
$\mathbf{u}^j$	displacement vector of corner point j of unit cell

u_Z, u_A	components of $\mathbf{u}$ with respect to base vectors $\mathbf{e}_Z$ and $\mathbf{e}_A$
V_0	initial volume of the graphene unit cell
$\hat{V}_{ext}$	operator for nucleus-electron interaction
V_{ext}	potential energy for nucleus-electron interaction
V_H	electrostatic electron-electron interaction potential
V_{KS}	Kohn-Sham potential
V_{xc}^{PBE}	PBE approximation of the exchange-correlation potential
w_k	weighting factors for chosen wave vector sampling points
$\mathbf{X}$	location vector throughout the graphene unit cell
X_Z, X_A, X_T	components of $\mathbf{X}$ with respect to base frame $\mathbf{e}_Z$, $\mathbf{e}_A$, $\mathbf{e}_T$ (Cartesian coordinates)
Y^{2D}	elastic Young's modulus associated with 2D elasticity in the graphene plane
Y^{3D}	elastic Young's modulus associated with pseudo-3D graphene material
$\mathbb{Z}$	set of integers
Z_k	atomic number of k-th nucleus
α_E	angle between base vectors $\mathbf{e}_Z$ and $\mathbf{e}_1^E$
α_π	angle between base vectors $\mathbf{e}_Z$ and $\mathbf{e}_1^\pi$
α_σ	angle between base vectors $\mathbf{e}_Z$ and $\mathbf{e}_1^\sigma$
β_1-β_3	scalar functions for constructing $\boldsymbol{\pi}$
γ_1-γ_7	scalar functions for constructing $\mathbb{C}$
Γ	center of the first Brillouin zone
δ	variation
δ_{mn}	Kronecker delta
ε_j	j-th one-electron Kohn-Sham eigenenergy / Lagrange multiplier
$\boldsymbol{\epsilon}^{\mathrm{ln}}$	logarithmic strain tensor
$\epsilon_{\mathrm{I}}^{\mathrm{ln}}, \epsilon_{\mathrm{II}}^{\mathrm{ln}}$	principal logarithmic strains, with directions $\mathbf{e}_1^E$ and $\mathbf{e}_2^E$
λ^{2D}	Lamé's first parameter associated with 2D elasticity in the graphene plane
λ^{3D}	Lamé's first parameter associated with pseudo-3D graphene material
$\lambda_{\mathrm{I}}, \lambda_{\mathrm{II}}$	principal stretches, with directions $\mathbf{e}_1^E$ and $\mathbf{e}_2^E$
ν	Poisson's ratio associated with elastic stiffness at infinitesimally small strains
ν^*	Poisson's ratio-type quantity for large deformations
ξ_1, ξ_2	natural coordinates of the CST-Finite Element
$\boldsymbol{\pi}$	2D second Piola-Kirchhoff stress tensor associated with the graphene plane
$\pi_{ZZ}, \pi_{ZA}, \pi_{AA}$	components of $\boldsymbol{\pi}$ with respect to base vectors $\mathbf{e}_Z$ and $\mathbf{e}_A$
$\pi_{11}^E, \pi_{12}^E, \pi_{22}^E$	components of $\boldsymbol{\pi}$ with respect to base vectors $\mathbf{e}_1^E$ and $\mathbf{e}_2^E$
$\pi_{\mathrm{I}}, \pi_{\mathrm{II}}$	principal stresses of $\boldsymbol{\pi}$, in directions $\mathbf{e}_1^\pi$ and $\mathbf{e}_2^\pi$
$\rho_{m,0}^{2D}$	initial mass density per area of graphene
$\rho_{m,0}^{3D}$	initial mass density per pseudo-volume of graphene
ρ^e	electronic (probability) density
$\boldsymbol{\sigma}$	2D Cauchy stress tensor, associated with the graphene plane
$\sigma_{11}^E, \sigma_{12}^E, \sigma_{22}^E$	components of $\boldsymbol{\sigma}$ with respect to base vectors $\mathbf{e}_1^E$ and $\mathbf{e}_2^E$
$\sigma_{\mathrm{I}}, \sigma_{\mathrm{II}}$	principal stresses of $\boldsymbol{\sigma}$, in directions $\mathbf{e}_1^\sigma$ and $\mathbf{e}_2^\sigma$
ϕ	areal dissipation

Φ	complex electronic wavefunction
Φ_j	j-th one-electron Kohn-Sham wavefunction
ψ_m	specific free energy (or Helmholtz energy per unit mass)
Ψ	Helmholtz free energy
Ω_{BZ}	volume of the first Brillouin zone
∇	nabla operator
$\otimes$	dyadic product
$\mathbf{1}$	second-order unit tensor
$\mathbb{I}$	symmetric fourth-order unit tensor
$\dot{(.)}$	derivative of quantity (.) with respect to time

5.1 Introduction

Graphene, the first true two-dimensional (2D) solid, consists of covalently bonded carbon atoms arranged in a monolayer honeycomb lattice. Since its isolation in 2004 [Novoselov et al., 2004], graphene has attracted considerable attention in the fields of chemistry, physics, and material science. Remarkable thermal, electronic, and mechanical properties of suspended graphene have been discovered [Lau et al., 2012]; the most famous ones are the high thermal conductivity, the weak uniform optical absorptivity, the extremely high electron mobility, and the mechanical strength and stiffness exceeding those of any other material [Balandin et al., 2008; Nair et al., 2008; Bolotin et al., 2008; Lee et al., 2008]. In addition, graphene exhibits several highly peculiar features, such as defects which may either reduce or increase the strength of graphene, or its electronic structure, which can be significantly modified through the application of mechanical strain [Galiotis et al., 2015; Wei et al., 2012; Bissett et al., 2014].

The outstanding mechanical properties of graphene have motivated remarkable studies linking the quantum mechanics-rooted Density Functional Theory (DFT), where the Schrödinger equation of a many electron system is solved by expressing the internal energy as a functional of the electronic density [Hohenberg and Kohn, 1964; Kohn and Sham, 1965], to classical theories of continuum mechanics, where the notions of "mechanical strength" and "mechanical stiffness" have actually been coined. In this context, DFT-simulated uniaxial stretching of four-atom unit cells revealed a Young's modulus, i.e. mechanical stiffness under uniaxial tension, of around 1 TPa [Liu et al., 2007]. These results were confirmed, and extended to the equal biaxial case, on unit cells with 4 and 32 atoms [Xu et al., 2012a]. Corresponding computations were based on a hyperelastic potential depending on the normal components of the Green-Lagrange strain tensor with respect to base vectors pointing into the zigzag and armchair directions, and on the first two invariants of the right Cauchy-Green tensor. Moreover, anisotropy of graphene was considered through dependence of the uniaxially and equally biaxially informed hyperelastic potential on the structural tensor [Kumar and Parks, 2015]. Such hyperelastic formulations have been used for structural mechanics computations concerning carbon nanotubes and nanocones [Ghaffari and Sauer, 2018].

The present paper concerns further refinement of the DFT-to-hyperelasticity conversion, with two threads of original contributions: (i) DFT-simulations relating to tens of thousands of arbitrary biaxial strain states provide a complete picture of deformation-driven energy landscapes of graphene; and (ii) the latter are represented, with decreasing prediction error, by a sequence of structure tensor-based polynomial hyperelastic models up to the fifth order. The concave characteristics of corresponding stress-strain relations give access to the failure limits of the 2D material, in terms of orientation-dependent stability regions [Kumar and Parks, 2015] in the principal strain space. Accordingly, the paper is structured as follows: In Section 5.2, we employ DFT for the quantification of the free energy of graphene in the ground state, as

function of arbitrary primitive lattice vectors characterizing different configurations of the systems. Thereafter, in Section 5.3, we convert the lattice vector configurations into continuum strain measures; and by deriving the free energy with respect to the former measures, we arrive at stress-strain relations for arbitrary deformation states, both with respect to the initial configuration as well as to the current one. Corresponding tangent stiffness tensors are also subjected to a stability analysis, in the line of an earlier contribution of Kumar and Parks [2015]. After presenting corresponding results (see Section 5.4), the paper is completed by a Discussion and Conclusion section (Section 5.5).

5.2 Density Functional Theory of graphene at ground state: free energies for arbitrary primitive lattice vectors

5.2.1 Basics of Density Functional Theory

Density functional theory (DFT) [Parr and Yang, 1989] is a particularly versatile and efficient tool for quantifying the ground energy state, i.e. the lowest possible energy level of atomistic systems.. This ground state is associated to zero absolute temperature, and at this temperature the internal energy $\bar{E}$ is equal to the Helmholtz free energy Ψ. Identification of internal and free energy is common when using DFT for deciphering the mechanics of graphene [Liu et al., 2007; Xu et al., 2012a; Kumar and Parks, 2015]. The starting point for DFT is the stationary *Schrödinger equation* for N electrons moving between fixed nuclei (Born-Oppenheimer nonrelativistic approximation [Born and Oppenheimer, 1927])

$$\hat{H}\,\Phi(\mathbf{r}_1, \mathbf{r}_2, \ldots, \mathbf{r}_{N_e}) = \bar{E}\,\Phi(\mathbf{r}_1, \mathbf{r}_2, \ldots, \mathbf{r}_{N_e})\,. \tag{5.1}$$

In (5.1), $\bar{E}$ is the internal energy of the system, $\hat{H}$ is the Hamiltonian, N_e is the total number of electrons, $\mathbf{r}_j$ denotes the spatial position of the j-th electron, $j = 1, 2, ..., N_e$; and Φ is the normalized complex many-body wavefunction fulfilling

$$\iint \ldots \int \Phi^*(\mathbf{r}_1, \mathbf{r}_2, \ldots, \mathbf{r}_{N_e})\,\Phi(\mathbf{r}_1, \mathbf{r}_2, \ldots, \mathbf{r}_{N_e})\,d\mathbf{r}_1 d\mathbf{r}_2 \ldots d\mathbf{r}_{N_e} = 1\,, \tag{5.2}$$

whereby Φ^* is the complex conjugate of Φ. The Hamiltonian operator $\hat{H}$ consists of three portions: the electron kinetic energy operator $\hat{T}_e$, the (Coulomb) electron-electron interaction operator $\hat{\mathcal{C}}$, and the potential energy (or nucleus-electron interaction) operator $\hat{V}_{\text{ext}}$. In mathematical terms,

$$\hat{H} = \hat{T}_e + \hat{\mathcal{C}} + \hat{V}_{\text{ext}}\,. \tag{5.3}$$

Thereby, the three individual mathematical operators read as

$$\hat{T}_e = -\sum_j^{N_e} \frac{\hbar^2}{2\,m_e}\nabla_j^2, \quad \hat{V}_{ext} = -\sum_j^{N_e}\sum_k^{N_n} \frac{e^2\,Z_k}{|\mathbf{r}_j - \mathbf{R}_k|}, \quad \hat{\mathcal{C}} = \sum_j^{N_e}\sum_{l<j} \frac{e^2}{|\mathbf{r}_j - \mathbf{r}_l|}\,, \tag{5.4}$$

where m_e is the mass of one electron (particle), e is the electron charge, $\hbar$ is the reduced Planck constant, N_n is the total number of nuclei, $\mathbf{R}_k$ and Z_k denote the spatial position and atomic number (positive charge) of the k-th nucleus, respectively; with $k = 1, 2, ..., N_n$; and ∇_j is the nabla operator acting on particle j, $\nabla_j = \partial/\partial\mathbf{r}_j$.

The complex normalized wavefunction is associated with the probability to find an electron at position $\mathbf{r}$, expressed through the so-called electronic (probability) *density* function, reading as [Parr and Yang, 1989]

$$\rho^e(\mathbf{r}) = N_e \iint \ldots \int \Phi^*(\mathbf{r}, \mathbf{r}_2, \ldots, \mathbf{r}_{N_e}) \, \Phi(\mathbf{r}, \mathbf{r}_2, \ldots, \mathbf{r}_{N_e}) \, d\mathbf{r}_2 d\mathbf{r}_3 \ldots d\mathbf{r}_{N_e} \, . \tag{5.5}$$

which, thanks to (5.2), fulfills

$$\int \rho^e(\mathbf{r}) \, d\mathbf{r} = N_e \, , \tag{5.6}$$

i.e. scanning the entire system domain, through many measurements targeting the presence of electrons, will reveal all the electrons present within this domain. Similarly, the average of many measurements of other observables leads to the expected values of these observables, such as the kinetic energy of the electrons

$$T_e[\Phi] = \iint \ldots \int \Phi^* \hat{T}_e \, \Phi \, d\mathbf{r}_1 d\mathbf{r}_2 \ldots d\mathbf{r}_{N_e} = \langle \Phi | \, \hat{T}_e \, | \Phi \rangle \, , \tag{5.7}$$

and from (5.1), the expected value for the internal energy follows as

$$\bar{E}[\Phi] = \iint \ldots \int \Phi^* \hat{H} \Phi \, d\mathbf{r}_1 d\mathbf{r}_2 \ldots d\mathbf{r}_{N_e} = \langle \Phi | \, \hat{H} \, | \Phi \rangle \geq \Psi \, , \tag{5.8}$$

where Ψ denotes the minimum of $\bar{E}$, hence Ψ is the ground state energy (which is identical to the free Helmholtz energy at zero Kelvin). According to the *Hohenberg-Kohn theorems* [Hohenberg and Kohn, 1964], the ground state is fully determined by the electronic density $\rho^e(\mathbf{r})$, as two different external potentials cannot deliver the same electronic density associated with the ground state. Hence, making also use of (5.8) in combination with (5.5), the ground state energy Ψ obeys to the following form

$$\Psi[\rho^e] = E_{ext}[\rho^e] + T_e[\rho^e] + E_{ee}[\rho^e], \quad E_{ext}[\rho^e] = -\sum_k^{N_n} \int \frac{e^2 \, Z_k}{|\mathbf{r} - \mathbf{R}_k|} \, \rho^e(\mathbf{r}) d\mathbf{r} \, , \tag{5.9}$$

with E_{ee} denoting the energy contribution coming from the (Coulomb) electron-electron interaction.

Next, reasonable approximations for T_e and E_{ee} are introduced. For this purpose, Kohn and Sham [1965] introduced a system of non-interacting electrons characterized by individual normalized single-electron wavefunctions $\Phi_1, \Phi_2, \ldots, \Phi_{N_e}$ fulfilling

$$\int \Phi_j^*(\mathbf{r}) \, \Phi_j(\mathbf{r}) d\mathbf{r} = 1 \, ; \quad \text{for} \quad j = 1, 2, ..., N_e \, , \tag{5.10}$$

with the corresponding simplified form of the electronic (probability) density reading as

$$\rho^e(\mathbf{r}) = \sum_j^{N_e} |\Phi_j(\mathbf{r})|^2 = \sum_j^{N_e} \Phi_j^*(\mathbf{r}) \, \Phi_j(\mathbf{r}) \, . \tag{5.11}$$

Following Bloch [1928], electron waves in a periodic lattice can be described by a continuous field of wave vectors $\mathbf{k}$ in the Brillouin zone Ω_{BZ}, see also Section 5.2.2. This leads to recasting (5.10) and (5.11) in the forms

$$\int_{UC} \Phi_j^*(\mathbf{r}, \mathbf{k})\, \Phi_j(\mathbf{r}, \mathbf{k})\, d\mathbf{r} = 1\,; \quad \text{for} \quad j = 1, 2, ..., N_e \quad \forall\, \mathbf{k} \in \Omega_{BZ}\,; \tag{5.12}$$

and

$$\rho^e(\mathbf{r}) = \sum_j^{N_e} \frac{1}{\Omega_{BZ}} \int_{\Omega_{BZ}} \Phi_j^*(\mathbf{r}, \mathbf{k})\, \Phi_j(\mathbf{r}, \mathbf{k})\, d\mathbf{k}\,, \tag{5.13}$$

where the spatial integral is evaluated over a periodic unit cell of the lattice, see also Section 5.2.2, and where N_e is the number of electrons in this unit cell. This approach of summing up wave contributions of the individual electrons is also adopted for the evaluation of the kinetic operator $\hat{T}_e$, so that the Kohn-Sham-Bloch approximation of the kinetic energy reads as

$$T_{e,0}[\rho^e] = \sum_j^{N_e} \frac{1}{\Omega_{BZ}} \int_{\Omega_{BZ}} \int_{UC} \Phi_j^*(\mathbf{r}, \mathbf{k}) \left(-\frac{\hbar^2}{2\, m_e} \nabla^2 \right) \Phi_j(\mathbf{r}, \mathbf{k})\, d\mathbf{r}\, d\mathbf{k}\,. \tag{5.14}$$

The classical electrostatic contribution to the electron-electron interaction energy E_{ee} is called Hartree energy E_H, and reads as [Hohenberg and Kohn, 1964]

$$E_H[\rho^e] = \frac{e^2}{2} \iint \frac{\rho^e(\mathbf{r})\, \rho^e(\mathbf{r}')}{|\mathbf{r} - \mathbf{r}'|}\, d\mathbf{r}\, d\mathbf{r}'\,. \tag{5.15}$$

The difference to the actual (unknown) value for $(T_e + E_{ee})$ is called exchange-correlation energy E_{xc}

$$E_{xc}[\rho^e] = (T_e[\rho^e] + E_{ee}[\rho^e]) - (T_{e,0}[\rho^e] + E_H[\rho^e])\,. \tag{5.16}$$

As an approximation to the exchange-correlaction energy, we adopt the popular generalized gradient approximation (GGA) of Perdew, Burke, and Ernzerhof (PBE) [Perdew et al., 1996, 1997], so that Eq. (5.9) can be transformed into the convenient format

$$\Psi[\rho^e] = E_{ext}[\rho^e] + T_{e,0}[\rho^e] + E_H[\rho^e] + E_{xc}^{PBE}[\rho^e]\,. \tag{5.17}$$

As Ψ denotes the minimum energy of the ground state, the minimization of the density functional (5.17) gives access to the actual value of Ψ, and identification of the minimum point is equivalent to finding the density and orbital state where the variation of Ψ vanishes

$$\min \Psi[\rho^e(\Phi_1^*, \Phi_2^*, \ldots, \Phi_{N_e}^*)] \quad \Leftrightarrow \quad \delta \Psi[\rho^e(\Phi_1^*, \Phi_2^*, \ldots, \Phi_{N_e}^*)] = 0\,. \tag{5.18}$$

Evaluation of the variational expression $(5.18)_2$ while considering the normalization condition (5.12), proposes the use of a Lagrange multiplier-enhanced energy expression $\mathcal{L}$ and its variation, according to

$$
\begin{aligned}
\delta\mathcal{L} &= \delta\mathcal{L}[\rho^e(\Phi_1^*, \Phi_2^*, \ldots, \Phi_{N_e}^*), \varepsilon_1(\mathbf{k}), \varepsilon_2(\mathbf{k}), \ldots, \varepsilon_{N_e}(\mathbf{k})] = \\
&= \delta \left[\Psi - \sum_i^{N_e} \int \varepsilon_i(\mathbf{k}) \left(\int \Phi_i^* \Phi_i\, d\mathbf{r} - 1 \right) d\mathbf{k} \right] \\
&= \sum_i^{N_e} \int \frac{d\Psi}{d\rho^e}[\rho^e(\Phi_1^*, \Phi_2^*, \ldots, \Phi_{N_e}^*)] \times \frac{\partial \rho^e}{\partial \Phi_i^*} \delta\Phi_i^* - \varepsilon_i(\mathbf{k}) \Phi_i \delta\Phi_i^*\, d\mathbf{k} = 0\,. \tag{5.19}
\end{aligned}
$$

As (5.19) needs to hold for any variations of the orbital conjugates, $\delta\Phi_i^*$, it yields N_e eigenvalue problem functionals in $\mathbf{k}$, which interestingly turn out to be all identical. They are all of the form

$$\left(-\frac{\hbar^2}{2\,m_e}\nabla^2 + V_{ext}(\mathbf{r}) + V_H[\rho^e] + V_{xc}^{PBE}[\rho^e]\right)\Phi_j(\mathbf{r},\mathbf{k}) = \varepsilon_j(\mathbf{k})\,\Phi_j(\mathbf{r},\mathbf{k}),$$

$$j = 1, 2, ..., \infty, \quad \forall\,\mathbf{k} \in \Omega_{BZ} \tag{5.20}$$

with the external, Hartree and the exchange correlation potentials reading as

$$V_{ext}(\mathbf{r}) = -\sum_k^{N_n}\frac{e^2\,Z_k}{|\mathbf{r}-\mathbf{R}_k|}\,,\ \ V_H[\rho^e] = \frac{dE_H[\rho^e]}{d\rho^e(\mathbf{r})} = e^2\int\frac{\rho^e(\mathbf{r}')}{|\mathbf{r}-\mathbf{r}'|}d\mathbf{r}'\,,$$

$$V_{xc}^{PBE}[\rho^e] = \frac{dE_{xc}^{PBE}[\rho^e]}{d\rho^e(\mathbf{r})}\,. \tag{5.21}$$

In (5.20), $\varepsilon_j(\mathbf{k})$ is called the j-th Kohn-Sham eigenenergy associated with wavevector $\mathbf{k}$, and the multiplicator of Φ_j in (5.20) is standardly called the Kohn-Sham potential

$$V_{\mathrm{KS}}[\rho^e] = V_{\mathrm{ext}}(\mathbf{r}) + V_H[\rho^e] + V_{xc}^{PBE}[\rho^e]. \tag{5.22}$$

In principle, the Kohn-Sham equations (5.20) with (5.22) give access to the orbitals Φ_j, which in turn, via (5.11) and (5.17), give access to the electronic density ρ^e and the ground state energy Ψ. Practically, this involves a number of computational steps, as described next.

5.2.2 DFT simulation procedure

All computations reported in the present paper are performed on a primitive *unit cell* of the crystal system (see Fig. 5.1): In *graphene*, a perfectly 2D monolayer of graphite, the undeformed sp^2 hybridized carbon atoms are arranged in a hexagonal lattice with lattice constant c. The latter quantifies the equilibrium bond length of two neighboring carbon atoms in the undeformed hexagonal graphene lattice. The smallest unit cell which is able to cover the bulk lattice upon periodic repetition contains two carbon atoms, see Fig. 5.1. In the initial configuration, such a unit cell is spanned by three *primitive lattice vectors* $\mathbf{a}_1^0$, $\mathbf{a}_2^0$, and $\mathbf{a}_3^0$: $\mathbf{a}_1^0$ and $\mathbf{a}_2^0$ are oriented at angles of -30° and 30° from the "armchair" direction $\mathbf{e}_A$, see Fig. 5.1(a), and vector $\mathbf{a}_3^0$ is perpendicular to the graphene plane, see Fig. 5.1(b). With respect to an orthonormal base frame $\{\mathbf{e}_Z, \mathbf{e}_A, \mathbf{e}_T\}$, the primitive lattice vectors read as

$$\mathbf{a}_1^0 = \frac{c}{2}\left(\sqrt{3}\,\mathbf{e}_Z + 3\,\mathbf{e}_A\right), \quad \mathbf{a}_2^0 = \frac{c}{2}\left(-\sqrt{3}\,\mathbf{e}_Z + 3\,\mathbf{e}_A\right), \quad \mathbf{a}_3^0 = h\,\mathbf{e}_T\,. \tag{5.23}$$

Since the employed program package VASP requires periodic boundary conditions in all three dimensions, the length of $\mathbf{a}_3^0$ defines the distance h between periodic images of the graphene sheet. $\mathbf{a}_3^0$ needs to be chosen large enough to avoid artefacts due to layer-layer interactions.

Positions within the unit cell and on its boundaries are described by position vector $\mathbf{X} = X_Z\,\mathbf{e}_Z + X_A\,\mathbf{e}_A + X_T\,\mathbf{e}_T$, see Fig. 5.1(b) for a Cartesian coordinate system consisting of the base frame $\{\mathbf{e}_Z, \mathbf{e}_A, \mathbf{e}_T\}$ and of an origin at the corner of one primitive cell. The initial positions of the two carbon atoms, C_1 and C_2, read as

$$\mathbf{X}_{C_1}^0 = \frac{1}{2}\mathbf{a}_3^0 = \frac{h}{2}\,\mathbf{e}_T, \quad \text{and} \quad \mathbf{X}_{C_2}^0 = \frac{1}{3}\mathbf{a}_1^0 + \frac{1}{3}\mathbf{a}_2^0 + \frac{1}{2}\mathbf{a}_3^0 = c\,\mathbf{e}_A + \frac{h}{2}\,\mathbf{e}_T\,. \tag{5.24}$$
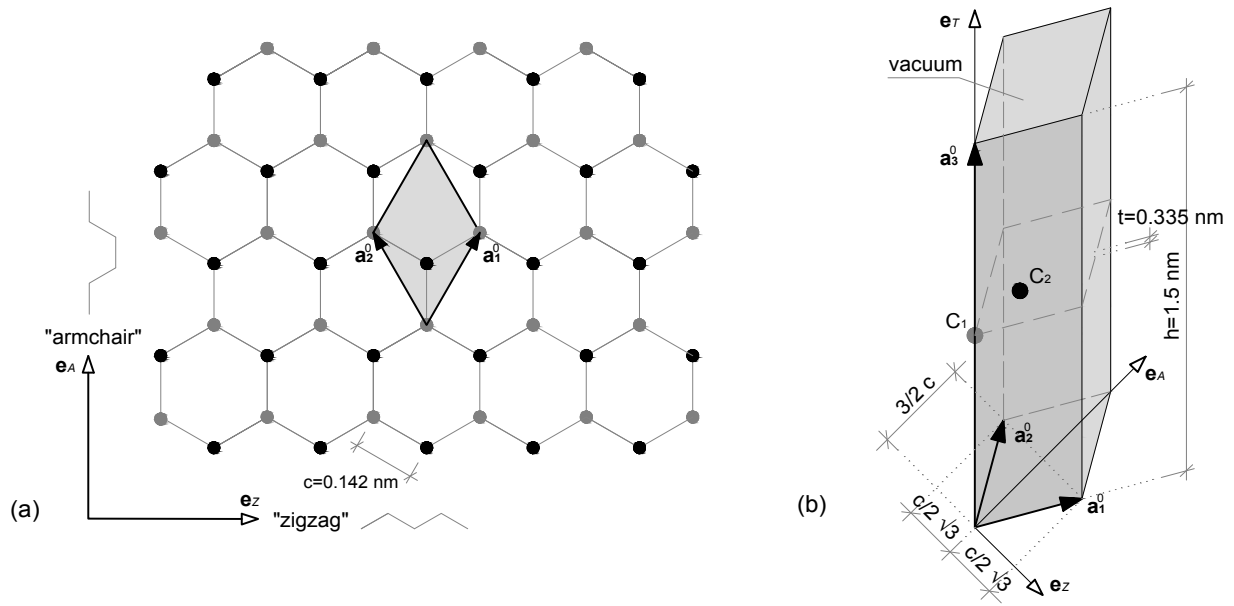
Fig. 5.1: Hexagonal carbon lattice of graphene modeled by periodic unit cells: (a) illustrations of typical unit cell in the graphene plane (spanned by base vectors $\mathbf{e}_Z$ and $\mathbf{e}_A$), with lattice constant $c = 0.142\,\text{nm}$; and (b) 3D geometry of the used primitive rhomboid unit cell with height h and effective thickness t; carbon atoms are indicated by C_1 and C_2.

The unit cell's initial area in the $\mathbf{e}_Z$-$\mathbf{e}_A$ plane and the initial volume of the unit cell follow as

$$A_0 = |\mathbf{a}_1^0 \times \mathbf{a}_2^0| = \frac{3\sqrt{3}}{2}\,c^2 = 2.5981\,c^2\,, \tag{5.25}$$

$$V_0 = \mathbf{a}_3^0 \cdot (\mathbf{a}_1^0 \times \mathbf{a}_2^0) = \frac{3\sqrt{3}}{2}\,h\,c^2 = 2.5981\,c^2\,h\,. \tag{5.26}$$

Furthermore, the mass of the unit cell m_{uc} is given by the two included carbon atoms, with

$$m_{uc} = 2\,m_C = 2 \times 12.0207\,\text{u}\,, \tag{5.27}$$

where [u] is the unified atomic mass unit (quantifying mass on an atomic scale), with $1\,\text{u} = 1.660539 \times 10^{-27}\,\text{kg}$.

Deformed states of the graphene unit cells, differing form the initial configuration, are quantified through deformation-related lattice vectors, reading in the $\{\mathbf{e}_Z, \mathbf{e}_A, \mathbf{e}_T\}$ base frame as

$$\mathbf{a}_1 = a_{1,Z}\,\mathbf{e}_Z + a_{1,A}\,\mathbf{e}_A\,, \quad \mathbf{a}_2 = a_{2,Z}\,\mathbf{e}_Z + a_{2,A}\,\mathbf{e}_A\,, \quad \mathbf{a}_3 = h\,\mathbf{e}_T\,, \tag{5.28}$$

whereby $\mathbf{a}_3 = \mathbf{a}_3^0$ (i.e. distances between the periodic images of the graphene sheet remain invariant). In order to reach a new energy minimum associated to such a deformed unit cell, the carbon atoms also need to change their position (ionic relaxation), see Fig. 5.2. This new energy minimum is higher than that associated with the undeformed configuration.

The entire periodic lattice is defined through the lattice point position vectors $\mathbf{R}_n$, reading as

$$\mathbf{R}_n = n_1\,\mathbf{a}_1 + n_2\,\mathbf{a}_2 + n_3\,\mathbf{a}_3 \quad \forall\, n_1, n_2, n_3 \in \mathbb{Z}\,. \tag{5.29}$$
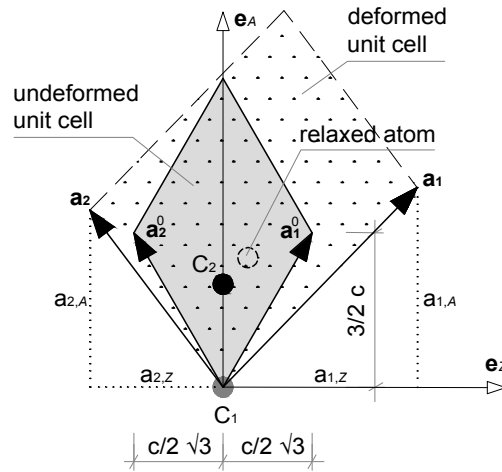
Fig. 5.2: Deformed and undeformed graphene unit cell in $\mathbf{e}_Z$-$\mathbf{e}_A$-plane, spanned by vectors according to (5.23) and (5.28), respectively, including initial and relaxed carbon atoms.

Any function f on this lattice is periodic, i.e. $f(\mathbf{r} + \mathbf{R}_n) = f(\mathbf{r}) \, \forall \, \mathbf{R}_n$, so that it is useful to write it as a Fourier series

$$f(\mathbf{r} + \mathbf{R}_n) = \sum_m f_m \exp[i\mathbf{G}_m \cdot \mathbf{r}] \exp[i\mathbf{G}_m \cdot \mathbf{R}_n] \, . \tag{5.30}$$

Periodicity implies $f(\mathbf{R}_n + \mathbf{r}) = f(\mathbf{R}_k + \mathbf{r})$ for any $n, k \in \mathbb{Z}$, and hence

$$\sum_m f_m \exp[i\mathbf{G}_m \cdot \mathbf{r}] \exp[i\mathbf{G}_m \cdot \mathbf{R}_n] = \sum_m f_m \, \exp[i\mathbf{G}_m \cdot \mathbf{r}]$$
$$\Rightarrow \quad \mathbf{G}_m \cdot \mathbf{R}_n = 2\,\pi\,N \quad \forall \, N \in \mathbb{Z} \, . \tag{5.31}$$

This relation induces a so-called reciprocal lattice in the form

$$\mathbf{G}_m = m_1 \, \mathbf{b}_1 + m_2 \, \mathbf{b}_2 + m_3 \, \mathbf{b}_3 \quad \forall \, m_1, m_2, m_3 \in \mathbb{Z} \, , \tag{5.32}$$

where $\mathbf{b}_1$, $\mathbf{b}_2$, and $\mathbf{b}_3$ are the *reciprocal lattice vectors* (see Fig. 5.3), defined as

$$\mathbf{b}_1 = 2\pi \frac{\mathbf{a}_2 \times \mathbf{a}_3}{\mathbf{a}_3 \cdot (\mathbf{a}_1 \times \mathbf{a}_2)} \, , \quad \mathbf{b}_2 = 2\pi \frac{\mathbf{a}_3 \times \mathbf{a}_1}{\mathbf{a}_3 \cdot (\mathbf{a}_1 \times \mathbf{a}_2)} \, , \quad \mathbf{b}_3 = 2\pi \frac{\mathbf{a}_1 \times \mathbf{a}_2}{\mathbf{a}_3 \cdot (\mathbf{a}_1 \times \mathbf{a}_2)} \, . \tag{5.33}$$

The reciprocal lattice vectors satisfy the duality relation

$$\mathbf{b}_m \cdot \mathbf{a}_n = 2\pi \, \delta_{mn} \, , \tag{5.34}$$

with δ_{mn} denoting the Kronecker delta ($\delta_{mn} = 1$ if $m = n$ and $\delta_{mn} = 0$ if $m \neq n$). For graphene, with primitive lattice vectors (5.23), the primitive reciprocal lattice vectors (in the initial undeformed configuration) read as

$$\mathbf{b}_1^0 = \frac{2\pi}{c} \left(\frac{1}{\sqrt{3}} \, \mathbf{e}_Z + \frac{1}{3} \, \mathbf{e}_A \right) , \quad \mathbf{b}_2^0 = \frac{2\pi}{c} \left(-\frac{1}{\sqrt{3}} \, \mathbf{e}_Z + \frac{1}{3} \, \mathbf{e}_A \right) , \quad \mathbf{b}_3^0 = \frac{2\pi}{h} \, \mathbf{e}_T \, , \tag{5.35}$$
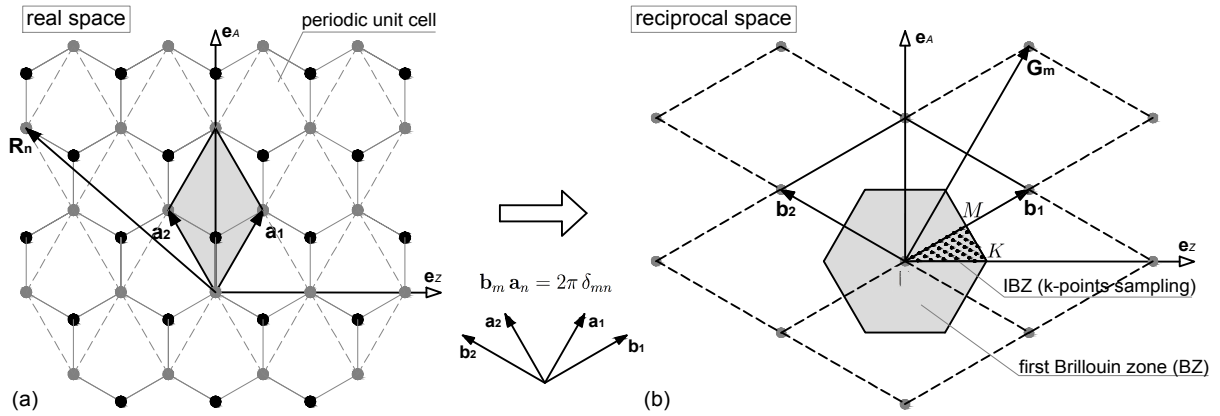
Fig. 5.3: Primitive unit cells in the graphene plane (spanned by base vectors $\mathbf{e}_Z$ and $\mathbf{e}_A$): (a) direct lattice generated by periodic rhomboid unit cell with primitive lattice vectors $\mathbf{a}_1$ and $\mathbf{a}_2$, and (b) reciprocal lattice generated by the first Brillouin zone (BZ) with primitive reciprocal lattice vectors $\mathbf{b}_1$, $\mathbf{b}_2$ and corresponding irreducible Brillouin zone (IBZ) characterized by high symmetry points Γ, M, K.

The electronic wavefunction on a periodic lattice can be conveniently written in terms of a Fourer series [Bloch, 1928]

$$\Phi_j(\mathbf{r}, \mathbf{k}) = \sum_m c_{jkm} \, \exp[i(\mathbf{k} + \mathbf{G}_m)\,\mathbf{r}] \,, \tag{5.36}$$

where wave vector $\mathbf{k}$ is regarded as a point in the reciprocal unit cell. For constructing the corresponding electronic density, we discretize the reciprocal space and employ the numerical integration scheme called *k-point sampling*, yielding

$$\rho^e(\mathbf{r}) = \sum_j^{N_e} \frac{1}{\Omega_{BZ}} \int_{\mathbf{k} \in BZ} \Phi_j^*(\mathbf{r}, \mathbf{k}) \, \Phi_j(\mathbf{r}, \mathbf{k}) \, d\mathbf{k} \approx \sum_j^{N_e} \sum_k^{N_k} w_k \, \Phi_{j,k}^*(\mathbf{r}) \, \Phi_{j,k}(\mathbf{r}) \,, \tag{5.37}$$

where w_k denotes the weighting factors for the chosen $\mathbf{k}$-points in the Brillouin zone (BZ), being associated with N_k wave vectors $\mathbf{k}_k$, $k = 1, 2, ..., N_k$; see Section 5.4.1 for further details. Substitution of (5.36) into (5.20) and considering the aforementioned k-point sampling yields the following set of generalized Kohn-Sham-Bloch eigenvalue problems for the first N_e eigenvalues

$$\left(-\frac{\hbar^2}{2\,m_e} \nabla^2 + V_{\mathrm{KS}}[\rho^e] \right) \Phi_{j,k}(\mathbf{r}) = \varepsilon_{j,k} \, \Phi_{j,k}(\mathbf{r}) \,,$$
$$j = 1, 2, ..., N_e \,, \quad k = 1, 2, ..., N_k \,, \tag{5.38}$$

with

$$\Phi_{j,k}(\mathbf{r}) = \sum_m c_{jkm} \, \exp[i(\mathbf{k}_k + \mathbf{G}_m)\,\mathbf{r}] \,. \tag{5.39}$$

The $(N_j \times N_k)$ eigenvalue problems (5.38)-(5.39), together with (5.37), are solved by means of (iterative) self-consistent field (SCF) cycles, see Fig. 5.4: From an initial guess for $\rho^e(\mathbf{r})$ and for a given $\mathbf{k}_k$, (5.38) provides a first estimate for the orbitals $\Phi_{j,k}$ following from the Fourier expansion coefficients c_{jkm} (5.39). The number of expansion coefficients is limited by a cut-off energy E_{cut}:

only those plane waves $|\mathbf{k}_k + \mathbf{G}_m|$ with a kinetic energy smaller than E_{cut} are included in the basis set

$$\frac{\hbar^2}{2m_e} |\mathbf{k}_k + \mathbf{G}_m|^2 < E_{cut} \,. \qquad (5.40)$$

Based on $\Phi_{j,k}$, we obtain a correspondingly updated estimate for $\rho^e(\mathbf{r})$ according to (5.37). The latter is used to re-evaluate V_{KS} (5.22), giving, via (5.38) and (5.39), access to further refined estimates for $\Phi_{j,k}$. This iterative process leads to estimates for $\rho^e(\mathbf{r})$, which converge to a solution for the electronic (probability) density field. The corresponding solution for the ground state

mix electronic densities
$\rho_{start}^{e,s+1}(\mathbf{r}) = f[\rho_{start}^{e,s}(\mathbf{r}), \rho_{new}^{e,s}(\mathbf{r})]$

start with initial electronic density
$\rho_{start}^{e,s}(\mathbf{r})$

no

compute output quantities ← yes — electronic density converged?

SCF cycles

calculate Kohn-Sham potential
$V_{KS} = f[\rho^e(\mathbf{r})]$

compute new electronic density
$\rho_{new}^{e,s}(\mathbf{r}) = \Sigma_j^{N_e} \Sigma_k^{N_k} w_k |\Phi_{j,k}(\mathbf{r})|^2$

solve Kohn-Sham equations
$\left(-\frac{\hbar^2}{2m}\nabla^2 + V_{KS}\right) \Phi_{j,k}(\mathbf{r}) = \varepsilon_{j,k} \, \Phi_{j,k}(\mathbf{r})$
$j = 1, 2, ..., N_e \quad k = 1, 2, ..., N_k$
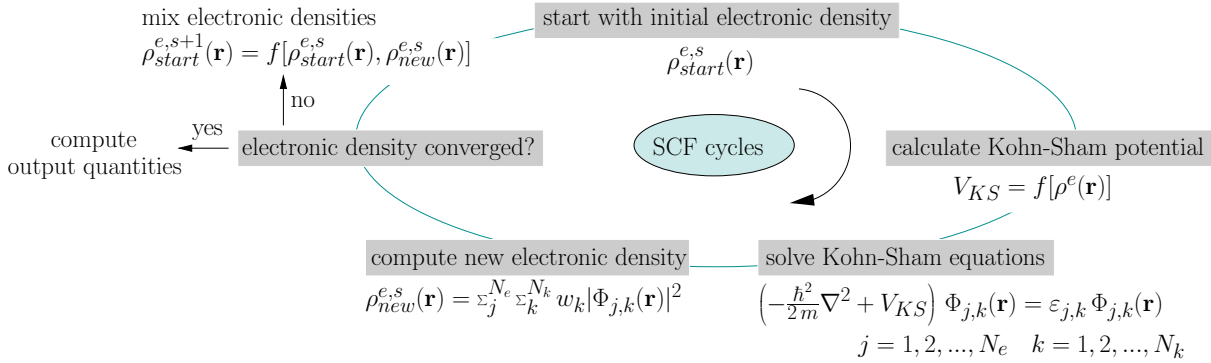
Fig. 5.4: Self-consistent field (SCF) cycles in DFT: Initial guess of the electronic density $\rho_{\mathrm{start}}^e(\mathbf{r})$ for calculating the Kohn-Sham potential V_{KS} and solving the Kohn-Sham equation for the one-electron wavefunction $\Phi_{j,k}(\mathbf{r})$. After computing $\rho_{new}^e(\mathbf{r})$, this process is repeated until convergence is reached.

energy can be related to the sum of the Kohn-Sham eigenenergies ε_j as follows: Multiplication of the Kohn-Sham equation (5.38) from the left with $\Phi_{j,k}^*$, integration over space, summation over the number of electrons N_e, and weighted summation over the N_k $\mathbf{k}_k$-points, while considering (5.13), (5.14), and (5.22), yields

$$T_{e,0}[\rho^e] = \sum_j^{N_e} \sum_k^{N_k} w_k \, \varepsilon_{j,k} - E_{ext}[\rho^e] - \int V_{xc}^{PBE}[\rho^e] \, \rho^e(\mathbf{r}) \, d\mathbf{r} - e^2 \iint \frac{\rho^e(\mathbf{r}) \, \rho^e(\mathbf{r}')}{|\mathbf{r} - \mathbf{r}'|} d\mathbf{r} \, d\mathbf{r}' \,. \quad (5.41)$$

Substitution of (5.41) into (5.17), finally delivers a more convenient form for calculating the internal energy at the ground state, reading as [Kohn and Sham, 1965]

$$\Psi[\rho^e] = \sum_j^{N_e} \sum_k^{N_k} w_k \, \varepsilon_{j,k} - E_H[\rho^e] + E_{xc}^{PBE}[\rho^e] - \int V_{xc}^{PBE}[\rho^e] \, \rho^e(\mathbf{r}) \, d\mathbf{r} \,. \quad (5.42)$$

We use the *Vienna Ab initio Simulation Package* (VASP, version 5.4.4) [Kresse and Hafner, 1993, 1994; Kresse and Furthmüller, 1996a,b] for all DFT calculations, using the following settings:

1. The convergence threshold for the self-consistency cycle of the Kohn-Sham equations in DFT (see Fig. 5.4) is set to 10^{-8} eV[1] for the electronic relaxation.

2. A conjugate gradient algorithm [Hestenes and Stiefel, 1952; Press et al., 1986] is used for ionic relaxation (i.e. the ions change their position for reaching an energy minimum), whereby the convergence threshold for the free energy change is set to 10^{-7} eV.

---

[1]Electronvolt eV is an empirical unit of energy equal to approximately 1.602×10^{-19} J, and is commonly used within atomic physics.

3. The Perdew-Burke-Ernzerhof (PBE) functional [Perdew et al., 1996, 1997] is chosen as exchange-correlation functional.

4. The projector-augmented wave (PAW) potentials [Blöchl, 1994; Kresse and Joubert, 1999] for the carbon ionic cores supplied with VASP are chosen.

5. The tetrahedron method with Blöchl corrections [Blöchl et al., 1994] is chosen for proper treatment of the occupancies around the Fermi energy, with the smearing width being set to 0.1 eV.

5.3 Continuum mechanical description of graphene

5.3.1 Deformation measure – Green-Lagrange strain tensor

Next, we convert the lattice vectors (5.28) from the DFT simulations into a strain field associated with the unit cell. As 2D strain measure, we choose the Green-Lagrange strain tensor $\mathbf{E}$ [Salençon, 2001; Fung and Tong, 2001]

$$\mathbf{E} = \frac{1}{2}\left[\frac{\partial \mathbf{u}}{\partial \mathbf{X}} + \left(\frac{\partial \mathbf{u}}{\partial \mathbf{X}}\right)^T + \left(\frac{\partial \mathbf{u}}{\partial \mathbf{X}}\right)^T \cdot \frac{\partial \mathbf{u}}{\partial \mathbf{X}}\right] = \sum_{k=1}^{2}\sum_{l=1}^{2} E_{kl}\,\mathbf{e}_k \otimes \mathbf{e}_l\,, \qquad (5.43)$$

where $\otimes$ denotes the dyadic product. This conversion is realized by means of two Finite Elements of the *constant strain triangle* (CST) type, see Fig. 5.5 for illustration of elements with height b^0 and width $2\,a^0$. According to the dimensions of the unit cell in the initial configuration [see (5.23) and Fig. 5.1(b)], the initial measures a^0 and b^0 are defined as

$$a^0 = \frac{\sqrt{3}}{2}\,c = a^0_{1,Z} = -a^0_{2,Z} \quad \text{and} \quad b^0 = \frac{3}{2}\,c = a^0_{1,A} = a^0_{2,A}\,. \qquad (5.44)$$

The 2D displacement field $\mathbf{u}(\mathbf{X})$ of one CST Finite Element is constructed from the displacements $\mathbf{u}^j$ of its three corner points j, with corresponding displacement vector components being collected into the mathematical vector $\mathbf{q}$. The aforementioned corner displacements can be directly related to the deformed and undeformed lattice vectors, through

$$\mathbf{u}^1 = 0\,, \quad \mathbf{u}^2 = \mathbf{a}_1 - \mathbf{a}^0_1\,, \quad \text{and} \quad \mathbf{u}^3 = \mathbf{a}_2 - \mathbf{a}^0_2\,, \qquad (5.45)$$

where we considered a fixed origin of the unit cell vectors in corner 1. In order to obtain a continuous displacement field over the entire CST Finite Element, we introduce a matrix of linear shape functions $\boldsymbol{\mathcal{N}}$:

$$\boldsymbol{\mathcal{N}} = \begin{bmatrix} \mathcal{N}_1 & 0 & \mathcal{N}_2 & 0 & \mathcal{N}_3 & 0 \\ 0 & \mathcal{N}_1 & 0 & \mathcal{N}_2 & 0 & \mathcal{N}_3 \end{bmatrix}\,. \qquad (5.46)$$

For the CST^I element, the components of the linear shape function matrix read as [Bathe and Wilson, 1976; Zienkiewicz and Taylor, 2000]

$$\mathcal{N}_1^I = 1 - \xi_1 - \xi_2\,, \quad \mathcal{N}_2^I = \xi_1\,, \quad \mathcal{N}_3^I = \xi_2\,, \qquad (5.47)$$

in natural coordinates (ξ_1 and ξ_2, see Fig. 5.6), and

$$\mathcal{N}_1^I \;=\; 1 - \frac{X_A}{b^0}\,,$$
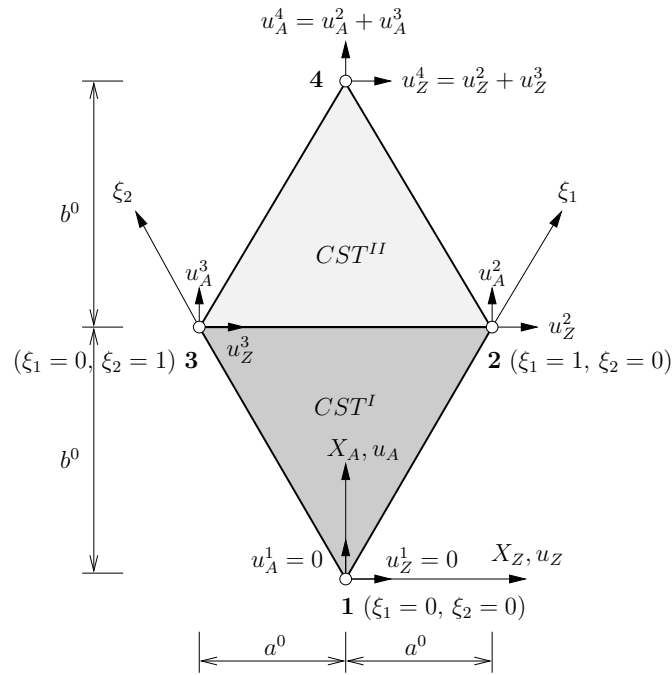
Fig. 5.5: Nodal corner displacements of the unit cell, consisting of two CST Finite Elements CST^I and CST^{II}.
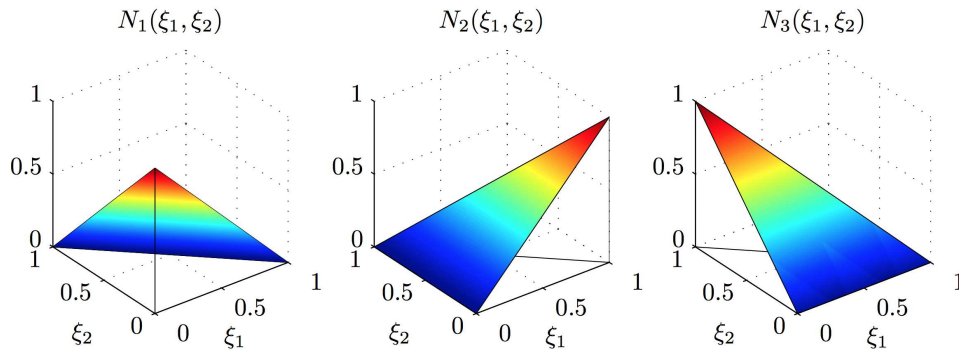
Fig. 5.6: Linear shape functions $\mathcal{N}_i$ in natural coordinates for CST Finite Elements.

$$
\begin{aligned}
\mathcal{N}_2^I &= \frac{1}{2}\left(\frac{X_Z}{a^0} + \frac{X_A}{b^0}\right), \\
\mathcal{N}_3^I &= \frac{1}{2}\left(\frac{X_A}{b^0} - \frac{X_Z}{a^0}\right),
\end{aligned}
\tag{5.48}
$$

in Cartesian coordinates, respectively. Therefore, focusing on Cartesian coordinates, while considering (5.45), the 2D displacement field $\mathbf{u}^I(\mathbf{X})$ of the CST^I element reads as

$$
\mathbf{u}^I(\mathbf{X}) = \boldsymbol{\mathcal{N}}^I(\mathbf{X}) \cdot \mathbf{q}^I =
\begin{bmatrix}
\mathcal{N}_1^I & 0 & \mathcal{N}_2^I & 0 & \mathcal{N}_3^I & 0 \\
0 & \mathcal{N}_1^I & 0 & \mathcal{N}_2^I & 0 & \mathcal{N}_3^I
\end{bmatrix}
\cdot
\begin{bmatrix}
0 \\
0 \\
a_{1,Z} - a^0 \\
a_{1,A} + a^0 \\
a_{2,Z} - b^0 \\
a_{2,A} - b^0
\end{bmatrix},
\tag{5.49}
$$

with the resulting component u_Z^I in $\mathbf{e}_Z$-direction reading as

$$u_Z^I = X_Z \left(\frac{a_{1,Z} - a_{2,Z}}{2\,a^0} - 1 \right) + X_A \left(\frac{a_{1,Z} + a_{2,Z}}{2\,b^0} \right), \tag{5.50}$$

and the component u_A^I in $\mathbf{e}_A$-direction reading as

$$u_A^I = X_Z \left(\frac{a_{1,A} - a_{2,A}}{2\,a^0} \right) + X_A \left(\frac{a_{1,A} + a_{2,A}}{2\,b^0} - 1 \right). \tag{5.51}$$

From this continuous displacement field, we determine the 2D Green-Lagrange strain tensor $\mathbf{E}$ according to (5.43), yielding the components

$$
\begin{aligned}
E_{ZZ}^I &= \frac{\partial u_Z^I}{\partial X_Z} + \frac{1}{2}\left[\left(\frac{\partial u_Z^I}{\partial X_Z}\right)^2 + \left(\frac{\partial u_A^I}{\partial X_Z}\right)^2\right] \\
&= \frac{a_{1,Z} - a_{2,Z}}{2\,a^0} - 1 + \frac{1}{2}\left[\left(\frac{a_{1,Z} - a_{2,Z}}{2\,a^0} - 1\right)^2 + \left(\frac{a_{1,A} - a_{2,A}}{2\,a^0}\right)^2\right],
\end{aligned}
\tag{5.52}
$$

$$
\begin{aligned}
E_{ZA}^I = E_{AZ}^I &= \frac{1}{2}\left[\frac{\partial u_Z^I}{\partial X_A} + \frac{\partial u_A^I}{\partial X_Z} + \frac{\partial u_Z^I}{\partial X_Z}\frac{\partial u_Z^I}{\partial X_A} + \frac{\partial u_A^I}{\partial X_Z}\frac{\partial u_A^I}{\partial X_A}\right] \\
&= \frac{1}{2}\left[\left(\frac{a_{1,Z} + a_{2,Z}}{2\,b^0}\right) + \left(\frac{a_{1,A} - a_{2,A}}{2\,a^0}\right)\right. \\
&\qquad \left. + \left(\frac{a_{1,Z} - a_{2,Z}}{2\,a^0} - 1\right)\left(\frac{a_{1,Z} + a_{2,Z}}{2\,b^0}\right) + \left(\frac{a_{1,A} - a_{2,A}}{2\,a^0}\right)\left(\frac{a_{1,2} + a_{2,A}}{2\,b^0} - 1\right)\right],
\end{aligned}
\tag{5.53}
$$

$$
\begin{aligned}
E_{AA}^I &= \frac{\partial u_A^I}{\partial X_A} + \frac{1}{2}\left[\left(\frac{\partial u_Z^I}{\partial X_A}\right)^2 + \left(\frac{\partial u_A^I}{\partial X_A}\right)^2\right] \\
&= \frac{a_{1,A} + a_{2,A}}{2\,b^0} - 1 + \frac{1}{2}\left[\left(\frac{a_{1,Z} + a_{2,Z}}{2\,b^0}\right)^2 + \left(\frac{a_{1,A} + a_{2,A}}{2\,b^0} - 1\right)^2\right].
\end{aligned}
\tag{5.54}
$$

Expectedly, we arrive at *constant* components of the Green-Lagrange strain tensor of the CST^I element, being independent of the position vector $\mathbf{X}$. Due to the *periodicity* requirement of the lattice, the displacements of the four corner points of the unit cell cannot be specified arbitrarily. In more detail, the opposite edges of the initial rhomboid unit cell must remain parallel during the cell's deformation. Hence, we obtain the following constraints for the displacements of the corner point 4

$$\mathbf{u}^4 = \mathbf{u}^2 + \mathbf{u}^3 = \mathbf{a}_1^0 - \mathbf{a}_1 + \mathbf{a}_2 - \mathbf{a}_2^0. \tag{5.55}$$

Considering these geometrical constraints on the displacements, the shape functions related to the CST^{II} element read as

$$
\begin{aligned}
\mathcal{N}_2^{II}(\mathbf{X}) &= \frac{1}{2}\left(\frac{X_Z}{a^0} - \frac{X_A}{b^0} + 2\right), \\
\mathcal{N}_3^{II}(\mathbf{X}) &= \frac{1}{2}\left(-\frac{X_Z}{a^0} - \frac{X_A}{b^0} + 2\right),
\end{aligned}
$$

$$\mathcal{N}_4^{II}(\mathbf{X}) \;=\; \frac{X_A}{b^0} - 1 \,, \tag{5.56}$$

with the corresponding displacement field reading as

$$\mathbf{u}^{II}(\mathbf{X}) = \boldsymbol{\mathcal{N}}^{II}(\mathbf{X}) \cdot \mathbf{q}^{II} = \begin{bmatrix} \mathcal{N}_1^{II} & 0 & \mathcal{N}_2^{II} & 0 & \mathcal{N}_3^{II} & 0 \\ 0 & \mathcal{N}_1^{II} & 0 & \mathcal{N}_2^{II} & 0 & \mathcal{N}_3^{II} \end{bmatrix} \cdot \begin{bmatrix} a_{1,Z} - a^0 \\ a_{1,A} + a^0 \\ a_{2,Z} - b^0 \\ a_{2,A} - b^0 \\ a_{1,Z} + a_{2,Z} \\ a_{1,A} + a_{2,A} - 2\,b^0 \end{bmatrix} . \tag{5.57}$$

Insertion of (5.56) into (5.57), and subsequent insertion of the corresponding result into (5.43) yields strain components which are identical to those given in (5.52)-(5.54). Hence, the entire unit cell is characterized by the homogeneous strain tensor components given in (5.52)-(5.54).

5.3.2 DFT-based hyperelastic potential

For large deformation studies of graphene, we here resort to the concept of hyperelasticity for anisotropic materials [Salençon, 2001; Truesdell and Noll, 1965; Rajagopal, 2011]: The specific free energy ψ_m (i.e. free energy per mass) is considered as a function of the Green-Lagrange strain tensor $\mathbf{E}$ and of the structural tensor $\mathbb{P}$

$$\psi_m = \Psi/m_{uc} = \psi_m(\mathbf{E}, \mathbb{P}) \,. \tag{5.58}$$

Thereby, Ψ is obtained from DFT-simulations associated with different strain states $\mathbf{E}$ whose principal directions deviate by different angles α_E from the zigzag and armchair directions, see Fig. 5.7 and Appendix A (5.A.4). The hexagonal lattice structure of graphene is reflected by a
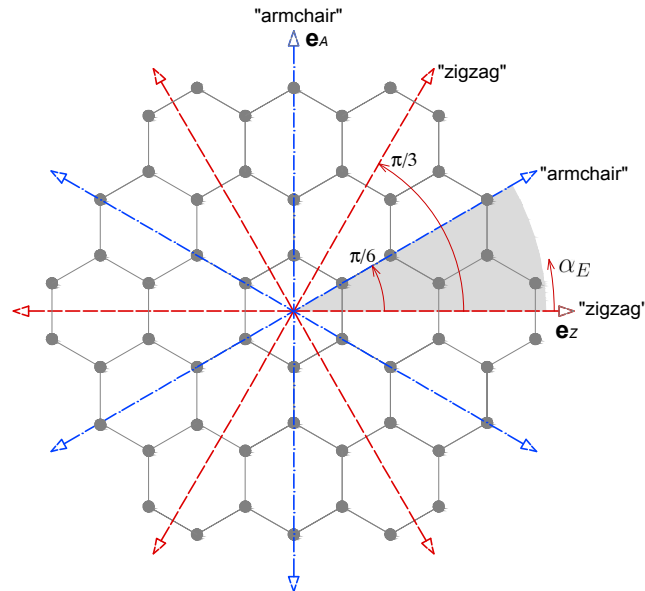
Fig. 5.7: Geometrical properties of symmetry and periodicity of the graphene honeycomb lattice: The full material behavior can be described by material directions between the zigzag and armchair direction (see shaded region).

sixth-order structural tensor of the form [Zheng, 1994; Zheng and Boehler, 1994]

$$
\begin{aligned}
\mathbb{P} &= \mathrm{Re}[(\mathbf{e}_Z + i\,\mathbf{e}_A) \otimes (\mathbf{e}_Z + i\,\mathbf{e}_A) \otimes (\mathbf{e}_Z + i\,\mathbf{e}_A) \otimes (\mathbf{e}_Z + i\,\mathbf{e}_A) \otimes (\mathbf{e}_Z + i\,\mathbf{e}_A) \otimes (\mathbf{e}_Z + i\,\mathbf{e}_A)] \\
&= \mathbf{M} \otimes \mathbf{M} \otimes \mathbf{M} - (\mathbf{M} \otimes \mathbf{N} \otimes \mathbf{N} + \mathbf{N} \otimes \mathbf{M} \otimes \mathbf{N} + \mathbf{N} \otimes \mathbf{N} \otimes \mathbf{M})\,,
\end{aligned} \tag{5.59}
$$

where we employed the following second-order tensors

$$
\mathbf{M} = \mathbf{e}_Z \otimes \mathbf{e}_Z - \mathbf{e}_A \otimes \mathbf{e}_A\,, \quad \mathbf{N} = \mathbf{e}_Z \otimes \mathbf{e}_A + \mathbf{e}_A \otimes \mathbf{e}_Z\,. \tag{5.60}
$$

The structural tensor is invariant under all orthogonal transformations $\mathbf{Q}$ forming the symmetry group SO of a hexagonal lattice [Zheng, 1994]

$$
\langle \mathbf{Q} \rangle\, \mathbb{P} = \mathbb{P} \quad \text{with} \quad (\langle \mathbf{Q} \rangle\, \mathbb{P})_{ijklmn} = Q_{io} Q_{jp} Q_{kq} Q_{lr} Q_{ms} Q_{nt} P_{opqrst}\,. \tag{5.61}
$$

Namely, graphene's SO group consists of tensors $\mathbf{Q}_{rot}$ associated with rotations $(n\,\pi/3)$ measured from the zigzag direction, and of tensors $\mathbf{Q}_{ref}$ associated with reflections about the zigzag and the armchair directions (see also Fig. 5.7)

$$
\forall\, n, l \in \mathbb{Z}: \; \mathbf{Q} \in SO =
$$
$$
= \left\{ \mathbf{Q}_{rot} = \begin{bmatrix} \cos(n\,\pi/3) & \sin(n\,\pi/3) \\ -\sin(n\,\pi/3) & \cos(n\,\pi/3) \end{bmatrix}, \; \mathbf{Q}_{ref} = \begin{bmatrix} \cos(l\,\pi/3) & \sin(l\,\pi/3) \\ \sin(l\,\pi/3) & -\cos(l\,\pi/3) \end{bmatrix} \right\}\,. \tag{5.62}
$$

Under all these rotations and reflections of the principal directions of the strain tensor, as well as of the point group defining the hexagonal lattice of graphene, the specific free energy remains invariant, according to

$$
\psi_m(\mathbf{E}, \mathbb{P}) = \psi_m(\mathbf{Q}^T\, \mathbf{E}\, \mathbf{Q}, \langle \mathbf{Q} \rangle\, \mathbb{P}) \quad \text{for} \quad \mathbf{Q} \in SO\,. \tag{5.63}
$$

Invariability requirement (5.63) can be met by making the free energy function dependent on three invariants

$$
\psi_m = \psi_m(I_1, I_3, I_3)\,, \tag{5.64}
$$

with these invariants reading as

$$
\begin{aligned}
I_1 &= \mathrm{tr}\mathbf{E} = E_{ZZ} + E_{AA}\,, \\
I_2 &= \frac{1}{2}\left[(\mathrm{tr}\mathbf{E})^2 - \mathrm{tr}\left(\mathbf{E}^2\right)\right] = E_{ZZ}\, E_{AA} - E_{ZA}^2\,, \\
I_3 &= [(\mathbb{P} : \mathbf{E}) : \mathbf{E}] : \mathbf{E} = (\mathbf{M} : \mathbf{E})^3 - 3(\mathbf{M} : \mathbf{E})(\mathbf{N} : \mathbf{E})^2 \\
&= E_{ZZ}^3 - 3\,E_{ZZ}^2 E_{AA} + 3\,E_{ZZ}\, E_{AA}^2 - E_{AA}^3 - 12\,E_{ZA}^2(E_{ZZ} - E_{AA})\,,
\end{aligned} \tag{5.65}
$$

where (:) denotes the second-order tensor contraction. In (5.65), I_1 and I_2 are isotropic principal invariants of the strain tensor, and the principal invariant I_3 takes into account the influence of the principal strain direction of $\mathbf{E}$ onto the mechanical response of graphene. In order to allow for higher order dependencies of the specific free energy on the components of the Green-Lagrange strain tensor $\mathbf{E}$, we construct a number of so-called main invariants, denoted by J_1 to J_{11}. Thereby, the first nine main invariants are associated with isotropic material behavior and hence with I_1 and I_2; they read as

$$
\begin{aligned}
I_1^2 - 2\,I_2 &= J_1 &= E_{ZZ}^2 + 2\,E_{ZA}^2 + E_{AA}^2\,, \\
I_1^3 - 3\,I_1\,I_2 &= J_2 &= E_{ZZ}^3 + 3\,E_{ZA}^2(E_{ZZ} + E_{AA}) + E_{AA}^3\,,
\end{aligned}
$$

$$
\begin{aligned}
I_1 I_2 = \quad J_3 \quad &= E_{ZZ}^2 E_{AA} - E_{ZA}^2 (E_{ZZ} + E_{AA}) + E_{ZZ} E_{AA}^2 \,, \\
I_1^4 - 4 I_1^2 I_2 + 2 I_2^2 = \quad J_4 \quad &= E_{ZZ}^4 + 4 E_{ZA}^2 (E_{ZZ}^2 + E_{ZZ} E_{AA} + E_{AA}^2) + E_{AA}^4 \,, \\
I_2^2 = \quad J_5 \quad &= E_{ZZ}^2 E_{AA}^2 - 2 E_{ZA}^2 E_{ZZ} E_{AA} + E_{ZA}^4 \,, \\
I_1^2 I_2 - 2 I_2^2 = \quad J_6 \quad &= E_{ZZ}^3 E_{AA} + E_{ZZ} E_{AA}^3 \\
&\quad + E_{ZA}^2 (2 E_{ZZ} E_{AA} - E_{ZZ}^2 - E_{AA}^2 - 2 E_{ZA}^2) \,, \\
I_1^5 - 5 I_1^3 I_2 + 5 I_1 I_2^2 = \quad J_7 \quad &= E_{ZZ}^5 + 5 E_{ZA}^4 (E_{ZZ} + E_{AA}) + E_{AA}^5 \\
&\quad + 5 E_{ZA}^2 (E_{ZZ}^3 + E_{ZZ}^2 E_{AA} + E_{ZZ} E_{AA}^2 + E_{AA}^3) \,, \\
I_1^3 I_2 - 3 I_1 I_2^2 = \quad J_8 \quad &= E_{ZZ}^4 E_{AA} - 3 E_{ZA}^4 (E_{ZZ} + E_{AA}) + E_{ZZ} E_{AA}^4 \\
&\quad - E_{ZA}^2 (E_{ZZ}^3 - 3 E_{ZZ}^2 E_{AA} - 3 E_{ZZ} E_{AA}^2 + E_{AA}^3) \,, \\
I_1 I_2^2 = \quad J_9 \quad &= E_{ZZ}^3 E_{AA}^2 + E_{ZA}^4 (E_{ZZ} + E_{AA}) + E_{ZZ}^2 E_{AA}^3 \\
&\quad - 2 E_{ZA}^2 (E_{ZZ}^2 E_{AA} + E_{ZZ} E_{AA}^2) \,,
\end{aligned}
\tag{5.66}
$$

and the last two main invariants are associated with anisotropic material behavior and hence they involve I_3 as well,

$$
\begin{aligned}
I_3 I_1 = \quad J_{10} \quad &= E_{ZZ}^4 - 2 E_{ZZ}^3 E_{AA} + 3 E_{ZZ} E_{AA}^3 - E_{AA}^4 \\
&\quad - 12 E_{ZA}^2 (E_{ZZ}^2 - E_{AA}^2), \\
I_3 \left(I_1^2 - 2 I_2 \right) = \quad J_{11} \quad &= E_{ZZ}^5 - 3 E_{ZZ}^4 E_{AA} + 4 E_{ZZ}^3 E_{AA}^2 - 4 E_{ZZ}^2 E_{AA}^3 \\
&\quad + 3 E_{ZZ} E_{AA}^4 - E_{AA}^5 - 14 E_{ZA}^2 (E_{ZZ}^3 - E_{AA}^3) \\
&\quad + 18 E_{ZA}^2 (E_{ZZ}^2 E_{AA} - E_{ZZ} E_{AA}^2) \\
&\quad + 24 E_{ZA}^4 (E_{ZZ} - E_{AA}).
\end{aligned}
\tag{5.67}
$$

Finally, the principal and main invariants (5.65)-(5.67) allow for constructing a hyperelastic function of the specific free energy in the format

$$
\begin{aligned}
\psi_m(I_1, I_3, I_3) \quad = \quad & c_1 I_1 + c_2 I_2 + c_3 I_3 \\
& + c_4 J_1 + c_5 J_2 + c_6 J_3 + c_7 J_4 + + c_8 J_5 \\
& + c_9 J_6 + c_{10} J_7 + c_{11} J_8 + c_{12} J_9 + c_{13} J_{10} + c_{14} J_{11} \,,
\end{aligned}
\tag{5.68}
$$

where c_1-c_{14} are polynomial fitting coefficients (dimension energy per unit mass) determined by DFT.

5.3.3 Lagrangian stress-strain relations, tangent elasticity tensor, and stability limits

The specific free energy of graphene readily gives access to the material behavior in terms of mechanical stresses, via the zero dissipation requirement of elasticity, which in Lagrangian representation reads as

$$
\phi = \boldsymbol{\pi} : \dot{\mathbf{E}} - \rho_{m,0}^{2D} \, \dot{\psi}_m = 0 \,, \qquad \text{with} \qquad \dot{\psi}_m = \frac{\partial \psi_m}{\partial \mathbf{E}} : \dot{\mathbf{E}} = 0 \,.
\tag{5.69}
$$

In (5.69), we explicitly consider the "real" two-dimensionality of graphene, by introducing the initial areal mass density as $\rho_{m,0}^{2D} = m_{uc}/A_0$, the areal dissipation ϕ (i.e. energy per area per time which is irreversibly lost for potential mechanical work), and the areal second Piola-Kirchhoff

tensor $\boldsymbol{\pi}$ (with dimension "force over length"). Validity of (5.69) for any time rates $\dot{\mathbf{E}}$ delivers the 2D material law of hyperelasticity in the format:

$$\boldsymbol{\pi} = \rho_{m,0}^{2D} \, \frac{\partial \psi_m}{\partial \mathbf{E}}(I_1, I_2, I_3) = \rho_{m,0}^{2D} \sum_{k=1}^{3} \frac{\partial \psi_m}{\partial I_k} \cdot \frac{\partial I_k}{\partial \mathbf{E}} \,, \tag{5.70}$$

Hence, considering the derivatives of the principal invariants with respect to the Green-Lagrange strain tensor,

$$\begin{aligned}
\frac{\partial I_1}{\partial \mathbf{E}} &= \mathbf{1} \,, \\
\frac{\partial I_2}{\partial \mathbf{E}} &= I_1 \, \mathbf{1} - \mathbf{E} \,, \\
\frac{\partial I_3}{\partial \mathbf{E}} &= \mathbf{S} \quad \text{with} \quad \mathbf{S} = 3 \left[(\mathbf{M} : \mathbf{E})^2 - (\mathbf{N} : \mathbf{E})^2 \right] \mathbf{M} - 6 \left[(\mathbf{M} : \mathbf{E})(\mathbf{N} : \mathbf{E}) \right] \mathbf{N} \,,
\end{aligned} \tag{5.71}$$

results in the expression for the 2D second Piola-Kirchhoff stress tensor

$$\boldsymbol{\pi} = \rho_{m,0}^{2D} \left[\beta_1 \, \mathbf{1} + \beta_2 \, \mathbf{E} + \beta_3 \, \mathbf{S} \right] \,, \tag{5.72}$$

with

$$\begin{aligned}
\beta_1 &= c_1 + c_2 \, I_1 - 3 \, c_5 \, I_2 + c_6 \left(I_1^2 + I_2 \right) - 4 \, c_7 \, I_1 \, I_2 + 2 \, c_8 \, I_1 \, I_2 + c_9 \left(I_1^3 - 2 \, I_1 \, I_2 \right) \\
&\quad + 5 \, c_{10} \left(I_2^2 - I_1^2 \, I_2 \right) + c_{11} \left(I_1^4 - 3 \, I_2^2 - 3 \, I_1^2 \, I_2 \right) + c_{12} \left(I_2^2 + 2 \, I_1^2 \, I_2 \right) + c_{13} I_3 \,, \\
\beta_2 &= -c_2 + 2 \, c_4 + 3 \, c_5 \, I_1 - c_6 \, I_1 + 4 \, c_7 \left(I_1^2 - I_2 \right) - 2 \, c_8 \, I_2 + c_9 \left(4 \, I_2 - I_1^2 \right) \\
&\quad + 5 \, c_{10} \left(I_1^3 - 2 \, I_1 \, I_2 \right) + c_{11} \left(6 \, I_1 \, I_2 - I_1^3 \right) - 2 \, c_{12} \, I_1 \, I_2 + 2 \, c_{14} \, I_3 \,, \\
\beta_3 &= c_3 + c_{13} \, I_1 + c_{14} \left(I_1^2 - 2 \, I_2 \right) \,,
\end{aligned} \tag{5.73}$$

where $\mathbf{1}$ is the second-order unit tensor and c_1-c_{14} are DFT-based polynomial fitting coefficients also appearing in (5.68). As unstrained graphene relates to zero stresses, we readily see that $c_1 = 0$. The components of (5.72) with respect to base frame $\mathbf{e}_Z$-$\mathbf{e}_A$, $\boldsymbol{\pi} = \sum_{i=Z,A} \sum_{j=Z,A} \pi_{ij} \, \mathbf{e}_i \otimes \mathbf{e}_j$, read as

$$\begin{aligned}
\pi_{ZZ} &= \rho_{m,0}^{2D} \left[\beta_1 + \beta_2 \, E_{ZZ} + \beta_3 \, S_{ZZ} \right] \,, \\
\pi_{ZA} = \pi_{AZ} &= \rho_{m,0}^{2D} \left[\beta_1 + \beta_2 \, E_{ZA} + \beta_3 \, S_{ZA} \right] \,, \\
\pi_{AA} &= \rho_{m,0}^{2D} \left[\beta_1 + \beta_2 \, E_{AA} + \beta_3 \, S_{AA} \right] \,,
\end{aligned} \tag{5.74}$$

with

$$\begin{aligned}
S_{ZZ} &= 3 \left(E_{ZZ} - E_{AA} \right)^2 - 12 \, E_{ZA}^2 \,, \\
S_{ZA} &= 12 \, E_{ZA} \left(E_{AA} - E_{ZZ} \right) \,, \\
S_{AA} &= -3 \left(E_{ZZ} - E_{AA} \right)^2 + 12 \, E_{ZA}^2 \,.
\end{aligned} \tag{5.75}$$

In general, the principal directions of the strain tensor $\mathbf{E}$ and of the stress tensor $\boldsymbol{\pi}$ do not coincide. This can be seen from writing Eq.(5.72) in terms of components with respect to

base frame $\mathbf{e}_1^E$-$\mathbf{e}_2^E$, $\boldsymbol{\pi} = \sum_{i=1}^2 \sum_{j=1}^2 \pi_{ij}^E \, \mathbf{e}_i^E \otimes \mathbf{e}_j^E$, see (5.A.3), (5.A.7), and (5.A.8) in Appendix A, yielding

$$
\begin{aligned}
\pi_{11}^E &= \rho_{m,0}^{2D} \left[\beta_1 + \beta_2 \, E_\mathrm{I} + 3 \, \beta_3 \, (E_\mathrm{I} - E_\mathrm{II})^2 \cos(6\alpha_E) \right], \\
\pi_{12}^E = \pi_{21}^E &= -3 \, \rho_{m,0}^{2D} \, \beta_3 \, (E_\mathrm{I} - E_\mathrm{II})^2 \sin(6\alpha_E), \\
\pi_{22}^E &= \rho_{m,0}^{2D} \left[\beta_1 + \beta_2 \, E_\mathrm{II} - 3 \, \beta_3 \, (E_\mathrm{I} - E_\mathrm{II})^2 \cos(6\alpha_E) \right].
\end{aligned}
\tag{5.76}
$$

According to $(5.76)_2$, the shear components π_{12}^E only vanish if the principal strain directions coincide with the zigzag direction $\mathbf{e}_Z$ or the armchair direction $\mathbf{e}_A$; i.e. for $\alpha_E = n\,\pi/6 \ \forall\, n \in \mathbb{Z}$. Only then, the principal directions of strain and stress coincide. In general, the angle between base vectors $\mathbf{e}_Z$ and $\mathbf{e}_1^\pi$ follows from

$$
\alpha_\pi = \alpha_E + \frac{1}{2} \left[\tan^{-1} \left(\frac{-6 \, \beta_3 \, (E_\mathrm{I} - E_\mathrm{II})^2 \sin(6\alpha_E)}{\beta_2 \, (E_\mathrm{I} - E_\mathrm{II}) + 6 \, \beta_3 (E_\mathrm{I} - E_\mathrm{II})^2 \cos(6\alpha_E)} \right) \right].
\tag{5.77}
$$

whereby α_E is the angle between $\mathbf{e}_Z$ and $\mathbf{e}_1^E$.

Stress increments follow from derivation of (5.72),

$$
d\boldsymbol{\pi} = \mathbb{C} : d\mathbf{E},
\tag{5.78}
$$

with the tangent elasticity tensor being defined as

$$
\mathbb{C} = \frac{\partial \boldsymbol{\pi}}{\partial \mathbf{E}} (I_1, I_2, I_3) = \rho_{m,0}^{2D} \frac{\partial^2 \psi_m}{\partial \mathbf{E} \, \partial \mathbf{E}} (I_1, I_2, I_3).
\tag{5.79}
$$

Use of the derivatives of the principal invariants (5.71) as well as

$$
\begin{aligned}
\frac{\partial \mathbf{E}}{\partial \mathbf{E}} &= \mathbb{I}, \\
\frac{\partial^2 I_3}{\partial \mathbf{E} \, \partial \mathbf{E}} = \frac{\partial \mathbf{S}}{\partial \mathbf{E}} &= \mathbb{S} \quad \text{with} \quad \mathbb{S} = 6 \left[(\mathbf{M} : \mathbf{E}) \, \mathbf{M} \otimes \mathbf{M} - (\mathbf{N} : \mathbf{E}) \, \mathbf{M} \otimes \mathbf{N} \right. \\
&\qquad\qquad \left. - (\mathbf{N} : \mathbf{E}) \, \mathbf{N} \otimes \mathbf{M} - (\mathbf{M} : \mathbf{E}) \, \mathbf{N} \otimes \mathbf{N} \right],
\end{aligned}
\tag{5.80}
$$

yields the expression for the tangent elasticity tensor in the format

$$
\begin{aligned}
\mathbb{C} &= \rho_{m,0}^{2D} \left[\gamma_1 \, \mathbb{I} + \gamma_2 \, (\mathbf{1} \otimes \mathbf{1}) + \gamma_3 \, (\mathbf{1} \otimes \mathbf{E} + \mathbf{E} \otimes \mathbf{1}) + \gamma_4 \, (\mathbf{E} \otimes \mathbf{E}) \right. \\
&\qquad \left. + \gamma_5 \, (\mathbf{1} \otimes \mathbf{S} + \mathbf{S} \otimes \mathbf{1}) + \gamma_6 \, (\mathbf{E} \otimes \mathbf{S} + \mathbf{S} \otimes \mathbf{E}) + \gamma_7 \, \mathbb{S} \right],
\end{aligned}
\tag{5.81}
$$

with

$$
\begin{aligned}
\gamma_1 &= -c_2 + 2\,c_4 + 3\,c_5 \, I_1 - c_6 \, I_1 + 4\,c_7 \left(I_1^2 - I_2 \right) - 2\,c_8 \, I_2 + c_9 \left(4\,I_2 - I_1^2 \right) \\
&\quad + 5\,c_{10} \left(I_1^3 - 2\,I_1 \, I_2 \right) + c_{11} \left(6\,I_1 \, I_2 - I_1^3 \right) - 2\,c_{12} \, I_1 \, I_2 + 2\,c_{14} \, I_3 = \beta_2, \\
\gamma_2 &= c_2 - 3\,c_5 \, I_1 + 3\,c_6 \, I_1 - 4\,c_7 \left(I_1^2 + I_2 \right) + 2\,c_8 \left(I_1^2 + I_2 \right) + c_9 \left(I_1^2 - 2\,I_2 \right) \\
&\quad - 5\,c_{10} \, I_1^3 + c_{11} \left(I_1^3 - 12\,I_1 \, I_2 \right) + c_{12} \left(6\,I_1 \, I_2 + 2\,I_1^3 \right), \\
\gamma_3 &= 3\,c_5 - c_6 + 4\,c_7 \, I_1 - 2\,c_8 \, I_1 + 2\,c_9 \, I_1 + \\
&\quad + 5\,c_{10} \left(I_1^2 - 2\,I_2 \right) + 3\,c_{11} \left(I_1^2 + 2\,I_2 \right) - 2\,c_{12} \left(I_1^2 + I_2 \right),
\end{aligned}
$$

$$\gamma_4 = 4\,c_7 + 2\,c_8 - 4\,c_9 + 10\,c_{10}\,I_1 - 6\,c_{11}\,I_1 + 2\,c_{12}\,I_1\,,$$

$$\gamma_5 = c_{13}\,,$$

$$\gamma_6 = 2\,c_{14}\,,$$

$$\gamma_7 = c_3 + c_{13}\,I_1 + c_{14}\left(I_1^2 - 2\,I_2\right) = \beta_3\,, \tag{5.82}$$

where $\mathbb{I} = 1/2\left[\delta_{ik}\delta_{jl} + \delta_{il}\delta_{jk}\right]\mathbf{e}_i \otimes \mathbf{e}_j \otimes \mathbf{e}_k \otimes \mathbf{e}_l$ is the symmetric fourth-order unit tensor, with δ_{mn} denoting the Kronecker delta ($\delta_{mn} = 1$ if $m = n$ and $\delta_{mn} = 0$ if $m \neq n$). It is noted, that the components of the elasticity tensor are *not constant*, but depend on the current strain state, i.e. on the components of the Green-Lagrange strain tensor. Since we consider large deformations, stress-strain relations are highly non-linear, in turn resulting in non-linear components of the elasticity tensor as function of the Green-Lagrange strain tensor. The components of (5.81) with respect to base frame $\mathbf{e}_1^E$-$\mathbf{e}_2^E$, $\mathbb{C} = \sum_{i=1}^2 \sum_{j=1}^2 \sum_{k=1}^2 \sum_{l=1}^2 C_{ijkl}^E\,\mathbf{e}_i^E \otimes \mathbf{e}_j^E \otimes \mathbf{e}_k^E \otimes \mathbf{e}_l^E$, see (5.A.3), (5.A.7)-(5.A.10) in Appendix A, read as

$$\begin{aligned}
C_{1111}^E &= \rho_{m,0}^{2D}\Big[\gamma_1 + \gamma_2 + 2\,\gamma_3\,E_\mathrm{I} + \gamma_4\,E_\mathrm{I}^2 + 6\,(\gamma_5 + \gamma_6\,E_\mathrm{I})(E_\mathrm{I} - E_\mathrm{II})^2\cos(6\alpha_E) \\
&\quad + 6\,\gamma_7\,(E_\mathrm{I} - E_\mathrm{II})\cos(6\alpha_E)\Big]\,, \\
C_{2222}^E &= \rho_{m,0}^{2D}\Big[\gamma_1 + \gamma_2 + 2\,\gamma_3\,E_\mathrm{II} + \gamma_4\,E_\mathrm{II}^2 - 6\,(\gamma_5 + \gamma_6\,E_\mathrm{II})(E_\mathrm{I} - E_\mathrm{II})^2\cos(6\alpha_E) \\
&\quad + 6\,\gamma_7\,(E_\mathrm{I} - E_\mathrm{II})\cos(6\alpha_E)\Big]\,, \\
C_{1122}^E &= \rho_{m,0}^{2D}\Big[\gamma_2 + \gamma_3\,(E_\mathrm{I} + E_\mathrm{II}) + \gamma_4\,E_\mathrm{I}\,E_\mathrm{II} - 3\,\gamma_6\,(E_\mathrm{I} - E_\mathrm{II})^3\cos(6\alpha_E) \\
&\quad - 6\,\gamma_7\,(E_\mathrm{I} - E_\mathrm{II})\cos(6\alpha_E)\Big] \quad = \quad C_{2211}^E\,, \\
C_{1112}^E &= \rho_{m,0}^{2D}\Big[-3\,(\gamma_5 + \gamma_6\,E_\mathrm{I})(E_\mathrm{I} - E_\mathrm{II})^2\sin(6\alpha_E) \\
&\quad - 6\,\gamma_7\,(E_\mathrm{I} - E_\mathrm{II})\sin(6\alpha_E)\Big] \quad = \quad C_{1121}^E = C_{1211}^E = C_{2111}^E\,, \\
C_{2212}^E &= \rho_{m,0}^{2D}\Big[-3\,(\gamma_5 + \gamma_6\,E_\mathrm{II})(E_\mathrm{I} - E_\mathrm{II})^2\sin(6\alpha_E) \\
&\quad + 6\,\gamma_7\,(E_\mathrm{I} - E_\mathrm{II})\sin(6\alpha_E)\Big] \quad = \quad C_{1222}^E = C_{2122}^E = C_{2221}^E\,, \\
C_{1212}^E &= \rho_{m,0}^{2D}\big[1/2\,\gamma_1 - 6\,\gamma_7\,(E_\mathrm{I} - E_\mathrm{II})\cos(6\alpha_E)\big] \quad = \quad C_{2112}^E = C_{2121}^E = C_{1221}^E\,. \tag{5.83}
\end{aligned}$$

The elastic behavior is stable, as long as $\mathbb{C}$ is positive definite, implying that the determinant of $\mathbb{C}$, as well as all sub-determinants are positive. Once the determinant or any of the sub-determinants of $\mathbb{C}$ become zero, the stability limit is reached [Born, 1940; Hill and Milstein, 1977; Mouhat and Coudert, 2014]. Mathematically, these determinants read as

$$\begin{aligned}
\det\mathbb{C} &= +2\,C_{1111}^E\,C_{2222}^E\,C_{1212}^E + 2\,C_{1122}^E\,C_{2212}^E\,C_{1211}^E + 2\,C_{1112}^E\,C_{2211}^E\,C_{1222}^E \\
&\quad -2\,C_{1112}^E\,C_{2222}^E\,C_{1211}^E - 2\,C_{1122}^E\,C_{2211}^E\,C_{1212}^E - 2\,C_{1111}^E\,C_{2212}^E\,C_{1222}^E \\
&= 0\,, \tag{5.84}
\end{aligned}$$

and

$$\det\mathbb{C}^{*,1} = C_{1111}^E\,C_{2222}^E - C_{1122}^E\,C_{2211}^E = 0\,, \qquad \det\mathbb{C}^{*,2} = C_{1111}^E = 0\,, \tag{5.85}$$

where $\mathbb{C}^{*,j}$ are principal minors (determinants of the submatrices of $\mathbb{C}^{*,j}$ starting from the upper-left matrix corner). For principal strain directions in zigzag direction $\mathbf{e}_Z$ or armchair direction $\mathbf{e}_Z$, Eq. (5.84) reduces to $(5.85)_1$. Substitution of (5.83) into (5.84) and (5.85) yields

the following elastic stability limits of graphene, as function of the principal strains and the angle α_E between $\mathbf{e}_Z$ and $\mathbf{e}_1^E$,

$$
\begin{aligned}
&\big[\gamma_1 + \gamma_2 + 2\,\gamma_3\,E_\mathrm{I} + \gamma_4\,E_\mathrm{I}^2 + 6\,(\gamma_5 + \gamma_6\,E_\mathrm{I})(E_\mathrm{I} - E_\mathrm{II})^2 \cos(6\alpha_E) + 6\,\gamma_7\,(E_\mathrm{I} - E_\mathrm{II})\cos(6\alpha_E)\big] \times \\
&\times \big[\gamma_1 + \gamma_2 + 2\,\gamma_3\,E_\mathrm{II} + \gamma_4\,E_\mathrm{II}^2 - 6\,(\gamma_5 + \gamma_6\,E_\mathrm{II})(E_\mathrm{I} - E_\mathrm{II})^2 \cos(6\alpha_E) + 6\,\gamma_7\,(E_\mathrm{I} - E_\mathrm{II})\cos(6\alpha_E)\big] \times \\
&\times [1/2\,\gamma_1 - 6\,\gamma_7\,(E_\mathrm{I} - E_\mathrm{II})\cos(6\alpha_E)] \\
&+ \big[\gamma_2 + \gamma_3\,(E_\mathrm{I} + E_\mathrm{II}) + \gamma_4\,E_\mathrm{I}\,E_\mathrm{II} - 3\,\gamma_6\,(E_\mathrm{I} - E_\mathrm{II})^3 \cos(6\alpha_E) - 6\,\gamma_7\,(E_\mathrm{I} - E_\mathrm{II})\cos(6\alpha_E)\big] \times \\
&\times \big[-3\,(\gamma_5 + \gamma_6\,E_\mathrm{II})(E_\mathrm{I} - E_\mathrm{II})^2 \sin(6\alpha_E) + 6\,\gamma_7\,(E_\mathrm{I} - E_\mathrm{II})\sin(6\alpha_E)\big] \times \\
&\times \big[-3\,(\gamma_5 + \gamma_6\,E_\mathrm{I})(E_\mathrm{I} - E_\mathrm{II})^2 \sin(6\alpha_E) - 6\,\gamma_7\,(E_\mathrm{I} - E_\mathrm{II})\sin(6\alpha_E)\big] \\
&+ \big[-3\,(\gamma_5 + \gamma_6\,E_\mathrm{I})(E_\mathrm{I} - E_\mathrm{II})^2 \sin(6\alpha_E) - 6\,\gamma_7\,(E_\mathrm{I} - E_\mathrm{II})\sin(6\alpha_E)\big] \times \\
&\times \big[\gamma_2 + \gamma_3\,(E_\mathrm{I} + E_\mathrm{II}) + \gamma_4\,E_\mathrm{I}\,E_\mathrm{II} - 3\,\gamma_6\,(E_\mathrm{I} - E_\mathrm{II})^3 \cos(6\alpha_E) - 6\,\gamma_7\,(E_\mathrm{I} - E_\mathrm{II})\cos(6\alpha_E)\big] \times \\
&\times \big[-3\,(\gamma_5 + \gamma_6\,E_\mathrm{II})(E_\mathrm{I} - E_\mathrm{II})^2 \sin(6\alpha_E) + 6\,\gamma_7\,(E_\mathrm{I} - E_\mathrm{II})\sin(6\alpha_E)\big] \\
&- \big[-3\,(\gamma_5 + \gamma_6\,E_\mathrm{I})(E_\mathrm{I} - E_\mathrm{II})^2 \sin(6\alpha_E) - 6\,\gamma_7\,(E_\mathrm{I} - E_\mathrm{II})\sin(6\alpha_E)\big]^2 \times \\
&\times \big[\gamma_1 + \gamma_2 + 2\,\gamma_3\,E_\mathrm{II} + \gamma_4\,E_\mathrm{II}^2 - 6\,(\gamma_5 + \gamma_6\,E_\mathrm{II})(E_\mathrm{I} - E_\mathrm{II})^2 \cos(6\alpha_E) + 6\,\gamma_7\,(E_\mathrm{I} - E_\mathrm{II})\cos(6\alpha_E)\big] \\
&- \big[\gamma_2 + \gamma_3\,(E_\mathrm{I} + E_\mathrm{II}) + \gamma_4\,E_\mathrm{I}\,E_\mathrm{II} - 3\,\gamma_6\,(E_\mathrm{I} - E_\mathrm{II})^3 \cos(6\alpha_E) - 6\,\gamma_7\,(E_\mathrm{I} - E_\mathrm{II})\cos(6\alpha_E)\big]^2 \times \\
&\times [1/2\,\gamma_1 - 6\,\gamma_7\,(E_\mathrm{I} - E_\mathrm{II})\cos(6\alpha_E)] \\
&- \big[\gamma_1 + \gamma_2 + 2\,\gamma_3\,E_\mathrm{I} + \gamma_4\,E_\mathrm{I}^2 + 6\,(\gamma_5 + \gamma_6\,E_\mathrm{I})(E_\mathrm{I} - E_\mathrm{II})^2 \cos(6\alpha_E) + 6\,\gamma_7\,(E_\mathrm{I} - E_\mathrm{II})\cos(6\alpha_E)\big] \times \\
&\times \big[-3\,(\gamma_5 + \gamma_6\,E_\mathrm{II})(E_\mathrm{I} - E_\mathrm{II})^2 \sin(6\alpha_E) + 6\,\gamma_7\,(E_\mathrm{I} - E_\mathrm{II})\sin(6\alpha_E)\big]^2 \\
&= 0\,,
\end{aligned}
\tag{5.86}
$$

$$
\begin{aligned}
&\big[\gamma_1 + \gamma_2 + 2\,\gamma_3\,E_\mathrm{I} + \gamma_4\,E_\mathrm{I}^2 + 6\,(\gamma_5 + \gamma_6\,E_\mathrm{I})(E_\mathrm{I} - E_\mathrm{II})^2 \cos(6\alpha_E) + 6\,\gamma_7\,(E_\mathrm{I} - E_\mathrm{II})\cos(6\alpha_E)\big] \times \\
&\times \big[\gamma_1 + \gamma_2 + 2\,\gamma_3\,E_\mathrm{II} + \gamma_4\,E_\mathrm{II}^2 - 6\,(\gamma_5 + \gamma_6\,E_\mathrm{II})(E_\mathrm{I} - E_\mathrm{II})^2 \cos(6\alpha_E) + 6\,\gamma_7\,(E_\mathrm{I} - E_\mathrm{II})\cos(6\alpha_E)\big] \\
&- \big[\gamma_2 + \gamma_3\,(E_\mathrm{I} + E_\mathrm{II}) + \gamma_4\,E_\mathrm{I}\,E_\mathrm{II} - 3\,\gamma_6\,(E_\mathrm{I} - E_\mathrm{II})^3 \cos(6\alpha_E) - 6\,\gamma_7\,(E_\mathrm{I} - E_\mathrm{II})\cos(6\alpha_E)\big]^2 \\
&= 0\,,
\end{aligned}
\tag{5.87}
$$

$$
\begin{aligned}
&\big[\gamma_1 + \gamma_2 + 2\,\gamma_3\,E_\mathrm{I} + \gamma_4\,E_\mathrm{I}^2 + 6\,(\gamma_5 + \gamma_6\,E_\mathrm{I})(E_\mathrm{I} - E_\mathrm{II})^2 \cos(6\alpha_E) + 6\,\gamma_7\,(E_\mathrm{I} - E_\mathrm{II})\cos(6\alpha_E)\big] \\
&= 0\,.
\end{aligned}
\tag{5.88}
$$

Alternatively, the elasticity of graphene can be quantified in terms of Eulerian quantities, i.e in measures associated with the current (deformed) configurations, such as the Cauchy stress tensor and the logarithmic strain tensor, see Appendix B.

5.3.4 Poisson effects

The Poisson effect is traditionally defined in linear isotropic elasticity, where uniaxial stress leads to a multi-dimensional, shear strain-free deformation state characterized by Poisson's ratio ν [Greaves et al., 2011], according to

$$
\pi_\mathrm{II} = \rho_{m,0}^{2D}\,\frac{\partial \psi_m}{\partial E_\mathrm{II}} = 0 \quad \Rightarrow \quad \nu = -\frac{E_\mathrm{II}}{E_\mathrm{I}}\,.
\tag{5.89}
$$

In this isotropic case, the principal directions of stress and strain coincide; and this coincidence is encountered with graphene only in very special circumstances, namely for infinitesimally small strains, or for finite strains with the principal directions coinciding with the zigzag- and the armchair directions, see (5.76).

Hence, we need to extend the notion of the Poisson effect beyond this application regime, and we do so by regarding $(5.89)_1$ as an energy minimization problem, looking for a minimum

of ψ_m as a function of E_{II}, with E_{I} being fixed. Corresponding specification of the invariants (5.65)-(5.67) for base frame $\mathbf{e}_1^E$-$\mathbf{e}_2^E$ (see (5.A.5)-(5.A.6) in Appendix A) and variation of the specific free energy (5.68) with respect to the transverse strain $E_{\mathrm{II},min}$, delivers the following formula for the sought transverse strains:

$$
\begin{aligned}
\frac{\partial \psi_m}{\partial E_{\mathrm{II}}} \;=\;\; & c_1 + c_2\, E_{\mathrm{I}} + c_6\, E_{\mathrm{I}}^2 + c_9\, E_{\mathrm{I}}^3 + c_{11}\, E_{\mathrm{I}}^4 - (3\, c_3\, E_{\mathrm{I}}^2 + 2\, c_{13}\, E_{\mathrm{I}}^3 + 3\, c_{14}\, E_{\mathrm{I}}^4) \cos(6\alpha_E) \\[4pt]
& + E_{\mathrm{II},min} \left[2\, c_4 + 2\, c_6\, E_{\mathrm{I}} + 2\, c_8\, E_{\mathrm{I}}^2 + 2\, c_{12}\, E_{\mathrm{I}}^3 (6\, c_3\, E_{\mathrm{I}} + 8\, c_{14}\, E_{\mathrm{I}}^3) \cos(6\alpha_E) \right] \\[4pt]
& + E_{\mathrm{II},min}^2 \left[3\, c_5 + 3\, c_9 E_{\mathrm{I}} + 3\, c_{12} E_{\mathrm{I}}^2 - (3\, c_3 - 6\, c_{13}\, E_{\mathrm{I}} + 12\, c_{14}\, E_{\mathrm{I}}^2) \cos(6\alpha_E) \right] \\[4pt]
& + E_{\mathrm{II},min}^3 \left[4\, c_7 + 4\, c_{11}\, E_{\mathrm{I}} - (4\, c_{13} - 12\, c_{14}\, E_{\mathrm{I}}) \cos(6\alpha_E) \right] \\[4pt]
& + E_{\mathrm{II},min}^4 \left[5\, c_{10} - 5\, c_{14}\, \cos(6\alpha_E) \right] = 0\,.
\end{aligned}
\tag{5.90}
$$

The calculated Poisson's ratio type quantity for large deformations is denoted as ν^*

$$
\nu^* = -\frac{E_{\mathrm{II},min}}{E_{\mathrm{I}}}\,.
\tag{5.91}
$$

5.4 Results

5.4.1 Convergence studies of DFT-simulations

When using VASP along with the described computational DFT-settings in Sec. 5.2.2, the free energy of an undeformed graphene unit cell can be regarded as converged once a cut-off energy E_{cut} of 400 eV (5.40), and a $25 \times 25 \times 1$ Monkhorst-Pack grid [Monkhorst and Pack, 1976] according to (5.37) are chosen, see Fig. 5.8. The converged free energy is set to zero, in accordance with (5.68). Corresponding energy minimization for determination of the lattice constant of
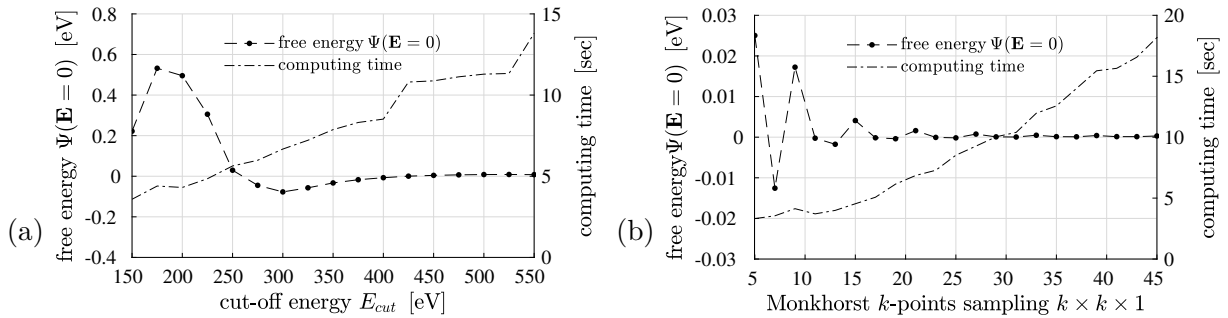
Fig. 5.8: Convergence study and related computing time (running on the Vienna Scientific Cluster [VSC3, 2014] with 2×INTEL Xeon E5-2650v2 CPUs (2.6 GHz, 8 cores) and 128 GB RAM) of the free energy $\Psi(\mathbf{E} = 0)$ for an undeformed graphene unit cell, as function of (a) the cut-off energy E_{cut}, and of (b) the Monkhorst-Pack k-points sampling.

graphene yields, $c = 0.1425\,\mathrm{nm} = 1.425\,\text{Å}^2$, see Fig. 5.9.

For a strained graphene unit cell, we obtain the same convergence thresholds. However, due to the need for ionic relaxation and the lack of symmetries, the computational effort increases compared to the unstrained case, see Fig. 5.10.

---

[2]Angstrom Å is a unit of length, with $1\,\text{Å} = 1 \times 10^{-10}\,\mathrm{m}$ often used for expressing sizes at the atomic scale.
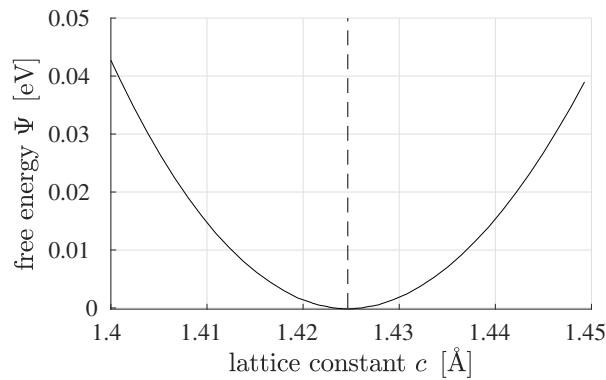
Fig. 5.9: Lattice constant for an undeformed hexagonal graphene lattice according to (5.23), obtained by DFT-energy minimization.
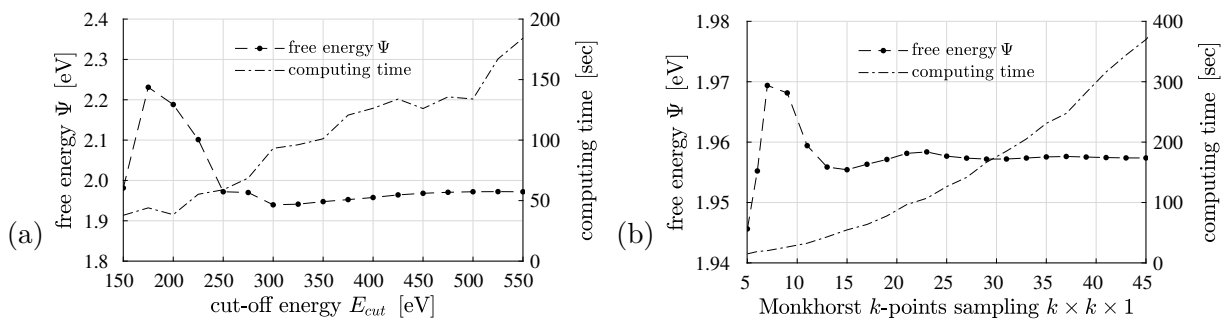
Fig. 5.10: Convergence study and related computing time (running on the Vienna Scientific Cluster [VSC3, 2014] with 2×INTEL Xeon E5-2650v2 CPUs (2.6 GHz, 8 cores) and 128 GB RAM) of the free energy Ψ for a strained graphene unit cell ($E_{\mathrm{I}} = 0.22$, $E_{\mathrm{II}} = -0.095$, $\alpha_E = \pi/9$), as function of (a) the cut-off energy E_{cut}, and of (b) the Monkhorst k-points sampling.

5.4.2 Energy landscapes of graphene under general deformations – DFT fitting coefficients

18207 VASP-based simulations according to Section 5.2.2, for principal strains E_{I} and E_{II} ranging from -0.14 to 0.28 and for loading angles α_E ranging from 0 to $\pi/6$, provide the energy landscapes depicted in Fig. 5.11. It can be observed that the energy levels obviously depend on the principal strain directions with respect to the material directions $\mathbf{e}_Z$ ("zigzag") and $\mathbf{e}_A$ ("armchair"), in particular so for "shear-type" loading where $E_{\mathrm{I}} \approx -E_{\mathrm{II}}$ (compare energy values associated with left upper and right lower corners of Figs. 5.11(b)-(h)). This shear-driven anisotropy effect is also reflected in the energy-strain diagrams of Fig. 5.12; showing 4.6% material direction-dependent energy difference under uniaxial strain states versus 12.5% under shear strain states.

Fitting the aforementioned landscapes by a polynomial of fifth order as given in (5.68) yields the coefficients given in Tab. 5.1. Thereby, the maximum difference between VASP-derived and fitted energy levels is always less than 1%. When prescribing the same maximum error level, a fourth-order polynomial with the fitted coefficients given Tab. 5.2 allows for representation of the energy landscape for principal strains ranging from -0.03 to 0.28. In the same sense, a third-order polynomial (see Tab. 5.3 for correspondingly fitted coefficients) allows for representation of the energy landscape for principal strains ranging from -0.02 to 0.07; and a second-order polynomial with $c_2 = 0.8556$ eV/u and $c_4 = 2.4175$ eV/u, which actually represents isotropic linear elastic
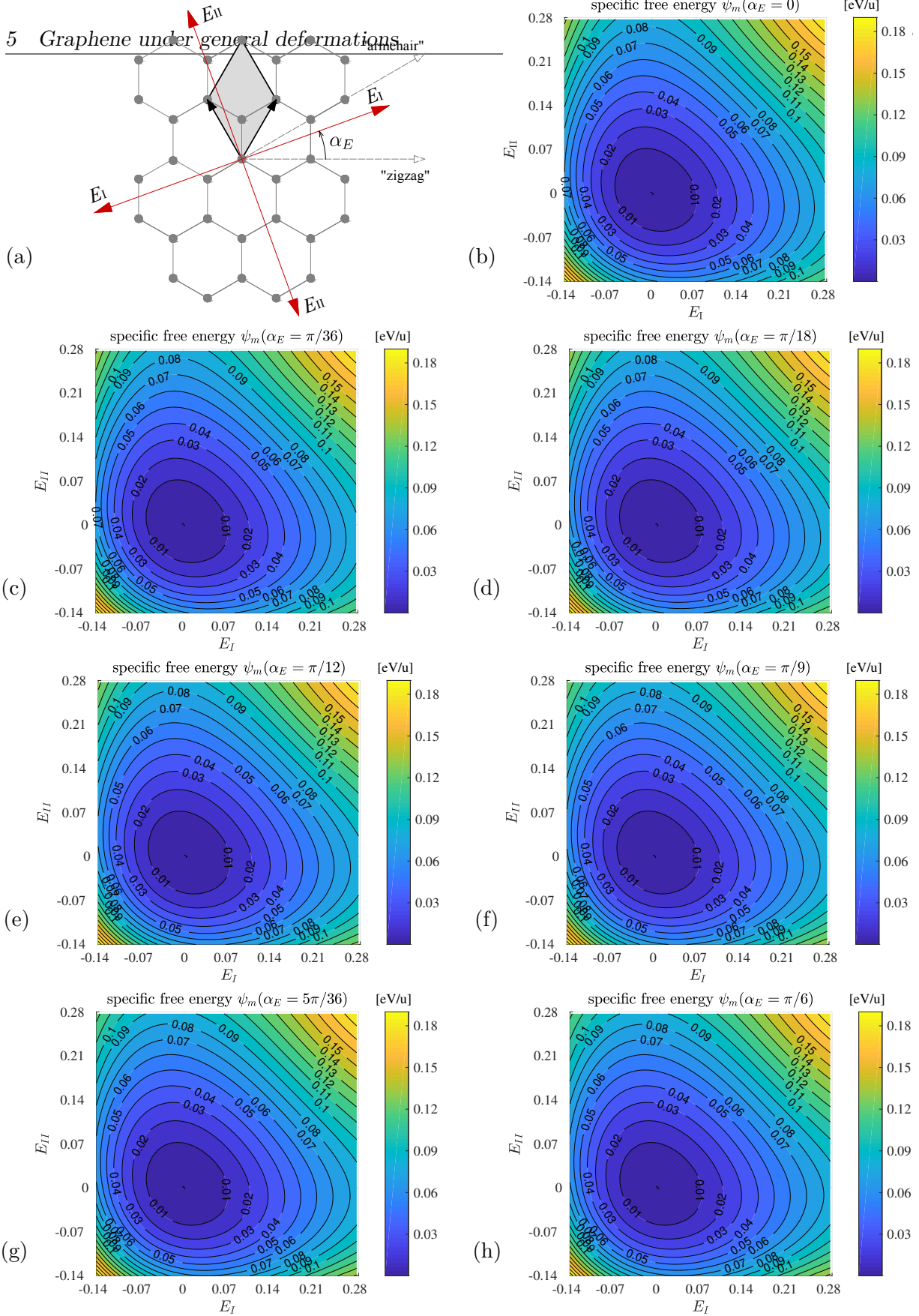
Fig. 5.11: DFT-results of the specific free energy ψ_m for suspended graphene as function of biaxial principle Green-Lagrange strains E_{I} and E_{II} with corresponding directions $\alpha_E = \{0, \frac{\pi}{36}, \frac{\pi}{18}, \frac{\pi}{12}, \frac{\pi}{9}, \frac{5\pi}{36}, \frac{\pi}{6}\}$.
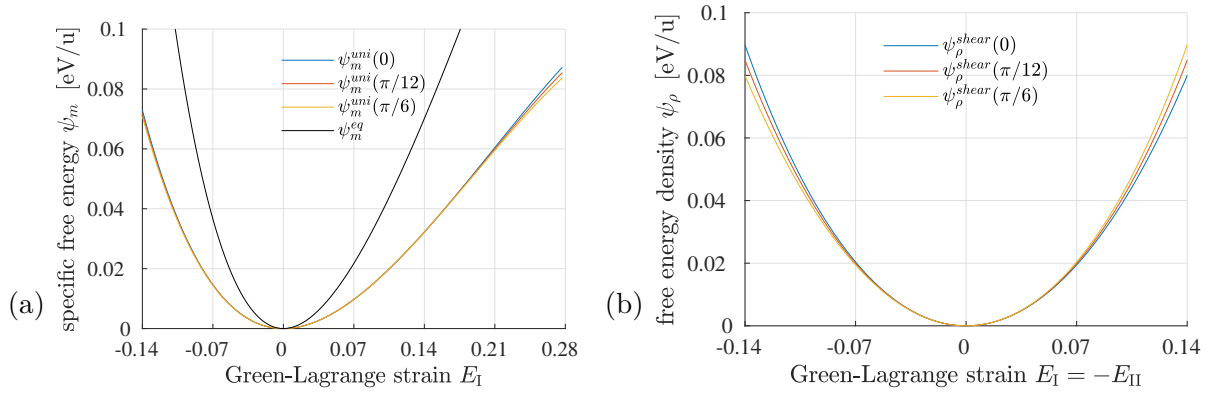
Fig. 5.12: Fitted specific free energy ψ_m for various principal strain directions $\alpha_E = \{0, \frac{\pi}{12}, \frac{\pi}{6}\}$, arising from (a) uniaxial ($E_{\mathrm{II}} = 0$) and equi-biaxial ($E_{\mathrm{I}} = E_{\mathrm{II}}$) strain states, and (b) shear strain states ($E_{\mathrm{I}} = -E_{\mathrm{II}}$).

Tab. 5.1: Fitting coefficients c_1-c_{14} of the specific free energy in form of a polynomial of fifth order, valid for a Green-Lagrange strain-range between -0.14 and +0.28; physical unit of the coefficients [eV/u].

c_1	c_2	c_3	c_4	c_5	c_6	c_7
0	0.8556	-0.1546	2.4175	-6.9294	-3.7008	12.1361

c_8	c_9	c_{10}	c_{11}	c_{12}	c_{13}	c_{14}
11.6114	9.05715	-14.8505	-10.9763	-9.6888	1.3425	-1.7422

Tab. 5.2: Fitting coefficients c_1-c_{14} of the specific free energy in form of a polynomial of fourth order, valid for a Green-Lagrange strain-range between -0.03 and +0.28; physical unit of the coefficients [eV/u].

c_1	c_2	c_3	c_4	c_5	c_6	c_7
0	0.8556	-0.2188	2.4175	-6.2698	-2.7062	5.7182

c_8	c_9	c_{10}	c_{11}	c_{12}	c_{13}	c_{14}
8.01272	1.7379	0	0	0	1.1773	0

material behavior, is sufficient, in the sense of the aforementioned 1% error, for principal strains ranging from -0.007 to 0.007. In turn, the aforementioned polynomials of lower order are only valid for the corresponding strain-range – otherwise the differences compared to the DFT-based results amount to 131 % for a polynomial of second order, 109 % for a polynomial of third order, and 13 % for a polynomial of fourth order, when applied for large strain regions.

Also Poisson's ratio ν^* according to (5.90) and (5.91) depends on the loading angle α_E (between zigzag direction and the direction of principlal strain E_{I}), as can be seen in Fig. 5.13. Only for infinitesimally small strains, the values of the Poisson *function* ν^* reach the classical Poisson's ratio of graphene, $\nu^*(\mathbf{E} \to 0) = \nu = 0.176954$.

Tab. 5.3: Fitting coefficients c_1-c_{14} of the specific free energy in form of a polynomial of third order, valid for a Green-Lagrange strain-range between -0.02 and +0.07; physical unit of the coefficients [eV/u].

c_1	c_2	c_3	c_4	c_5	c_6	c_7
0	0.8556	-0.1507	2.4175	-6.0597	-2.7913	0

c_8	c_9	c_{10}	c_{11}	c_{12}	c_{13}	c_{14}
0	0	0	0	0	0	0
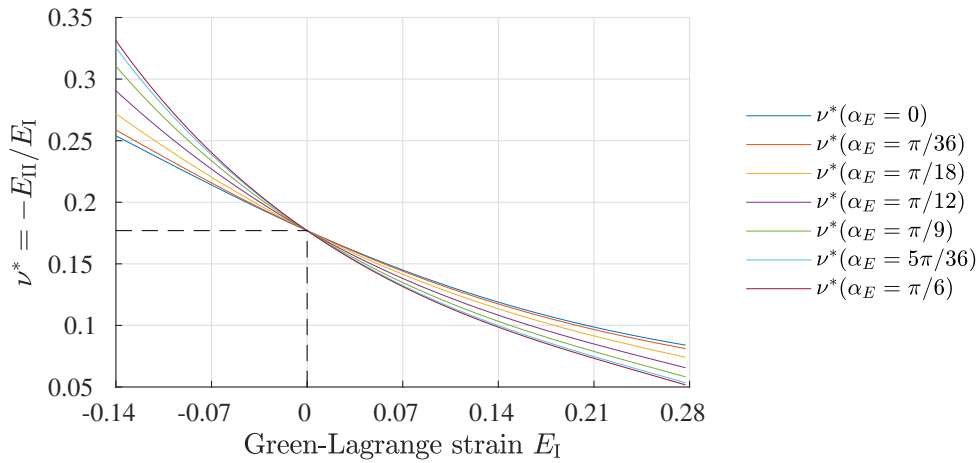
Fig. 5.13: Ratio ν^* of the negative energy-minimizing transverse strain E_{II} to the longitudinal engineering strain E_{I} according to (5.90) and (5.91), evaluated for various principal strain directions $\alpha_E = \{0, \frac{\pi}{36}, \frac{\pi}{18}, \frac{\pi}{12}, \frac{\pi}{9}, \frac{5\pi}{36}, \frac{\pi}{6}\}$.

5.4.3 Stress-strain relations and corresponding elasticity tensor

Knowing the stress components of $\boldsymbol{\pi}$ as function of the strain tensor $\mathbf{E}$, we can provide general *nonlinear stress-strain relations* of these energetic-conjugate quantities. This is shown for the normal stress components π_{11}^E and π_{22}^E (with respect to base vectors $\mathbf{e}_1^E$ and $\mathbf{e}_2^E$) for various principal strain directions $\alpha_E = \{0, \frac{\pi}{18}, \frac{\pi}{9}, \frac{\pi}{6}\}$, see Figs. 5.14 and 5.15. Maximum differences between results in zigzag and armchair direction amount to 35 % for π_{11}^E and 25 % for π_{22}^E. The discussed deviation of the principal strain direction of $\mathbf{E}$ and the principal stress direction of $\boldsymbol{\pi}$ (see Sec. 5.3.3) can be illustrated by the shear components π_{12}^E (with respect to base vectors $\mathbf{e}_1^E$ and $\mathbf{e}_2^E$), see Fig. 5.16. Obviously, only principal strains in graphene's zigzag and armchair direction result in vanishing shear stresses, indicating the same principal strain and stress directions.

Furthermore, the relations of the energetic-conjugate pair of Cauchy stresses and logarithmic strains of Appendix B, (5.B.11)-(5.B.12), are exemplarily shown for general principal strain states in graphene's zigzag direction, with respect to base vectors $\mathbf{e}_1^E$ and $\mathbf{e}_2^E$, see Fig. 5.17. It is clearly seen that the stress-strain landscapes of the energetic-conjugate measures $\boldsymbol{\pi}$ and $\mathbf{E}$ (see Figs. 5.14 and 5.15) and the energetic-conjugate measures $\boldsymbol{\sigma}$ and $\boldsymbol{\epsilon}^{ln}$ (see Fig. 5.17) are different in shape and magnitude, while both do show the anisotropic behavior of graphene.

The corresponding tangent modulus of Lagrangian stress-strain relations (5.72), namely the derived elasticity tensor (5.81) is evaluated for various principal strain directions α_E, once more demonstrating the strong anisotropic behavior of graphene in large strain regions. The components of the elasticity tensor C_{1111}^E, C_{2222}^E, and C_{1122}^E (with respect to base vectors $\mathbf{e}_1^E$
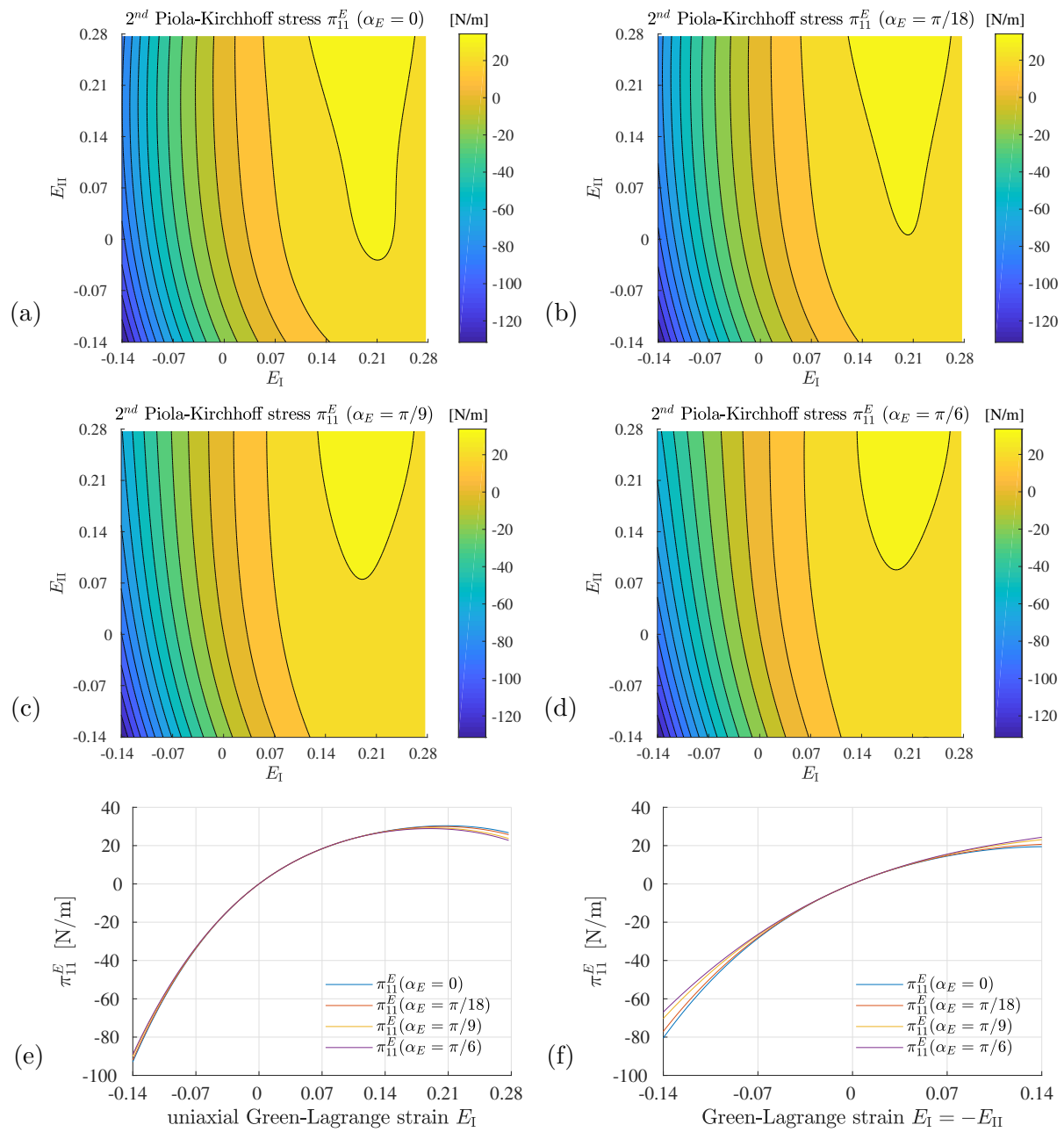
Fig. 5.14: Second Piola-Kirchhoff stresses π_{11}^E (with respect to base vectors $\mathbf{e}_1^E$ and $\mathbf{e}_2^E$) of suspended graphene for various principal strain directions $\alpha_E = \{0, \frac{\pi}{18}, \frac{\pi}{9}, \frac{\pi}{6}\}$: (a)-(d) general principle strain states, (e) uniaxial strain states ($E_{\mathrm{II}} = 0$), and (f) shear strain states ($E_{\mathrm{I}} = -E_{\mathrm{II}}$).

and $\mathbf{e}_2^E$) are again exemplarily shown for principal strain directions $\alpha_E = \{0, \frac{\pi}{18}, \frac{\pi}{9}, \frac{\pi}{6}\}$, see Figs. 5.18-5.20. Maximum differences between results in zigzag and armchair direction amount to 36 % for C_{1111}^E, 56 % for C_{2222}^E, and 175 % for C_{1122}^E.

The components of the elasticity tensor (as exemplarily shown in Figs. 5.18-5.20) are further used for predicting elastic stability limits of graphene. The limits given by Eqs. (5.86), (5.87), and (5.88), are indicated by red, blue and green curves in Fig. 5.21; while grey area relates to values of E_{I} and E_{II} where all three determinants given in (5.86)-(5.88) are positive, i.e. to
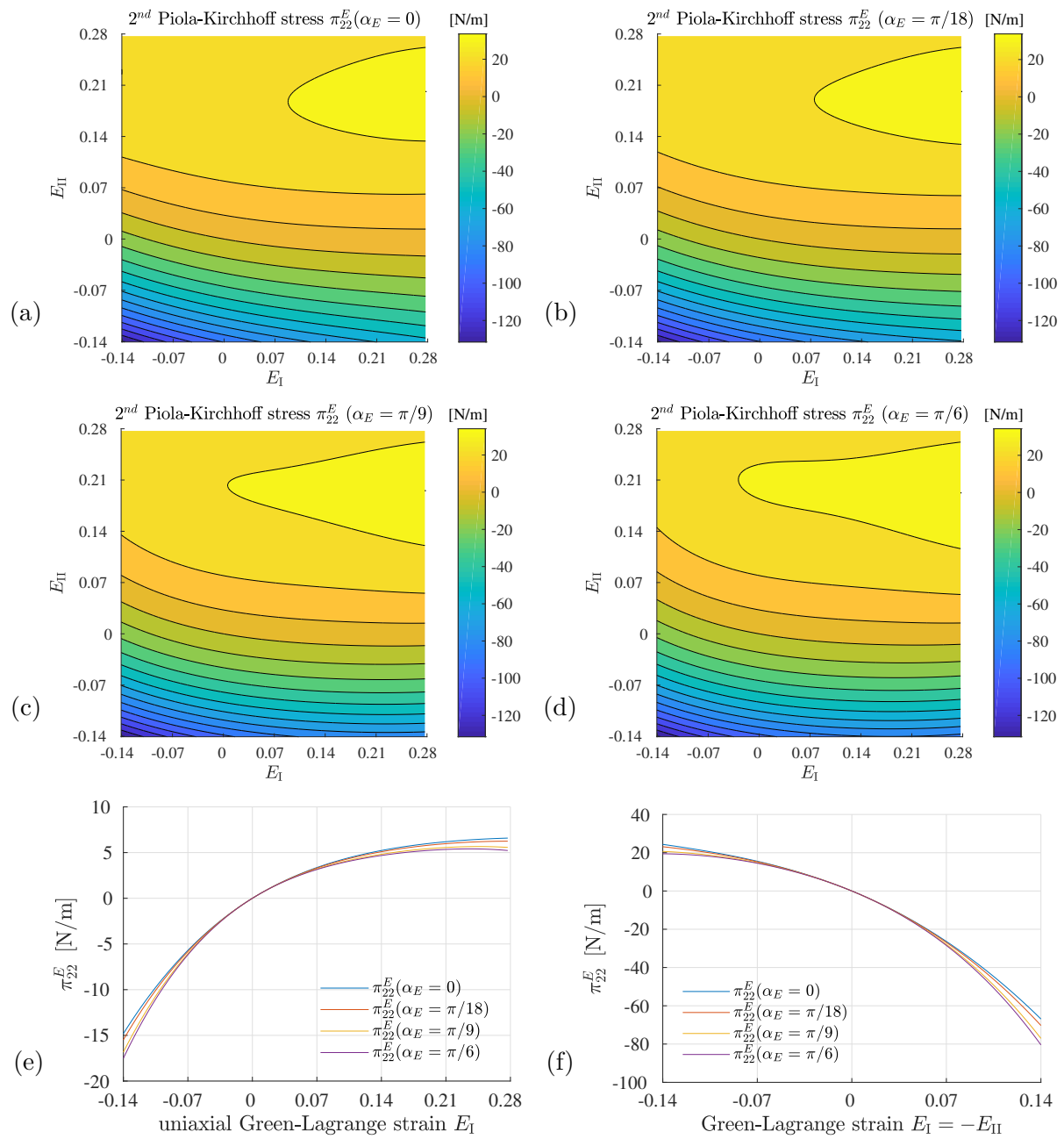
Fig. 5.15: Second Piola-Kirchhoff stress π_{22}^E (with respect to base vectors $\mathbf{e}_1^E$ and $\mathbf{e}_2^E$)) of suspended graphene for various principal strain directions $\alpha_E = \{0, \frac{\pi}{18}, \frac{\pi}{9}, \frac{\pi}{6}\}$: (a)-(d) general principle strain states, (e) uniaxial strain states ($E_{\mathrm{II}} = 0$), and (f) shear strain states ($E_{\mathrm{I}} = -E_{\mathrm{II}}$).

strains under which the material is stable. We observe that the "larger" determinants (red, green) provide quasi-identical stability limits, while the "smaller" determinant (blue) cuts off a physically meaningless mirror image provided by the "larger" determinants.

As discussed for the Poisson effect, graphene is only isotropic in the case of infinitesimal small strains, $\mathbf{E} \to 0$, resulting in components of the elasticity tensor, $C_{1111,0} = C_{2222,0} = 2\,\rho_{m,0}^{2D}\,c_4$ and $C_{1122,0} = C_{2211,0} = \rho_{m,0}^{2D}\,c_2$, which can be used for obtaining 2D isotropic elastic constants of graphene: Taking into account the definitions of the polynomial fitting coefficients c_2 and c_4
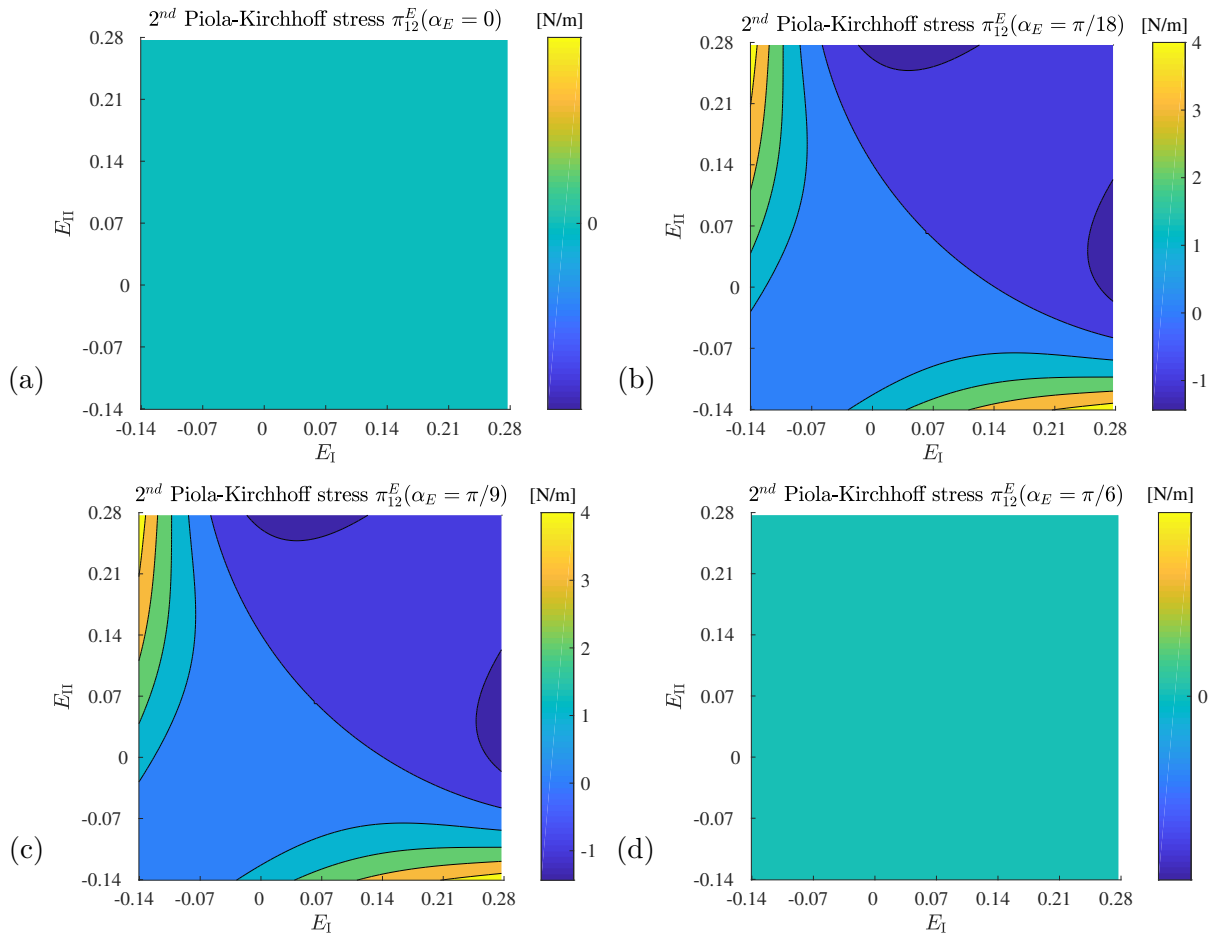
Fig. 5.16: Second Piola-Kirchhoff stresses π_{12}^E (with respect to base vectors $\mathbf{e}_1^E$ and $\mathbf{e}_2^E$) of suspended graphene for various principal strain directions $\alpha_E = \{0, \frac{\pi}{18}, \frac{\pi}{9}, \frac{\pi}{6}\}$: (a)-(d) general principle strain states, indicating that principal strain and stress directions only coincide for material directions $\alpha_E = \{0, \frac{\pi}{6}\}$.

(Tab. 5.1) and the initial area mass density $\rho_{A,0} = m_{uc}/A_0 = 4.555\,\mathrm{u/\mathring{A}}^2$, yields the following elastic constants, namely the elastic Young's modulus (dimension force per unit length)

$$Y^{2D} = C_{1111,0} - \frac{C_{1122,0}^2}{C_{1111,0}} = \rho_{m,0}^{2D}\left(2\,c_4 - \frac{c_2^2}{2\,c_4}\right) = 21.336\,\mathrm{eV/\mathring{A}}^2 = 341.84\,\mathrm{N/m}\,, \tag{5.92}$$

and the in-plane Poisson's ratio

$$\nu = \frac{C_{1122,0}}{C_{1111,0}} = \frac{c_2}{2\,c_4} = 0.176954\,, \tag{5.93}$$

where the latter is in full agreement with the observed investigations of the energy-minimizing Poisson-effect, see Fig. 5.13. These constants can then be used to obtain related elastic constants, namely the 2D shear modulus (Lamé's second parameter)

$$G^{2D} = \frac{E}{2(1+\nu)} = 9.064\,\mathrm{eV/\mathring{A}}^2 = 145.22\,\mathrm{N/m}\,, \tag{5.94}$$
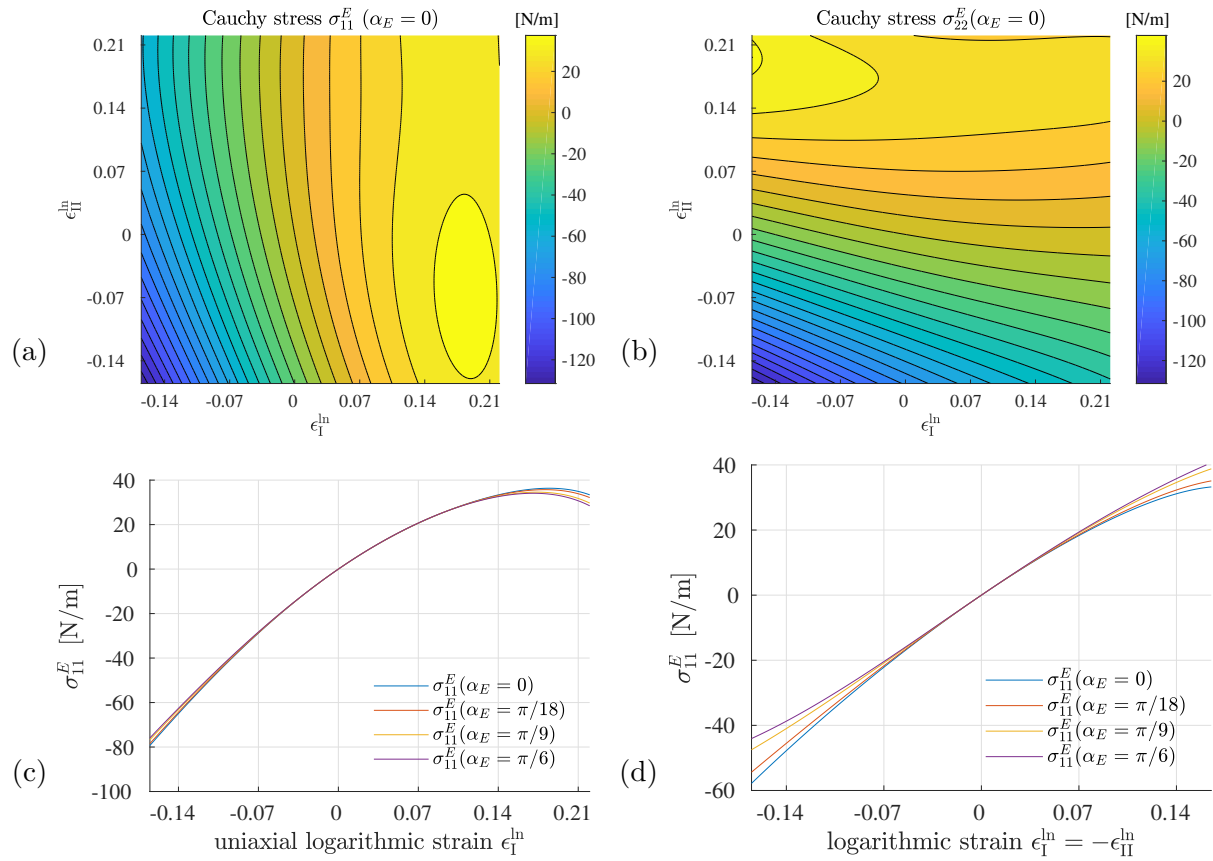
Fig. 5.17: Cauchy stresses (with respect to base vectors $\mathbf{e}_1^E$ and $\mathbf{e}_2^E$) of suspended graphene for various principal strain directions: (a)-(b) stress components σ_{11}^E and σ_{22}^E for general principle strain states with $\alpha_E = 0$, (c) uniaxial strain states ($\epsilon_{\mathrm{II}}^{\mathrm{ln}} = 0$), and (d) shear strain states ($\epsilon_{\mathrm{I}}^{\mathrm{ln}} = -\epsilon_{\mathrm{II}}^{\mathrm{ln}}$).

and the 2D Lamé's first parameter

$$\lambda^{2D} = \frac{E\,\nu}{(1+\nu)(1-2\,\nu)} = 4.965 \, \mathrm{eV/\mathring{A}}^2 = 79.55 \, \mathrm{N/m}\,. \tag{5.95}$$

Although graphene is a 2D material, it is common to assign an effective thickness to graphene. This is a useful practice for obtaining stress and stiffness quantities with dimension force per unit area, which can be compared to other 3D materials. Therefore, this effective thickness is assumed to be equal to the interlayer distance of graphite, $t_0 = 3.35\mathring{A}$ [Franklin, 1951; Brandt et al., 1988]. Use of this initial graphene thickness t_0 and incorporation of the resulting initial mass density per pseudo-volume, $\rho_{m,0}^{3D} = m_{uc}/(A_0\,t_0) = 1.3598 \, \mathrm{u/\mathring{A}}^3$, into the provided hyperelastic model, yields the following corresponding pseudo-3D elastic constants (dimension force per unit area)

$$
\begin{aligned}
Y^{3D} &= \rho_{m,0}^{3D}\left(2\,c_4 - \frac{c_2^2}{2\,c_4}\right) = 6.369 \, \mathrm{eV/\mathring{A}}^3 = 1020.43 \, \mathrm{GPa} = Y^{2D}/t_0\,, \\[6pt]
G^{3D} &= \frac{E}{2(1+\nu)} = 2.706 \, \mathrm{eV/\mathring{A}}^3 = 433.50 \, \mathrm{GPa} = G^{2D}/t_0\,, \\[6pt]
\lambda^{3D} &= \frac{E\,\nu}{(1+\nu)(1-2\,\nu)} = 1.482 \, \mathrm{eV/\mathring{A}}^3 = 237.46 \, \mathrm{GPa} = \lambda^{2D}/t_0\,,
\end{aligned} \tag{5.96}
$$
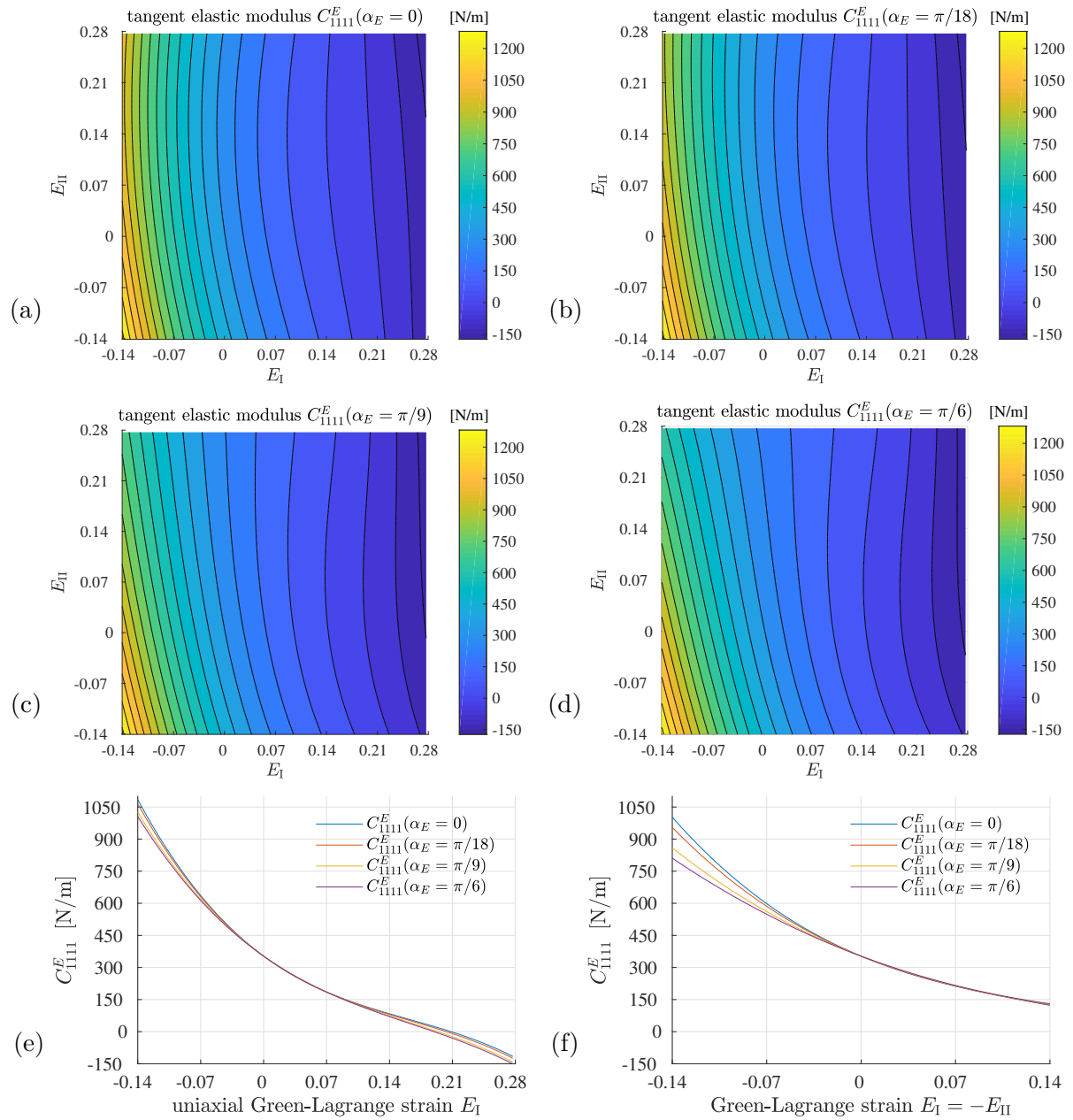
Fig. 5.18: Component C_{1111}^E of the elasticity tensor $\mathbb{C}$ (with respect to base vectors $\mathbf{e}_1^E$ and $\mathbf{e}_2^E$) of suspended graphene for various principal strain directions $\alpha_E = \{0, \frac{\pi}{18}, \frac{\pi}{9}, \frac{\pi}{6}\}$: (a)-(d) general principle strain states, (e) uniaxial strain states ($E_{\mathrm{II}} = 0$), and (f) shear strain states ($E_{\mathrm{I}} = -E_{\mathrm{II}}$).

while the dimensionless in-plane Poisson's ratio is unaffected by the effective thickness and remains constant, see (5.93).

5.5 Discussion and conclusion

An invariant-based hyperelastic material model of suspended graphene for general strain states was derived, based on energy calculations by Density Functional Theory. These DFT-calculations
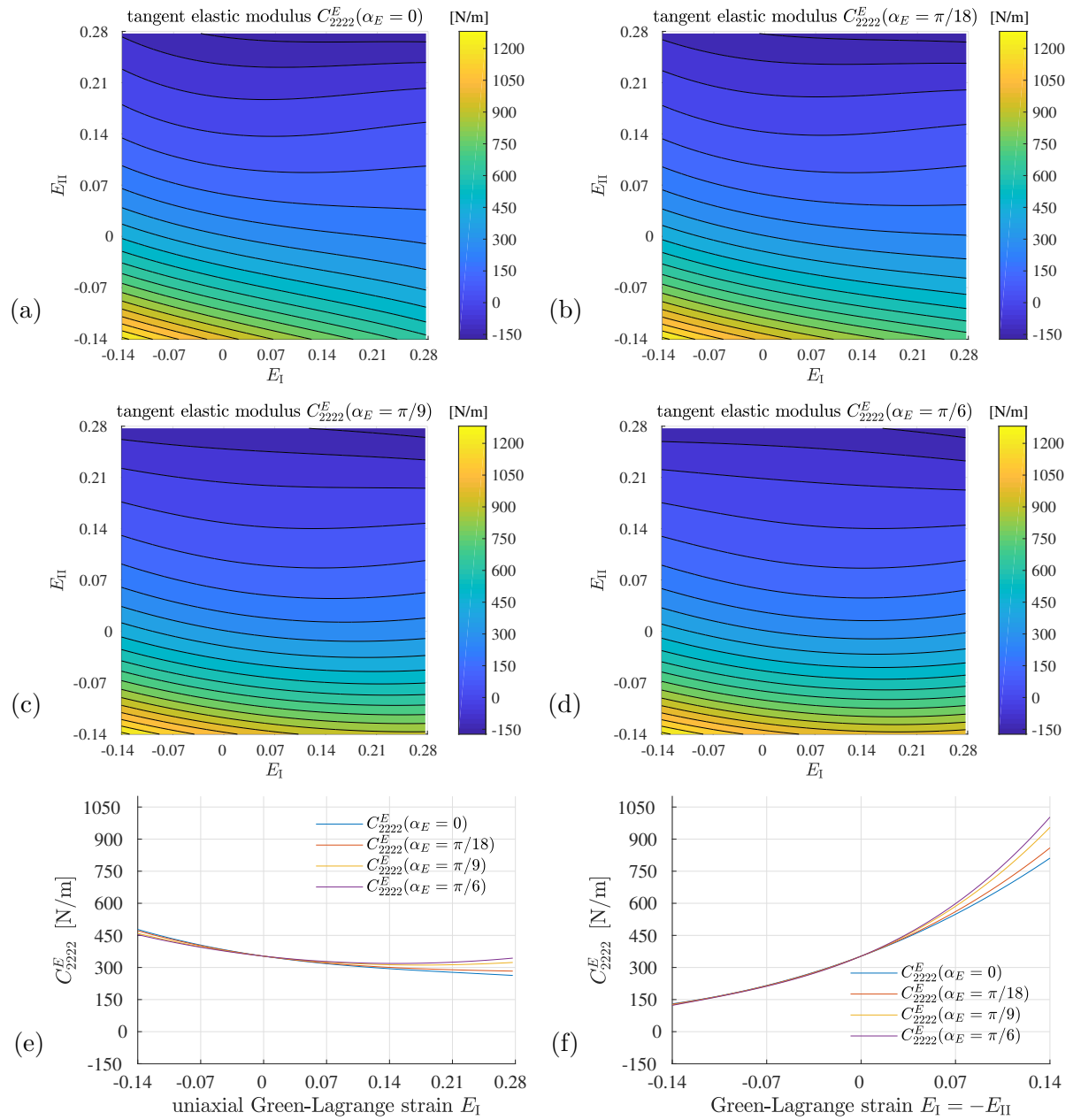
Fig. 5.19: Component C^E_{2222} of the elasticity tensor $\mathbb{C}$ (with respect to base vectors $\mathbf{e}^E_1$ and $\mathbf{e}^E_2$) of suspended graphene for various principle strain directions $\alpha_E = \{0, \frac{\pi}{18}, \frac{\pi}{9}, \frac{\pi}{6}\}$: (a)-(d) general principle strain states, (e) uniaxial strain states ($E_{\mathrm{II}} = 0$), and (f) shear strain states ($E_{\mathrm{I}} = -E_{\mathrm{II}}$).

were performed for tens of thousands of strain states giving access to polynomial fitting coefficients of the hyperelastic formulation of the specific free energy. In this context, the provided specific free energy function contains an invariant information regarding the applied strain tensor, as well as the geometric characteristics of graphene in form of a structural tensor accounting for the anisotropic structural behavior of graphene. Maximum energy differences between DFT and the hyperelastic model are as low as 1%. The consequently derived hyperelastic constitutive equations, namely the expressions for the stress tensors and elasticity tensor, are valid for both infinitesimal small deformations and large general deformations up to 1.25 for tensile stretches
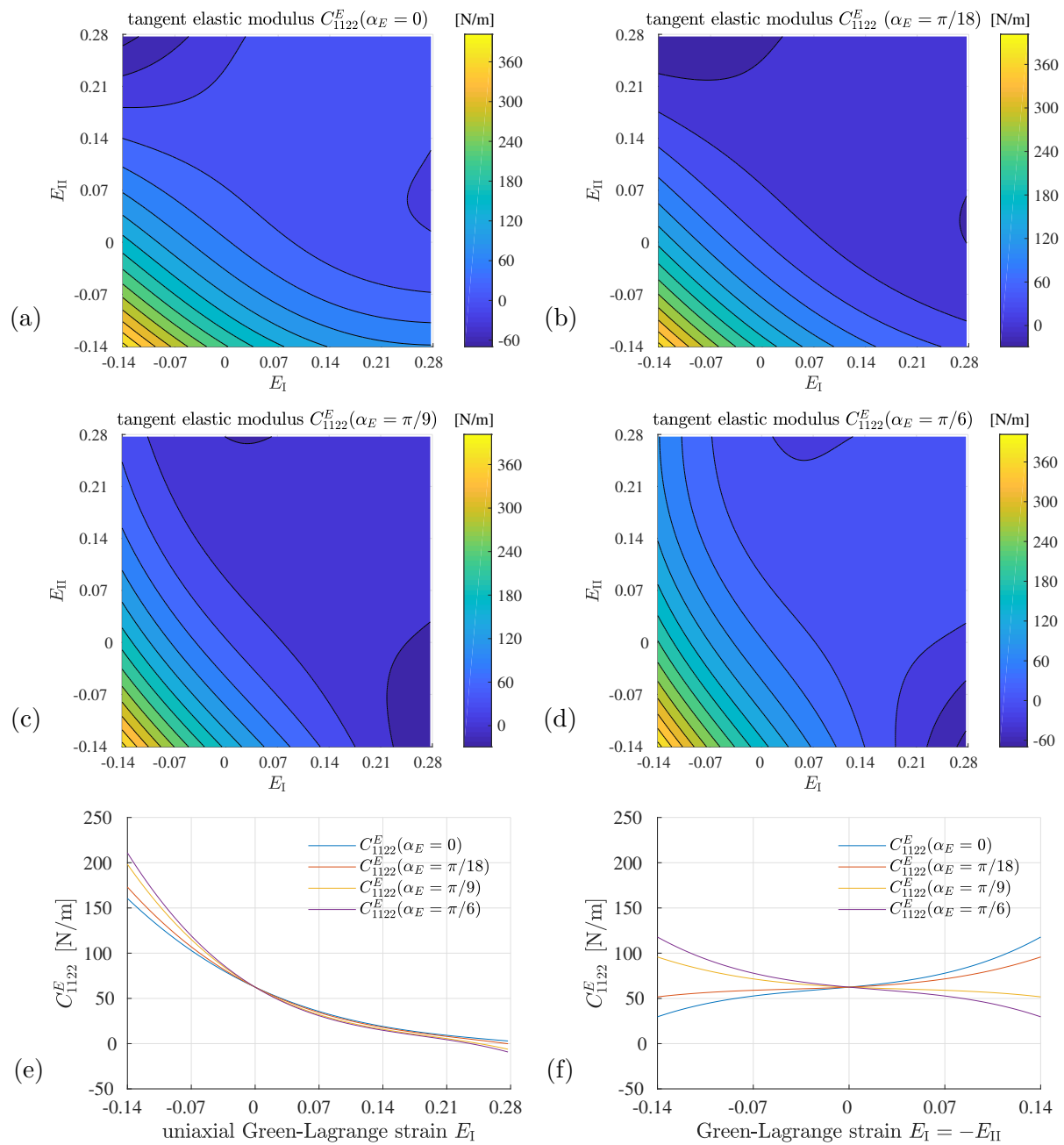
Fig. 5.20: Component C_{1122}^E of the elasticity tensor $\mathbb{C}$ (with respect to base vectors $\mathbf{e}_1^E$ and $\mathbf{e}_2^E$) of suspended graphene for various principal strain directions $\alpha_E = \{0, \frac{\pi}{18}, \frac{\pi}{9}, \frac{\pi}{6}\}$: (a)-(d) general principle strain states, (e) uniaxial strain states ($E_{\mathrm{II}} = 0$), and (f) shear strain states ($E_{\mathrm{I}} = -E_{\mathrm{II}}$).

and 0.85 for compressive stretches, respectively. For the first time, we have shown that in general, there is a deviation of the principal directions of the Green-Lagrange strain tensor imposed onto the unit cell, and the corresponding principal directions of both the second Piola-Kirchhoff and the Cauchy stress tensor. Only in zigzag and armchair directions, the aforementioned strain and stress directions coincide. All this is relevant for the finite strain domain, while it is well known that graphene is isotropic in the context of infinitesimal strains. Furthermore, we have provided an extensive overview on the anisotropy features of graphene, starting with the specific free
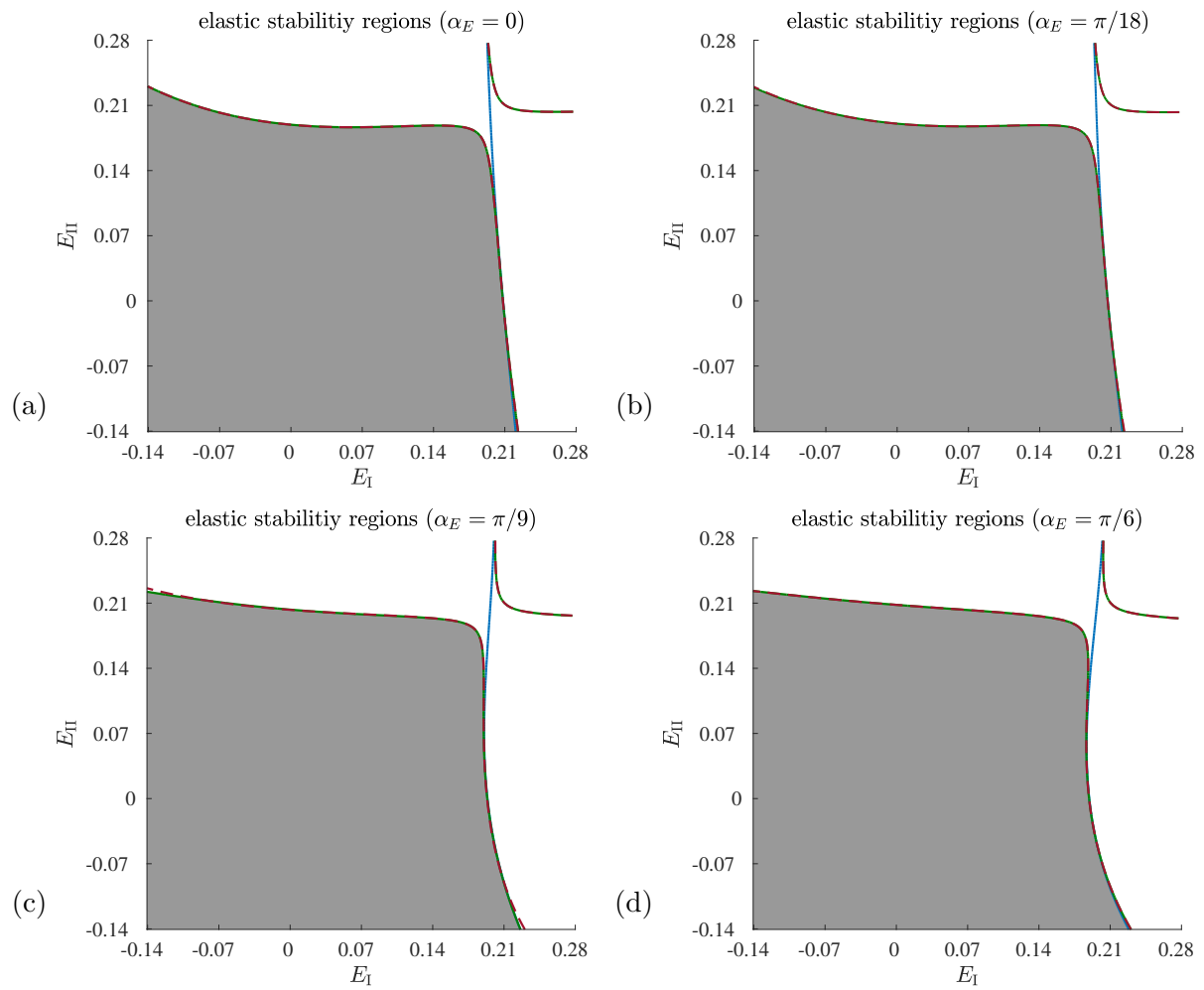
Fig. 5.21: Elastic stability limits according to (5.86)-(5.88) of suspended graphene for various principal strain directions $\alpha_E = \{0, \frac{\pi}{18}, \frac{\pi}{9}, \frac{\pi}{6}\}$: (a)-(d) elastic stability regions (see shaded regions) for general principle strain states, where the red line, green line, and blue line indicate stability criteria (5.86), (5.87) and (5.88), respectively.

energy, via the Poisson ratio-type quantity for large deformations, to the stress-strain relations and stiffnesses. Namely, differences between the zigzag and armchair direction amount to 16.5 % for the specific free energy, 45 % for the Poisson effect, 35 % for normal components of the second Piola-Kirchhoff stress tensor, and 175 % for shear components of the elasticity tensor. Analyzing the elastic stability limits of graphene, we provided stable strain regions according to a positive definite elasticity tensor. In this context, we straightforwardly extended the predictions of Kumar and Parks [2015] (unique strain states in zigzag and armchair direction) to general strain states for various material directions.

As regards material symmetry, the structure of graphene is unaltered in observation under certain orthogonal transformations $\mathbf{Q} \in SO$, see (5.62). These orthogonal tensors are in agreement with the work of Pitteri and Zanzotto [2003], as far as the symmetries of crystal lattices and their classification are concerned. For a hexagonal lattice, the symmetry group SO consists of orthogonal reflection tensors characterizing the six-fold symmetry axis, as well as of orthogonal rotation tensors associated with rotations of $\pi/3$, $2\pi/3$, π, $4\pi/3$, and $5\pi/3$ [Pitteri and Zanzotto, 2003]. In addition, the orthogonal transformations (5.62), together with invariability requirement

(5.63), are fully consistent with the landmark approaches for simple materials pioneered by Noll, which were later extended to implicit constitutive relations by Rajagopal [2015]. According to the theory of simple materials, the deformation gradient $\mathbf{F}$ is mapped onto the Cauchy stress tensor $\boldsymbol{\sigma}$ through the constitutive expression [Noll, 1958, 1972; Truesdell and Noll, 1965]

$$\boldsymbol{\sigma} = \mathcal{B}\left[\mathbf{F}(\mathbf{X}, t)\right] . \tag{5.97}$$

In (5.97), $\mathcal{B}$ is a general response functional which assigns the deformation gradient tensor to the symmetric Cauchy stress tensor $\boldsymbol{\sigma}$. For simple materials, the aforementioned orthogonal transformations $\mathbf{Q}$ belong to the material symmetry group SO if the following condition holds

$$\mathbf{Q}\,\mathcal{B}\left[\mathbf{F}(\mathbf{X}, t)\right]\mathbf{Q}^T = \mathcal{B}\left[\mathbf{Q}\,\mathbf{F}(\mathbf{X}, t)\,\mathbf{Q}^T\right] . \tag{5.98}$$

Thus, symmetry condition (5.98) states that the stress tensor is unaffected by orthogonal transformations $\mathbf{Q} \in SO$. (5.98) obviously holds for the right-hand side of Eq. (5.72), in combination with the expressions (5.71), so that the Piola-Kirchhoff stress tensor "inherits" the hexagonal symmetries, and then hands them over to the Cauchy stress tensor through the classical relation (5.B.1): In terms of components with respect to base frame $\mathbf{e}_1^E$-$\mathbf{e}_2^E$ (5.76), we obtain identical stress components for rotations of $n\,\pi/3$, $\forall\,n \in \mathbb{Z}$. Still, Eq. (5.72), which is based on the tensors $\mathbf{M}$ and $\mathbf{N}$ through $(5.71)_3$, fully defines the hexagonal symmetry; hence Eq. (5.72) together with Eq. (5.71) effectively *specify* Noll's general formalism given through (5.97) and (5.98), for the investigated case of graphene.

As regards elastic stiffness properties of graphene, the obtained elastic constants of the provided hyperelastic model for infinitesimal small strains are compared to the following reported values from experimental measurements: Lee et al. [2008] measured elastic properties of free-standing graphene membranes by nanoindentation in an atomic force microscope (AFM). These properties were evaluated in the framework of isotropic hyperelastic Finite Element analyses. Clark et al. [2013] used PeakForce QNM (quantitative nanomechanical mapping) atomic force microscopy imaging to map the nanomechanical properties of suspended graphene membranes. These properties where again fitted by Lee's isotropic material model [Lee et al., 2008]. Sen et al. [2010] used high-resolution optical and scanning electron microscopy (SEM) imaging and tearing angles were measured through digital-image processing. Corresponding elastic properties of graphene were evaluated by combining these experimental studies and first-principles ReaxFF molecular dynamics. Furthermore, Politano and Chiarello [2015] analyzed the average elastic properties, based on the investigation of acoustic phonon dispersion in graphite and in graphene using high-resolution energy loss spectroscopy (HREELS). The measured elastic constants of the aforementioned experiments can be found in Tab.5.4. Comparison of the literature according to computational quantum-mechanics shows, that molecular dynamics simulations using Tersoff- and REBO-potentials [Lu and Huang, 2009; Lu et al., 2011; Saavedra Flores et al., 2015; Singh and Patel, 2015] underestimates the elastic Young's modulus and overestimates the Poisson's ratio, when compared to DFT-based and experimental values, see Tab.5.5. However, our derived elastic constants are in good agreement with reported values from the aforementioned experimental measurements [Lee et al., 2008; Clark et al., 2013; Sen et al., 2010; Politano and Chiarello, 2015]; as well as with DFT-based computational methods [Liu et al., 2007; Xu et al., 2012a; Kumar and Parks, 2015]. Besides the validation of elastic constants for infinitesimal small strains, large deformation can be validated by incorporating the provided hyperelastic model in the constitutive equations of a 2D membrane theory. This is the topic of ongoing research.

Tab. 5.4: Elastic Young's modulus, represented in 2D and 3D (assuming a graphene thickness of 3.35 Å), and Poisson's ratio of graphene stemming from experimental data in literature.

literature	experimental method	Young's modulus Y^{3D} [GPa]	Young's modulus Y^{2D} [N/m]	Poisson's ratio ν [-]
Lee et al. [2008]	AFM experiments on membranes, evaluated by FE analyses	1015 ± 150	340 ± 50	–
Clark et al. [2013]	QNM-AFM experiments on membranes, evaluated by FE analyses	1045 ± 150	350 ± 50	–
Sen et al. [2010]	High-resolution optical- and SEM images on membranes, evaluated by molecular simulations	1010.0	338.4	–
Politano and Chiarello [2015]	Acoustic phonon dispersion ("ultrasonics")	1020.9	342.0	0.190

Tab. 5.5: Elastic Young's modulus, represented in 2D and 3D (assuming a graphene thickness of 3.35 Å), and Poisson's ratio of graphene stemming from the present hyperelastic model compared to computational data in literature.

literature	computational method	Young's modulus Y^{3D} [GPa]	Young's modulus Y^{2D} [N/m]	Poisson's ratio ν [-]
Present model	DFT-PBE	1020.4	341.8	0.177
Liu et al. [2007]	DFT-LDA	1046.9	350.7	0.186
Xu et al. [2012a]	DFT-PBE	1045.4	350.2	0.220
Kumar and Parks [2015]	DFT-GGA	1041.8	349.2	0.203
Majidi [2017]	DFT-PBE	1104.5	370.0	0.150
Cadelano et al. [2009]	TB	931.3	312.0	0.310
Lu and Huang [2009]	MD-REBO	725.4	243.0	0.398
Saavedra Flores et al. [2015]	MD-Tersoff	836.0	284.2	0.410
Singh and Patel [2015]	MD-REBO	726.6	243.4	0.397

Acknowledgments

5.A Invariants of the specific free energy for principal strain states

The components of the Green-Lagrange strain tensor with respect to base vectors $\mathbf{e}_Z$ and $\mathbf{e}_A$ (5.52)-(5.54) can be transformed to a base frame in principal strain directions $\mathbf{e}_1^E$ and $\mathbf{e}_2^E$. Thus, the characteristic polynomial of the eigenvalue problem,

$$\det(\mathbf{E} - E_j \mathbf{1}) = E_j^2 - (E_{ZZ} + E_{AA}) E_j + (E_{ZZ} E_{AA} - E_{ZA}^2) = 0 \,, \tag{5.A.1}$$

has to be solved for the eigenvalues E_j. This delivers the principal strains,

$$
\begin{aligned}
E_{\mathrm{I}} &= \frac{E_{ZZ} + E_{AA}}{2} + \sqrt{\left(\frac{E_{ZZ} - E_{AA}}{2}\right)^2 + (E_{ZA})^2} \,, \\
E_{\mathrm{II}} &= \frac{E_{ZZ} + E_{AA}}{2} - \sqrt{\left(\frac{E_{ZZ} - E_{AA}}{2}\right)^2 + (E_{ZA})^2} \,,
\end{aligned} \tag{5.A.2}
$$

which are components of a Green-Lagrange strain tensor with vanishing shear strain components,

$$\mathbf{E} = E_{\mathrm{I}} \, \mathbf{e}_1^E \otimes \mathbf{e}_1^E + E_{\mathrm{II}} \, \mathbf{e}_2^E \otimes \mathbf{e}_2^E \,. \tag{5.A.3}$$

The corresponding base frame of components (5.A.2) is rotated by an angle α_E, relative to the initial base frame $\mathbf{e}_Z$-$\mathbf{e}_A$, reading as

$$\alpha_E = \frac{1}{2} \left[\tan^{-1}\left(\frac{2\,E_{ZA}}{E_{ZZ} - E_{AA}} \right) + \pi \cdot H\left(E_{AA} - E_{ZZ} \right) \right] \,, \tag{5.A.4}$$

with H being the Heaviside step function ($H(x) = 1$ if $x > 0$ and $H(x) = 0$ otherwise).

The 2D principal invariants of the Green-Lagrange strain tensor (5.A.3) and of the structural tensor (5.59) are provided as function of principal strain measures in form of

$$
\begin{aligned}
I_1 &= \mathrm{tr}\mathbf{E} = E_{\mathrm{I}} + E_{\mathrm{II}} \,, \\
I_2 &= \frac{1}{2} \left[(\mathrm{tr}\mathbf{E})^2 - \mathrm{tr}\left(\mathbf{E}^2 \right) \right] = E_{\mathrm{I}} \, E_{\mathrm{II}} \,, \\
I_3 &= \left[(\mathbb{P} : \mathbf{E}) : \mathbf{E} \right] : \mathbf{E} = (\mathbf{M} : \mathbf{E})^3 - 3(\mathbf{M} : \mathbf{E})(\mathbf{N} : \mathbf{E})^2 = \\
&= (E_{\mathrm{I}} - E_{\mathrm{II}})^3 \cos(6\,\alpha_E) \,.
\end{aligned} \tag{5.A.5}
$$

The corresponding main invariants J_1-J_{11} read as

$$
\begin{aligned}
I_1^2 - 2\,I_2 = \quad J_1 \;\; &= E_{\mathrm{I}}^2 + E_{\mathrm{II}}^2 \,, \\
I_1^3 - 3\,I_1\,I_2 = \quad J_2 \;\; &= E_{\mathrm{I}}^3 + E_{\mathrm{II}}^3 \,, \\
I_1\,I_2 = \quad J_3 \;\; &= E_{\mathrm{I}}^2 \, E_{\mathrm{II}} + E_{\mathrm{I}} \, E_{\mathrm{II}}^2 \,, \\
I_1^4 - 4\,I_1^2\,I_2 + 2\,I_2^2 = \quad J_4 \;\; &= E_{\mathrm{I}}^4 + E_{\mathrm{II}}^4 \,, \\
I_2^2 = \quad J_5 \;\; &= E_{\mathrm{I}}^2 \, E_{\mathrm{II}}^2 \,, \\
I_1^2\,I_2 - 2\,I_2^2 = \quad J_6 \;\; &= E_{\mathrm{I}}^3 \, E_{\mathrm{II}} + E_{\mathrm{I}} \, E_{\mathrm{II}}^3 \,, \\
I_1^5 - 5\,I_1^3\,I_2 + 5\,I_1\,I_2^2 = \quad J_7 \;\; &= E_{\mathrm{I}}^5 + E_{\mathrm{II}}^5 \,, \\
I_1^3\,I_2 - 3\,I_1\,I_2^2 = \quad J_8 \;\; &= E_{\mathrm{I}}^4 \, E_{\mathrm{II}} + E_{\mathrm{I}} \, E_{\mathrm{II}}^4 \,, \\
I_1\,I_2^2 = \quad J_9 \;\; &= E_{\mathrm{I}}^3 \, E_{\mathrm{II}}^2 + E_{\mathrm{I}}^2 \, E_{\mathrm{II}}^3 \,, \\
I_3\,I_1 = \quad J_{10} \;\; &= (E_{\mathrm{I}} - E_{\mathrm{II}})^3 (E_{\mathrm{I}} + E_{\mathrm{II}}) \cos(6\,\alpha_E) \,, \\
I_3 \left(I_1^2 - 2\,I_2 \right) = \quad J_{11} \;\; &= (E_{\mathrm{I}} - E_{\mathrm{II}})^3 (E_{\mathrm{I}}^2 + E_{\mathrm{II}}^2) \cos(6\,\alpha_E) \,.
\end{aligned} \tag{5.A.6}
$$

Furthermore, the components of the second-order tensor $\mathbf{S}$ (5.71), namely the derivative of the principal invariant I_3 with respect to the Green-Lagrange strain tensor $\mathbf{E}$, read as

$$\mathbf{S} = S_{11}^E\,\mathbf{e}_1^E \otimes \mathbf{e}_1^E + S_{12}^E\,(\mathbf{e}_1^E \otimes \mathbf{e}_2^E + \mathbf{e}_2^E \otimes \mathbf{e}_1^E) + S_{22}^E\,\mathbf{e}_2^E \otimes \mathbf{e}_2^E\,, \tag{5.A.7}$$

with

$$
\begin{aligned}
S_{11}^E &= 3\,(E_\mathrm{I} - E_\mathrm{II})^2 \cos(6\alpha_E)\,, \\
S_{12}^E &= -3\,(E_\mathrm{I} - E_\mathrm{II})^2 \sin(6\alpha_E)\,, \\
S_{22}^E &= -3\,(E_\mathrm{I} - E_\mathrm{II})^2 \cos(6\alpha_E)\,.
\end{aligned}
\tag{5.A.8}
$$

The corresponding components of the fourth-order tensor $\mathbb{S}$ (5.80), namely the derivative of the principal invariant $\mathbf{S}$ with respect to the Green-Lagrange strain tensor $\mathbf{E}$, read as

$$
\begin{aligned}
\mathbb{S} = {}& +S_{1111}^E\,\mathbf{e}_1^E \otimes \mathbf{e}_1^E \otimes \mathbf{e}_1^E \otimes \mathbf{e}_1^E + S_{2222}^E\,\mathbf{e}_2^E \otimes \mathbf{e}_2^E \otimes \mathbf{e}_2^E \otimes \mathbf{e}_2^E \\
& +S_{1122}^E\,\big(\mathbf{e}_1^E \otimes \mathbf{e}_1^E \otimes \mathbf{e}_2^E \otimes \mathbf{e}_2^E + \mathbf{e}_2^E \otimes \mathbf{e}_2^E \otimes \mathbf{e}_1^E \otimes \mathbf{e}_1^E\big) \\
& +S_{1212}^E\,\big(\mathbf{e}_1^E \otimes \mathbf{e}_2^E \otimes \mathbf{e}_1^E \otimes \mathbf{e}_2^E + \mathbf{e}_2^E \otimes \mathbf{e}_1^E \otimes \mathbf{e}_1^E \otimes \mathbf{e}_2^E \\
& \qquad\quad +\mathbf{e}_2^E \otimes \mathbf{e}_1^E \otimes \mathbf{e}_2^E \otimes \mathbf{e}_1^E + \mathbf{e}_1^E \otimes \mathbf{e}_2^E \otimes \mathbf{e}_2^E \otimes \mathbf{e}_1^E\big) \\
& +S_{1112}^E\,\big(\mathbf{e}_1^E \otimes \mathbf{e}_1^E \otimes \mathbf{e}_1^E \otimes \mathbf{e}_2^E + \mathbf{e}_1^E \otimes \mathbf{e}_1^E \otimes \mathbf{e}_2^E \otimes \mathbf{e}_1^E \\
& \qquad\quad +\mathbf{e}_1^E \otimes \mathbf{e}_2^E \otimes \mathbf{e}_1^E \otimes \mathbf{e}_1^E + \mathbf{e}_2^E \otimes \mathbf{e}_1^E \otimes \mathbf{e}_1^E \otimes \mathbf{e}_1^E\big) \\
& +S_{1222}^E\,\big(\mathbf{e}_1^E \otimes \mathbf{e}_2^E \otimes \mathbf{e}_2^E \otimes \mathbf{e}_2^E + \mathbf{e}_2^E \otimes \mathbf{e}_1^E \otimes \mathbf{e}_2^E \otimes \mathbf{e}_2^E \\
& \qquad\quad +\mathbf{e}_2^E \otimes \mathbf{e}_2^E \otimes \mathbf{e}_1^E \otimes \mathbf{e}_2^E + \mathbf{e}_2^E \otimes \mathbf{e}_2^E \otimes \mathbf{e}_2^E \otimes \mathbf{e}_1^E\big)\,,
\end{aligned}
\tag{5.A.9}
$$

with

$$
\begin{aligned}
S_{1111}^E = S_{2222}^E &= +6\,(E_\mathrm{I} - E_\mathrm{II}) \cos(6\alpha_E)\,, \\
S_{1122}^E = S_{1212}^E &= -6\,(E_\mathrm{I} - E_\mathrm{II}) \cos(6\alpha_E)\,, \\
S_{1112}^E &= -6\,(E_\mathrm{I} - E_\mathrm{II}) \sin(6\alpha_E)\,, \\
S_{1222}^E &= +6\,(E_\mathrm{I} - E_\mathrm{II}) \sin(6\alpha_E)\,.
\end{aligned}
\tag{5.A.10}
$$

5.B   Eulerian stress-strain relations

Stress states actually occur in the deformed configuration. Hence, we are also interested in the stress measures related to the deformed configuration, i.e. in the Cauchy stresses, reading as

$$\boldsymbol{\sigma} = \frac{1}{J}\,\mathbf{F} \cdot \boldsymbol{\pi} \cdot \mathbf{F}^T\,, \quad \text{with} \quad J = \det\mathbf{F}\,. \tag{5.B.1}$$

The Cauchy stresses are energetically conjugated to the logarithmic strains [Hencky, 1928; Xiao et al., 1997]

$$\boldsymbol{\epsilon}^{\mathrm{ln}} = \ln\sqrt{\mathbf{F}\,\mathbf{F}^T}\,, \tag{5.B.2}$$

with the deformation gradient

$$\mathbf{F} = \frac{\partial \mathbf{u}^I}{\partial \mathbf{X}} + \mathbf{1} \,. \tag{5.B.3}$$

The components of the deformation gradient in the $\mathbf{e}_Z$-$\mathbf{e}_A$ base frame read as

$$F_{ZZ} = \frac{\partial u_Z^I}{\partial X_Z} + 1 = \frac{a_{1,Z} - a_{2,Z}}{2\,a^0} \,, \tag{5.B.4}$$

$$F_{ZA} = \frac{\partial u_Z^I}{\partial X_A} = \frac{a_{1,Z} + a_{2,Z}}{2\,b^0} \,, \tag{5.B.5}$$

$$F_{AZ} = \frac{\partial u_A^I}{\partial X_Z} = \frac{a_{1,A} - a_{2,A}}{2\,a^0} \,, \tag{5.B.6}$$

$$F_{ZZ} = \frac{\partial u_A^I}{\partial X_A} + 1 = \frac{a_{1,A} + a_{2,A}}{2\,b^0} \,, \tag{5.B.7}$$

noting that in general the deformation gradient is not symmetric. Regarding principal strain states with direction $\mathbf{e}_1^E$, and $\mathbf{e}_2^E$ according to (5.A.3)-(5.A.4), the deformation gradient is a function of principal stretches, λ_I and λ_II (eigenvalues), reading as

$$\mathbf{F} = \lambda_\mathrm{I}\,\mathbf{e}_1^E \otimes \mathbf{e}_1^E + \lambda_\mathrm{II}\,\mathbf{e}_2^E \otimes \mathbf{e}_2^E \,. \tag{5.B.8}$$

Accordingly, the logarithmic strain tensor with respect to base frame $\mathbf{e}_1^E$-$\mathbf{e}_2^E$ reads as

$$\boldsymbol{\epsilon}^{\ln} = \ln \lambda_\mathrm{I}\,\mathbf{e}_1^E \otimes \mathbf{e}_1^E + \ln \lambda_\mathrm{II}\,\mathbf{e}_2^E \otimes \mathbf{e}_2^E \,. \tag{5.B.9}$$

Thus, use of the logarithmic strain (5.B.2) in (5.B.1), while considering (5.72) and

$$\mathbf{E} = \frac{1}{2}\left(\mathbf{F}^T\,\mathbf{F} - \mathbf{1}\right), \qquad \mathbf{F}\,\mathbf{F}^T = \exp[2\,\boldsymbol{\epsilon}^{\ln}], \qquad J = \exp[(\epsilon_\mathrm{I}^{\ln} + \epsilon_\mathrm{II}^{\ln})], \tag{5.B.10}$$

yields the energetic-conjugate stress-strain relation

$$\begin{aligned}
\boldsymbol{\sigma} = {} & \frac{\rho_{m,0}^{2D}\,\exp[2\,\boldsymbol{\epsilon}^{\ln}]}{\exp[\epsilon_\mathrm{I}^{\ln} + \epsilon_\mathrm{II}^{\ln}]}\left[\beta_1\,\mathbf{1} + \frac{\beta_2}{2}\left(\exp[2\,\boldsymbol{\epsilon}^{\ln}] - \mathbf{1}\right)\right] \\
& + \frac{\rho_{m,0}^{2D}}{\exp[\epsilon_\mathrm{I}^{\ln} + \epsilon_\mathrm{II}^{\ln}]}\left[\beta_3\,\mathbf{F}\,\mathbf{S}\,\mathbf{F}^T\right],
\end{aligned} \tag{5.B.11}$$

with $\epsilon_\mathrm{I}^{\ln}$ and $\epsilon_\mathrm{II}^{\ln}$ as the principal logarithmic strains, see (5.B.9). The components of (5.B.11) with respect to base frame $\mathbf{e}_1^E$-$\mathbf{e}_2^E$, $\boldsymbol{\sigma} = \sum_{i=1}^2 \sum_{j=1}^2 \sigma_{ij}\,\mathbf{e}_i^E \otimes \mathbf{e}_j^E$, read as

$$\begin{aligned}
\sigma_{11}^E = {} & \rho_{m,0}^{2D}\left[\beta_1 + \frac{\beta_2}{2}\left(\exp[2\,\epsilon_\mathrm{I}^{\ln}] - 1\right)\right. \\
& \left. + \frac{3\,\beta_3}{4}\left(\exp[2\,\epsilon_\mathrm{I}^{\ln}] - \exp[2\,\epsilon_\mathrm{II}^{\ln}]\right)^2 \cos(6\alpha_E)\right] \exp[\epsilon_\mathrm{I}^{\ln} - \epsilon_\mathrm{II}^{\ln}], \\
\sigma_{12}^E = \sigma_{21}^E = {} & -\rho_{m,0}^{2D}\,\frac{3\,\beta_3}{4}\left(\exp[2\,\epsilon_\mathrm{I}^{\ln}] - \exp[2\,\epsilon_\mathrm{II}^{\ln}]\right)^2 \sin(6\alpha_E)\,, \\
\sigma_{22}^E = {} & \rho_{m,0}^{2D}\left[\beta_1 + \frac{\beta_2}{2}\left(\exp[2\,\epsilon_\mathrm{II}^{\ln}] - 1\right)\right. \\
& \left. - \frac{3\,\beta_3}{4}\left(\exp[2\,\epsilon_\mathrm{I}^{\ln}] - \exp[2\,\epsilon_\mathrm{II}^{\ln}]\right)^2 \cos(6\alpha_E)\right] \exp[\epsilon_\mathrm{II}^{\ln} - \epsilon_\mathrm{I}^{\ln}],
\end{aligned}$$

$$\tag{5.B.12}$$

where we used the identities, $E_{\mathrm{I}} = \frac{1}{2}\left(\exp[2\,\epsilon_{\mathrm{I}}^{\ln}] - 1\right)$ and $E_{\mathrm{II}} = \frac{1}{2}\left(\exp[2\,\epsilon_{\mathrm{II}}^{\ln}] - 1\right)$, for the components of $\mathbf{S}$ (5.A.8) and for the principal invariants apperaing in the scalar functions β_j. In analogy to the second Piola-Kirchhoff stress tensor, the direction of the principal component σ_{I} of the Cauchy stress tensor reads as

$$\alpha_\sigma = \alpha_E + \frac{1}{2}\left[\tan^{-1}\left(\frac{2\,\sigma_{12}^E}{\sigma_{11}^E - \sigma_{22}^E}\right)\right]\,, \tag{5.B.13}$$

describing the angle between base vectors $\mathbf{e}_Z$ and $\mathbf{e}_1^\sigma$.

Chapter 6

A membrane theory for circular graphene sheets, based on a hyperelastic material model for large deformations

Authored by: Raphael Höller, Florian Libisch, and Christian Hellmich

Abstract

Large deflections relevant for suspended circular graphene sheets with simply supported boundaries are computed by a theory for 2D membranes subjected to several types of vertical axisymmetric forces, based on the Principle of Virtual Power. Corresponding constitutive stress-strain relations are provided in an invariant fashion in form of a nonlinear anisotropic hyperelastic material model for graphene, which is basically fitted by the quantum mechanics-rooted density functional theory. When approximating the deflections through Navier-type Fourier series, the Principle of Virtual Power yields a nonlinear algebraic system of equations. In this context, the iterative Newton-Raphson solution procedure provides the Fourier coefficients of the aforementioned series representation. The latter converges, with increasing number of series members, to the true solution for the membrane deflections. The new computational efficient method is applied to relevant problems in mechanical engineering of graphene, and it is validated through comparison of the numerical results it provides, with predictions obtained from experimental nanoindentaion measurements.

Contribution of the author: The author of the present thesis developed the PVP-based membrane theory for circular graphene sheets undergoing large deformations, characterized by nonlinear hyperelastic stress-strain relations. Furthermore, he performed extensive literature research, prepared the Matlab code for the iterative series-based solution procedure, and documented most of the manuscript.

List of symbols

$\mathbf{a}_i$	vector containing amplitudes $a_{m,i}$ for each iteration step i associated to Newton-Raphson method
a_m	Fourier coefficient of deflection approximation
$\dot{\hat{a}}_t$	Fourier coefficient in approximation of virtual velocity
c_i	DFT-based fitting coefficients for hyperelastic material model
$\hat{\mathbf{d}}$	virtual Eulerian strain rate
$\mathbf{e}_r, \mathbf{e}_\varphi, \mathbf{e}_z$	base vectors of cylindrical coordinate system
$\mathbf{E}$	Green-Lagrange strain tensor
E_{rr}	normal component of $\mathbf{E}$ in the r-direction
$\dot{\hat{\mathbf{E}}}$	virtual Green-Lagrange strain rate
$\dot{\hat{E}}_{rr}$	normal component of $\dot{\hat{\mathbf{E}}}$ in the r-direction
$\mathbf{f}$	volume force vector
$\mathbf{f}^{NR}$	vector containing functions f_t^{NR} associated to Newton-Raphson method
f_t^{NR}	multivariate function of the nonlinear system of equations
$\mathbf{F}$	deformation gradient
F_{rr}	normal component of $\mathbf{F}$ in teh r-direction
$F_{\varphi\varphi}$	normal component of $\mathbf{F}$ in the φ-direction
F_{zz}	normal component of $\mathbf{F}$ in the z-direction
F_{zr}	shear component of $\mathbf{F}$ in the r-z-plane
h	effective thickness of graphene
i	index of summation / of vector component
I_1, I_3	principal invariants of the strain and structural tensor
$\mathbf{J}$	Jacobian matrix associated to Newton-Raphson method
$J_{tj,i}$	elements of $\mathbf{J}$ for each iteration step i
j	index of summation / of vector component
k	index of summation / of vector component
l	index of summation / of vector component
m	index of summation / of vector component
M_{jklt}^{I}	"stiffness matrix element" associated to deformation amplitudes of third power
M_{jklmnt}^{II}	"stiffness matrix element" associated to deformation amplitudes of fifth power
M_{jklmnt}^{III}	"stiffness matrix element" associated to deformation amplitudes of seventh power
n	index of summation / of vector component
$\mathbf{n}$	outward normal vector onto the boundaries of deformed continuum
$\mathbf{N}$	outward normal vector onto the boundaries of undeformed membrane
$n_{L,rr}$	internal normal force per unit length in the r-direction
N_m	number of Fourier series members approximating the deflection
N_t	number of Fourier series members approximating the virtual velocity
$P_{L,z}$	single force acting in vertical direction (z)
$\overline{p}_{L,z}$	vertical surface load per unit area, acting over specific circular area
$p_{L,z}$	vertical surface load per unit area, acting over entire membrane
PVP	Principle of Virtual Power
$\mathcal{P}^{ext}$	virtual power of external forces

$\mathcal{P}^{int}$	virtual power of internal forces
q	index of summation / of vector component
r	radial coordinate of the cylindrical coordinate system
R	radius of the membrane
R_T	radius of the surface load $\overline{p}_{L,z}$
$\mathbf{S}$	derivative of the principal invariant I_3 with respect to $\mathbf{E}$
S_{rr}	component of $\mathbf{S}$ in the r-direction,
	characterizing graphene's anisotropic material behavior
s	index of summation / of vector component
t	index of summation / of vector component
$\mathbf{T}$	traction vector
$\mathbf{u}$	displacement vector
$\hat{\mathbf{u}}$	virtual displacement vector
u_z	deflection of the membrane
$\hat{u}_z$	virtual deflection of the membrane
$\hat{\mathbf{v}} = \dot{\hat{\mathbf{u}}}$	virtual velocity vector
v_z	component of $\hat{\mathbf{v}}$ in the z-direction
V_t^p	"load vector element" associated to surface load
	acting on entire membrane
$V_t^{\overline{p}}$	"load vector element" associated to surface load
	acting on circular area
V_t^P	"load vector element" associated to single force
w_m	m-th deflection mode associated to 2D Fourier series
$\mathbf{x}$	location vector throughout the deformed membrane
$\mathbf{X}$	location vector throughout the undeformed membrane
z	vertical coordinate of the cylindrical coordinate system
$\beta_1, \beta_2, \beta_3$	scalar functions of the hyperelastic material model for graphene
λ	scaling factor
$\boldsymbol{\pi}$	second Piola-Kirchhoff stress tensor
π_{rr}	normal component of $\boldsymbol{\pi}$ in the r-direction
π_{rz}	shear component of $\boldsymbol{\pi}$ in the r-z-plane
π_{zz}	normal component of $\boldsymbol{\pi}$ in the z-direction
π_{rr}^{2D}	normal component of 2D second Piola-Kirchhoff stress tensor
$\rho_{m,0}^{2D}$	initial mass density per area of graphene
$\boldsymbol{\sigma}$	Cauchy stress tensor
$\sum$	summation operator
φ	azimuth of the cylindrical coordinate system

6.1 Introduction

Two-dimensional (2D) graphene membranes, consisting of carbon atoms arranged in a hexagonal lattice, attract considerable attention in the fields of chemistry, physics, and material science [Balandin et al., 2008; Bolotin et al., 2008; Lee et al., 2008; Castro Neto et al., 2009; Lau et al., 2012]. As regards membrane theories for computing the deflections of suspended graphene sheets, several methods have been used up to the present day: Atomistic models of graphene membranes have been developed by molecular dynamics simulations using interatomic Lennard-Jones potentials and Tersoff-Brenner potentials [Neek-Amal and Peeters, 2010; Fang et al., 2011; Shakouri et al., 2011; Samadikhah et al., 2012], as well as by truss-type models consisting of beam elements for simulating covalently bonded carbon atoms in a hexagonal graphene lattice

[Sakhaee-Pour et al., 2008; Sakhaee-Pour, 2009; Rouhi and Ansari, 2012]. The by far most popular method for the solution of mechanical deformations is that of the Finite Element method, which has been the basis for many scientific contributions up to the present day [Gil et al., 2010; Scarpa et al., 2010; Larsson and Samadikhah, 2011; Xu et al., 2012a,b; Wei and Kysar, 2012; Jiang et al., 2014; Seifoori and Hajabdollahi, 2015; Ghaffari et al., 2018]. Besides mechanical deformations, vibrational analysis of graphene sheets were performed indicating its fundamental frequencies and mode shapes [Sadeghi and Naghdabadi, 2010; Mianroodi et al., 2011; Wang et al., 2013; Jiang et al., 2014].

However, for a circular graphene membrane, simply supported at its boundary, a more computationally efficient Fourier-series based theory can be provided: Therefore, we resort to the Principle of Virtual Power (PVP) [Germain, 1972, 1973a,b; Germain et al., 1983; Maugin, 1980, 2013; Touratier, 1991; Salençon, 2001; Höller et al., 2019], which we specify for the kinematic characteristics of a 2D graphene membrane in bending mode, see Section 6.2. In this context, we consider large deformations using Lagrangian quantities, namely the Green-Lagrange strain and the energetically conjugated second Piola-Kichhoff stress. Corresponding stress-strain relations are linked by a nonlinear, anisotropic hyperelastic material model of graphene [Höller et al., 2020a], based on the Density Functional Theory (DFT) [Hohenberg and Kohn, 1964; Kohn and Sham, 1965]. Furthermore, the investigated circular membranes are subjected to several types of axisymmetric vertical forces, namely to single forces or to distributed surface loads acting on circular areas, whereby the action points and the areas form axisymmetric patterns. Such kinds of concentrated loads allow for consideration of nanoindentation of free-standing graphene membranes [Lee et al., 2008]. In Section 6.3, the PVP-based governing equation is used for constructing a nonlinear algebraic system of equations for determining the sought deflection function. The latter is expanded into Fourier series according to Navier's proposal [Navier, 1823] and the unknown Fourier coefficients of the nonlinear multivariate system of equation are solved iteratively by means of the Newton-Raphson method [Ortega and Rheinboldt, 2000]. Section 6.4 is devoted to numerical investigations in the form of three representative examples, and of comparison of respective results with experimental measurements. Finally, concluding remarks are provided in Section 6.5. Appendix A contains the elements of the algebraic system of equations for the three aforementioned numerical examples, in order to solve the unknown Fourier coefficients.

6.2 Kinematics and stress resultants of suspended graphene membranes for large deformations – reviewed in the context of the Principle of Virtual Power

6.2.1 Basics

The Principle of Virtual Power (PVP) is an efficient and safe method for constructing energetically consistent theories of structural members, as documented by Germain [1972, 1973a,b] and Maugin [1980, 2013]. Setting our focus point on 2D graphene membranes, we start with the formulation of the PVP for a standard 3D continuum, in the format put forward by Germain and followers [Maugin, 2013; Touratier, 1991; Salençon, 2001; Höller et al., 2019; Borino and Polizzotto, 2014],

$$\mathcal{P}^{ext} + \mathcal{P}^{int} = 0 \,, \tag{6.1}$$

with

$$\mathcal{P}^{ext} \quad = \quad + \int\limits_{V} \mathbf{f}(\mathbf{x}) \cdot \hat{\mathbf{v}}(\mathbf{x}) \, dV + \int\limits_{S} \mathbf{T}(\mathbf{n}, \mathbf{x}) \cdot \hat{\mathbf{v}}(\mathbf{x}) \, dS \,, \tag{6.2}$$

$$\mathcal{P}^{int} \quad = \quad - \int\limits_{V} \boldsymbol{\sigma} : \hat{\mathbf{d}} \, dV \,, \tag{6.3}$$

where $\mathcal{P}^{ext}$ and $\mathcal{P}^{int}$ denote the virtual power of the external forces and of the internal forces, respectively; $\mathbf{x}$ denotes the actual location vectors throughout the continuum and at its boundaries with outward normals $\mathbf{n}$; $\mathbf{f}$ denotes volume forces; $\mathbf{T}$ denotes traction (surface) forces; $\hat{\mathbf{v}}$ denotes the virtual velocity; $\boldsymbol{\sigma}$ denotes the Cauchy stress; and $\hat{\mathbf{d}}$ denotes the virtual Eulerian strain rate. The Principle of Virtual Power implies both kinematic compatibility and equilibrium of the solid continuum.

In the case of circular membranes, undergoing large deformations, we formulate strains and stresses as a function of the location vector $\mathbf{X}$ in the undeformed configuration (Lagrangian representation). Any position within the surface of such a membrane is described by a cylindrical coordinate system, with an origin located in center of the membrane, and with base vectors $\mathbf{e}_r, \mathbf{e}_\varphi$, and $\mathbf{e}_z$. The latter is orthogonal to the undeformed membrane and the azimuth of $\varphi = 0$ corresponds to a base vector $\mathbf{e}_r$ pointing in the so-called "zigzag" direction of graphene. Thus, for describing large deformations, the following virtual power of external and internal forces are provided in Lagrangian representation

$$\mathcal{P}^{ext} \quad = \quad \int\limits_{0}^{R} \int\limits_{0}^{2\pi} \hat{\mathbf{v}}(\mathbf{X}) \cdot \mathbf{F} \cdot \boldsymbol{\pi}(\mathbf{X}) \cdot \mathbf{N}(\mathbf{X}) \; r \, d\varphi \, dr \,, \tag{6.4}$$

$$\mathcal{P}^{int} \quad = \quad - \int\limits_{0}^{R} \int\limits_{0}^{2\pi} \int\limits_{-\frac{h}{2}}^{+\frac{h}{2}} \boldsymbol{\pi} : \dot{\hat{\mathbf{E}}} \; r \, dz \, d\varphi \, dr \,, \tag{6.5}$$

where $\mathbf{X}$ denotes the initial location vectors throughout the membrane with outward normals $\mathbf{N}$ and radius R; $\mathbf{F}$ denotes the deformation gradient; $\boldsymbol{\pi}$ denotes the second Piola-Kirchhoff stress tensor; and $\dot{\hat{\mathbf{E}}}$ denotes the virtual Green-Lagrange strain rate. It is noted, that we neglected volume force vectors due to the infinitesimal small thickness of graphene (single layer of carbon atoms), see Section 6.2.2.

6.2.2 Kinematics

2D graphene membranes in so-called bending mode are characterized by the following kinematic features:

1. The thickness of graphene is negligible *small* [Castro Neto et al., 2009; Lau et al., 2012], such that all straight lines (generators) orthogonal to the undeformed membrane remain, throughout the deformation process, *straight*, constant in length, and *orthogonal* to the undeformed membrane plane.

2. All points of a generator have, in good approximation, the same displacement in the z-direction, namely the deflection u_z, see Fig. 6.1.

3. The deflections are *large* when compared to the thickness of the membrane.

4. Axisymmetric loads result in axisymmetric patterns of the displacements.

5. Stretching stiffness is dominant over negligible shear and bending stiffnesses.
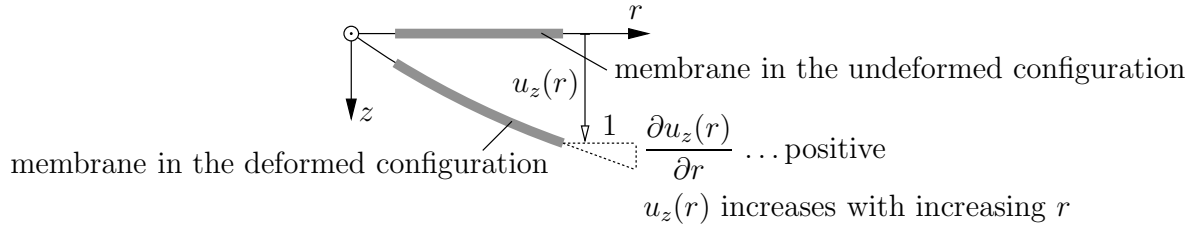
Fig. 6.1: Sideview in the *r*-*z*-plane of a graphene membrane in the undeformed and in the deformed configuration.

Under the aforementioned kinematic conditions, the displacement field of the membrane reads as

$$\mathbf{u}(\mathbf{X}) = u_z(r)\,\mathbf{e}_z\,, \tag{6.6}$$

and the corresponding virtual velocity field follows from a virtual displacement field of the form

$$\hat{\mathbf{u}}(\mathbf{X}) = \hat{u}_z(r)\,\mathbf{e}_z\,. \tag{6.7}$$

Namely, temporal derivation of (6.7) yields the virtual velocity field as

$$\hat{\mathbf{v}}(\mathbf{X}) = \dot{\hat{\mathbf{u}}}(\mathbf{X}) = \hat{v}_z(r)\,\mathbf{e}_z\,, \tag{6.8}$$

with $\hat{v}_z$ as the temporal derivative of the time-dependent virtual displacement $\hat{u}_z$.

Displacement field (6.6) implies a Green-Lagrange strain tensor $\mathbf{E}$ [Salençon, 2001]

$$\mathbf{E} = \frac{1}{2}\left[\frac{\partial\mathbf{u}}{\partial\mathbf{X}} + \left(\frac{\partial\mathbf{u}}{\partial\mathbf{X}}\right)^T + \left(\frac{\partial\mathbf{u}}{\partial\mathbf{X}}\right)^T\cdot\frac{\partial\mathbf{u}}{\partial\mathbf{X}}\right] = \sum_{i=r,\varphi,z}\sum_{j=r,\varphi,z} E_{ij}\,\mathbf{e}_i\otimes\mathbf{e}_j\,, \tag{6.9}$$

with non-zero components reading as

$$E_{rr}(r) \;=\; \frac{1}{2}\left(\frac{\partial u_z(r)}{\partial r}\right)^2\,, \tag{6.10}$$

where the transverse shear strains are neglected due to the infinitesimal small thickness of the 2D membrane. Derivation of (6.10) with respect to the time, and substitution of the occuring time derivatives of displacements by virtual velocities, yields

$$\dot{\hat{\mathbf{E}}} = \dot{\hat{E}}_{rr}\,\mathbf{e}_r\otimes\mathbf{e}_r\,, \tag{6.11}$$

with

$$\dot{\hat{E}}_{rr}(r) \;=\; \frac{\partial u_z(r)}{\partial r}\,\frac{\partial\hat{v}_z(r)}{\partial r}\,. \tag{6.12}$$

Thus, the virtual Green-Lagrange strain rate (appearing in the virtual power of internal forces) depends on both the virtual velocity $\hat{v}_z$ and the actual deflection u_z indicating a non-linearity in the structural problem.

Furthermore, displacement field (6.6) implies a deformation gradient, $\mathbf{F} = \mathbf{1} + \partial\mathbf{u}/\partial\mathbf{X}$ (appearing in the virtual power of external forces), reading as

$$\mathbf{F} = F_{rr}\,\mathbf{e}_r \otimes \mathbf{e}_r + F_{\varphi\varphi}\,\mathbf{e}_\varphi \otimes \mathbf{e}_\varphi + F_{zr}\,\mathbf{e}_z \otimes \mathbf{e}_r + F_{zz}\,\mathbf{e}_z \otimes \mathbf{e}_z\,, \tag{6.13}$$

with

$$F_{rr} = 1\,, \quad F_{\varphi\varphi} = 1\,, \quad F_{zr} = \frac{\partial u_z(r)}{\partial r}\,, \quad \text{and} \quad F_{zz} = 1\,. \tag{6.14}$$

6.2.3 Virtual Power of internal forces and corresponding hyperelastic material model of graphene

As regards specification of the virtual power of internal forces (6.5) for the kinematic characteristics of graphene membranes undergoing large deformations, the virtual Green-Lagrange strain rates (6.12) imply that only stresses π_{rr} perform power along the virtual strain rates $\dot{\hat{E}}_{rr}$. Hence, the virtual power of the internal forces reads as

$$\begin{aligned}
\mathcal{P}^{int} &= -\int\limits_0^R \int\limits_0^{2\pi} \int\limits_{-\frac{h}{2}}^{+\frac{h}{2}} \pi_{rr}(r)\,\dot{\hat{E}}_{rr}(r)\,r\,dz\,d\varphi\,dr \\[2mm]
&= -\int\limits_0^R \int\limits_0^{2\pi} \int\limits_{-\frac{h}{2}}^{+\frac{h}{2}} \pi_{rr}(r)\left[\frac{\partial u_z(r)}{\partial r}\,\frac{\partial \hat{v}_z(r)}{\partial r}\right]\,r\,dz\,d\varphi\,dr\,.
\end{aligned} \tag{6.15}$$

Eq. (6.15) indicates that the membrane-specific "degrees of freedom" $\frac{\partial u_z(r)}{\partial r}\,\frac{\partial \hat{v}_z(r)}{\partial r}$ induce internal stress resultants on which they produce power, namely internal forces per unit length

$$n_{L,rr}(r) = \int\limits_{-\frac{h}{2}}^{+\frac{h}{2}} \pi_{rr}(r)\,dz \equiv \pi_{rr}^{2D}(r)\,. \tag{6.16}$$

Stress resultant (6.16) can be interpreted as the normal component of the 2D second Piola-Kirchhoff stress tensor in $\mathbf{e}_r$ direction acting on a 2D solid. For a hexagonal graphene lattice, the nonlinear, anisotropic material behavior is described by the following hyperelastic stress-strain relation [Höller et al., 2020a]

$$n_{L,rr} = \rho_{m,0}^{2D}\left[\beta_1 + \beta_2\,E_{rr} + \beta_3\,S_{rr}\right]\,. \tag{6.17}$$

In Eq. (6.17), $\rho_{m,0}^{2D}$ is the initial mass density per area of graphene; β_1, β_2, and β_3 are scalars depending on graphene's DFT-based material fitting coefficients c_i and principal invariants I_i of the strain and structural tensor [Höller et al., 2020a][1]

$$\begin{aligned}
\beta_1 &= c_2\,I_1 + c_6\,I_1^2 + c_9\,I_1^3 + c_{13}\,I_3 \\
\beta_2 &= -c_2 + 2\,c_4 + (3\,c_5 - c_6)I_1 + (4\,c_7 - c_9)I_1^2\,, \\
\beta_3 &= c_3 + c_{13}\,I_1\,,
\end{aligned} \tag{6.18}$$

---

[1] The fitting coefficients within the used hyperelastic material model of graphene are valid for Green-Lagrange strains between -0.03 and +0.28 [Höller et al., 2020a, Table 2].

with

$$I_1 = E_{rr}, \quad I_3 = E_{rr}^3 \cos(6\varphi). \tag{6.19}$$

S_{rr} refers to the anisotropic behavior and is the component of the second-order tensor, $\mathbf{S} = \partial I_3 / \partial \mathbf{E}$, reading as,

$$S_{rr} = 3\, E_{rr}^2 \cos(6\varphi), \tag{6.20}$$

characterizing the influence of the strain of E_{rr} onto the mechanical response of graphene.

Back-insertion of (6.16) together with (6.17)-(6.19) into the power expression (6.15), yields the virtual power of internal forces in the following form

$$
\begin{aligned}
\mathcal{P}^{int} \;=\; & -\rho_{m,0}^{2D} \int\limits_0^R \int\limits_0^{2\pi} \Big[2\, c_4\, E_{rr} + 3 \left(c_5 + c_3 \cos(6\varphi) \right) E_{rr}^2 \\
& + 4 \left(c_7 + c_{13} \cos(6\varphi) \right) E_{rr}^3 \Big] \times \left[\frac{\partial u_z(r)}{\partial r}\, \frac{\partial \hat{v}_z(r)}{\partial r} \right] r\, d\varphi\, dr.
\end{aligned}
\tag{6.21}
$$

Substitution of the Green-Lagrange strain (6.10) results in

$$
\begin{aligned}
\mathcal{P}^{int} \;=\; & -\rho_{m,0}^{2D} \int\limits_0^R \int\limits_0^{2\pi} \Bigg[c_4 \left(\frac{\partial u_z(r)}{\partial r} \right)^2 + \frac{3}{4} \left(c_5 + c_3 \cos(6\varphi) \right) \left(\frac{\partial u_z(r)}{\partial r} \right)^4 \\
& + \frac{1}{2} \left(c_7 + c_{13} \cos(6\varphi) \right) \left(\frac{\partial u_z(r)}{\partial r} \right)^6 \Bigg] \times \left[\frac{\partial u_z(r)}{\partial r}\, \frac{\partial \hat{v}_z(r)}{\partial r} \right] r\, d\varphi\, dr.
\end{aligned}
\tag{6.22}
$$

6.2.4 Virtual Power of external forces and PVP-based governing equation

Evaluation of (6.4) for the virtual velocity (6.8) and for the deformation gradient (6.13)-(6.14), yields when considering a membrane with outward normals $\mathbf{N} = \mathbf{e}_z$

$$
\begin{aligned}
\mathcal{P}^{ext} \;=\; & +\int\limits_0^R \int\limits_0^{2\pi} \hat{\mathbf{v}}(\mathbf{X}) \cdot \mathbf{F} \cdot \boldsymbol{\pi}(\mathbf{X}) \cdot \mathbf{e}_z\, r\, d\varphi\, dr \\
\;=\; & +\int\limits_0^R \int\limits_0^{2\pi} \hat{v}_z(r) \cdot \left(\pi_{zz}(r) + \frac{\partial u_z(r)}{\partial r} \pi_{rz}(r) \right) r\, d\varphi\, dr.
\end{aligned}
\tag{6.23}
$$

Eq. (6.23) indicates that the membrane-specific degree of freedom $\hat{v}_z(r)$ induces external Lagrangian stress resultants on which power is produced, namely vertical Lagrangian surface loads (dimension force per unit area), reading as

$$p_{L,z}(r) = \pi_{zz}(r) + \frac{\partial u_z(r)}{\partial r} \pi_{rz}(r). \tag{6.24}$$

Substitution of (6.24) into the power expression (6.23) yields the virtual power of external forces in the following form

$$\mathcal{P}^{ext} = +\int\limits_0^R \int\limits_0^{2\pi} p_{L,z}(r)\, \hat{v}_z(r)\, r\, d\varphi\, dr. \tag{6.25}$$

As regards more complex loading cases, Eq. (6.25) can be straightforwardly extended to membranes loaded by surface loads per unit area $p_{L,z}(r)$ over the entire membrane, distributed forces $\overline{p}_{L,z}$ over the centered circular area of radius R_T, and vertical single forces $P_{L,z}$ acting in the center of the membrane, see Fig. 6.2. In this context, the virtual power of external forces for
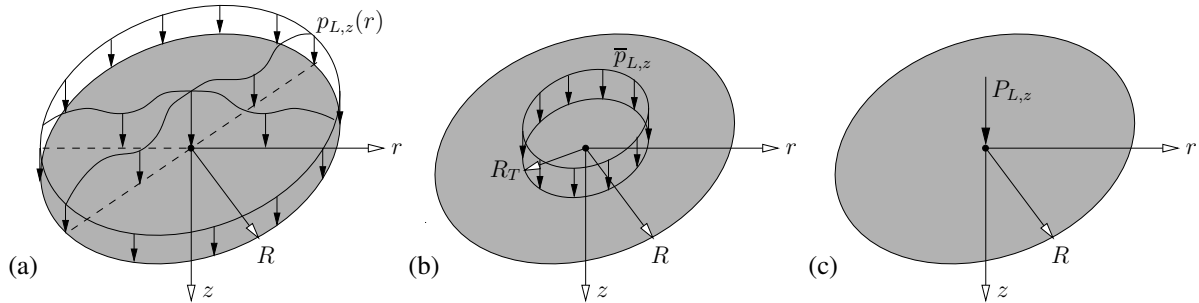
Fig. 6.2: (a) Vertical surface load $p_{L,z}(r)$ non-uniformly distributed over the entire membrane; (b) vertical surface load $\overline{p}_{L,z}$ uniformly distributed over a centered circular area of radius R_T; and (c) vertical single force $P_{L,z}$ acting in the center of the membrane.

a circular membrane subjected to axisymmetric loads reads as

$$\mathcal{P}^{ext} = + \int\limits_{0}^{R}\int\limits_{0}^{2\pi} p_{L,z}(r)\,\hat{v}_z(r)\,r\,d\varphi\,dr + \overline{p}_{L,z}\int\limits_{0}^{R_T}\int\limits_{0}^{2\pi}\hat{v}_z(r)\,r\,d\varphi\,dr + P_{L,z}\,\hat{v}_z(r)\Big|_{r=0}. \tag{6.26}$$

Insertion of the expression for the virtual power of internal forces (6.22) as well as of the expression for the virtual power of external forces (6.26), into the PVP (6.1), yields

$$\mathcal{P}^{ext} + \mathcal{P}^{int} =$$
$$+ \int\limits_{0}^{R}\int\limits_{0}^{2\pi} p_{L,z}(r)\,\hat{v}_z(r)\,r\,d\varphi\,dr + \overline{p}_{L,z}\int\limits_{0}^{R_T}\int\limits_{0}^{2\pi}\hat{v}_z(r)\,r\,d\varphi\,dr + P_{L,z}\,\hat{v}_z(r)\Big|_{r=0}$$
$$- \rho_{m,0}^{2D}\int\limits_{0}^{R}\int\limits_{0}^{2\pi}\left[c_4\left(\frac{\partial u_z(r)}{\partial r}\right)^2 + \frac{3}{4}\left(c_5 + c_3\cos(6\varphi)\right)\left(\frac{\partial u_z(r)}{\partial r}\right)^4\right.$$
$$\left. + \frac{1}{2}\left(c_7 + c_{13}\cos(6\varphi)\right)\left(\frac{\partial u_z(r)}{\partial r}\right)^6\right] \times \left[\frac{\partial u_z(r)}{\partial r}\,\frac{\partial\hat{v}_z(r)}{\partial r}\right] r\,d\varphi\,dr = 0. \tag{6.27}$$

The PVP in the format (6.27) is the basis for the determination of the sought deflection function $u_z(r)$. Therefore, the latter is expanded into a Fourier series, which leads to the so-called Galerkin method, as described in Section 6.3.

6.3 Mathematical solution procedure

The Principle of Virtual Power in the format (6.27) can also be used for constructing a *nonlinear* algebraic system of equations giving access to the deflection function $u_z(r)$. For this purpose,

we resort to Navier [1823], representing the axisymmetric deflection function as a series of trigonometric functions, i.e. a Fourier series

$$u_z(r) = \sum_{m=1}^{N_m} a_m \, w_m(r) \,, \tag{6.28}$$

where a_m are unknown Fourier coefficients (amplitudes), and w_m denote corresponding trigonometric functions reading as

$$w_m(r) = \cos\left(\frac{m \, r \, \pi}{2 \, R}\right) \quad \text{for} \quad m = 1, 3, 5 \dots \,. \tag{6.29}$$

Subscripts m refer to the number of waves related to the trigonometric functions, with N_m as the total number of employed deflection modes. (6.29) automatically ensures a circular membrane with simply supported boundaries, i.e. deflection modes are zero for $r = R$: $w_m(R) = 0$.

Similar choices are made for the virtual velocities $\hat{v}_z(r)$, through introduction of Ansatz functions identical to those in Eq. (6.28),

$$\hat{v}_z(r) = \sum_{t=1}^{N_t} \dot{\hat{a}}_t \, w_t(r) \,, \tag{6.30}$$

with the virtual velocity coefficient $\dot{\hat{a}}_t$. Insertion of (6.28) and of (6.30) into Eq. (6.27), yields the following Galerkin-type solution scheme

$$
\begin{aligned}
&\mathcal{P}^{ext} + \mathcal{P}^{int} = \\
&\sum_{t=1}^{N_t} \dot{\hat{a}}_t \left\{ \int_0^R \int_0^{2\pi} p_{L,z} \, w_t \, r \, d\varphi \, dr + \overline{p}_{L,z} \int_0^{R_T} \int_0^{2\pi} w_t \, r \, d\varphi \, dr + P_{L,z} \, w_t \Big|_{r=0} \right. \\
&- \rho_{m,0}^{2D} \int_0^R \int_0^{2\pi} \left[c_4 \left(\sum_{m=1}^{N_m} a_m \frac{\partial w_m}{\partial r} \right)^2 + \frac{3}{4} \, (c_5 + c_3 \cos(6\varphi)) \left(\sum_{m=1}^{N_m} a_m \frac{\partial w_m}{\partial r} \right)^4 \right. \\
&+ \left. \frac{1}{2} \, (c_7 + c_{13} \cos(6\varphi)) \left(\sum_{m=1}^{N_m} a_m \frac{\partial w_m}{\partial r} \right)^6 \right] \times \left(\sum_{m=1}^{N_m} a_m \frac{\partial w_m}{\partial r} \right) \frac{\partial w_t}{\partial r} \, r \, d\varphi \, dr \left. \right\} \\
&= 0 \,.
\end{aligned}
\tag{6.31}
$$

After simplification, we further obtain a more suitable solution scheme

$$
\begin{aligned}
&\mathcal{P}^{ext} + \mathcal{P}^{int} = \\
&\sum_{t=1}^{N_t} \dot{\hat{a}}_t \left\{ \int_0^R \int_0^{2\pi} p_{L,z} \, w_t \, r \, d\varphi \, dr + \overline{p}_{L,z} \int_0^{R_T} \int_0^{2\pi} w_t \, r \, d\varphi \, dr + P_{L,z} \, w_t \Big|_{r=0} \right. \\
&- 2 \, \pi \, \rho_{m,0}^{2D} \, c_4 \sum_{j,k,l=1}^{N_m} a_j \, a_k \, a_l \int_0^R \frac{\partial w_j}{\partial r} \frac{\partial w_k}{\partial r} \frac{\partial w_l}{\partial r} \frac{\partial w_t}{\partial r} \, r \, dr \\
&- \frac{3}{2} \, \pi \, \rho_{m,0}^{2D} \, c_5 \sum_{j,k,l,m,n=1}^{N_m} a_j \, a_k \, a_l \, a_m \, a_n \int_0^R \frac{\partial w_j}{\partial r} \frac{\partial w_k}{\partial r} \frac{\partial w_l}{\partial r} \frac{\partial w_m}{\partial r} \frac{\partial w_n}{\partial r} \frac{\partial w_t}{\partial r} \, r \, dr
\end{aligned}
$$

$$-\pi \, \rho_{m,0}^{2D} \, c_7 \sum_{j,k,l,m,n,q,s=1}^{N_m} a_j \, a_k \, a_l \, a_m \, a_n \, a_q \, a_s \int\limits_0^R \frac{\partial w_j}{\partial r} \frac{\partial w_k}{\partial r} \frac{\partial w_l}{\partial r} \frac{\partial w_m}{\partial r} \frac{\partial w_n}{\partial r} \frac{\partial w_q}{\partial r} \frac{\partial w_s}{\partial r} \frac{\partial w_t}{\partial r} \, r \, dr \Bigg\}$$

$$= 0 \,. \tag{6.32}$$

Requiring validity of (6.32) for any combinations of the virtual coefficients $\dot{a}_t$, yields a nonlinear system of N_t algebraic equations for the unknowns a_m, reading as

$$f_t = V_t^p + V_t^{\overline{p}} + V_t^P - \sum_{j,k,l=1}^{N_m} a_j \, a_k \, a_l \, M_{jklt}^I - \sum_{j,k,l,m,n=1}^{N_m} a_j \, a_k \, a_l \, a_m \, a_n \, M_{jklmnt}^{II}$$

$$- \sum_{j,k,l,m,n,q,s=1}^{N_m} a_j \, a_k \, a_l \, a_m \, a_n \, a_q \, a_s \, M_{jklmnqst}^{III} = 0 \,, \qquad \text{for} \quad t = 1, 3, ..., N_t \,, \tag{6.33}$$

with

$$M_{jklt}^I = 2 \, \pi \, \rho_{m,0}^{2D} \, c_4 \int\limits_0^R \frac{\partial w_j}{\partial r} \frac{\partial w_k}{\partial r} \frac{\partial w_l}{\partial r} \frac{\partial w_t}{\partial r} \, r \, dr \,, \tag{6.34}$$

as the stiffness matrix elements associated to deformation amplitudes of third power (see Appendix A, Eq. (6.A.4), for analytical expressions concerning (6.34));

$$M_{jklmnt}^{II} = \frac{3}{2} \, \pi \, \rho_{m,0}^{2D} \, c_5 \int\limits_0^R \frac{\partial w_j}{\partial r} \frac{\partial w_k}{\partial r} \frac{\partial w_l}{\partial r} \frac{\partial w_m}{\partial r} \frac{\partial w_n}{\partial r} \frac{\partial w_t}{\partial r} \, r \, dr \,, \tag{6.35}$$

as the stiffness matrix elements associated to deformation amplitudes of fifth power (see Appendix A, Eq. (6.A.5), for analytical expressions concerning (6.35));

$$M_{jklmnqst}^{III} = \pi \, \rho_{m,0}^{2D} \, c_7 \int\limits_0^R \frac{\partial w_j}{\partial r} \frac{\partial w_k}{\partial r} \frac{\partial w_l}{\partial r} \frac{\partial w_m}{\partial r} \frac{\partial w_n}{\partial r} \frac{\partial w_q}{\partial r} \frac{\partial w_s}{\partial r} \frac{\partial w_t}{\partial r} \, r \, dr \,, \tag{6.36}$$

as the stiffness matrix elements associated to deformation amplitudes of seventh power (see Appendix A, Eq. (6.A.6), for analytical expressions concerning (6.36));

$$V_t^p = \int\limits_0^R \int\limits_0^{2\pi} p_{L,z} \, w_t \, r \, d\varphi \, dr \,, \tag{6.37}$$

as the load vector elements associated to general surface loads acting on the entire membrane, respectively (see Appendix A, Eq. (6.A.1), for analytical expressions concerning (6.37), specified for constant and cosine-type loads);

$$V_t^{\overline{p}} = \overline{p}_{L,z} \int\limits_0^{R_T} \int\limits_0^{2\pi} w_t \, r \, d\varphi \, dr \,, \tag{6.38}$$

as the load vector elements associated to the distributed load acting over the centered circular area of radius R_T (see Appendix A, Eq. (6.A.2), for analytical expressions concerning (6.38));

$$V_t^P = P_{L,z} \, w_t \Big|_{r=0} \,, \tag{6.39}$$

as the load vector elements associated to single forces acting in the center of the membrane (see Appendix A, Eq. (6.A.3), for analytical expressions concerning (6.39)). The corresponding approximative solution for $u_z(r)$ is the more precise the more series deflection members (being N_m in number) are employed.

As regards solving the derived nonlinear multivariate system of equations (6.33), we resort to the iterative Newton-Raphson method [Ortega and Rheinboldt, 2000] being defined as

$$\mathbf{a}_{i+1} = \mathbf{a}_i - \mathbf{J}^{-1}(\mathbf{a}_i) \cdot \mathbf{f}(\mathbf{a}_i),\tag{6.40}$$

where vector $\mathbf{a}_i = [a_{1,i}, a_{3,i}, ..., a_{N_m,i}]^T$ contains the unknown amplitudes $a_{m,i}$ for each iteration step i; vector $\mathbf{f} = [f_{1,i}, f_{3,i}, ..., f_{N_t,i}]^T$ contains each line t of the nonlinear system of equation according to (6.33); and $\mathbf{J}$ is the so-called Jacobian matrix as the partial derivative of $\mathbf{f}$ with respect to the amplitudes $\mathbf{a}$. Thus, the elements of the $N_t \times N_j$ Jacobian matrix for iteration step i, when specified for (6.33), read as

$$
\begin{aligned}
J_{tj,i} = \frac{\partial f_{t,i}}{\partial a_{j,i}} \quad = \quad &-3\sum_{k,l=1}^{N_m} a_k\, a_l\, M^I_{jklt} - 5\sum_{k,l,m,n=1}^{N_m} a_k\, a_l\, a_m\, a_n\, M^{II}_{jklmnt} \\
&-7\sum_{k,l,m,n,q,s=1}^{N_m} a_l\, a_l\, a_m\, a_n\, a_q\, a_s\, M^{III}_{jklmnqst}.
\end{aligned}
\tag{6.41}
$$

According to the first iteration step, $i = 0$, an initial estimate for the amplitudes $\mathbf{a}_0$ can be directly calculated using a reduced system of equation, including deflection amplitudes up to the third power, namely

$$V^p_t + V^{\overline{p}}_t + V^P_t - \sum_{j,k,l=1}^{N_m} a_{j,0}\, a_{k,0}\, a_{l,0}\, M^I_{jklt} = 0, \qquad \text{for} \quad t = 1, 3, ..., N_t.\tag{6.42}$$

Based on the initial estimate $\mathbf{a}_0$, the Newton-Raphson iteration process (6.40) is repeated until convergence is reached.

6.4 Application to circular graphene membranes and validation by means of AFM experiments

The structural problem (6.33)-(6.39) is now applied to the analysis of a free-standing circular graphene membrane of $R = 500\,\text{nm}$ radius, simply supported at its boundary. In the following, this membrane is subjected to different axisymmetric mechanical loads as constant and cosine-type loads $p_{L,z}(r)$ over the entire membrane, respectively, as well as distributes loads $\overline{p}_{L,z}$ over a circular area of radius R_T (see Fig. 6.3), each of them resulting in a force of $F = 500\,\text{nN}$. Corresponding results will be presented in a dimensionless way, which does not only comprise the actual deformations arising from the aforementioned material, structural, and loading characteristics, but which reflects infinitely many additional problems which are associated with different membrane radii and different mechanical loads. In more detail, we consider a dimensional analysis [Barenblatt, 1996] of the deflection function (6.28) arising from the solution of (6.33), together with (6.34) to (6.39). This yields the following dimensionless relations

$$\frac{u_z}{R} = \frac{u_z}{R}\left(\frac{r}{R}, \frac{R_T}{R}, \frac{c_3}{c_4}, \frac{c_5}{c_4}, \frac{c_7}{c_4}, \frac{c_{13}}{c_4}, \frac{p_{L,z}\,R}{\rho^{2D}_{m,0}\,c_4}, \frac{\overline{p}_{L,z}\,R}{\rho^{2D}_{m,0}\,c_4}\right).\tag{6.43}$$
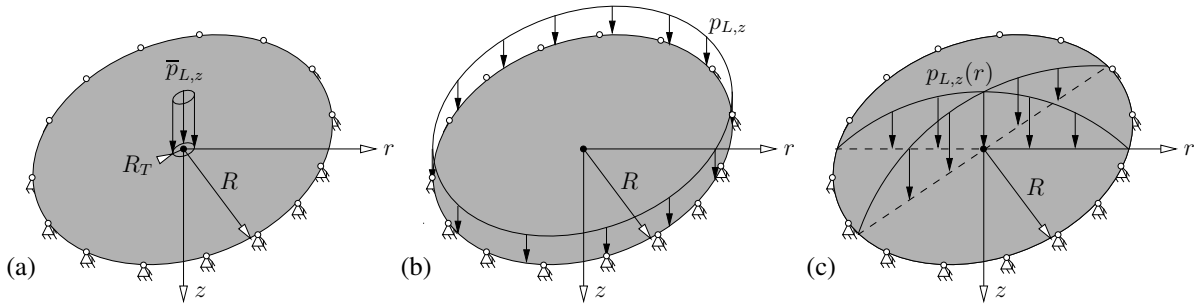
Fig. 6.3: Circular graphene membrane with simply supported boundaries and radius R, subjected to (a) vertical load $\overline{p}_{L,z}$ distributed over a centered circular area of radius R_T, (b) uniform vertical surface load $p_{L,z}$, and (c) non-uniform vertical cosine-type load $p_{L,z}(r)$.

(6.43) elucidates that the basic dimensionless functions $[u_z/R]$ depend on geometrical characteristics, in-plane stiffness constants of graphene [Höller et al., 2020a], and dimensionless quantities related to mechanical loadings, so as to deliver dimensionless quantities related to deflections. These relations, depicted in the format of $[u_z/R](r/R = R_T/R = c_3/c_4 = c_5/c_4 = c_7/c_4 = c_{13}/c_4 = p_{L,z} R/(\rho_{m,0}^{2D} c_4) = \overline{p}_{L,z} R/(\rho_{m,0}^{2D} c_4) = \text{constant})$ in Figures 6.4, 6.6, and 6.7, are valid for any change $R \to \lambda R$, once $r \to \lambda r$, $R_T \to \lambda R_T$, $p_{L,z} \to p_{L,z}/\lambda$, and $\overline{p}_{L,z} \to \overline{p}_{L,z}/\lambda$.

6.4.1 Example 1/Validation: Circular graphene membrane subjected to a concentrated load

The membrane is subjected to a vertical load $\overline{p}_{L,z}$, which is distributed over the centered circular area of radius $R_T = 16.5\,\text{nm}$, see Fig. 6.3(a). This concentrated load represents the tip of a nanoindentation of free-standing graphene membranes as experimentally measured by Lee et al. [2008]. It is noted that the relation between the Eulerian loading area dS and the Lagrangian loading area dS_0,

$$dS_0\, N_z = \frac{dS}{\det \mathbf{F}}\, n_z\,, \tag{6.44}$$

results in equivalent loading areas of the indenter, $dS_0 = dS$, when considering $\det \mathbf{F} = 1$ according to (6.13) and (6.14), as well as a horizontal tangent of the aforementioned tip with outward normals $N_z = n_z = -1$.

The approximative solution for the dimensionless maximum deflection $[u_z/R]$ located at $r = 0$ can be regarded as converged once $N_m = 16$ series members are employed, see Fig. 6.4(c). With Matlab version R2012b [Mathworks, 2012] running on a computer AMD Phenom(tm) II X6 1090T with 8GB RAM, this related to 24.4 seconds computing time, see Fig. 6.4(d). Considering corresponding fields, the maximum deflections occur at the center of the membrane, see Fig. 6.4(a-b).

For validation of the provided structural problem according to (6.33)-(6.39), the results of force-displacement curves are compared to those stemming from experimental measurements by Lee et al. [2008] performed with an atomic force microscope (AFM). In this context, a circular graphene membrane of radius $R = 500\,\text{nm}$ is subjected to the indenter tip, representing a resulting force F up to $1000\,\text{nN}$ acting on a circular area of radius R_T of $16.5\,\text{nm}$ and $27.5\,\text{nm}$, respectively, see Fig. 6.5. Maximum differences between experimental measurements and series-based results of the deflections $u_{z,max}$ are as low as $0.27\,\%$ for $F = 500\,\text{nN}$, and $1.44\,\%$ for $F = 1000\,\text{nN}$.
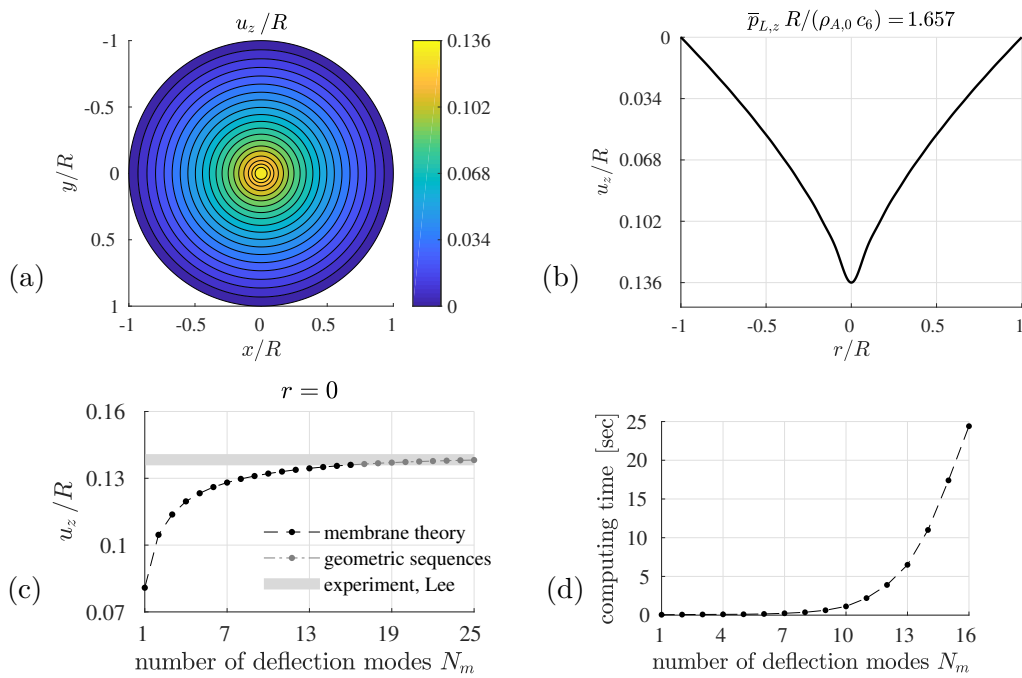
Fig. 6.4: Dimensionless deflections $[u_z/R]$ in circular graphene membrane, with simply supported boundary, subjected to a concentrated surface load $\overline{p}_{L,z}\,R/(\rho_{m,0}^{2D}\,c_6) = 1.657$: (a) deflections in entire membrane, (b) deflections in r-z-plane, (c) convergence study of the dimensionless deflection located at $r = 0$ as a function of the number of deflection modes N_m, and (d) corresponding computing time for results associated to one point of the plate.
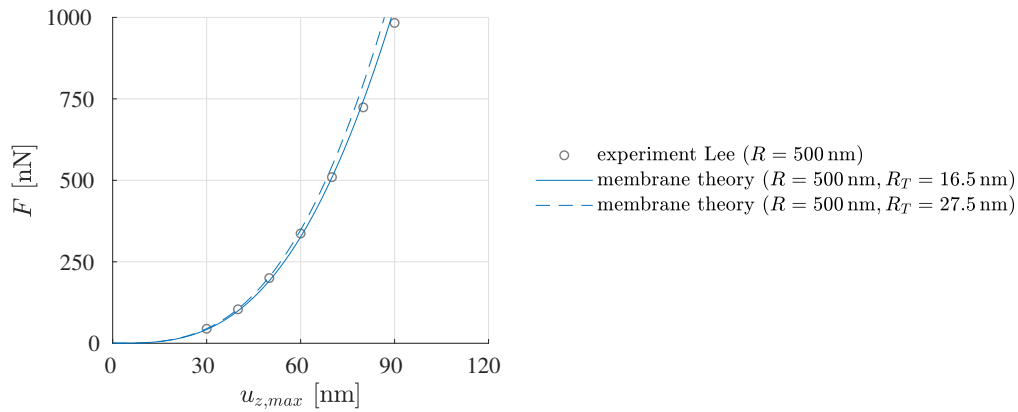
Fig. 6.5: Validation of series-based solution procedure (6.33) according to example 1 by experimental measurements, as provided by Lee et al. [2008] using AFM nanoindentation.

6.4.2 Example 2: Circular graphene membrane subjected to an uniform surface load

The membrane is subjected to an uniform surface load $p_{L,z}(r) = \text{constant} = p_{L,z}$, representing the deadload of a graphene membrane for example, see Fig. 6.3(b). The approximative solution for the dimensionless maximum deflection $[u_z/R]$ at the membrane's center can be regarded as converged once $N_m = 7$ series members are employed, see Fig. 6.6(c). With Matlab version R2012b running on a computer AMD Phenom(tm) II X6 1090T with 8GB RAM, this related to

Fig. 6.6: Dimensionless deflections $[u_z/R]$ in circular graphene membrane, with simply supported boundary, subjected to constant surface load $p_{L,z}\,R/(\rho_{m,0}^{2D}\,c_6) = 0.0018$: (a) deflections in entire membrane, (b) deflections in r-z-plane, (c) convergence study of the dimensionless deflection located at $r = 0$ as a function of the number of deflection modes N_m, and (d) corresponding computing time for results associated to one point of the plate.

0.2 seconds computing time, see Fig. 6.6(d). Considering corresponding fields, the maximum deflections occur at the center of the membrane, see Figs. 6.6(a-b).

6.4.3 Example 3: Circular graphene membrane subjected to a cosine-type surface load

The membrane is subjected to a cosine-type surface load $p_{L,z}(r) = p_{L,z}\cos(r\,\pi/(2\,R))$, representing an external pressure for example, see Fig. 6.3(c). The approximative solution for the dimensionless deflection $[u_z/R]$ at the membrane's center can be regarded as converged once $N_m = 8$ series members are employed, see Fig. 6.7(c). With Matlab version R2012b running on a computer AMD Phenom(tm) II X6 1090T with 8GB RAM, this related to 0.3 seconds computing time, see Fig. 6.7(d). Considering corresponding fields, the maximum deflections occur at the center of the membrane, see Figs. 6.7(a-b).

6.5 Conclusion

The Principle of Virtual Power, with rigorous discrimination of internal versus external forces, was applied to the problem of a circular suspended graphene membrane, simply supported at its boundary, and subjected to different axisymmetric mechanical loads. As regards material behavior of graphene, the DFT-based hyperelastic material model [Höller et al., 2020a] was used, and the resulting Fourier series-based nonlinear algebraic system of equations was solved by the iterative Newton-Raphson method. The aforementioned solution procedure also appears
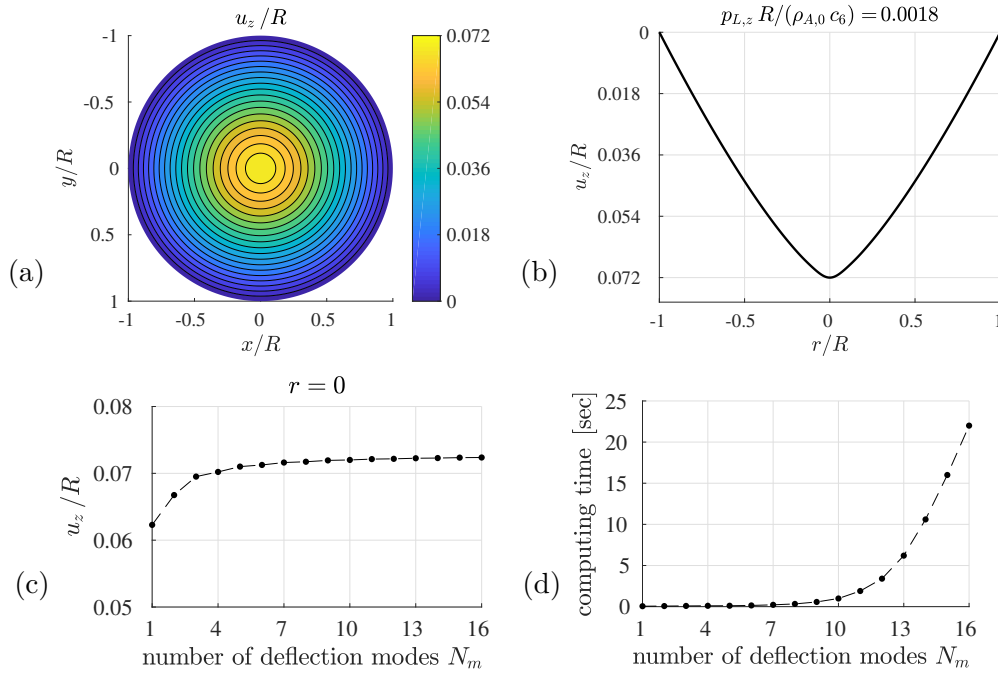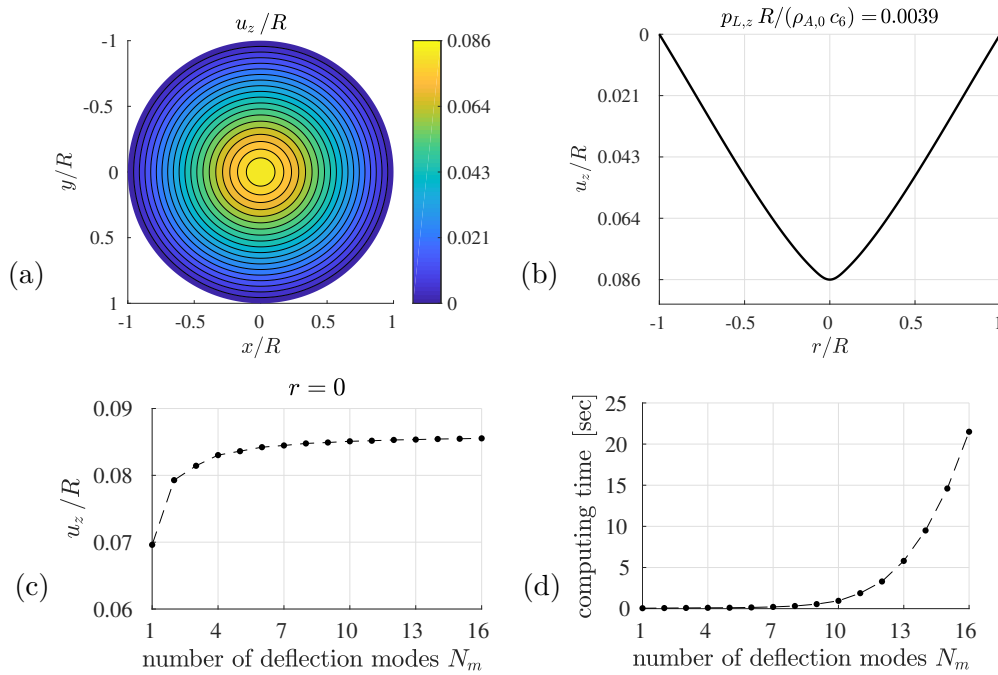
Fig. 6.7: Dimensionless deflections $[u_z/R]$ in circular graphene membrane, with simply supported boundary, subjected to a cosine-type surface load $p_{L,z}\,R/(\rho_{m,0}^{2D}\,c_6) = 0.0039$: (a) deflections in entire membrane, (b) deflections in r-z-plane, (c) convergence study of the dimensionless deflection located at $r = 0$ as a function of the number of deflection modes N_m, and (d) corresponding computing time for results associated to one point of the plate.

as an efficient and computational fast method for modeling specific mechanical problems of graphene membranes. The numerical results are validated by experimental measurements as presented by Lee et al. [2008] using AFM nanoindentation, being in good agreement up to large deformations. We regard this as an interesting example for energetically consistent formulations appearing as the basis for particularly relevant and reliable solutions to the growing field of the structural mechanics of graphene. Such a energetically consistent theory is comparable to other nonlinear problems regarding large deformations as the analyses of laminated composite beams using the principle of virtual work and a finite element approximation in a total Lagrangian manner [Pagani and Carrera, 2017]; of inflated circular hyperelastic membranes based on the variational method including a Mooney-Rivlin strain energy [Patil and DasGupta, 2013]; and of the nonlinear vibration response of a neo-Hookean membrane obtained by means of the Galerkin method [Gonçalves et al., 2009].

Acknowledgments

6.A Stiffness matrix and load vector elements

In order to determine the unknown coefficients a_m, we have to solve the system of algebraic equations (6.33) together with the corresponding stiffness matrix and load vector elements

(6.34)-(6.39), for the employed trigonometric functions of type $w_m(r)$, see (6.29). First, we provide the load vector elements for any combinations of $t = 1, 3, ..., N_t$:

(i) Load vector element associated to the constant and cosine-type surface load $p_{L,z}(r)$ acting on the entire membrane:

$$V_t^p = \int\limits_0^R \int\limits_0^{2\pi} p_{L,z}\, w_t\, r\, d\varphi\, dr \tag{6.A.1}$$

$$= \begin{cases} p_{L,z}\, \dfrac{4\,R^2\left[\pi\,t\,\sin\left(\frac{\pi\,t}{2}\right) - 2\right]}{\pi\,t^2} & p_{L,z}(r) = p_{L,z}, \\[2ex] p_{L,z}\, \dfrac{R^2(\pi^2 - 4)}{2\,\pi} & \text{for} \quad p_{L,z}(r) = p_{L,z}\cos\left(\frac{r\,\pi}{2\,R}\right), \quad t = 1 \\[2ex] p_{L,z}\, \dfrac{8\,R^2\left[2\,t\,\sin\left(\frac{\pi\,t}{2}\right) - t^2 - 1\right]}{\pi\,(t^2 - 1)^2} & p_{L,z}(r) = p_{L,z}\cos\left(\frac{r\,\pi}{2\,R}\right), \quad t \neq 1, \end{cases}$$

(ii) Load vector element associated to the distributed load $\overline{p}_{L,z}$ acting over the centered circular area of radius R_T:

$$V_t^{\overline{p}} = \overline{p}_{L,z} \int\limits_0^{R_T} \int\limits_0^{2\pi} w_t\, r\, d\varphi\, dr = \overline{p}_{L,z}\, \frac{4\,R\left[\pi\,t\,R_T\,\sin\left(\frac{\pi\,t\,R_T}{2\,R}\right) - 4\,R\sin^2\left(\frac{\pi\,t\,R_T}{4\,R}\right)\right]}{\pi\,t^2}, \tag{6.A.2}$$

(iii) Load vector element associated to single forces $P_{L,z}$ acting in the center of the membrane:

$$V_t^P = P_{L,z}\, w_t\Big|_{r=0} = P_{L,z}. \tag{6.A.3}$$

Next, we provide the stiffness matrix elements M_{jklt}^I, M_{jklmnt}^{II}, and $M_{jklmnrst}^{III}$, for any combinations of j, k, l, m, n, q, s, and t up to the chosen number of 16 deflection modes (with $N_m = 31$) being sufficient for various mechanical loading cases, see Sec.6.4:

1. Stiffness matrix elements associated to deformation amplitudes of third power:

$$\begin{aligned} M_{jklt}^I &= 2\,\pi\,\rho_{m,0}^{2D}\,c_4 \int\limits_0^R \frac{\partial w_j}{\partial r}\frac{\partial w_k}{\partial r}\frac{\partial w_l}{\partial r}\frac{\partial w_t}{\partial r}\, r\, dr \\[1ex] &= \rho_{m,0}^{2D}\,c_4 \frac{j\,k\,l\,t\,\pi^5}{8\,R^4} \int\limits_0^R \sin\left(\frac{j\,r\,\pi}{2\,R}\right)\sin\left(\frac{k\,r\,\pi}{2\,R}\right) \times \\[1ex] &\quad \times \sin\left(\frac{l\,r\,\pi}{2\,R}\right)\sin\left(\frac{t\,r\,\pi}{2\,R}\right)\, r\, dr \\[1ex] &= \frac{\rho_{m,0}^{2D}\,c_4}{R^2}\, A_{jklt}^I, \qquad \text{for} \quad j, k, l, t = 1, 3, ..., 31. \end{aligned} \tag{6.A.4}$$

2. Stiffness matrix elements associated to deformation amplitudes of fifth power:

$$M_{jklmnt}^{II} = \frac{3}{2}\,\pi\,\rho_{m,0}^{2D}\,c_5 \int\limits_0^R \frac{\partial w_j}{\partial r}\frac{\partial w_k}{\partial r}\frac{\partial w_l}{\partial r}\frac{\partial w_m}{\partial r}\frac{\partial w_n}{\partial r}\frac{\partial w_t}{\partial r}\, r\, dr$$

$$
\begin{aligned}
&= \frac{3}{2}\,\rho_{m,0}^{2D}\,c_5\,\frac{j\,k\,l\,m\,n\,t\,\pi^7}{64\,R^6}\,\times\\
&\quad\int_0^R \sin\left(\frac{j\,r\,\pi}{2\,R}\right)\sin\left(\frac{k\,r\,\pi}{2\,R}\right)\sin\left(\frac{l\,r\,\pi}{2\,R}\right)\,\times\\
&\quad\times \sin\left(\frac{m\,r\,\pi}{2\,R}\right)\sin\left(\frac{n\,r\,\pi}{2\,R}\right)\sin\left(\frac{t\,r\,\pi}{2\,R}\right)\,r\,dr\\
&= \frac{\rho_{m,0}^{2D}\,c_5}{R^4}\,A_{jklmnt}^{II}\,,
\end{aligned}
$$

$$
\text{for}\quad j,k,l,m,n,t = 1,3,...,31\,. \tag{6.A.5}
$$

3. Stiffness matrix elements associated to deformation amplitudes of seventh power:

$$
\begin{aligned}
M_{jklmnqst}^{III} &= \rho_{m,0}^{2D}\,\pi\,c_7 \int_0^R \frac{\partial w_j}{\partial r}\frac{\partial w_k}{\partial r}\frac{\partial w_l}{\partial r}\frac{\partial w_m}{\partial r}\frac{\partial w_n}{\partial r}\frac{\partial w_q}{\partial r}\frac{\partial w_s}{\partial r}\frac{\partial w_t}{\partial r}\,r\,dr\\
&= \rho_{m,0}^{2D}\,c_7\,\frac{j\,k\,l\,m\,n\,q\,s\,t\,\pi^9}{256\,R^8}\,\times\\
&\quad\int_0^R \sin\left(\frac{j\,r\,\pi}{2\,R}\right)\sin\left(\frac{k\,r\,\pi}{2\,R}\right)\sin\left(\frac{l\,r\,\pi}{2\,R}\right)\sin\left(\frac{m\,r\,\pi}{2\,R}\right)\,\times\\
&\quad\times \sin\left(\frac{n\,r\,\pi}{2\,R}\right)\sin\left(\frac{q\,r\,\pi}{2\,R}\right)\sin\left(\frac{s\,r\,\pi}{2\,R}\right)\sin\left(\frac{t\,r\,\pi}{2\,R}\right)\,r\,dr\\
&= \frac{\rho_{m,0}^{2D}\,c_7}{R^6}\,A_{jklmnqst}^{III}\,,
\end{aligned}
$$

$$
\text{for}\quad j,k,l,m,n,q,s,t = 1,3,...,31\,. \tag{6.A.6}
$$

The dimensionless stiffness matrix elements A_{jklt}^{I}, A_{jklmnt}^{II}, and $A_{jklmnqst}^{III}$ are provided in form of an electronic data set for up 16 deflection modes, see Appendix B. Since the trigonometric functions of form $\sin(j\,r\,\pi/(2\,R))$, appearing in (6.A.4)-(6.A.6), are of similar shape, the ordering of the matrix indices can be chosen arbitrarily. Thus, it is sufficient to calculate matrix elements for indices in descending order, $j \geq k \geq l \geq m \geq n \geq q \geq s \geq t$, which then can be used for other chosen ordering of the indices[2].

6.B Supplementary material

The supplementary data associated with this article can be found, in the online version, at https://owncloud.tuwien.ac.at/index.php/s/7FvfmXCsqdfOPKt.

---

[2]For example, one obtains identical results for dimensionless stiffness matrix elements A_{jklt}^{I} with indices of form $A_{3111}^{I} = A_{1311}^{I} = A_{1131}^{I} = A_{1113}^{I}$. The same holds for the matrix elements A_{jklmnt}^{II} and $A_{jklmnqst}^{III}$.

Chapter 7

Conclusions and perspectives

7.1 Summary and conclusions of the present thesis

In the present thesis, 2D continuum mechanical theories for thin plates and membranes undergoing both small and large deformations were developed. On the one hand, we focused on computational efficiency taking advantage of the smallness of the thickness as well as of the assumptions regarding the displacement field of such structural elements; on the other hand, a new level of precision for constitutive material models and for energetically consistent principles, including external loads and internal strains and stresses of the continuum, is provided:

As regards structural problems of thin plates, we applied the Principle of Virtual Power to a thermoelastic Kirchhoff plate with free boundaries resting on elastic Winkler foundations. The rectangular plates were subjected to vertical single forces, surface loads acting on specific rectangular areas, and to temperature-induced eigencurvatures of the plate. The resulting PVP-based governing equation for a "freely swimming" plate allowed for overcoming spurious external moments and shear forces acting on the plates boundaries, as they are encountered with the widely used plate theories of the Vlasov-type. The sought deflections were approximated through 2D Fourier series, which were used in the Principle of Virtual Power for constructing a linear algebraic system of equations, giving access to the deflection field. The derived energetically consistent Fourier series-based solution procedure appears as an efficient alternative to the standardly applied Finite Element method. Namely, it may reduce computing times by a factor of almost forty for symmetrical loading cases. This thermoelastic continuum model of thin plates serves as the basis for particularly relevant and reliable solutions in pavement engineering, namely concrete slabs for roads and airfields, as well as for floor screeds in building construction. In this context, the new solution method was used for thin concrete pavements subjected to temperature gradients along the plate's thickness direction. This was motivated by simulations of extreme weather events, i.e. hail showers, following significant solar heating at the top surface of the plate. The temperature gradients were transferred to temperature-induced eigencurvatures of the Kirchhoff plate resulting in bending stresses. Since solar heating of the top surface induce partial separation (negative deflections) of the plate from the subgrade, the corresponding subgrade reaction forces are equal to zero, and hence the Winkler foundation is active in compression only. The solution for this problem was determined iteratively, i.e. starting from a constant Winkler modulus of subgrade reaction along the entire bottom surface of the plate, the resulting areas of negative deflections were assumed to have a zero Winkler modulus. Based on the inhomogeneous Winkler foundation, this iterative process was repeated until convergence was reached. Top-down scaling (using multiscale material modeling) of the macroscopic stresses to the microscopic stresses of the concrete constituents show that these stresses are likely to reach the tensile strength of concrete.

As regards membranes undergoing large deformations, we focused on the first true 2D material graphene, an one-atom thick hexagonal lattice of carbon atoms, with a mechanical strength and stiffness exceeding those of any other material. While graphene mechanics are commonly

derived under uniaxial and equi-biaxial strain states, we here presented a fully anisotropic free energy function reflecting DFT-simulations associated with tens of thousands of arbitrary biaxial strain states on the nanoscopic level. Corresponding fitting coefficients for invariant structure tensor-based polynomial models up to the fifth order are provided, where maximum energy differences between DFT and the hyperelastic model are as low as 1%. The consequently derived hyperelastic constitutive equations overcome the transition between the quantum mechanics-rooted DFT-simulations and classical continuum mechanics, resulting in expressions for stress and elasticity tensors. Thereby, we have shown a deviation of the principal directions of the Green-Lagrange strain tensor and the corresponding principal directions of both the second Piola-Kirchhoff and the Cauchy stress tensor. Only in zigzag and armchair directions, the aforementioned strain and stress directions coincide. Analyzing the elastic stability limits of graphene, we determined stable strain regions according to a positive definite elasticity tensor. Furthermore, we provided an extensive overview on the anisotropy features of graphene, starting with the free energy density, via the Poisson ratio-type quantity for large deformations, to the stress-strain relations and stiffnesses, with differences amounting to 175%. All this is relevant for the finite strain domain, while it is well known that graphene is isotropic in the context of infinitesimal strains – we here specified a Poisson's ratio of 0.177 and an elastic Young's modulus of 342 N/m, being in good agreement with reported values from experimental measurements. Besides the validation of elastic constants for infinitesimal small strains, large deformation can be validated by incorporating the provided stress-strain relations of the hyperelastic model into a 2D membrane theory. This was done for circular graphene membranes with simply supported boundaries, subjected to several vertical axisymmetric mechanical loads. The Principle of Virtual Power was applied to this membrane problem, resulting in a Fourier series-based nonlinear algebraic system of equations, which was solved iteratively for the unknown deflections of the graphene membrane. The numerical results of the solution procedure are validated by experimental measurements using AFM nanoindentation, being in good agreement up to large deformations.

We regard the developed 2D mechanics of the present thesis, in form of both quantum mechanics dealing with atoms and electrons and classical continuum mechanics on the macroscopic level of concrete, as refined and accurate energetically consistent continuum models. The computationally efficient solution procedures appear as the basis for material science and structural mechanics of thin concrete slabs and graphene membranes.

7.2 Future research studies – continuum mechanics with electromagnetic interactions

Future research on the mechanics of graphene involve theories for advanced continuum mechanics, as the description of the interaction between mechanical deformations and electromagnetic fields. As regards standard 3D continua, we provide an introduction of such a theory, based on the accomplishments of Prof. Gérard A. Maugin [Maugin and Eringen, 1977, 1990; Maugin, 1988, 2009]: In this theory, electromagnetic fields are in strong interaction with mechanical deformation, resulting in nonlinear electromagnetic constitutive equations. For the description of advanced continuum mechanics involving electromagnetic interactions, we have to start with definitions of electromagnetic fields, as well as electromagnetic forces in deformed continua. Subsequently, we are able to obtain stresses and equilibrium conditions, which differ significantly from the purely mechanical case. Furthermore, based on the electromagnetic forces and stresses, we are able to specify the Principle of Virtual Power for electromagnetic deformable continua, which in turn are used for the thermodynamical description of the continuum.

7.2.1 Electromagnetic fields – Maxwell's equations in deformable continua

The electromagnetic field is the combination of an electric field and of a magnetic field, whereby the electric field is produced by stationary charges, and the magnetic field by currents (moving charges). The interaction between the electromagnetic field, charges, and currents can be described by *Maxwell's equations*, as proposed by the physicist and mathematician James Clerk Maxwell (1831-1879). The macroscopic formulations of Maxwell's equations[1] in a fixed Galilean frame, at time t, consist of

(i) *Gauss's law*

$$\nabla \cdot \mathbf{D} = \rho_{q,f} \,, \tag{7.1}$$

describing the relationship between the electric displacement and the density of free electric charges.

(ii) *Gauss's law for magnetism*

$$\nabla \cdot \mathbf{B} = 0 \,, \tag{7.2}$$

stating that there exist no magnetic monopoles.

(iii) *Faraday's law of induction*

$$\nabla \times \mathbf{E} = -\frac{\partial \mathbf{B}}{\partial t} \,, \tag{7.3}$$

describing how a time varying magnetic field induces an electric field.

(iv) and *Ampere-Maxwell's law*

$$\nabla \times \mathbf{H} = \frac{\partial \mathbf{D}}{\partial t} + \mathbf{J}_f \,, \tag{7.4}$$

stating that an electric current can be generated by magnetic fields and by time varying electric displacements.

In Eq. (7.1)-(7.4), $\mathbf{E}$ is the electric field vector[2] (dimension force per electric charge), $\mathbf{D}$ is the electric displacement vector (dimension electric charge per area), $\mathbf{B}$ is the magnetic field- or magnetic flux vector (dimension force per electric charge per velocity), $\mathbf{H}$ is the induced magnetic field strength vector (dimension electric charge per time per length), $\mathbf{J}_f$ is the free electric current density vector (dimension electric charge per time per area), $\rho_{q,f}$ is the density of free electric charges (dimension electric charge per volume), $\times$ is the cross product, and $\nabla = (\partial/\partial x_1, ..., \partial/\partial x_n)$ is the nabla operator. In order to complete the set of Maxwell's equations, the electric field and electric displacement, as well as the magnetic field and magnetic field strength are related as follows

$$\mathbf{D} = \epsilon_0 \, \mathbf{E} + \mathbf{P} \,, \qquad \mathbf{H} = \frac{1}{\mu_0} \mathbf{B} - \mathbf{M} \,, \tag{7.5}$$

with $\mathbf{P}$ being the electric polarization density vector (dimension electric charge per area), $\mathbf{M}$ being the magnetization density vector (dimension electric charge per time per length), $\epsilon_0 = 8.854 \times 10^{-12} \, [\mathrm{C}^2 \, \mathrm{N}^{-1} \, \mathrm{m}^{-2}]$ being the electric permittivity of vacuum, and $\mu_0 = 4 \, \pi \, \times \, 10^{-7} \, [\mathrm{N} \, \mathrm{s}^2 \, \mathrm{C}^{-2}]$ being the magnetic permeability of vacuum. The relations in (7.5) can be further specialized, when taking into account the identities

$$\mathbf{P} = \epsilon_0 \, \chi_e \mathbf{E} \quad \text{and} \quad \mathbf{M} = \chi_m \mathbf{H} \,, \tag{7.6}$$

---

[1] The macroscopic Maxwell's equations are also called *Maxwell's equations in matter* and are represented in Si units.

[2] In Appendix A, $\mathbf{E}$ is the electric field vector, not the Green-Lagrange strain tensor, which will be denoted as $\boldsymbol{\mathcal{E}}$ subsequently.

with $\boldsymbol{\chi}_e$ and $\boldsymbol{\chi}_m$ as the electric susceptibility and the magnetic susceptibility, respectively. The latter are dimensionless second-order tensors indicating the degree of polarization of a material in response to an applied electric field, and the degree of magnetization of a material in response to an applied magnetic field, respectively. Substitution of (7.6) into (7.5), while taking into account the relative electric permittivity tensor (also called dielectric tensor), $\boldsymbol{\epsilon}_r = \mathbf{1} + \boldsymbol{\chi}_e$, and the relative permeability tensor $\boldsymbol{\mu}_r = \mathbf{1} + \boldsymbol{\chi}_m$, yields

$$\mathbf{D} = \epsilon_0\,\boldsymbol{\epsilon}_r \mathbf{E}\,, \qquad \mathbf{H} = \frac{1}{\mu_0}\boldsymbol{\mu}_r^{-1}\,\mathbf{B}\,. \tag{7.7}$$

In this fixed Galilean frame (also called laboratory frame), the electromagnetic fields are *not invariant*, i.e. they involve partial time derivatives and are observer's dependent. Hence, in order to obtain Maxwell's equations in deformable continua, which are form invariant under the Galilean transformations, the following transformations of electromagnetic fields are required [Maugin, 1988]:

$$
\begin{aligned}
\widetilde{\rho}_{q,f} &= \rho_{q,f}\,, \\
\widetilde{\mathbf{J}}_f &= \mathbf{J}_f - \rho_{q,f}\,\mathbf{v}\,, \\
\widetilde{\mathbf{E}} &= \mathbf{E} + \mathbf{v}\times\mathbf{B}\,, \\
\widetilde{\mathbf{D}} &= \mathbf{D} + \epsilon_0\,\mathbf{v}\times\mathbf{B}\,, \\
\widetilde{\mathbf{P}} &= \mathbf{P}\,, \\
\widetilde{\mathbf{B}} &= \mathbf{B} - \epsilon_0\,\mu_0\,\mathbf{v}\times\mathbf{E}\,. \\
\widetilde{\mathbf{M}} &= \mathbf{M} + \mathbf{v}\times\mathbf{P}\,, \\
\widetilde{\mathbf{H}} &= \mathbf{H} - \mathbf{v}\times\mathbf{D}\,,
\end{aligned}
\tag{7.8}
$$

with

$$\widetilde{\mathbf{D}} = \epsilon_0\,\widetilde{\mathbf{E}} + \widetilde{\mathbf{P}} \quad \text{and} \quad \widetilde{\mathbf{H}} = \frac{1}{\mu_0}\widetilde{\mathbf{B}} - \widetilde{\mathbf{M}}\,, \tag{7.9}$$

where $\mathbf{v}$ is the velocity field.

Knowing the electromagnetic fields (7.8)-(7.9), we can transform Maxwell's equations (7.1)-(7.4) to a moving frame for a *deformed continuum*. Exemplarily, this is done for the Ampere-Maxwell's law: Substitution of $(7.8)_2$ and $(7.8)_8$ into (7.4) and taking into account the Gauss's law (7.1) yields

$$\nabla\times\widetilde{\mathbf{H}} = \left[\frac{\partial\mathbf{D}}{\partial t} + \nabla\times(\mathbf{D}\times\mathbf{v}) + \mathbf{v}(\nabla\cdot\mathbf{D})\right] + \widetilde{\mathbf{J}}_f \quad \Leftrightarrow \quad \nabla\times\widetilde{\mathbf{H}} = \overset{*}{\mathbf{D}} + \widetilde{\mathbf{J}}_f\,, \tag{7.10}$$

where the expression inside the square bracket is an objective upper-convected (Oldroyd) type time derivative of $\mathbf{D}$, denoted by $\overset{*}{\mathbf{D}}$. This objective time derivative can be used for any vector arbitrary $\boldsymbol{\mathcal{V}}$ in form of [3]

$$\overset{*}{\boldsymbol{\mathcal{V}}} = \frac{\partial\boldsymbol{\mathcal{V}}}{\partial t} + \nabla\times(\boldsymbol{\mathcal{V}}\times\mathbf{v}) + \mathbf{v}(\nabla\cdot\boldsymbol{\mathcal{V}}) = \frac{D\boldsymbol{\mathcal{V}}}{Dt} - (\boldsymbol{\mathcal{V}}\cdot\nabla)\mathbf{v} + \boldsymbol{\mathcal{V}}(\nabla\cdot\mathbf{v})\,, \tag{7.11}$$

which proves to be valuable for the description of electromagnetic deformable continua. On the right hand side of (7.11), $D\boldsymbol{\mathcal{V}}/Dt$ is the material derivative of an arbitrary vector $\boldsymbol{\mathcal{V}}$, which

---

[3]The relation between the derived time derivative $\overset{*}{\boldsymbol{\mathcal{V}}}$ (7.11) and the Oldroyd time derivative, denoted by $\overset{\triangledown}{\boldsymbol{\mathcal{V}}}$, reads as follows: $\overset{*}{\boldsymbol{\mathcal{V}}} = \overset{\triangledown}{\boldsymbol{\mathcal{V}}} + \boldsymbol{\mathcal{V}}(\nabla\cdot\mathbf{v})$.

will be denoted by $\overset{\circ}{\boldsymbol{\mathcal{V}}}$ subsequently. The same transformation procedure is used to obtain the Faraday's law of induction in a moving frame for a deformed continuum. Substitution of $(7.8)_3$ into (7.3) and taking into account the Gauss's law for magnetism (7.2) yields

$$\nabla \times \widetilde{\mathbf{E}} = -\left[\frac{\partial \mathbf{B}}{\partial t} + \nabla \times (\mathbf{B} \times \mathbf{v}) + \mathbf{v}(\nabla \cdot \mathbf{B})\right] \quad \Leftrightarrow \quad \nabla \times \widetilde{\mathbf{E}} = -\overset{*}{\mathbf{B}}. \tag{7.12}$$

Hence, by means of the upper-convective type time derivative (7.11), we re-formulate the Maxwell's equations for deformed continua, reading as

$$\nabla \cdot \mathbf{D} = \rho_{q,f}, \qquad \nabla \cdot \mathbf{B} = 0,$$

$$\nabla \times \widetilde{\mathbf{E}} = -\overset{*}{\mathbf{B}}, \qquad \nabla \times \widetilde{\mathbf{H}} = \overset{*}{\mathbf{D}} + \widetilde{\mathbf{J}}_f. \tag{7.13}$$

7.2.2 Macroscopic electromagnetic force, couple, and power

Starting from the microscopic expressions of the electromagnetic force, couple, and power – based on the *electron theory of Lorentz*[4] – we derive the sought macroscopic electromagnetic contributions of deformed continua, using a spatial averaging procedure.

Macroscopic *electromagnetic forces* are forces which act on a volume element dV of a continuum, caused by electromagnetic fields. These electromagnetic force vectors per unit volume $\mathbf{f}^{em}(\mathbf{x})$ are defined in the deformed configuration (Eulerian representation) at the position $\mathbf{x}$, in analogy to the mechanical force vector per unit volume $\mathbf{f}(\mathbf{x})$ in pure continuum mechanics, see Sec. 2.2. Let us start with the aforementioned microscopic electromagnetic forces $\partial \mathbf{f}^\alpha$ acting on the electric particle charge ∂q^α, located at

$$\mathbf{r}^\alpha = \mathbf{r} + \boldsymbol{\xi}^\alpha \quad \text{with} \quad \alpha = 1, 2, ... \in V_{RVE}, \tag{7.14}$$

where $\mathbf{r}$ being the position vector of the mass center M of the representative volume element V_{RVE}, and $\boldsymbol{\xi}^\alpha$ being the distance vector between the mass center M and particle charge ∂q^α in the V_{RVE}, see Fig. 7.1(a). The velocity vector $\mathbf{v}^\alpha = D\mathbf{r}^\alpha/Dt$ at particle α can be reformulated as
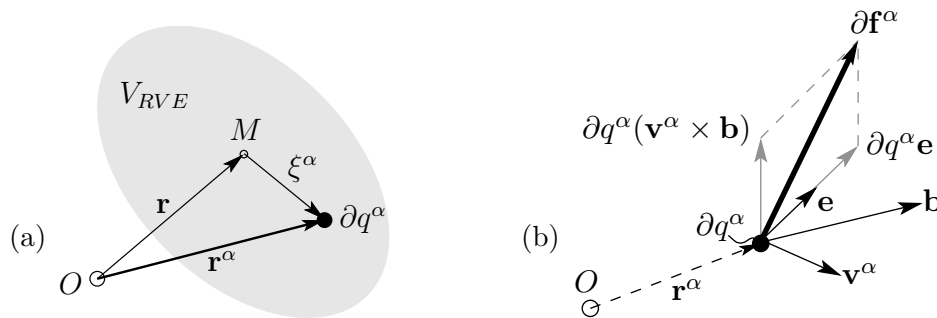
Fig. 7.1: (a) Microscopic electric particle charge ∂q^α and its coordinates of an representative volume element V_{RVE}, and (b) scheme of the microscopic Lorentz force $\partial \mathbf{f}^\alpha$ acting on a particle charge ∂q^α.

$$\mathbf{v}^\alpha = \mathbf{v} + \dot{\boldsymbol{\xi}}^\alpha + \hat{\mathbf{v}}^\alpha \quad \text{with} \quad \alpha = 1, 2, ... \in V_{RVE}, \tag{7.15}$$

---

[4]The theory is named after the physicist Hendrik Antoon Lorentz (1853-1928).

where $\mathbf{v}$ is the mean velocity field of the representative volume element V_{RVE}, and $\hat{\mathbf{v}}$ is the fluctuation velocity. The electron theory of Lorentz states, that the microscopic Lorentz force $\partial\mathbf{f}^\alpha$ is the combination of the electric and magnetic force on a particle charge ∂q^α due to the microscopic electric field vector $\mathbf{e}$ and microscopic magnetic field vector $\mathbf{b}$, see Fig. 7.1(b). Hence, the microscopic electromagnetic force acting on a point charge reads as

$$\partial\mathbf{f}^\alpha = \partial q^\alpha \left[\mathbf{e}(\mathbf{r}^\alpha) + \mathbf{v}^\alpha \times \mathbf{b}(\mathbf{r}^\alpha)\right].\tag{7.16}$$

Substitution of the definitions of the position vector $\mathbf{r}^\alpha$ (7.14) and the velocity $\mathbf{v}^\alpha$ (7.15) of the particle charge ∂q^α into (7.16), as well as making use of the averaging procedure, yields the macroscopic electromagnetic force

$$\mathbf{f}^{em} = \frac{1}{V_{RVE}} \sum_{\alpha \in V_{RVE}} \partial q^\alpha \left[\mathbf{e}(\mathbf{r} + \boldsymbol{\xi}^\alpha) + (\mathbf{v} + \dot{\boldsymbol{\xi}}^\alpha + \hat{\mathbf{v}}^\alpha) \times \mathbf{b}(\mathbf{r} + \boldsymbol{\xi}^\alpha)\right].\tag{7.17}$$

Considering the following macroscopic electromagnetic fields [Maugin, 1988]

$$\begin{aligned}
\rho_{q,f}(\mathbf{r},t) &= \frac{1}{V_{RVE}} \sum_{\alpha \in V_{RVE}} \partial q^\alpha,\\[4pt]
\widetilde{\mathbf{J}}_f(\mathbf{r},t) &= \frac{1}{V_{RVE}} \sum_{\alpha \in V_{RVE}} \partial q^\alpha \hat{\mathbf{v}}^\alpha(\mathbf{r},t),\\[4pt]
\mathbf{P}(\mathbf{r},t) &= \frac{1}{V_{RVE}} \sum_{\alpha \in V_{RVE}} \partial q^\alpha \boldsymbol{\xi}^\alpha(\mathbf{r},t),\\[4pt]
\widetilde{\mathbf{M}}(\mathbf{r},t) &= \frac{1}{V_{RVE}} \sum_{\alpha \in V_{RVE}} \frac{1}{2c} \partial q^\alpha \boldsymbol{\xi}^\alpha(\mathbf{r},t) \times \dot{\boldsymbol{\xi}}^\alpha(\mathbf{r},t),
\end{aligned}\tag{7.18}$$

and performing a Taylor series expansion about $\mathbf{r}$, where at most quadratic terms are considered, lead to the following equivalent expressions for the macroscopic electromagnetic force per unit volume [Maugin, 1988]:

$$\mathbf{f}^{em} = \rho_{q,f}\widetilde{\mathbf{E}} + \left(\widetilde{\mathbf{J}}_f + \overset{*}{\mathbf{P}}\right) \times \mathbf{B} + (\mathbf{P}\cdot\nabla)\widetilde{\mathbf{E}} + (\nabla\mathbf{B})\cdot\widetilde{\mathbf{M}},\tag{7.19}$$

$$\mathbf{f}^{em} = \rho_{q,f}\mathbf{E} + \mathbf{J}_f \times \mathbf{B} + (\nabla\mathbf{E})\cdot\mathbf{P} + (\nabla\mathbf{B})\cdot\mathbf{M} + \frac{D(\mathbf{P}\times\mathbf{B})}{Dt}.\tag{7.20}$$

Eq. (7.20) can be interpreted as follows: The first two terms represent the Lorentz force density acting on a charged particle; the third term is the Kelvin force density acting on the electric dipole moment; the fourth term is the force density acting on the magnetic dipole moment; and the last term is an electrodynamic effect accounting for the deformation of the continuum.

Macroscopic *electromagnetic couples* are moments, which act on a volume element dV of a continuum, caused by electromagnetic fields. Again, we start with the microscopic description, i.e. based on the position vector (7.14) and velocity vector (7.15) of the particle charge ∂q^α, we define the microscopic electromagnetic couple as the moment about the origin of coordinates O, with distance $\mathbf{r}^\alpha$ between the origin and the corresponding microscopic electromagnetic forces $\partial\mathbf{f}^\alpha$ of the representative volume element (see Fig. 7.1),

$$\partial\mathbf{c}^\alpha = \mathbf{r}^\alpha \times \partial q^\alpha \left[\mathbf{e}(\mathbf{r}^\alpha) + \mathbf{v}^\alpha \times \mathbf{b}(\mathbf{r}^\alpha)\right].\tag{7.21}$$

Substitution of the definitions of the position vector $\mathbf{r}^\alpha$ (7.14) and the velocity $\mathbf{v}^\alpha$ (7.15) of the RVE into (7.21), as well as making use of the averaging procedure, yields the macroscopic electromagnetic couple

$$\mathbf{c}^{em} = \frac{1}{V_{RVE}} \sum_{\alpha \in V_{RVE}} (\mathbf{r} + \boldsymbol{\xi}^\alpha) \times \partial q^\alpha \left[\mathbf{e}(\mathbf{r} + \boldsymbol{\xi}^\alpha) + (\mathbf{v} + \dot{\boldsymbol{\xi}}^\alpha + \hat{\mathbf{v}}^\alpha) \times \mathbf{b}(\mathbf{r} + \boldsymbol{\xi}^\alpha) \right] . \tag{7.22}$$

Subsequently, for the derivation of useful expressions for the electromagnetic couple, we use the same procedure as presented for the derivation of macroscopic electromagnetic forces. Thus, the expression for the electromagnetic couple per unit volume read as [Maugin, 1988]

$$\mathbf{c}^{em} = \mathbf{x} \times \mathbf{f}^{em} + \widetilde{\mathbf{c}}^{em}, \quad \text{with} \quad \widetilde{\mathbf{c}}^{em} = \mathbf{P} \times \widetilde{\mathbf{E}} + \widetilde{\mathbf{M}} \times \mathbf{B}, \tag{7.23}$$

noting that $\widetilde{\mathbf{c}}^{em}$ is called *ponderomotive couple*.

In order to formulate thermodynamical descriptions of our electromagnetic deformable continuum, we need to derive macroscopic expressions for the *electromagnetic power* per unit volume p^{em}. As before, we start with the microscopic expression of the electromagnetic power reading as

$$\partial p^\alpha = \partial q^\alpha \, \mathbf{v}^\alpha \cdot \mathbf{e}(\mathbf{r}^\alpha) . \tag{7.24}$$

Substitution of the definitions of the position vector $\mathbf{r}^\alpha$ (7.14) and the velocity $\mathbf{v}^\alpha$ (7.15) of the RVE into (7.24), as well as making use of the averaging procedure, yields the macroscopic electromagnetic power

$$p^{em} = \frac{1}{V_{RVE}} \sum_{\alpha \in V_{RVE}} \partial q^\alpha \, (\mathbf{v} + \dot{\boldsymbol{\xi}}^\alpha + \hat{\mathbf{v}}^\alpha) \cdot \mathbf{e}(\mathbf{r} + \boldsymbol{\xi}^\alpha) . \tag{7.25}$$

Once again, use the homogenization procedure (7.18) as presented for the derivation of electromagnetic forces, yields the following expressions for the electromagnetic power per unit volume [Maugin, 1988]

$$p^{em} = \mathbf{f}^{em} \cdot \mathbf{v} + \widetilde{\mathbf{J}}_f \cdot \widetilde{\mathbf{E}} + \rho \, \widetilde{\mathbf{E}} \cdot \dot{\mathbf{p}} - \widetilde{\mathbf{M}} \cdot \dot{\mathbf{B}}, \tag{7.26}$$

using the identity

$$\rho \, \dot{\mathbf{p}} = \overset{*}{\mathbf{P}} + (\nabla \cdot \mathbf{P})\mathbf{v}, \tag{7.27}$$

where $\mathbf{p} = \mathbf{P}/\rho$ is the *electric polarization per unit mass*. The identity (7.27) can be proved by the following considerations:

$$\dot{\mathbf{P}} = \rho \, \dot{\mathbf{p}} + \dot{\rho} \, \mathbf{p}, \quad \text{with}^5 \quad \dot{\rho} = -\rho \, (\nabla \cdot \mathbf{v}) \tag{7.28}$$

resulting in

$$\rho \, \dot{\mathbf{p}} = \dot{\mathbf{P}} + \mathbf{P} \, (\nabla \cdot \mathbf{v}) \quad \Leftrightarrow \quad \rho \, \dot{\mathbf{p}} = \overset{*}{\mathbf{P}} + (\nabla \cdot \mathbf{P})\mathbf{v}. \tag{7.29}$$

7.2.3 Stresses of electromagnetic deformable continua

Electromagnetic fields not only cause electromagnetic forces, couples and powers, but of course also electromagnetic stress tensors. In other words, the Cauchy stress tensor in Eulerian representation,

---

[5]The material derivative of the mass density $\dot{\rho}$ can be obtained by means of the the conservation of mass and of the Reynolds transport theorem: $\frac{D}{Dt} \int_V \rho \, dV = \int_V \left[\frac{\partial \rho}{\partial t} + \nabla \cdot (\rho \, \mathbf{v}) \right] dV = 0$. Since this equation is valid for any size of a continuum, the differential form of the so-called continuity equation reads as $\frac{\partial \rho}{\partial t} + \nabla \cdot (\rho \, \mathbf{v}) = 0$ or $\dot{\rho} = -\rho \, (\nabla \cdot \mathbf{v})$.

or the second Piola-Kirchhoff stress tensor in Lagrangian representation are strongly linked with electromagnetic interactions. In the electromagnetic case, these interactions motivates us to call them *electromagnetic Cauchy stress tensor* and *electromagnetic second Piola-Kirchhoff stress tensor*, respectively.

In analogy to the pure mechanical case in Sec. 2.2, we can describe surface and volume forces acting on electromagnetic deformable continua. Thus, as an extension to the traction vectors $\mathbf{T}(\mathbf{x}, \mathbf{n})$ and mechanical force density vectors $\mathbf{f}(\mathbf{x})$, we introduce the derived electromagnetic force density vectors $\mathbf{f}^{em}(\mathbf{x})$ (dimension force per volume) and electromagnetic couples $\mathbf{c}^{em}(\mathbf{x})$ (dimension moment per volume), see Sec. 7.2.2. For this continuous force system, we can
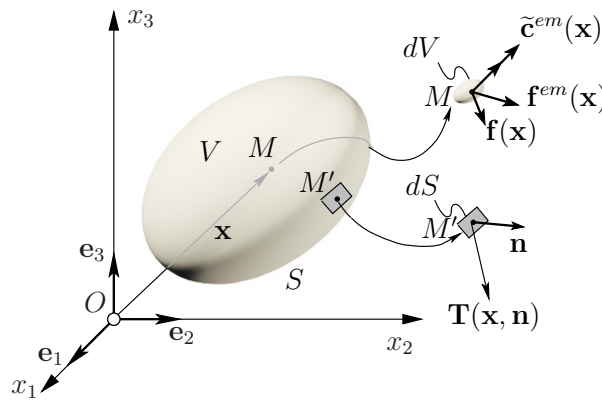
Fig. 7.2: Mechanical volume forces $\mathbf{f}\,dV$, electromagnetic volume forces $\mathbf{f}^{em}dV$, ponderomotive couples $\widetilde{\mathbf{c}}^{em}dV$, and surface forces $\mathbf{T}dS$, acting on an electromagnetic continuum in the *deformed* configuration.

reformulate the well-known equilibrium conditions (2.40) and (2.41) as follows: The volume integral of force equilibrium condition is extended by the electromagnetic force density $\mathbf{f}^{em}$, reading as[6]

$$\int_V \left[\mathbf{f}(\mathbf{x}) + \mathbf{f}^{em}(\mathbf{x})\right] dV + \int_S \mathbf{T}(\mathbf{x}, \mathbf{n})\, dS = 0\,, \tag{7.30}$$

and the volume integral of the moment equilibrium is extended by the electromagnetic couple $\mathbf{c}^{em}$, reading as

$$\int_V \left(\mathbf{x} \times \left[\mathbf{f}(\mathbf{x}) + \mathbf{f}^{em}(\mathbf{x})\right] + \widetilde{\mathbf{c}}^{em}(\mathbf{x})\right) dV + \int_S \mathbf{x} \times \mathbf{T}(\mathbf{x}, \mathbf{n})\, dS = 0\,, \tag{7.31}$$

considering the definition of the electromagnetic couple, $\mathbf{c}^{em} = \mathbf{x} \times \mathbf{f}^{em} + \widetilde{\mathbf{c}}^{em}$. For the definition of the stress tensor in the deformed configuration, again we consider a tetrahedron of arbitrary size ($h \to 0$), see Fig. 2.4b. Therefore, the "tetrahedron-lemma" (2.44), induces the existence of the *electromagnetic Cauchy stress tensor* $\boldsymbol{\sigma}^{em}$

$$\mathbf{T}(\mathbf{n}) = \boldsymbol{\sigma}^{em} \cdot \mathbf{n}\,. \tag{7.32}$$

---

[6]In the dynamic case (where the velocity of motions can not be neglected), Eqs. (7.30) and (7.31) must be extended to $\int_V \left[\mathbf{f}(\mathbf{x}) + \mathbf{f}^{em}(\mathbf{x})\right] dV + \int_S \mathbf{T}(\mathbf{x}, \mathbf{n})\, dS = \int_V \rho \frac{\partial^2 \mathbf{x}}{\partial t^2}\, dV$ and $\int_V \left(\mathbf{x} \times \left[\mathbf{f}(\mathbf{x}) + \mathbf{f}^{em}(\mathbf{x})\right] + \widetilde{\mathbf{c}}^{em}(\mathbf{x})\right) dV + \int_S \mathbf{x} \times \mathbf{T}(\mathbf{x}, \mathbf{n})\, dS = \int_V \mathbf{x} \times \rho \frac{\partial^2 \mathbf{x}}{\partial t^2}\, dV$, respectively, with ρ as the mass density in point $\mathbf{x}$. These equilibrium conditions are only applicable, if the position vectors are measured in a spatially fixed or Galilean coordinate system.

Use of (7.32) in equilibrium condition (7.30), as well as use of Gauss's divergence theorem for an arbitrary body (integrand must vanish) yields the local force equilibrium condition[7]

$$\mathbf{f}(\mathbf{x}) + \mathbf{f}^{em}(\mathbf{x}) + \operatorname{div}\boldsymbol{\sigma}^{em}(\mathbf{x}) = 0\,. \tag{7.33}$$

Hence, equilibrium condition (7.33) in notation of components of an orthnormal basis $\mathbf{e}_1$, $\mathbf{e}_2$, $\mathbf{e}_3$ reads as

$$f_1 + f_1^{em} + \frac{\partial \sigma_{11}^{em}}{\partial x_1} + \frac{\partial \sigma_{12}^{em}}{\partial x_2} + \frac{\partial \sigma_{13}^{em}}{\partial x_3} = 0\,, \tag{7.34}$$

$$f_2 + f_2^{em} + \frac{\partial \sigma_{21}^{em}}{\partial x_1} + \frac{\partial \sigma_{22}^{em}}{\partial x_2} + \frac{\partial \sigma_{23}^{em}}{\partial x_3} = 0\,, \tag{7.35}$$

$$f_3 + f_3^{em} + \frac{\partial \sigma_{31}^{em}}{\partial x_1} + \frac{\partial \sigma_{32}^{em}}{\partial x_2} + \frac{\partial \sigma_{33}^{em}}{\partial x_3} = 0\,. \tag{7.36}$$

In order to prove the symmetry properties of the electromagnetic Cauchy stress tensor, we refer to the moment equilibrium condition (7.31) in notation of components of an orthogonal basis $\mathbf{e}_1$, $\mathbf{e}_2$, $\mathbf{e}_3$

$$\begin{aligned}
\left[\int_V (x_2(f_3 + f_3^{em}) - x_3(f_2 + f_2^{em}) + \widetilde{c}_1^{em})\,dV + \int_S (x_2 T_3 - x_3 T_2)\,dS\right] \mathbf{e}_1 &\quad+ \\
\left[\int_V (x_3(f_1 + f_1^{em}) - x_1(f_3 + f_3^{em}) + \widetilde{c}_2^{em})\,dV + \int_S (x_3 T_1 - x_1 T_3)\,dS\right] \mathbf{e}_2 &\quad+ \\
\left[\int_V (x_1(f_2 + f_2^{em}) - x_2(f_1 + f_1^{em}) + \widetilde{c}_3^{em})\,dV + \int_S (x_1 T_2 - x_2 T_1)\,dS\right] \mathbf{e}_3 &\quad= \quad 0\,, \quad (7.37)
\end{aligned}$$

which requires that the three expressions in the brackets are equal to zero. In the following, we regard to the multiplier of $\mathbf{e}_1$: Use of Cauchy's formula (7.32), and the local force equilibrium conditions (7.35) and (7.36), as well as use of Gauss's divergence theorem yields

$$\begin{aligned}
0 = \int_V \Bigg(&-x_2 \frac{\partial \sigma_{31}^{em}}{\partial x_1} - x_2 \frac{\partial \sigma_{32}^{em}}{\partial x_2} - x_2 \frac{\partial \sigma_{33}^{em}}{\partial x_3} + x_3 \frac{\partial \sigma_{21}^{em}}{\partial x_1} + x_3 \frac{\partial \sigma_{22}^{em}}{\partial x_2} + x_3 \frac{\partial \sigma_{23}^{em}}{\partial x_3} + \widetilde{c}_1^{em} \\
&+ x_2 \frac{\partial \sigma_{31}^{em}}{\partial x_1} + \sigma_{32}^{em} + x_2 \frac{\partial \sigma_{32}^{em}}{\partial x_2} + x_2 \frac{\partial \sigma_{33}^{em}}{\partial x_3} - x_3 \frac{\partial \sigma_{21}^{em}}{\partial x_1} - x_3 \frac{\partial \sigma_{22}^{em}}{\partial x_2} - \sigma_{23}^{em} - x_3 \frac{\partial \sigma_{23}^{em}}{\partial x_3} \Bigg) dV = 0\,.
\end{aligned}$$
$$\tag{7.38}$$

Since Eq. (7.38) is valid for any body, the integrand must vanish, and we obtain

$$\sigma_{23}^{em} = \sigma_{32}^{em} + \widetilde{c}_1^{em}\,. \tag{7.39}$$

Analogous transformations of the multipliers of $\mathbf{e}_2$ and $\mathbf{e}_3$ in (7.37) delivers

$$\sigma_{13}^{em} = \sigma_{31}^{em} - \widetilde{c}_2^{em} \quad \text{and} \quad \sigma_{12}^{em} = \sigma_{21}^{em} + \widetilde{c}_3^{em}\,, \tag{7.40}$$

which allows us to write in general (considering the definition of the ponderomotive couple $\widetilde{\mathbf{c}}^{em}$ (7.23))

$$\sigma_{ij}^{em} = \sigma_{ji}^{em} + P_i \widetilde{E}_j - P_j \widetilde{E}_i + \widetilde{M}_i B_j - \widetilde{M}_j B_i \quad \forall i \neq j\,. \tag{7.41}$$

---

[7]In the dynamic case (where the velocity of motions can not be neglected), Eq. (7.33) must be extended to $\mathbf{f}(\mathbf{x}) + \mathbf{f}^{em}(\mathbf{x}) + \operatorname{div}\boldsymbol{\sigma}^{em}(\mathbf{x}) = \rho \frac{\partial^2 \mathbf{x}}{\partial t^2}$.

Hence, in the case of electromagnetic deformable continua, we can state that the electromagnetic Cauchy stress tensor $\boldsymbol{\sigma}^{em}$ in general is *not symmetric*,

$$\boldsymbol{\sigma}^{em} \neq (\boldsymbol{\sigma}^{em})^T \,, \tag{7.42}$$

due to the influence of the ponderomotive couple $\widetilde{\mathbf{c}}^{em}$, which in turn is caused by the interaction between the electromagnetic fields ($\widetilde{\mathbf{E}}$ and $\mathbf{B}$) and the polarization and magnetization fields ($\mathbf{P}$ and $\widetilde{\mathbf{M}}$), respectively. The components of the ponderomotive couple $\widetilde{c}_i^{em}$ can be interpreted as follows: These electromagnetic contributions represent internal "spins" (moments per unit volume) of an infinitesimal volume element. In this context, the component $\widetilde{c}_1^{em}$ is defined as the positive moment per unit volume around the $\mathbf{e}_1$ axis, $\widetilde{c}_2^{em}$ is defined as the negative moment per unit volume around the $\mathbf{e}_2$ axis, and $\widetilde{c}_3^{em}$ is defined as the positive moment per unit volume around the $\mathbf{e}_3$ axis, see see Fig. 7.3.
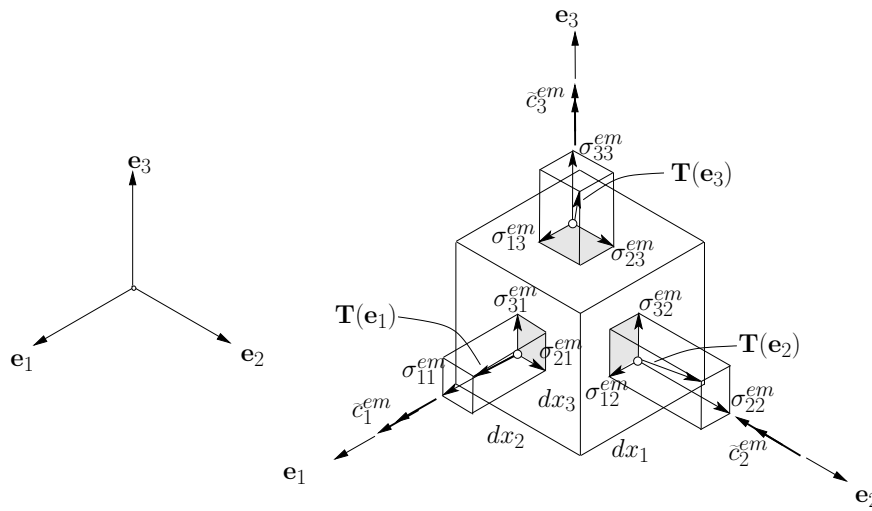
Fig. 7.3: Interpretation of the components of the electromagnetic Cauchy stress tensor $\boldsymbol{\sigma}^{em}$ and of the ponderomotive couple $\widetilde{\mathbf{c}}^{em}$.

The proved existence of the (nonsysmmetric) electromagnetic Cauchy stress tensor $\boldsymbol{\sigma}^{em}$ (7.32) motivates us to introduce alternative (symmetric) stress tensors, which useful for the thermodynamic description of the continuum. Use of the derived symmetry-properties (7.39)-(7.41), gives us access to construct components of a symmetric second order tensor:

$$\sigma_{ij}^{em} + P_j \widetilde{E}_i + \widetilde{M}_j B_i = \sigma_{ji}^{em} + P_i \widetilde{E}_j + \widetilde{M}_i B_j \quad \forall i \neq j \,. \tag{7.43}$$

In this context, the expressions on the left-hand side are denoted as $\overline{\sigma}_{ij}^{em}$ and the expressions on the right-hand side are denoted as $\overline{\sigma}_{ji}^{em}$, reading as

$$\overline{\sigma}_{ij}^{em} = \overline{\sigma}_{ji}^{em} \,, \tag{7.44}$$

with

$$\overline{\sigma}_{ij}^{em} = \sigma_{ij}^{em} + \widetilde{E}_i P_j + B_i \widetilde{M}_j \quad \text{and} \quad \overline{\sigma}_{ji}^{em} = \sigma_{ji}^{em} + \widetilde{E}_j P_i + B_j \widetilde{M}_i \,. \tag{7.45}$$

These tensor components are part of the so-called *generalized electromagnetic Cauchy stress tensor* $\overline{\boldsymbol{\sigma}}^{em}$. In tensor notation, the generalized (symmetric) electromagnetic Cauchy stress tensor is defined as

$$\overline{\boldsymbol{\sigma}}^{em} = \boldsymbol{\sigma}^{em} + \widetilde{\mathbf{E}} \otimes \mathbf{P} + \mathbf{B} \otimes \widetilde{\mathbf{M}} = (\overline{\boldsymbol{\sigma}}^{em})^T \,. \tag{7.46}$$

In the case of large deformations, we have to formulate the stress tensor as a function of the particle position vector $\mathbf{X}$ in the *undeformed* reference configuration (Lagrangian representation), in accordance with Sec. 2.3. Thus, by means of the deformation gradient $\mathbf{F}$ and the corresponding Jacobi-determinant $J = \det\mathbf{F}$, we can re-formulate the definition of the second Piola-Kirchhoff stress tensor for electromagnetic deformable continua

$$\boldsymbol{\pi}^{em} = J\,\mathbf{F}^{-1}\cdot\boldsymbol{\sigma}^{em}\cdot\mathbf{F}^{-T}\,. \tag{7.47}$$

In analogy, the (symmetric) generalized electromagnetic second Piola-Kirchhoff stress tensor reads as

$$\overline{\boldsymbol{\pi}}^{em} = J\,\mathbf{F}^{-1}\cdot\overline{\boldsymbol{\sigma}}^{em}\cdot\mathbf{F}^{-T}\,. \tag{7.48}$$

7.2.4 The Principle of Virtual Power of electromagnetic deformable continua

Since the Principle of Virtual Power is a versatile method for the formulation of complex theories, this method is used for the theory of electromagnetic deformable continua. In analogy, our starting point of all considerations is the investigation of power characteristics of forces in equilibrium, acting on a continuous body. Thus, an continuous force system of mechanical volume force densities $\mathbf{f}$, electromagnetic force densities $\mathbf{f}^{em}$, and traction force densities $\mathbf{T}$ perform virtual power densities $d\mathcal{P}$ along geometrically compatible virtual velocities $\hat{\mathbf{v}}$ (see Fig. 7.4). Integration of the volume- and traction terms over the volume and surface, respectively, delivers the following virtual power expression

$$\mathcal{P} = \int_V [\mathbf{f}(\mathbf{x}) + \mathbf{f}^{em}(\mathbf{x})]\cdot\hat{\mathbf{v}}(\mathbf{x})\,dV + \int_S \mathbf{T}(\mathbf{x},\mathbf{n})\cdot\hat{\mathbf{v}}(\mathbf{x})\,dS\,, \tag{7.49}$$

representing the power of forces acting on an electromagnetic deformable continuum. Use of
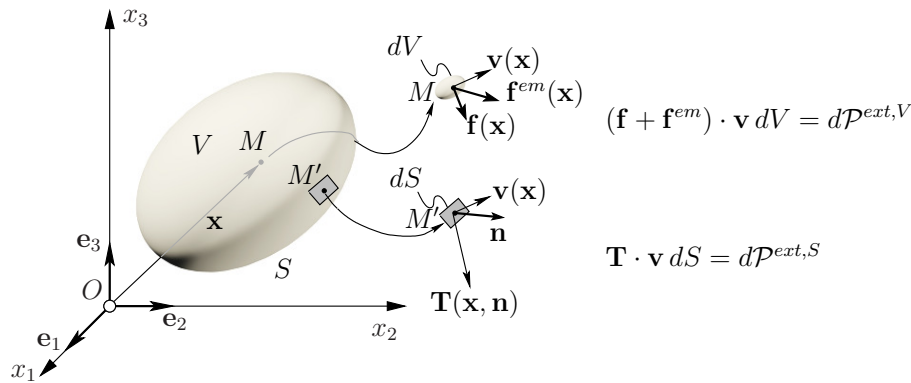
Fig. 7.4: Power of volume and traction forces acting on an electromagnetic deformable continuum.

Cauchy's formula (7.32) and Gauss's divergence theorem yields

$$\mathcal{P} = \int_V \left([\mathbf{f} + \mathbf{f}^{em}]\cdot\hat{\mathbf{v}} + \mathrm{div}(\hat{\mathbf{v}}\cdot\boldsymbol{\sigma}^{em})\right)dV = \int_V \left([\mathbf{f} + \mathbf{f}^{em}]\cdot\hat{\mathbf{v}} + \mathrm{grad}\hat{\mathbf{v}} : \boldsymbol{\sigma}^{em} + \hat{\mathbf{v}}\cdot\mathrm{div}\boldsymbol{\sigma}^{em}\right)dV\,. \tag{7.50}$$

Taking into account the local equilibrium condition (7.33), delivers the expression

$$\mathcal{P} = \int_V \boldsymbol{\sigma}^{em} : \mathrm{grad}\hat{\mathbf{v}}\,dV\,. \tag{7.51}$$

It is noted, that we are *not* allowed to introduce the virtual Eulerian strain rate (2.63) since the electromagnetic Cauchy stress in *not symmetric.* The power expressions (7.49) and (7.51), result in the sought Principle of Virtual Power of electromagnetic deformable continua in Eulerian representation, reading as

$$\mathcal{P}^{ext} + \mathcal{P}^{int} = 0 \,, \tag{7.52}$$

with

$$\mathcal{P}^{ext} = + \int_V [\mathbf{f}(\mathbf{x}) + \mathbf{f}^{em}(\mathbf{x})] \cdot \hat{\mathbf{v}}(\mathbf{x})\, dV + \int_S \mathbf{T}(\mathbf{x}, \mathbf{n}) \cdot \hat{\mathbf{v}}(\mathbf{x})\, dS \,, \tag{7.53}$$

$$\mathcal{P}^{int} = - \int_V \boldsymbol{\sigma}^{em} : \nabla \hat{\mathbf{v}}\, dV \,, \tag{7.54}$$

In order to represent the Principle of Virtual Power as a function of objective strain rates, the commonly used (virtual) Eulerian strain rate $\hat{\mathbf{d}}$ requires a symmetric stress tensor in (7.54). Thus, we incorporate the introduced symmetric generalized Cauchy stress tensor $\overline{\boldsymbol{\sigma}}^{em}$ as defined in (7.46). In this context, the Principle of Virtual Power (7.52)-(7.54) is extended by vanishing virtual electromagnetic power expressions reading as [Maugin, 1988]

$$\mathcal{P}^{ext} = + \int_V [\mathbf{f} + \mathbf{f}^{em}] \cdot \hat{\mathbf{v}}\, dV + \int_S \mathbf{T} \cdot \hat{\mathbf{v}}\, dS + \int_V (\rho\, \widetilde{\mathbf{E}} \cdot \dot{\hat{\mathbf{p}}} + \rho\, \mathbf{B} \cdot \dot{\hat{\boldsymbol{\mu}}})\, dV \,, \tag{7.55}$$

$$\mathcal{P}^{int} = - \int_V \boldsymbol{\sigma}^{em} : \nabla \hat{\mathbf{v}}\, dV - \int_V (\rho\, \widetilde{\mathbf{E}} \cdot \dot{\hat{\mathbf{p}}} + \rho\, \mathbf{B} \cdot \dot{\hat{\boldsymbol{\mu}}})\, dV \,, \tag{7.56}$$

where $\hat{\mathbf{p}} = \hat{\mathbf{P}}/\rho$ is the virtual electric polarization per unit mass, and $\hat{\boldsymbol{\mu}} = \widehat{\widetilde{\mathbf{M}}}/\rho$ is the virtual magnetization per unit mass. In the following, we the expression of the virtual power of internal forces (7.56) is transformed as follows: Use of the expressions for the electric polarization and magnetization per unit mass

$$\rho\, \dot{\hat{\mathbf{p}}} = \overset{*}{\hat{\mathbf{P}}} + (\mathbf{P} \cdot \nabla) \hat{\mathbf{v}} \quad \text{and} \quad \rho\, \dot{\hat{\boldsymbol{\mu}}} = \overset{*}{\widehat{\widetilde{\mathbf{M}}}} + (\widetilde{\mathbf{M}} \cdot \nabla) \hat{\mathbf{v}} \,, \tag{7.57}$$

and taking into account the identities[8]

$$\widetilde{\mathbf{E}} (\mathbf{P} \cdot \nabla) \hat{\mathbf{v}} = (\widetilde{\mathbf{E}} \otimes \mathbf{P}) : \nabla \hat{\mathbf{v}} \,, \qquad \mathbf{B} (\widetilde{\mathbf{M}} \cdot \nabla) \hat{\mathbf{v}} = (\mathbf{B} \otimes \widetilde{\mathbf{M}}) : \nabla \hat{\mathbf{v}} \,, \tag{7.58}$$

results in

$$\mathcal{P}^{int} = - \int_V \left(\left[\boldsymbol{\sigma}^{em} + \widetilde{\mathbf{E}} \otimes \mathbf{P} + \mathbf{B} \otimes \widetilde{\mathbf{M}} \right] : \nabla \hat{\mathbf{v}} + \widetilde{\mathbf{E}} \cdot \overset{*}{\hat{\mathbf{P}}} + \mathbf{B} \cdot \overset{*}{\widehat{\widetilde{\mathbf{M}}}} \right) dV \,, \tag{7.59}$$

where the expression in the square bracket equals to the definition of the generalized electromagnetic Cauchy stress tensor $\overline{\boldsymbol{\sigma}}^{em}$ (7.46). Considering the relation deriving from the symmetry

---

[8]The transformations for the identities are examplarily shown for (7.58)$_1$ starting with $\widetilde{\mathbf{E}} (\mathbf{P} \cdot \nabla) \hat{\mathbf{v}} = \widetilde{\mathbf{E}} (\nabla \hat{\mathbf{v}}) \mathbf{P}$. Since the gradient can be seen as a dyadic product in form of $\nabla \hat{\mathbf{v}} = \hat{\mathbf{v}} \otimes \nabla$, we can make the following transformation: $\widetilde{\mathbf{E}} (\hat{\mathbf{v}} \otimes \nabla) \mathbf{P} = (\widetilde{\mathbf{E}} \otimes \mathbf{P}) : (\hat{\mathbf{v}} \otimes \nabla) = (\widetilde{\mathbf{E}} \otimes \mathbf{P}) : \nabla \hat{\mathbf{v}}$ with : as the second-order tensor contraction.

of the generalized stress tensor ($\overline{\boldsymbol{\sigma}}^{em} : \nabla\hat{\mathbf{v}} = \overline{\boldsymbol{\sigma}}^{em} : \hat{\mathbf{d}}$), yields an equivalent formulation of the Principle of Virtual Power in the format

$$\mathcal{P}^{ext} + \mathcal{P}^{int} = 0\,, \tag{7.60}$$

with

$$\mathcal{P}^{ext} \;=\; + \int_V [\mathbf{f} + \mathbf{f}^{em}] \cdot \hat{\mathbf{v}}\, dV + \int_S \mathbf{T} \cdot \hat{\mathbf{v}}\, dS + \int_V (\rho\, \widetilde{\mathbf{E}} \cdot \dot{\hat{\mathbf{p}}} + \rho\, \mathbf{B} \cdot \dot{\hat{\boldsymbol{\mu}}})\, dV\,, \tag{7.61}$$

$$\mathcal{P}^{int} \;=\; - \int_V (\overline{\boldsymbol{\sigma}}^{em} : \hat{\mathbf{d}} + \widetilde{\mathbf{E}} \cdot \overset{*}{\hat{\mathbf{P}}} + \mathbf{B} \cdot \overset{*}{\widetilde{\hat{\mathbf{M}}}})\, dV\,. \tag{7.62}$$

Obviously, the virtual power of internal forces (7.62) only contains objective time rates, such as the Eulerian strain rate $\mathbf{d}$, and the upper-convected type time derivatives of the electric polaritzation and of the magnetization, respectively.

In the case of large deformations, we make use of the definition of the symmetric generalized second Piola-Kirchhoff stress tensor $\overline{\boldsymbol{\pi}}^{em}$ (7.48), the relation between the Eulerian strain rate $\mathbf{d}$ and the Green-Lagrange strain tensor $\boldsymbol{\mathcal{E}}$ (2.67), as well as of the following definitions of electromagnetic field vectors in Lagrangian representation (described by the subscript π) [Maugin, 1988]

$$\mathbf{E}_\pi = \widetilde{\mathbf{E}} \cdot \mathbf{F}\,, \qquad \mathbf{B}_\pi = \mathbf{B} \cdot \mathbf{F}\,, \qquad \mathbf{M}_\pi = J\, \mathbf{F}^{-1}\, \widetilde{\mathbf{M}}\,, \qquad \mathbf{P}_\pi = J\, \mathbf{F}^{-1}\, \mathbf{P}\,, \qquad \mathbf{J}_{\pi,f} = J\, \mathbf{F}^{-1}\, \widetilde{\mathbf{J}}_f\,. \tag{7.63}$$

Furthermore, the (objective) material derivatives of the Lagrangian electric polarization and magnetization are defined as[9]

$$\dot{\mathbf{P}}_\pi = J\, \mathbf{F}^{-1}\, \overset{*}{\mathbf{P}} \quad \text{and} \quad \dot{\mathbf{M}}_\pi = J\, \mathbf{F}^{-1}\, \overset{*}{\widetilde{\mathbf{M}}}\,. \tag{7.64}$$

Use of these definitions as well as of the identity of volume changes, $dV = J\, dV_0$, in the expressions for the virtual power of external forces (7.61) and for the virtual power of internal forces (7.62) results in the sought formulation of the Principle of Virtual Power in Lagrangian representation reading as

$$\mathcal{P}^{ext} + \mathcal{P}^{int} = 0\,, \tag{7.65}$$

with

$$\mathcal{P}^{ext} \;=\; + \int_{V_0} J\, (\mathbf{f}[\boldsymbol{\varphi}(\mathbf{X})] + \mathbf{f}^{em}[\boldsymbol{\varphi}(\mathbf{X})]) \cdot \hat{\mathbf{v}}\, dV_0 + \int_{S_0} \mathbf{F} \cdot \boldsymbol{\pi}^{em} \cdot \mathbf{N} \cdot \hat{\mathbf{v}}\, dS_0 + \int_{V_0} \rho_0\, (\widetilde{\mathbf{E}} \cdot \dot{\hat{\mathbf{p}}} + \mathbf{B} \cdot \dot{\hat{\boldsymbol{\mu}}})\, dV_0\,, \tag{7.66}$$

$$\mathcal{P}^{int} \;=\; - \int_{V_0} (\overline{\boldsymbol{\pi}}^{em} : \dot{\hat{\boldsymbol{\mathcal{E}}}} + \mathbf{E}_\pi \cdot \dot{\hat{\mathbf{P}}}_\pi + \mathbf{B}_\pi \cdot \dot{\hat{\mathbf{M}}}_\pi)\, dV_0\,. \tag{7.67}$$

---

[9]The material derivatives of the Lagrangian electric polarization and magnetization can be proved using the chain rule: $\dot{\mathbf{P}}_\pi = \dot{J}\, \mathbf{F}^{-1}\, \mathbf{P} - J\, \mathbf{F}^{-2}\, \dot{\mathbf{F}}\, \mathbf{P} + J\, \mathbf{F}^{-1}\, \dot{\mathbf{P}}$, with $\dot{J} = J\, (\nabla \cdot \mathbf{v})$ and $\dot{\mathbf{F}} = (\nabla \mathbf{v})\, \mathbf{F}$. Substitution of $\dot{J}$ and $\dot{\mathbf{F}}$ results in $\dot{\mathbf{P}}_\pi = J\, \mathbf{F}^{-1}\, [\dot{\mathbf{P}} + (\nabla \cdot \mathbf{v})\, \mathbf{P} - (\nabla \cdot \mathbf{P})\, \mathbf{v}]$, where the expression in the square bracket is the convective time derivative of $\mathbf{P}$ as defined in (7.11). The same procedure is done for the material derivative of the Lagrangian magnetization $\dot{\mathbf{M}}_\pi$.

7.2.5 Thermodynamics and constitutive laws of electromagnetic deformable continua

The developments of thermodynamics for deformable continua (see Section 2.4) can be straightforwardly extended to more complex material behavior. In addition to conventional thermoelasticity, we here present an extension to electromagnetism by means of the derived electromagnetic power as well as of the Principle of Virtual Power for electromagnetic deformable continua.

First, we start with the thermodynamical description in the deformed configuration (Eulerian representation). The conservation of all forms of energy in the case of electromagnetic deformable continua is formulated as follows (*first law of thermodynamics*): mechanical work, electromagnetic energy, and heat given to a body per unit time is equal to the increase of its *internal energy* E[10]

$$\dot{E} = \int_V \rho\,\dot{e}_m\,dV = \int_V \mathbf{f}\cdot\mathbf{v}\,dV + \int_S \mathbf{T}\cdot\mathbf{v}\,dS - \int_S \mathbf{q}\cdot\mathbf{n}\,dS + \int_V r\,dV + \int_V p^{em}\,dV\,, \qquad (7.68)$$

where e_m is the gravimetric internal energy density (energy per unit mass); r is the per unit volume and per time Eulerian heat supply; $\mathbf{q}$ is the heat flux vector (heat per unit area) in Eulerian representation; and p^{em} is the electromagnetic power per unit volume. Substituting the expression for the electromagnetic power (7.26) into (7.68) yields

$$\int_V \rho\,\dot{e}_m\,dV = \int_V [\mathbf{f}+\mathbf{f}^{em}]\cdot\mathbf{v}\,dV + \int_S \mathbf{T}\cdot\mathbf{v}\,dS - \int_S \mathbf{q}\cdot\mathbf{n}\,dS + \int_V r\,dV + \int_V (\widetilde{\mathbf{J}}_f\cdot\widetilde{\mathbf{E}} + \rho\,\widetilde{\mathbf{E}}\cdot\dot{\mathbf{p}} - \widetilde{\mathbf{M}}\cdot\dot{\mathbf{B}})\,dV\,. \tag{7.69}$$

In order to obtain thermodynamic laws, including objective time rates, we introduce the *gravimetric generalized internal energy density* $\overline{e}_m$ as well as the gravimetric generalized free energy density $\overline{\psi}_m$ reading as [Maugin, 1988]

$$\overline{e}_m = e_m + \boldsymbol{\mu}\cdot\mathbf{B}\,, \qquad \overline{\psi}_m = \overline{e}_m - Ts_m = \psi_m + \boldsymbol{\mu}\cdot\mathbf{B}\,, \qquad (7.70)$$

where $\boldsymbol{\mu}$ is the magnetization per unit mass. Thus, considering the generalized energy densities in (7.69) yields a more natural form, since the electric polarization and magnetization are used as independent variables for electromagnetic effects

$$\int_V \rho\,\dot{\overline{e}}_m\,dV = \int_V [\mathbf{f}+\mathbf{f}^{em}]\cdot\mathbf{v}\,dV + \int_S \mathbf{T}\cdot\mathbf{v}\,dS - \int_S \mathbf{q}\cdot\mathbf{n}\,dS + \int_V r\,dV + \int_V (\widetilde{\mathbf{J}}_f\cdot\widetilde{\mathbf{E}} + \rho\,\widetilde{\mathbf{E}}\cdot\dot{\mathbf{p}} + \rho\,\mathbf{B}\cdot\dot{\boldsymbol{\mu}})\,dV\,. \tag{7.71}$$

Use of the Principle of Virtual Power (7.60)-(7.62), as well as the divergence theorem, allows the reformulation of the law of energy conservation (7.71) in local form (integrands must vanish)

$$\rho\,\dot{\overline{e}}_m = \overline{\boldsymbol{\sigma}}^{em}:\mathbf{d} - \mathrm{div}\mathbf{q} + r + \widetilde{\mathbf{J}}_f\cdot\widetilde{\mathbf{E}} + \widetilde{\mathbf{E}}\cdot\overset{*}{\mathbf{P}} + \mathbf{B}\cdot\overset{*}{\widetilde{\mathbf{M}}}\,. \qquad (7.72)$$

Thereby, the conversion of heat energy into effective mechanical energy is limited, which is expressed by the *second law of thermodynamics*:

$$\dot{S} = \int_V \rho\,\dot{s}_m\,dV \geq \int_V \frac{r}{T}\,dV - \int_S \frac{\mathbf{q}\cdot\mathbf{n}}{T}\,dS\,, \qquad (7.73)$$

---

[10]In Eq. (7.68), the identitiy $\dot{E} = \int_V \rho\,\dot{e}_m\,dV$ can be proved as follows: Use of the Reynolds transport theorem in the definition of the rate of the internal energy, $\dot{E} = \frac{D}{Dt}\int_V e\,dV = \frac{D}{Dt}\int_V \rho\,e_m\,dV$, results in $\int_V \left[\frac{\partial(\rho\,e_m)}{\partial t} + \nabla\cdot(\rho\,e_m\,\mathbf{v})\right]dV = \int_V \left[e_m\left(\frac{\partial\rho}{\partial t} + \nabla\cdot(\rho\mathbf{v})\right) + \rho\left(\frac{\partial e_m}{\partial t} + \mathbf{v}\cdot\nabla e_m\right)\right]dV$. Taking into account the conservation of mass in form of the continuity equation, $\frac{\partial\rho}{\partial t} + \nabla\cdot(\rho\mathbf{v}) = 0$, (see also (7.28)) and the definition of the material derivative yields $\dot{E} = \int_V \rho\left(\frac{\partial e_m}{\partial t} + \mathbf{v}\cdot\nabla e_m\right)dV = \int_V \rho\,\dot{e}_m\,dV$.

where s_m is the gravimetric internal entropy density (entropy per unit mass), and T is the absolute Temperature. Use of the divergence theorem, allows the reformulation of (7.73) for any body (integrands must vanish) and yields the local form of the second law of thermodynamics

$$\rho\,T\dot{s}_m + \mathrm{div}\mathbf{q} - \frac{\mathbf{q}}{T}\cdot\mathrm{grad}T - r \geq 0\,. \tag{7.74}$$

Combining the generalized local form of the law of energy conservation (7.72) and the local form of the second law if thermodynamics (7.74), as well as considering the definition of the generalized free energy density (7.70), allows us to represent an generalized formulation of the *Clausius-Duhem inequality*,

$$\phi = \overline{\boldsymbol{\sigma}}^{em} : \mathbf{d} - \rho\,\dot{\overline{\psi}}_m - \rho\,s_m\dot{T} - \frac{\mathbf{q}}{T}\cdot\mathrm{grad}T + \widetilde{\mathbf{J}}_f\cdot\widetilde{\mathbf{E}} + \widetilde{\mathbf{E}}\cdot\overset{*}{\mathbf{P}} + \mathbf{B}\cdot\overset{*}{\widetilde{\mathbf{M}}} \geq 0\,, \tag{7.75}$$

including objective time rates and the symmetric mechanical stress tensor.

In the case of large deformations, we refer to the considerations of hyperelastic materials representing the free energy density as a function of the Green-Lagrange strain tensor: Based on the introduced first law of thermodynamics in form of generalized energy densities (7.71), we can present an equivalent expression in Lagrangian representation, using the *gravimetric generalized intenal energy density* $\overline{e}_m = \overline{e}/\rho$ as well as the identity for volume changes

$$\dot{E} = \int_{V_0}\rho_0\,\dot{\overline{e}}_m\,dV_0 = +\int_{V_0}J\,(\mathbf{f}[\boldsymbol{\varphi}(\mathbf{X})] + \mathbf{f}^{em}[\boldsymbol{\varphi}(\mathbf{X})])\cdot\mathbf{v}\,dV_0 + \int_{S_0}\mathbf{F}\cdot\boldsymbol{\pi}^{em}\cdot\mathbf{N}\cdot\mathbf{v}\,dS_0$$
$$-\int_{S_0}\mathbf{Q}\cdot\mathbf{N}\,dS_0 + \int_{V_0}R\,dV_0 + \int_{V_0}(J\,\widetilde{\mathbf{J}}_f\cdot\widetilde{\mathbf{E}} + \rho_0\,\widetilde{\mathbf{E}}\cdot\dot{\mathbf{p}} + \rho_0\,\mathbf{B}\cdot\dot{\boldsymbol{\mu}})\,dV_0\,, \tag{7.76}$$

where ρ_0 is the initial volumetric mass density; $R = r\,J$ is the per unit volume and per time Lagrangian heat supply; and $\mathbf{Q} = J\,\mathbf{q}\,\mathbf{F}^{-T}$ is the heat flux vector (heat per unit area) in Lagrangian representation. Use of the Principle of Virtual Power (7.65)-(7.67) as well as the divergence theorem, allows the reformulation of (7.76) for any body (integrands must vanish)

$$\rho_0\,\dot{\overline{e}}_m = \overline{\boldsymbol{\pi}}^{em} : \dot{\boldsymbol{\mathcal{E}}} - \mathrm{div}_{\mathbf{X}}\mathbf{Q} + R + \mathbf{J}_{\pi,f}\cdot\mathbf{E}_\pi + \mathbf{E}_\pi\cdot\dot{\mathbf{P}}_\pi + \mathbf{B}_\pi\cdot\dot{\mathbf{M}}_\pi\,, \tag{7.77}$$

taking into account the nabla-operator as a function of the particle position vector $\mathbf{X}$ in the undeformed configuration $\nabla_{\mathbf{X}} = \left(\frac{\partial}{\partial X_1}, ..., \frac{\partial}{\partial X_n}\right)$. Eq. (7.77) is the local form of the law of energy conservation (in the case of electromagnetic deformable continua) in Lagrangian representation.

The second law of thermodynamics, see (2.79) and (7.73), respectively, can be tranformed into the Lagrangian representation by using the *gravimetric intenal entropy density* $s_m = s/\rho$ (entropy per unit mass) as well as the identity for volume changes (2.94):

$$\frac{\partial S}{\partial t} = \int_{V_0}\rho_0\,\dot{s}_m\,dV_0 \geq \int_{V_0}\frac{R}{T}\,dV_0 - \int_{S_0}\frac{\mathbf{Q}\cdot\mathbf{N}}{T}\,dS_0\,, \tag{7.78}$$

Use of the divergence theorem, allows the reformulation of (7.78) for any body (integrands must vanish) and yields the local form of the second law of thermodynamics in Lagrangian representation

$$\rho_0\,T\,\dot{s}_m + \mathrm{div}_{\mathbf{X}}\mathbf{Q} - \frac{\mathbf{Q}}{T}\cdot\mathrm{grad}_{\mathbf{X}}T - R \geq 0\,. \tag{7.79}$$

Again, we link the local forms of the second law of thermodynamics (7.79) and first law of thermodynamics (7.77), yielding

$$\phi = \overline{\boldsymbol{\pi}}^{em} : \dot{\boldsymbol{\mathcal{E}}} - \rho_0 \dot{\overline{\psi}}_m - \rho_0 \, s_m \dot{T} - \frac{\mathbf{Q}}{T} \cdot \text{grad}_{\mathbf{X}} T + \mathbf{J}_{\pi,f} \cdot \mathbf{E}_\pi + \mathbf{E}_\pi \cdot \dot{\mathbf{P}}_\pi + \mathbf{B}_\pi \cdot \dot{\mathbf{M}}_\pi \geq 0 \,. \quad (7.80)$$

where we considered the energy differentiation, $\overline{e}_m = \overline{\psi}_m + T s_m$. This inequality is called *generalized Lagrangian Clausius-Duhem inequality for electromagnetic deformable continua.*

As described in Sec. 2.4, the gravimetric generalized free energy density $\overline{\psi}_m$ is a function of so-called *state variables*: In the case of thermoelasticity, there are two such state variables, namely the Green-Lagrange strain tensor $\boldsymbol{\mathcal{E}}$ and the absolute temperature T. Additionally, there can be other quantities of energetic changes, e.g. electromagnetism or plasticity of the continuum. In the case of electromagnetic deformable continua, the state variables can be straightforwardly extended to the Lagrangian electric polarization $\mathbf{P}_\pi$ and to the Lagrangian magnetization $\mathbf{M}_\pi$. Hence, we assume the following dependence of the gravimetric generalized free energy density of type

$$\overline{\psi}_m = \overline{\psi}_m(\boldsymbol{\mathcal{E}}, T, \mathbf{P}_\pi, \mathbf{M}_\pi) \,. \quad (7.81)$$

Use of the dependence (7.81), the dissipation inequality (7.80) can be reformulated as follows

$$\phi = \overline{\boldsymbol{\pi}}^{em} : \dot{\boldsymbol{\mathcal{E}}} - \rho_0 \left(\frac{\partial \overline{\psi}_m}{\partial \boldsymbol{\mathcal{E}}} : \dot{\boldsymbol{\mathcal{E}}} + \frac{\partial \overline{\psi}_m}{\partial T} : \dot{T} + \frac{\partial \overline{\psi}_m}{\partial \mathbf{P}_\pi} : \dot{\mathbf{P}}_\pi + \frac{\partial \overline{\psi}_m}{\partial \mathbf{M}_\pi} : \dot{\mathbf{M}}_\pi \right)$$

$$- \rho_0 \, s_m \dot{T} - \frac{\mathbf{Q}}{T} \cdot \text{grad}_{\mathbf{X}} T + \mathbf{J}_{\pi,f} \cdot \mathbf{E}_\pi + \mathbf{E}_\pi \cdot \dot{\mathbf{P}}_\pi + \mathbf{B}_\pi \cdot \dot{\mathbf{M}}_\pi \geq 0 \,. \quad (7.82)$$

This inequality must be valid for any evolutions of the Green-Lagrange strain tensor $\boldsymbol{\mathcal{E}}$, the absolute temperature T (and temperature gradients), as well as for the electromagnetic fields $\mathbf{E}_\pi$, $\mathbf{B}_\pi$, $\mathbf{J}_{\pi,f}$, $\mathbf{P}_\pi$, and $\mathbf{M}_\pi$. Therefore, the fulfillment of the dissipation inequality (7.82) implies constitutive laws of electromagnetic deformable continua in the reference configuration

$$\overline{\boldsymbol{\pi}}^{em} = \rho_0 \frac{\partial \overline{\psi}_m}{\partial \boldsymbol{\mathcal{E}}}(\boldsymbol{\mathcal{E}}, T, \mathbf{P}_\pi, \mathbf{M}_\pi) \,,$$

$$s_m = -\frac{\partial \overline{\psi}_m}{\partial T}(\boldsymbol{\mathcal{E}}, T, \mathbf{P}_\pi, \mathbf{M}_\pi) \,,$$

$$\mathbf{E}_\pi = \rho_0 \frac{\partial \overline{\psi}_m}{\partial \mathbf{P}_\pi}(\boldsymbol{\mathcal{E}}, T, \mathbf{P}_\pi, \mathbf{M}_\pi) \,,$$

$$\mathbf{B}_\pi = \rho_0 \frac{\partial \overline{\psi}_m}{\partial \mathbf{M}_\pi}(\boldsymbol{\mathcal{E}}, T, \mathbf{P}_\pi, \mathbf{M}_\pi) \,. \quad (7.83)$$

Knowing the derived stress tensor, and electromagnetic fields in Lagrangian representation, we finally can provide a set of constitutive laws in Eulerian representation, using the reciprocal of (7.48) and (7.63)

$$\overline{\boldsymbol{\sigma}}^{em} = \rho \, \mathbf{F} \cdot \frac{\partial \overline{\psi}_m}{\partial \boldsymbol{\mathcal{E}}}(\boldsymbol{\mathcal{E}}, T, \mathbf{P}_\pi, \mathbf{M}_\pi) \cdot \mathbf{F}^T \,,$$

$$s = -\rho \frac{\partial \overline{\psi}_m}{\partial T}(\boldsymbol{\mathcal{E}}, T, \mathbf{P}_\pi, \mathbf{M}_\pi) \,,$$

$$\widetilde{\mathbf{E}} = \rho_0 \frac{\partial \overline{\psi}_m}{\partial \mathbf{P}_\pi}(\boldsymbol{\mathcal{E}}, T, \mathbf{P}_\pi, \mathbf{M}_\pi) \cdot \mathbf{F}^{-1} \,,$$

$$\widetilde{\mathbf{B}} \quad = \quad \rho_0 \, \frac{\partial \overline{\psi}_m}{\partial \mathbf{M}_\pi}(\boldsymbol{\mathcal{E}}, T, \mathbf{P}_\pi, \mathbf{M}_\pi) \cdot \mathbf{F}^{-1} \, . \tag{7.84}$$

Finally, based on the definition of the generalized electromagnetic Cauchy stress tensor (7.46), we are able to calculate the (nonsymmetric) electromagnetic Cauchy stress tensor reading as

$$\boldsymbol{\sigma}^{em} = \overline{\boldsymbol{\sigma}}^{em} - \widetilde{\mathbf{E}} \otimes \mathbf{P} - \mathbf{B} \otimes \widetilde{\mathbf{M}} \, . \tag{7.85}$$

Bibliography

Abell, G. C. Empirical chemical pseudopotential theory of molecular and metallic bonding. *Physical Review B*, 31:6184–6196, 1985.

Alungbe, G. D., Tia, M., and Bloomquist, D. G. Effect of aggregate, water/cement ratio, and curing on the coefficient of linear thermal expansion of concrete. *Transportation Research Record: Journal of the Transportation Research Board*, 1335:44–51, 1992.

Balandin, A. A., Ghosh, S., Bao, W., Calizo, I., Teweldebrhan, D., Miao, F., and Lau, C. N. Superior thermal conductivity of single-layer graphene. *Nano Letters*, 8(3):902–907, 2008.

Barenblatt, G. I. *Scaling, Self-similarity, and intermediate Asymptotics.* Cambridge University Press, Cambridge, England, 1st edition, 1996.

Bathe, K.-J. and Wilson, E. L. *Numerical Methods in Finite Element Analysis.* Prentice-Hall, 1976.

Bažant, Z. P. and Kaplan, M. F. *Concrete at high temperatures: material properties and mathematical models.* Longman, Burnt Mill, UK, 1996.

Bažant, Z. P. and Vorel, J. Energy-conservation error due to use of green-naghdi objective stress rate in commercial finite-element codes and its compensation. *Journal of Applied Mechanics*, 81:021008, 2014.

Bažant, Z. P., Gattu, M., and Vorel, J. Work conjugacy error in commercial Finite-Element codes: its magnitude and how to compensate for it. *Proceedings of the Royal Society A: Mathematical, Physical and Engineering Sciences*, 468:3047–3058, 2012.

Belshe, M., Mamlouk, M. S., Kaloush, K. E., and Rodezno, M. Temperature gradient and curling stresses in concrete pavement with and without open-graded friction course. *Journal of Transportation Engineering*, 137(10):723–729, 2010.

Benveniste, Y. A new approach to the application of Mori-Tanaka's theory in composite materials. *Mechanics of Materials*, 6(2):147–157, 1987.

Bissett, M. A., Tsuji, M., and Ago, H. Strain engineering the properties of graphene and other two-dimensional crystals. *Physical Chemistry Chemical Physics*, 16:11124, 2014.

Blab, R. and Harvey, J. Modelling measured 3D tire contact stress in a viscoelastic FE pavement model. *Int. J. Geomech.*, 2(3):271–290, 2002.

Bloch, F. Über die Quantenmechanik der Elektronen in Kristallgittern [On the quantum mechanics of electrons in crystal lattices]. *Zeitschrift für Physik*, 52:555–600, 1928. in German.

Blöchl, P. E. Projector augmented-wave method. *Physical Review B*, 50:17953, 1994.

Blöchl, P. E., Jepsen, O., and Anderson, O. K. Improved tetrahedron method for brillouin-zone integrations. *Physical Review B*, 49:16223–16233, 1994.

Bolotin, K. I., Sikes, K. J., Klima, M., Fudenberg, G., Hone, J., Kim, P., and Stormer, H. L. Ultrahigh electron mobility in suspended graphene. *Solid State Communications*, 146:351–355, 2008.

Bonnell, D. G. R. and Harper, F. C. The thermal expansion of concrete. Engineering research. *Journal of the Institution of Civil Engineers*, 33(4):320–330, 1950.

Borino, G. and Polizzotto, C. A method to transform a nonlocal model into a gradient one within elasticity and plasticity. *European Journal of Mechanics-A/Solids*, 46:30–41, 2014.

Born, M. On the stability of crystal lattices. I. *Mathematical Proceedings of the Cambridge Philosophical Society*, 36:160–172, 1940.

Born, M. and Oppenheimer, R. Zur Quantentheorie der Molekeln [On the quantum theory of molecules]. *Annalen der Physik*, 84(20):457–484, 1927. in German.

Bowles, J. E. *Foundation analysis and design*. McGraw-Hill International Book Company, 1997.

Bradbury, R. D. *Reinforced concrete pavements*. Wire Reinforcement Institute, Washington D.C., 1938.

Brandt, N. B., Chudinov, S. M., and Ponomarev, Y. G. *Semimetals: 1. Graphite and Its Compounds*. North-Holland, 1988.

Cadelano, E., Palla, P. L., Giordano, S., and Colombo, L. Nonlinear elasticity of monolayer graphene. *Physical Review Letters*, 102:235502, 2009.

Caliendo, C. and Parisi, A. Stress prediction model for airport pavements. *Journal of Transportation Engineering*, 136,(7):664–677, 2010.

Castro Neto, A. H., Guinea, F., Peres, N. M. R., Novoselov, K. S., and Geim, A. K. The electronic properties of graphene. *Reviews of Modern Physics*, 81:109–155, 2009.

Changnon, S. A. Increasing major hail losses in the U.S. *Climatic Change*, 96(1-2):161–166, 2009.

Chen, W.-F. and Duan, L. *Bridge Engineering Handbook: Fundamentals, Superstructure Design, Substructure Design, Seismic Design, and Construction and Maintenance*. CRC Press, 2nd edition, 2014.

Choubane, B. and Tia, M. Nonlinear temperature gradient effect on maximum warping stresses in rigid pavements. *Transportation Research Record: Journal of the Transportation Research Board*, 1370(1):11, 1992.

Choubane, B. and Tia, M. Analysis and verification of thermal-gradient effects on concrete pavement. *Journal of Transportation Engineering*, 121(1):75–81, 1995.

Chung, Y. and Shin, H.-C. Characterization of the coefficient of thermal expansion and its effect on the performance of Portland cement concrete pavements. *Canadian Journal of Civil Engineering*, 38(2):175–183, 2010.

Clark, N., Oikonomou, A., and Vijayaraghavan, A. Ultrafast quantitative nanomechanical mapping of suspended graphene. *Physica Status Solidi B*, 250(12):2672–2677, 2013.

Das, B. *Principles of Foundation Engineering*. Cengage Learning, 2010.

Delatte, N. *Concrete Pavement Design, Construction and Performance.* Taylor & Francis, 2008.

Deplazes, A. *Constructing Architecture: Materials, Processes, Structures. A Handbook.* Birkhäuser, 2008.

Dettling, H. *Die Wärmedehnung des Zementsteines, der Gesteine und der Betone [Thermal expansion of cement pastes, aggregates, and concretes].* Dr.-Ing. dissertation, Technische Hochschule Stuttgart, Germany, 1962.

Dlubal. *RFEM – FEM Structural Analysis Software.* Dlubal Software GmbH, Am Zellweg 2, 93464 Tiefenbach, Germany, 2016.

Eisenmann, J. *Betonfahrbahnen [Concrete pavements].* Wilhem Ernst & Sohn, Berlin, München, Düsseldorf, 1979. In German.

Emanuel, J. H. and Hulsey, J. L. Prediction of the thermal coefficient of expansion of concrete. *Journal of the American Concrete Institute*, 74(4):149–155, 1977.

Eshelby, J. D. The determination of the elastic field of an ellipsoidal inclusion, and related problems. *Proceedings of the Royal Society A: Mathematical, Physical and Engineering Sciences*, 241(1226):376–396, 1957.

Fang, T.-H., Wang, T. H., Yang, J.-C., and Hsiao, Y.-J. Mechanical characterization of nanoindented graphene via molecular dynamics simulations. *Nanoscale Research Letters*, 6: 481, 2011.

Fo-van, C. and Siao-mei, H. A free rectangular plate on elastic foundation. *Applied Mathematics and Mechanics*, 5(3):1317–1324, 1984.

Franklin, R. E. The structure of graphitic carbons. *Acta Crystallographica.*, 4:253–261, 1951.

Fu, Y. F., Wong, Y. L., Poon, C. S., Tang, C. A., and Lin, P. Experimental study of micro/macro crack development and stress-strain relations of cement-based composite materials at elevated temperatures. *Cement and Concrete Research*, 34(5):789–797, 2004a.

Fu, Y. F., Wong, Y. L., Tang, C. A., and Poon, C. S. Thermal induced stress and associated cracking in cement-based composite at elevated temperatures – Part I: Thermal cracking around single inclusion. *Cement and Concrete Composites*, 26(2):99–111, 2004b.

Fu, Y. F., Wong, Y. L., Tang, C. A., and Poon, C. S. Thermal induced stress and associated cracking in cement-based composite at elevated temperatures – Part II: Thermal cracking around multiple inclusions. *Cement and Concrete Composites*, 26(2):113–126, 2004c.

Fung, Y. C. and Tong, P. *Classical and Computational Solid Mechanics.* Advanced Series in Engineering Science. World Scientific, Singapore, 1 edition, 2001.

Galiotis, C., Frank, O., Koukaras, E. N., and Sfyris, D. Graphene mechanics: Current status and perspectives. *Annual Review of Chemical and Biomolecular Engineering*, 6:121–140, 2015.

Germain, P. Sur l'application de la méthode des puissances virtuelles en mécanique des milieux continus [on the application of the method of virtual power in continuum mechanics]. *Comptes Rendus de l' Académie des Sciences Paris*, 274(Série A):1051–1055, 1972. in French.

Germain, P. La méthode des puissances virtuelles en mécanique des milieu continus [The principle of virtual power in solid mechanics]. *Journal de mécanique*, 12(2):235–274, 1973a. in French.

Germain, P. The method of virtual power in continuum mechanics. Part 2: Microstructure. *SIAM Journal on Applied Mathematics*, 25(3):556–575, 1973b.

Germain, P., Nguyen, Q. S., and Suquet, P. Continuum thermodynamics. *Transactions of the ASME*, 50:1010–1020, 1983.

Ghabezloo, S. Micromechanical analysis of the effect of porosity on the thermal expansion coefficient of heterogeneous porous materials. *International Journal of Rock Mechanics and Mining Sciences*, 55:97–101, 2012.

Ghaffari, R. and Sauer, R. A. A new efficient hyperelastic finite element model for graphene and its application to carbon nanotubes and nanocones. *Finite Elements in Analysis and Design*, 146:42–61, 2018.

Ghaffari, R., Duong, T. X., and Sauer, R. A. A new shell formulation for graphene structures based on existing ab-initio data. *International Journal of Solids and Structures*, 135:37–60, 2018.

Gil, A. J., Adhikari, S., Scarpa, F., and Bonet, J. The formation of wrinkles in single-layer graphene sheets under nanoindentation. *Journal of Physics: Condensed Matter*, 22:145302, 2010.

Gonçalves, P. B., Soares, R. M., and Pamplona, D. Nonlinear vibrations of a radially stretched circular hyperelastic membrane. *Journal of Sound and Vibration*, 327:231–248, 2009.

Gould, P. L. *Analysis of Shells and Plates.* Springer-Verlag, 1988.

Greaves, G. N., Greer, A. L., Lakes, R. S., and Rouxel, T. Poisson's ratio and modern materials. *Nature Materials*, 10:823–837, 2011.

Grédiac, M., Pierron, F., Avril, S., and Toussaint, E. The virtual fields method for extracting constitutive parameters from full-field measurements: a review. *Strain*, 42:233–253, 2006.

Green, G. On the laws of reflexion and refraction of light at the common surface of two non-crystallized media. *Transactions of the Cambridge Philosophical Society*, 7:245–269, 1837.

Hajek, J. *Common Airport Pavement Maintenance Practices.* Transportation Research Board, 2011.

Hellmich, C. *Skriptum zur Vorlesung "Festigkeitslehre" [Lecture notes "strenght of materials"].* Institute for Mechanics of Materials and Structures, Vienna University of Technology, Karlspl. 13/202 A-1040 Vienna, Austria, 2012. in German.

Hellmich, C. *Skriptum zur Vorlesung "Ingenieurmechanik" [Lecture notes "engineering mechanics"].* Institute for Mechanics of Materials and Structures, Vienna University of Technology, Karlspl. 13/202 A-1040 Vienna, Austria, 2018. in German.

Hencky, H. Über die Form des Elastizitätsgesetzes bei idealen elastischen Stoffen. *Zeitschrift für Technische Physik*, 9:214–247, 1928. in German.

Hestenes, M. R. and Stiefel, E. Methods of conjugate gradients for solving linear systems. *Journal of Research of the National Bureau of Standards*, 49(6):409–436, 1952.

Hill, R. and Milstein, F. Principles of stability analysis of ideal crystals. *Physical Review B*, 15 (6):3087–3096, 1977.

Hohenberg, P. and Kohn, W. Inhomogeneous electron gas. *Physical Review*, 136:B864–B871, 1964.

Höller, R. *Bedded plate - versus layered half space - based modeling of floating floor screeds: implications for design.* TU Wien, Vienna, Austria, 2017. Diploma Thesis.

Höller, R., Aminbaghai, M., Eberhardsteiner, L., Eberhardsteiner, J., Blab, R., Pichler, B., and Hellmich, C. Rigorous amendment of Vlasov's theory for thin elastic plates on elastic Winkler foundations, based in the Principle of Virtual Power. *European Journal of Mechanics-A/Solids*, 73:449–482, 2019.

Höller, R., Smejkal, V., Libisch, F., and Hellmich, C. Energy landscape of graphene under general deformations: DFT-to-hyperelasticity upscaling. *International Journal of Engineering Science (under review)*, 2020a.

Höller, R., Libisch, F., and Hellmich, C. A membrane theory for circular graphene sheets, based on a hyperelastic material model for large deformations. *Submitted to Mechanics of Advanced Materials and Structures*, 2020b.

Hooke, R. *De Potentia Restitutiva, or of Spring. Explaining the Power of Springing Bodies.* London, 1678.

Ioannides, A. and Peng, J. Finite Element simulation of crack growth in concrete slabs: Implications for pavement design. In *Fifth International Workshop on Fundamental Modeling of Concrete Pavements, Istanbul, Turkey*, pages 56–68, 2004.

Ioannides, A. M. and Khazanovich, L. Nonlinear temperature effects on multilayered concrete pavements. *Journal of Transportation Engineering*, 124(2):128–136, 1998.

Jelenić, G. and Saje, M. A kinematically exact space finite strain beam model - finite element formulation by generalized virtual work principle. *Computer Methods in Applied Mechanics and Engineering*, 120:131–161, 1995.

Ji, W., Waas, A. M., and Bažant, Z. P. Errors caused by non-work-conjugate stress and strain measures and necessary corrections in Finite Element programs. *Journal of Applied Mechanics*, 77:044504, 2010.

Jiang, S., Shi, S., and Wang, X. Nanomechanics and vibration analysis of graphene sheets via a 2D plate model. *Journal of Physics D: Applied Physics*, 47:045104, 2014.

Jun-Yu, T. Remarks of some problems for rectangular thin plates with free edges on elastic foundations. *Applied Mathematics and Mechanics*, 12(4):415–420, 1991.

Kameswara Rao, N. S. V. *Foundation Design: Theory and Practice.* John Wiley & Sons (Asia) Pte Ltd, 2011.

Kang, L.-C., Wu, C.-H., and Steele, C. R. Fourier series of ploygonal plate bending: A very large plate element. *Applied Mathematics and Computation*, 67:197–225, 1995.

Ke-rang, W. Thick rectangular plates with free edges on elastic foundations. *Applied Mathematics and Mechanics*, 11(9):869–879, 1990.

Ko, J., Lee, P. S., and Bathe, K.-J. The MITC4+ shell element and its performance. *Computers and Structures*, 169:57–86, 2016.

Kohler, E. and Kannekanti, V. *Influence of the coefficient of thermal expansion on the cracking of jointed concrete pavements.* London, CRC Press, 2008.

Kohn, W. and Sham, L. J. Self-consistent equations including exchange and correlation effects. *Physical Review*, 140:A1133–A1138, 1965.

Königsberger, M., Pichler, B., and Hellmich, C. Micromechanics of ITZ-aggregate interaction in concrete, part I: Stress concentration. *Journal of the American Ceramic Society*, 97(2): 535–542, 2014a.

Königsberger, M., Pichler, B., and Hellmich, C. Micromechanics of ITZ-aggregate interaction in concrete, part II: Strength upscaling. *Journal of the American Ceramic Society*, 97(2):543–551, 2014b.

Königsberger, M., Hlobil, M., Delsaute, B., Staquet, S., Hellmich, C., and Pichler, B. Hydrate failure in ITZ governs concrete strength: A micro-to-macro validated engineering mechanics model. *Cement and Concrete Research*, 103:77–94, 2018.

Kresse, G. and Furthmüller, J. Efficiency of ab-initio total energy calculations for metals and semiconductors using a plane-wave basis set. *Computational Materials Science*, 6:15–50, 1996a.

Kresse, G. and Furthmüller, J. Efficient iterative schemes for ab initio total-energy calculations using a plane-wave basis set. *Physical Review B*, 54:11169, 1996b.

Kresse, G. and Hafner, J. Ab initio molecular dynamics for liquid metals. *Physical Review B*, 47: 558, 1993.

Kresse, G. and Hafner, J. Ab initio molecular-dynamics simulation of the liquid-metal-amorphous-semiconductor transition in germanium. *Physical Review B*, 49:14251, 1994.

Kresse, G. and Joubert, D. From ultrasoft pseudopotentials to the projector augmented-wave method. *Physical Review B*, 59:1758, 1999.

Kumar, S. and Parks, D. M. On the hyperelastic softening and elastic instabilities in graphene. *Proceedings of the Royal Society A: Mathematical, Physical and Engineering Sciences*, 471: 20140567, 2015.

Kundalwal, S. I. Review on micromechanics of nano- and micro-fiber reinforced composites. *Polymer Composites*, 39(12):4243–4274, 2018.

Kundalwal, S. I. and Ray, M. C. Thermoelastic properties of a novel fuzzy fiber-reinforced composite. *Journal of Applied Mechanics*, 80(6):061011, 2013.

Kundalwal, S. I. and Ray, M. C. Effect of carbon nanotube waviness on the effective thermoelastic properties of a novel continuous fuzzy fiber reinforced composite. *Composites Part B: Engineering*, 57:199–209, 2014.

Kundalwal, S. I. and Ray, M. C. Smart damping of fuzzy fiber reinforced composite plates using 1–3 piezoelectric composites. *Journal of Vibration and Control*, 22(6):1526–1546, 2016.

Kunz, M., Sander, J., and Kottmeier, C. Recent trends of thunderstorm and hailstorm frequency and their relation to atmospheric characteristics in southwest Germany. *International Journal of Climatology: A Journal of the Royal Meteorological Society*, 29(15):2283–2297, 2009.

Lang, H.-J. *Bodenmechanik und Grundbau [Soil mechanics and foundation engineering]*. Springer, 2010. in German.

Larsson, R. and Samadikhah, K. Atomistic continuum modeling of graphene membranes. *Computational Materials Science*, 50:1744–1753, 2011.

Lau, C. N., Bao, W., and Velasco, J. Properties of suspended graphene membranes. *Materialstoday*, 15(6):238–245, 2012.

Lee, C., Wei, X., Kysar, J. W., and Hone, J. Measurement of the elastic properties and intrinsic strength of monolayer graphene. *Science*, 321:385–388, 2008.

Lennard-Jones, J. On the determination of molecular fields. *Proceedings of the Royal Society A: Mathematical, Physical and Engineering Sciences*, 106(738):463–477, 1924.

Liu, F., Ming, P., and Li, J. Ab initio calculation of ideal strength and phonon instability of graphene under tension. *Physical Review B*, 76:064120, 2007.

Liu, S., Liu, X., Guan, X. F., He, P. F., and Yuan, Y. A stochastic multi-scale model for predicting the thermal expansion coefficient of early-age concrete. *CMES: Computer Modeling in Engineering and Sciences*, 92(2):173–191, 2013.

Louhghalam, A. and Ulm, F.-J. Risk of pavement fracture due to eigenstresses at early ages and beyond. *Journal of Engineering Mechanics*, 142(12):04016105, 2016.

Love, A. E. H. On the small free vibrations and deformations of elastic shells. *Philosophical Transactions of the Royal Society (London)*, Series A(17):491–549, 1888.

Lu, Q. and Huang, R. Nonlinear mechanics of single-atomic-layer graphene sheets. *International Journal of Applied Mechanics*, 1(3):443–467, 2009.

Lu, Q., Gao, W., and Huang, R. Atomistic simulation and continuum modeling of graphene nanoribbons under uniaxial tension. *Modelling and Simulation in Materials Science and Engineering*, 19:054006, 2011.

Mahboub, K. C., Liu, Y., and Allen, D. L. Evaluation of temperature responses in concrete pavement. *Journal of Transportation Engineering*, 130(3):395–401, 2004.

Majidi, R. Density functional theory study on structural and mechanical properties of graphene, t-graphene, and r-graphyne. *Theoretical Chemistry Accounts*, 136:109, 2017.

Mallela, J., Abbas, A., Harman, T., Rao, C., Liu, R., and Darter, M. Measurement and significance of the coefficient of thermal expansion of concrete in rigid pavement design. *Transportation Research Record: Journal of the Transportation Research Board*, (1919):38–46, 2005.

Mang, H. A. and Hofstetter, G. *Festigkeitslehre [Strength of Materials]*. Springer-Verlag, 2000. in German.

Masad, E., Taha, R., and Muhunthan, B. Finite-Element analysis of temperature effects on plain-jointed concrete pavements. *Journal of Transportation Engineering*, 122(5):388–398, 1996.

Mathworks, I. *Matlab*. 1 Apple Hill Drive, Natick, MA 01760-2098, USA, R2012b edition, 2012.

Maugin, G. A. The method of virtual power in continuum mechanics: application to coupled fields. *Acta Mechanica*, 35(1):1–70, 1980.

Maugin, G. A. *Continuum mechanics of electromagnetic solids.* North-Holland, 1988.

Maugin, G. A. On modelling electromagnetomechanical interactions in deformable solids. *International Journal of Advances in Engineering Sciences and Applied Mathematics*, 1(25): 25–32, 2009.

Maugin, G. A. The principle of virtual power: from eliminating metaphysical forces to providing an efficient modelling tool. *Continuum Mechanics and Thermodynamics*, 25:127–146, 2013.

Maugin, G. A. and Eringen, A. C. On the equations of the electrodynamics of deformable bodies of finite extent. *Journal de Mécanique*, 16(1):101–147, 1977.

Maugin, G. A. and Eringen, A. C. *Electrodynamics of continua I: Foundations and Solid Media.* Springer-Verlag, 1990.

Maugin, G. A. and Goudjo, C. The equations of soft-ferromagnetic elastic plates. *International Journal of Solids and Structures*, 18(10):889–912, 1982.

McCarthy, L. M., Gudimettla, J. M., Crawford, G. L., Guercio, M. C., and Allen, D. Impacts of variability in coefficient of thermal expansion on predicted concrete pavement performance. *Construction and Building Materials*, 93:711–719, 2015.

McCullough, B. F., Zollinger, D., and Dossey, T. Evaluation of the performance of Texas pavements made with different coarse aggregates. Technical report, University of Texas at Austin. Center for Transportation Research, 2000.

Mermin, N. D. Cristalline order in two dimensions. *Physical Review*, 176:250–254, 1968.

Meyers, S. L. Thermal expansion characteristics of hardened cement paste and of concrete. In *Highway Research Board Proceedings*, volume 30, pages 193–203, 1951.

Mianroodi, J. R., Niaki1, S. A., Naghdabadi, R., and Asghari, M. Nonlinear membrane model for large amplitude vibration of single layer graphene sheets. *Nanotechnology*, 22:305703, 2011.

Mitchell, L. J. Thermal expansion tests on aggregates, neat cements, and concretes. In *Proceedings of the American Society for Testing and Materials*, volume 53, pages 963–977, 1953.

Mohamed, A. and Hansen, W. Effect of nonlinear temperature gradient on curling stress in concrete pavements. *Transportation Research Record: Journal of the Transportation Research Board*, (1568):65–71, 1997.

Mohamed, A. R. and Hansen, W. Prediction of stresses in concrete pavements subjected to non-linear gradients. *Cement and Concrete Composites*, 18(6):381–387, 1996.

Mondal, P., Shah, S. P., and Marks, L. D. Nanomechanical properties of interfacial transition zone in concrete. In *Nanotechnology in Construction 3*, pages 315–320. Springer, 2009.

Monkhorst, H. J. and Pack, J. D. Special points for brillouin-zone integrations. *Physical Review B*, 13(12):5188–5192, 1976.

Mori, T. and Tanaka, K. Average stress in matrix and average elastic energy of materials with misfitting inclusions. *Acta Metallurgica*, 21(5):571–574, 1973.

Mouhat, F. and Coudert, F. Necessary and sufficient elastic stability conditions in various crystal systems. *Physical Review B*, 90:224104, 2014.

Mukhopadhyay, A. K., Neekhra, S., and Zollinger, D. G. Preliminary characterization of aggregate coefficient of thermal expansion and gradation for paving concrete. Technical Report 0-1700-5, Texas Transportation Institute, Texas, United States, 2007.

Naik, T. R., Kraus, R. N., and Kumar, R. Influence of types of coarse aggregates on the coefficient of thermal expansion of concrete. *Journal of Materials in Civil Engineering*, 23(4):467–472, 2011.

Nair, R. R., Blake, P., Grigorenko, A. N., Novoselov, K. S., Booth, T. J., Stauber, T., Peres, N. M. R., and Geim, A. K. Fine structure constant defines visual transparency of graphene. *Science*, 320:1308, 2008.

National Cooperative Highway Research Program. Guide for mechanistic-empirical design of new and rehabilitated pavement structures. Final report, NCHRP Project 1-37A, Transportation Research Board Washington, DC, United States, 2004.

Navier, C. L. M. H. Extrait des recherches sur la flexion des plans élastiques [Excerpt from research on bending of elastic planes]. *Bulletin des Sciences de la Société. Philomathique de Paris*, 5:92–102, 1823. in French.

Neek-Amal, M. and Peeters, F. M. Continuum-molecular modelling of graphene. *Physical Review B*, 81:235421, 2010.

Neto, M. A., Amaro, A., Roseiro, L., Cirne, J., and Leal, R. *Engineering Computation of Structures: The Finite Element Method*. Springer-Verlag, 2015.

Nishizawa, T., Ozeki, T., Katoh, K., and Matsui, K. Finite Element model analysis of thermal stresses of thick airport concrete pavement slabs. *Transportation Research Record: Journal of the Transportation Research Board*, (2095):3–12, 2009.

Noll, W. A mathematical theory of the mechanical behavior of continuous media. *Archive for Rational Mechanics and Analysis*, 2:197–226, 1958.

Noll, W. A new mathematical theory of simple materials. *Archive for Rational Mechanics and Analysis*, 48:1–50, 1972.

Novoselov, K. S., Geim, A. K., Morozov, S. V., Jiang, D., Zhang, Y., Dubonos, S. V., Grigorieva, I. V., and Firsov, A. A. Electric field effect in atomically thin carbon films. *Science*, 306: 666–669, 2004.

Ollivier, J. P., Maso, J. C., and Bourdette, B. Interfacial transition zone in concrete. *Advanced Cement Based Materials*, 2(1):30–38, 1995.

Ortega, J. and Rheinboldt, W. *Iterative Solution of Nonlinear Equations in Several Variables (Classics in Applied Mechanics)*. SIAM, 2000.

Pagani, A. and Carrera, E. Large-deflection and post-buckling analyses of laminated composite beams by Carrera unified formulation. *Composite Structures*, 170:40–52, 2017.

Pan, E. Static response of a transversely isotropic and layered half-space to general surface loads. *Physics of the Earth and Planetary Interiors*, 54:353–363, 1989.

Pane, I., Hansen, W., and Mohamed, A. Three-dimensional Finite Element study on effects of nonlinear temperature gradients in concrete pavements. *Transportation Research Record: Journal of the Transportation Research Board*, (1629):58–66, 1998.

Parr, R. G. and Yang, W. *Density-Functional Theory of Atoms and Molecules*. Oxford University Press., 1989.

Patil, A. and DasGupta, A. Finite inflation of an initially stretched hyperelastic circular membrane. *European Journal of Mechanics A/Solids*, 41:28–36, 2013.

Pech, A., Müller, W., and Zach, F. *Fußböden [Floors]*. Birkhäuser, 2016. in German.

Pech, A., Kolbitsch, A., and Zach, F. *Tragwerke [Structures]*. Birkhäuser, 2018. in German.

Perdew, J. P., Burke, K., and Ernzerhof, M. Generalized gradient approximation made simple. *Physical Review Letters*, 77:3865, 1996.

Perdew, J. P., Burke, K., , and Ernzerhof, M. Erratum: Generalized gradient approximation made simple. *Physical Review Letters*, 78:1396, 1997.

Pichler, B. and Dormieux, L. Cracking risk of partially saturated porous media – Part I: Microporoelasticity model. *International Journal for Numerical and Analytical Methods in Geomechanics*, 34(2):135–157, 2010a.

Pichler, B. and Dormieux, L. Cracking risk of partially saturated porous media – Part II: Application to drying shrinkage. *International Journal for Numerical and Analytical Methods in Geomechanics*, 34(2):159–186, 2010b.

Pichler, B. and Hellmich, C. Estimation of influence tensors for eigenstressed multiphase elastic media with nonaligned inclusion phases of arbitrary ellipsoidal shape. *Journal of Engineering Mechanics*, 136(8):1043–1053, 2010.

Pitteri, M. and Zanzotto, G. *Continuum Models for Phase Transitions and Twinning in Crystals*. CRC Press, 1th edition, 2003.

Politano, A. and Chiarello, G. Probing the young's modulus and poisson's ratio in graphene/metal interfaces and graphite: a comparative study. *Nano Research*, 8:1847–1856, 2015.

Polizzotto, C. From the Euler-Bernoulli beam to the Timoshenko one through a sequence of Reddy-type shear deformable beam models of increasing order. *European Journal of Mechanics-A/Solids*, 53:62–74, 2015.

Polizzotto, C. Variational formulations and extra boundary conditions within stress gradient elasticity theory with extensions to beam and plate models. *International Journal of Solids and Structures*, 80:405–419, 2016.

Press, W. H., Flannery, B. P., Teukolsky, S. A., and Vetterling, W. T. *Numerical recipes*. Cambridge University Press, New York, 1986.

Rajagopal, K. R. Conspectus of concepts of elasticity. *Mathematics and Mechanics of Solids*, 16 (5):536–562, 2011.

Rajagopal, K. R. A note on the classification of anisotropy of bodies defined by implicit constitutive relations. *Mechanics Research Communications*, 64:38–41, 2015.

Ramesh, G., Sotelino, E. D., and Chen, W. F. Effect of transition zone on elastic moduli of concrete materials. *Cement and Concrete Research*, 26(4):611–622, 1996.

Ray, M. C. and Kundalwal, S. I. A thermomechanical shear lag analysis of short fuzzy fiber reinforced composite containing wavy carbon nanotubes. *European Journal of Mechanics-A/Solids*, 44:41–60, 2014.

Reddy, J. N. *Theory and Analysis of elastic Plates and Shells*. CRC Press, 2nd edition, 2007.

Rouhi, S. and Ansari, R. Atomistic finite element model for axial buckling and vibration analysis of single-layered graphene sheets. *Physica E*, 44:764–772, 2012.

Saavedra Flores, E. I., Ajaj, R. M., Adhikari, S., Dayyani, I., Friswell, M. I., and Castro-Triguero, R. Hyperelastic tension of graphene. *Applied Physics Letters*, 106:061901, 2015.

Sadeghi, M. and Naghdabadi, R. Nonlinear vibrational analysis of single-layer graphene sheets. *Nanotechnology*, 21:105705, 2010.

Sakhaee-Pour, A. Elastic buckling of single-layered graphene sheet. *Computational Materials Science*, 45:266–270, 2009.

Sakhaee-Pour, A., Ahmadian1, M. T., and Naghdabadi, R. Vibrational analysis of single-layered graphene sheets. *Nanotechnology*, 19:085702, 2008.

Sakyi-Bekoe, K. *Assessment of the coefficient of thermal expansion of Alabama concrete*. Master thesis, Auburn University, Alabama, United States, 2008.

Salençon, J. *Handbook of Continuum Mechanics*. Springer-Verlag, 2001.

Samadikhah, K., Larsson, R., Bazooyar, F., and Bolton, K. Continuum-molecular modelling of graphene. *Computational Materials Science*, 53:37–43, 2012.

Scarpa, F., Adhikari, S., Gil, A. J., and Remillat, C. The bending of single layer graphene sheets: the lattice versus continuum approach. *Nanotechnology*, 21:125702, 2010.

Schrödinger, E. An undulatory theory of the mechanics of atoms and molecules. *Physical Review*, 28(6):1049–1070, 1926.

Scrivener, K. L., Crumbie, A. K., and Laugesen, P. The interfacial transition zone (ITZ) between cement paste and aggregate in concrete. *Interface Science*, 12(4):411–421, 2004.

Seifoori, S. and Hajabdollahi, H. Impact behavior of single-layered graphene sheets based on analytical model and molecular dynamics simulation. *Applied Surface Science*, 351:565–572, 2015.

Sen, D., Novoselov, K. S., Reis, P. M., and Buehler, M. J. Tearing graphene sheets from adhesive substrates produces tapered nanoribbons. *Small*, 6(10):1108–1116, 2010.

Sevčík, I. *3D Finite Elements with rotational degrees of freedom*. FEM Consulting s.r.o, Brno, Czech Republic.

Shakouri, A., Ng, T. Y., and Lin, R. M. A new rebo potential based atomistic structural model for graphene sheets. *Nanotechnology*, 22:295711, 2011.

Shi, X. P., Fwa, T. F., and Tan, S. A. Warping stresses in concrete pavements on Pasternak foundation. *Journal of Transportation Engineering*, 119(6):905–913, 1993.

Shi, X. P., Tan, S. A., and Fwa, T. F. Rectangular thick plate with free edges on Pasternak foundation. *Journal of Engineering Mechanics*, 120(5):971–988, 1994.

Shi, X. P., Fwa, T. F., Hu, Y., and Zhang, J. Thick-plate model for warping stresses in concrete pavements. *International Journal of Pavement Engineering*, 1(2):107–117, 2000.

Simeonov, P. and Ahmad, S. Effect of transition zone on the elastic behavior of cement-based composites. *Cement and Concrete Research*, 25(1):165–176, 1995.

Singh, S. and Patel, B. P. Nonlinear elastic properties of graphene sheet under finite deformation. *Composite Structures*, 119:412–421, 2015.

Slater, J. C. and Koster, G. F. Simplified LCAO method for the periodic potential problem. *Physical Review*, 94:1498–1524, 1954.

Stenzel, G. Beton-Bodenplatten für Hallen- und Freiflächen: Konstruktion und Bemessung [Concrete base plates for indoor and outdoor applications: layout and design]. *Beton- und Stahlbetonbau, Ernst & Sohn, Berlin, München, Düsseldorf*, 100(4):277–288, 2005. In German.

Straughan, W. T. Analysis of plates on elastic foundation. Phd thesis, Texas Tech University, 1990.

Sumarac, D. and Krasulja, M. Damage of plain concrete due to thermal incompatibility of its phases. *International Journal of Damage Mechanics*, 7(2):129–142, 1998.

Tasneem, K., Kim, S.-H., Kim, J., Nam, B. H., and Park, Y. Effects of aggregate mineralogy on the thermal expansion behavior of concrete. In *Proceedings of the 2nd Transportation and Development Institute Congress*, pages 163–172, Orlando, United States, 2014.

Teller, L. W. and Sutherland, E. C. The structural design of concrete pavements, Part 2: Observation effects of variations in temperature and moisture on the size, shape and stress resistance of concrete pavement slabs. Technical report, Bureau of Public Roads, United States, 1935.

Teller, L. W. and Sutherland, E. C. The structural design of concrete pavements, Part 5: An experimental study of the westergaard analysis of stress conditions in concrete pavement slabs of uniform thickness. Technical report, Public Roads Administration, United States, 1943.

Tersoff, G. New empirical approach for the structure and energy of covalent systems. *Physical Review B*, 37:6991–7000, 1988.

Terzaghi, K. *Theoretical Soil Mechanics*. John Wiley & Sons, Inc, 1943.

Terzaghi, K. *Soil Mechanics in Engineering Practice*. John Wiley & Sons, Inc, 1948.

Thomlinson, J. Temperature variations and consequent stresses produced by daily and seasonal temperature cycles in concrete slabs. *Concrete Constructional Engineering*, 36(6):298–307, 1940.

Timoshenko, S. and Woinowsky-Krieger, S. *Theory of Plates and Shells*. McGraw-Hill, New York, 2nd edition, 1959.

Touratier, M. An efficient standard plate theory. *International Journal of Engineering Science*, 29(8):901–916, 1991.

Truesdell, C. and Noll, W. *The Nonlinear Field Theories of Mechanics, in Handbuch der Physik (Ed. S. Flügge)*, volume III/3. Springer-Verlag, 1965.

Turhan, A. A consistent Vlasov model for analysis of plates on elastic foundation using the Finite Element method. Phd thesis, Texas Tech University, 1992.

Ullrich, M. Abschätzung der Untergrundverhältnisse am Bahnkörper anhand des Bettungsmoduls [Estimation of subsoil atatus at railroads based on the modulus of subgrade reaction]. *Eisenbahntechnische Rundschau*, 5:31–38, 2016. in German.

Ulrik Nilsen, A. and Monteiro, P. J. M. Concrete: A three phase material. *Cement and Concrete Research*, 23(1):147–151, 1993.

Ventsel, E. and Krauthammer, T. *Thin Plates and Shells: Theory, Analysis, and Applications*. Marcel Dekker, Inc, 2001.

Vlasov, V. Z. and Leont'ev, N. N. *Beams, Plates and Shells on Elastic Foundations*. Israel Program for Scientific Translations, Jerusalem, 1966.

von Kármán, T. *Encyklopädie der mathematischen Wissenschaften [Encyclopady of Mathematical Sciences]*, volume IV, chapter Festigkeitsproblem im Maschinenbau, 311-385. Verlag von B. G. Teubner, 1910. in German.

VSC3. Vienna Scientific Cluster (VSC3). *VSC Research Center, TU Wien, Operngasse 11/E057-09, Vienna, Austria*, 2014.

Wang, C. G., Lan, L., Liu, Y. P., Tan, H. F., and He, X. D. Vibration characteristics of wrinkled single-layered graphene sheets. *International Journal of Solids Structures*, 50:1812–823, 2013.

Wang, H., Binder, E., Mang, H. A., Yuan, Y., and Pichler, B. Multiscale structural analysis inspired by exceptional load cases concerning the immersed tunnel of the Hong Kong-Zhuhai-Macao Bridge. *Underground Space*, 3(4):252–267, 2018a.

Wang, H., Hellmich, C., Yuan, Y., Mang, H. A., and Pichler, B. May reversible water uptake/release by hydrates explain the thermal expansion of cement paste? – Arguments from an inverse multiscale analysis. *Cement and Concrete Research*, 113:13–26, 2018b.

Wang, H., Höller, R., Aminbaghai, M., Hellmich, C., Yuan, Y., Mang, H. A., and Pichler, B. L. A. Concrete pavements subjected to hail showers: A semi-analytical thermoelastic multiscale analysis. *Engineering Structures*, 200:109677, 2019a.

Wang, H., Mang, H. A., Yuan, Y., and Pichler, B. Multiscale thermoelastic analysis of the thermal expansion coefficient and of microscopic thermal stresses of mature concrete. *Materials*, 12:2689, 2019b.

Wei, X. and Kysar, J. W. Experimental validation of multiscale modeling of indentation of suspended circular graphene membranes. *International Journal of Solids and Structures*, 49: 3201–3209, 2012.

Wei, Y., Wuu, J., Yin, H., Shi, X., Yang, R., and Dresselhaus, M. The nature of strength enhancement and weakening by pentagon–heptagon defects in graphene. *Nature Materials*, 11: 759–763, 2012.

Wei, Y., Gao, X., Wang, F., and Zhong, Y. Nonlinear strain distribution in a field-instrumented concrete pavement slab in response to environmental effects. *Road Materials and Pavement Design*, pages 1–14, 2017.

Westergaard, H. M. Stresses in concrete pavements computed by theoretical analysis. *Public Roads*, 7:25–35, 1926.

Westergaard, H. M. Analysis of stresses in concrete pavements due to variations of temperature. In *Highway Research Board Proceedings*, volume 6, pages 201–215, 1927.

Westergaard, H. M. Stresses in concrete runways of airports. *Proc. of the 19th Annual Meeting of the Highway Research Board, Washington, D.C.*, 19:197–205, 1939.

Westergaard, H. M. New formulas for stresses in concrete pavements of airfields. *American Society of Civil Engineers Transactions*, 113:425–444, 1948.

William, G. W. and Shoukry, S. N. 3D Finite Element analysis of temperature-induced stresses in dowel jointed concrete pavements. *International Journal of Geomechanics*, 1(3):291–307, 2001.

Winkler, E. *Die Lehre von der Elasticitaet und Festigkeit: mit besonderer Rücksicht auf ihre Anwendung in der Technik [Lessons on elasticity and strength of materials: with special consideration of their application in technology]*. Dominicus, Prague, 1867. In German.

Won, M. Improvements of testing procedures for concrete coefficient of thermal expansion. *Transportation Research Record: Journal of the Transportation Research Board*, 1919:23–28, 2005.

Wyrzykowski, M., McDonald, P. J., Scrivener, K. L., and Lura, P. Water redistribution within the microstructure of cementitious materials due to temperature changes studied with ^{1}H NMR. *The Journal of Physical Chemistry C*, 121(50):27950–27962, 2017.

Xiang-sheng, C. The bending, stability and vibration of rectangular plates with free edges on elastic foundation. *Applied Mathematics and Mechanics*, 9(6):573–578, 1988.

Xiang-sheng, C. A free rectangular plate on elastic foundation. *Applied Mathematics and Mechanics*, 13(10):977–982, 1992.

Xiao, H., Bruhns, O. T., and Meyers, A. Logarithmic strain, logarithmic spin and logarithmic rate. *Acta Mechanica*, 124:89–105, 1997.

Xu, M., Paci, J. T., Oswald, J., and Belytschko, T. A constitutive equation for graphene based on density functional theory. *International Journal of Solids and Structures*, 49:2582–2589, 2012a.

Xu, M., Tabarraei, A., Paci, J. T., Oswald, J., and Belytschko, T. A coupled quantum/continuum mechanics study of graphene fracture. *International Journal of Fracture*, 172:163–173, 2012b.

Yao, S. and Yih, H. A free rectangular plate on the two-parameter elastic foundation. *Applied Mathematics and Mechanics*, 8(4):325–338, 1987.

Zaoui, A. Continuum micromechanics: Survey. *Journal of Engineering Mechanics*, 128(8):808–816, 2002.

Zhang, J., Fwa, T. F., Tan, K. H., and Shi, X. P. Model for nonlinear thermal effect on pavement warping stresses. *Journal of Transportation Engineering*, 129(6):695–702, 2003.

Zhang, J.-L., Vida, C., Yuan, Y., Hellmich, C., Mang, H. A., and Pichler, B. A hybrid analysis method for displacement-monitored segmented circular tunnel rings. *Engineering Structures*, 148:839–856, 2017.

Zheng, Q.-S. Theory of representations for tensor functions. *Applied Mechanics Review*, 47(11): 545–587, 1994.

Zheng, Q.-S. and Boehler, J. P. The description, classification, and reality of material and physical symmetries. *Acta Mechanica*, 102:73–89, 1994.

Zhou, C., Huang, B., and Shu, X. Micromechanical model for predicting coefficient of thermal expansion of concrete. *Journal of Materials in Civil Engineering*, 25(9):1171–1180, 2013.

Zhou, C., Shu, X., and Huang, B. Predicting concrete coefficient of thermal expansion with an improved micromechanical model. *Construction and Building Materials*, 68:10–16, 2014.

Zienkiewicz, O. C. and Taylor, R. L. *The Finite element method.* Butterworth-Heinemann, 5th edition, 2000.

Curriculum Vitae

Dipl.-Ing. Raphael HÖLLER

PERSONAL INFORMATION

Date of birth:	16.03.1991
Place of birth:	Vienna
Nationality:	Austria
Address:	Augasse 9, A-2482 Münchendorf

EDUCATION

March 2017 - June 2020	Doctoral programme in Engineering Science – Civil Engineering Vienna University of Technology
August 2015 - January 2017	Master programme – Civil Engineering Vienna University of Technology Structural Engineering (Diploma eximination passed with distinction)
March 2011 - August 2015	Bachelor programme – Civil Engineering Vienna University of Technology
September 2005 - June 2010	Höhere Technische Lehranstalt Mödling Building Construction (Matura passed with distinction)

WORK EXPERIENCE

March 2017 - June 2020	Institute for Mechanics of Materials and Structures Vienna University of Technology *University Assistant*
February 2012 - February 2017	Civil engineering office DI Gerhard Kidery, Vienna *Structural Engineer*

CONFERENCE PRESENTATIONS

October 19-22, 2019	*Multiaxial Hyperelasticity of Graphene*, 2nd International Conference on Mechanics of Advanced Materials and Structures (ICMAMS), Nanjing, China
October 7-8, 2019	*Rigorous Amendment of Vlasov's Theory for Thin Elastic Plates on Elastic Winkler Foundations, based on the Principle of Virtual Power*, China-Austria Forum for Postgraduates of Civil Engineering, Vienna, Austria
September 18-20, 2019	*Multiaxial Hyperelasticity of Graphene*, Doctoral College – TU-D Retreat, Langenlois, Austria
February 18-22, 2019	*Rigorous Amendment of Vlasov's Theory for Thin Elastic Plates on Elastic Winkler Foundations, based on the Principle of Virtual Power*, 90th Annual Meeting of the International Association of Applied Mathematics and Mechanics (GAMM), Vienna, Austria
September 24-26, 2018	*Continuum Nanomechanics of Suspended Graphene Membranes with Electro-Mechanical Couplings*, Doctoral College – TU-D Retreat, Langenlois, Austria
June 17-20, 2018	*Rigorous Amendment of Vlasov's Theory for Thin Elastic Plates on Elastic Winkler Foundations*, 1st International Conference on Mechanics of Advanced Materials and Structures (ICMAMS), Turin, Italy
September 25-27, 2017	*Continuum Nanomechanics of Suspended Graphene Membranes*, Doctoral College – TU-D Retreat, Langenlois, Austria